

UNIVERSITAT POLITÈCNICA DE VALÈNCIA
DEPARTAMENTO DE MÁQUINAS Y MOTORES TÉRMICOS



DOCTORAL THESIS

COMPUTATIONAL STUDY ON THE NON-REACTING FLOW
IN LEAN DIRECT INJECTION GAS TURBINE COMBUSTORS
THROUGH EULERIAN-LAGRANGIAN LARGE-EDDY
SIMULATIONS

Presented by:

Mr. Mario Belmar Gil

Supervised by:

Dr. Marcos Carreres Talens

*in fulfillment of the requirements for the degree of
Doctor of Philosophy*

Valencia, November 2020

Ph.D. Thesis

COMPUTATIONAL STUDY ON THE NON-REACTING FLOW
IN LEAN DIRECT INJECTION GAS TURBINE COMBUSTORS
THROUGH EULERIAN-LAGRANGIAN LARGE-EDDY
SIMULATIONS

Written by: Mr. Mario Belmar Gil
Supervised by: Dr. Marcos Carreres Talens

Thesis committee:

Chairman: Prof. Antonio Torregrosa Huguet
Secretary: Dr. Daniel Mira Martínez
Member: Dr. Peter Kelly Senecal

Thesis committee substitutes:

Chairman: Prof. José María Desantes Fernández
Secretary: Prof. Jacobo Porteiro Fresco
Member: Dr. Jorge Martínez López

Valencia, November 2020

Abstract

Aeronautical gas turbine engines present the main challenge of increasing the efficiency of the cycle while keeping the pollutant emissions below stringent restrictions. This has led to the design of new injection-combustion strategies working on more risky and problematic operating points such as those close to the lean extinction limit. In this context, the Lean Direct Injection (LDI) concept has emerged as a promising technology to reduce oxides of nitrogen (NO_x) for next-generation aircraft power plants.

In LDI combustors, a highly swirling air is admitted into the combustor where the liquid fuel is directly injected at a lean equivalence ratio close to the lean blow-out limit. The turbulent swirling flow promotes both the atomisation of the injected liquid sheet and the mixing of the atomised sprays and generates a high-turbulent recirculation region downstream of the injection system that considerably increases the flame stability limits. Therefore, an accurate characterisation of the degree of atomisation of the liquid spray fuel, the turbulent dispersion and evaporation of liquid drops and the fuel-air mixing quality is deemed to be essential since these phenomena strongly influence the subsequent combustion performance and pollutant emissions.

In this scenario, Computational Fluid Dynamics (CFD) methods have become an essential component in the design process of gas turbine combustion systems due to its suitability to optimise key performance indicators through fast and cheap parametric studies. Specifically, Large Eddy Simulations (LES) are considered to be the next-generation numerical design tool for predicting and investigating the generation and evolution of coherent flow structures in swirl-stabilised gas turbine combustors both in reacting and non-reacting conditions. The characterisation of the non-reacting flow is a crucial step in LDI combustor research since the success or failure of ignition (and re-ignition at high-altitude) is governed by the local conditions just before ignition, especially on the mixture quality and the turbulence level at the near-injection region.

In this context, this thesis aims at contributing to the knowledge of the governing physical mechanisms within an LDI burner and to provide analysis tools for a deep characterisation of such complex flows. In order to do so, a numerical CFD methodology capable of reliably modelling the 2-phase non-reacting flow in an academic LDI burner has been developed in an Eulerian-Lagrangian framework, using the U-RANS and LES turbulence approaches. The LDI combustor taken as a reference to carry out the investigation is the laboratory-scale swirled-stabilised CORIA Spray Burner. The multi-scale problem is addressed by solving the complete inlet flow path through the swirl

vanes and the combustor through two different CFD codes involving two different meshing strategies: an automatic mesh generation with adaptive mesh refinement (AMR) algorithm through CONVERGE™ and a more traditional static meshing technique in OpenFOAM®.

On the one hand, a methodology to obtain an optimal mesh strategy using AMR has been defined, and its benefits against traditional fixed mesh approaches have been exploited. In this way, the applicability of grid control tools available in CONVERGE™ such as fixed embedding and AMR has been demonstrated to be an interesting option to face this type of multi-scale problem. The results highlight an optimisation of the use of the computational resources and better accuracy in the simulations carried out with the presented methodology.

On the other hand, the use of CFD tools has been combined with the application of systematic advanced modal decomposition techniques (i.e., Proper Orthogonal Decomposition and Dynamic Mode Decomposition). The numerical identification of the main acoustic modes in the chamber have proved their potential when studying the characteristics of the most powerful coherent flow structures of strongly swirled jets in a LDI burner undergoing vortex breakdown (VBB). Besides, the implementation of these mathematical procedures has allowed both retrieving information about the flow dynamics features and providing a systematic approach to identify the main mechanisms that sustain instabilities in the combustor. Last, this analysis has also allowed identifying some key features of swirl spray systems such as the complex pulsating, intermittent and cyclical spatial patterns related to the Precessing Vortex Core (PVC).

Finally, the validated methodology is exploited through a Design of Experiments (DoE) to quantify the influence of critical design factors on the non-reacting flow. In this way, the individual contribution of some functional parameters (namely the number of swirler vanes, the swirler vane angle, the combustion chamber width and the axial position of the nozzle tip) into both the flow field pattern, the spray size distribution and the occurrence of instabilities in the combustion chamber are evaluated throughout a Taguchi's orthogonal array L9. Such a statistical study has supposed a good starting point for subsequent studies of injection, atomisation and combustion on LDI burners.

Resumen

El principal desafío en los motores turbina de gas empleados en aviación reside en aumentar la eficiencia del ciclo termodinámico manteniendo las emisiones contaminantes por debajo de las rigurosas restricciones. Ésto ha conll-evado la necesidad de diseñar nuevas estrategias de inyección/combustión que operan en puntos de operación peligrosos por su cercanía al limite inferior de apagado de llama. En este contexto, el concepto Lean Direct Injection (LDI) ha emergido como una tecnología prometedora a la hora de reducir los óxidos de nitrógeno (NO_x) emitidos por las plantas propulsoras de los aviones de nueva generación.

En los quemadores de flujo continuo LDI, el combustible líquido se inyecta en unas proporciones de mezcla pobre directamente en la cámara de combustión, donde se encuentra un flujo de aire coaxial altamente torbellinado. Este flujo altamente turbulento promueve tanto la atomización de la película de combustible líquida como el mezclado del spray atomizado con el aire, a la vez que genera una zona de recirculación inmediatamente aguas abajo del sistema de inyección que incrementa de manera considerable el límite de estabilidad de la llama. Por tanto, se requiere de una caracterización precisa del grado de atomización del combustible líquido, la dispersión turbulenta y evaporación de las gotas de combustible y la calidad de la mezcla aire-combustible, ya que estos fenómenos influyen fuertemente en el rendimiento de la combustión y las emisiones contaminantes posteriores.

En este escenario, los métodos basados en la de Dinámica de Fluidos Computacional (CFD) se han convertido en un componente esencial en el proceso de diseño de sistemas de combustión de turbinas de gas por su idoneidad para optimizar indicadores clave de desempeño a través de estudios paramétricos rápidos y relativamente poco costosos. Concretamente, las simulaciones basadas en tratamientos de turbulencia LES se consideran la herramienta de diseño numérico de la siguiente generación para predecir e investigar la generación y evolución de estructuras de flujo coherentes en cámaras de combustión de turbinas de gas, tanto en condiciones reactivas como no reactivas. La caracterización del flujo inerte es un primer paso crucial en la investigación de quemadores LDI, ya que el éxito o el fracaso de la ignición (y la re-ignición a gran altitud) viene determinado por las condiciones locales presentes momentos antes de la ignición, especialmente por la calidad de la mezcla y el nivel de turbulencia en la región cercana a la inyección.

En este contexto, la presente tesis tiene como objetivos contribuir al conocimiento de los mecanismos físicos que rigen el comportamiento de un quemador LDI y proporcionar herramientas de análisis para una profunda

caracterización de las complejas estructuras de flujo de turbulento generadas en el interior de la cámara de combustión. Para ello, se ha desarrollado una metodología numérica basada en CFD capaz de modelar el flujo bifásico no reactivo en el interior de un quemador LDI académico mediante enfoques de turbulencia U-RANS y LES en un marco Euleriano-Lagrangiano. El quemador LDI tomado como referencia para llevar a cabo la investigación es el quemador académico CORIA Spray Burner. La resolución numérica de este problema multiescala se aborda mediante la descripción completa del flujo a lo largo de todos los elementos que constituyen la maqueta experimental, incluyendo su paso por el swirler y entrada a la cámara de combustión. Ésto se lleva a cabo través de dos códigos CFD que involucran dos estrategias de mallado diferentes: una basada en algoritmos de generación y refinamiento automático de la malla (AMR) a través de CONVERGE™ y otra técnica de mallado estático más tradicional mediante OpenFOAM®.

Por un lado, se ha definido una metodología para obtener una estrategia de mallado óptima mediante el uso del AMR y se han explotado sus beneficios frente a los enfoques tradicionales de malla estática. De esta forma, se ha demostrado que la aplicabilidad de las herramientas de control de malla disponibles en CONVERGE™ como el refinamiento fijo (fixed embedding) y el AMR son una opción muy interesante para afrontar este tipo de problemas multiescala. Los resultados destacan una optimización del uso de los recursos computacionales y una mayor precisión en las simulaciones realizadas con la metodología presentada.

Por otro lado, el uso de herramientas CFD se ha combinado con la aplicación de técnicas de descomposición modal avanzadas (Proper Orthogonal Decomposition and Dynamic Mode Decomposition). La identificación numérica de los principales modos acústicos en la cámara de combustión ha demostrado el potencial de estas herramientas al permitir caracterizar las estructuras de flujo coherentes generadas como consecuencia de la rotura de los vórtices (VBB) y de los chorros fuertemente torbellinados presentes en el quemador LDI. Además, la implementación de estos procedimientos matemáticos ha permitido tanto recuperar información sobre las características de la dinámica de flujo como proporcionar un enfoque sistemático para identificar los principales mecanismos que sustentan las inestabilidades en la cámara de combustión. Por último, este análisis también ha permitido identificar algunas características clave en sistemas con presencia de flujo altamente torbellinado, así como revelar los patrones pulsantes, intermitentes y cíclicos relacionados con el Precessing Vortex Core (PVC).

Finalmente, la metodología validada ha sido explotada a través de un

Diseño de Experimentos (DoE) para cuantificar la influencia de los factores críticos de diseño en el flujo no reactivo. De esta manera, se ha evaluado la contribución individual de algunos parámetros funcionales (el número de palas del swirler, el ángulo de dichas palas, el ancho de la cámara de combustión y la posición axial del orificio del inyector) en los patrones del campo fluido, la distribución del tamaño de gotas del combustible líquido y la aparición de inestabilidades en la cámara de combustión a través de una matriz ortogonal L9 de Taguchi. Este estudio estadístico supone un punto de partida para posteriores estudios de inyección, atomización y combustión en quemadores LDI.

Resum

El principal desafiament als motors turbina de gas utilitzats a la aviació resideix en augmentar l'eficiència del cicle termodinàmic mantenint les emissions contaminants per davall de les rigoroses restriccions. Aquest fet comporta la necessitat de dissenyar noves estratègies d'injecció/combustió que radiquen en punts d'operació perillosos per la seva aproximació al límit inferior d'apagat de flama. En aquest context, el concepte Lean Direct Injection (LDI) sorgeix com a eina innovadora a l'hora de reduir els òxids de nitrogen (NO_x) emesos per les plantes propulsores dels avions de nova generació.

En els cremadors LDI, el combustible líquid s'injecta en unes proporcions de mescla pobre directament en la càmera de combustió, on es troba un flux d'aire coaxial arremolinat. Aquest flux altament turbulent promou l'atomització de la pel·lícula de combustible líquid i el mesclat l'esprai amb el aire. Al mateix temps també genera una zona de recirculació immediatament aigües avall del sistema d'injecció que incrementa de forma considerable el límit d'estabilitat de la flama. Per tant, es requereix d'una caracterització precisa del grau d'atomització del combustible líquid, de la dispersió turbulenta, de l'evaporació de les gotes de combustible i de la qualitat de la mescla aire-combustible, ja que estos fenòmens influeixen notòriament en el rendiment de la combustió i les posteriors emissions contaminants.

En aquest escenari, els mètodes de Dinàmica de Fluids Computacional (CFD) s'han convertit en un component essencial del procés de disseny de sistemes de combustió de turbines de gas, ja que són idonis al optimitzar indicadors clau de l'acompliment mitjançant estudis paramètrics ràpids i relativament poc costosos. Concretament, les simulacions basades en un tractament de turbulència LES es consideren la ferramenta de disseny numèric de la següent generació per tal de predir i investigar la generació i evolució d'estructures de flux coherents en càmeres de combustió de turbines de gas, tant en condicions reactives com no reactives. La caracterització del flux inert és un primer pas en la investigació de cremadors LDI, ja que l'èxit o el fracàs de la ignició (i la re-ignició a gran altitud), ve determinat per les condicions locals presents moments abans, principalment per la qualitat de la mescla i el nivell de turbulència en la regió propera a la injecció.

Sota aquest context, aquesta tesis té com a objectius contribuir al coneixement dels mecanismes físics que regeixen el comportament d'un cremador LDI i proporcionar ferramentes d'anàlisi per a una profunda caracterització de les complexes estructures de flux turbulent generades a l'interior de la càmera de combustió. Per tal de dur-ho a terme s'ha desenvolupat una metodologia numèrica basada en CFD capaç de modelar el flux bifàsic no reactiu a

l'interior d'un cremador LDI acadèmic mitjançant els enfocaments de turbulència U-RANS i LES en un marc Eulerià-Lagrangià. El cremador LDI pres com a referència per a fer la investigació, é el cremador acadèmic CORIA Spray Burner. La resolució numèrica d'aquest problema multiescala s'aborda mitjançant la resolució completa del flux al llarg de tots els elements que constitueixen la maqueta experimental, incloent el seu pas pel swirler i l'entrada a la càmera de combustió. Açò es duu a terme a través de dos codis CFD que involucren estratègies de mallat diferents: una basada en la generació automàtica de la malla i en l'algoritme de refinament adaptatiu (AMR) amb CONVERGE™ i l'altra que es basa en una tècnica de mallat estàtic més tradicional amb OpenFOAM®.

D'una banda, s'ha definit una metodologia per tal d'obtindre una estratègia de mallat òptima mitjançant l'ús de l'AMR i s'han explotat els seus beneficis front als enfocaments tradicionals de malla estàtica. D'aquesta forma, s'ha demostrat que l'aplicabilitat de les ferramentes de control de malla disponibles en CONVERGE™ com el refinament fixe (fixed embedding) i l'AMR són una opció molt interessant per tal d'afrontar aquest tipus de problemes multiescala. Els resultats destaquen una optimització de l'ús dels recursos computacionals i una major precisió en les simulacions realitzades amb la metodologia presentada.

D'altra banda, l'ús d'eines CFD s'ha combinat amb l'aplicació de tècniques de descomposició modal avançades (Proper Orthogonal Decomposition and Dynamic Mode Decomposition). La identificació numèrica dels principals modes acústics a la càmera de combustió ha demostrat el potencial d'aquestes ferramentes al permetre caracteritzar les estructures de flux coherents generades com a conseqüència del trencament dels vòrtex (VBB) i dels raigs fortament arremolinats presents al cremador LDI. A més, la implantació d'estos procediments matemàtics ha permès recuperar informació sobre les característiques de la dinàmica del flux i proporcionar un enfocament sistemàtic per tal d'identificar els principals mecanismes que sustenten les inestabilitats a la càmera de combustió. Per últim, aquest anàlisi també ha possibilitat identificar algunes característiques clau en sistemes amb presència de flux altament arremolinat, així com revelar els patrons polsants, intermitents i cíclics relacionats amb el Precessing Vortex Core (PVC).

Finalment, la metodologia validada ha sigut explotada a través d'un Disseny d'Experiments (DoE) per tal de quantificar la influència dels factors crítics de disseny en el flux no reactiu. D'aquesta manera, s'ha avaluat la contribució individual d'alguns paràmetres funcionals (el nombre de pales del swirler, l'angle de les pales, l'amplada de la càmera de combustió i la posició axial de

l'orifici de l'injector) en els patrons del camp fluid, la distribució de la mida de gotes del combustible líquid i l'aparició d'inestabilitats en la càmera de combustió mitjançant una matriu ortogonal L9 de Taguchi. Aquest estudi estadístic és un bon punt de partida per a futurs estudis de injecció, atomització i combustió en cremadors LDI.

“The writer Umberto Eco belongs to that small class of scholars who are encyclopedic, insightful, and non-dull. He is the owner of a large personal library (containing thirty thousand books), and separates visitors into two categories: those who react with “Wow! Signore, professore dottore Eco, what a library you have! How many of these books have you read?” and the others -a very small minority- who get the point that a private library is not an ego-boosting appendage but a research tool. Read books are far less valuable than unread ones. The library should contain as much of what you don’t know as your financial means, mortgage rates and the currently tight real-estate market allows you to put there. You will accumulate more knowledge and more books as you grow older, and the growing number of unread books on the shelves will look at you menacingly. Indeed, the more you know, the larger the rows of unread books. Let us call this collection of unread books an anti-library.”

—Nassim N. Taleb, *The Black Swan*

A mi abuelo

Me gustaría aprovechar esta oportunidad para agradecer a todas aquellas personas que de un modo u otro han contribuido a la consecución de este trabajo. Se cierra un ciclo de 10 años en la UPV y si tuviese que escoger una única cosa con la que quedarme, sería sin lugar a dudas la calidad (y cantidad) de las relaciones forjadas con tantas personas excepcionales con las que he tenido la suerte de coincidir.

En primer lugar, quisiera agradecer y expresar mi más sincera admiración por mi tutor y director, Marcos Carreres. Su absoluta implicación unida a sus valores sobre la manera de trabajar, razonar y cuidar los detalles en busca de la excelencia han supuesto una referencia y fuente de inspiración constante para lograr sacar mi máximo potencial. No exagero al asegurar que todas las charlas, debates y consejos recibidos por su parte (tanto en el ámbito profesional como en el personal) me han ayudado a crecer y a convertirme en una mejor persona. Me siento realmente afortunado y agradecido de haber podido compartir contigo tantas cosas durante estos 4 años, amigo.

Asimismo, debo expresar mi gratitud al Instituto CMT-Motores Térmicos, y en especial al Profesor Francisco Payri y Profesor José María Desantes por darme la oportunidad de trabajar en el desarrollo de una nueva línea de investigación en este reconocido y prestigioso centro de investigación.

En este sentido, también debo mencionar aquí a las personas que me acogieron y ayudaron a desarrollar la estancia (aunque de manera virtual) en su centro de investigación (CORIA): F.X. Demoulin y Diego Farrando.

De igual manera, me siento en deuda con todos mis compañeros del equipo de inyección, liderado de manera ejemplar por Raul Payri. Gracias a los profesores que han colaborado y aportado en algún momento su granito de arena a esta Tesis: Javi, Jaime, Pedro, Gabriela y Joaquín. Gracias a los doctorandos del grupo que se han terminado convirtiendo en amigos, con especial cariño a Abian y Armando, con los que he podido compartir de manera íntegra toda esta "aventura". Gracias a Dani, Sebas, Jesús, Mary, Santi, Alberto, Vincenzo, Tomás, Kike, María, César, Rami, Victor y Javi. Y por supuesto, gracias a mis compañeros de despacho por aguantarme días tras día: David Jaramillo, Marco (mil gracias por toda la ayuda que me ofreciste, especialmente en mi primer año) y Lucas (infinitas nuestras tardes de risas/confesiones tan necesarias). Mención importante merecen también José Enrique y Omar, siempre dispuestos a echar una mano con los montajes y ensayos experimentales. No quisiera olvidarme tampoco del personal de secretaría y su ayuda a la hora de simplificar la burocracia (gracias Amparo), y del personal de limpieza (Toñi).

Me siento en la obligación de remarcar que el alcance de esta Tesis no habría sido el mismo de no ser por la ayuda directa de un conjunto de personas.

En primer lugar, aquellos proyectandos que he tenido la suerte de dirigir y que con su trabajo y dedicación han ido impulsando el avance de la investigación: Agustín, Carlos, Mael, Dorian, Alicia y David. Igual de importante ha sido la ayuda recibida de algunos compañeros de la línea de combustión, sin los cuales el proyecto no habría arrancado tan bien orientado: Ricardo, José Manuel e Iván, muchísimas gracias por vuestro trabajo y consejos. Por último, agradecer la enorme y encomiable ayuda de Jorge, permitiendo extender el alcance de los resultados y dotar de mayor rigor científico esta Tesis.

Tampoco puedo dejar de mencionar a mis amigos de la carrera por su apoyo constante y por tan buenas experiencias compartidas: Lledó, Juanpa, Coy, Julián y Feng. Algunos de ellos también he tenido la suerte de tenerlos cerca durante esta última etapa: Abian (nuevamente), Guille, Natalia y María. Además, quiero reconocer la importancia de los equipos de fútbol de la UPV y de la liga de Quart de Poblet, tan necesarios tanto para desconectar como para vivir y celebrar grandes triunfos.

Por supuesto, no me puedo olvidar de mis amigos del “grupo del 92” de Malilla. Me siento especialmente afortunado de haber podido disfrutar de tantas experiencias con vosotros, e ilusionado de las que todavía están por venir: Tarek (gracias por el apoyo absoluto e incondicional durante tantos años, debes sentirte parte fundamental de este logro), Guillem, Borja, Campi y Olmeda. Además, debo destacar las grandes charlas con Quique, cuya capacidad de sacrificio e instinto de superación y mejora diaria ha supuesto una inspiración en muchos momentos.

De manera especial debo agradecer a mi familia por la gran educación y apoyo recibidos. Gracias a mis padres y hermano por habérmelo dado absolutamente todo y haber hecho más llevadera esta etapa (y todas las anteriores). Siento que he jugado con mucha ventaja por todas las facilidades que me habeis puesto y quiero que os sintais totalmente participes de esta Tesis, ya que es el fiel reflejo de todo lo que he recibido de vosotros. Además, quiero reconocer la gran labor que mi tío Antonio José y mi tía Ana han tenido en mi desarrollo.

Y por supuesto, mención especial para mi abuelo. Dudo haber escogido este camino de no ser por todos los ratos que pasabas conmigo de pequeño enseñándome matemáticas y ciencia del espacio con tan solo 5 años. Desde luego, esos aprendizajes despertaron algo dentro de mí y desde entonces han marcado mi camino. Es algo que siempre recordaré con cariño. Esta Tesis va por ti.

Y por último, no puedo terminar esta sección de otra manera más que agradeciendo a la persona que más me ha apoyado y que más ha tenido que aguantar todo lo que esta difícil etapa conlleva: Raquel, tu frescura y apoyo

incesante han sido indispensables para mí, y me resulta imposible explicar y agradecer con palabras la importancia que has tenido en la consecución de este logro. Tu manera de ver la vida, de ilusionarte y de ser feliz dándole valor a los pequeños detalles que muchas veces pasamos por alto pero que todos tenemos a nuestro alcance debería estudiarse en las escuelas. Estoy seguro de que de esta manera el mundo sería un lugar mucho mejor. Gracias por enseñarme tanto.

Contents

Contents	i
List of Figures	v
List of Tables	xi
Nomenclature	xiii
1 Introduction	1
1.1 General context	1
1.2 Objectives and methodology	7
1.3 Thesis outline	10
References	11
2 Fundamentals of the LDI system	17
2.1 Introduction	17
2.2 Lean Direct Injection system	19
2.2.1 General Features of Swirling Flows	19
2.2.1.1 Swirling Flow Structures	21
2.2.2 Injection Systems in Gas Turbine Combustors	23
2.3 Governing Equations	26
2.3.1 Two-Phase Spray Characteristics	26
2.3.2 Gas-Phase Equations	28
2.3.3 Discrete-Phase Equations	31
2.4 Spray Formation	32
2.4.1 Spray Sub-processes	33
2.4.1.1 Atomisation Process	33

2.4.1.2	Drop Drag and Deformation	39
2.4.1.3	Drop-Turbulence Interactions	40
2.4.1.4	Drop Collision and Coalescence	41
2.4.1.5	Evaporation Process	44
2.4.2	Spray Characterisation	46
2.4.2.1	Drop size	46
2.4.2.2	Drop Size Distribution	48
2.4.2.3	Spray Penetration	49
2.4.2.4	Spray Cone Angle	49
	References	51
3	Literature Review	59
3.1	Introduction	59
3.2	Experimental Studies on LDI Burners	60
3.3	Computational Studies on LDI Burners	71
3.4	Studies based on Advanced Spectral Analysis	83
	References	84
4	Computational Methodology	105
4.1	Introduction	105
4.2	CFD Modeling	106
4.2.1	Navier-Stokes Equations	107
4.2.2	Turbulence Modeling	108
4.2.2.1	Unsteady Reynolds-Averaged Navier-Stokes (U-RANS)	111
4.2.2.2	Large Eddy Simulations (LES)	114
4.2.3	Spray Modelling	115
4.2.3.1	The Euler-Lagrange Approach	116
4.2.3.2	Atomisation and Drop Breakup Modelling	118
4.2.3.3	Turbulent Dispersion Modelling of Spray Drops	126
4.2.3.4	Drop Collision and Coalescence Modelling	128
4.2.3.5	Drop Evaporation Modelling	131
4.2.4	Numerical Methods	133
4.3	Pre-processing	135
4.3.1	Computational Domain and Boundary Conditions	136
4.3.1.1	Gaseous-fueled case	136
4.3.1.2	Liquid-fueled case	138
4.3.2	Computational Grid	140
4.3.2.1	CONVERGE™ Mesh	140
4.3.2.2	OpenFOAM© Mesh	142

4.3.3	Numerical Algorithms and Discretisation Schemes . . .	144
4.3.3.1	Numerical Setup in CONVERGE™	144
4.3.3.2	Numerical Setup in OpenFOAM©	146
4.4	Post-processing	147
4.4.1	Algorithms for Gaseous and Liquid Phase Characterisation	147
4.4.1.1	Definition of a Quality Parameter	147
4.4.1.2	Algorithm for liquid-phase post-processing . .	150
4.4.2	Modal Decomposition Techniques	152
4.4.2.1	Proper Orthogonal Decomposition (POD) . . .	155
4.4.2.2	Dynamic Mode Decomposition (DMD)	157
4.4.2.3	Spectral Analysis Procedure	159
	References	159
5	Computational Model Validation	167
5.1	Introduction	167
5.2	Gaseous-Fueled Reference Case	168
5.2.1	Evaluation of the mesh and turbulence models influence	168
5.2.1.1	Mesh sensitivity study for OpenFOAM simulations	168
5.2.1.2	Mesh parametric study for CONVERGE simulations	171
5.2.2	LES Quality Assessment	182
5.2.3	Numerical results: Validation and discussion	184
5.2.3.1	Flow Characterisation	184
5.2.3.2	Mean Features	191
5.3	Liquid-Fueled Reference Case	198
5.3.1	Flow Characterisation	198
5.3.2	Mean Features	201
5.3.2.1	Carrier Phase	201
5.3.2.2	Dispersed Phase	204
5.4	Conclusions	213
	References	215
6	Spectral Analysis	219
6.1	Introduction	219
6.2	Gaseous-fueled Case	220
6.2.1	Fast Fourier Transform (FFT) Analysis	220
6.2.2	Proper Orthogonal Decomposition (POD) Analysis . . .	223
6.2.3	Dynamic Mode Decomposition (DMD) Analysis	228

6.3	Liquid-fueled Case	231
6.3.1	Proper Orthogonal Decomposition (POD) Analysis . . .	232
6.3.2	Dynamic Mode Decomposition (DMD) Analysis	235
6.4	Conclusions	239
	References	241
7	Analysis of the influence of the combustor geometrical features on the non-reacting flow	245
7.1	Introduction	245
7.2	Design of Experiments (DoE)	246
7.3	Statistical Analysis of Variance (ANOVA)	249
7.3.1	Definition of the response variables	249
7.3.2	Statistical Analysis (linear)	251
7.3.3	Discussion about non-linearity on the response variables	266
7.3.4	Multiple Response Optimisation	269
7.4	Spectral Analysis	270
7.5	Conclusions	277
	References	279
8	Conclusions and Future Works	281
8.1	Conclusions	281
8.2	Future works	288
A	Full set of results for the L9 orthogonal array parametric study on the geometrical features	293
	Global Bibliography	301

List of Figures

1.1	Left: Schematic of an RQL combustor. Right: NO_x trends related to equivalence ratio, defined as the ratio of the actual fuel/air ratio to the stoichiometric fuel/air ratio.	3
1.2	Left: Schematic of a radial-staged Dual Annular Combustor (DAC). Right: Schematic of a Twin Annular Premixing Swirler (TAPS) combustor.	3
2.1	Diagram showing the phenomena and interactions occurring in a Lean Direct Injection system.	18
2.2	Typical swirler assemblies used in GT combustors.	20
2.3	Characteristic flow features present in a swirl injection system.	24
2.4	Schematic for (a) pressure atomisers and (b) twin-fluid atomisers.	26
2.5	Schematic representation of spray regimes for liquid injection from a single hole nozzle.	27
2.6	Picture showing the three primary atomisation regimes: rim (left), wavy (center) and perforated-sheet (right) modes.	35
2.7	Scheme of secondary atomisation regimes.	37
2.8	Effect of Stokes number on particle dispersion in large-scale turbulent structures.	41
2.9	Schematic of a binary collision of two moving drops.	42
2.10	Analytical regions for binary drop collisions.	44
3.1	Comparison of the NO_x emission levels between: LDI and RQL schemes (left); LDI and LPP schemes (right).	61
3.2	Multi-Point LDI module with 25 fuel injectors and air swirlers.	64
3.3	Schematic drawing of the PRECCISNTA LDI burner.	66
3.4	Schematic drawing of the MERCATO test rig.	67

3.5	PVC structure identified at the MERCATO test rig through an iso-surface of Q-criterion at different times.	74
3.6	Left: Global view of the VESTA combustor. Right: Ignition sequence revealed through the evolution of the flame front.	75
3.7	3D flame view of the shape flame through an iso-surface of a progress variable in a 2634-million cells DNS on the PRECCIN-STA Burner.	77
3.8	Spray ignition sequence predicted by LES within the CORIA Spray Burner	78
4.1	Time evolution of a given local variable computed through RANS, LES and DNS turbulence approaches.	109
4.2	Energy spectrum of turbulent flow as a function of the wave numbers for RANS, LES and DNS turbulence approaches.	110
4.3	Schematic representation of the DPM coupling between continuous and discrete phases.	117
4.4	Relation between liquid sheet thickness t_s and half spray cone angle θ in pressure swirl atomisers.	120
4.5	Conceptual representation of the liquid sheet flow at the exit of a hollow cone pressure swirl atomiser.	122
4.6	Sample three-cell of a one-dimensional spatial domain	134
4.7	Numerical procedure to solve the discretised transport equations.	136
4.8	Overview of the CORIA single burner computational domain.	137
4.9	Sketch of the swirl-injection system showing both gaseous premixed (left) and non-premixed (right) injection strategies.	138
4.10	Sketch of the swirl-injection system showing the liquid spray injection strategy.	139
4.11	Computational mesh illustrating the strategy considered in CONVERGE™.	142
4.12	Computational mesh illustrating the strategy considered in OpenFOAM®.	143
4.13	Overview of the measurement transverse cross-section where experimental data are available for comparison with CFD simulations	149
4.14	Diagram of the algorithm implemented in Python to post-process the liquid-phase statistics.	152
4.15	Parcel detection plane in cylindrical coordinates.	152
5.1	Mesh Sensitivity Study for RANS, U-RANS and LES OpenFOAM® simulations.	170
5.2	Influence of the grid control tools on the <i>NMSE-Centerline</i> value.	173

5.3	Influence of the U-RANS turbulence models on the <i>NMSE-Centerline</i> , <i>NMSE-Mean-Stations</i> and <i>NMSE-RMS-Stations</i> values.	178
5.4	Influence of the SGS LES turbulence models on the <i>NMSE-Centerline</i> , <i>NMSE-Mean-Stations</i> and <i>NMSE-RMS-Stations</i> values.	180
5.5	Assessment of the LES quality through two different criteria. . . .	183
5.6	Mean (time-averaged) axial velocity field in a mid x-plane and streamlines patterns showing the characteristic flow pattern at 200 ms.	185
5.7	Vortex Breakdown Bubble identified using an iso-surface of zero mean streamwise velocity at 200 ms.	186
5.8	Contours of instantaneous (left) and time-averaged (right) axial velocity, and time-averaged tangential velocity at 200 ms.	187
5.9	Instantaneous visualization of the Precessing Vortex Core identified through a pressure iso-surface of the instantaneous pressure $\bar{p} = 101.1$ kPa at 200 ms.	188
5.10	Time evolution of the PVC in one cycle of the precession motion. PVC is identified using an iso-surface of the instantaneous pressure $\bar{p} = 101.1$ kPa.	189
5.11	Left: Instantaneous iso- Q criterion ($Q = 10^7$) in the swirler and the combustor at 200 ms. Right: Instantaneous iso-surface of the tangential vorticity component (15000 s^{-1}) through the combustion chamber at 200 ms.	190
5.12	Snapshot of the vorticity magnitude field in a central x -cut plane at 200 ms.	191
5.13	Mean (time-averaged) and RMS velocity components in a central x -cut plane through the combustion chamber of the Dynamic Smagorinsky LES with CONVERGE TM	193
5.14	Mean and RMS Axial Velocity profiles obtained in U-RANS and LES simulations with CONVERGE TM (CG) and OpenFOAM [©] (OF) at 5 axial locations.	194
5.15	Mean and RMS Radial Velocity profiles obtained in U-RANS and LES simulations with CONVERGE TM (CG) and OpenFOAM [©] (OF) at 5 axial locations.	195
5.16	Mean and RMS Tangential Velocity profiles obtained in U-RANS and LES simulations with CONVERGE TM (CG) and OpenFOAM [©] (OF) at 5 axial locations.	196
5.17	Mean Axial Velocity Profile along with the central axis of the burner.	197
5.18	Left: Mean (time-averaged) axial velocity field in a central x -cut plane. Right: Instantaneous visualization of the PVC and VBB structures at 200 ms.	199

5.19	Representation of the instantaneous parcels at two instants for LISA and TAB simulations in CONVERGE TM	200
5.20	Gaseous Mean and RMS Axial Velocity profiles obtained in TAB cases with CONVERGE TM (CG) and OpenFOAM [®] (OF) at 4 axial locations.	202
5.21	Gaseous Mean and RMS Tangential Velocity profiles obtained in TAB cases with CONVERGE TM (CG) and OpenFOAM [®] (OF) at 4 axial locations.	203
5.22	Liquid Mean and RMS Axial Velocity profiles obtained in TAB and LISA cases with CONVERGE TM (CG) and TAB case with OpenFOAM [®] (OF) at 3 axial locations.	205
5.23	Liquid Mean and RMS Radial Velocity profiles obtained in TAB and LISA cases with CONVERGE TM (CG) and TAB case with OpenFOAM [®] (OF) at 3 axial locations.	206
5.24	Sauter Mean Diameters (D_{32}) profiles obtained in TAB and LISA cases with CONVERGE TM (CG) and TAB case with OpenFOAM [®] (OF) at 4 axial locations.	207
5.25	Particle size distribution obtained in TAB and LISA cases with CONVERGE TM (CG) and TAB case with OpenFOAM [®] (OF) at 2 spatial locations.	208
5.26	Liquid Mean and RMS Axial Velocity profiles classified by size groups obtained in TAB case with CONVERGE TM (CG) at 4 axial locations.	209
5.27	Liquid Mean and RMS Radial Velocity profiles classified by size groups obtained in TAB case with CONVERGE TM (CG) at 4 axial locations.	210
5.28	Liquid Mean and RMS Tangential Velocity profiles classified by size groups obtained in TAB case with CONVERGE TM (CG) at 4 axial locations.	211
5.29	Liquid-gas mean slip velocity magnitude classified by size groups in TAB case with CONVERGE TM (CG) at 4 axial locations.	212
6.1	Sound Pressure Level (SPL) amplitude of the static pressure signal at eight representative locations and 3D streamlines pattern.	221
6.2	FFT amplitude of the static pressure signal recorded at 1 million random probes within the domain.	222
6.3	Pareto chart showing the singular values associated with POD modes Ψ_2 to Ψ_{208} and the aggregate contribution to the remaining energy after discarding the first mode related to the mean homogeneous pressure.	224

6.4	Power Spectral Density of the time coefficient associated with POD modes $\Psi_2 - \Psi_{17}$ in the frequency domain.	225
6.5	Spatial distribution of POD modes $\Psi_2 - \Psi_{13}$ and $\Psi_{50}, \Psi_{100}, \Psi_{150}$ and Ψ_{200} within the combustor.	226
6.6	Frontal view of the spatial distribution of the first four POD modes $\Psi_2 - \Psi_5$. Both mode pairs describe rotating structures with the same frequency with azimuthal wavenumber $ m = 1$ for modes Ψ_2 and Ψ_3 and with $ m = 2$ for modes Ψ_4 and Ψ_5	227
6.7	Normalised relevance of the spectrum of DMD modes, highlighting the eight most coherent modes at the frequencies of interest.	228
6.8	Spatial distribution of the eight more coherent DMD modes within the combustor.	230
6.9	Frontal view of the spatial distribution of four DMD modes.	230
6.10	Power Spectral Density of the time coefficient associated with POD modes $\Psi_2 - \Psi_{17}$ obtained from the 3-D pressure signal in the frequency domain.	233
6.11	Power Spectral Density of the time coefficient associated with POD modes $\Psi_2 - \Psi_{17}$ obtained from the 3-D mass fuel fraction signal in the frequency domain.	234
6.12	Spatial distribution of the first five pressure (top) and fuel (bottom) POD modes $\Psi_2 - \Psi_6$ within the combustor.	235
6.13	Normalised relevance of the spectrum of DMD modes obtained from the 3D pressure signal.	236
6.14	Normalised relevance of the spectrum of DMD modes obtained from the 3D mass fuel fraction signal.	236
6.15	Spatial distribution of the more coherent pressure (top) and fuel (bottom) DMD modes within the combustor.	237
7.1	Zoom to the swirler system to illustrate the modifications in key features	248
7.2	Definition of the response variables considered to characterise the self-excited structures identified through an iso-surface of zero mean streamwise velocity	250
7.3	Contours of time-averaged axial velocity at 200 ms for the simulations of the L9 array.	252
7.4	Contours of time-averaged tangential velocity at 200 ms for the simulations of the L9 array.	253
7.5	P-values for the defined response variables.	259
7.6	Representation of the spray pattern (instantaneous parcels), fuel reaction rate (dark-coloured) and PVC (red) at 200m for the simulations of the L9 array.	261

7.7	Liquid spray penetration profiles for the simulations of the L9 array.	262
7.8	Evolution of the Swirl Number along the swirler.	265
7.9	Dispersion values of some example response variables as a function of a given design parameter. Blue circles: the values of the response variable for each of the 9 simulations. Red squares: average of the 3 values for each level of the considered geometric factor.	267
7.10	Power Spectral Density and spatial distribution of the time coefficient associated with POD modes $\Psi_2 - \Psi_{17}$ obtained from the 3D pressure signal for the reference case.	271
7.11	Power Spectral Density and spatial distribution of the time coefficient associated with POD modes $\Psi_2 - \Psi_{17}$ obtained from the 3D pressure signal for the simulations of the L9 array.	272
7.12	Dispersion values of the spectral response variables for each design parameter.	276
A.1	Dispersion values of the response variables for each design parameter (1 of 7).	294
A.2	Dispersion values of the response variables for each design parameter (2 of 7).	295
A.3	Dispersion values of the response variables for each design parameter (3 of 7).	296
A.4	Dispersion values of the response variables for each design parameter (4 of 7).	297
A.5	Dispersion values of the response variables for each design parameter (5 of 7).	298
A.6	Dispersion values of the spectral response variables for each design parameter (6 of 7).	299
A.7	Dispersion values of the spectral response variables for each design parameter (7 of 7).	300

List of Tables

2.1	Swirling Flow features in LDI burners.	22
3.1	Experimental works on LDI combustors.	70
3.2	Numerical works on LDI combustors.	82
4.1	Operating and boundary conditions of the gaseous-fueled cases for both premixed and non-premixed injection strategies.	138
4.2	Operating and boundary conditions of the liquid-fueled case.	139
4.3	Numerical setup of the simulations performed in CONVERGE TM and OpenFOAM [®]	145
4.4	Strengths and weaknesses of POD and DMD techniques.	154
5.1	Characteristics of the six meshes proposed to study the non-reactive premixed gaseous-fueled case in OpenFOAM [®]	169
5.2	Parameters considered to assess the influence of the CONVERGE TM grid control tools for Standard k- ϵ U-RANS simulations.	172
5.3	Accuracy and computational requirements concerning the CONVERGE TM optimal mesh case and OpenFOAM [®] reference case simulations (Standard k- ϵ U-RANS turbulence model).	175
5.4	Accuracy and computational requirements concerning the two dynamic Smagorinsky LES in CONVERGE TM to evaluate the influence of the AMR algorithm.	176
5.5	Performance and computational requirements of the SGS LES models for the two meshing strategies considered.	181
6.1	Strouhal numbers for the main frequencies identified using FFT, POD and DMD techniques.	231

6.2	Main frequencies of the coherent flow structures of the liquid-fueled and gaseous-fueled cases identified using POD and DMD techniques.	239
7.1	Geometrical parameters and levels considered to conduct the parametric study (values of the baseline geometry in bold)	247
7.2	Taguchi's orthogonal array L9 proposed to study the influence of the geometrical parameters on the non-reacting field	248
7.3	Definition of the response variables considered for the analysis of variance.	251
7.4	Values of the response variables considered for the analysis of variance for the simulations of the L9 array (1/2).	254
7.5	Values of the response variables considered for the analysis of variance for the simulations of the L9 array (2/2).	254
7.6	Results of the analysis of variance for the the maximum axial velocity of the swirled jet.	256
7.7	P-values for the defined response variables.	258
7.8	Geometrical parameters values of the optimal cases resulted from two Multiple Response Optimisation (MRO) analysis	270
7.9	Frequency and amplitude associated to the POD modes obtained from the 3-D pressure signal for the simulations of the L9 array.	273
7.10	P-values for the response variables of the spectral analysis.	275

Nomenclature

Acronyms

ACARE	Advisory Council for Aeronautics Research in Europe.
AMR	Adaptive Mesh Refinement.
ANOVA	ANalysis Of VAriance.
CAEP	Committee on Aviation Environmental Protection.
CFD	Computational Fluid Dynamics.
CFL	Courant-Friedrichs-Lewy number.
CMC	Conditional Moment Closure.
CPU	Central Processing Unit
CRSB	Coria Rouen Spray Burner.
CTRZ	Central Toroidal Recirculation Zone.
DACRS	Dual-Annular Counter-Rotating Swirling Combustor.
DAC	Dual-Annular Combustor.
DDM	Discrete Droplet Model.
DILU	Diagonal Incomplete LU.
DMD	Dynamic Mode Decomposition.
DNS	Direct Numerical Simulation.
DOE	Design Of Experiments.
DPS	Discrete Phase Model.
DSD	Droplet Size Distribution.
DTF	Dynamically Thickened-Flame.
EE	Eulerian-Eulerian.

ELSA	Eulerian Lagrangian Spray Atomization.
EL	Eulerian-Lagrangian.
FDF	Filtered mass-Density Function.
FFT	Fast Fourier Transform.
FGM	Flamelet-Generated Manifold.
FSD	Flame Surface Density.
GAMG	Geometric-Algebraic Multigrid.
GEAE	General Electric Aircraft Engines.
GT	Gas Turbine.
ICAO	International Civil Aviation Organisation.
ICE	Internal Combustion Engine.
KH	Kelvin-Helmholtz.
KIAI	Knowledge for Ignition, Acoustics and Instabilities.
LDA	Laser Doppler Anemometry.
LDI	Lean Direct Injection.
LDV	Laser Doppler Velocimetry.
LEM	Linear Eddy Mixing.
LES	Large Eddy Simulation.
LIF	Laser Induced Fluorescence.
LISA	Linearised Instability Sheer Atomisation.
LPP	Lean Premixed Prevaporised.
MERCATO	Experimental Means for Research in Air-breathing Combustion by Optical Techniques.
MILD	Moderate or Intense Low-oxygen Dilution.
MP	Multi-Point.
MUSCL	Monotonic Upstream-Centered Scheme for Conservation Laws.
NASA	National Aeronautics and Space Administration.
NCC	National Combustion Code.
NMSE	Normalised Mean Square Error.
NS	Navier-Stokes.
PBiCG	Preconditioned Bi-Conjugate Gradient.
PCA	Principal Component Analysis.
PDF	Probability Density Function.
PISO	Pressure Implicit with Splitting of Operators.
PIV	Particle Image Velocimetry.

PLIF	Planar Laser Induced Fluorescence.
POD	Proper Orthogonal Decomposition.
PRECCINSTA	PREdiction and Control of Combustion INSTAbilities for industrial gas turbines.
PVC	Precessing Vortex Core.
RANS	Reynolds-Averaged Navier-Stokes.
REDIM	Reaction-Diffusion Manifold.
RMS	Root Mean Square.
RNG	Renormalisation Group.
ROM	Reduced-Order Model.
RQL	Rich-Burn/Quick-Quench/Lean-Burn.
RSM	Reynolds Stress Model.
RT	Rayleigh-Taylor.
SGS	Sub-Grid Scale.
SMD	Sauter Mean Diameter.
SMR	Sauter Mean Radius.
SPL	Sound Pressure Level.
SVD	Singular Value Decomposition.
SWJ	Swirled Jet.
TAB	Taylor Analogy Breakup.
TAPS	Twin Annular Premixing Swirler.
TARS	Triple Annular Research Swirler.
U-RANS	Unsteady Reynolds-Averaged Navier-Stokes.
UCH	Unburned hydrocarbons.
VBB	Vortex Breakdown Bubble.
VOF	Volume of Fluid.
WALE	Wall-Adapting Local Eddy-viscosity.
WAVE	Surface Wave Instability Atomisation.

Greek symbols

α	Collision angle formed by the trajectory between two colliding drops.
α_h	Heat transfer coefficient.
α_i	DMD modal amplitude.
α_{SWJ}	Half Swirled Jet cone angle.
δ	Characteristic size of a large-scale flow structure.

ΔP_{loss}	Pressure loss of the flow across the swirler.
Δ_e	Spatial filter cut-off width in LES.
Δ_l	Drop diameter ratio.
δ_{ij}	Kronecker delta function.
η_{bu}	Liquid sheet length at breakup event in the LISA model.
λ	Thermal conductivity.
λ_i	DMD modal eigenvalue.
Λ_s	Wavelength responsible for breaking up the liquid sheet in the LISA model.
λ_{eff}	Effective thermal conductivity.
μ	Dynamic Viscosity.
μ_g	Gas molecular viscosity.
μ_t	Turbulent dynamic Viscosity.
ν	Kinematic Viscosity.
ν_l	Liquid kinematic viscosity.
ν_t	Turbulent kinematic viscosity.
ν_{num}	Numerical viscosity in LES.
ν_{sgs}	Sub-grid scale viscosity in LES.
ω	Specific rate of turbulent energy dissipation.
ω_L	Complex form of the wave growth rate in the LISA model.
Ω_s	Maximum growth rate of wave disturbance on the liquid sheet in the LISA model.
ω_T	Droplet oscillation frequency in TAB model.
ϕ	General flow variable.
Φ_i	DMD modal shape
Ψ_i	POD modal shape
ρ	Density.
Σ	POD modal amplitude matrix
σ	Variance in a Gaussian probability distribution.
σ_i	POD modal eigenvalue.
σ_l	Surface tension at the boundary among the liquid and the gas.
τ	Total (laminar + turbulent) viscous stress tensor.
τ_g	Viscous stress tensor of the gas-phase.
τ_{bu}	Breakup time.
τ_{ij}	Reynolds stresses.

τ_{PVC}	Rotation period of the precessing vortex core.
τ_{rot}	Rotation time scale associated with the VBB.
θ	Half spray cone angle.
θ_g	Gas-phase void fraction.
ε	Turbulent dissipation rate.
$\hat{\Delta}_e$	Test level filter in LES.

Latin symbols

\dot{f}_{bu}	Source term originated from droplet breakup.
\dot{f}_{coll}	Source term originated from droplet collision.
\dot{m}	Mass flow rate.
\dot{Q}^c	Source term related to chemical reactions.
\dot{Q}^s	Source term related to spray interactions.
A	Swirler vane angle.
A_a	Air core area within a pressure swirl atomiser.
a_i	Temporal evolution of the POD modes.
A_o	Discharge orifice area of a pressure swirl atomiser.
A_{DMD}	DMD modal amplitude matrix.
B	Mass transfer number.
b_{crit}	Critical impact parameter.
C_D	Drag coefficient of the droplet.
c_l	Specific heat of liquid drops.
C_S	Smagorinsky coefficient.
D	Mass diffusion coefficient.
d_L	Diameter of the liquid ligament.
d_l	Diameter of the liquid drop.
d_o	Discharge orifice diameter of a pressure swirl atomiser.
D_t	Mass diffusion coefficient for turbulent cases.
D_{10}	Arithmetic mean diameter.
D_{32}	Sauter mean diameter.
D_{ext}	Injector swirl chamber diameter.
D_{iag}	Diagonal matrix of DMD modal amplitudes.
E_i	Relevance of a given DMD mode.
F	Drop acceleration.
f	Frequency.

F_D	Drag force on a drop.
f_d	Droplet distribution function.
f_E	Fraction of energy dissipated in the collision between droplets.
g	Gravitational acceleration.
G_x	Axial flux of axial momentum.
G_θ	Axial flux of angular momentum.
h	Specific enthalpy.
I	Specific internal energy.
I_l	Internal energy of liquid drops.
IQ_k	Index of quality based on the resolved turbulent kinetic energy in LES.
IQ_ν	Index of quality based on the viscosity in LES.
J	Heat flux vector.
k	Turbulent kinetic energy.
K_s	Wave number corresponding to the maximum growth rate.
K_t	Conductivity coefficient for turbulent cases.
k_v	Velocity coefficient related to the injector design in LISA model.
k_{mod}	Modelled Turbulent kinetic energy in LES.
k_{res}	Resolved Turbulent kinetic energy in LES.
L_{CRZ}	Length of the corner recirculation zone.
$L_{SWJ}^{0.2ref}$	SWJ length with velocity 20% of reference case.
$L_{VBB,bot}$	Length of the vortex breakdown bubble bottle-neck.
$L_{VBB,top}$	Maximum length of the vortex breakdown bubble.
m	Wavenumber of a travelling azimuthal wave associated to a POD/DMD mode.
N	Axial position of the nozzle tip.
N_p	Number of drops in a parcel.
N_T	Number of temporal snapshots.
Nu	Nusselt number.
Oh	Ohnesorge number.
P	Fluid pressure.
P_c	Probability of collision between a pair of parcels.
p_g	Thermodynamic pressure of the gas-phase.
p_{DN}	Probable drop number per unit of volume.
p_{inj}	Operating injection pressure of the atomiser.

Pr	Prandtl number.
Pr_t	Turbulent Prandtl number.
q	Parameter to account the dispersion among drop sizes.
R	Radius of the swirler.
r	Drop radii.
r_o	Discharge orifice radius of a pressure swirl atomiser.
Re	Reynolds number.
Re_c	Collision Reynolds number.
Re_d	Drop Reynolds number.
S	Number of swirler vanes.
S_d	Source term that represents the interactions with the discrete phase.
S_S	Source terms in the transport equations.
S_W	Swirl number.
S_{CRZ}	Size of the corner recirculation zone.
S_{ij}	Mean strain rate tensor.
S_{spray}	Spray penetration.
Sc	Schmidt number.
Sc_t	Turbulent Schmidt number.
Sh	Sherwood number.
Str	Strouhal number.
SS	Sum of Squares.
St	Stokes number.
T	Temperature.
t	Time.
T_d	Drop temperature.
T_g	Gas temperature.
t_l	Liquid film thickness at the injection plane.
t_s	Liquid sheet thickness.
u	Gaseous velocity.
u'	Gaseous turbulent velocity.
U_{CRZ}^{min}	Minimum axial velocity at the corner recirculation zone.
U_{CTRZ}^{min}	Minimum axial velocity at the CTRZ.
U_{SWJ}^{max}	Maximum axial velocity at the SWJ.
V	Matrix of the sequence of temporal snapshots used in POD and DMD.

v	Liquid velocity.
V_c	Cell volume.
V_d	Dispersed-phase volume.
v_{rel}	Relative velocity between two colliding drops.
V_{SWJ}^{max}	Maximum tangential velocity at the SWJ.
W	Combustion chamber width.
w	Gaseous-liquid interface velocity.
W_g	Molecular weight of the gas-phase.
W_{CRZ}	Width of the corner recirculation zone.
W_{f_v}	Molecular weight of the vapour fuel.
W_{VBB}	Maximum width of the VBB).
We	Weber number.
We_c	Collision Weber number.
We_{crit}	Critical Weber number (threshold for the onset of drop breakup).
x	Non-dimensional impact parameter.
y	Drop distortion.
y^+	Non-dimensional boundary layer distance.
Y_m	Mass fraction of specie m .
Y_{f_v}	Fuel mass fraction in the computational cell.
$Y_{f_v}^*$	Fuel mass fraction at the drop surface.

Subscripts

θ	Tangential component.
f_v	Fuel vapour.
g	Gas phase.
l	Liquid phase.
r	Radial component.
z	Axial component.

Chapter 1

Introduction

*“A mistake is not something to be determined after the fact,
but in light of the information available until that point.”*

—Nassim N. Taleb

1.1 General context

The study of advanced aeronautical gas turbine engines is controlled by increasingly stringent environmental regulations. The aviation industry continues its expansion and aeronautical engines have to rely on the combustion of fuels of high energy fuels since hybrid systems are still in a very early phase of research. An underlying problem in combustor design is that of achieving easy ignition, wide burning range, high-combustion efficiency and minimum pollutant emissions in a single, fixed combustion zone supplied with fuel from a single injection point. As some of these requirements conflict, the outcome is inevitably a compromise of some kind [1].

Current aero-engines must satisfy the regulations imposed since the 90s by organisms such as the ICAO-CAEP and the Advisory Council for Aviation Research and Innovation in Europe (ACARE), which drives companies to continuously innovate the engine designs by reducing both the fuel consumption and the pollutant and noise emissions. The goals proposed for 2050 by ACARE are mainly focused on reducing CO₂ emissions by 75% per passenger and kilometre, NO_x emissions by 90% and noise by 65% with respect to the year 2000 [2]. Meanwhile, the mitigation of other pollutants such as CO,

unburned hydrocarbons (UHC) and soot have also received serious attention because of the adverse impacts on health and the environment. Each of these pollutants have been considerably reduced in modern gas turbines, except for NO_x , whose limits have become ever more stringent in the last two decades. NO_x production is mostly governed by the combustor operating conditions, the fuel and air injection scheme, the fuel-air mixing, and the combustion process. In this context, the development of a clean and efficient injection-combustion strategy is crucial since emissions are primarily governed by the combustion process [3].

The modern aero-engines technology so far employed has been based on the Rich-Burn/Quick-Quench/Lean-Burn (RQL) concept introduced in 1980 [4] (see Figure 1.1 left). In this system, the combustion stability is enhanced through the generation of a rich burning primary region. This rich-burn zone minimises the NO_x production as a result of relatively low temperatures and oxygen concentrations (see the right side of Figure 1.1). Then, a rapid mixing is forced at the intermediate region to avoid the considerable generation of pollutants (high route NO_x path in the right side of Figure 1.1) associated with the local formation of stoichiometric conditions. This transition towards the lean-burn zone has to be carefully controlled to minimise CO, UHC and soot formation. Finally, in this lean dilution zone, the high concentrations of CO and hydrocarbon species from the primary zone are oxidized. The RQL technology has proved to be very prosperous for aero-engine applications since it presents both a better ignition and lean blowout performance and a lower NO_x generation when comparing with conventional combustors.

Nevertheless, even if some possible developments can still be expected from the RQL design, its potential to further decrease NO_x emissions is limited. In such circumstances, the stringent restrictions are forcing the development of alternative modern low emissions combustion technologies for aero gas turbine engines relying on innovative injection-combustion concepts, such as *lean combustion*. This strategy is characterised by forcing the burner to operate with an excess of air to drastically reduce the flame temperature.

The fuel-staged combustion was the first approach introduced in this *lean combustion* framework. In staged combustors, the fuel is injected into a constant airflow distribution and shifted between the two or more combustion zones employed by the burner (arranged either in parallel or in series) in an attempt to sustain a constant temperature. In this respect, the Dual Annular Combustor (DAC) was developed by General Electric for civil aircraft engines [6] based on a parallel/radial staging strategy (see left side of Figure 1.2). The DAC was designed with a pilot stage in the outer annulus (optimised to

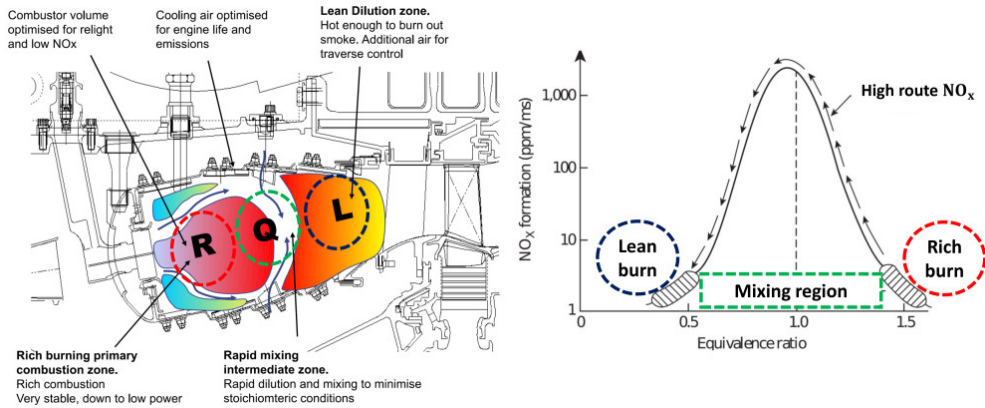


Figure 1.1: Left: Schematic of an RQL combustor. Right: NO_x trends related to equivalence ratio, defined as the ratio of the actual fuel/air ratio to the stoichiometric fuel/air ratio [1, 5].

operate at low-power operation points such as start-up, altitude relight and engine idle) and a main stage in the inner one, optimised for high-power settings. Nevertheless, several issues related both to the uniformity performance of the exit temperature profile during intermediate power settings (i.e., both chambers operating far away from their optimum design points) and to the increased design complexity limited the application of this kind of technology.

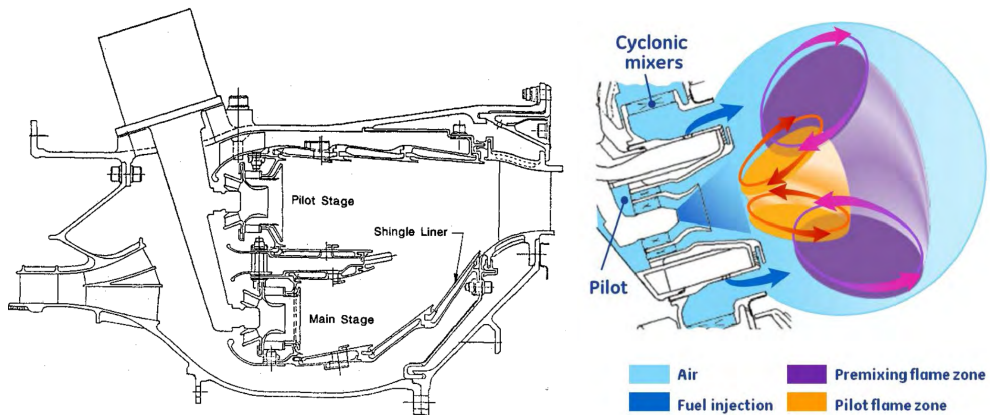


Figure 1.2: Left: Schematic of a radial-staged Dual Annular Combustor (DAC) [6]. Right: Schematic of a Twin Annular Premixing Swirler (TAPS) combustor [7].

Therefore, both aero-engine researchers and manufacturers focused the attention on Single Staged Combustors. The most relevant burner employing this technology and currently the only lean-burn combustion system employed on a certified aircraft engine is the GE-TAPS (Twin Annular Premixing Swirler). The TAPS configuration (see right side of Figure 1.2) is based on two co-annular swirling flow streams produced by a staged pilot injector and a main lean direct multi-point injection. On the one hand, the pilot injection system employs a high-flow simplex pressure atomiser surrounded by two co-rotating swirlers assisting the atomisation of the fuel spray for engine startup and low-power operations. On the other hand, the main-mixer consists of a radial swirler (cyclone) and a cavity where discrete transversed fuel jets are injected [7, 8]. The interaction between the swirling jets from the pilot and the main-mixer is of paramount importance to generate the optimal aerodynamic and thermal scenarios needed to meet the performance and design requirements. In this respect, further investigation for the sake of an additional reduction of emission levels has led to the TAPS II configuration [9] during the last years.

The most extensively used RQL technology and the existing DAC concept mentioned above are expected to be phased out since further optimization is no longer contributing to any notable enhancement in their ability for reducing NO_x . This has led the aviation gas turbine industry to move toward the development of lean combustion technologies with lower emissions levels while satisfying all operability requirements. In this context, the Lean Premixed Prevaporised (LPP) [10] and the Lean Direct Injection (LDI) [11] concepts have emerged as potential candidates to replace the current combustion systems for future aero gas turbine engines.

On the one hand, the LPP concept is based on getting complete evaporation of the fuel and full mixing of fuel and air before combustion. In this way, NO_x emissions are drastically reduced since droplet burning is avoided (thus eliminating “hot spots” from the combustion zone) and the combustion is produced at lean conditions (low flame temperature). The main shortcoming of the LPP technology is the prolonged time required to entirely vaporise and mix the fuel at low-power conditions. This may result in autoignition or flashback phenomena in the fuel preparation channel. In this way, additional cost and complexity concerns are associated with this system in order to mitigate these operational risks (through the use of staged combustion or variable geometry), severely compromising and affecting its durability and maintainability.

On the other hand, the LDI scheme is expected to further reduce the NO_x emissions while maintaining the other emissions criteria and performing stably

under all operating conditions (experiments have demonstrated its good flame-holding ability and wide stability limits), especially at high-temperature and high-pressure conditions [1]. In the LDI concept, the air is swirled upstream of a venturi section, and the fuel is injected radially into the airstream from the venturi throat section in order to produce a lean mixture. Hence, the swirling air-flow is used both for atomizing the injected liquid jets, mixing the atomised sprays and generating a recirculating region downstream, which acts as an aerodynamic flame holder. Thus, suitable atomisation and quick and uniform fuel-air mixing are achieved in a short period enabling low-temperature combustions with low NO_x levels. Furthermore, the LDI strategy mitigates the risks of auto-ignition and flashback since the fuel is directly injected into the combustion zone.

The main challenge of LDI burners lies then in efficiently mixing the air and fuel before the reaction is completed, thus avoiding high NO_x levels due to the high flame temperature peaks that would be formed from regions presenting high local fuel concentrations. Furthermore, LDI combustors may be prone to cause unstable combustion since they operate close to the lean extinction limit. Consequently, detailed analyses of the flow dynamics and heat release generated in the mixing regions are essential during preliminary design stages.

In this frame, the injection-swirler system present in LDI combustors has been widely studied due to its key role on fuel atomisation, vaporisation and air-fuel mixing process, setting the scenario in which combustion will take place, thus importantly affecting its characteristics. Numerous studies, both experimental and computational, have been carried out during the last years in order to increase the knowledge about the fundamental features of the LDI concept. The first studies in LDI burners were conducted experimentally considering configurations with radial swirlers and using natural gas instead of liquid fuel [12]. Subsequently, research on the injection of liquid fuel began to be generalised, studying the effect of atomisation and evaporation and confirming the ability of LDI burners to reduce NO_x emissions [13]. Specific studies on the atomisation of liquid fuel [14, 15] indicated significant influence of the turbulence induced by the swirler in the distribution of fuel droplet size in the chamber.

Recently, several burners with simplified geometries have been designed for the experimental study of the non-stationary phenomena of the LDI injection, including both single-injector and multi-injector configurations and premixed and non-premixed cases, highlighting the PRECCINSTA combustor of the DLR [16], a high-pressure test-rig in TU-Darmstadt [17], the MERCATO model developed in ONERA [18] and the CORIA burner installed in CORIA

[19]. These facilities have been used to develop studies on the probability of ignition, flame stability analysis and characterisation of the reacting flow and combustion.

However, the high cost of experimental tools and techniques for the study of LDI combustors have forced the development of computational tools that model the relevant phenomena (i.e., air turbulence, fuel atomisation, air/fuel mixing, etc.) thus allowing the evaluation and prediction of the main flow structures generated within the burner in a fast and accurate form. In this way, Computational Fluid Dynamics (CFD) has become a fundamental technique for design purposes over the last years [20]. Simulations at an industry level have been typically performed considering a RANS (Reynolds-Average Navier-Stokes) approach, where the mean flow is modelled and the turbulence effects are included through ad-hoc models. Nevertheless, considering the high level of unsteadiness and turbulence that usually characterise the lean burn devices, these models are inadequate to describe the underlying complexity. Hence, computational methods have been evolving over the last years towards scale-resolving procedures, such as Large Eddy Simulation (LES), where the unsteady characteristics of spray flames can be appreciated.

In this scenario, the LDI computational studies carried out report a wide range of phenomena occurred inside these burners, from prediction of the ignition [21] and extinction [22] of the flame, to detailed characterisations of the dynamics of the spray-turbulence-flame interactions [23]. Most of these numerical studies take as reference the academic geometries mentioned above to validate their models based on readily available experimental data. Nevertheless, many uncertainties still characterise this technology and further investigation on this injection-combustion strategy related to typical phenomena suffered in lean systems such as flame stability, thermo-acoustic oscillations and ignition performances is required.

Lately, several thematic projects on the topic of Advanced Low-NO_x Combustion Technologies were launched in the framework of the *Clean Sky* (a public-private partnership between the European Commission and the European aeronautics industry) in order to establish a roadmap for future combustion technology for the mid-term (EIS 2035) and long-term (EIS 2050). The low-NO_x technologies proposed are currently under investigation, ranging from the development of a new Lean Azimuthal Flame concept based on MILD combustion [24] or a Compact Helical Arranged Combustor with lean Lifted Flames [25] to more innovative technologies related to the electrochemical suppression of NO_x generation in the primary combustion zone and the electromagnetic decomposition of NO_x molecules in the engine exhaust [26].

Nevertheless, these concepts are at a very early stage, and further investigation is required to clarify their viability and applicability.

1.2 Objectives and methodology

The purpose of this thesis is to shed light on the field of Lean Direct Injection (LDI) combustors to assess the viability of this low- NO_x swirled-stabilised strategy in replacing the actual aero-engines technology. Swirl combustion (considering gaseous fuels or sprays) constitutes the cornerstone of most of the present thermal power generation systems, especially in the field of Gas Turbine engines. In this context, the development and establishment of reliable numerical tools play a vital role as a crucial alternative to traditional experiments to effectively design, model and optimise these complex systems. Nevertheless, numerical CFD simulations of these devices are usually computationally unaffordable since they imply a multi-scale problem.

The main objective of the investigation is to develop a numerical tool capable of reliably modelling the 2-phase non-reacting flow in an academic LDI burner, using the U-RANS and LES approaches, and the subsequent exploitation of the models to evaluate the influence of geometrical factors of the burner on the phenomena of turbulent flow structures generation, fuel atomisation, evaporation and formation of the gaseous air-fuel mixture. Characterising the non-reacting flow is a crucial step in LDI combustor research since the success or failure of ignition (and re-ignition at high-altitude) is known to directly depend on local conditions just before ignition, especially on the mixture quality and the turbulence level at the near-injection region. The LDI combustor taken as a reference to carry out the investigation is the laboratory-scale¹ swirled-stabilised CORIA Spray Burner because of its extensive experimental data available in the literature [27–29]. The problem will be addressed by solving the complete inlet flow path through the swirl vanes and the combustor through two different CFD codes involving two different meshing strategies: an automatic mesh generation with adaptive mesh refinement (AMR) algorithm through CONVERGETM and a more traditional static meshing technique in OpenFOAM[®].

With all, the partial objectives of the present thesis may be summarised as follows:

¹A laboratory-scale combustor allows reducing the magnitude of the challenge in terms of required computational resources while retaining the underlying fundamental phenomena present in full-scale systems.

1. To define a robust methodology in order to establish an optimal meshing strategy that allows characterising the flow field in the CORIA LDI burner through several grid control tools, and the exploitation of its benefits against traditional mesh approaches in this kind of multi-scale problem. Such a strategy could provide the user with a more automated mesh generation to study this kind of problem with less computational resources than traditional approaches, without compromising accuracy.
 - a) To evaluate automatic grid control tools and the turbulence model influence through a mesh parametric study, with special attention to the Adaptive Mesh Refinement algorithm. AMR techniques have proved to be a remarkably efficient approach to reduce mesh elements while performing accurate simulations, especially those involving complex flows with moderate Reynolds numbers.
 - b) To develop a rigorous procedure to quantify the CFD performance considering discrepancies between predicted and experimentally measured values, thus making it possible to assign an overall score for a quantitative comparison between simulations. For this purpose, an specific quality parameter has been adopted to quantify the accuracy of turbulent numerical statistics regarding the agreement with the experimental database available in the literature.
2. To develop systematic computational algorithms to automatically post-process the raw data extracted from gaseous fuel and spray simulations used for comparison, validation and identification of physical mechanisms.
3. To solve the reference gaseous fuel case, which presents a reduced complexity when compared to the spray fuel case, in order to validate the gaseous-phase resolution and evaluate the methodology established.
 - a) To characterise the flow topology and assess the flow pattern typical of highly swirled configurations. The macroscopical analysis of the main turbulent features given by the unsteady flow visualisation allows identifying the large coherent structures within the combustor resulting in periodic hydrodynamic disturbances and instabilities.
 - b) To implement different filtering techniques (i.e., Fast Fourier Transform) and data-driven modal decomposition procedures (i.e., Proper Orthogonal Decomposition and Dynamic Mode Decomposition) for a further characterisation of the unsteady flow structures generated within the combustion chamber.

4. To apply the defined methodology and the spectral analysis tools to solve the reference spray fuel case, which involves an accurate modelling of all those phenomena associated to the liquid phase: atomisation², breakup, drop turbulent dispersion, drop collisions, evaporation and air/fuel mixing.
5. Once validated for the gaseous fuel and spray reference cases, the developed methodology will allow analysing the effect of key geometric features of the burner on the generation of flow structures, atomisation of the fuel and formation of the air-fuel mixture. Such a parametric study should also allow identifying geometric solutions that reduce the formation of emissions pollutants and increase the performance of future aviation engines.

Therefore, the use of CFD tools has been combined with the development of systematic advanced modal decomposition techniques (previously validated against experimental results) given their proved potential when studying the characteristics of the most powerful coherent structures of strongly swirled jets in a Lean Direct Injection burner undergoing vortex breakdown. The implementation of these mathematical procedures allows both retrieving information about the flow dynamics features and providing a systematic approach to identify the main mechanisms that sustain instabilities in the combustor. This makes it possible to determine not only the governing helical coherent structures generated within the burner but also to understand the periodic physics underlying hydrodynamic instabilities. The characterisation of non-reacting instabilities is of primary interest since one of the biggest problems of the LDI technology is the eventual flame blowouts and the consequent re-ignition in altitude from a non-reacting field.

This work has been performed in the frame of the *Departamento de Máquinas y Motores Térmicos* at *Universitat Politècnica de València* (Spain), which has a long expertise in the study of the diesel injection process following experimental and computational approaches alike [30–37]. Recently, the group has entered the aviation industry, through the funding of public projects such as those granted by Clean Sky with European Union funds under the Horizon 2020 program. In addition, national projects such as CHEST (development of combustion and emission models in GT engines) are being led and projects with the industry have been carried out with companies such as

²The accuracy of the predictions strongly depends on the models (and its correct calibration) adopted for spray atomisation.

Donaldson. In this frame, a laboratory-scale atmospheric continuous-flow LDI test rig (both confined and non confined configurations) has been designed and developed at the department to experimentally investigate this injection/combustion strategy, whose first measurements have been recently published [38]. Simultaneously, this thesis constitutes the development and establishment of the basis and state of the art in the research centre to first investigate the atomisation and evaporation phenomena in the LDI technology numerically, thus giving further insights in the following years.

In the last years, the CONVERGE™ CFD package has been extensively used in the investigation of Internal Combustion engines [39–42] due to both its automated mesh generation and the adaptive mesh refinement algorithm, which allow maximising accuracy and computational efficiency. Despite the wide application of AMR to flows involving shocks or chemical reactions, there have been fewer investigations regarding the implementation of AMR to turbulent flows. Nevertheless, some recent studies have been carried out to expand the use of this code to the aero-engine framework [43–47].

1.3 Thesis outline

This thesis is organised in eight chapters, including the present introduction (*Chapter 1*). In *Chapter 2*, the fundamentals of the Lean Direct Injection (LDI) concept are exposed. Special attention is given both to the swirler and the injection system since its coupled performance is critical for the viability and success of the described strategy. Due to their relevance in the combustion process, the theory of non-reactive spray-related phenomena (e.g., atomisation and breakup, dispersion, mixing and evaporation) and the resulting spray is described as well.

Chapter 3 offers a detailed description of the state of the art on how the LDI systems have been experimentally studied and numerically modelled by other authors through laboratory-scale test rigs and CFD approaches, respectively. The kind of spectral studies employing the mathematical decomposition procedures mentioned above cannot be performed without high-resolution (both in time and space) 3D data sets, only available in the very recent past. For this reason, the most relevant works on flow characterisation on the dynamics of the governing helical coherent structures within LDI combustors are also outlined in this chapter.

A description of the methodology in terms of the computational tools on which this thesis is based is presented in *Chapter 4*. This includes those sub-models that are required to predict the flow and spray behaviour and to

perform realistic spray simulations. Not only the solver equations and sub-models are presented in this chapter, but also the strategy followed in the case set-ups for both the gaseous fuel and spray simulations (pre-processing) and the procedure developed to post-process the raw 3D data extracted from them. The recent incursion of advanced modal decomposition techniques that allow further investigating the underlying physics in LDI systems is also presented.

Chapter 5 provides a validation of the CFD codes against different literature test cases taken as a reference involving both gaseous and spray fuel configurations. In the first place, a robust methodology to establish an optimal meshing strategy concerning gaseous fuel injections is defined by quantitatively and qualitatively comparing the CFD outcomes with the experimental reference measurements. Secondly, the derived methodology is used to simulate spray fuel cases to complete the validation assessment concerning all the liquid-phase sub-models considered. Meanwhile, the quality and reliability of such simulations (focused on Large Eddy Simulations) are evaluated based on turbulent criteria before analysing the results obtained.

Meanwhile, *Chapter 6* deals with the spectral analysis as a result of the application of different modal decomposition tools to the gaseous and spray fuel reference cases. In this way, the results presented in *Chapter 5* are here confirmed, justified and extended thanks to the implementation of Proper Orthogonal Decomposition (POD) and Dynamic Mode Decomposition (DMD) techniques.

Once the CFD codes are calibrated and validated against the reference cases, the predictive capabilities of the proposed methodology are exploited in *Chapter 7* through a parametric study. In this way, this thesis is extended to analyse the effect of the key geometrical aspects of the burner on the generation of flow structures, atomisation of the fuel and formation of the air-fuel mixture.

Finally, the last chapter (*Chapter 8*) draws the main conclusions of this thesis synthesizing the main findings of the investigation and showing possible directions on which to orient future research in the LDI strategy.

References

- [1] Lefebvre, A. and Ballal, D. *Gas turbine combustion: alternative fuels and emissions*. 3rd edition. Taylor and Francis, 2010.
- [2] *Report of the High Level Group on Aviation Research*. Tech. rep. European Commission. 2011. DOI: 10.2777/50266.

- [3] Liu, Y. et al. “Review of modern low emissions combustion technologies for aero gas turbine engines”. In: *Progress in Aerospace Sciences* 94 (2017), pp. 12–45. DOI: 10.1016/j.paerosci.2017.08.001.
- [4] Mosier, S. and R., Pierce. “Advanced Combustion Systems for Stationary Gas Turbine Engines: Volume 1 Review and Preliminary Evaluation”. In: *U.S. Environmental Protection Agency Technical Report EPA-600/7-80-017a* (1980).
- [5] Puggelli, S. “Towards a unified approach for Large Eddy Simulation of turbulent spray flames”. PhD thesis. Universita degli studi Firenze, 2018.
- [6] Bahr, D. “Technology for the design of high temperature rise combustors”. In: *Journal of Propulsion and Power* 3 (1987), pp. 179–186. DOI: 10.2514/3.22971.
- [7] Mongia, H. “TAPS: A Fourth Generation Propulsion Combustor Technology for Low Emissions”. In: *AIAA International Air and Space Symposium and Exposition* July (2003), pp. 1–11. DOI: 10.2514/6.2003-2657.
- [8] Cooper, J. et al. “Fuel nozzle assembly for reduced exhaust emissions”. Google Patent 6389815. 2002.
- [9] Stickles, R. and Barrett, J. *TAPS II Technology Final Report*. Tech. rep. 2013.
- [10] Russell, P., Beal, G., and Hinton, B. “Low NO_x heavy fuel combustor concept program”. In: *NASA Technical Report NASA-CR-165512* (1981).
- [11] Alkabie, H., Andrews, G., and Ahmad, N. “Lean Low NO_x Primary Zones Using Radial Swirlers”. In: *Turbo Expo: Power for Land, Sea and Air*. 1988. DOI: 10.1115/88-GT-245.
- [12] Alkabie, H. and Andrews, G. “Reduced NO_x Emissions Using Low Radial Swirler Vane Angles”. In: *Proceedings of the ASME: International Gas Turbine and Aeroengine Congress and Exposition*. Orlando, Florida (USA), 1991. DOI: 10.1115/91-GT-363.
- [13] Shaffar, S. and Samuelsen, G. “A Liquid Fueled, Lean Burn, Gas Turbine Combustor Injector”. In: *Combustion Science and Technology* 139.1 (1998), pp. 41–57. DOI: 10.1080/00102209808952080.
- [14] Cai, J, Tacina, R., and Jeng, S. “The Structure of a Swirl-Stabilized Reacting Spray Issued From an Axial Swirler”. In: *43rd AIAA Aerospace Sciences Meeting and Exhibit*. January. 2005.

- [15] Hicks, Y., Heath, C., Anderson, R., and Tacina, K. “Investigations of a Combustor Using a 9-Point Swirl-Venturi Fuel Injector: Recent Experimental Results”. In: *20th International Symposium on Air Breathing Engines (ISABE)*. Göteborg (Suecia), 2011.
- [16] Weigand, P., Meier, W., Duan, X., Stricker, W., and Aigner, M. “Investigations of swirl flames in a gas turbine model combustor: I. Flow field, structures, temperature, and species distributions”. In: *Combustion and Flame* 144.1-2 (2006), pp. 205–224. DOI: 10.1016/j.combustflame.2005.07.010.
- [17] Janus, B., Dreizier, A., and Janicka, J. “Experiments on swirl stabilized non-premixed natural gas flames in a model gasturbine combustor”. In: *Proceedings of the Combustion Institute* 31 II (2007), pp. 3091–3098. DOI: 10.1016/j.proci.2006.07.014.
- [18] Linassier, G. et al. “Application of numerical simulations to predict aircraft combustor ignition”. In: *Comptes Rendus Mécanique* 341.1-2 (2013), pp. 201–210. DOI: 10.1016/J.CRME.2012.11.009.
- [19] Barré, D. et al. “Flame propagation in aeronautical swirled multi-burners: Experimental and numerical investigation”. In: *Combustion and Flame* 161.9 (2014), pp. 2387–2405. DOI: 10.1016/j.combustflame.2014.02.006.
- [20] Versteeg, H. and Malalasekera, W. *Introduction to Computational Fluid Dynamics: The finite volume method*. 2nd Edition. Pearson Education Limited, 2007. DOI: 10.2514/1.22547.
- [21] Marchione, T., Ahmed, S., and Mastorakos, E. “Ignition of turbulent swirling n-heptane spray flames using single and multiple sparks”. In: *Combustion and Flame* 156.1 (2009), pp. 166–180. DOI: 10.1016/J.COMBUSTFLAME.2008.10.003.
- [22] Tyliszczak, A., Cavaliere, D., and M. “LES/CMC of Blow-off in a Liquid Fueled Swirl Burner”. In: *Flow, Turbulence and Combustion* 92.1 (2014), pp. 237–267. DOI: 10.1007/s10494-013-9477-5.
- [23] Patel, N. and Menon, S. “Simulation of spray-turbulence-flame interactions in a lean direct injection combustor”. In: *Combustion and Flame* 153 (2008), pp. 228–257. DOI: 10.1016/j.combustflame.2007.09.011.
- [24] *Development of the Lean Azimuthal Flame as an Innovative aviation gas turbine low-NOX combustion concept*. 2020. URL: <https://cordis.europa.eu/project/id/831804> (visited on 02/11/2020).

- [25] *Compact Helical Arranged combustors with lean LIFTed flames*. 2020. URL: <https://cordis.europa.eu/project/id/831881> (visited on 02/11/2020).
- [26] *Innovative Technologies of Electrochemical Suppression and Electromagnetic Decomposition for NOx Reduction in Aeroengines*. 2020. URL: <https://cordis.europa.eu/project/id/831848> (visited on 02/11/2020).
- [27] Cordier, M. “Allumage et propagation de flamme dans les écoulements fortement swirlés : études expérimentales et numériques”. PhD thesis. Institut National des sciences appliquees (INSA), 2013.
- [28] Cordier, M., Vandael, A., Cabot, G., Renou, B., and Boukhalfa, A. “Laser-Induced Spark Ignition of Premixed Confined Swirled Flames”. In: *Combustion Science and Technology* 185.3 (2013), pp. 379–407. DOI: 10.1080/00102202.2012.725791.
- [29] Barré, D. “Simulation Numerique De L’Allumage Dans Les Chambres De Combustion Aeronautiques”. PhD thesis. Institut National Polytechnique de Toulouse (INP Toulouse), 2014.
- [30] Salvador, F.J. “Estudio teórico experimental de la influencia de la geometría de toberas de inyección Diésel sobre las características del flujo interno y del chorro”. PhD thesis. Universitat Politècnica de València, 2003.
- [31] Gimeno, J. “Desarrollo y aplicación de la medida de flujo de cantidad de movimiento de un chorro Diesel”. PhD thesis. Universitat Politècnica de València, 2008. DOI: 10.4995/Thesis/10251/8306.
- [32] Bracho, G. “Experimental and theoretical study of the direct diesel injection process at low temperatures”. PhD thesis. Universitat Politècnica de València, 2011.
- [33] De la Morena, J. “Estudio de la influencia de las características del flujo interno en toberas sobre el proceso de inyección Diesel en campo próximo”. PhD thesis. Universitat Politècnica de València, 2011.
- [34] Martí-Aldaraví, P. “Development of a computational model for a simultaneous simulation of internal flow and spray break-up of the Diesel injection process”. PhD thesis. Universitat Politècnica de València, 2014. DOI: 10.4995/Thesis/10251/43719.
- [35] Carreres, M. “Thermal Effects Influence on the Diesel Injector Performance through a Combined 1D Modelling and Experimental Approach”. PhD thesis. Universitat Politècnica de València, 2016.

- [36] Viera, A. “Effect of multiple injection strategies on the diesel spray formation and combustion using optical diagnostics”. PhD thesis. Universitat Politècnica de València, 2019.
- [37] Crialesi, M. “Analysis of primary atomization in sprays using Direct Numerical Simulation”. PhD thesis. Universitat Politècnica de València, 2019.
- [38] Payri, R., Salvador, F., Gimeno, J., and Cardona, S. “Experimental study of the influence of the boundary conditions on the atomization process in an unconfined atmospheric burner”. In: *ILASS - Europe 2019, 29th Conference on Liquid Atomization and Spray Systems*. Paris, France, 2019.
- [39] Torregrosa, A., Broatch, A., García-Tíscar, J., and Gomez-Soriano, J. “Modal decomposition of the unsteady flow field in compression-ignited combustion chambers”. In: *Combustion and Flame* 188 (2018), pp. 469–482. DOI: 10.1016/j.combustflame.2017.10.007.
- [40] Broatch, A., Novella, R., Gomez-Soriano, J., Pal, P., and Som, S. “Numerical Methodology for Optimization of Compression-Ignited Engines Considering Combustion Noise Control”. In: *SAE International Journal of Engines* 11.6 (2018), pp. 625–642. DOI: 10.4271/2018-01-0193.
- [41] Xu, L. et al. “Experimental and modeling study of liquid fuel injection and combustion in diesel engines with a common rail injection system”. In: *Applied Energy* 230 (2018), pp. 287–304. DOI: 10.1016/j.apenergy.2018.08.104.
- [42] Broatch, A., Olmeda, P., Margot, X., and Gomez-Soriano, J. “Numerical simulations for evaluating the impact of advanced insulation coatings on H2 additivated gasoline lean combustion in a turbocharged spark-ignited engine”. In: *Applied Thermal Engineering* 148.November 2018 (2019), pp. 674–683. DOI: 10.1016/j.applthermaleng.2018.11.106.
- [43] Drennan, S. and Kumar, G. “Demonstration of an Automatic Meshing Approach for Simulation of a Liquid Fueled Gas Turbine with Detailed Chemistry”. In: *AIAA Propulsion and Energy Forum 2014* 3 of 9 (2014), pp. 2590–2597. DOI: 10.1081/E-EEE2-120046011.
- [44] Drennan, S., Kumar, G., Steinthorsson, E., and Mansour, A. “Unsteady Simulations of a low NOx LDI combustor for environmentally responsible aviation engines”. In: *Turbine Technical Conference and Exposition GT2015* (2015).

- [45] Kumar, G. and Drennan, S. “A CFD Investigation of Multiple Burner Ignition and Flame Propagation with Detailed Chemistry and Automatic Meshing”. In: *AIAA Propulsion and Energy 2016 Conference 4 of 9* (2016), pp. 20–54. DOI: 10.1081/E-EEE2-120046011.
- [46] Payri, R., Novella, R., Carreres, M., and Belmar-Gil, M. “Study about the influence of an automatic meshing algorithm on numerical simulations of a Gaseous-Fueled Lean Direct Injection (LDI) Gas Turbine Combustor in Non-Reactive conditions”. In: *ILASS - Europe 2019, 29th Conference on Liquid Atomization and Spray Systems*. Paris, France, 2019.
- [47] Payri, R., Novella, R., Carreres, M., and Belmar-Gil, M. “Modeling gaseous non-reactive flow in a lean direct injection gas turbine combustor through an advanced mesh control strategy”. In: *Proceedings of the Institution of Mechanical Engineers, Part G: Journal of Aerospace Engineering* 234.11 (2020), pp. 1788–1810. DOI: 10.1177/0954410020919619.

Chapter 2

Fundamentals of the LDI system

“No problem can be solved from the same level of consciousness that created it”

—Albert Einstein

2.1 Introduction

The present chapter is mainly focused on the fundamentals of the Lean Direct Injection (LDI) concept. Special attention is given both to the swirler and the injection system in Section 2.2, since its coupled performance is critical for the viability and success of the described strategy. In these devices, gas and fuel dispersion, continuous phase turbulence, dispersed phase collisions, evaporation, mixing and combustion co-occur. Furthermore, such phenomena are characterised by different time and spatial scales, and need to be taken into account to achieve a correct prediction of the engine performance. For this reason, in order to improve the quality of the air-fuel mixture and then the combustion efficiency, the dynamics of the swirling flows and the spray formation should be understood entirely. In this way, the equations governing the numerous spray regimes are presented in Section 2.3.

A summary of the physics involved in this turbulent spray process is shown in Figure 2.1 and detailed in Section 2.4. A spray is generally considered as a system of liquid droplets immersed in a gaseous phase. In the particular case

regarding non-reactive two-phase flow studied in the present thesis, the gas turbulence conducts to dispersion or macro-mixing (arrow 1), and the local structure evolves as a consequence of the molecular diffusion or micro-mixing (2), which in turn depends on the turbulent length scales (3). The resulting mass fraction and temperature distributions will be decisive for cases involving combustion (4), where the heat release and expansion alters the turbulent velocity statistics (5). On the other hand, the liquid and gaseous phase turbulence influence each other due to momentum exchange (9). In this way, liquid fuel droplets get dispersed due to droplet turbulence (6) and evaporated (7) due to local temperature and vapour gradients, which in turn are influenced by gas dispersion (11), micro-mixing (13) and the droplet vapour boundary layer thickness, result of the local velocity difference (8 and 10).

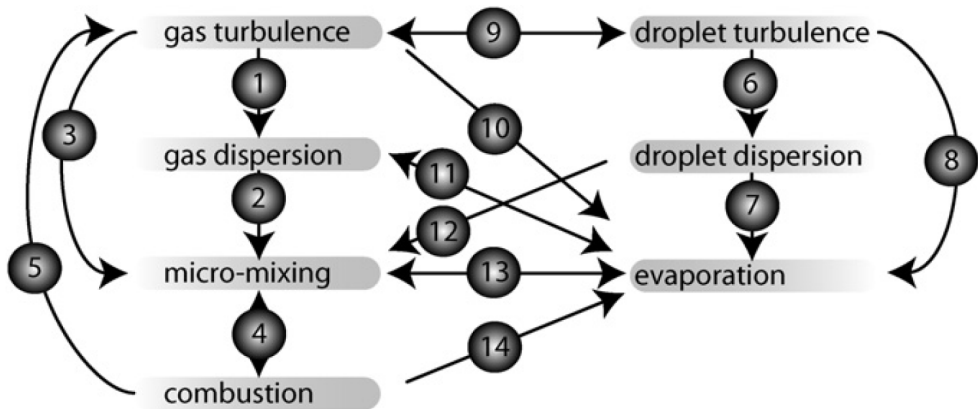


Figure 2.1: Diagram showing the phenomena and interactions occurring in a Lean Direct Injection system [1].

In this context, modelling the fundamental mechanisms and the complexity of the turbulent spray combustion scenario shown in Figure 2.1 stands as a tremendous task¹. Meanwhile, in order to develop and establish advanced modeling and predictive capabilities in LDI burners, it seems reasonable to first aim at progressing in individual non-reactive sub-areas like liquid injection, atomisation and breakup, dispersion, mixing and evaporation, whose theory is described in Section 2.4.

¹Note that essential phenomena such as atomisation and droplet collisions are not included in the diagram of Figure 2.1.

2.2 Lean Direct Injection system

The Lean Direct Injection (LDI) scheme has become a potential low- NO_x alternative to replace the current combustion systems for future gas turbines engines thanks to its substantial reduction in pollutant emissions levels, as introduced in Section 1.1. In this concept, a highly swirling air is admitted into the combustor where the liquid fuel is directly injected at a lean equivalence ratio close to the lean blow-out limit. Therefore, the liquid fuel must be quickly atomised, mixed, vaporised, and ignited directly within the combustion chamber in the shortest distance and time. This requirement highlights the importance of the swirler system (discussed in Section 2.2.1), which plays a crucial role as a turbulence generator. In this way, the turbulent flow promotes the atomisation of the injected liquid jets, the mixing of the atomised sprays and generates a recirculating region downstream of the injection system that considerably increases the flame stability limits. Meanwhile, the existing technologies of liquid injection systems for GT engines are presented in Section 2.2.2.

2.2.1 General Features of Swirling Flows

Swirling flows have been intensely examined outside the field of the turbulent combustion community due to the difficulty to accurately characterise (experimentally or numerically) such complex motions accurately (see the reviews by Sarpkaya [2], Syred et al. [3], Escudier et al. [4, 5], Gupta et al. [6] and Lucca-Negro et al. [7]). In order to understand the injector/swirler dynamics and the air-fuel mixing process in Lean Direct Injection burners it is necessary to know both the key features of swirling spray systems and the parameters that characterise them [8].

The swirling flow within conventional Gas Turbine combustors is typically generated through a tangential injection of the air into an axial flow or by employing inclined vanes. In this way, typical swirler assemblies used in GT burners (shown in Figure 2.2), can include many variants of helical vanes or radial/tangential swirlers to deflect the flow and generate the desired level of air-fuel mixing to reach an efficient combustion. On the one hand, in a helical-vane swirl injector (see Figure 2.2(a)), the fuel is injected into the swirling airflow immediately downstream of the swirler vanes and mixed in the combustion chamber itself. Meanwhile, in a radial swirler (see Figure 2.2(b)), the fuel is delivered from the nozzle placed on the centre of the swirler and eventually dispersed into the radially injected swirling air. Finally, swirl can also be generated by a tangential swirl injector system (i.e., without using

swirling vanes) like the one shown in Figure 2.2(c), in which the airflow is released into a premixing chamber through tangential air slots that span the complete axial length of the premixing chamber.

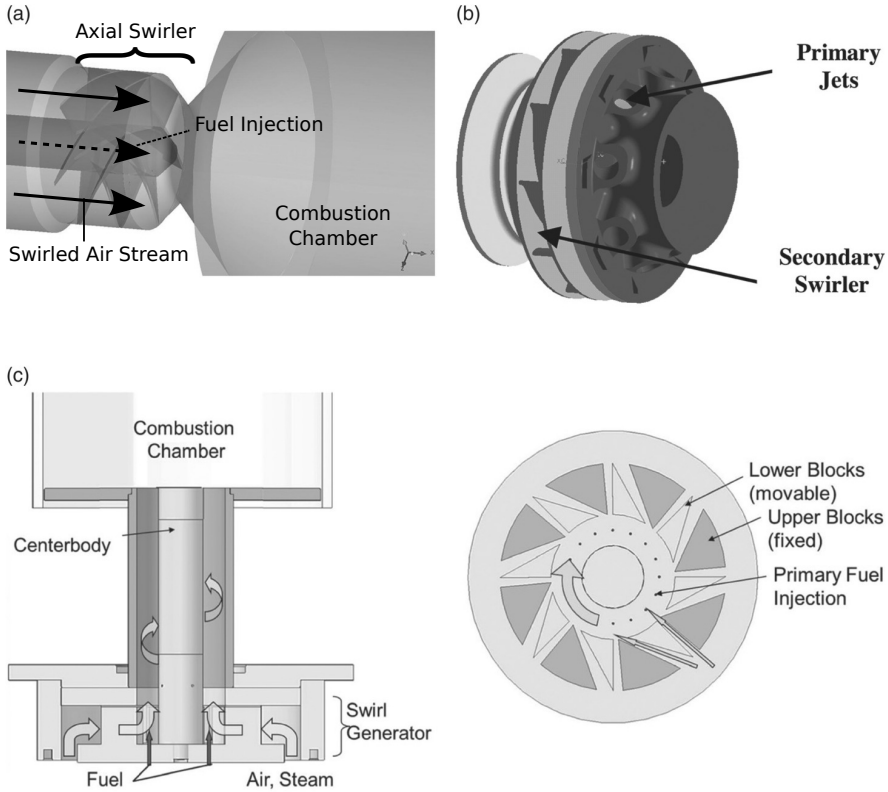


Figure 2.2: Typical swirler assemblies used in GT combustors. (a) Helical-vane swirler (axial swirler) [9]; (b) radial swirler [10]; (c) tangential swirler [11].

In a swirl-stabilised LDI burner, the degree of mixing depends mainly on the intensity of the swirl, quantified by the non-dimensional swirl number S_W . The swirl number was defined by Chigier and Beer [12] (and later simplified by Sheen et al. [13]) as the ratio of the axial flux of the tangential momentum to the product of the axial momentum flux and a characteristic radius:

$$S_W = \frac{G_\theta}{G_x R} \quad (2.1)$$

where the G_θ and G_x are the axial flux of angular momentum and axial momentum, respectively, which can be expressed as:

$$G_\theta = \int_0^R (U_\theta r) \rho U_x 2\pi r dr \quad (2.2a)$$

$$G_x = \int_0^R (U_x) \rho U_x 2\pi r dr + \int_0^R p 2\pi r dr = \int_0^R \rho \left[U_x^2 - \frac{1}{2} U_\theta^2 \right] 2\pi r dr \quad (2.2b)$$

In Eq. (2.2), U_θ and U_x denote the azimuthal and axial velocity components, p is the pressure, and R is the radius of the swirler. The swirl number is a local variable depending on the axial distance from the combustion chamber inlet since it decreases as progressing downstream from the injection plane due to the dissipation. Therefore, it needs to be evaluated at a given axial location. Nevertheless, for comparison purposes and after some simplifications [14], the swirl number can be defined at the swirler exit as:

$$S_W = \frac{2}{3} \tan \phi \quad (2.3)$$

where ϕ is the swirler vane angle. Therefore, since the axial flow in a GT engine is typically determined by operational margins, the swirl number can be only ultimately increased by rising the tangential momentum of the airflow (i.e., increasing the swirler vane angle) rather than by reducing the axial flow.

2.2.1.1 Swirling Flow Structures

Based on the swirl number, swirling flows can be divided into two groups: weak swirling flows ($S_W < 0.6$), in which the axial pressure gradients are insufficient to cause recirculation, and strong swirling flows ($S_W > 0.6$), in which the strong radial and axial pressure gradients near the swirler exit origin a phenomenon known as Vortex Breakdown Bubble (VBB), assisting in the formation of a Central Toroidal Recirculation Zone (CTRZ). The main interests and drawbacks of imposing a swirling motion to the reactive flow in a GT combustor are summarised in Table 2.1. Nevertheless, the turbulent swirling flow also plays a crucial role in the previous non-reactive scenario (as already stated) by promoting both the atomisation of the injected liquid sheets and the mixing and dispersion of the atomised sprays.

The characteristic flow structures typically generated within the combustion chamber (illustrated on Figure 2.3) depend on the swirl number and can be summarised as:

Interests	Drawbacks
To generate large recirculation zones, which:	
1. Improve the combustion process by the velocity fluctuations induced by rotating flow.	1. Extreme rotation can have harmful consequences on a small flame kernel by causing both an excessively high turbulence level and strong shear stress rates at the peripheric boundary of the CTRZ.
2. Have propitious impacts on the propagation mechanisms during both the ignition phase, the flame attachment and the inter-injector propagation.	2. When the CTRZ is extremely wide, the flame can flashback into the injection systems.
3. Have a beneficial effect by pushing the flame kernel upstream thanks to reverse velocity, thus anchoring and stabilising the flame rapidly on the nozzle tip.	3. For high swirl numbers, the CTRZ may oscillate, causing large perturbations (source of combustion instabilities).
4. Locally increase the flow residence time, which helps capturing the hot gas, thus:	
4.1. promoting the combustion process,	
4.2. reducing the size of the combustion chamber.	

Table 2.1: Swirling Flow features in LDI burners.

- **Central Toroidal Recirculation Zone (CTRZ).** This region can be understood as the cornerstone of recent designs of GT combustion chambers. The CTRZ appears for high swirl numbers (typically above 0.6) and is usually established along the swirler axis. The formation of a CTRZ is the result from both the radial pressure gradient generated by the swirled vane-guided rotating flow, which presents a significant azimuthal velocity component, and the flow expansion through the swirler outlet region (combustion chamber inlet). In this way, the radial pressure radial gradient and axial velocity component decay as a consequence

of the expansion, thus generating a negative axial pressure gradient involving reverse flow [6, 15, 16].

- **Corner Recirculation Zones (CRZ)**. In confined configurations of LDI burners, the abrupt flow expansion at the swirler outlet region is partially regulated by recirculating flow bubbles which are potentially present at the outer corners [3, 6].
- **Precessing Vortex Core (PVC) and Vortex Breakdown Bubble (VBB)**. The central vortex core located both in the internal passages of the swirler and within the CTRZ becomes destabilised under particular conditions (still unpredictable and not completely understood) giving rise to the PVC [6]. The VBB can be described as the formation of a free stagnation point and a recirculation zone with a surrounding 3D spiral flow in the core. When the central vortex core starts precessing around the combustor axis of symmetry at a given frequency, it produces hydrodynamic instabilities. The frequency of precession is a function of the combustor design and the swirl intensity at the inlet. This unstable mode, typically related to the VBB, can be defined as the Precessing Vortex Core (PVC). The PVC structure coincides with a vorticity helical-shaped tube usually located at the periphery of the CTRZ and induces a highly local flow rotation in the direction of the swirl motion. Besides, this resulting instability can provoke significant oscillations of the CTRZ in both axial and tangential directions, being at the same time highly dependent on the overall CTRZ and CRZ interactions [17].

Meanwhile, a rotation time scale associated with the PVC can be defined to identify some unsteady flow structures, as shown in Eq. (2.4):

$$\tau_{rot} = \frac{2\pi R_i}{U_{\theta,i}} \quad (2.4)$$

where R_i is the mean radius of the convergent inlet and $U_{\theta,i}$ is the mean tangential (azimuthal) velocity component in the inlet plane of the combustion chamber.

2.2.2 Injection Systems in Gas Turbine Combustors

Spray nozzles can be classified based on resulting spray features (discussed in Section 2.4.2), such as mass flow rate, liquid mass distribution, spray pattern,

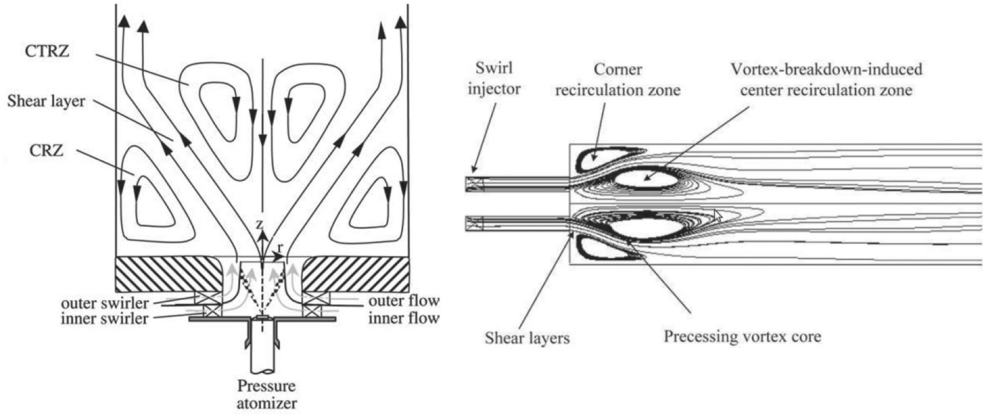


Figure 2.3: Characteristic flow features present in a swirl injection system [14].

spray angle, spray impact, and droplet size. The fuel delivery system of an aircraft gas turbine engine must accomplish the following general tasks:

- To deliver the required amount of fuel into the combustion chamber in an uninterrupted way.
- To enhance the atomisation phenomenon in order to increase the air-fuel interface surface thus accelerating the fuel evaporation process.
- To develop an air-fuel mixture to optimize engine performance under several operating conditions.

Therefore, the final objective of the injection system is to generate a cloud of fuel droplets that maximizes the surface of contact between the liquid fuel and the gas-phase, thus enhancing mass and heat exchanges, promoting evaporation in turn. To achieve this, a highly turbulent area is generated in the region near the injection that facilitates atomisation and mixing phenomena. This can be achieved by different mechanical processes, giving rise to the various existing technologies providing different types of spray patterns [18–20]:

- **Pressure atomisers.** This typology takes advantage of the difference in pressure between the pressurized fuel line and the combustion chamber to force the swirling liquid film to emanate through a small hole resulting

in liquid fragmentation. This is achieved forcing the fluid into a rotational motion by fitting a swirl chamber before dispensing it from the nozzle. The main variations of pressure atomisers are shown on the left side of Figure 2.4, including plain-orifice, simplex, duplex, dual-orifice, fan spray and spill return nozzles. The main advantage is that the degree of atomisation achieved is not a function of the air flow (i.e., the final droplet size is independent of the engine's operating conditions). On the contrary, among the disadvantages is the possible obstruction of the injection holes due to their small size, requiring adjacent pressurization systems that increase the complexity and weight of the engine.

- **Twin-fluid nozzles.** In these nozzles, a high-velocity airflow is conducted in contact with a liquid stream, either within the nozzle (internal mix) or outside of the nozzle (external mix). Twin-fluid nozzles can be classified depending both on the airflow rate (air velocity and quantity) used in the atomising process and the way it is contacted with the liquid. These variations are shown on the right side of Figure 2.4, including air-blasting (e.g., simple, pre-filming and plain-jet air-blasts), air-assisting (e.g., internal mixing and external mixing) and effervescent [21] nozzles. The most commonly employed in GT combustors is the pre-filming air-blast, which employs a simple concept whereby fuel at low pressure impacts into internal passage walls, and the resulting liquid film (driven by the airflow towards an atomising lip) is disintegrated into small droplets. Nevertheless, since this technology relies on the air momentum to atomise the fuel, it can be too low to ensure a proper atomisation at low power operation (e.g., during in-flight relight).
- **Vaporisers.** These are pipes located in the primary zone of the combustion chamber through which evaporated fuel is injected due to the high heat flux from the flame. In more recent variants, the fuel and air are mixed and heated within the vaporiser, so most of the mixture leaves the vaporiser as a collection of droplets impinging on the primary zone of the combustor where they are finally heated and vaporised by the high temperatures. Nevertheless, this can be highly detrimental to the tube lifetime due to the high thermal stresses to which it is subjected.

The small droplets resulting from the primary atomisation and breakup processes are then mixed by the turbulent flow generated by the swirler system, thus promoting partially-premixed and pollutant-free combustion. The injection system employed in the present numerical investigation consists of a

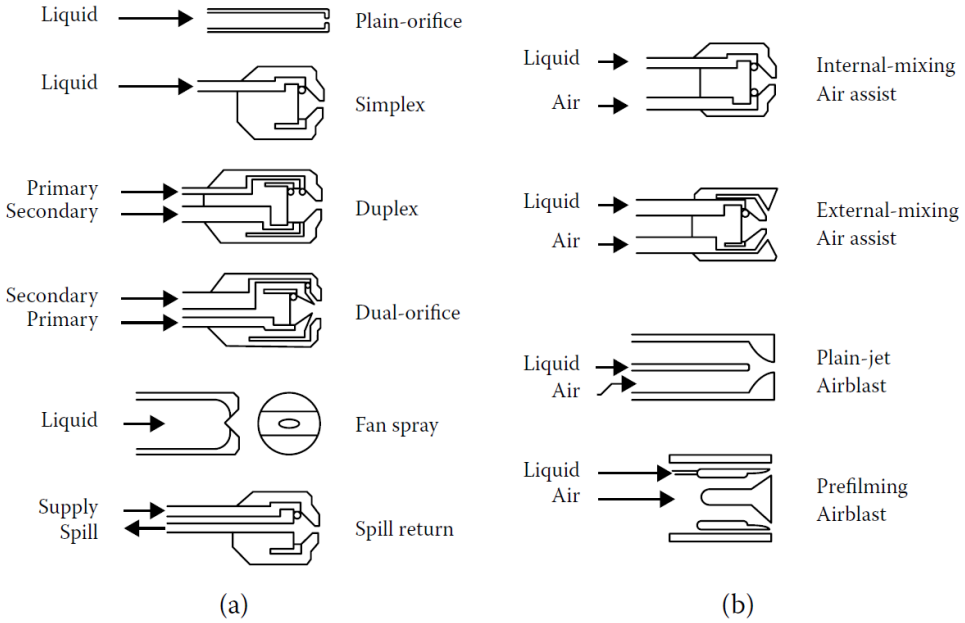


Figure 2.4: Schematic for (a) pressure atomisers and (b) twin-fluid atomisers [18].

simplex pressure swirl atomiser replicating the experimental test rig considered for the model validation. For further details on the types of atomisers, the reader may also refer to the works by Lefebvre [18] and Ashgriz [20].

2.3 Governing Equations

Sprays commonly found in an LDI burner can be considered as a system of droplets immersed in a gaseous phase. In this context, sprays belong to a specific type of two-phase flow (Section 2.3.1), which includes a gaseous phase as the continuum (Section 2.3.2) and a liquid phase as a discrete form (Section 2.3.3). The equations governing the numerous spray regimes are briefly described as follows.

2.3.1 Two-Phase Spray Characteristics

The essential spray regimes found in the liquid fuel injection from a single hole atomiser are summarised in Figure 2.5, where they are classified depending on the volume fraction occupied by the disperse phase. It can be seen that

near the injector nozzle, in a region typically known as dense spray regime, the dispersed phase fills a significant volume fraction (above 10^{-3}) of the two-phase mixture. In this region, dynamics are dominated by the discrete phase and droplet collision and coalescence occur frequently. Meanwhile, in the intermediate regime, the dispersed phase volume fraction ranges between 10^{-6} and 10^{-3} , and the drop size is reduced due to drop breakup and evaporation phenomena. Finally, in the dilute spray regime, droplet collisions can be neglected since the drops become isolated with negligible mass and volume (i.e., dispersed phase volume fractions lower than 10^{-6}) compared to that of the surrounding gas. Hence, some isolated drop correlations [22] can be used here to characterise the mass, momentum and energy exchanges between liquid and gaseous phases.

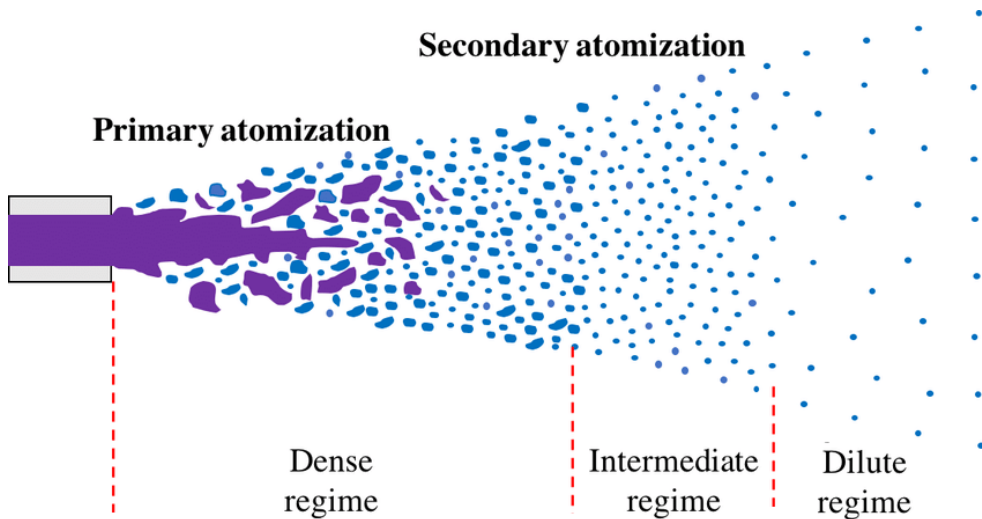


Figure 2.5: Schematic representation of spray regimes for liquid injection from a single hole nozzle [23].

In regions concerning the dilute spray regime, the drops can be tracked using the spray equation [22], discussed in Section 2.3.3. In this way, the evolution of a droplet is described through the droplet distribution function f_d , which has 9 independent variables: three drop position coordinates \mathbf{x} , three velocity components \mathbf{v} , the drop radius r , the drop temperature T_d and the time t . Therefore,

$$p_{DN} = f_d(\mathbf{x}, r, \mathbf{v}, T_d, t) d\mathbf{x} dr d\mathbf{v} dT_d \quad (2.5)$$

is the probable drop number per unit of volume located in the physical space between $(\mathbf{x}, \mathbf{x} + d\mathbf{x})$ and time t with drop radii in the interval $(r, r + dr)$, velocity in the interval $(\mathbf{v}, \mathbf{v} + d\mathbf{v})$ and temperatures in the interval $(T_d, T_d + dT_d)$. Note that the temperature is considered uniform within the drop. The total fraction of volume occupied by the gaseous phase (i.e., the gas-phase void fraction, θ_g) can be computed in the intermediate and dilute regions by integrating the liquid volume (i.e., the dispersed-phase volume V_d) over all the drops:

$$\theta_g = 1 - \int_{V_d} \left(\iiint \frac{4}{3} \pi f_d dr d\mathbf{v} dT_d \right) dV_d / V_d \quad (2.6)$$

On the other hand, in the intermediate spray regime shown in Figure 2.5 the drops can affect the state of the gas and, even though their discrete volume fraction is still low, they have a significant mass compared to the gas-phase.

Finally, in the dense spray regime, the liquid volume fraction is much higher, and the effects of the drops interactions (i.e., collisions and coalescence) become important, thus influencing the exchange rates. Here, there is a need to make a distinction between the *primary atomisation* region, where intact liquid core starts to disintegrate into ligaments, and the *secondary atomisation* region, where the ligaments complete the breakup phenomenon into a spray. O'Rourke [24] suggested a practical definition for the transition between the *primary* and *secondary atomisation* regions of the dense regime when $\theta_g < 0.9$. Nevertheless, the applicability of the coupling terms between liquid and gaseous phases in this region is not clear yet. Furthermore, there is no current single model that can handle the entire breakup process, and thus most spray simulations model the spray from its characteristics in the intermediate or dilute regime.

2.3.2 Gas-Phase Equations

The dynamics of a gaseous fluid flow are governed by equations that describe the conservation of mass, momentum and energy, supplemented by ad-hoc equations to describe the turbulence. Meanwhile, the interactions between the liquid and gaseous phases are accounted for by considering exchange functions through source terms.

On the one hand, in the absence of spray drops, the gas-phase mass conservation can be written as:

$$\int_{V_g} \left(\frac{\partial \rho_g}{\partial t} + \nabla \cdot (\rho_g \mathbf{u}) \right) dV_g = 0 \quad (2.7)$$

where ρ_g and \mathbf{u} are the gas density and velocity, respectively. Note that when the liquid drops are not present, the volume occupied by the gas (V_g) represents the total volume (V_T).

On the other hand, when liquid drops are present, the differential form of the gas-phase mass conservation equation can be expressed as follows:

$$\int_{V_T} \left(\frac{\partial \rho}{\partial t} + \nabla \cdot (\rho \mathbf{u}) \right) dV_T = - \int_{S_d} \rho_g (\mathbf{u} - \mathbf{w}) \cdot \mathbf{n}_d dA \quad (2.8)$$

where ρ is the gas mass per unit volume of the mixture, S_d refers to the inner surfaces of the control volume in contact with the drops, \mathbf{w} is the gas-liquid interface velocity and dA is an element of total surface area. Here, the total volume is V_T , consisting of the volume of the gas (V_g) and the volume filled by the drops (V_d). The source/sink of gas mass due to evaporation/condensation of the drops is denoted by the integral of the right-hand side of Eq. (2.8). This change of liquid mass due to drop evaporation can be calculated considering the hypothesis of spherical drops as:

$$\frac{\partial}{\partial t} \left(\frac{4}{3} \pi r^3 \rho_l \right) = \int_{Surf_d} \rho_l (\mathbf{w} - \mathbf{v}) \cdot \mathbf{n}_d dA \quad (2.9)$$

where ρ_l is the liquid density, \mathbf{v} is the drop velocity, and integration is performed over the drop surface. From mass conservation, the right-hand sides of Eqs. (2.8) and (2.9) must be equal. When Eq. (2.9) is summed over all of the drops and constant liquid density is assumed, Eq. (2.8) becomes the final form of the mass conservation equation, which can be written as follows:

$$\frac{\partial \rho}{\partial t} + \nabla \cdot (\rho \mathbf{u}) = - \iiint \rho_l 4\pi r^2 \dot{R} f_d dr dv dT_d \quad (2.10)$$

where \dot{R} is the time rate of change of drop radius r , and T_d is the drop temperature.

Similar derivations can be followed for the momentum and the energy conservation equations. The linear momentum conservation for a single droplet can be expressed as:

$$\frac{4}{3} \pi r^3 \rho_l \mathbf{F} = \int_{Surf_d} [\rho_g (\mathbf{u} - \mathbf{v})(\mathbf{v} - \mathbf{w}) \cdot \mathbf{n} - p_g \mathbf{n} + \tau_g \cdot \mathbf{n} + \sigma_l \nabla \cdot \mathbf{n}] dA \quad (2.11)$$

where \mathbf{F} is the drop acceleration, τ_g and p_g are the viscous stress tensor and the thermodynamic pressure of the of the gas-phase, respectively.

Similar considerations for the energy conservation of a single drop give place to terms that account both for the energy required to heat the drop and for the work associated with the normal stresses and heat transfer. These source terms are further described in Section 2.3.3.

On the other hand, the mass conservation equation can be generalized for a mixture of reacting gases. In this way, the equation for species m and its corresponding source terms arising from the evaporated spray and chemical reactions can be described as:

$$\frac{\partial \rho_m}{\partial t} + \nabla \cdot (\rho_m \mathbf{u}) = \nabla \cdot \left[\rho D \nabla \cdot \left(\frac{\partial \rho_m}{\rho} \right) \right] + \dot{\rho}_m^c + \dot{\rho}^s \delta_{m1} \quad (2.12)$$

where ρ_m is the mass density of species m , ρ is the total mass density, D is the diffusion coefficient, $\dot{\rho}_m^c$ is the source term due to chemical reactions, and $\dot{\rho}^s \delta_l$ corresponds to the source term due to the evaporation of the species, where δ_l is the Kronecker delta function referred to the liquid-phase.

The momentum conservation equation for the fluid mixture can be expressed including the turbulence modelling as follows:

$$\frac{\partial \rho \mathbf{u}}{\partial t} + \nabla \cdot (\rho \mathbf{u} \mathbf{u}) = -\nabla p - \nabla \cdot \left(\frac{2}{3} \rho k \right) + \nabla \tau + F^s + \rho g \quad (2.13)$$

where P is the fluid pressure, k is the turbulent kinetic energy, τ is the total (laminar + turbulent) viscous stress tensor, F^s is the rate of momentum increment per unit volume because of the spray, and g is the body force, which is assumed to be constant. The viscous stress tensor can be related to the diffusion coefficient (D) and written in Newtonian form as follows:

$$\tau = \rho D \left[\left(\nabla \mathbf{u} + \nabla \mathbf{u}^T \right) - \frac{2}{3} \nabla \cdot \mathbf{u} \mathbf{I} \right] \quad (2.14)$$

where \mathbf{I} is a unit dyadic.

Finally, the energy conservation equation can be described as:

$$\frac{\partial \rho I}{\partial t} + \nabla \cdot (\rho \mathbf{u} I) = -P \nabla \cdot \mathbf{u} - \nabla \cdot J + \rho \varepsilon + \dot{Q}^c + \dot{Q}^s \quad (2.15)$$

where I is the specific internal energy, J is the heat flux vector, ε is the turbulent dissipation rate, and \dot{Q}^c and \dot{Q}^s are the source terms related to chemical reactions (i.e., heat release) and spray interactions, respectively.

The effects concerning the turbulent heat conduction and enthalpy diffusion are considered in the heat flux vector J , which can be expressed as follows:

$$J = -\lambda \nabla T - \rho D \sum_m h_m \nabla(\rho_m/\rho) \quad (2.16)$$

where λ is the thermal conductivity, T is the gas temperature, and h_m is the specific enthalpy of species m .

The transport of mass, momentum, and energy is severely influenced by the diffusion term D , as can be inferred from Eq. (2.12) to (2.16), which in turn is related to the transport of turbulent kinetic energy k and its corresponding dissipation rate ε as follows:

$$D = C_\mu \frac{k^2}{\varepsilon} \quad (2.17)$$

where C_μ is a constant. Both the turbulent kinetic energy and its dissipation rate need to be modelled by selecting a suitable turbulence model. The classical turbulence approaches available for turbulent flow computations are described in Chapter 4.

2.3.3 Discrete-Phase Equations

The governing equation of the discrete phase [22], also known as spray equation, describes the evolution of the droplet distribution through a distribution function f , which represents the probable number of droplets as follows:

$$P_{DN} = f(\mathbf{x}, r, \mathbf{v}, T_d, y, \dot{y}, t) d\mathbf{x} dr d\mathbf{v} dT_d dy d\dot{y} \quad (2.18)$$

In this way, the distribution function has 11 independent variables: three drop position coordinates \mathbf{x} , the drop radius coordinate r , three velocity components \mathbf{v} , the drop temperature T_d , the drop distortion y , the rate of change of drop distortion \dot{y} , and time t .

The time rate of change of the distribution function f can be obtained by solving a form of the spray equation, as follows:

$$\frac{\partial f}{\partial t} + \nabla_{\mathbf{x}} \cdot (f\mathbf{v}) + \nabla_{\mathbf{v}} \cdot (f\mathbf{F}) + \frac{\partial}{\partial r}(fR) + \frac{\partial}{\partial T_d}(f\dot{T}_d) + \frac{\partial}{\partial y}(f\dot{y}) + \frac{\partial}{\partial \dot{y}}(f\ddot{y}) = \dot{f}_{coll} + \dot{f}_{bu} \quad (2.19)$$

where the quantities \mathbf{F} , R , \dot{T}_d and \dot{y} are the time rates of changes of velocity, radius, temperature and oscillation velocity (\dot{y}) of an individual droplet, respectively. Meanwhile, the source terms originated from droplet collision and breakup are referred as \dot{f}_{coll} and \dot{f}_{bu} , respectively.

By solving the spray equation, the exchange functions $\dot{\rho}^s$, F^s , and \dot{Q}^s can be calculated by summing the rate of mass, momentum and energy for all the drops existing in the spray at position \mathbf{x} and time t . Then, it can be used in the mixture equations of mass -Eq. (2.12)-, momentum -Eq. (2.13)- and internal energy -Eq. (2.15)- conservation presented in Section 2.3.2.

The mass source term $\dot{\rho}^s$ is introduced by the vaporization of the spray, and can be written as follows:

$$\dot{\rho}^s = - \int f \rho_l 4\pi r^2 R \, d\mathbf{v} \, dr \, dT_d \, dy \, d\dot{y} \quad (2.20)$$

Meanwhile, the exchange function F^s , arising from force of the droplet to the gas due to droplet drag, can be expressed as:

$$F^s = - \int f \rho_l \left(\frac{4}{3} \pi r^3 \mathbf{F}' + 4\pi r^2 R \mathbf{v} \right) \, d\mathbf{v} \, dr \, dT_d \, dy \, d\dot{y} \quad (2.21)$$

where $\mathbf{F}' = \mathbf{F} - g$.

Finally, the source term \dot{Q}^s accounts both for the energy release from the evaporating drop to the gas, the heat transfer into the drop, and the work done by turbulent fluctuations, and can be computed as:

$$\dot{Q}^s = - \int f \rho_l \left[4\pi r^2 R \left[I_l + \frac{1}{2} (\mathbf{v} - \mathbf{u})^2 \right] + \frac{4}{3} \pi r^3 \left[c_l \dot{T}_d + \mathbf{F}' \cdot (\mathbf{v} - \mathbf{u} - \mathbf{u}') \right] \right] \, d\mathbf{v} \, dr \, dT_d \, dy \, d\dot{y} \quad (2.22)$$

where I_l and c_l are the internal energy and specific heat of liquid drops, respectively. The term $(\mathbf{v} - \mathbf{u})$ corresponds to the relative velocity between the liquid droplet and gas (previously denoted as \mathbf{w}), and \mathbf{u}' is the turbulent velocity of the gas-phase.

2.4 Spray Formation

Sprays are commonly defined as two-phase flows, consisting of systems of droplets (liquid phase) immersed into a continuum (gaseous phase). In Gas

Turbine burners, liquid fuel sheets can be injected through several pressure swirl or air-blast nozzles, as introduced in Section 2.2.2. Nevertheless, given that the typical liquid fuels are not sufficiently volatile to produce the required volume of vapour for combustion, they need to be atomised into a large number of droplets. In this way, the aerodynamic forces cause the disintegration of the liquid sheets, first into ligaments (*primary atomisation*), and then into droplets (*secondary atomisation* or secondary breakup). Breakup occurs when the magnitude of the disruptive force just exceeds the consolidating surface tension force [25]. Finally, the fuel droplets evaporate and the gaseous fuel is mixed with the air to produce a suitable mixture.

The atomisation process considerably influences the spray dispersion and evaporation rate by increasing the total surface of the liquid fuel, which in turn affects significantly the combustion process. It is therefore clear that the degree of atomisation and evaporation plays a crucial role in the performance of an LDI burner. In these possible scenarios related to turbulent spray combustion, the spray quality is expected to affect the stability limits, combustion efficiency and pollutant emission levels.

Thus, a detailed understanding of the fundamentals of the existing spray regimes and sub-processes (Section 2.4.1) is mandatory. However, there exists a substantial lack of knowledge concerning specific details of the spray development. This lack of knowledge arises from the spray complexity, making it difficult to experimentally capture or computationally resolve all regimes associated to the breakup process, even in simple canonical problems [26]. These complications can be attributed to both the extreme operating conditions, the geometrical complexity of injectors, and the difficulties arising by dense spray measurements. Meanwhile, the essential spray characteristics, such as the shape and penetration of the spray, drop velocity, and drop size distribution are discussed in Section 2.4.2.

2.4.1 Spray Sub-processes

This section briefly discusses the basic principles of various sub-processes associated to the spray phenomena, including the atomisation and drop breakup, drop drag and deformation, turbulent dispersion, drop collision and coalescence, and spray evaporation.

2.4.1.1 Atomisation Process

The atomisation process is responsible for transforming the bulk liquid emerging from the injector into small drops by disrupting the consolidating surface

tension. This phenomena consists first in the destabilisation of the liquid film because of the growth of initially small disturbances over the liquid surface to generate ligaments and large drops (*primary atomisation*), and then on the subsequent rupture of these ligaments in smaller drops (*secondary atomisation* or *secondary breakup*). In this way, the joint action of these two atomisation processes define the particular properties of the fuel spray, including size, distribution, and velocity of liquid drops.

Primary Atomisation

The *primary atomisation* process and subsequent development of the liquid sheet are governed mainly by the relative velocity between the liquid and the surrounding gas-phase and the physical properties of both fluids. When increasing the initial velocity of the liquid sheet emerging from an atomiser (by increasing the operating pressure), the sheet is expanded against the consolidating surface tension force. In this condition, a leading-edge is formed at a given axial position from the injection plane where the equilibrium between inertial and surface tension forces is reached.

According to the study conducted by Fraser and Eisenklam [27] about liquid sheets, three different primary atomisation modes may be distinguished depending on the velocity of the liquid at the atomiser outlet, described as *rim*, *wave*, and *perforated-sheet* disintegration regimes.

For low injection velocities, surface tension forces cause the free edge of the liquid sheet to contract into a thick rim, promoting the sheet rupture into droplets by a mechanism resembling the disintegration of a free jet (*rim mode*). As can be seen on the left side of Figure 2.6, the resulting drops remain to move in the injected direction but staying connected to the sheet surface through small filaments that further break up into ordered files of drops. This kind of atomisation tends to produce both large size droplets and multiple small satellite droplets.

For higher injection velocities, the emergence and growth of wave motions on the sheet surface, which corresponds to a half or full wavelength of the oscillation, cause some areas of the sheet to turn away before the leading edge is formed (*wave mode*). Both the air action and liquid turbulence disintegrate these areas, which immediately get contracted due to the surface tension, precluding the establishment of a regular system of threads, as shown in center of Figure 2.6. In these conditions, the disintegration is extremely irregular, and thus drop sizes are much more diverse.

Finally, for very high injection velocities, many holes emerge in the sheet and are outlined by rims generated from the liquid that was inserted initially

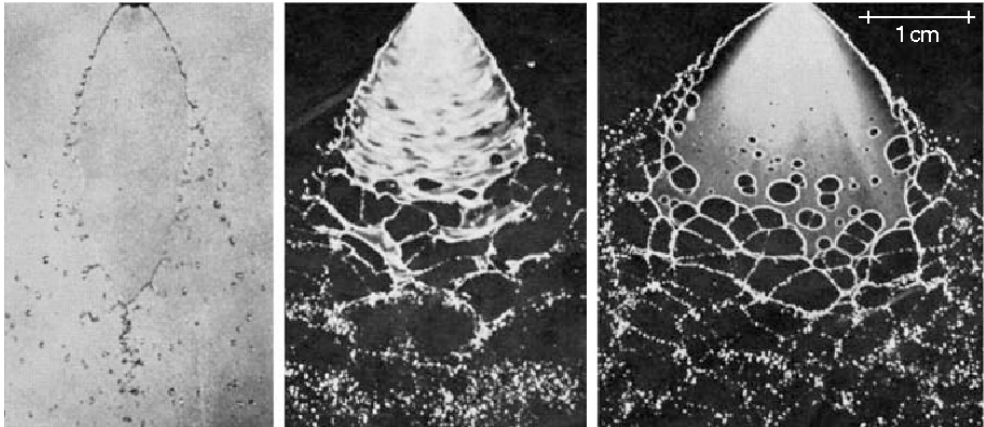


Figure 2.6: Picture showing the three primary atomisation regimes: rim (left), wavy (center) and perforated-sheet (right) modes.

inside (*perforated-sheet mode*). These holes proliferate in dimension until the rims of nearby holes coalesce, thus originating the irregular ligaments shown on the right side of Figure 2.6, which subsequently break up into varying-size droplets.

In general, pressure-swirl atomisers discharging fuel in the form of liquid sheets frequently manifest all these three disintegration modes (even co-occurring), whose relative magnitude dictates the resulting drop size distribution. For instance, Dombrowski, Eisenklam, Fraser, and co-workers [27–33] contributed in the 50s and 60s to give valuable insight into the mechanisms of liquid sheet disintegration by means of a large number of experiments including a wide variety of liquids. In this way, they established that the holes in the liquid sheet are the main precursors of ligaments, concluding that (1) liquid sheets with high surface tension and viscosity are most resistant to disruption and (2) the effect of liquid density on sheet disintegration is negligibly small [28].

More recently, many formulations have been proposed for flexible design tools, based on linear stability analysis or more complex forms that account for both non-linear temporal and spatial waves. The literature in this area is extensive, so for more detailed information on this topic, the reader may refer to the work by Sirignano et al. [34, 35], Senecal et al. [36], Lin [37], and Dumouchel [38]. Some of these formulations will be further discussed in Section 4.2.3, where some liquid-phase models that have given rise to implementation in numerical simulations are presented.

Secondary Atomisation

Once the initial liquid sheet disintegration has formed a collection of ligaments and droplets, the spray atomisation continues governed by the same balance of forces already explained, producing the so-called *secondary atomisation* or secondary break-up. Nevertheless, this disruption process is remarkably different due to the difference in the shape of the droplets.

In this force balance, the relative velocity between the fuel drops and the surrounding air (i.e., the aerodynamic force) tends to break these droplets into new smaller drops. On the opposite side, the forces associated to the surface tension tend to retain the original spherical shape of the drop. Therefore, higher relative velocities are required to disintegrate the smaller droplets because of their high curvature and surface tension.

A quantitative characterisation of the mechanisms involved in the drop breakup processes can be stated based on the Weber number (We). In this way, the Weber number can be defined as the ratio between the aerodynamic disruptive forces and the consolidating surface tension force, as shown in Eq. (2.23):

$$We = \frac{\rho_g \|\mathbf{w}\|^2 d_l}{\sigma_l} \quad (2.23)$$

where ρ_g is the density of the gaseous-phase (air), \mathbf{w} denotes the relative velocity between the liquid fuel and the surrounding air introduced in Section 2.3.2, σ_l represents the surface tension at the boundary among the liquid and the gas, and d_l is the diameter of the liquid drop.

In this scenario, an initial condition for drop breakup can be established when the aerodynamic drag is just equal to the consolidating surface tension force, thus defining a critical Weber number acting as a threshold for the onset of drop breakup:

$$C_D \frac{1}{2} \rho_g \|\mathbf{w}\|^2 \frac{\pi}{4} d_l^2 = \pi d_l \sigma_l$$

$$We_{crit} = \left(\rho_g \|\mathbf{w}\|^2 d_l / \sigma_l \right)_{crit} = 8 / C_D \quad (2.24)$$

where C_D denotes the drag coefficient of the droplet.

Meanwhile, the Ohnesorge dimensionless number (Oh) was defined according to Eq. (2.25) as the ratio between the viscous and both inertial and surface tension forces in order to account the liquid viscosity on drop breakup:

$$Oh = \frac{\sqrt{We}}{Re} = \frac{\mu_l}{\rho_l \sigma_l d_l} \quad (2.25)$$

where Re is the Reynolds number, and μ_l , ρ_l are the liquid viscosity and density, respectively.

Based on the Weber number, secondary atomisation regimes have been traditionally classified into five main groups [39–43], as depicted in the Figure 2.7, which are contained into two different stages: first stage and second stage. On the one hand, all the drops in the first stage undergo (regardless of their atomisation regime) a disk-shaped profile as a consequence of non-uniform air velocity and pressure distributions throughout the drop surface. At this stage, the drop further flattens with an increase in Bernoulli pressure difference, and finally forms a disk-shaped profile. On the other hand, during the second stage, the distorted droplets experience different disintegration depending on the breakup regime.

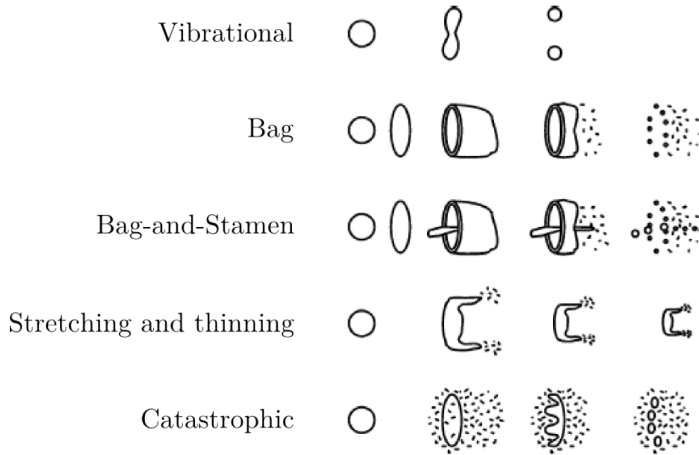


Figure 2.7: Scheme of secondary atomisation regimes according to Wierzba [40]

Following the classification in Figure 2.7, for $Oh \leq 1$ and $We < 12$, aerodynamic forces provoke only slight distortions and oscillations that are not able to break the drops, limiting their effect to small perturbations on its shape.

However, a small increment in the relative velocity would propitiate the first breakup regime (i.e., *vibrational* atomisation), in which the deformation of the droplet surface progressively grows up until causing its division.

During the second breakup regime (i.e., *bag* breakup, corresponding to $12 \leq We \leq 20$), flow separation around the deformed drop leads to a positive pressure difference between the leading stagnation point and the wake. This tends to blow the center of the drop downstream resulting in the formation of the bag, while the outer edge forms a toroidal ring to which the bag is attached [44], ending up with disintegration in many small droplets [45]. Meanwhile, the third breakup regime holds a strong resemblance, with the only difference that a ligament is generated inside the bag giving place to new droplets of relatively large size.

In the fourth breakup regime (i.e., sheet *stretching and thinning*, for $We \leq 100$), ambient phase inertia causes the continuous formation of a sheet at the drop periphery [43], which rapidly evolves into ligaments, and disintegrates into a multitude of small droplets. This process remains until the droplet is entirely fragmented, or until it has accelerated to the point at which aerodynamic forces are negligible. In this last case, a core drop remains after secondary atomisation [46].

Finally, in the fifth breakup regime (i.e., *catastrophic* breakup, for $We > 100$), unstable surface Rayleigh-Taylor waves are generated on the leading edge of the deformed drop due to the acceleration of the dense drop into the lighter ambient [47]. These waves produce a small number of large ligaments that, in turn, break up into smaller fragments.

Nonetheless, although progress has been made in characterising the atomisation process, there is still much uncertainty about the breakup regimes, atomisation mechanisms and fluctuations in the liquid-gas interface in cases concerning high speed drops. In fact, as the air velocity increases, aerodynamic instabilities, turbulence and viscous effects become more important and the process becomes even more difficult to characterise. Therefore, further investigation on this topic is still required. Even so, many analytical models have been developed to try to predict drop breakup behavior, among which are the Taylor Analogy Breakup (TAB) model [48], ETAB [49], Droplet Deformation Breakup Model [50], and the Unified Spray Breakup (USB) model [51]. Some of these formulations will be further discussed in Section 4.2.3, where numerical models used in this thesis are presented. For further details on these models, the reader may also refer to the work by Ashgriz [52].

2.4.1.2 Drop Drag and Deformation

Liquid properties such as the spatial location, velocity, and penetration of a given drop in the continuum gas-phase are influenced by the experimented acceleration, which in turn, depends on the drop drag. Furthermore, drops are subjected to shape variations during the breakup process, resulting in a dynamic behaviour of the drop drag, which can also affect the properties of the gas medium. Therefore, these drag variations need to be considered during the drop breakup phenomena to correctly predict the drop and gas properties.

Drop drag is usually quantified by the drag coefficient C_D , which was introduced in Eq. (4.39a). For thin sprays considering spherical drops, the C_D can be determined as a function of the drop Reynolds number [53]:

$$C_{D,sphere} = \begin{cases} \frac{24}{Re_d} \left(1 + \frac{1}{6} Re_d^{2/3}\right), & Re_d \leq 1000 \\ 0.424, & Re_d \geq 1000 \end{cases} \quad (2.26)$$

On the other hand, the drop drag coefficient for thick sprays and $Re_d \leq 1000$ can be written, according to O'Rourke [24, 54], as:

$$C_{D,sphere} = \frac{24}{Re_d} \left(\theta_g^{-2.65} + Re_d^{2/3} \theta_g^{1.78} / 6 \right) \quad (2.27)$$

where θ_g is the local void fraction.

Meanwhile, the drop drag coefficient can be affected at given conditions involving high relative velocities because of the oscillation and distortion of the drops during the breakup process [53, 55]. At such conditions, the oscillation amplitude is considered in the C_D calculation as follows:

$$C_D = C_{D,sphere} (1 + 2.632y) \quad (2.28)$$

where y is the drop distortion from sphericity. Once the breakup process has started, the drop distortion can be calculated from the spring-mass analogy equation:

$$\frac{d^2y}{dt^2} = \frac{2}{3} \frac{\rho_g \mathbf{w}^2}{\rho_l r^2} - \frac{8\sigma_l}{\rho_l r^3} y - \frac{5\mu_l}{\rho_l r^2} \frac{dy}{dt} \quad (2.29)$$

where $\frac{dy}{dt}$ denotes the oscillation velocity (\dot{y}), and $\frac{d^2y}{dt^2}$ is the time rate of change of \dot{y} (\ddot{y}).

As a consequence, in the limit of no drop distortion (i.e., $y = 0$) the drag coefficient computed from Eq. (2.28) corresponds to that of a spherical drop. On the other hand, at maximum distortion levels (i.e., $y = 1$), a drag coefficient of a disk (about 3.6 times higher than $C_{D,sphere}$) is obtained. Therefore, the drag coefficient of a given distorting drop during the breakup process can be found among the drag coefficient of a sphere and a disk.

2.4.1.3 Drop-Turbulence Interactions

The dispersion of liquid drops into a turbulent gas-phase results in a modulation of the turbulence intensity associated to the large scale vortical structures of the carrier phase. These drop-turbulence interactions occur principally due to the modification of both the turbulence properties by the motion of drops and the inter-phase transport rates by turbulent fluctuations. In this way, a part of the turbulent gaseous kinetic energy is consumed to disperse the spray drops [56]. Nevertheless, the wakes generated by large drops (i.e., drops larger than one-tenth of the turbulent integral scale) can also act as a source of turbulent energy and thus increase the gaseous turbulent kinetic energy [57]. Therefore, the magnitude of these opposite effects needs to be evaluated in order to determine the overall result in terms of the modification of the turbulence levels [58].

Based on experimental observations, it was demonstrated that the organised rotating motion of the large-scale structures could enhance the dispersion of intermediate size particles [57]. Furthermore, it was observed that small drops had a tendency to follow the large-scale gaseous vortex structures, whereas the larger drops left the large eddies [59]. The relevance of these features is described by the Stokes number (St), which is defined as a ratio of the aerodynamic response time of a droplet suspended in a flow field and the time scale associated to the large-scale flow vortices:

$$St = \frac{\tau_m}{\tau_F} = \frac{\rho_l d_l^2 \|\mathbf{w}_s\|}{18\mu\delta} \quad (2.30)$$

where \mathbf{w}_s is the relative velocity between the liquid fuel particle and the surrounding large-scale structure and δ is the characteristic size of the structure.

The aerodynamic response time of a droplet can be understood as an indicator of the responsiveness of a given particle to a change in gas velocity. In fact, the effects of the large-scale structures on particle dispersion can be estimated by means of the Stokes number, as shown in Figure 2.8. In this way,

droplets presenting low Stokes numbers tend to follow the streamlines of the surrounding fluid and thus get dispersed. On the other hand, droplets with large Stokes numbers are dominated by its inertia (i.e., the particle to fluid dispersion ratio becomes less than unity), and the large-scale vortices have insufficient time to influence them. Meanwhile, droplets exhibiting intermediate sizes (i.e., presenting Stokes numbers close to the unity) are expected to be centrifuged by the vortex, as represented in Figure 2.8.

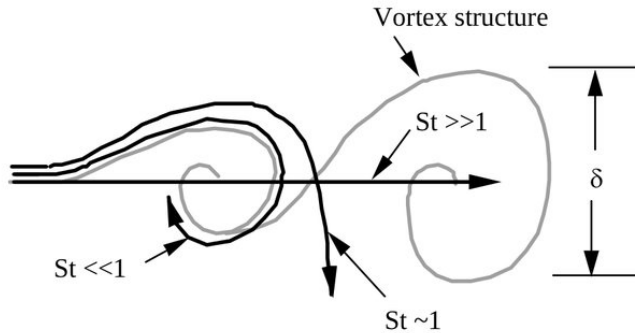


Figure 2.8: Effect of Stokes number on particle dispersion in large-scale turbulent structures [59].

Therefore, it can be concluded that a turbulent carrier phase strongly influences the trajectory and motion of small drops. Furthermore, the production rate of turbulent kinetic energy is reduced as a consequence of these interactions between small drops and the gas-phase eddies.

2.4.1.4 Drop Collision and Coalescence

Spray characteristics in the dense regime can be significantly modified due to drop collision and coalescence [54]. At the same time and location that the atomisation takes place, interactions among droplets (i.e., the coalescence phenomenon and bouncing of droplets) also occur. Therefore, many efforts have been made in the past to provide an insight into the collision outcomes and the parameters that allow categorising droplet interactions [53].

In this respect, Ashgriz and Givi [60] classified the types of drop collisions into four general groups, namely *bouncing*, *coalescence*, *separation*, and *shattering* collisions. In *bouncing* collision, the contact of the drop surfaces is restricted by the intervening gas film resulting in drops bouncing after the contact. Meanwhile, *coalescence* collision occurs when two droplets collide

and merge permanently to create a single drop. On the other hand, *separation* collision (or temporary coalescence) refers to interactions where droplets coalesce temporarily with a subsequent separation into two or more droplets. Finally, *shattering* collision befalls in the presence of high relative velocities, leading to the disintegration of the interacting drops into a cluster of numerous radially-expelled droplets.

Nevertheless, more recent phenomenological observations [61, 62] have demonstrated the presence of many sub-categories within the four generalised mentioned before, depending basically on the operating conditions. In this way, the drop collision outcomes are governed by parameters such as the relative velocity of the two droplets, the thermophysical properties of the liquid drop (i.e., density, viscosity, and surface tension), the drop diameters and velocities, and the density and velocity of the surrounding gas-phase. Another variable that affects the resultant state is the impact parameter (X), which is proportional to the distance between the centers of the pair drops involved [61]. Nonetheless, the main parameter in a binary collision is the relative velocity of the two drops (see Figure 2.9), which can be written as:

$$\mathbf{v}_{rel} = \left(\mathbf{v}_1^2 + \mathbf{v}_2^2 - 2\mathbf{v}_1\mathbf{v}_2 \cos \alpha \right)^{\frac{1}{2}} \quad (2.31)$$

where \mathbf{v}_1 and \mathbf{v}_2 are the velocities of the larger (collector) and smaller drops respectively, and α is the collision angle formed between their trajectories.

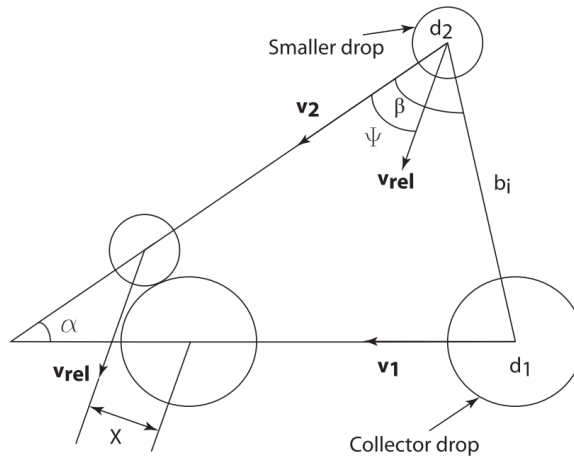


Figure 2.9: Schematic of a binary collision of two moving drops [61].

The main parameters that govern the collision phenomenon can be classified into five dimensionless numbers: the collision Reynolds number (Re_c), the collision Weber number (We_c), the drop diameter ratio (Δ_l), the non-dimensional impact parameter (x), and the Weber number of the surrounding gas-phase (We), previously defined in Eq. (2.23). The rest of the affected parameters can be defined as:

$$Re_c = \frac{\rho_l d_1 \mathbf{v}_{rel}}{\mu_l} \quad (2.32a)$$

$$We_c = \frac{\rho_l d_2 \mathbf{v}_{rel}^2}{\sigma_l} \quad (2.32b)$$

$$\Delta_l = \frac{d_2}{d_1} \quad (2.32c)$$

$$x = \frac{2X}{d_1 + d_2} \quad (2.32d)$$

where d_1 and d_2 are the diameters of the large and small drops, respectively.

Ashgriz and Poo [61] collected data gathered from binary water drop collisions with multiple Reynolds numbers ranging from 500 to 4000 to demonstrate the influence of the parameters mentioned above on the collision outcome. They observed that the Reynolds number and the gaseous-phase Weber number did not manifest a significant relevance in the outcome of the collision, which in general depends on the forces acting on the combined pair of droplets. Therefore, for low Reynolds and low Weber numbers, the main parameters governing the collision outcomes are the impact parameter, the drop diameter ratio, and the collision Weber number.

Figure 2.10 summarises the collision regimes of drops from observations for a wide range of collision Weber numbers ($5 \leq We_c \leq 100$) and all possible impact parameters ($0 \leq x \leq 1$) for two equal-size drops [61]. On the one hand, at low collision Weber numbers (i.e., at low relative velocities of the concerning drops), surface tension forces are more significant than liquid inertia forces, and permanent coalescence occurs for any value of the impact parameter ($x = 0$ denotes a frontal collision, whereas $x = 1$ refers to a tangential collision). On the other hand, while the drop collision Weber number is increased, liquid inertia forces dominate, and either stretching or reflexive separation modes manifest, depending on the impact parameter. Moreover, satellite drops are formed during the collision around the involved drops in a process known as

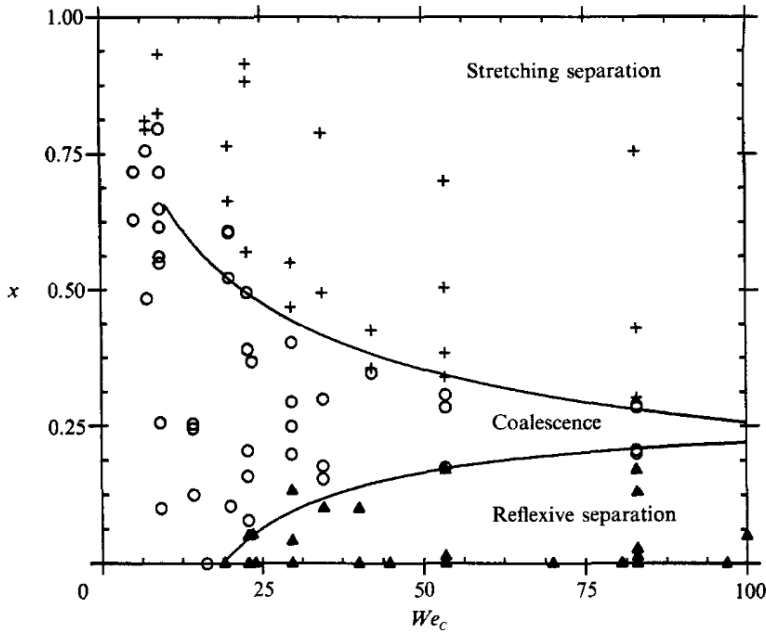


Figure 2.10: Analytical regions for binary drop collisions with $\Delta_l = 1.0$ (+: stretching separation; O: coalescence; ▲: reflexive separation) [61].

grazing collision [24]. Finally, at very high collision Weber numbers, the two droplets get fragmented after colliding, thus generating small droplets [63].

The model considered in this thesis to predict the collision outcome from two colliding parcels (each parcel containing a given number of drops) is discussed in Section 4.2.3.

2.4.1.5 Evaporation Process

In addition to the spray break-up and fuel-air mixing processes, the evaporation of liquid drops also has a notable influence on the ignition, combustion, and production of pollutants. The energy required for the evaporation process is transferred from the hot gaseous phase present at the combustion chamber to the colder fuel drops through conductive, convective, and radiative heat transfer [64]. This results, in turn, in a diffusive and convective mass transfer of fuel vapour from the drops surface into the gas. During the heat transfer process, the drops heat up and lose part of their mass by vaporisation and diffusion to the surrounding gas. The rates of heat and mass transfer are affected by the drop Reynolds number (Re_d). Nevertheless, the drop Reynolds

number fluctuates during the drop life as a consequence of variation both in the drop diameter and the drop velocity. Therefore, there is a substantial connection between the evaporation rate and the gas conditions (i.e., pressure, temperature, and transport properties).

A general discussion about droplet vaporisation can be found in the books of Sirignano [65] and Crowe et al. [66], and the work of Sazhin [67]. Besides, evaporation models concerning multiple degrees of complexity and addressing different features of the evaporation process (orientated to different applications) are described in the investigations of Abraham and Magi [68], Abramzon and Sirignano [69], Aouina et al. [70], Ayoub and Reitz [71], Lippert and Reitz [72], Renksizbulut et al. [73, 74] and Zhu et al. [75].

The whole continuum-based evaporation models proposed in the works mentioned above can be summarised in the following six categories [65], which are classified in order of increasing complexity:

1. Constant droplet temperature models where the drop temperature is constant throughout the evaporation process.
2. Infinite liquid-conductivity models, where the drop temperature is time-varying but uniform.
3. Conduction limit models which consider the transient heating process in the droplet.
4. Effective conductivity models which take the internal drop recirculation into account via adjustment of the internal liquid conductivity.
5. Vortex models which describe the drop heating by considering the internal flow.
6. Models based on the full solution of the Navier-Stokes equations.

As far as the complexity of the models is increased, both the predictions accuracy and the computational resources get considerably more significant. Since many of these evaporation models have been developed for CFD spray simulations, where millions of droplets have to be considered, computational cost emerges as the main issue. Therefore, in practical cases, the models employed are limited to the second and third category.

The standard approach considered in this thesis to describe the evaporation process is presented in Section 4.2.3.

2.4.2 Spray Characterisation

In the context of the processes concerning the spray formation and atomisation presented in Section 2.4.1, several existing parameters can provide a proper description and characterisation of the spray appearance and structure. The essential spray properties of most GT aero-engines, namely the drop size, drop size distribution, spray angle, and drop penetration determine the spray quality and are discussed in this section.

2.4.2.1 Drop size

The drop size is a valuable indicator of the quality and performance of the injection system, and allows both understanding the atomisation process and defining the degree of atomisation. However, the droplets formed spread over an extensive range of diameter values, presenting a significant variability both spatially and temporally. Furthermore, the evaporation process, which also occurs at ambient conditions, continues reducing the drop sizes while moving downstream of the combustor. Therefore, a statistical approach is usually employed to define a characteristic drop diameter rather than a deterministic measurement. In this way, Mugele and Evans [76] classified these descriptions suggesting the notation of Eq. (2.33):

$$D_{pq} = \left(\frac{\sum_{i=1}^{N_d} N_{d,i} D_i^p}{\sum_{i=1}^{N_d} N_{d,i} D_i^q} \right)^{\frac{1}{p-q}} \quad (2.33)$$

where i denotes the size range considered, $N_{d,i}$ is the number of droplets in size range i , and D_i represents the middle diameter of size range i . Numerous classes of diameter may be defined from Eq. (2.33) based on the values given to p and q . The most employed diameters in the spray characterisation in aero-gas turbine application are the arithmetic mean diameter (D_{10} , for $p = 1$ and $q = 0$) and the Sauter Mean Diameter (SMD or D_{32} , for $p = 3$ and $q = 2$). The SMD can be interpreted as the diameter of the drops of a mono-disperse spray having the same volume-to-surface ratio as the entire poly-disperse spray. Therefore, low SMD values are characteristic of a high surface drop with respect to its volume and thus are an effective indicator of good performance and efficiency of the atomiser.

Many specific empirical correlations of the SMD have been proposed for the injection systems usually employed in GT combustors reviewed in Section 2.2.2. For instance, a comprehensive empirical equation for the SMD of drops

for pressure swirl atomiser, in terms of both the atomiser parameters and the liquid properties, takes the form given by Eq. (2.34) [77, 78]:

$$D_{32} \propto \sigma_l^a \nu_l^b \dot{m}_l^c \Delta P_l^d \quad (2.34)$$

where σ_l , ν_l and \dot{m}_l are the surface tension, kinematic viscosity and mass flow rate of liquid fuel, respectively, and ΔP_l refers to the operating injection pressure of the atomiser. Meanwhile, a , b , c and d are the exponents that need to be calibrated.

Later on, Lefebvre [79] made an effort to propose a formulation for predicting the SMD of a pressure swirl atomiser including the effects of both the external aerodynamic forces and the disrupting forces within the emerging liquid. As introduced in Section 2.4.1, the disturbances experimented within the flow have a substantial influence on sheet disintegration. For this reason, the development of waves on the liquid sheet surface produced because of the relative velocity between the liquid and the surrounding gas-phase plays a significant role in the atomisation through the production of unstable ligaments and should be taken into account [80]. In this way, the derived equation for the SMD [79] takes the following form:

$$D_{32} = 4.52 \left(\frac{\sigma_l^{0.5} \nu_l}{\rho_g^{0.5} \Delta P_l} \right)^{0.5} (t_l \cos \theta)^{0.25} + 0.39 \left(\frac{\sigma_l \nu_l}{\rho_g \Delta P_l} \right)^{0.25} (t_l \cos \theta)^{0.75} \quad (2.35)$$

where t_l is the liquid film thickness at the injection plane and θ refers to the half spray cone angle.

In the case of pressure swirl atomisers, the liquid film thickness is related to the air core area as follows:

$$\frac{A_a}{A_o} = \frac{(d_o - 2t_l)^2}{d_o^2} \quad (2.36)$$

where A_a and A_o represent the air core and the discharge orifice areas, respectively, and d_o is the discharge orifice diameter.

Several empirical correlations have been proposed to estimate the liquid film thickness [81, 82]. Most of such expressions show a high dependence on atomiser geometry and the independence from the liquid properties and the atomiser operating conditions. Nevertheless, notable variations are obtained on the film thickness values predicted due to the limited amount of experimental data used to establish the correlation [25].

The existing expressions of characteristic drop sizes from pressure swirl atomisers may be used in the specific cases simulated in this thesis only as a starting point. Then, the exact values needed for the calibration of the atomisation models will be adjusted to properly fit the available experimental data under consideration.

2.4.2.2 Drop Size Distribution

The broad spectrum of different drops sizes produced by an atomiser at a given operating condition makes it necessary to characterise the specific distribution around a given mean size value. Knowledge of the droplet size distribution in a spray in GT combustors is essential for further accurate predictions about spray flame and contaminant emissions. Nevertheless, since the hydrodynamic and aerodynamic phenomena associated with both atomisation and sheet disintegration processes are not still mathematically included in the existing theories, several empirical models have long been proposed to describe the particle size distribution. Most commonly accepted distribution functions include normal, log-normal, upper limit, log-hyperbolic, Nukiyama-Tanasawa [83], Chi-Squared [84], and Rosin-Rammler [85] distributions. However, out of these analytical approaches, there is no unique model able to represent all drop-size data, so that comparative evaluations are required to clarify the one that best fits the available experimental data.

The drop size distribution model proposed by Rosin-Rammler [85] is the most employed approach in many spray-related fields since it provides an adequate match over a wide drop size range. In this correlation, an exponential relationship between the droplet diameter D_l and the mass fraction of drops holding a diameter higher than D_l (Y_{D_l}) is assumed:

$$Y_{D_l} = 1 - Q = \exp - \left(\frac{D_l}{D_l} \right)^q \quad (2.37)$$

where D_l is the mean diameter, Q refers to the fraction of the total volume containing drops with a diameter smaller than D_l , and q represents a quantification of the spreads of drop sizes in the spray (i.e., the higher the value of q the more uniformity in the spray drop sizes by having more smaller drops). The constant values of D_l and q must be determined and calibrated from experimental data.

A significant interest in the drop distribution given by the Rosin-Rammler expression is that the whole range of representative diameter values are mainly connected by means of the spread parameter. Furthermore, Eq. (2.37) can be

implemented to any range of drop sizes, including the very fine drops within the dense region shown in Figure 2.5, where experimental measurements are not always possible. Nevertheless, the Rosin-Rammler prediction has been sometimes found to deviate from the experimental data for the bigger drops. For this reason, a modified expression has been proposed, as shown in Eq. (2.38):

$$1 - Q = \exp - \left(\frac{\ln D_l}{\ln \bar{D}_l} \right)^q \quad (2.38)$$

The modified expression has been demonstrated to provide a better representation of large drops for different configurations of pressure-swirl and air-blast atomisers [86, 87].

2.4.2.3 Spray Penetration

The penetration of a spray is defined as the maximum distance reached by the spray into the quiescent surrounding medium within the combustion chamber. This parameter can be a crucial indicator to identify combustion and emissions issues. In this way, both an insufficiency in the air-fuel mixing process and the chance of fuel impingement on the combustor walls can be anticipated due to an under-penetration or an over-penetration of the spray, respectively.

The spray penetration is determined by the balance among the kinetic energy of the emerging liquid sheet from the nozzle and the aerodynamic resistance of the surrounding gaseous-phase. As the atomisation process increases the spray surface, the higher frictional losses to the gas-phase cause a gradual dissipation of the liquid kinetic energy up to the point in which the fuel trajectory is mainly influenced by the joint action of the surrounding medium and gravity.

While some expressions have been proposed to predict the spray tip penetration in Internal Combustion Engines, minimal information is available on the penetration of the spray for pressure-swirl atomisers operating in GT combustors. In this way, only a few general considerations have been published, stating that the spray penetration in simplex atomisers is inversely proportional to the cube root of the ambient gas pressure. For further details on this topic, the reader may refer to the work by Lefebvre [88].

2.4.2.4 Spray Cone Angle

The spray spreading angle is defined as the angle included between the two straight lines delimiting the spray cone. According to the momentum con-

servation, the spray angle is strongly related to the spray penetration (i.e., the larger the spray angle, the more the resistance from the surrounding gas stream, and thus the lower penetration of spray drops) and has a notable influence on fuel atomisation. In fact, this parameter plays a crucial role in driving the air entrainment in the spray and hence promoting the fuel-air mixing (i.e., intensifying the interactions between spray drops and the surrounding medium), evaporation (i.e., leading to a more efficient exchange of mass and energy between phases), and combustion (i.e., improving ignition performance and flame blow-out limits) processes.

The spray produced by a pressure-swirl atomiser is characterised by presenting a cone shape (solid-cone or hollow-cone²) and a wide-spreading angle. The bulk of the liquid sheet or drops is then located near the spray periphery, forming an annulus pattern. The first reported studies conducted on pressure-swirl atomisers under the assumption of non-viscous liquid fuel illustrated the importance of both the nozzle geometry, fuel properties, and gas-phase density on the spray cone angle [25]. In this way, several initial formulations were proposed to derive the half-cone angle assuming a constant axial velocity across the liquid film [89], as shown in Eq. (2.39):

$$\tan \theta_m = \tan \theta - \left(1 - \frac{t_l}{d_o}\right) \quad (2.39)$$

Later on, Rizk and Lefebvre [90] derived a dimensionally-correct equation to predict the spray cone angle considering viscous liquids, which can be written as:

$$2\theta_m = 6 \left(\frac{A_P}{d_o D_S}\right)^{-0.15} \left(\frac{\Delta P_l d_o^2 \rho_l}{\mu_l}\right)^{0.11} \quad (2.40)$$

where $2\theta_m$ refers to the mean cone angle in the region close to the nozzle, A_P is the total area of the inlet ports, and D_S represents the injector swirl chamber diameter.

Equation (2.40) highlights the dependence among the liquid injection pressure and liquid properties on spray angle. Nevertheless, even though the expression provides an useful insight, the effects of ambient pressure on the

²In hollow-cone pressure swirl atomisers most of the droplets are concentrated at the outer edge of a conical spray pattern thus providing both a better atomization and radial liquid distribution. For this reason, it is often preferred for many industrial processes, especially for combustion applications.

spray cone angle are still not considered. In this way, Ortman and Lefebvre [91] carried out several tests on different simplex pressure-swirl atomisers using kerosene as liquid fuel to evaluate the effects of gas pressure on the spray cone angle. Their results show how as far as the surrounding gas pressure is increased over atmospheric conditions, the spray angle is substantially narrowed. Nevertheless, this angle contraction becomes less prominent when the increase in ambient pressure continues, and finally, a critical condition is reached in which further rise in gas pressure does not influence the spray spreading angle. For further details on this topic, the reader may refer to the work by Lefebvre [25].

References

- [1] Jenny, P., Roekaerts, D., and Beishuizen, N. “Modeling of turbulent dilute spray combustion”. In: *Progress in Energy and Combustion Science* 38.6 (2012), pp. 846–887. DOI: 10.1016/j.pecs.2012.07.001.
- [2] Sarpkaya, T. “On stationary and travelling vortex breakdowns”. In: *Journal of Fluid Mechanics* 45.3 (1971), pp. 545–559. DOI: 10.1017/S0022112071000181.
- [3] Syred, N. and Beér, J. “Combustion in swirling flows: A review”. In: *Combustion and Flame* 23.2 (1974), pp. 143–201. DOI: 10.1016/0010-2180(74)90057-1.
- [4] Escudier, M. and Zehnder, N. “Vortex-flow regimes”. In: *Journal of Fluid Mechanics* 115 (1982), pp. 105–121. DOI: 10.1017/S0022112082000676.
- [5] Escudier, M. “Vortex breakdown: Observations and explanations”. In: *Progress in Aerospace Sciences* 25.2 (1988), pp. 189–229. DOI: 10.1016/0376-0421(88)90007-3.
- [6] Gupta, A., Lilley, D., and Syred, N. *Swirl flows*. Abacus Press, 1984.
- [7] Lucca-Negro, O. and O’Doherty, T. “Vortex breakdown: A review”. In: *Progress in Energy and Combustion Science* 27 (2001), pp. 431–481. DOI: 10.1016/S0360-1285(00)00022-8.
- [8] Beér, J. and Chigier, N. *Combustion aerodynamics*. London, Applied Science Publishers, 1972.
- [9] Patel, N. and Menon, S. “Simulation of spray-turbulence-flame interactions in a lean direct injection combustor”. In: *Combustion and Flame* 153 (2008), pp. 228–257. DOI: 10.1016/j.combustflame.2007.09.011.

- [10] Giridharan, M., Mongia, H., and Jeng, S. "Swirl Cup Modeling Part VIII : Spray Combustion in CFM-56 Single Cup Flame Tube". In: *AIAA Paper* January (2003), pp. 1–11.
- [11] Terhaar, S., Bobusch, B., and Paschereit, C. "Effects of outlet boundary conditions on the reacting flow field in a swirl-stabilized burner at dry and humid conditions". In: *Journal of Engineering for Gas Turbines and Power* 134.11 (2012), pp. 1–9. DOI: 10.1115/1.4007165.
- [12] Chigier, N. and Beer, J. "Velocity and Static-Pressure Distributions in Swirling Air Jets Issuing From Annular and Divergent Nozzles". In: *Journal of Basic Engineering* 86.4 (1964), pp. 788–796. DOI: 10.1115/1.3655954.
- [13] Sheen, H., Chen, W., Jeng, S., and Huang, T. "Correlation of swirl number for a radial-type swirl generator". In: *Experimental Thermal and Fluid Science* 12.4 (1996), pp. 444–451. DOI: [https://doi.org/10.1016/0894-1777\(95\)00135-2](https://doi.org/10.1016/0894-1777(95)00135-2).
- [14] Huang, Y. and Yang, V. "Dynamics and stability of lean-premixed swirl-stabilized combustion". In: *Progress in Energy and Combustion Science* 35.4 (2009), pp. 293–364. DOI: 10.1016/J.PECS.2009.01.002.
- [15] Lilley, D. "Swirl Flows in Combustion: A Review". In: *AIAA Journal* 15.8 (1977), pp. 1063–1078. DOI: 10.2514/3.60756.
- [16] Syred, N. and Dahman, K. "Effect of high levels of confinement upon the aerodynamics of swirl burners". In: *Journal of Energy* 2.1 (1978), pp. 8–15. DOI: 10.2514/3.47950.
- [17] Valera-Medina, A., Syred, N., and Griffiths, A. "Visualisation of isothermal large coherent structures in a swirl burner". In: *Combustion and Flame* 156 (2009), pp. 1723–1734. DOI: 10.1016/J.COMBUSTFLAME.2009.06.014.
- [18] Lefebvre, A. *Atomization and Sprays*. Hemisphere Publishing Corporation, 1989.
- [19] Lefebvre, A. and Ballal, D. *Gas turbine combustion: alternative fuels and emissions*. 3rd edition. Taylor and Francis, 2010.
- [20] Ashgriz, N. "Handbook of atomization and sprays: theory and applications". In: Springer Science and Business Media, 2011. Chap. 24 - Spray Nozzles.
- [21] Sovani S. Sojka, P. and Lefebvre, A. "Effervescent Atomization". In: *Progress in Energy and Combustion Science* 27 (2001), pp. 483–521.

- [22] Williams, F. *Combustion Theory*. 2nd edition. Taylor and Francis, 1985.
- [23] Elghobashi, S. and Truesdell, G. “On the two way interaction between homogeneous turbulence and dispersed solid particles. I: Turbulence modification”. In: *Physics of Fluids A: Fluid Dynamics* 5.7 (1993), pp. 1790–1801. DOI: 10.1063/1.858854.
- [24] O’Rourke, P. “Collective Drop Effects on Vaporizing Liquid Sprays”. PhD thesis. Princeton University, 1981.
- [25] Lefebvre, A. “Properties of Sprays”. In: *Particle and Particle Systems Characterization* 6.1-4 (1989), pp. 176–186. DOI: 10.1002/ppsc.19890060129.
- [26] Li, X. and Soteriou, M. “High-fidelity simulation of fuel atomization in a realistic swirling flow injector”. In: *Atomization and Sprays* 23 (2013), pp. 1049–1078. DOI: 10.1615/AtomizSpr.2013007395.
- [27] Fraser, R. and Eisenklam, P. “Research into the performance of atomizers for liquids”. In: *Journal of the Imperial College Chemical Engineering Society* 7 (1953), pp. 52–68.
- [28] Dombrowski, N. and Fraser, R. “A photographic investigation into the disintegration of liquid sheets”. In: *Journal of Mathematical and Physical Sciences* 247 (1954), pp. 101–130. DOI: 10.1098/rsta.1954.0014.
- [29] Fraser, R. “Liquid fuel atomization”. In: *Sixth Symposium (International) on Combustion*. New York, United States of America, 1957, pp. 687–701.
- [30] Fraser, R., Eisenklam, P., Dombrowski, N., and Hasson, D. “Drop formation from rapidly moving sheets”. In: *Journal of American Institute of Chemical Engineers* 8.5 (1962), pp. 672–680.
- [31] Dombrowski, N. and Johns, W. “The aerodynamic instability and disintegration of viscous liquid sheets”. In: *Journal of Chemical Engineering Science* 18 (1963), pp. 203–214.
- [32] Fraser, R., Dombrowski, N., and Routley, J. “The atomization of a liquid sheet by an impinging air stream”. In: *Journal of Chemical Engineering Science* 18 (1963), pp. 339–353.
- [33] Crapper, G. and Dombrowski, N. “A note on the effect of forced disturbances on the stability of thin liquid sheets and on the resulting drop size”. In: *International Journal of Multiphase Flow* 10.6 (1984), pp. 731–736.

- [34] Rangel, R. and Sirignano, W. "The linear and non-linear shear instability of a fluid sheet". In: *Physics of Fluids* 3 (1999), pp. 2392–2400.
- [35] Mehring, C. and Sirignano, W. "Review of theory of distortion and disintegration of liquid streams". In: *Progress in Energy and Combustion Science* 26 (2000), pp. 609–655.
- [36] Senecal, P. et al. "Modeling high-speed viscous liquid sheet atomization". In: *International Journal of Multiphase Flow* 25 (1999), pp. 1073–1097. DOI: 10.1016/S0301-9322(99)00057-9.
- [37] Lin, S. *Breakup of Liquid Sheets and Jets*. Cambridge University Press, 2003. DOI: 10.1017/CB09780511547096.
- [38] Dumouchel, C. "On the experimental investigation on primary atomization of liquid streams". In: *Experiments in Fluids* 45 (2008), pp. 371–422.
- [39] Krzeczkowski, S. "Measurement of liquid droplet disintegration mechanisms". In: *International Journal of Multiphase Flow* 6.3 (1980), pp. 227–239. DOI: 10.1016/0301-9322(80)90013-0.
- [40] Wierzba, A. "Deformation and breakup of liquid drops in a gas stream at nearly critical Weber numbers". In: *Experiments in Fluids* 9.1-2 (1990), pp. 59–64. DOI: 10.1007/BF00575336.
- [41] Wu, P. and Faeth, G. "Aerodynamic effects primary breakup of turbulent liquids". In: *Atomization and Sprays* 3 (1993), pp. 265–289.
- [42] Faeth, G., Hsiang, L., and Wu, P. "Structure and breakup properties of sprays". In: *International Journal Of Multiphase Flow* 21 (1995), pp. 99–127.
- [43] Liu, Z. and Reitz, R. "An analysis of the distortion and breakup mechanisms of high speed liquid drops". In: *International Journal of Multiphase Flow* 23.4 (1997), pp. 631–650. DOI: 10.1016/S0301-9322(96)00086-9.
- [44] Han, J. and Tryggvason, G. "Secondary breakup of axisymmetric liquid drops. II. Impulsive acceleration". In: *Physics of Fluids* 13.6 (2001), pp. 1554–1565. DOI: 10.1063/1.1370389.
- [45] Chou, W. and Faeth, G. "Temporal properties of secondary drop breakup in the bag breakup regime". In: *International Journal of Multiphase Flow* 24.6 (1998), pp. 889–912. DOI: 10.1016/S0301-9322(98)00015-9.

- [46] Hsiang, L. and Faeth, G. “Near-limit drop deformation and secondary breakup”. In: *International Journal of Multiphase Flow* 18.5 (1992), pp. 635–652. DOI: 10.1016/0301-9322(92)90036-G.
- [47] Joseph, D., Belanger, J., and Beavers, G. “Breakup of a liquid drop suddenly exposed to a high-speed airstream”. In: *International Journal of Multiphase Flow* 25 (1999), pp. 1263–1303. DOI: 10.1016/j.ijmultiphaseflow.2003.11.004.
- [48] O’Rourke, P. and Amsden, A. “The tab method for numerical calculation of spray droplet breakup”. In: *SAE Technical Papers* (1987). DOI: 10.4271/872089.
- [49] Tanner, F. “Liquid jet atomization and droplet breakup modeling of non-evaporating diesel fuel sprays”. In: *SAE Technical Papers* 412 (1997). DOI: 10.4271/970050.
- [50] Ibrahim, E., Yang, H., and Przekwas, A. “Modeling of spray droplets deformation and breakup”. In: *Journal of Propulsion and Power* 9.4 (1993), pp. 651–654. DOI: 10.2514/3.23672.
- [51] Chryssakis, C. and Assanis, D. “A unified fuel spray breakup model for internal combustion engine applications”. In: *Atomization and Sprays* 18 (2008), pp. 375–426. DOI: 10.1615/AtomizSpr.v18.i5.10.
- [52] Ashgriz, N. “Handbook of atomization and sprays: theory and applications”. In: Springer Science and Business Media, 2011. Chap. 6 - Droplet Deformation and Breakup.
- [53] Liu, A., Mather, D., and Reitz, R. “Modeling the Effects of Drop Drag and Breakup on Fuel Sprays”. In: *International Congress Exposition*. SAE International, 1993. DOI: <https://doi.org/10.4271/930072>.
- [54] O’Rourke, P. and Bracco, F. “Modelling of drop interactions in thick sprays and a comparison with experiments”. In: *Stratified Charge Automotive Engine, IMechE*. 1980.
- [55] Hwang, S., Liu, Z., and Reitz, R. “Breakup mechanisms and drag coefficients of high speed vaporizing liquid drops”. In: *Atomization and Sprays* 6.3 (1996). DOI: 10.1615/AtomizSpr.v6.i3.60.
- [56] Faeth, G. “Evaporation and combustion of sprays”. In: *Progress in Energy and Combustion Science* 9.1 (1983), pp. 1–76. DOI: [https://doi.org/10.1016/0360-1285\(83\)90005-9](https://doi.org/10.1016/0360-1285(83)90005-9).
- [57] Crowe, C. “Modeling turbulence in multiphase flow”. In: *Engineering Turbulence Modelling and Experiments* (1993), pp. 899–913. DOI: <https://doi.org/10.1016/B978-0-444-89802-9.50088-5>.

- [58] Yuan, Z. and Michaelides, E. “Turbulence modulation in particulate flows: A theoretical approach”. In: *International Journal of Multiphase Flow* 18.5 (1992), pp. 779–785. DOI: [https://doi.org/10.1016/0301-9322\(92\)90045-I](https://doi.org/10.1016/0301-9322(92)90045-I).
- [59] Crowe, C., Chung, J., and Troutt, T. “Particle mixing in free shear flows”. In: *Progress in Energy and Combustion Science* 14.3 (1988), pp. 171–194. DOI: [https://doi.org/10.1016/0360-1285\(88\)90008-1](https://doi.org/10.1016/0360-1285(88)90008-1).
- [60] Ashgriz, N. and Givi, P. “Binary collision dynamics of fuel droplets”. In: *International Journal of Heat and Fluid Flow* 8.3 (1987), pp. 205–210. DOI: 10.1016/0142-727X(87)90029-4.
- [61] Ashgriz, N. and Poo, J. “Coalescence and separation in binary collisions of liquid drops”. In: *Journal of Fluid Mechanics* 221 (1990), pp. 183–204. DOI: 10.1017/S0022112090003536.
- [62] Jia, X., Yang, J., Zhang, J., and Ni, M. “An experimental investigation on the collision outcomes of binary liquid metal droplets”. In: *International Journal of Multiphase Flow* 116 (1992), pp. 80–90. DOI: 10.1016/j.ijmultiphaseflow.2019.04.008.
- [63] Qian, J. and Law, C. “Regimes of coalescence and separation in droplet collision”. In: *Journal of Fluid Mechanics* 331 (1997), pp. 59–80. DOI: 10.1017/S0022112096003722.
- [64] Abramzon, B. and Sirignano, W. “Approximate theory of a single droplet vaporization in a convective field: effects of variable properties, Stefan flow and transient liquid heat”. In: *Proceedings of the American Society of Mechanical Engineers*. Honolulu, Hawaii, United States of America, 1987.
- [65] Sirignano, W. *Fluid Dynamics and Transport of Droplets and Sprays*. 2nd Edition. New York, USA: Cambridge University Press, 2010.
- [66] Crowe, C., Sommerfeld, M., Schwarzkopf, J., and Tsuji, Y. *Multiphase Flows with Droplets and Particles*. 2nd Edition. New York, USA: Taylor and Francis.
- [67] Sazhin, S. “Advanced models of fuel droplet heating and evaporation”. In: *Progress in Energy and Combustion Science* 32 (2006), pp. 162–214. DOI: 10.1016/j.pecs.2005.11.001.
- [68] Abraham, J. and Magi, V. “A Model for Multicomponent Droplet Vaporization in Sprays”. In: *SAE Transactions* 107 (1998), pp. 603–613. DOI: 10.2307/44736555.

- [69] Abramzon, B. and Sirignano, W. “Droplet vaporization model for spray combustion calculations”. In: 32.9 (1988), pp. 1605–1618. DOI: 10.2514/6.1988-636.
- [70] Aouina, Y., Maas, U., Gutheil, E., Riedel, U., and Warnatz, J. “Mathematical modeling of droplet heating, vaporization, and ignition including detailed chemistry”. In: *Combustion Science and Technology* 173 (2001), pp. 1–29. DOI: 10.1080/00102200108935842.
- [71] Ayoub, N. and Reitz, R. “Multidimensional Computation of Multi-component Spray Vaporization and Combustion”. In: *International Congress Exposition*. SAE International, 1995. DOI: 10.4271/950285.
- [72] Lippert, A. and Reitz, R. “Modeling of Multicomponent Fuels Using Continuous Distributions with Application to Droplet Evaporation and Sprays”. In: *International Fuels and Lubricants Meeting and Exposition*. SAE International, 1997. DOI: <https://doi.org/10.4271/972882>.
- [73] Renksizbulut, M., Nafziger, R., and Li, X. “A mass transfer correlation for droplet evaporation in high-temperature flows”. In: *Chemical Engineering Science* 46 (1991), pp. 2351–2358.
- [74] Renksizbulut, M., Bussmann, M., and Li, X. “A Droplet Vaporization Model for Spray Calculations”. In: *Particle and Particle Systems Characterization* 9.1â4 (1992), pp. 59–65. DOI: 10.1002/ppsc.19920090110.
- [75] Zhu, G., Reitz, R., Xin, J., and Takabayashi, T. “Modelling characteristics of gasoline wall films in the intake port of port fuel injection engines”. In: *International Journal of Engine Research* 2.4 (2001), pp. 231–248. DOI: 10.1243/1468087011545451.
- [76] Mugele, R. and Evans, H. “Droplet Size Distribution in Sprays”. In: *Industrial and Engineering Chemistry* 43.6 (1951), pp. 1317–1324. DOI: 10.1021/ie50498a023.
- [77] Radcliffe, A. “Fuel Injection, High Speed Aerodynamics and Jet Propulsion”. In: *Technical Report XID* 11 (1960), p. 84.
- [78] Kennedy, J. “High weber number SMD correlations for pressure atomizers”. In: *Journal of Engineering for Gas Turbines and Power* 108.1 (1986), pp. 191–195. DOI: 10.1115/1.3239870.
- [79] Lefebvre, A. “The prediction of sauter mean diameter for simplex pressure-swirl atomisers”. In: *Atomisation Spray Technology* 3.1 (1987), pp. 37–51.

- [80] Wang, X. and Lefebvre, A. "Mean drop sizes from pressure-swirl nozzles". In: *Journal of Propulsion and Power* 3.1 (1987), pp. 11–18. DOI: 10.2514/3.22946.
- [81] H., Simmons and C., Harding. "Some effects on using water as a test fluid in fuel nozzle spray analysis". In: ASME Paper 80-GT-90, 1980.
- [82] Lefebvre, A. and Suyari, M. "Film thickness measurements in a simplex swirl atomizer". In: *Journal of Propulsion and Power* 2.6 (1986), pp. 528–533. DOI: 10.2514/3.22937.
- [83] Nukiyama, S. and Tanasawa, Y. "Experiments on the atomization of liquids in an airstream". In: *Trans. Soc. Mech. Eng. Jpn* 5 (1939), pp. 68–75.
- [84] Amsden, A. "KIVA-3V: A block-structured KIVA program for engines with vertical or canted valves". In: *Los Alamos National Laboratory Technical Report LA-13313-MS* (1997).
- [85] Rosin, P. and Rammler, E. "The laws governing the fineness of powdered coal". In: *Journal of the Institute of Fuel* 7 (1933), pp. 29–36.
- [86] Custer, J. and Rizk, N. "Influence of design concept and liquid properties on fuel injector performance". In: *Journal of Propulsion and Power* 4.4 (1988), pp. 378–384. DOI: 10.2514/3.23077.
- [87] Rizk, N. and Mongia, H. "Performance of hybrid airblast atomizers under low power conditions". In: *30th Aerospace Sciences Meeting and Exhibit*. 1992. DOI: 10.2514/6.1992-463.
- [88] Lefebvre, A.H. "Factors controlling gas turbine combustion performance at high pressures". In: *Cranfield International Symposium Series* 10 (1968), pp. 211–226.
- [89] Joyce, J. "The Atomisation of Liquid Fuels". In: *The Journal of the Royal Aeronautical Society* 58.518 (1954). DOI: 10.1017/S0368393100097832.
- [90] Rizk, N. and Lefebvre, A. "Prediction of velocity coefficient and spray cone angle for simplex swirl atomizers". In: *Proc. 3rd Int. Conf. Liquid Atomization and Spray Systems, 111C/2/1-16*. 1985. DOI: 10.2514/6.1992-463.
- [91] Ortman, J. and Lefebvre, A. "Fuel distributions from pressure-swirl atomizers". In: *Journal of Propulsion and Power* 1 (1985), pp. 11–15. DOI: 10.2514/3.22752.

Chapter 3

Literature Review

“We have far too many ways to interpret past events for our own good.”

—Nassim N. Taleb

3.1 Introduction

The present thesis explores the non-reacting swirling flow field in Lean Direct Injection (LDI) gas turbine combustors by means of Large-Eddy Simulations in an Eulerian-Lagrangian framework. The fundamentals of the LDI concept were presented in Chapter 2. However, an in-depth literature review is required to understand the current state of the art and to frame the objectives of this investigation.

In the recent past, a significant effort has been made on measuring and simulating the swirling flow in gas turbine combustors regarding different injection strategies and swirler types. Nevertheless, even though these flows are employed in most engine designs, its chaotic swirling nature hinders both experimental measurements (see Section 3.2) and numerical computations (see Section 3.3), implying several phenomena are still not understood. For instance, since the spray is injected into a burning 3D turbulent flow field in the combustion chamber, quantitative experimental measurements of spray breakup in dense spray regimes are currently inconceivable. As a consequence, most experiments have been limited to measure global characteristics of the spray further downstream of the nozzle where a more diluted spray is accessible by optical techniques. This in turn also implies severe difficulties for

numerical simulations since the required approximations to set up the initial spray formation and the atomisation processes profoundly impact the accuracy of the predictions.

In addition, given the dynamic interactions and high-turbulent large-scale coherent structures present within an LDI combustor, gathering knowledge about the underlying fluid mechanisms governing the system is not an easy task. In this way, a more in-depth frequency-related analysis becomes necessary for a better characterisation on the dynamics of the governing helical coherent structures. Therefore, a brief review regarding the existing works about spectral analysis and recent modal decomposition techniques is presented as well in Section 3.4.

3.2 Experimental Studies on LDI Burners

This section briefly presents the main experimental works available in the literature about the LDI (Lean Direct Injection) strategy from the early measurements to our days. For a complete review of the working principles of modern low emissions combustion technologies for aero gas turbine engines, the reader may also refer to the work by Liu et al. [1].

The LDI concept emerged in the 90s as a low-NO_x alternative to the RQL combustion schemes traditionally used in aero gas turbine engines, and as an evolution of the LPP (Lean Premixed Prevaporized) combustion concept introduced by NASA in the 70s and investigated in the 80s [2]. Indeed, the LDI design was pretended to combine the good stability and lean blowout performance of the traditional RQL combustors with the low-NO_x levels reported by LPP systems.

At first, most works focused on globally measuring pollutant emissions. The first reported study on the direct injection concept was carried out at the University of Leeds by Al-Kabie and Andrews [3]. Their work dealt with the then called high-shear combustion system employing radial swirlers and using natural gas instead of liquid fuel [4, 5]. They reported similar low-NO_x levels and greater flame stability than LPP combustors.

Similar works were carried out some years later by McVey et al. [6] and Hayashi et al. [7] confirming the wide stability limits and the good performance in the NO_x emission levels pointed out by Al-Kabie and Andrews [3]. In this sense, the high residence time associated with the large vortex-breakdown recirculation region generated in these swirl-stabilised devices did not seem to adversely impact the NO_x formation.

With regard to these three approaches, Tacina [8] made a comparison between the NO_x emission levels of LDI [3, 9, 10], RQL [11–15] and LPP [16, 17] combustion systems at different operating conditions. The main findings are compiled in Figure 3.1. As it can be seen, LDI combustors presented similar NO_x levels than LPP systems (lower than traditional RQL systems) but without presenting the narrow stability limits and the susceptibility to autoignition/flashback reported by the LPP combustion concept.

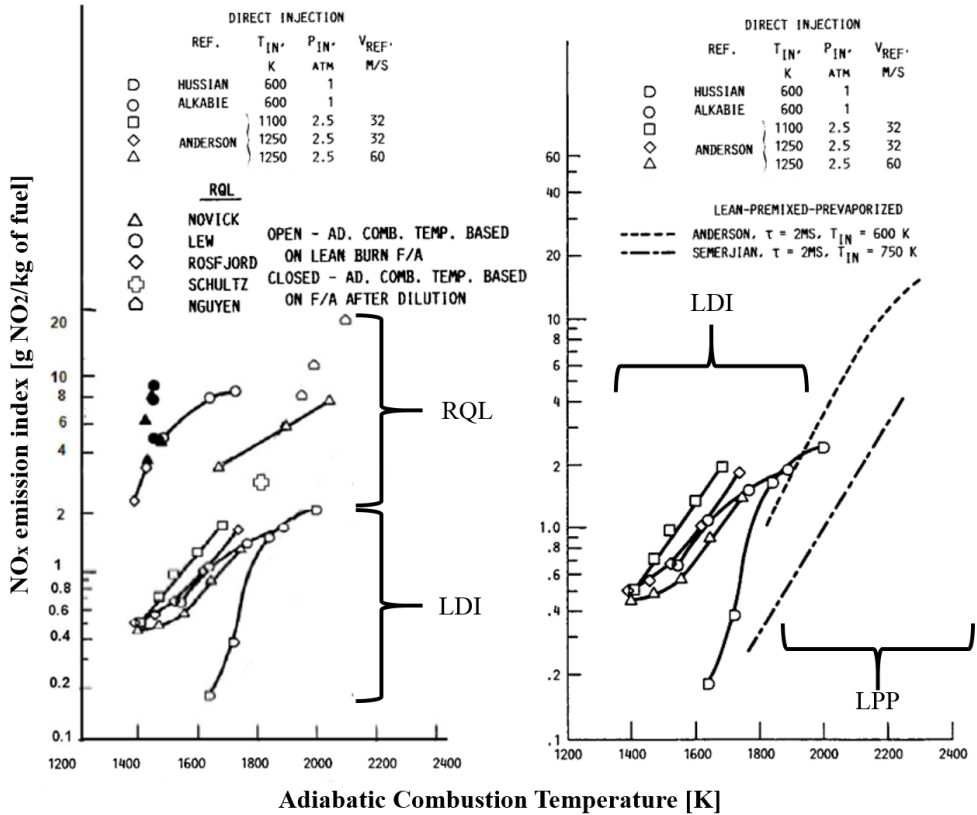


Figure 3.1: Comparison of the NO_x emission levels between: LDI and RQL schemes (left); LDI and LPP schemes (right) [8].

Nevertheless, since these results were obtained with gaseous fuels, the challenge was then to produce the same low- NO_x levels with liquid fuels. It is important to note that for liquid fuel injections, the NO_x emissions are highly dependent both on the atomisation and vaporisation degree, together with the mixing quality achieved before combustion.

Subsequently, research on the injection of liquid fuel began to be generalised. Andrews et al. [18] studied the effect of atomisation and evaporation and confirmed the potential of LDI burners to reach the NO_x emissions of the LPP combustors even with liquid fuels. However, specific studies on the atomisation of liquid fuel [19] indicated significant influence of the turbulence induced by the swirler in the distribution of fuel droplet size in the chamber, and thus in the NO_x emissions. The influence was more accused when operating at high-pressure conditions, highlighting the importance of achieving a proper non-reacting flow field before the injection/combustion occurs.

So far, the only results that had been paid attention to were based on global NO_x emissions. From this moment, once the potential of LDI technology in reducing NO_x levels was contrasted, the scientific community started to invest more efforts in researching the LDI concept as a real alternative to traditional RQL systems. This fact, together with the development of modern optical techniques based on non-intrusive laser diagnostics, pushed many research centres to develop laboratory-scale LDI test rigs. The turbulent flow field within swirl-stabilised combustors had been visualised for a long time using the Laser-Doppler Velocimetry (LDV) technique [20]. Nevertheless, the Phase Doppler Anemometry (PDA) technique irruption allowed improving the comprehension of spray dynamics and droplet characteristics, since it is used to characterise both gaseous and liquid phases statistics as mean and fluctuating velocity and diameter [21–24].

Although some more recent optical diagnostic methods have been developed over the last few years [25–27], there still exist uncertainties when getting an accurate prediction for both carrier and disperse phases close to the nozzle exit. For this reason, most experimental observations have been reduced to measurements in the diluted regime employing contrasted techniques such as LDV, PDA or LIF. For a complete review of the current non-intrusive diagnostic techniques employed in the experimental research of gas turbine combustors, the reader may also refer to the work by Ruan et al. [28].

As previously stated, many laboratory-scale with simplified geometries have been designed in the recent years for the experimental study of the unsteady phenomena of the LDI injection. These designs included different gaseous and injection strategies (e.g. dual annular, twin annular, single, multi-point -MP-, etc.) and swirler types (e.g. axial, radial, counter-swirl, helical, cyclone, single stage, etc.). This resulted in high-resolution measurements in terms of resolving both the fluid-dynamic characteristics of the swirling flow and the interaction between gaseous and liquid phases, which is highly valuable for current modellers. A review of laboratory gaseous-fueled swirl

burners for model validation may be found in [29]. The most relevant experimental gaseous and liquid-fueled LDI combustor designs for investigation are summarised in Table 3.1 together with their more significant features and contributions.

One of the first studies that thoroughly characterised an LDI combustor was performed in 2000 by Meier et al. [30] at the DLR. They developed the Tecflam Swirl Burner for confined natural gas flames and reported measurements of velocity, temperature, mixture fraction, and species concentrations. These results provided an extensive experimental database that allowed to validate combustion models.

Later on, some efforts were made to implement strategies that ensure quick and uniform air-fuel mixing. In this sense, Tacina et al. [31–33] implemented the multi-point injection concept in LDI burners (MP-LDI), containing multiple fuel injection tips and multi-burning zones. In the MP-LDI strategy, each fuel injector is composed of a pressure swirl atomiser in the centre and a discrete-jet air swirler on the outside (see Figure 3.2). Experiments were performed with modules including 25 [33], 36 [31] and 49 [32] fuel injectors at chamber conditions up to 810 K and 27 bar. They concluded that splitting the fuel injections into several injector devices resulted not only in proper atomisation and a more homogeneous mixture but also in a shortening of the fuel residence time, thus resulting in lower NO_x generation. Nevertheless, advances in the combustion efficiency at operating conditions close to the lean extinction limit were still required.

Archer and Gupta [34] examined the effect of swirl and combustion in a single-element double-concentric swirl LDI burner under non-reacting and reacting conditions using gaseous fuel. They concluded that co-swirl configurations could lead both to a more elongated flowfield and a more symmetrical and stable flame when compared to counter-swirl cases. This influence was attributed to the creation of a less energetic and dynamic flowfield.

A similar approach was followed by Li and Gutmark [35], who investigated the effects of different swirler configurations on the central recirculation zone, velocity fields, temperature distributions, flame structure and emission levels in isothermal and reacting cases. The results in the Triple Annular Research Swirler (TARS) assembly highlighted the role of the turbulence pattern in LDI combustion and the connection between the Damkohler number and NO_x production for both gaseous and liquid fuels.

One year later, Cai et al. [36] carried out non-reacting and combustion measurements in the single-element NASA LDI combustor at ambient temperature and pressure conditions. They found that the high-swirling flow

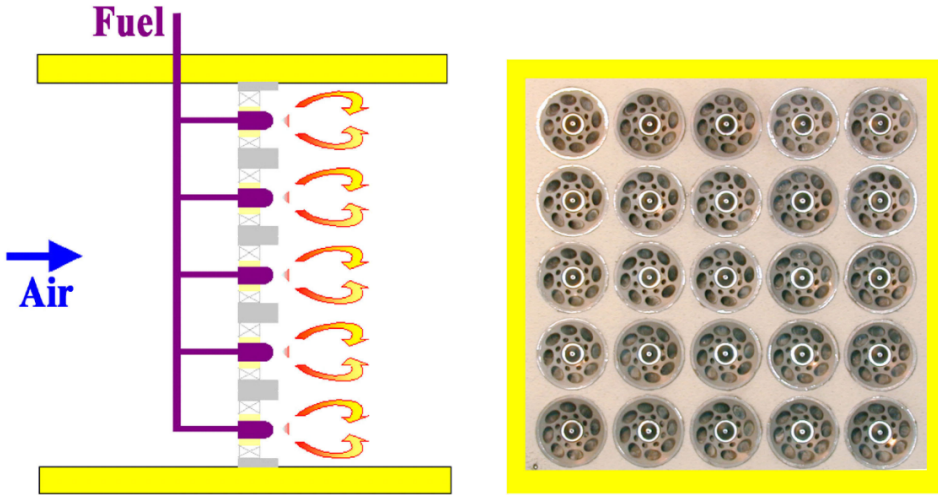


Figure 3.2: Multi-Point LDI module with 25 fuel injectors and air swirlers [33].

caused by the helicoidal swirler blades provided uniform drop size profiles. Furthermore, they reported higher mean and fluctuating gaseous velocities and a smaller central recirculation zone generated in the reacting case. Later studies by Yi and Santavicca [37] were focused on studying combustion instabilities and the resulting flame structure under thermoacoustic oscillations excited by external and background disturbances. In addition, a very recent parametric investigation has been reported by Gejji et al. [38] based on a high-pressure model of the single-element NASA LDI combustor. In this way, the behaviour of self-excited combustion dynamics was characterised and the effects of the combustor geometry, air temperature and global equivalence ratio were described.

Special consideration must be given to the work by Janus et al. [39], who successfully applied the planar laser-induced fluorescence (PLIF) technique to represent the behaviour of detached flames at elevated pressure and swirling conditions in the high-pressure TURBOMECA LDI burner installed in TU-Darmstadt. They considered gaseous-fueled injections in a confined configuration to characterise the reaction zone in terms of flame shape and mean stabilisation and exposed the influence of pressure on the flame structure and the complex coherent flow structures (e.g., Vortex Breakdown Bubble, Precessing Vortex Core). In addition, they concluded that the combustion rate was governed by the turbulent flame spreading rather than diffusive transport. Subsequent studies [40] allowed to better characterise the reacting fields

in terms of the flame lift-off height, the mean reaction progress or the flame surface density.

Similar works were carried out some years later by Weigand et al. [41], Meier et al. [42], and Sadanandan et al. [43] in the dual-radial swirler PREC-CINSTA LDI combustor of the DLR (see Figure 3.3), which was explicitly intended for thermoacoustic instability studies. Both pulsating and non-pulsating flames were studied at atmospheric conditions for gaseous fuels in order to determine the influence of the turbulence on the local flame characteristics. They provided a useful data set as a basis for validating reacting simulations with well-defined boundary conditions and a wide range of results concerning the flow field, flame structure, species concentration, mixture fraction and temperature profiles. More recent liquid-fueled measurements at high-pressures up to 20 bar have been reported in the so-called Generic Single Sector Combustor (GENRIG) by Meier et al. [44]. In addition, Stöhr et al. [45] investigated the mechanisms of the interaction between the PVC and the turbulent swirl flame for different Damköhler numbers. According to their results, strong PVC-flame interactions were observed for all tested conditions. This interaction enhanced the supply of heat and radicals to the unburned gas, thus favouring the ignition, but also caused a significant aerodynamic stretch of the reaction zones, which could lead locally to the flame extinction.

Al-Abdeli and Masri [46] also investigated the effect of instabilities such as Vortex Breakdown Bubble (VBB) and Precessing Vortex Core (PVC) on flame stability. To this end, the Sydney Swirl Burner at The University of Sydney relied on aerodynamic induction of swirl through tangential ports instead of the so far geometrical swirl generation via radial vanes. Other results such as velocity fields, blow-off/lift-off characteristics of several natural gas flames, and the coherent instability modes [47] were also available to validate numerical models. Meanwhile, a second copy of the burner was installed at Sandia National Laboratories to acquire compositional field data [48] and to obtain further insight in turbulence-chemistry interactions [49]. More recent studies concerning liquid-fueled injections in the so-called Sydney Spray Burner [50, 51] also provided an extensive database of spray-related results in terms of droplet dispersion and evaporation and droplet-turbulence-flame interactions.

The MERCATO test-rig shown Figure 3.4 was developed at ONERA [52] for the study of two-phase flows. In particular, it was intended to provide in-depth physical knowledge of ignition sequences in realistic aero combustion chambers at high altitudes with liquid fuel injection. Detailed experimental data in non-reacting [53] and reacting [54, 55] conditions for both purely gaseous flow and evaporating two-phase flow were employed to develop and

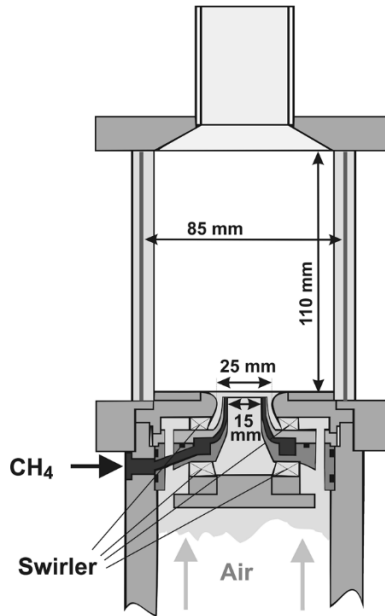


Figure 3.3: Schematic drawing of the PRECCISNTA LDI burner [41].

validate ignition models, which could be later coupled with the ONERA CFD code (CEDRE) to predict the ignition/re-ignition phenomena, especially in altitude conditions [56, 57].

With regard to the multi-point injection strategy, the same swirl-injector module introduced in 2005 in the work mentioned above by Cai et al. [36] was adopted as the baseline 9-point swirl-venturi (SV) LDI configuration developed by the NASA Glenn Research Centre [59]. In 2007, Fu et al. [60] reported the first detailed measurements on mean and fluctuating gaseous velocity components for the multi-point co- and counter-swirling cases. The results revealed a complicated flowfield near the injectors and the absence of a central recirculation zone in both multi-point cases when compared with the single-element case. This influence was attributed to the high turbulence and strong interactions among the adjacent swirler-injectors near the swirler exit. Later on, in 2010, Heath et al. [61] conducted a set of liquid-fueled (JET-A) experiments at high-pressure (10-13 atm) and high-temperature (672-828 K) conditions to determine the potential of the MP-LDI strategy in next-generation aircraft powerplants. They measured both gaseous and liquid velocities (mean and RMS), and fuel drop sizes at very-lean conditions (equivalence ratios between 0.41 and 0.45). They found that the 9-point LDI burner was extremely effi-

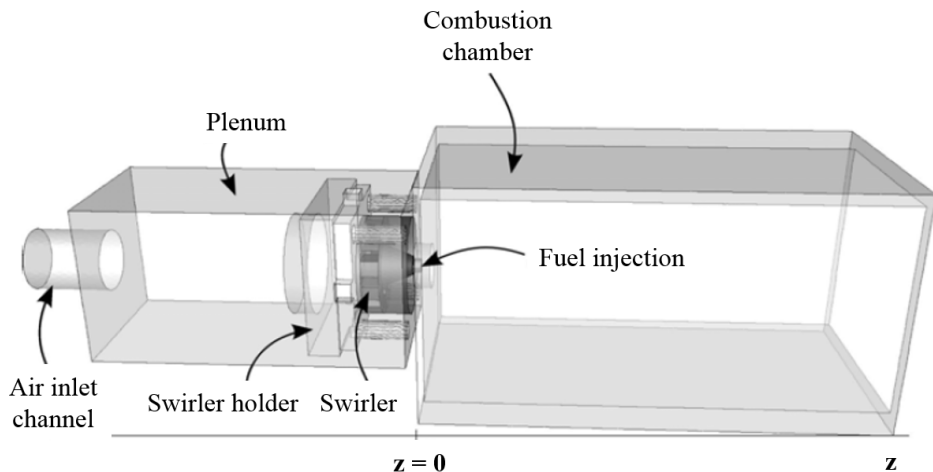


Figure 3.4: Schematic drawing of the MERCATO test rig [58].

cient atomising the fuel since the reported average arithmetic mean diameters (D_{10}) were typically less than $20\ \mu\text{m}$ and all the droplets (including the largest ones) were vaporised entirely within the first 15 mm from the nozzle. Hicks et al. [62] also investigated in 2012 the 9-point swirl-venturi LDI configuration at the same conditions than Heath et al. [61]. They reported gaseous and liquid properties and expanded the study to visualise the flame structure for two different cases: on the one hand, equally splitting the fuel injections (JP8) into all injectors, and on the other hand, just feeding the central injector. According to the results, the burning region in the central injection case extended considerably downstream since the local equivalence ratio was much higher than for the evenly-fueled configuration. The authors also reported local burning influence for each element and limited flame interaction between injectors.

Some years later (2014), three second-generation SV-LDI configurations were developed by Tacina et al. [63] at the NASA Glenn Research Centre based on the baseline 9-point SV-LDI hardware mentioned above [59]. These three variations showed better low-power operability than the original 9-point configuration, and the landing-takeoff NO_x emissions were expected to be around 85% below the CAEP/6 standards [64]. Tacina et al. [65] studied combustion dynamics and found that substituting half of the main-stage fuel flow from the simplex main-1 stage by the airblast main-2 stage (maintaining the overall equivalence ratio) could significantly reduce the NO_x emissions. It is important to note that a third-generation 7-point swirl-venturi lean-direct-

injection (SV-LDI-3) combustor [66] is currently under investigation.

Other novel experimental LDI facilities have also been designed by Delft and Cambridge research groups to improve the knowledge of the droplets-turbulence-flame interactions and enhance the modeling capabilities of turbulent spray reacting flows. On the one hand, the Delft Spray Burner was designed by Correia-Rodrigues et al. [67, 68] to study spray combustion in Moderate or Intense Low-oxygen Dilution (MILD) non-swirled co-flow conditions. On the other hand, the Cambridge Spray Burner was updated by Yuan et al. [69, 70] from the gaseous bluff-body swirl burner [71] to investigate the local flame structure, the reaction zones and the local quenching holes along with the flame sheet at conditions close to blow-off limits.

Finally, the last LDI test rig here reviewed is the confined burner developed and installed at CORIA¹ [72]. The experimental setup is composed of all the elements found in a standard combustor: plenum, radial swirler, combustion chamber and convergent exhaust. The CORIA burner has been tested both for gaseous [73] and spray [74] fuel cases considering both single-point [75] and multi-point [76] injection strategies, leading to a complete database for validating CFD codes. More recently, a new atmospheric unconfined non-swirled configuration known as CORIA Rouen Spray Burner (CRSB) [77, 78] has been proposed to evaluate the droplet-flame interactions and quantify the fuel droplet properties in terms of size, velocity and temperature across the flame front. Last, very-recent quantitative measurements of NO_x concentrations have been reported by Mulla et al. [79] in dilute spray flames within the CRSB.

As a conclusion about the current state of knowledge, the understanding of the dynamic spray structure is deemed to be crucial for the fulfilment of the ignition/re-ignition and combustion stability requirements. As reviewed, even though aircraft engines operate under high-pressure conditions, most of the laboratory-scale combustors are usually studied at ambient conditions, typically operating at 1 bar. Thus, comprehensive research on the influence of high-pressure conditions in LDI devices is an area with limited progress. On the other hand, although several experimental works have also dealt recently with multiple injectors, these studies are only addressed in a qualitative sense, and further investigation is required to shed light on complex phenomena such as ignition cycle, interactions among injectors and combustion dynamics in more realistic configurations.

¹The laboratory-scale CORIA Spray Burner is taken as a reference to carry out the present investigation.

Author	Year	Test rig	Swirler-injector system	Operating conditions	Relevant results
Meier et al. [30]	2000	Tecflam Swirl Burner	Annular nozzle Axial swirler	298 K 1 atm	2D Gas velocity 2D Temperature profiles Species concentration
Tacina et al. [31]	2002	Open flame tube testing	MP simplex (5x5) Radial swirler	505 to 810 K 1 to 27 atm	NO _x emissions SMD distribution
Archer et al. [34]	2003	Double concentric swirl burner	Central pipe Radial swirler	298 K 1 atm	2D Gas velocity 2D Vorticity
Li et al. [35]	2004	TARS LDI burner	Simplex Triple axial swirler	298 K 1 atm	NO _x and CO emissions 3D Gas velocity 2D Temperature profiles
Cai et al. [36]	2005	NASA LDI burner	Simplex Axial swirler	298 and 503 K 1 atm	3D Gas velocity 2D Spray velocity Drop size distribution
Janus et al. [39, 40]	2005	TURBOMECA LDI burner	Central tube Radial swirler	623 K 2 to 6 atm	3D Gas velocity Fuel distribution Flame structure
Weigand et al. [41, 42, 44]	2006-2012	PRECCINSTA/ GENRIG Burner	Central pipe/simplex Radial swirlers	295 to 850 K 1 to 20 atm	3D Gas velocity Temperature profiles Flame structure

Continued on next page

Author	Year	Test rig	Swirler-injector system	Operating conditions	Relevant results
Al-Abdeli et al. [46, 51]	2007-2011	Sydney Swirl/Spray Burner	Central tube/Simplex Tangential swirler	298 K 1 atm	3D Gas and spray velocity Flame structure
García-Rosa et al. [52, 54, 57]	2007-2011	MERCATO test rig	Simplex Radial swirler	233 to 463 K 1 to 4 atm	3D Gas and spray velocity Spray size distribution Re-ignition sequences
Fu et al. [60-62]	2007-2012	NASA 9-point SV-LDI Burner	Simplex Axial swirler	298 to 828 K 1 to 13 atm	3D Gas and spray velocity Spray size distribution Flame structure
Renou et al. [73, 74]	2013-2019	CORIA Spray Burner	Simplex Radial swirler	298 to 416 K 1 atm	3D Gas and spray velocity Spray size distribution Flame structure NO _x emissions
Tacina et al. [63-65]	2014-2016	Second-generation NASA 9-point SV-LDI Burner	Simplex/airblast Axial swirler	535 to 810 K 7 to 18 atm	NO _x and CO emissions
Roekaerts et al. [67, 68]	2015	Delft Spray Burner	Simplex No swirler	298K 1 atm	3D Gas and spray velocity Spray size distribution Flame structure
Yuan et al. [69, 70]	2015-2018	Cambridge Spray Burner	Simplex Radial swirler	298K 1 atm	Flame structure Species concentration

Table 3.1: *Experimental works on LDI combustors.*

3.3 Computational Studies on LDI Burners

This section intends to provide a clear vision of state of the art concerning computational investigations on LDI carried out by some authors from the early numerical methods to our days. Unlike experimental approaches, which can be notably time-consuming and expensive, numerical simulations allow diminishing the number of experimental tests, avoiding the installation of expensive diagnostic tools and allowing the access to information at locations not accessible to optical or sensors measurements. In this way, Computational Fluid Dynamics (CFD) simulations (see Section 4.2) have emerged as a valuable complementary research tool, enabling to acquire a better understanding of the complex unsteady processes that occur in the injection systems, such as the vortex breakdown bubble (VBB) and the precessing vortex core (PVC). With this knowledge, it is more accessible to circumscribe and improve the performance of the LDI system under different operating conditions [80]. The exponential rise in computing power has also been utilised to further develop and test several spray and combustion sub-models in simpler geometries [81–87].

A vast number of computational researches on LDI combustors have been carried out in the last two decades oriented to study the behaviour of the spray breakup, droplet dispersion in swirling flow and mixing under different operating conditions. Given the high turbulence and unsteadiness associated to the swirling motion inside the combustor, the Unsteady Reynolds-Averaged Navier Stokes (U-RANS) turbulence modeling approach precludes a complete analysis of the flow characteristics. U-RANS simulations model the turbulence and only resolve statistically steady flow structures, failing in predicting turbulence fluctuation statistics accurately and, thus, resulting insufficient in to represent the complexity of LDI combustors. Recently, some Direct Numerical Simulation (DNS) investigations of swirling spray combustion have been performed [88–90] in which all the scale structures of scalar and velocities fluctuations are solved. Nevertheless, these simulations are still limited to canonical flow configurations and low Reynolds numbers since its expensive computational cost limits its application in practical flows. Therefore, Large Eddy Simulations (LES) have emerged as a realistic alternative and has been applied in most numerical studies to investigate the generation and evolution of the fully transient coherent structures in swirl-stabilised combustors. In LES, the governing equations are filtered to separate the large-scale turbulence, solved by the discretised equation; and small-scale turbulence, modeled through the sub-grid scales models to represent the effects of unresolved small-

scale fluid motions. A comprehensive description of turbulence approaches is presented in Section 4.2.2.

Concerning the numerical modeling approaches for simulating multiphase flow systems used in conventional swirling spray combustors, the Eulerian-Eulerian (EE), Eulerian-Lagrangian (EL) and hybrid methods should be highlighted (see Section 4.2.3). Since in the Eulerian-Eulerian formulation both carrier and disperse phases are solved using a common Eulerian framework [91–93], a consistent numerical method can be used for both phases, thus taking advantage of scalable, high-performance parallel computing. However, this approach requires substantial modeling effort for the disperse phase and is considered expensive for polydisperse systems. Meanwhile, in the Eulerian-Lagrangian method, the conventional Eulerian framework is used to compute the carrier phase, and a Lagrangian tracking is performed to the disperse phase calculation [94]. Despite its slower statistical convergence and inefficient parallelisation, this approach is the most common method to simulate the swirling spray in LDI burners due to its robustness and capability to model complex phenomena such as droplet breakup and interactions. In recent years, hybrid methods have been developed, joining the Eulerian-Eulerian formulation near the nozzle with the Eulerian-Lagrangian approach further downstream to simulate the complete breakup process [95].

One of the first simulations was performed in 2002 by Sankaran and Menon [96], who carried out an LES of a cylindrical dump combustor similar to the dual-annular counter-rotating swirling (DACRS) gas turbine burner of GE Aircraft Engines (GEAE). They may have been the first authors to numerically study the effect of the swirl strength on the transient interactions between fuel spray dispersion, vaporisation, fuel-air mixing and heat release in a realistic LDI configuration. According to the results, enhanced droplet dispersion and fuel-air mixing were manifested when increasing the swirl intensity. They also reported that a central toroidal recirculation zone (generated as a result of a vortex breakdown process) only occurred under high-swirl conditions and demonstrated how its size was reduced in the presence of combustion and heat release.

In 2007, Stein and Kempf [97] and Malalasekera et al. [98] conducted non-reacting and reacting gaseous-fueled LES computations of the Sydney Swirl Burner [46] with the PUFFIN CFD code [99]. Some efforts were focused on predicting key features of swirling flames with moderate-resource approaches such as the laminar flamelet model. They reported good agreement overall with experimental data on the velocity, mixture and temperature profiles. Besides, the LES also predicted the collar-like structures generated near the

necking vicinity of the flame. However, some discrepancies were reported on the species and temperature results in some regions of the swirling flame, indicating that the steady laminar flamelet model could not be quite adequate for such cases.

Some years later, Chrigui et al. [100] (2013) and El-Asrag and Braun [101] (2015) performed Eulerian-Lagrangian LES of the liquid-fueled Sydney Spray Burner [51]. Chrigui et al. [100] considered the FGM tabulated chemistry to study an ethanol spray flame. General agreement with experimental data was reported, especially in the combustion properties, such as flame height. Meanwhile, El-Asrag and Braun [101] focused the study on the non-reacting spray properties. The effect of U-RANS turbulence closure models on the turbulent drop dispersion, drop size distribution and spray evolution was investigated for an ethanol spray flame. A strong impact on the predicted spray trajectory and dispersion characteristics were reported when moving from isotropic turbulence models (e.g., $k-\epsilon$ and SST $k-\omega$) to non-isotropy modeling (e.g., Reynolds Stress Model). Most recently, several simulations have been performed on the Sydney Spray Burner in order to assess more advanced combustion models (e.g., artificially thickened flame method [102, 103] and multi-regime flamelet coupled with the dynamic thickened flame model [104, 105]) that allow overcoming the limitations reported in the past by Malalasekera et al. [98].

At CERFACS, several two-phase flow LES of the MERCATO test rig were performed between 2007 and 2011 by Lamarque [106], Sanjosé et al. [107] and Senoner et al. [108] for reacting conditions and by Sanjosé et al. [109] and Jones et al. [110] for an isothermal case (see Figure 3.5). In this sense, Eulerian-Eulerian (EE) and Eulerian-Lagrangian (EL) simulations were conducted with the in-house AVBP CFD code and the implemented FIM-UR (Fuel Injection Method by Upstream Reconstruction) methodology to initialise the drop size and velocity distributions without resolving primary atomisation. In both EE and EL approaches, a constant diameter was set for the injected spray taken from the mean diameter of the drop distribution measured experimentally. According to the authors, both approaches yielded liquid velocity fields in good agreement with measurements, and the opening angle and rotation of the spray were correctly captured. Nevertheless, the monodisperse description of the spray hindered a proper prediction of mean droplet diameters. From similar studies, polydispersion was known to influence on cold spray dispersion but no significant changes on the flame shape and structure [111]. On the other hand, the EE simulation exhibited smoother evaporation, whereas EL case results revealed detached “pockets” of intense evaporation, as also reported by Jaegle et al. [112]. Finally, strong inhomogeneities and unsteady structures on the dispersed phase were reported and attributed to the PVC.

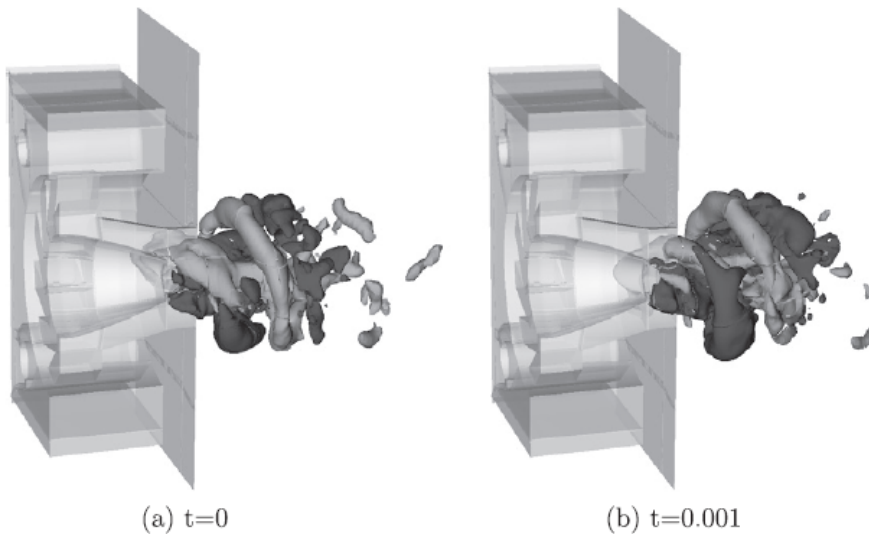


Figure 3.5: PVC structure identified at the MERCATO test rig through an iso-surface of Q -criterion at different times [110].

Later on, in 2008, Boileau et al. [113] performed an LES study of the ignition sequence within the full annular VESTA combustor built by TURBOMECA (see the left side of Figure 3.6) using an Eulerian-Eulerian framework. The fuel spray was assumed to be entirely atomised, so the distribution of liquid droplets was directly injected. They analysed the flame propagation between the 18 sectors that composed the combustion chamber, each one presenting its own swirler/injector system (see right side of Figure 3.6). Results also showed how the presence of a vortex breakdown bubble generated strong recirculation zones in which the flame was stabilised and modulated during ignition. Nevertheless, the lack of detailed experimental data hindered any possible validation. One year later, Staffelbach et al. [114] conducted 45-million elements LES to capture the self-excited instabilities generated throughout the full annular geometry. They found that two superimposed rotating modes at 740 Hz with different amplitudes modulated both the flow rate and the flame location through the 18 burners. The presence of these azimuthal modes was found to lead to local heat release fluctuations induced by flame oscillations and eventual flashback.

Special consideration must be given to the work by Patel and Menon [115], who successfully carried out an LES to represent the behaviour of the spray-turbulence interactions within an LDI combustor, as done in the present thesis.

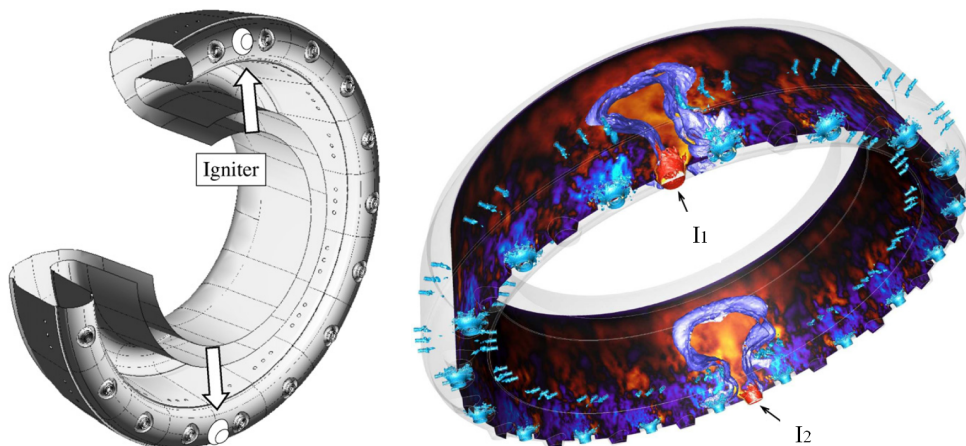


Figure 3.6: Left: Global view of the VESTA combustor. Right: Ignition sequence revealed through the evolution of the flame front [113].

In addition, they made a particular effort to numerically determine spray-flame interactions in the single-element NASA LDI burner [36]. The simulations were performed using the NASA in-house National Combustion Code (NCC) developed by Liu et al. [116] with a lagrangian formulation (Discrete Droplet Model, DDM) to represent the spray. Results were achieved at predicting both the spray dispersion through the PVC structure and the flame stabilisation within the VBB. Besides, they reported drop-drop and drop-gas correlations for several breakup models (KH and TAB). With regard to the spray behaviour, they concluded that the spray velocity and drop size distribution were strongly influenced by the incoming turbulent swirling flow.

With regard to the single-element NASA LDI burner [36], Liu et al. [117] also performed several reacting two-phase simulations with the NCC code for the single-element LDI using U-RANS and LES methods and diverse validated sub-grid models for turbulent mixing and combustion (i.e., well-mixed model, eddy-break-up model [118], thickened flame model [119], flamelet-based model [120], conditional moment closure -CMC- method [121], filtered mass density function/probability density function -FDF/PDF- method [122] and linear eddy mixing -LEM- model [115]). Liu reported the simultaneous presence of both premixed, partially-premixed and non-premixed flames in the burner and confirmed the enhancement of spray particle dispersion hinted by Patel and Menon [115] as a consequence of the PVC. Meanwhile, Davoudzadeh et al. [123] and Dewanji and Rao [124, 125] also investigated the non-reacting and reacting flow in the single-element [36] and multi-point [60] NASA LDI

combustors through U-RANS and LES approaches. On the one hand, the mean velocity components exhibited by Davoudzadeh et al. [123] showed some discrepancy with experimental data at the entrance of the combustion chamber due to a poor grid refinement (0.86 million cells). On the other hand, the simulations of Dewanji and Rao [124, 125] captured the unsteady turbulent flow structures at the border of the neighbouring swirlers and evaluated the spray velocity and drop size distribution for several spray models. In this way, they showed how the shear layers emerging from adjacent swirlers in the multi-point LDI configuration played a major role in the spray dispersion and mixing when compared to the single-element LDI burner. Finally, more recent non-reacting and two-phase reacting flow CFD analysis with the NCC code of the NASA third-generation lean-direct-injection (SV-LDI-3) combustor [66] can be found in the work by Ajmani et al. [126].

In 2011, Luo et al. [127] conducted a Direct Numerical Simulation to study the spray combustion in a simplified coaxial dump LDI combustor [128] based on the design of a Pratt and Whitney gas-turbine engine. The case setup was evaluated from previous LES of Moin and Apte [85] and Mahesh et al. [129]. A log-normal drop size distribution of n-heptane was injected in an Eulerian-Lagrangian framework, and the secondary breakup was not considered. Results exhibited a complex flame structure, composed of premixed and non-premixed combustion regions, as previously reported by Liu et al. [117]. They also found that premixed flames, although covering a small volume than diffusion flames, contributed more than 70% to the total heat release rate.

As important milestones, Moureau et al. [130] were the first to consider a real lab-scale burner to conduct Direct Numerical Simulations (DNS) in complex LDI geometries. In this way, they performed a 2634-million tetrahedral cells² DNS on the PRECCINSTA Burner [41] to gain insight into the flame dynamics and structure (see Figure 3.7). The boundary layers were not resolved ($y^+ \geq 10$ in all regions) since the authors suggested them to have a minimal impact on such flow, at least for the flame-turbulence interaction under study. The DNS computation, initialised from a converged solution of a 329-million elements LES, required 16 384 cores during 80 hours to simulate 1.9 ms of physical time, corresponding to the Precessing Vortex Core characteristic time scale. DNS results were employed to calibrate and evaluate existing combustion models based on premixed flamelet and presumed probability density functions. Nevertheless, some limitations were reported concerning the heat transfer treatment in the corner recirculation zones.

²It is important to note that tetrahedron-based meshes count about eight times more elements than hexahedron-based meshes with the same resolution.

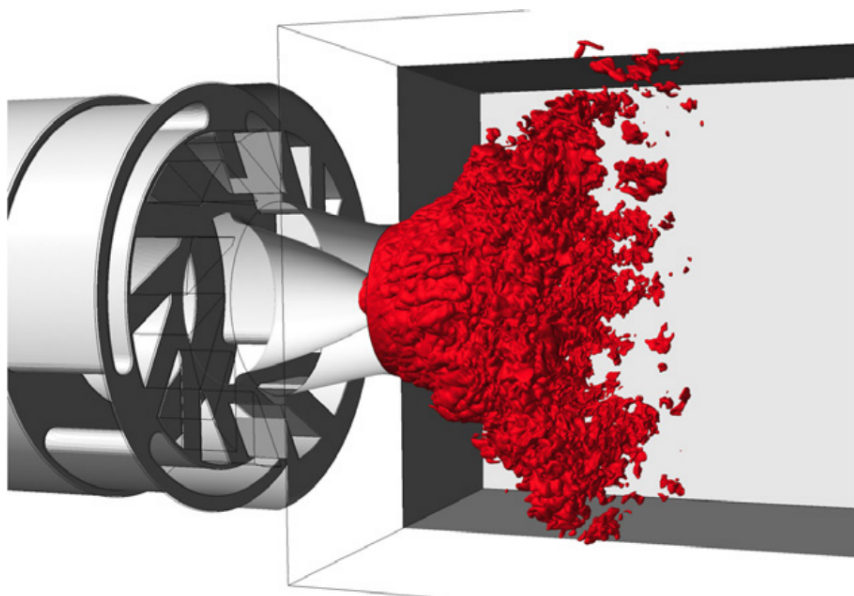


Figure 3.7: 3D flame view of the shape flame through an iso-surface of a progress variable in a 2634-million cells DNS on the PRECCINSTA Burner [130].

Some years later, Jones et al. [131] investigated the turbulent mixing, spray dispersion and evaporation and combustion in the GENRIG burner installed at the DLR [44] at both reacting and non-reacting conditions in an Eulerian-Lagrangian LES framework. The essential flow features were well reproduced through the in-house BOFFIN-CFD code, but some discrepancies were reported in the recirculation zone. This was attributed both to the uncertainty in the inlet spray boundary conditions and to the questioned suitability of the Lagrangian formulation for the liquid phase close to the nozzle.

Similar works were carried out a few years later by Wang et al. [132, 133], who performed detailed comparisons of the performances of several turbulent combustion models (i.e., dynamically thickened-flame -DTF- model, flame surface density -FSD- model and Reaction-Diffusion Manifold -REDIM-technique) for turbulent premixed swirling flames within the PRECCINSTA Burner [41]. According to the authors, the plenum and the atmosphere were not included into the discretised computational domain (solved with the in-house LESOCC2C CFD code) to avoid the interactions between the turbulent flame and acoustics of the system, which were known to be susceptible to the inlet and outlet boundary conditions. Good agreement between the LES and

experimental data was reported for the velocity statistics, the concentrations of the main species and temperature. However, the prediction of the minor species distribution exhibited substantial differences between the tested combustion models. Most recently, Ramaekers et al. [134] analysed the influence of the LES sub-grid scale model on the non-reacting mean and fluctuating values of velocity within a slightly modified version of the PRECCINSTA Burner equipped with a double-curved convex nozzle. To this end, the performance of both Smagorinsky (varying the subgrid viscosity constant value) and Dynamic Smagorinsky cases was assessed through several LES index quality indicators. According to the solution, the predicted opening angle of the swirling jet within the combustion chamber was strongly affected by the subgrid viscosity.

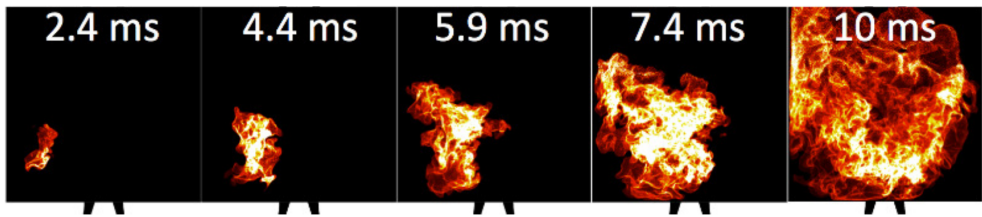


Figure 3.8: Spray ignition sequence predicted by LES within the CORIA Spray Burner [135].

Finally, the gaseous-configuration of the CORIA LDI burner [73] has been studied numerically at premixed [75, 76] and non-premixed [136] conditions in single [75, 136] and multi-injector [76] burner configurations with both the AVBP and the in-house YALES2 [137] CFD codes. In this sense, Barré et al. [76] conducted high-fidelity LES to analyse the impact of the flow structures on the ignition sequences and flame propagation. In their work, supported by experiments, they also performed simulations varying the distance between injectors. They concluded that increasing spacing between consecutive injectors directly affected the flame propagation mode and thus the ignition delay. Besides, they identified a critical distance, above which propagation occurred not only in the spanwise direction but also in the axial direction. Finally, very-recent two-phase flow LES were conducted in 2019 by Collin-Bastiani et al. [135] on the liquid-fueled CORIA Spray Burner [74]. Their study was focused on the influence of initial flow conditions on the flame structure and spray ignition. In addition, they analysed the overall temporal evolution of the ignition process (see Figure 3.8) and the transient spray-flame interaction. Results suggested that the flame kernel evolution and the success of ignition were strongly influenced by the local non-reacting turbulence intensity and presence of droplets at the sparking location.

Author	Year	Test rig	Turbulence modeling	Grid resolution and numerical method	Relevant results
Sankaran et al. [96]	2002	DACRS Burner	Smago. LES	0.85 M structured cells 2 nd order time and space EL approach	3D Gas velocity Spray Visualisation Unsteady structures
Davoudzadeh et al. [123]	2006	NASA 9-p LDI Burner [60]	U-RANS (low-Re k- ϵ)	0.86 M structured cells 4-step Runge-Kutta Gaseous-fueled case	3D Gas velocity
Patel and Menon [115]	2008	NASA LDI Burner [36]	LEM-LES	2.06 M structured cells 2 nd order time and space EL approach	3D Gas and spray velocity Spray size distribution Unsteady structures Flame structure
Boileau et al. [113]	2008	VESTA combustor	LES (WALE)	19 M unstructured cells 3-step Runge-Kutta EE approach	Species concentration Ignition sequence Flame propagation Flame structure
Malalasekera et al. [98]	2008	Sydney Swirl Burner [46]	Smago. LES	3.4 M structured cells 2 nd order time and space EL approach	3D Gas velocity Species concentration Temperature profiles

Continued on next page

Author	Year	Test rig	Turbulence modeling	Grid resolution and numerical method	Relevant results
Staffelbach et al. [114]	2009	VESTA combustor	Smago. LES	42 M structured cells 2 nd order time and space Gaseous-fueled case	Spectral Analysis (pressure) Heat release (flame response) Temperature fields
Liu et al. [117]	2011	NASA LDI Burner [36]	U-RANS LEM-LES	0.86 M structured cells 2 nd order time and space EL approach	Assess combustion models Unsteady structures Temperature profiles
Sanjosé et al. [109]	2011	MERCATO test rig [52]	LES (WALE)	3.5 M unstructured cells 2-step Runge-Kutta EE and EL approach	3D Gas and spray velocity Spray size distribution Unsteady structures Species concentration
Luo et al. [127]	2011	Coaxial Combustor Model [128]	DNS	75 M structured cells 2 nd order time and space EL approach	Evaporation rates Species concentration Flame structure Temperature distribution
Moureau et al. [130]	2011	PRECCINSTA Burner [41]	DNS	2634 M unstructured cells 4-step Runge-Kutta Gaseous-fueled case	3D Gas velocity Species concentration Flame structure

Continued on next page

Author	Year	Test rig	Turbulence modeling	Grid resolution and numerical method	Relevant results
Jones et al. [110]	2012	MERCATO test rig [52]	Smago. LES	3.7 M unstructured cells 2 nd order time and space EE and EL approach	3D Gas and spray velocity Spray size distribution Spectral Analysis (PSD)
Barré et al. [76]	2014	Multi-point CORIA LDI Burner [76]	LES (WALE)	43.1 M structured cells 3 rd order time and space Gaseous-fueled case	3D Gas velocity Ignition sequences Flame propagation Flame structure
Jones et al. [131]	2014	GENRIG Burner [44]	LES (Dyn. Smago.)	2.2 M structured cells 2 nd order time and space EL approach	3D Gas and spray velocity Spray size distribution Unsteady structures Flame structure
El-Asrag et al. [101]	2015	Sydney Spray Burner [51]	U-RANS (k- ϵ , k- ω , RSM)	1.05 structured cells 2 nd order time and space EL approach	3D Gas and spray velocity Spray size distribution
Esclapez et al. [136]	2015	Single-point CORIA LDI Burner [73]	LES (WALE)	22 M structured cells 3 rd order time and space Gaseous-fueled case	3D Gas velocity Species concentration Ignition probability maps

Continued on next page

Author	Year	Test rig	Turbulence modeling	Grid resolution and numerical method	Relevant results
Dewanji et al. [125]	2015	NASA 9-p LDI Burner [60]	U-RANS (k- ϵ) Smago. LES	8.7 M structured cells 2 nd order time and space EL approach	3D Gas and spray velocity Spray size distribution Unsteady structures Temperature profiles
Wang et al. [133]	2016	PRECCINSTA Burner [41]	LES (Dyn. Smago.)	8.5 M structured cells 3-step Runge-Kutta Gaseous-fueled case	3D Gas velocity Species concentration Spectral analysis (PSD)
Ajmani et al. [126]	2017	Third-gen. NASA SV-LDI Burner [66]	U-RANS (k- ϵ) TFN/VLES	22 M unstructured cells 2 nd order time and space EL approach	3D Gas velocity Species concentration Temperature contours
Ramaekers et al. [134]	2018	PRECCINSTA Burner [41]	LES (Smago. and Dyn. Smago.)	8.4 M structured cells 2 nd order time and space Gaseous-fueled case	3D Gas velocity Unsteady structures LES quality indicators
Bastiani et al. [135]	2019	CORIA Spray Burner [74]	LES (WALE)	60 M unstructured cells 2 nd order time and space EL approach	3D Gas and spray velocity Ignition sequences Spray-flame interaction Flame structure

Table 3.2: Numerical works on LDI combustors.

3.4 Studies based on Advanced Spectral Analysis

As reviewed, traditional experimental measurements (see Section 3.2) and numerical simulations (see Section 3.3) on LDI burners have resulted in 2D or 3D snapshots data, thus providing a meaningful insight about the turbulent flow field within the combustor and illustrating how the coherent structures are much stronger than small scales fluctuations. In most of those works, snapshot datasets were averaged in order to extract ensemble-averaged and root-mean-square (RMS) fields for quantitative comparisons. The shortcoming of that approach is that a significant fraction of the information contained in the snapshots was lost, especially the dynamic interaction and evolution of the large-scale coherent structures. Such phenomena are strongly unsteady and three-dimensional, being complex to study experimentally and even numerically.

In this context, advanced statistical data processing techniques based on linear-algebra tools such as the Proper Orthogonal Decomposition (POD) and the Dynamic Mode Decomposition (DMD) have emerged in the recent past with the aim of shedding some light on the flow diagnostics to characterise their structure and extract complementary information. These two powerful tools complement each other and have been applied to extract the low-order coherent structures acting as precursors of the global self-sustained oscillations. A brief review is shown in this section regarding the existing works in which these techniques have been applied. A comprehensive description of the theoretical background is presented in Section 4.4.2.

On the one hand, Lumley [138] was the first to use the Proper Orthogonal Decomposition (POD) technique to track the behaviour of coherent structures in turbulent flows. From then on, POD has been extensively used to analyse many different complex flows. In the reciprocating Internal Combustion Engine (ICE) field, POD has been applied to analyse issues such as acoustic impact and spark-ignition misfire both experimentally [139–144] and numerically [145], and more recently to study pressure resonance phenomena [146] through CFD simulations. Meanwhile, in aeronautical research, POD has demonstrated to be useful for multiple applications such as the analysis of the aircraft engine noise [147–149] and the optimisation of compressors [150, 151] and turbines [152], being also able to identify from external aerodynamic fluctuations [153] to wing aeroelastic responses [154].

Specifically, aero-engine combustors have been experimentally investigated through POD decomposition techniques. Based on the PIV measurements, the presence of a Vortex Breakdown Bubble (VBB) and a Precessing Vortex Core

(PVC) have been partially revealed and characterised in strongly swirling jets using modal decomposition analysis both in non-reacting [155–162] and reacting [45, 163–166] conditions. Nevertheless, as a consequence of experimental diagnosis shortcomings (e.g., the sampling frequency of the Stereo PIV system can be sometimes much smaller than the PVC frequency [157]), temporal and spatial-detailed CFD simulations have emerged as a potential tool to successfully characterise the coherent structures within the combustor through pressure, vorticity and species signals decomposition rather than dealing just with velocity. In this way, the POD technique applied to numerical studies has characterised the VBB and the transition to helical breakdown modes in non-reacting conditions [80, 167, 168], the combustion dynamics and flame interactions in reacting conditions [115, 169–172] and the impact of variations of thermal load and global equivalence ratio on combustion acoustics noise levels [173, 174].

On the other hand, the Dynamic Mode Decomposition technique [175, 176] has been used in recent turbulent flow investigations [177, 178]. So far, this post-processing tool has been limitedly employed for simple modal flow decomposition in reciprocating engines [145, 146]. In fact, even in gas turbine research, its application to the combustion problem is still scarce, focused on experimental PIV data analysis based on velocity and vorticity fields [179, 180]. It has been only in the very recent years when DMD has been successfully applied both to experimental aero-engine investigations, such as cavity flows [181], fan [182] and combustion noise [183–185], and to CFD studies to a lesser extent (e.g., radial [151] and centrifugal [186] compressors, and swirled-stabilised lean combustors [187]), where DMD has allowed obtaining flame structures and dominant acoustic modes.

References

- [1] Liu, Y. et al. “Review of modern low emissions combustion technologies for aero gas turbine engines”. In: *Progress in Aerospace Sciences* 94 (2017), pp. 12–45. DOI: 10.1016/j.paerosci.2017.08.001.
- [2] Russell, P., Beal, G., and Hinton, B. “Low NO_x heavy fuel combustor concept program”. In: *NASA Technical Report NASA-CR-165512* (1981).
- [3] Al-Kabie, H. and Andrews, G. “Ultra low NO_x emissions for gas and liquid fuels using radial swirlers”. In: *Proceedings of the ASME Turbo Expo*. Vol. 3. 1989. DOI: 10.1115/89-GT-322.

- [4] Al-Kabie, H. and Andrews, G. "Radial swirlers with peripheral fuel injection for ultra-low NO_x emissions". In: *Proceedings of the ASME Turbo Expo*. Vol. 3. 1990. DOI: 10.1115/90-GT-102.
- [5] Alkabie, H. and Andrews, G. "Reduced NO_x Emissions Using Low Radial Swirler Vane Angles". In: *Proceedings of the ASME: International Gas Turbine and Aeroengine Congress and Exposition*. Orlando, Florida (USA), 1991. DOI: 10.1115/91-GT-363.
- [6] McVey, J. et al. "Evaluation of low NO_x combustor concepts for aeroderivative gas turbine engines". In: *ASME 1992 International Gas Turbine and Aeroengine Congress and Exposition*. Vol. 3. 1992. DOI: 10.1115/92-GT-133.
- [7] Hayashi, S., Yamada, H., Shimodaira, K., and Machida, T. "NO_x emissions from non-premixed, direct fuel injection methane burners at high-temperature and elevated pressure conditions". In: *Symposium (International) on Combustion 27.2* (1998), pp. 1833–1839. DOI: 10.1016/S0082-0784(98)80025-8.
- [8] Tacina, R. "Low NO_x potential of gas turbine engines". In: *28th Aerospace Sciences Meeting*. 1990, pp. 1–19. DOI: 10.2514/6.1990-550.
- [9] Hussain, U., Andrews, G., Cheung, W., and Shahabadi, A. "Low NO_x Primary Zones Using Jet Mixing Shear Layer Combustion". In: *Proceedings of the ASME Turbo Expo*. Vol. 3. 1988. DOI: 10.1115/88-GT-308.
- [10] Anderson, D. "Ultra-Lean Combustion at High Inlet Temperatures". In: *Proceedings of the ASME Turbo Expo*. Vol. 2. 1989. DOI: 10.1115/81-GT-44.
- [11] Novick, A. and Troth, D. "Low NO_x heavy fuel combustor concept". In: *NASA Technical Report NASA-CR-165367* (1981).
- [12] Lew, H., Carl, D., Vermes, G., and DeZubay, E. "Low NO_x heavy fuel combustor concept program. Phase 1: Combustion technology generation". In: *NASA Technical Report NASA-CR-165482* (1981).
- [13] Rosfjord, T. "Evaluation of synthetic fuel character effects on rich-lean stationary gas turbine combustion systems. Vol. 1: Subscale test program". In: *Electric Power Research Institute Technical Report AP-2822* (1981).
- [14] Schultz, D. and Wolfbrandt, G. "Flame tube parametric studies for control of fuel bound nitrogen using rich-lean two stage combustion". In: *NASA Technical Report NASA-TM-81472* (1980).

- [15] Nguyen, L. and Bittker, D. "Investigation of low NO_x staged combustor concept in high-speed civil transport engines". In: *NASA Technical Report NASA-TM-101977* (1989).
- [16] Anderson, D. "Effect of Equivalence Ratio and Dwell Time on Exhaust Emissions From an Experimental Premixing Prevaporizing Burner". In: *NASA Technical Report NASA-TMX-71592* (1975).
- [17] Semerjian, H., Ball, I., and A., Vranos. "Pollutant Emissions from Partially Mixed Turbulent Flames". In: *17th International Symposium on Combustion*, pp. 679–6879.
- [18] Andrews, G., N., Escott, A., Al-Shaikhly, and H., Al-Kabie. "Counter-rotating radial swirlers for low NO_x emissions with passage fuel injection". In: *International Symposium on Air Breathing Engines (ISABE)*. 1995.
- [19] Shaffar, S. and Samuelsen, G. "A Liquid Fueled, Lean Burn, Gas Turbine Combustor Injector". In: *Combustion Science and Technology* 139.1 (1998), pp. 41–57. DOI: 10.1080/00102209808952080.
- [20] Chen, R. and Driscoll, J. "The role of the recirculation vortex in improving fuel-air mixing within swirling flames". In: *Symposium (International) on Combustion* 22.1 (1989), pp. 531–540. DOI: [https://doi.org/10.1016/S0082-0784\(89\)80060-8](https://doi.org/10.1016/S0082-0784(89)80060-8).
- [21] Hadeif, R. and Lenze, B. "Measurements of droplets characteristics in a swirl-stabilized spray flame". In: *Experimental Thermal and Fluid Science* 30.2 (2005), pp. 117–130. DOI: 10.1016/J.EXPTHERMFLUSCI.2005.05.002.
- [22] Soltani, M., Ghorbanian, K., Ashjaee, M., and Morad, M. "Spray characteristics of a liquid-liquid coaxial swirl atomizer at different mass flow rates". In: *Aerospace Science and Technology* 9.7 (2005), pp. 592–604. DOI: 10.1016/J.AST.2005.04.004.
- [23] Hadeif, R. and Lenze, B. "Effects of co- and counter-swirl on the droplet characteristics in a spray flame". In: *Chemical Engineering and Processing: Process Intensification* 47.12 (2008), pp. 2209–2217. DOI: 10.1016/J.CEP.2007.11.017.
- [24] Tratnig, A. and Brenn, G. "Drop size spectra in sprays from pressure-swirl atomizers". In: *International Journal of Multiphase Flow* 36.5 (2010), pp. 349–363. DOI: 10.1016/J.IJMULTIPHASEFLOW.2010.01.008.

- [25] Linne, M., Paciaroni, M., Berrocal, E., and Sedarsky, D. “Ballistic imaging of liquid break-up processes in dense sprays”. In: *Proceedings of Combustion Institute* 32.2 (2009), pp. 2147–2161. DOI: 10.1016/j.proci.2008.07.040.
- [26] Desantes, J., Salvador, F., Lopez, J., and De la Morena, J. “Study of mass and momentum transfer in diesel sprays based on X-ray mass distribution measurements and on a theoretical derivation”. In: *Experiments in Fluids* 50.2 (2011), pp. 233–246. DOI: 10.1007/s00348-010-0919-8.
- [27] Reddemann, M., Mathieu, F., and Kneer, R. “Transmitted light microscopy for visualizing the turbulent primary breakup of a microscale liquid jet”. In: *Experiments in Fluids* 54.11 (2013), p. 1607. DOI: 10.1007/s00348-013-1607-2.
- [28] Ruan, C. et al. “Principles of non-intrusive diagnostic techniques and their applications for fundamental studies of combustion instabilities in gas turbine combustors: A brief review”. In: *Aerospace Science and Technology* 84 (2019), pp. 585–603. DOI: 10.1016/j.ast.2018.10.002.
- [29] Al-Abdeli, Yasir M. and Masri, Assaad R. “Review of laboratory swirl burners and experiments for model validation”. In: *Experimental Thermal and Fluid Science* 69 (2015), pp. 178–196. DOI: 10.1016/j.expthermflusci.2015.07.023.
- [30] Meier, W., Keck, O., Noll, B., Kunz, O., and Stricker, W. “Investigations in the TECFLAM swirling diffusion flame: Laser Raman measurements and CFD calculations”. In: *Applied Physics B: Lasers and Optics* 71.5 (2000), pp. 725–731. DOI: 10.1007/s003400000436.
- [31] Tacina, R., Wey, C., Laing, P., and Mansour, A. “A low NO_x lean-direct injection, multipoint integrated module combustor concept for advanced aircraft gas turbines”. In: *NASA Technical Report NASA-TM-211347* (2002).
- [32] Tacina, R., Mao, C., and Wey, C. “Experimental Investigation of a Multiplex Fuel Injector Module for Low Emission Combustors”. In: *41st Aerospace Sciences Meeting and Exhibit*. 2003, pp. 1–16.
- [33] Tacina, R., Mao, C., and Wey, C. “Experimental investigation of a multiplex fuel injector module with discrete jet swirlers for low emission combustors”. In: *NASA Technical Report NASA-TM-212918* (2004).

- [34] Archer, S. and Gupta, A. “Effect of Swirl and Combustion on Flow Dynamics in Lean Direct Injection Gas Turbine Combustion”. In: *41st Aerospace Sciences Meeting and Exhibit, AIAA 2003-1343*. 2003, pp. 1–9. DOI: 10.1115/DETC2003/CIE-48253.
- [35] Li, Guoqiang and Gutmark, Effie. “Effects of Swirler Configurations on Flow Structures and Combustion Characteristics”. In: vol. 1. 2004. DOI: 10.1115/GT2004-53674.
- [36] Cai, J, Tacina, R., and Jeng, S. “The Structure of a Swirl-Stabilized Reacting Spray Issued From an Axial Swirler”. In: *43rd AIAA Aerospace Sciences Meeting and Exhibit*. January. 2005.
- [37] Yi, T. and Santavicca, D. “Combustion Instability in a Turbulent Liquid-Fueled Swirl-Stabilized LDI Combustor”. In: *Experiments, to be presented at the 45th AIAA/ASME/SAE/ASEE Joint Propulsion Conference & Exhibition*. Denver, Colorado (USA), 2009.
- [38] Gejji, R., Huang, C., Fugger, C., Yoon, C., and Anderson, W. “Parametric investigation of combustion instabilities in a single-element lean direct injection combustor”. In: *International Journal of Spray and Combustion Dynamics* 11 (2018), p. 1756827718785851. DOI: 10.1177/1756827718785851.
- [39] Janus, B, Dreizler, A, and Janicka, J. “Experimental Study on Stabilization of Lifted Swirl Flames in a Model GT Combustor”. In: *Flow, Turbulence and Combustion* 75.1 (2005), pp. 293–315. DOI: 10.1007/s10494-005-8583-4.
- [40] Janus, B., Dreizler, A., and Janicka, J. “Experiments on swirl stabilized non-premixed natural gas flames in a model gasturbine combustor”. In: *Proceedings of the Combustion Institute* 31 II (2007), pp. 3091–3098. DOI: 10.1016/j.proci.2006.07.014.
- [41] Weigand, P., Meier, W., Duan, X., Stricker, W., and Aigner, M. “Investigations of swirl flames in a gas turbine model combustor: I. Flow field, structures, temperature, and species distributions”. In: *Combustion and Flame* 144.1-2 (2006), pp. 205–224. DOI: 10.1016/j.combustflame.2005.07.010.
- [42] Meier, W., Weigand, P., Duan, X., and Giezendanner-Thoben, R. “Detailed characterization of the dynamics of thermoacoustic pulsations in a lean premixed swirl flame”. In: *Combustion and Flame* 150.1-2 (2007), pp. 2–26. DOI: 10.1016/j.combustflame.2007.04.002.

- [43] Sadanandan, R., Stöhr, M., and Meier, W. “Simultaneous OH-PLIF and PIV measurements in a gas turbine model combustor”. In: *Applied Physics B: Lasers and Optics* 90.3-4 (2008), pp. 609–618. DOI: 10.1007/s00340-007-2928-8.
- [44] Meier, Ulrich, Heinze, Johannes, Freitag, Stefan, and Hassa, Christoph. “Spray and flame structure of a generic injector at aeroengine conditions”. In: *Journal of Engineering for Gas Turbines and Power* 134.3 (2012), pp. 1–9. DOI: 10.1115/1.4004262.
- [45] Stöhr, M, Arndt, C M, and Meier, W. “Effects of Damköhler number on vortex-flame interaction in a gas turbine model combustor”. In: *Proceedings of the Combustion Institute* 34.2 (2013), pp. 3107–3115. DOI: <https://doi.org/10.1016/j.proci.2012.06.086>.
- [46] Al-Abdeli, Y. and Masri, A. “Turbulent Swirling Natural Gas Flames: Stability Characteristics, Unsteady Behavior and Vortex Breakdown”. In: *Combustion Science and Technology* 179.1-2 (2007), pp. 207–225. DOI: 10.1080/00102200600809092.
- [47] Al-Abdeli, Y., Masri, A., Marquez, G., and Starner, S. “Time-varying behaviour of turbulent swirling nonpremixed flames”. In: *Combustion and Flame* 146.1 (2006), pp. 200–214. DOI: <https://doi.org/10.1016/j.combustflame.2006.03.009>.
- [48] Masri, A., Kalt, P., and Barlow, R. “The compositional structure of swirl-stabilised turbulent nonpremixed flames”. In: *Combustion and Flame* 137.1 (2004), pp. 1–37. DOI: <https://doi.org/10.1016/j.combustflame.2003.12.004>.
- [49] Masri, A., Kalt, P., Al-Abdeli, Y., and Barlow, R. “Turbulence-chemistry interactions in non-premixed swirling flames”. In: *Combustion Theory and Modelling* 11.5 (2007), pp. 653–673. DOI: 10.1080/13647830701213482.
- [50] Masri, A. and Gounder, J. “Turbulent Spray Flames of Acetone and Ethanol Approaching Extinction”. In: *Combustion Science and Technology* 182.4-6 (2010), pp. 702–715. DOI: 10.1080/00102200903467754.
- [51] Gounder, J., Kourmatzis, A., and Masri, A. “Turbulent piloted dilute spray flames: Flow fields and droplet dynamics”. In: *Combustion and Flame* 159.11 (2012), pp. 3372–3397. DOI: <https://doi.org/10.1016/j.combustflame.2012.07.014>.

- [52] García-Rosa, N. “Phénomènes d’allumage d’un foyer de turbomachine en conditions de haute altitude”. PhD thesis. Institut Supérieur de l’Aéronautique et de l’Espace - ONERA, 2008.
- [53] Lecourt, R., Rossoni, Laurent, Goyer, Stephen, and Linassier, Guillaume. “Gas Phase Velocity Measurements in a Swirled Air/Kerosene Burning Spray downstream from an Actual Turbojet Injection System”. In: *50th AIAA/ASME/SAE/ASEE Joint Propulsion Conference*. 2014. DOI: 10.2514/6.2014-3659.
- [54] Linassier, G., Lecourt, R., Villedieu, P., Lavergne, G., and Verdier, H. “Numerical and Experimental study of aircraft engine ignition”. In: *ILASS - Europe 2010, 23rd Annual Conference on Liquid Atomization and Spray Systems*. 2010, pp. 1–10.
- [55] Lecourt, R., Linassier, G., and Lavergne, G. “Detailed Characterisation of a Swirled Air/Kerosene Spray in Reactive and Non-Reactive Conditions Downstream From an Actual Turbojet Injection System”. In: *Proceedings of the ASME Turbo Expo*. Vol. 2. 2011, pp. 185–194. DOI: 10.1115/GT2011-45173.
- [56] Lecourt, R., Bismes, G., and Heid, G. “Experimental Investigation of Ignition of an Air-Kerosene Spray in Altitude Conditions”. In: *International Symposium on Air Breathing Engines (ISABE)*. 2009.
- [57] García-Rosa, N., Linassier, G., Lecourt, R., Villedieu, P., and Lavergne, G. “Experimental and Numerical Study of High-Altitude Ignition of a Turbojet Combustor”. In: *Heat Transfer Engineering* 32 (2011), pp. 949–956. DOI: 10.1080/01457632.2011.556377.
- [58] Senoner, J. “Simulation aux Grandes Échelles de l’écoulement diphasique dans un bruleur aéronautique par une approche Euler-Lagrange”. PhD thesis. Institut National Polytechnique de Toulouse - CERFACS, 2010.
- [59] Tacina, R., Lee, P., and Wey, C. “A Lean-Direct-Injection Combustor Using a 9 Point Swirl-Venturi Fuel Injector”. In: *International Symposium on Air Breathing Engines (ISABE)*. 2005.
- [60] Fu, Y., Jeng, S., and Tacina, R. “Characteristics of the swirling flow in a multipoint LDI combustor”. In: *45th AIAA Aerospace Sciences Meeting, AIAA 2007-846*. 2007. DOI: 10.2514/6.2007-846.

- [61] Heath, C., Hicks, Y., Anderson, R., and Locke, R. “Optical Characterization of a Multipoint Lean Direct Injector for Gas Turbine Combustors: Velocity and Fuel Drop Size Measurements.” In: *Proceedings of the ASME Turbo Expo*. Vol. 2. 2010, pp. 791–802. DOI: 10.1115/GT2010-22960.
- [62] Hicks, Y., Heath, C., Anderson, R., and Tacina, K. “Investigations of a Combustor Using a 9-Point Swirl-Venturi Fuel Injector: Recent Experimental Results”. In: *20th International Symposium on Air Breathing Engines (ISABE)*. Göteborg (Suecia), 2011.
- [63] Tacina, K., Chang, C., He, Z., Dam, B., and Mongia, H. “A Second Generation Swirl-Venturi Lean Direct Injection Combustion Concept”. In: *NASA Technical Report NASA-E-662715* (2014).
- [64] Tacina, Kathleen M. et al. “A comparison of three second-generation swirl-venturi lean direct injection combustor concepts”. In: *52nd AIAA/SAE/ASEE Joint Propulsion Conference, 2016*. 2016. DOI: 10.2514/6.2016-4891.
- [65] Tacina, R. et al. “An assessment of combustion dynamics in a low-NOx second-generation swirl-venturi lean direct injection combustion concept”. In: *International Symposium on Air Breathing Engines (ISABE)*. 2015.
- [66] Tacina, K., Podboy, D., Dam, B., and Lee, F. “A Third-Generation Swirl-Venturi Lean Direct Injection Combustor With a Prefilming Pilot Injector”. In: 2019. DOI: 10.1115/GT2019-90484.
- [67] Correia-Rodrigues, H., Tummers, M., van-Veen, E., and Roekaerts, D. “Spray flame structure in conventional and hot-diluted combustion regime”. In: *Combustion and Flame* 162.3 (2015), pp. 759–773. DOI: <https://doi.org/10.1016/j.combustflame.2014.07.033>.
- [68] Correia-Rodrigues, H., Tummers, M., van-Veen, E., and Roekaerts, D. “Effects of coflow temperature and composition on ethanol spray flames in hot-diluted coflow”. In: *International Journal of Heat and Fluid Flow* 51 (2015), pp. 309–323. DOI: <https://doi.org/10.1016/j.ijheatfluidflow.2014.10.006>.
- [69] Yuan, R., Kariuki, J., Dowlut, A., Balachandran, R., and Mastorakos, E. “Reaction zone visualisation in swirling spray n-heptane flames”. In: *Proceedings of the Combustion Institute* 35.2 (2015), pp. 1649–1656. DOI: <https://doi.org/10.1016/j.proci.2014.06.012>.

- [70] Yuan, R., Kariuki, J., and Mastorakos, E. “Measurements in swirling spray flames at blow-off”. In: *International Journal of Spray and Combustion Dynamics* 10.3 (2018), pp. 185–210. DOI: 10.1177/1756827718763559.
- [71] Cavaliere, D., Kariuki, J., and Mastorakos, E. “A Comparison of the Blow-Off Behaviour of Swirl-Stabilized Premixed, Non-Premixed and Spray Flames”. In: *Flow, Turbulence and Combustion* 91.2 (2013), pp. 347–372. DOI: 10.1007/s10494-013-9470-z.
- [72] Cordier, M. “Allumage et propagation de flamme dans les écoulements fortement swirlés : études expérimentales et numériques”. PhD thesis. Institut National des sciences appliquees (INSA), 2013.
- [73] Cordier, M., Vandel, A., Cabot, G., Renou, B., and Boukhalfa, A. “Laser-Induced Spark Ignition of Premixed Confined Swirled Flames”. In: *Combustion Science and Technology* 185.3 (2013), pp. 379–407. DOI: 10.1080/00102202.2012.725791.
- [74] Marrero-Santiago, J. et al. “Experimental study of airflow velocity, fuel droplet size-velocity and flame structure in a confined swirled jet-spray flame”. In: *ILASS - Europe 2016, 27th Conference on Liquid Atomization and Spray Systems*. September. Brighton, United Kingdom, 2016.
- [75] Barré, D., Kraushaar, M., Staffelbach, G., Moureau, V., and Gicquel, L. “Compressible and low Mach number LES of a swirl experimental burner”. In: *3rd INCA Colloquim* 341.1-2 (2013), pp. 277–287. DOI: 10.1016/j.crme.2012.11.010.
- [76] Barré, D. et al. “Flame propagation in aeronautical swirled multi-burners: Experimental and numerical investigation”. In: *Combustion and Flame* 161.9 (2014), pp. 2387–2405. DOI: 10.1016/j.combustflame.2014.02.006.
- [77] Verdier, A. et al. “Experimental study of local flame structures and fuel droplet properties of a spray jet flame”. In: *Proceedings of the Combustion Institute* 36.2 (2017), pp. 2595–2602. DOI: 10.1016/j.proci.2016.07.016.
- [78] Verdier, A. et al. “Local extinction mechanisms analysis of spray jet flame using high speed diagnostics”. In: *Combustion and Flame* 193 (2018), pp. 440–452. DOI: 10.1016/J.COMBUSTFLAME.2018.03.032.
- [79] Mulla, I., Godard, G., Cabot, G., Grisch, F., and Renou, B. “Quantitative imaging of nitric oxide concentration in a turbulent n-heptane spray flame”. In: *Combustion and Flame* 203 (2019), pp. 217–229. DOI: 10.1016/j.combustflame.2019.02.005.

- [80] Kim, S., Menon, S., and Darin, J. “Large-Eddy Simulation of a High-Pressure, Single-Element Lean Direct-Injected Gas-Turbine Combustor”. In: *52nd Aerospace Sciences Meeting*. 2014. DOI: 10.2514/6.2014-0131.
- [81] Caraeni, D., Bergström, C., and Fuchs, L. “Modeling of liquid fuel injection, evaporation and mixing in a gas turbine burner using large eddy simulations”. In: *Flow, Turbulence and Combustion* 65.2 (c), pp. 223–244. DOI: 10.1023/A:1011428926494.
- [82] Apte, S.V., Gorokhovski, M., and Moin, P. “LES of atomizing spray with stochastic modeling of secondary breakup”. In: *International Journal of Multiphase Flow* 29.9 (2003), pp. 1503–1522. DOI: 10.1016/S0301-9322(03)00111-3.
- [83] Raman, V. and Pitsch, H. “Large-eddy simulation of a bluff-body-stabilized non-premixed flame using a recursive filter-refinement procedure”. In: *Combustion and Flame* 142.4 (2005), pp. 329–347. DOI: 10.1016/j.combustflame.2005.03.014.
- [84] Menon, S. and Patel, N. “Subgrid Modeling for Simulation of Spray Combustion in Large-Scale Combustors”. In: *AIAA Journal* 44.4 (2006), pp. 709–723. DOI: 10.2514/1.14875.
- [85] Moin, P. and Apte, S. “Large-eddy simulation of realistic gas turbine combustors”. In: *AIAA Journal* 44.4 (2006), pp. 698–708.
- [86] El-Asrag, H. and Menon, S. “Large eddy simulation of bluff-body stabilized swirling non-premixed flames”. In: *Proceedings of the Combustion Institute* 31 II (2007), pp. 1747–1754. DOI: 10.1016/j.proci.2006.07.251.
- [87] Riber, E., Moureau, V., García-Rosa, M., Poinso, T., and Simonin, O. “Evaluation of numerical strategies for large eddy simulation of particulate two-phase recirculating flows”. In: *Journal of Computational Physics* 228.2 (2009), pp. 539–564. DOI: 10.1016/j.jcp.2008.10.001.
- [88] Reveillon, J. and Demoulin, F. X. “Evaporating droplets in turbulent reacting flows”. In: *Proceedings of the Combustion Institute* 31 II (2007), pp. 2319–2326. DOI: 10.1016/j.proci.2006.07.114.
- [89] Pera, C. and Reveillon, J. “Direct numerical simulation of spray flame/acoustic interactions”. In: *Proceedings of the Combustion Institute* 31 II (2007), pp. 2283–2290. DOI: 10.1016/j.proci.2006.07.153.

- [90] Neophytou, A., Mastorakos, E., and Cant, R. S. “DNS of spark ignition and edge flame propagation in turbulent droplet-laden mixing layers”. In: *Combustion and Flame* 157.6 (2010), pp. 1071–1086. DOI: 10.1016/j.combustflame.2010.01.019.
- [91] Boileau, M. et al. “Investigation of Two-Fluid Methods for Large Eddy Simulation of Spray Combustion in Gas Turbines”. In: *Flow, Turbulence and Combustion* 80.3 (2007), pp. 291–321. DOI: 10.1007/s10494-007-9123-1.
- [92] Ménard, T, Tanguy, S, and Berlemont, A. “Coupling level set/VOF/ghost fluid methods: Validation and application to 3D simulation of the primary break-up of a liquid jet”. In: *International Journal of Multiphase Flow* 33.5 (2007), pp. 510–524. DOI: 10.1016/j.ijmultiphaseflow.2006.11.001.
- [93] Desjardins, O., Moureau, V., and Pitsch, H. “An accurate conservative level set/ghost fluid method for simulating turbulent atomization”. In: *Journal of Computational Physics* (2008). DOI: 10.1016/j.jcp.2008.05.027.
- [94] Apte, S., Mahesh, K., Gorokhovski, M., and Moin, P. “Stochastic modeling of atomizing spray in a complex swirl injector using large eddy simulation”. In: *Proceedings of the Combustion Institute* 32.2 (2009), pp. 2257–2266. DOI: 10.1016/j.proci.2008.06.156.
- [95] Arienti, M., Li, X., Soteriou, M., Eckett, C., and Jensen, R. “Coupled Level-Set/Volume-of-Fluid Method for the Simulation of Liquid Atomization in Propulsion Device Injectors”. In: *AIAA/ASME/SAE/ASEE Joint Propulsion Conference* July (2010), pp. 1–10.
- [96] Sankaran, V. and Menon, S. “LES of spray combustion in swirling flows”. In: *Journal of Turbulence* 3 (2002). DOI: 10.1088/1468-5248/3/1/011.
- [97] Stein, O. and Kempf, A. “LES of the Sydney swirl flame series: A study of vortex breakdown in isothermal and reacting flows”. In: *Proceedings of the Combustion Institute* 31 II (2007), pp. 1755–1763. DOI: 10.1016/j.proci.2006.07.255.
- [98] Malalasekera, W., Ranga-Dinesh, K., Ibrahim, S., and Masri, A. “LES of recirculation and vortex breakdown in swirling flames”. In: *Combustion Science and Technology* 180.5 (2008), pp. 809–832. DOI: 10.1080/00102200801894018.
- [99] Kirkpatrick, M. “A large eddy simulation code for industrial and environmental flows”. PhD thesis. The University of Sydney, 2002.

- [100] Chrigui, M., Masri, A., Sadiki, A., and Janicka, J. “Large eddy simulation of a polydisperse ethanol spray flame”. In: *Flow, Turbulence and Combustion* 90.4 (2013), pp. 813–832. DOI: 10.1007/s10494-013-9449-9.
- [101] El-Asrag, Hossam A. and Braun, Markus. “Effect of turbulence non-isotropy modeling on spray dynamics for an evaporating Acetone spray jet”. In: *International Journal of Multiphase Flow* 68 (2015), pp. 100–120. DOI: 10.1016/j.ijmultiphaseflow.2014.10.009.
- [102] Rittler, A., Proch, F., and Kempf, A. “LES of the Sydney piloted spray flame series with the PFGM/ATF approach and different sub-filter models”. In: *Combustion and Flame* 162 (2015), pp. 1575–1598. DOI: 10.1016/J.COMBUSTFLAME.2014.11.025.
- [103] Dressler, L., Sacomano Filho, F., Sadiki, A., and Janicka, J. “Influence of Thickening Factor Treatment on Predictions of Spray Flame Properties Using the ATF Model and Tabulated Chemistry”. In: *Flow, Turbulence and Combustion* (2020). DOI: 10.1007/s10494-020-00149-7.
- [104] Hu, Y. and Kurose, R. “Nonpremixed and premixed flamelets LES of partially premixed spray flames using a two-phase transport equation of progress variable”. In: *Combustion and Flame* 188 (2018), pp. 227–242. DOI: <https://doi.org/10.1016/j.combustflame.2017.10.004>.
- [105] Hu, Y., Kai, R., Kurose, R., Gutheil, E., and Olguin, H. “Large eddy simulation of a partially pre-vaporized ethanol reacting spray using the multiphase DTF/flamelet model”. In: *International Journal of Multiphase Flow* 125 (2020), p. 103216. DOI: 10.1016/j.ijmultiphaseflow.2020.103216.
- [106] Lamarque, N. “Schémas numériques et conditions limites pour la simulation aux grandes échelles de la combustion diphasique dans les foyers d’hélicoptère”. PhD thesis. Institut National Polytechnique de Toulouse - CERFACS, 2007.
- [107] Sanjosé, M. et al. “LES of two-phase reacting flows”. In: *Proceedings of the Summer Program (Center for Turbulence Research)* (2008), pp. 251–263.
- [108] Senoner, J. et al. “Eulerian and Lagrangian Large-Eddy Simulations of an evaporating two-phase flow”. In: *Comptes Rendus Mécanique* 337.6-7 (2009), pp. 458–468. DOI: 10.1016/J.CRME.2009.06.002.

- [109] Sanjosé, M. et al. “Fuel injection model for Euler-Euler and Euler-Lagrange large-eddy simulations of an evaporating spray inside an aeronautical combustor”. In: *International Journal of Multiphase Flow* 37.5 (2011), pp. 514–529. DOI: 10.1016/j.ijmultiphaseflow.2011.01.008.
- [110] Jones, W. P., Lettieri, C., Marquis, A. J., and Navarro-Martinez, S. “Large Eddy Simulation of the two-phase flow in an experimental swirl-stabilized burner”. In: *International Journal of Heat and Fluid Flow* 38 (2012), pp. 145–158. DOI: 10.1016/j.ijheatfluidflow.2012.09.001.
- [111] Vié, A., Jay, S., Cuenot, B., and Massot, M. “Accounting for polydispersion in the eulerian large eddy simulation of the two-phase flow in an aeronautical-type burner”. In: *Flow, Turbulence and Combustion* 90.3 (2013), pp. 545–581. DOI: 10.1007/s10494-012-9440-x.
- [112] Jaegle, F. et al. “Eulerian and Lagrangian spray simulations of an aeronautical multipoint injector”. In: *Proceedings of the Combustion Institute* 33 (2011), pp. 2099–2107. DOI: 10.1016/j.proci.2010.07.027.
- [113] Boileau, M., Staffelbach, G., Cuenot, B., Poinso, T., and Bérat, C. “LES of an ignition sequence in a gas turbine engine”. In: *Combustion and Flame* 154.1-2 (2008), pp. 2–22. DOI: 10.1016/j.combustflame.2008.02.006.
- [114] Staffelbach, G., Gicquel, L., Boudier, G., and Poinso, T. “Large Eddy Simulation of self excited azimuthal modes in annular combustors”. In: *Proceedings of the Combustion Institute* 32 II.2 (2009), pp. 2909–2916. DOI: 10.1016/j.proci.2008.05.033.
- [115] Patel, N. and Menon, S. “Simulation of spray-turbulence-flame interactions in a lean direct injection combustor”. In: *Combustion and Flame* 153 (2008), pp. 228–257. DOI: 10.1016/j.combustflame.2007.09.011.
- [116] Liu, N., Shih, T., and Wey, T. “Comprehensive combustion modeling and simulation: Recent progress at NASA Glenn Research Center”. In: *International Symposium on Air Breathing Engines (ISABE)*. 2007.
- [117] Liu, N., Shih, T., and Wey, C. “Numerical Simulations of Two-Phase Reacting Flow in a Single-Element Lean Direct Injection (LDI) Combustor Using NCC”. In: *NASA Technical Report NASA/TM-217031* (2011).

- [118] Kirtas, M., Patel, N., Sankaran, S., and Menon, S. “Large-Eddy Simulation of a Swirl-Stabilized, Lean Direct Injection Spray Combustor”. In: *Proceedings of the ASME Turbo Expo*. 2006, pp. 903–914. DOI: 10.1115/GT2006-91310.
- [119] Legier, J., Poinso, T., and Veynante, D. “Dynamically Thickened Flame LES model for Premixed and Non-premixed Turbulent Combustion”. In: *Proceedings of the Summer Program, Center for Turbulence Research (Stanford University)* (2000), pp. 157–168.
- [120] Knudsen, E. and Pitsch, H. “Large Eddy Simulation of a Spray Combustor Using a Multi-regime Flamelet Approach”. In: *Annual Research Briefs, Center for Turbulence Research (Stanford University)* (2010), pp. 337–350.
- [121] Sreedhara, S. and Huh, K. “Assessment of closure schemes in second-order conditional moment closure against DNS with extinction and ignition”. In: *Combustion and Flame* 143.4 (2005). DOI: 10.1016/j.combustflame.2005.08.015.
- [122] James, S., Zhu, J., and Anand, M. “Large eddy simulations of turbulent flames using the filtered density function model”. In: *Proceedings of the Combustion Institute* 31.2 (2007), pp. 1737–1745. DOI: 10.1016/j.proci.2006.07.160.
- [123] Davoudzadeh, F., Liu, N., and Moder, J. “Investigation of swirling air flows generated by axial swirlers in a flame tube”. In: *Proceedings of the ASME Turbo Expo 1* (2006), pp. 891–902. DOI: 10.1115/GT2006-91300.
- [124] Dewanji, D. and Rao, A. “Spray combustion modeling in lean direct injection combustors, part I: Single-element LDI”. In: *Combustion Science and Technology* 187.4 (2015), pp. 537–557. DOI: 10.1080/00102202.2014.965810.
- [125] Dewanji, D. and Rao, A. “Spray combustion modeling in lean direct injection combustors, part II: Multi-point LDI”. In: *Combustion Science and Technology* 187.4 (2015), pp. 558–576. DOI: 10.1080/00102202.2014.958476.
- [126] Ajmani, K., Mongia, H., and Lee, P. “CFD evaluation of a 3rd generation LDI combustor”. In: *53rd AIAA/SAE/ASEE Joint Propulsion Conference, 2017*. 2017. DOI: 10.2514/6.2017-5017.

- [127] Luo, K., Pitsch, H., Pai, M. G., and Desjardins, O. “Direct numerical simulations and analysis of three-dimensional n-heptane spray flames in a model swirl combustor”. In: *Proceedings of the Combustion Institute* 33.2 (2011), pp. 2143–2152. DOI: 10.1016/j.proci.2010.06.077.
- [128] Sommerfeld, M. and Qiu, H. “Detailed measurements in a swirling particulate two-phase flow by a phase-Doppler anemometer”. In: *International Journal of Heat and Fluid Flow* 12.1 (1991), pp. 20–28. DOI: 10.1016/0142-727X(91)90004-F.
- [129] Mahesh, K. et al. “Large-eddy simulation of reacting turbulent flows in complex geometries”. In: *Journal of Applied Mechanics* 73.3 (2006), p. 374. DOI: 10.1115/1.2179098.
- [130] Moureau, V., Domingo, P., and Vervisch, L. “From Large-Eddy Simulation to Direct Numerical Simulation of a lean premixed swirl flame: Filtered laminar flame-PDF modeling”. In: *Combustion and Flame* 158.7 (2011), pp. 1340–1357. DOI: 10.1016/j.combustflame.2010.12.004.
- [131] Jones, W., Marquis, A., and Vogiatzaki, K. “Large-eddy simulation of spray combustion in a gas turbine combustor”. In: *Combustion and Flame* 161.1 (2014), pp. 222–239. DOI: 10.1016/j.combustflame.2013.07.016.
- [132] Wang, P., Platova, N., Fröhlich, J., and Maas, U. “Large Eddy Simulation of the PRECCINSTA burner”. In: *International Journal of Heat and Mass Transfer* 70 (2014), pp. 486–495. DOI: 10.1016/j.ijheatmasstransfer.2013.11.025.
- [133] Wang, P., Fröhlich, J., Maas, U., He, Z., and Wang, C. “A detailed comparison of two sub-grid scale combustion models via large eddy simulation of the PRECCINSTA gas turbine model combustor”. In: *Combustion and Flame* 164 (2016), pp. 329–345. DOI: 10.1016/j.combustflame.2015.11.031.
- [134] Ramaekers, W., Tap, F., and Boersma, B. “Subgrid Model Influence in Large Eddy Simulations of Non-reacting Flow in a Gas Turbine Combustor”. In: *Flow, Turbulence and Combustion* 100.2 (2018), pp. 457–479. DOI: 10.1007/s10494-017-9853-7.
- [135] Collin-Bastiani, F. et al. “A joint experimental and numerical study of ignition in a spray burner”. In: *Proceedings of the Combustion Institute* 37.4 (2019), pp. 5047–5055. DOI: 10.1016/j.proci.2018.05.132.

- [136] Esclapez, L., Riber, E., and Cuenot, B. “Ignition probability of a partially premixed burner using les”. In: *Proceedings of the Combustion Institute* 35.3 (2015), pp. 3133–3141. DOI: 10.1016/j.proci.2014.07.040.
- [137] Moureau, V., Domingo, P., and Vervisch, L. “Design of a massively parallel CFD code for complex geometries”. In: *Comptes Rendus Mecanique* 339.2 (2011), pp. 141–148. DOI: 10.1016/j.crme.2010.12.001.
- [138] Lumley, J. “The structure of inhomogeneous turbulent flows”. In: *Atmospheric Turbulence and Radio Wave Propagation (Eds. A.M. Yaglom and V.I. Tatarsky)* (1967), p. 166.
- [139] Fogleman, M., Lumley, J., Rempfer, D., and Haworth, D. In: *Journal of Turbulence* 5 (2004). DOI: 10.1088/1468-5248/5/1/023.
- [140] Danby, S. and Echehki, T. “Proper orthogonal decomposition analysis of autoignition simulation data of nonhomogeneous hydrogen-air mixtures”. In: *Combustion and Flame* 144.1-2 (2006), pp. 126–138. DOI: 10.1016/j.combustflame.2005.06.014.
- [141] Bizon, K., Continillo, G., Mancaruso, E., Merola, S., and Vaglieco, B. “POD-based analysis of combustion images in optically accessible engines”. In: *Combustion and Flame* 157.4 (2010), pp. 632–640. DOI: 10.1016/j.combustflame.2009.12.013.
- [142] Chen, H., Reuss, D., and Sick, V. “Analysis of misfires in a direct injection engine using proper orthogonal decomposition”. In: *Experiments in Fluids* 51.4 (2011), pp. 1139–1151. DOI: 10.1007/s00348-011-1133-z.
- [143] Chen, H., Hung, D., Xu, M., Zhuang, H., and Yang, J. “Proper orthogonal decomposition analysis of fuel spray structure variation in a spark-ignition direct-injection optical engine”. In: *Experiments in Fluids* 55.4 (2014), p. 1703. DOI: 10.1007/s00348-014-1703-y.
- [144] Bizon, K., Continillo, G., Lombardi, S., Sementa, P., and Vaglieco, B. “Independent component analysis of cycle resolved combustion images from a spark ignition optical engine”. In: *Combustion and Flame* 163 (2016), pp. 258–269. DOI: 10.1016/j.combustflame.2015.10.002.
- [145] Sakowitz, A. and Mihăescu M .and Fuchs, L. “Flow decomposition methods applied to the flow in an IC engine manifold”. In: *Applied Thermal Engineering* 65 (2014), pp. 57–65.

- [146] Torregrosa, A., Broatch, A., García-Tíscar, J., and Gomez-Soriano, J. “Modal decomposition of the unsteady flow field in compression-ignited combustion chambers”. In: *Combustion and Flame* 188 (2018), pp. 469–482. DOI: [10.1016/j.combustflame.2017.10.007](https://doi.org/10.1016/j.combustflame.2017.10.007).
- [147] Steinberg, A., Boxx, I., Stöhr, M., Carter, C., and Meier, W. “Flow-flame interactions causing acoustically coupled heat release fluctuations in a thermo-acoustically unstable gas turbine model combustor”. In: *Combustion and Flame* 157.12 (2010), pp. 2250–2266. DOI: [10.1016/j.combustflame.2010.07.011](https://doi.org/10.1016/j.combustflame.2010.07.011).
- [148] Caux-Brisebois, V., Steinberg, A., Arndt, C., and Meier, W. “Thermo-acoustic velocity coupling in a swirl stabilized gas turbine model combustor”. In: *Combustion and Flame* 161.12 (2014), pp. 3166–3180. DOI: [10.1016/j.combustflame.2014.05.020](https://doi.org/10.1016/j.combustflame.2014.05.020).
- [149] Meadows, J. and Agrawal, A. “Time-resolved PIV of lean premixed combustion without and with porous inert media for acoustic control”. In: *Combustion and Flame* 162.4 (2015), pp. 1063–1077. DOI: [10.1016/j.combustflame.2014.09.028](https://doi.org/10.1016/j.combustflame.2014.09.028).
- [150] Luo, J. “Design optimization of the last stage of a 4.5-stage compressor using a POD-based hybrid model”. In: *Aerospace Science and Technology* 76 (2018), pp. 303–314. DOI: <https://doi.org/10.1016/j.ast.2018.01.043>.
- [151] Broatch, A., García-Tíscar, J., Roig, F., and Sharma, S. “Dynamic mode decomposition of the acoustic field in radial compressors”. In: *Aerospace Science and Technology* 90 (2019), pp. 388–400. DOI: [10.1016/j.ast.2019.05.015](https://doi.org/10.1016/j.ast.2019.05.015).
- [152] Lengani, D. et al. “Identification and quantification of losses in a LPT cascade by POD applied to LES data”. In: *International Journal of Heat and Fluid Flow* 70 (2018), pp. 28–40. DOI: <https://doi.org/10.1016/j.ijheatfluidflow.2018.01.011>.
- [153] Güner, H., Thomas, D., Dimitriadis, G., and Terrapon, V. “Unsteady aerodynamic modeling methodology based on dynamic mode interpolation for transonic flutter calculations”. In: *Journal of Fluids and Structures* 84 (2019), pp. 218–232. DOI: [10.1016/j.jfluidstructs.2018.11.002](https://doi.org/10.1016/j.jfluidstructs.2018.11.002).
- [154] Rajpal, D., Gillebaart, E., and De Breuker, R. “Preliminary aeroelastic design of composite wings subjected to critical gust loads”. In: *Aerospace Science and Technology* 85 (2019), pp. 96–112. DOI: <https://doi.org/10.1016/j.ast.2018.11.051>.

- [155] Legrand, M., Nogueira, J., Lecuona, A., Nauri, S., and Rodríguez, P. “Atmospheric low swirl burner flow characterization with stereo PIV”. In: *Experiments in Fluids* 48 (2009), pp. 901–913. DOI: 10.1007/s00348-009-0775-6.
- [156] Oberleithner, K. et al. “Three-dimensional coherent structures in a swirling jet undergoing vortex breakdown: Stability analysis and empirical mode construction”. In: *Journal of Fluid Mechanics* 679 (2011), pp. 383–414. DOI: 10.1017/jfm.2011.141.
- [157] Oberleithner, K., Paschereit, C., Seele, R., and Wygnanski, I. “Formation of Turbulent Vortex Breakdown: Intermittency, Criticality, and Global Instability”. In: *AIAA Journal* 50 (2012), pp. 1437–1452. DOI: 10.2514/1.J050642.
- [158] Percin, M., Vanierschot, M., and Oudheusden, B. van. “Analysis of the pressure fields in a swirling annular jet flow”. In: *Experiments in Fluids* 58.12 (2017), p. 166. DOI: 10.1007/s00348-017-2446-3.
- [159] Alekseenko, S. et al. “Coherent structures in the near-field of swirling turbulent jets: A tomographic PIV study”. In: *International Journal of Heat and Fluid Flow* 70 (2018), pp. 363–379. DOI: <https://doi.org/10.1016/j.ijheatfluidflow.2017.12.009>.
- [160] Ianiro, A., Lynch, K., Violato, D., Cardone, G., and Scarano, F. “Three-dimensional organization and dynamics of vortices in multichannel swirling jets”. In: *Journal of Fluid Mechanics* 843 (2018), pp. 180–210. DOI: 10.1017/jfm.2018.140.
- [161] Vanierschot, M., Percin, M., and Van Oudheusden, B. “Double helix vortex breakdown in a turbulent swirling annular jet flow”. In: *Physical Review Fluids* 3.3 (2018). DOI: 10.1103/PhysRevFluids.3.034703.
- [162] Vanierschot, M. and Ogus, G. “Experimental investigation of the precessing vortex core in annular swirling jet flows in the transitional regime”. In: *Experimental Thermal And Fluid Science* 106 (2019), pp. 148–158.
- [163] Stöhr, M., Sadanandan, R., and Meier, W. “Phase-resolved characterization of vortex-flame interaction in a turbulent swirl flame”. In: *Experiments in Fluids* 51.4 (2011), pp. 1153–1167. DOI: 10.1007/s00348-011-1134-y.

- [164] Alekseenko, S., Dulin, V., Kozorezov, Y, and Markovich, D. “Effect of High-Amplitude Forcing on Turbulent Combustion Intensity and Vortex Core Precession in a Strongly Swirling Lifted Propane/Air Flame”. In: *Combustion Science and Technology* 184.10-11 (2012), pp. 1862–1890. DOI: 10.1080/00102202.2012.695239.
- [165] Reichel, T., Goeckeler, K., and Paschereit, O. “Investigation of Lean Premixed Swirl-Stabilized Hydrogen Burner With Axial Air Injection Using OH-PLIF Imaging”. In: *Journal of Engineering for Gas Turbines and Power* 137.11 (2015). DOI: 10.1115/1.4031181.
- [166] Karlis, E. et al. “Thermoacoustic phenomena in an industrial gas turbine combustor at two different mean pressures”. In: *AIAA SciTech Forum*. January. San Diego, California, 2019, pp. 1–17. DOI: 10.2514/6.2019-0675.
- [167] Ruith, M., Chen, P., Meiburg, E., and Maxworthy, T. “Three-dimensional vortex breakdown in swirling jets and wakes: Direct numerical simulation”. In: *Journal of Fluid Mechanics* 486.486 (2003), pp. 331–378. DOI: 10.1017/S0022112003004749.
- [168] Cozzi, F., Sharma, R., and Solero, G. “Analysis of coherent structures in the near-field region of an isothermal free swirling jet after vortex breakdown”. In: *Experimental Thermal and Fluid Science* 109 (2019), p. 109860. DOI: 10.1016/j.expthermflusci.2019.109860.
- [169] Huang, Y., Wang, S., and Yang, V. “Systematic Analysis of Lean-Premixed Swirl-Stabilized Combustion”. In: *Aiaa Journal* 44 (2006), pp. 724–740. DOI: 10.2514/1.15382.
- [170] Huang, Y. and Yang, V. “Dynamics and stability of lean-premixed swirl-stabilized combustion”. In: *Progress in Energy and Combustion Science* 35.4 (2009), pp. 293–364. DOI: 10.1016/J.PECS.2009.01.002.
- [171] Duwig, C., Ducruix, S., and Veynante, D. “Studying the Stabilization Dynamics of Swirling Partially Premixed Flames by Proper Orthogonal Decomposition”. In: *Journal of Engineering for Gas Turbines and Power* 134.10 (2012), p. 101501. DOI: 10.1115/1.4007013.
- [172] Mira, D. et al. “Numerical Characterization of a Premixed Hydrogen Flame Under Conditions Close to Flashback”. In: *Flow, Turbulence and Combustion* 104.2-3 (2020), pp. 479–507. DOI: 10.1007/s10494-019-00106-z.

- [173] Grimm, F., Dierke, J., Ewert, R., Noll, B., and Aigner, M. “Modelling of combustion acoustics sources and their dynamics in the PRECCINSTA burner test case”. In: *International Journal of Spray and Combustion Dynamics* 9.4 (2017), pp. 330–348. DOI: 10.1177/1756827717717390.
- [174] Grimm, F. et al. “Combustion Noise Dependency on Thermal Load and Global Equivalence Ratio in a Swirl-Stabilized Combustor”. In: *AIAA SciTech Forum*. 2019, pp. 1–24. DOI: 10.2514/6.2019-1582.
- [175] Schmid, P. “Dynamic mode decomposition of numerical and experimental data”. In: *Journal of Fluid Mechanics* 656 (2010), pp. 5–28. DOI: 10.1017/S0022112010001217.
- [176] Schmid, P. “Applications of the dynamic mode decomposition”. In: *Journal of Fluid Mechanics* 25.1 (2010), pp. 249–259.
- [177] Rowley, C., Mezi, I., Bagheri, S., Schlatter, P., and Henningson, D. “Spectral analysis of nonlinear flows”. In: *Journal of Fluid Mechanics* 641 (2009), pp. 115–127. DOI: 10.1017/S0022112009992059.
- [178] Chen, K., Tu, J., and Rowley, C. “Variants of dynamic mode decomposition: Boundary condition, Koopman, and fourier analyses”. In: *Journal of Nonlinear Science* 22.6 (2012), pp. 887–915. DOI: 10.1007/s00332-012-9130-9.
- [179] Richecoeur, F., Hakim, L., Renaud, A., and Zimmer, L. “DMD algorithms for experimental data processing in combustion”. In: *Center for Turbulence Research (Stanford University)*. 2012, pp. 459–468.
- [180] Sampath, Ramgopal and Chakravarthy, Satyanarayanan R. “Investigation of intermittent oscillations in a premixed dump combustor using time-resolved particle image velocimetry”. In: *Combustion and Flame* 172 (2016), pp. 309–325. DOI: 10.1016/j.combustflame.2016.06.018.
- [181] Vinha, N., Meseguer-Garrido, F., De Vicente, J., and Valero, E. “A dynamic mode decomposition of the saturation process in the open cavity flow”. In: *Aerospace Science and Technology* 52 (2016), pp. 198–206. DOI: 10.1016/j.ast.2016.02.036.
- [182] Daroukh, M., Moreau, S., Gourdain, N., Boussuge, J., and Sensiau, C. “Tonal Noise Prediction of a Modern Turbofan Engine With Large Upstream and Downstream Distortion”. In: *Journal of Turbomachinery* 141.2 (2019). DOI: 10.1115/1.4042163.

- [183] Renaud, A., Tachibana, S., Arase, S., and Yokomori, T. “Experimental Study of Thermo-Acoustic Instability Triggering in a Staged Liquid Fuel Combustor Using High-Speed OH-PLIF”. In: *Journal of Engineering for Gas Turbines and Power* 140.8 (2018), p. 081505. DOI: 10.1115/1.4038915.
- [184] Karlis, E., Liu, Y., Hardalupas, Y., and Taylor, A. “H₂ enrichment of CH₄ blends in lean premixed gas turbine combustion: An experimental study on effects on flame shape and thermoacoustic oscillation dynamics”. In: *Fuel* 254 (2019), p. 115524. DOI: 10.1016/j.fuel.2019.05.107.
- [185] Papadogiannis, D. et al. “Assessment of the Indirect Combustion Noise Generated in a Transonic High-Pressure Turbine Stage”. In: *Journal of Engineering for Gas Turbines and Power* 138.4 (2015). DOI: 10.1115/1.4031404.
- [186] Semlitsch, B. and Mihaescu, M. “Flow phenomena leading to surge in a centrifugal compressor”. In: *Energy* 103 (2016), pp. 572–587. DOI: 10.1016/j.energy.2016.03.032.
- [187] Kim, J., Jung, W., Hong, J., and Sung, H. “The Effects of Turbulent Burning Velocity Models in a Swirl-Stabilized Lean Premixed Combustor”. In: *International Journal of Turbo and Jet Engines* 35.4 (2018), pp. 365–372. DOI: 10.1515/tjj-2016-0053.

Chapter 4

Computational Methodology

“We humans are the victims of an asymmetry in the perception of random events. We attribute our successes to our skills, and our failures to external events outside our control, namely to randomness.”

—Nassim N. Taleb

4.1 Introduction

As introduced in Chapter 1, this thesis reports a non-reacting computational study of both gaseous and liquid-fueled injection cases in a laboratory-scale radial-swirled Lean Direct Injection (LDI) combustor. The problem is addressed by solving the complete inlet flow path through the swirl vanes and the combustor through two different CFD codes involving two different meshing strategies: an automatic mesh generation with adaptive mesh refinement (AMR) algorithm through CONVERGETM and a more traditional static meshing technique in OpenFOAM[®]. It is of primary interest to consider the flow across the plenum and swirler blades in order to remove any ambiguity in the inflow conditions as the flow dynamics and coherent structures within the combustion chamber are fundamentally characterised by the flow conditions at the exit of the swirler. The meshing stage constitutes one of the central challenges of the study, given that in the geometry of any LDI burner coexist sections with small characteristic sizes (e.g., the swirler, which needs to be discretised into very small elements to solve all the flow structures correctly) along with sections of very long length (e.g., the combustion chamber). The

discretisation of the entire domain in the small elements required in both the swirler and near-injection regions would imply a high total number of computational cells, notably increasing both the computational resources needed for each simulation and the simulation time itself. Therefore, the use of AMR needs to be explored since it allows starting the simulation from a coarse mesh and then refining on-the-fly in areas of the domain where it is required due to the high gradients detected in the relevant variables.

A reference gaseous fuel case will be considered to calibrate and validate the CFD codes and to carry out the mesh study and turbulence models (U-RANS and LES) evaluation before advancing to more complex spray fuel set-ups. The models associated with liquid phase atomisation and breakup, as well as the turbulence, are presented in Section 4.2 and need to be selected and calibrated correctly during the pre-processing stage (see Section 4.3) to represent realistic conditions in the vicinity of the injector. To this end, a Lagrangian point particle tracking and the parcel approximation¹ is considered. This approach groups drops of similar size, location and properties into a single parcel. Then, Lagrangian equations are solved for averaged properties of the parcel. As a result, the average and fluctuating components of the gas phase velocity, the distribution and correlation of liquid droplets sizes and velocities and their evaporation rate should be accurately reproduced. In this way, the systematic algorithms developed to automatically post-process the raw data extracted from gaseous fuel and spray simulations are shown in Section 4.4.

4.2 CFD Modeling

Computational Fluid Dynamics (CFD) deals with the resolution and analysis of systems involving fluid flow, heat transfer and associated phenomena such as chemical reactions through numerical simulations [1]. A validated CFD code allows to investigate systems where experiments could be challenging to perform (e.g., large systems at hazardous conditions or exceeding the typical performance limits) with an almost unlimited level of detail of results and a substantial reduction of costs associated to new designs. For such reasons, the aeronautical industry has been including CFD tools from the 1960s into the aircraft design, research and production stages. More recently, CFD methods

¹The number of drops can be huge (order of tens of millions) and are typically circumscribed to a relatively small region of the whole computational domain involving high (unapproachable) computational costs.

have also become an essential component in the design process of gas turbine combustion systems due to its suitability to optimise key performance indicators through fast and cheap parametric studies.

Nevertheless, the turbulent flow originated within an LDI combustor (see 2.2.1) implies a computational challenge since fluctuations occur over a broad spectrum of length scales. In fact, the turbulent Reynolds number for the swirling flow through a typical LDI laboratory-scaled combustor can be in the order of 10000 with an integral scale that is tens of centimetres, whereas the Kolmogorov scale is of the order of 100 μm , which is not much larger than the fuel droplet diameters [2, 3]. As a consequence, it is computationally unaffordable to resolve all the turbulent scales in an unsteady multiphase flow over the physical domain, thus requiring both modeling some terms and dealing with equations governing statistical properties in order to reduce the complexity and the computational cost [4].

This section presents the numerical modeling strategy considered to deal with the limitations mentioned above. First, the governing Navier-Stokes equations introduced in a general way in Section 2.3.2 are recapitulated in Section 4.2.1. Next, the available approaches to resolve or model the turbulence are presented in Section 4.2.2, with particular consideration to those employed in this study. In addition, Section 4.2.3 discusses the numerical spray sub-models employed to model the spray sub-processes (e.g., atomisation, drop breakup, drop distortion and drag, drop collision and coalescence, turbulent dispersion of spray drops and drop evaporation) in an Eulerian-Lagrangian framework. Finally, the numerical methods used in CONVERGETM and OpenFOAM[©] CFD codes involving both numerical algorithms and discretisation schemes are briefly introduced in Section 4.2.4.

4.2.1 Navier-Stokes Equations

The dynamics of the swirling flows within a gas turbine combustor are governed by the Navier-Stokes Equations, that describe the conservation of mass, momentum, energy and species. On the one hand, the turbulent compressible equations for mass transport and momentum transport can be synthesised in Eq. 4.1 and Eq. 4.2, respectively:

$$\frac{\partial \rho}{\partial t} + \frac{\partial(\rho u_i)}{\partial x_i} = S \quad (4.1)$$

$$\frac{\partial(\rho u_i)}{\partial t} + \frac{\partial(\rho u_i u_j)}{\partial x_j} = -\frac{\partial P}{\partial x_i} + \frac{\partial}{\partial x_j} \left[\mu \left(\frac{\partial u_i}{\partial x_j} + \frac{\partial u_j}{\partial x_i} \right) - \frac{2}{3} \mu \frac{\partial u_k}{\partial x_k} \delta_{ij} \right] + \frac{\partial \tau_{ij}}{\partial x_i} + S_i \quad (4.2)$$

In the above equations, S is the source term (e.g., evaporation for the mass conservation equation, and spray coupling or mass sources for the momentum equation) and τ_{ij} denotes the Reynolds stresses of the system ($\tau_{ij} = \rho u'_i u'_j$) which need to be modeled to provide mathematical closure and to account for turbulence effects (discussed in Section 4.2.2).

On the other hand, the compressible form of the energy and species equations are given by Eq. 4.3 and Eq. 4.4, respectively:

$$\frac{\partial \rho e}{\partial t} + \frac{\partial(\rho u_j e)}{\partial x_j} = -P \frac{\partial(\rho u_j)}{\partial x_j} + \sigma_{ij} \frac{\partial(\rho u_i)}{\partial x_j} + \frac{\partial}{\partial x_j} \left(K \frac{\partial T}{\partial x_j} \right) + \frac{\partial}{\partial x_j} \left(\rho D \sum_m h_m \frac{\partial Y_m}{\partial x_j} \right) + S \quad (4.3)$$

$$\frac{\partial \rho_m}{\partial t} + \frac{\partial(\rho_m u_j)}{\partial x_j} = + \frac{\partial}{\partial x_j} \left(\rho D \sum_m h_m \frac{\partial Y_m}{\partial x_j} \right) + S_m \quad (4.4)$$

Please note that the species transport solves for the mass fraction (Y_m) of all species in the system. For turbulent cases, the mass diffusion and conductivity coefficients are calculated by $D_t = \nu_t / Sc_t$ and $K_t = C_p \mu_t / Pr_t$ regarding turbulent viscosity and turbulent Schmidt-Prandtl numbers, respectively, that account for the presence of turbulence in mass transport and energy transport.

4.2.2 Turbulence Modeling

Turbulence significantly increases the momentum, energy and species rate of mixing through a convective process that results from the generation of unsteady 3-D rotational eddies with a broad range of spatial and temporal scales that interact with the flow in a dynamically complex motion. Due to the difficulty to deeply characterise analytically and even experimentally the turbulent flow, CFD simulations stands as a fundamental tool to capture and understand the chaotic effects due to turbulence. Nowadays, several methods for the treatment (modeling or resolving) of turbulent flows are available. They can be organised into the following three levels:

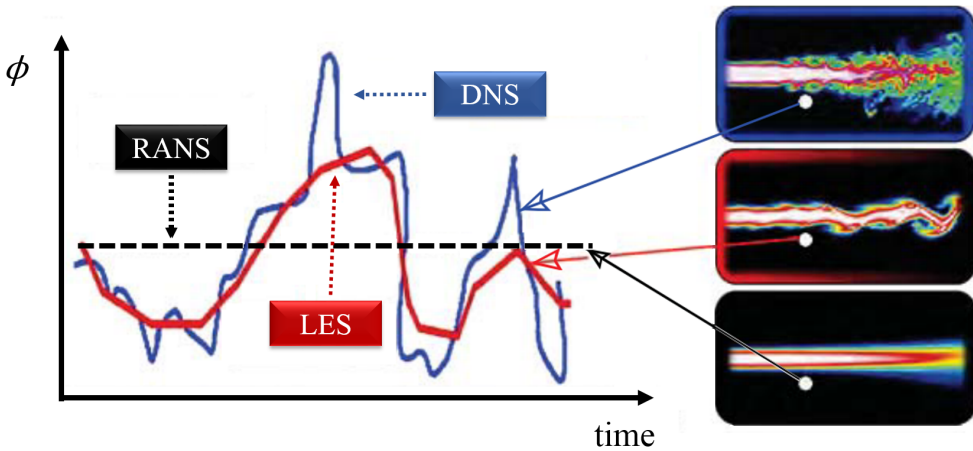


Figure 4.1: Time evolution of a given local variable computed through RANS, LES and DNS turbulence approaches.

- Reynolds-Averaged Navier-Stokes (RANS)** This approach only considers the influence of turbulence on mean flow properties by ensemble-averaging (not to be confused with time-averaging) the Navier-Stokes (NS) equations (see Section 2.3.2). Consequently, the flow variables predicted by RANS at a given spatial time is a constant mean quantity, as illustrated in Figure 4.1. The instantaneous flow variables are decomposed into an ensemble mean and a fluctuating term, thus giving rise to unclosed higher-order additional terms in the transport equations due to the interactions between the turbulent fluctuations. These new terms are modeled through additional transport equations included by traditional RANS turbulence models such as the $k-\varepsilon$ and the Reynolds stress models (discussed later). Since the computational power required to model the mean turbulent flow is reduced, this approach is considered as the pillar regarding flow calculations for engineering purposes over the last four decades.

Unsteady Reynolds-Averaged Navier-Stokes (U-RANS). It is a well-suited variation of the RANS approach able to capture (model) fluctuations or unsteady behaviour in the mean quantities. U-RANS method separates the time scale of mean motion and time scales of turbulent motion. Nevertheless, the underlying assumption in U-RANS is that the turbulent time scale is much lower than the mean flow time scale, so it catastrophically fails in modeling fluctuations in situations where this is not true (e.g., jet flows boundaries).

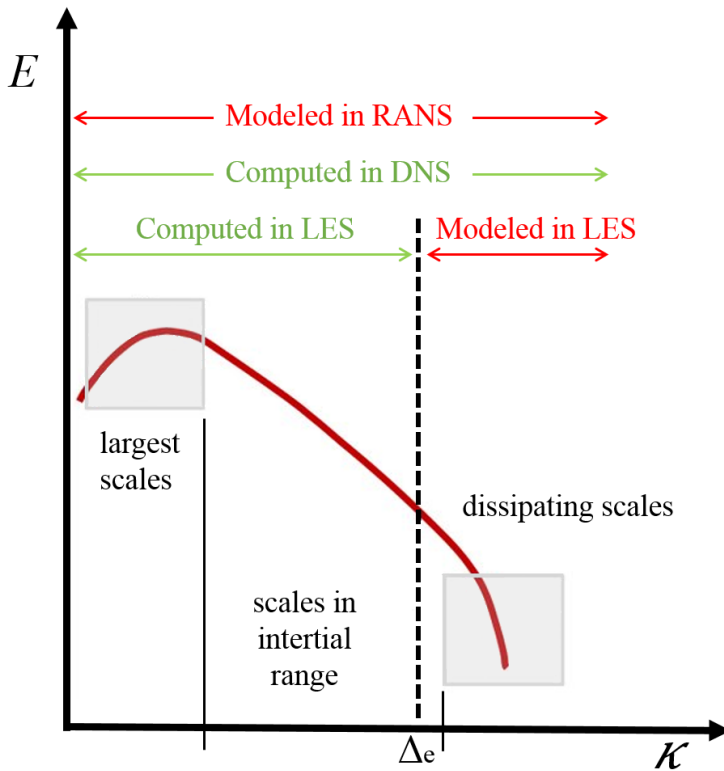


Figure 4.2: Energy spectrum of turbulent flow as a function of the wave numbers for RANS, LES and DNS turbulence approaches. Δ_e is the LES cut filter.

- Large-Eddy Simulation (LES)** This approach filters the NS equations spatially to separate the large-scale and small-scale turbulent structures. Then, the large-scale turbulence (integral scale, associated with the motions containing most of the kinetic energy) is solved by the discretised equations, whereas the small-scale turbulence (universal dissipative scales of the order of Kolmogorov scales) is modeled through the sub-grid scale (SGS) models. The spatial filter is usually related to the grid size and needs to be sufficiently small to let resolve a significant amount of energy associated to the larger eddies. This fact, together with the requirement of resolving transient flow equations, involves such demanding computing resources only affordable for research scale applications. However, the substantial progress in computing power and the appearance of massively parallel architectures have allowed LES to be

come available for widespread industrial applications where large-scale time-dependent flow features play an important role.

- **Direct Numerical Simulation (DNS)** In DNS, the full instantaneous NS equations (mean flow and all turbulent fluctuations) are computed without any model. In this way, the unsteady NS equations are explicitly solved on sufficiently fine grids that allow capturing all turbulent temporal and spatial scales (see Figure 4.1). Nevertheless, the prohibitive computational cost associated with the high Reynolds numbers found in industrial problems limits its application to academic cases in fundamental research in turbulence for moderate Reynolds [5].

The turbulent modeling approaches are summarised in Figure 4.2 in terms of the energy spectrum. As can be seen, all spatial frequencies corresponding to eddies of all sizes are modeled in RANS, and no turbulent energy is explicitly resolved. At the opposite side, DNS numerically solves all spatial and temporal turbulent scales without any turbulence model. Meanwhile, LES is found in an intermediate point between RANS and DNS. As mentioned above, LES explicitly solves for the large eddies above the spatial filter (Δ_e) and implicitly accounts for the small dissipating eddies through sub-grid scale (SGS) models. The U-RANS and LES turbulence approaches used in this study are briefly described below. A comprehensive description of the turbulence modeling can be found in [1].

4.2.2.1 Unsteady Reynolds-Averaged Navier-Stokes (U-RANS)

In U-RANS approach, the ensemble averaging of the equations introduces additional terms to represent the effects of turbulence: the Reynolds stresses, denoted as τ_{ij} in Eq. 4.2. The traditional U-RANS turbulence models are categorised based on the number of additional transport equations that need to be solved along with the governing Navier-Stokes equations of Section 4.2.1:

- Zero extra transport equations: mixing length model.
- One extra transport equations: Spalart-Allmaras model.
- Two extra transport equations: k - ε and k - ω model.
- Seven extra transport equations: Reynolds Stress Model (RSM).

A brief description of the U-RANS k- ε and Reynolds Stress models applied in this study is presented below.

k- ε model

The modeled Reynolds stresses for the two-equation k- ε turbulence model is given by Eq. (5):

$$\tau_{ij} = \overline{\rho \widetilde{u'_i u'_j}} = 2\mu_t S_{ij} - \frac{2}{3}\delta_{ij} \left(\rho k + \mu_t \frac{\partial \widetilde{u}_i}{\partial x_i} \right) \quad (4.5)$$

where $\bar{\cdot}$ denotes the ensemble mean and $\widetilde{\cdot}$ is the Favre average. The turbulent viscosity (μ_t), the mean strain rate tensor (S_{ij}), and the turbulent kinetic energy (k) are given by Eq. 4.6, Eq. 4.7 and Eq. 4.8, respectively:

$$\mu_t = C_\mu \rho \frac{k^2}{\varepsilon} \quad (4.6)$$

$$S_{ij} = \frac{1}{2} \left(\frac{\partial \widetilde{u}_i}{\partial x_j} + \frac{\partial \widetilde{u}_j}{\partial x_i} \right) \quad (4.7)$$

$$k = \frac{1}{2} \overline{u'_i u'_i} \quad (4.8)$$

Therefore, the k- ε model require two additional transport equations to obtain the turbulent viscosity through Eq. 4.6: one equation is needed for the turbulent kinetic energy (k) and one for the dissipation of turbulent kinetic energy (ε), reproduced respectively in Eq. (9) and Eq. (10):

$$\frac{\partial \rho k}{\partial t} + \frac{\partial (\rho u_i k)}{\partial x_i} = \tau_{ij} \frac{\partial u_i}{\partial x_j} + \frac{\partial}{\partial x_j} \left(\frac{\mu + \mu_t}{Pr_k} \frac{\partial k}{\partial x_j} \right) - \rho \varepsilon + \frac{C_S}{1.5} S_S \quad (4.9)$$

$$\begin{aligned} \frac{\partial \rho \varepsilon}{\partial t} + \frac{\partial (\rho u_i \varepsilon)}{\partial x_i} = & \frac{\partial}{\partial x_j} \left(\frac{\mu + \mu_t}{Pr_\varepsilon} \frac{\partial \varepsilon}{\partial x_j} \right) + C_{\varepsilon 3} \rho \varepsilon \frac{\partial u_i}{\partial x_i} + \\ & \left(C_{\varepsilon 1} \frac{\partial u_i}{\partial x_j} \tau_{ij} - C_{\varepsilon 2} \rho \varepsilon + C_S S_S \right) + S \end{aligned} \quad (4.10)$$

Where S is the user-defined source term and S_S is the source term that represents interactions with the discrete phase. The $C_{\varepsilon i}$ terms are model

constants that account for compression and expansion. The details of the existing k- ε variants, namely Standard, Realizable and RNG, can be found in [1].

Reynolds Stress Model (RSM)

The Reynolds Stress Model (RSM) solves an independent equation for each of the six Reynolds stresses and another one for the dissipation rate. The RSM approach is usually more suitable for simulating complex turbulent flows involving strong anisotropy (e.g., the strong swirl generated inside the combustor), since the model obviates the use of the isotropic turbulent-viscosity hypothesis [5]. Nevertheless, even though the transport equations for the Reynolds stresses can be written in the exact form, some of the terms in those equations are unknown and need to be modeled to ensure closure of the system.

The exact transport equation for the Reynolds stresses can be obtained from the Navier-Stokes equations and summarized as follows:

$$C_{ij} = D_{T,ij} + D_{M,ij} + P_{ij} + \phi_{ij} + \varepsilon_{ij} \quad (4.11)$$

where C_{ij} represents the convective term, $D_{T,ij}$ is the turbulent diffusion term, $D_{M,ij}$ is the molecular diffusion term, P_{ij} is the stress production term, ϕ_{ij} is the pressure-strain term and ε_{ij} is the dissipation term. These exact contributions are given by Eq. 4.12:

$$C_{ij} = \frac{\partial}{\partial t} (\bar{\rho} \widetilde{u'_i u'_j}) + \frac{\partial}{\partial x_j} (u_k \bar{\rho} \widetilde{u'_i u'_j}) \quad (4.12a)$$

$$D_{T,ij} = -\frac{\partial}{\partial x_k} \left(\bar{\rho} \widetilde{u'_i u'_j u'_k} + p \left(\delta_{kj} \widetilde{u'_i} + \delta_{ik} \widetilde{u'_j} \right) \right) \quad (4.12b)$$

$$D_{M,ij} = \frac{\partial}{\partial x_k} \left(\mu \frac{\partial}{\partial x_k} (\bar{\rho} \widetilde{u'_i u'_j}) \right) \quad (4.12c)$$

$$P_{ij} = -\bar{\rho} \left(\widetilde{u'_i u'_k} \frac{\partial u'_j}{\partial x_k} + \widetilde{u'_j u'_k} \frac{\partial u'_i}{\partial x_k} \right) \quad (4.12d)$$

$$\phi_{ij} = P \left(\frac{\partial \widetilde{u'_i}}{\partial x_j} + \frac{\partial \widetilde{u'_j}}{\partial x_i} \right) \quad (4.12e)$$

$$\varepsilon_{ij} = -2\mu \left(\widetilde{\frac{\partial u'_i}{\partial x_k} \frac{\partial u'_j}{\partial x_k}} \right) \quad (4.12f)$$

As stated previously, some of the terms need to be modeled to close the equations (i.e., the turbulent diffusion $D_{T,ij}$, the pressure-rate-of-strain ϕ_{ij} and the dissipation ε_{ij} terms) while the rest of them are directly calculated. The pressure-rate-of-strain term is generally considered to be the most important in terms of modeling since it serves to redistribute energy among the Reynolds stresses. In this study, the Launder-Reece-Rodi (LRR) RSM model [6] is used to evaluate ϕ_{ij} .

4.2.2.2 Large Eddy Simulations (LES)

In the LES approach, the field is decomposed into a resolved field ($\bar{\cdot}$) and a sub-grid field through a spatial filter operation [7]. The resolved velocity field is defined as a spatial average of the actual velocity field, unlike the ensemble average presented in RANS. When the LES decomposition is applied to the equation of momentum conservation, Eq. 4.13 is obtained:

$$\frac{\partial (\bar{\rho} \tilde{u}_i)}{\partial t} + \frac{\partial (\bar{\rho} \tilde{u}_i \tilde{u}_j)}{\partial x_j} = -\frac{\partial \bar{P}}{\partial x_i} + \frac{\partial \bar{\sigma}_{ij}}{\partial x_j} - \frac{\partial \tau_{ij}}{\partial x_j} \quad (4.13)$$

Most sub-grid scale LES models focus on modeling the expression for the sub-grid stress tensor, $\tau_{ij} = \bar{\rho} (\widetilde{u_i u_j} - \tilde{u}_i \tilde{u}_j)$. In the frame of the present investigation, the Smagorinsky, Dynamic Smagorinsky, and Dynamic Structure SGS LES models have been considered and are briefly presented here.

The Smagorinsky model is a zero-equation LES model (i.e., no additional transport equation is solved) which relates the turbulent viscosity to the magnitude of the strain rate tensor and cell size [8]. The model for the sub-grid stress tensor is given by:

$$\tau_{ij} = -2C_S^2 \Delta_e^2 \bar{S}_{ij} \sqrt{S_{ij} S_{ij}} \quad (4.14)$$

where Δ_e is the filter cut-off width represented Figure 4.2, which in this study is considered to be related to the cell volume V_c , as shown in Eq. 4.15:

$$\Delta_e = \sqrt[3]{V_c} \quad (4.15)$$

The main drawback of the Smagorinsky model is that the appropriate value of the Smagorinsky coefficient (C_S) is highly dependent on the flow regime. To solve this problem, the Dynamic Smagorinsky model provides a methodology to estimate the local value of C_S [9]. The formulation of a dynamic model requires a second filtering operation for which a test level filter ($\hat{\Delta}_e$) is designated. Finally, an expression for the dynamic coefficient can be derived:

$$C_{S-dynamic} = \frac{M_{ij}L_{ij}}{M_{kl}M_{kl}} \quad (4.16)$$

where L_{ij} is the Leonard stress term, and M_{ij} is function of the test filter ($\hat{\Delta}_e$) and the rate of strain tensor (S_{ij}). The reader may refer to [10] for more details about these terms.

Last, the Dynamic Structure model is characterised by not using turbulent viscosity to model the sub-grid stress tensor. This model adds the following transport equation for the sub-grid kinetic energy:

$$\frac{\partial k}{\partial t} + \bar{u}_i \frac{\partial k}{\partial x_i} = -\tau_{ij} \frac{\partial \bar{u}_i}{\partial x_j} - \varepsilon + \frac{\partial}{\partial x_i} \left(\frac{\nu_t}{\sigma_k} \frac{\partial k}{\partial x_i} \right) \quad (4.17)$$

This enforces a budget on the energy flow between the resolved and the sub-grid scales. To that end, the sub-grid stress tensor (τ_{ij}) must be a function of the sub-grid turbulent kinetic energy (k), resulting in a set of six Fredholm integral equations of the second kind that can be solved via an iterative method. Please refer to [11] for the complete derivation of the equations involved in the Dynamic Structure model.

4.2.3 Spray Modelling

In gas turbine applications, liquid fuels are usually injected into the combustion chamber through a spray atomiser (see Section 2.2.2), involving several sub-processes, as discussed in Section 2.4.1. Since the turbulent spray characteristics profoundly affect the overall combustion performance and pollutant emissions, a detailed comprehension and modelling of these sub-processes is mandatory. Nevertheless, the underlying physics of phenomena such as the atomisation process and gas-spray interactions are not well understood despite the vast theoretical and experimental investigations on turbulent spray combustion.

In recent years, progress in spray diagnostic techniques and computational modelling (together with the increasingly available computational power) has

allowed conducting more in-depth spray analysis, thus improving the understanding of turbulent swirled-stabilised spray combustors. The main challenge to correctly model and simulate these biphasic systems appears for two reasons: on the one hand due to the strongly coupled phenomena co-occurring such as turbulence, phase change and mass transfer between phases². On the other hand, because of the necessity to get a trade-off between computational efficiency (i.e., reduced mathematical models) while maintaining an accurate description of relevant processes (i.e., complex mathematical models and increase in CPU cost).

In this context, numerous spray breakup models have been developed to characterise fuel injection using CFD techniques. In this way, the primary atomisation of liquid sheets is modelled considering the increasing instabilities of the liquid/gas interface or a combination of turbulent disturbances and instability theories [12]. Meanwhile, the breakup or rupture of the fuel ligaments is typically modelled by means of a Discrete Phase Model (DPM) through a Lagrangian approach. Nevertheless, this approach only works precisely in regions where droplets are dispersed in the absence of liquid ligaments (i.e., in the intermediate and dilute regimes shown in Figure 2.5).

This section discusses the numerical spray sub-models employed to model the spray sub-processes³ presented in 2.4.1 in order to compute the spray fuel cases of the CORIA LDI combustor.

4.2.3.1 The Euler-Lagrange Approach

The Euler-Lagrange (EL) formulation is the most common approach to simulate swirling spray combustion in GT burners (see Chapter 3). In the EL method, a Lagrangian tracking of discrete drops (disperse phase) is performed whereas the carrier phase is computed through the conventional Eulearian framework. A significant assumption of the EL approach is that the liquid droplet is considered as a point particle (i.e., the flow field inside and around the particles is not resolved). In this way, drop effects are reflected through empirical correlations and the inter-phase interactions through exchange terms [13].

The Discrete Phase Model (DPM) present in CONVERGETM [14] and OpenFOAM© [15] solvers implements the EL formulation to predict the behaviour of the multiphase flow and is employed in the present thesis to compute

²In reactive cases, additional phenomena such as heat transfer between phases and chemical reactions need to be modelled.

³These include atomisation, drop breakup, drop distortion and drag, drop collision and coalescence, turbulent dispersion of spray drops and drop evaporation.

the turbulent swirling spray in the CORIA LDI combustor. In this way, the gaseous phase (considered as a continuum) is solved through the Navier-Stokes (NS) equations (see Section 2.3.2), whereas the liquid phase (considered as discrete particles) is computed through the Lagrangian equations (see Section 2.3.3) by tracking the particles throughout the determined flow field. In the two-way coupling considered in the DPM, the gas-phase affects liquid particles through drag, turbulence and momentum exchange, whereas the discrete phase interacts with the continuum through source terms in the NS equations for mass ($\dot{\rho}^s$), momentum (F^s) and energy (\dot{Q}^s), as illustrated in Figure 4.3.

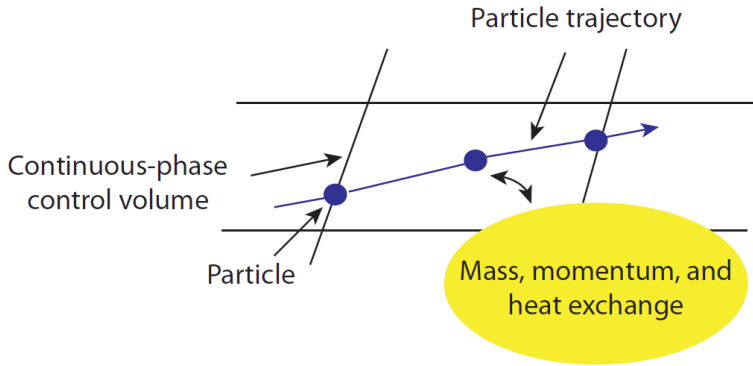


Figure 4.3: Schematic representation of the DPM coupling between continuous and discrete phases.

In the EL approach, the trajectories of the discrete particles are computed individually during the continuous phase calculation by integrating the force balance on the particle in a Lagrangian reference frame:

$$\frac{d\mathbf{v}}{dt} = F_D(\mathbf{v} - \mathbf{u}) + \frac{g_x(\rho_l - \rho_g)}{\rho_l} + F_x \quad (4.18)$$

where \mathbf{v} is the particle velocity, \mathbf{u} refers to the gas velocity, the term $F_D(\mathbf{v} - \mathbf{u})$ represents the drag force per unit particle mass, g_x is the gravitational acceleration, F_x is an additional force per unit particle (important under specific situations) and ρ_l and ρ_g are the liquid and gas density, respectively.

The term F_D related to the drag force in Eq. 4.18 can be written as [16]:

$$F_D = \frac{18\mu_g C_D Re}{\rho_l d_t^2} \frac{1}{24} \quad (4.19)$$

where μ_g is the gas molecular viscosity, d_l refers to the diameter of the liquid particle and C_D is the drag coefficient⁴. Meanwhile, the relative Reynolds number (Re) is defined as:

$$Re \equiv \frac{\rho_g d_l |\mathbf{v} - \mathbf{u}|}{\mu_g} \quad (4.20)$$

Finally, the drop parcel approximation is considered to calculate the spray in liquid fuel simulations. This approach introduces drop parcels into the computational domain at the injector location at a user-specified rate. Parcels represent a group of drops (particles) of similar size, location and properties (e.g., velocity, temperature). These drops are collected into single parcels before solving Lagrangian equations for averaged properties of each parcel. By using the concept of drop parcels to statistically represent the entire spray field, CONVERGETM and OpenFOAM[©] significantly reduce the computational resources of spray simulations.

4.2.3.2 Atomisation and Drop Breakup Modelling

A primary atomisation model yields both the initial and boundary conditions for the liquid fuel injection at the nozzle exit (i.e., spray drop distribution, drop velocities, temperature) and the disintegration at the near-nozzle region. The most commonly used primary atomisation models in spray simulations are the one developed by Huh et al. [17] for liquid jets, and the Linearised Instability Sheet Atomization (LISA) model [18, 19] for liquid sheets. Besides, the LISA model includes two parts: a general liquid sheet breakup mechanism and a liquid injection methodology specifically developed for pressure-swirl atomisers, so its use in the present thesis is justified.

On the other hand, several spray breakup mechanisms, including popular and widely used models based on the Kelvin-Helmholtz (KH, WAVE Model) and Rayleigh-Taylor (RT) instability mechanisms, and the Taylor Analogy Breakup (TAB) drop breakup model [20] have been proposed to predict the secondary atomisation or liquid spray drop breakup modelling. The WAVE model [21, 22] is based on a liquid jet stability analysis and is suitable for drop breakup in the stripping regime. Meanwhile, the RT model [23] considers RT waves arising on a very high-speed drop surface due to the rapid deceleration of the drops because of the drag force magnitude. Finally, the TAB model is based on Taylor's analogy [24] between an oscillating and distorting droplet

⁴Models for the drag coefficient (C_D) are presented in a following section.

and a spring-mass system and is generally well suited for low-Weber-number sprays.

The determination of the appropriate atomisation and breakup models (and the corresponding selection of model constants) for a particular spray simulation is not trivial. In essence, a trial and error procedure is habitually required. This section describes the theory behind the models used in this thesis to predict liquid atomisation (LISA model) and drop breakup (TAB model) and its implementation in the numerical simulations.

LISA Model

The LISA model is deemed to be well-suited for modelling both the injection (i.e., the liquid sheet formation) and the primary sheet atomisation (i.e., the sheet disintegration into ligaments) of pressure-swirl atomisers. The description of the liquid injection model is first presented followed by the disintegration model.

The methodology developed by Schmidt et al. [18] is used to initialize the size and velocity of injected sheet parcels. In a pressure swirl atomiser, an air-core enclosed by a liquid film is created inside the atomiser due to the centrifugal motion (see Section 2.2.2). The liquid mass flow rate (\dot{m}_l) can be expressed in terms of the film thickness (t_l), represented in Figure 4.4, as [19]:

$$\dot{m}_l = \pi \rho_l u_l t_l (d_o - t_l) \quad (4.21)$$

where d_o is the atomiser outlet diameter and u_l is the liquid axial velocity component at the nozzle outlet section. Nevertheless, since u_l is influenced by internal details of the atomiser (not always accessible or available), the model assumes the injector outlet velocity profile to be uniform [25], also assuming a dependence of the total velocity (U_l) to the known injection pressure (p_{inj}). The total exit velocity can be written as:

$$U_l = k_v \sqrt{\frac{2p_{inj}}{\rho_l}} \quad (4.22)$$

where k_v is the velocity coefficient related to the injector design and injection pressure [26], given by:

$$k_v = \max \left[0.7, \frac{4\dot{m}_l}{\pi d_o^2 \rho_l \cos \theta} \sqrt{\frac{\rho_l}{2p_{inj}}} \right] \quad (4.23)$$

where θ is the initial half spray cone angle⁵. In this way, Eq. 4.22 is used to initialise the velocity of the sheet parcels, the liquid axial velocity (u_l) being determined as:

$$u_l = U_l \cos \theta \quad (4.24)$$

Meanwhile, the initial liquid sheet thickness (t_s) can be related to the film thickness (t_l), as shown in Figure 4.4, through the following expression:

$$t_s = t_l \cos \theta \quad (4.25)$$

Therefore, both the sheet film thickness and the axial velocity are determined at the nozzle outlet through Eqs. 4.21 to 4.25. Furthermore, the model assumes a tangential liquid sheet velocity (w_l) to be identical to the radial velocity component (v_l) downstream of the injector exit [18], given by:

$$w_l = v_l = U_l \sin \theta \quad (4.26)$$

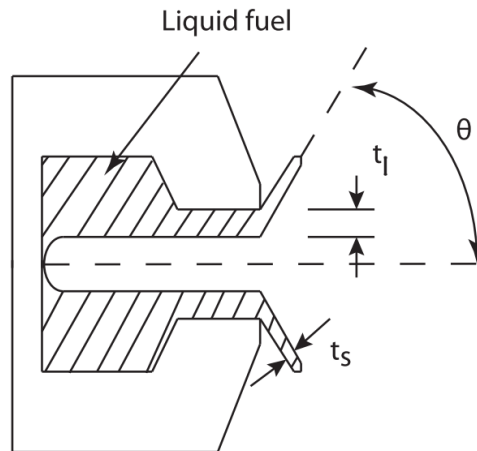


Figure 4.4: Relation between liquid sheet thickness t_s and half spray cone angle θ in pressure swirl atomisers [27].

On the other hand, the sheet disintegration stage in the LISA model considers the impact of the surrounding gas-phase, liquid viscosity and surface

⁵The spray cone angle is a design parameter but it is affected by the operating conditions (i.e, density and temperature in the combustion chamber).

tension. Senecal et al. [19] derived the following dispersion relation for the sinuous mode⁶ for a two-dimensional, viscous and incompressible liquid sheet with thickness t_s and relative velocity U_{rel} moving through a quiescent, inviscid, incompressible gas medium [12]:

$$\omega_L^2 \left[\tanh \left(k \frac{t_s}{2} \right) + \rho_{g,l} \right] + \omega_L \left[4\nu_l k^2 \tanh \left(k \frac{t_s}{2} \right) + 2i\rho_{g,l} k U_{rel} \right] + 4\nu_l^2 k^4 \tanh \left(k \frac{t_s}{2} \right) - 4\nu_l^2 k^3 L \tanh \left(L \frac{t_s}{2} \right) - \rho_{g,l} U_{rel}^2 k^2 + \frac{\sigma_l k^3}{\rho_l} = 0 \quad (4.27)$$

where $\omega_L = \omega_r + i\omega_i$ is the complex form of the wave growth rate, k is the wave number, ν_l is the liquid kinematic viscosity, σ_l is the liquid surface tension, $\rho_{g,l} = \rho_g/\rho_l$ and $L^2 = k^2 + \omega_L/\nu_l$. The maximum growth rate of the sinuous mode solution has shown to be always greater than or equal to the maximum growth rate of varicose waves for high velocity flows with values of $\rho_{g,l}$ significantly smaller than one.

Senecal et al. [19] performed an order of magnitude analysis to simplify Eq. 4.27 for use in multi-scale simulations. In this way, typical values from the inviscid solutions manifested that the second-order terms in viscosity can be neglected when compared to other terms. Furthermore, if short waves are assumed⁷ (i.e., $\tanh(k \frac{t_s}{2})$) and $\rho_{g,l} \ll 1$, the real part of the wave growth rate can be reduced to:

$$\omega_r = -2\nu_l k^2 + \sqrt{4\nu_l^2 k^4 + \rho_{g,l} U_{rel}^2 k^2 - \frac{\sigma_l k^3}{\rho_l}} \quad (4.28)$$

The LISA model adopts the physical mechanism of sheet disintegration proposed by Dombrowski and Johns [28] to predict the ligament sizes produced by the primary atomisation process. In this process, disintegration occurs due to the growth of waves on the surfaces generated by the aerodynamic forces acting on the liquid sheet. Once the waves reach a critical amplitude, fragments of the liquid are broken-off and contracted to form cylindrical ligaments

⁶The LISA model is based on the development of sinuous (anti-symmetric) waves on the liquid sheet inducing sheet disintegration into ligaments.

⁷Senecal et al. [19] analytically derived a critical Weber number of $We_g = \rho_g U_{rel}^2 t_s / (2\sigma) = 27/16$, below which long waves dominate the breakup process, and above which short waves dominate breakup. As the Weber number is typically well above 27/16 for sheet breakup in pressure-swirl atomizers, it is reasonable to assume that short waves are responsible for breakup.

that are believed to move normal to the ligament axis. The onset of ligament formation can be determined through an analogy with the prediction of the breakup length of cylindrical liquid jets [21]. In this way, when a disturbance generated at the liquid sheet reaches a length of η_{bu} at breakup, a breakup time τ_{bu} can be evaluated as:

$$\eta_{bu} = \eta_0 \exp(\Omega_s \tau_{bu}) \Rightarrow \tau_{bu} = \frac{1}{\Omega_s} \ln \left(\frac{\eta_{bu}}{\eta_0} \right) \quad (4.29)$$

where Ω_s is the maximum growth rate, obtained from Eq. 4.28 by maximizing ω_r as a function of k . Thus, the sheet will break up and ligaments will be formed having a length given by:

$$L_{bu} = U_l \tau_{bu} = \frac{U_l}{\Omega_s} \ln \left(\frac{\eta_{bu}}{\eta_0} \right) \quad (4.30)$$

where the quantity $\ln(\eta_{bu}/\eta_0)$ is typically set to 12 based on the work of Dombrowski and Hooper [29].

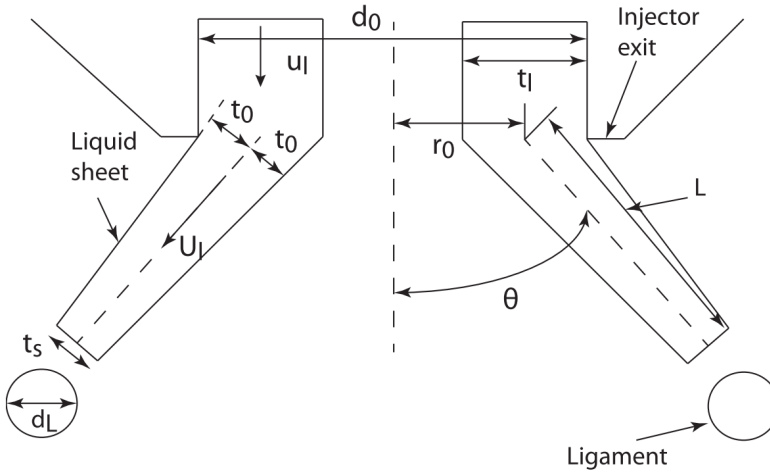


Figure 4.5: Conceptual representation of the liquid sheet flow at the exit of a hollow cone pressure swirl atomiser.

Once the sheet breakup length predicted by Eq. 4.30 is reached, ligaments with a given diameter (d_L) depending on the sheet thickness (t_s) are formed

(see Figure 4.5). The sheet thickness at the breakup length is obtained using the following correlation:

$$t_s = \frac{2r_0 t_0}{r_0 + L \sin \theta} \quad (4.31)$$

where r_0 is the radius at the injector exit, t_0 refers to the half sheet-thickness at the atomiser exit and L represents the sheet length (see Figure 4.5).

The resulting diameter of a ligament created by a short wave disturbance⁸ is given by the following expression [19]:

$$d_L = \sqrt{\frac{8t_s}{K_s}} \quad (4.32)$$

where K_s is the wave number corresponding to the maximum growth rate Ω_s .

Nevertheless, the LISA model in CONVERGETM and OpenFOAM[©] codes considers that the ligament diameter is linearly proportional to the wavelength (Λ_s) responsible for breaking up the liquid sheet:

$$d_L = C_{lisa} \Lambda_s = C_{lisa} \frac{2\pi}{K_s} \quad (4.33)$$

where C_{lisa} is a model constant.

Finally, the generation of drops from the disintegration of ligaments is considered to occur according to capillary instability analysis [28] when the amplitude of the unstable waves equals the radius of the ligament (i.e., one drop is created per wavelength). In this way, the resulting drop diameter is found from the following expression [19]:

$$d_D = 1.88d_L (1 + 3Oh)^{1/6} \quad (4.34)$$

where Oh is the Ohnesorge number, defined in Eq. 2.25.

In CONVERGETM and OpenFOAM[©] the parcels representing the liquid sheet do not directly interact with the gas phase and do not undergo collision, drag, evaporation, or turbulent dispersion. Once the sheet parcels travel a distance from the injector given by Eq. 4.30, the parcels are given a size

⁸Ligaments are assumed to be created in the liquid sheet once per wavelength.

predicted by Eq. 4.34 and are treated as normal parcels that undergo collision, drag, evaporation, turbulent dispersion, and are coupled to the gas [14, 15]. Finally, the TAB model is used to predict secondary drop breakup in the LISA model.

TAB Model

The TAB (Taylor Analogy Breakup) model [20] is based on Taylor's analogy between an oscillating and distorting droplet and a spring-mass system in order to compute drop distortion and breakup. In this way, the surface tension forces, the liquid viscosity effects and the gas aerodynamic forces are resembled by their analogous restoring forces of the spring, the damping forces and the external forces on the mass, respectively.

The governing equation of a damped, forced harmonic oscillator is given by:

$$m\ddot{x} = F - k_s x - d\dot{x} \quad (4.35)$$

where x is the displacement of the equator of the droplet from its undisturbed spherical position, F represents the external aerodynamic (drag) forces, k_s is the spring's constant representing the surface tension and d_s the damping parameter analogous to the viscous forces.

The physical connections of the coefficients of 4.35 are obtained from Taylor's analogy as:

$$\frac{F}{m} = C_F \frac{\rho_g |\mathbf{w}|^2}{\rho_l r_o} \quad (4.36a)$$

$$\frac{k_s}{m} = C_{k,s} \frac{\sigma}{\rho_l r_o^3} \quad (4.36b)$$

$$\frac{d_s}{m} = C_{d,s} \frac{\mu_l}{\rho_l r_o^2} \quad (4.36c)$$

where \mathbf{w} denotes the relative velocity between the droplet and the surrounding air introduced in Section 2.3.2, r_o is the undisturbed droplet radius (i.e., the drop radius prior to breakup), and C_F , $C_{k,s}$ and $C_{d,s}$ are dimensionless constants defined below.

Now, substituting the relationships of Eq. 4.36 in Eq. 4.35 and considering $y = x/(C_b r_o)$, a non-dimensional equation of the oscillator can be written:

$$\ddot{y} = \frac{C_F \rho_g}{C_b \rho_l} \frac{|\mathbf{w}|^2}{r_o^2} - \frac{C_{k,s} \sigma}{\rho_l r_o^3} y - \frac{C_{d,s} \mu_l}{\rho_l r_o^2} \dot{y} \quad (4.37)$$

where the constants have been determined to match experiments and theoretical results [30], resulting in the following values: $C_{k,s} = 8$, $C_{d,s} = 5$, $C_b = 1/2$ and $C_F = 1/3$.

The temporal response of y for under-damped drops can be defined from Eq. 4.37 if assuming constant relative velocity:

$$y(t) = We_c + \exp^{-\frac{t}{t_d}} \left[(y - We_c) \cos(\omega_T t) + \frac{1}{\omega_T} \left(\frac{dy}{dt}(0) + \frac{y(0) - We_c}{t_d} \right) \sin(\omega_T t) \right] \quad (4.38)$$

where

$$We_c = \frac{C_F}{C_{k,s} C_b} We_g \quad (4.39a)$$

$$\frac{1}{t_d} = \frac{C_{d,s}}{2} \frac{\mu_l}{\rho_l r_o^2} \quad (4.39b)$$

$$\omega_T^2 = C_{k,s} \frac{\sigma}{\rho_l r_o^3} - \frac{1}{t_d^2} \quad (4.39c)$$

These drop parameters We_c , t_d and ω_T^2 (droplet oscillation frequency) are first computed in the numerical implementation of the TAB model. Two possibilities arise from here: if the drop oscillation is negligible ($\omega_T^2 \leq 0$), no further breakup computations are executed for the droplet during the current time-step. Alternatively, if the drop oscillation presents positive values ($\omega_T^2 > 0$), the amplitude of the undamped oscillation is computed as:

$$A = \sqrt{(y - We_c)^2 + (y/\omega_T)^2} \quad (4.40)$$

The evaluation of A gives rise to two new possible scenarios. If $A + We_c \leq 1$, drop breakup does not occur during the current time-step. In this case, the distortion parameters y and \dot{y} are updated according to the following expressions:

$$y^{n+1} = We_c + \exp^{-\frac{\Delta t}{t_d}} \left[(y^n - We_c) \cos(\omega_T \Delta t) + \frac{1}{\omega_T} \left(\dot{y}^n + \frac{y^n - We_c}{t_d} \right) \sin(\omega_T \Delta t) \right] \quad (4.41a)$$

$$\begin{aligned} \dot{y}^{n+1} = & \frac{We_c - y^{n+1}}{t_d} + \\ & + \omega_T \exp^{-\frac{dt}{t_d}} \left[\frac{1}{\omega_T} \left(\dot{y}^n + \frac{y^n - We_c}{t_d} \right) \cos(\omega_T t) - (y^n - We_c) \sin(\omega_T t) \right] \end{aligned} \quad (4.41b)$$

where the superscript $n+1$ refers to the updated values and the superscript n refers to the previous values.

On the other hand, if $A+We_c > 1$, breakup is then predicted to occur and a breakup time is calculated considering that the drop oscillation is undamped for its first period [20]. Breakup is finally confirmed if the computational time-step is larger than the breakup time or if $y \geq 1$.

When breakup occurs, y is set to 1, \dot{y} is set to the corresponding undamped oscillation evaluated at the breakup time, and a perpendicular drop velocity component V_n is estimated through:

$$V_n = 0.5 r_o \dot{y} \quad (4.42)$$

The direction of V_n is randomly determined in a plane orthogonal to the drop relative velocity, and its magnitude is added to the drop velocity.

Finally, the breakup drop radius r is computed with the following formulation derived by O'Rourke and Amsden [20]:

$$r = \frac{r_o}{1 + \frac{8K}{20} y^2 + \frac{\rho_l r_o^3}{\sigma} \dot{y}^2 \left(\frac{6K-5}{120} \right)} \quad (4.43)$$

where K is a constant that must be calibrated experimentally by measuring drop sizes, and whose value has been set as $K = 10/3$ [20].

It should be noted that if a drop size distribution is specified to the TAB model (as done in this thesis), the radius calculated by Eq. 4.43 is the Sauter Mean Radius (SMR) of the distribution. In this case, once the new radius is computed, the number of drops for the parcel is updated to meet mass conservation.

4.2.3.3 Turbulent Dispersion Modelling of Spray Drops

The effects of the turbulent flow on the dispersion of spray drops (parcels) are predicted through a stochastic tracking method. Such approach adds an instantaneous fluctuating velocity \mathbf{u}'_i to the gas velocity \mathbf{u}_i in the particle trajectory before the integration of Eq. 4.18. Besides, source terms are included

both in RANS and LES turbulence models to account for the decrease of turbulent kinetic energy as a consequence of the work done by turbulent eddies to disperse the liquid spray droplets.

The source terms S_s also include the fluctuating component of the gas-phase velocity \mathbf{u}'_i :

$$S_s = -\frac{\sum_p N_p (F'_{D,i}|\mathbf{u}'_i|)_p}{V_c} \quad (4.44)$$

where the summation is over all the parcels in the cell, N_p is the number of drops in a parcel, V_c is the cell volume and

$$F'_{D,i} = -\frac{F_{D,i}}{|\mathbf{u}'_i| + |\mathbf{u}_i| - |\mathbf{v}'|}|\mathbf{u}'_i| \quad (4.45)$$

where $F_{D,i}$ is the drag force on a drop.

The O'Rourke turbulent dispersion model used in this study assumes that each discretised gaseous turbulent eddy is characterised by a Gaussian distribution for the random velocity fluctuation and a time scale. In this way, the fluctuating velocity components ($u'_{x,i}$, $u'_{y,i}$ and $u'_{z,i}$) follows a Gaussian probability distribution given by

$$G(u'_{k,i}) = \frac{1}{\sqrt{2\pi}\sigma} \exp\left(-\frac{(u'_{k,i})^2}{2\sigma^2}\right) \quad (4.46)$$

with a variance σ^2 proportional to the turbulent kinetic energy by a factor of $2/3k$ [31]. It can be shown that the cumulative distribution function for Eq. 4.46 is given by

$$\tilde{G}(u'_{k,i}) = \operatorname{erf}\left(\frac{u'_{k,i}}{\sqrt{2}\sigma}\right) = \operatorname{erf}(\zeta) \quad 0 < \zeta < 2 \quad (4.47)$$

where:

$$\zeta = \frac{u'_{k,i}}{\sqrt{(4/3)k}} \quad (4.48)$$

The Newton's method is used to numerically obtain the specific values of \tilde{G} through the inversion Eq. 4.47. These values are calculated once at the

start of the simulation and stored in a table. When a value of ζ is needed for a turbulent dispersion calculation, a random number YY between zero and one is selected which represents the chosen value of \tilde{G} . Then, the corresponding value of ζ is found by interpolating in the table [14]. Finally, once a value of ζ is selected, $u'_{k,i}$ is calculated⁹ using Eq. 4.48 and its sign is determined based on the parameter $XX = 1 - 2YY$.

The trajectory of each liquid drop is integrated according to the above procedure with the turbulent velocity field of the carrier phase until a turbulence correlation time (t_d) is reached and the drop leaves behind the eddy. This drop-eddy interaction time is defined as the lesser of the eddy breakup time (i.e., eddy characteristic lifetime) and the time taken by the droplet to travel across an eddy [32]:

$$t_d = \min \left(\frac{k}{\varepsilon}, c_{ps} \frac{k^{3/2}}{\varepsilon} \frac{1}{|\mathbf{u}'_i + \mathbf{u}_i - \mathbf{v}'|} \right) \quad (4.49)$$

where c_{ps} is an empirical constant and ε is the dissipation of turbulent kinetic energy.

4.2.3.4 Drop Collision and Coalescence Modelling

The fundamentals of drop collision and coalescence phenomena are presented in Chapter 2. Nevertheless, computing drop collision for the vast collection of drops that coexist in liquid spray LDI burners is computationally prohibitive. An efficient collision and coalescence model together with the parcel concept described in a previous section needs to be considered to estimate the number of droplet (parcel) collisions and their outcomes in a relatively computationally efficient way. It can be seen that for N drops present in a liquid spray, each having $N - 1$ possible collision partners, the number of possible collision pairs is approximately $(1/2)N^2$. Without the parcel approximation, this N^2 -dependence would render the collision calculation computationally prohibitive for the millions of drops that may exist in a simulation. Since a parcel can represent hundreds or thousands of drops, the CPU cost of the collision calculation is significantly reduced.

In order to further reduce the computational cost, the O'Rourke collision and coalescence model [33] is used in this study. The O'Rourke algorithm considers a stochastic estimation of collisions and assumes that parcels can collide only if they are placed in the same eulerian cell. In this way, CONVERGETM

⁹Note that this process is conducted for each of the three components of $u'_{k,i}$.

and OpenFOAM® only perform a collision calculation for a pair of parcels. The parcel including bigger drops is known as the collector, whereas the parcel containing smaller drops is known as the droplet. In the following description, a subscript of 1 is adopted for the collector parcel, while a subscript of 2 is used for the droplet parcel.

On the one hand, the collision frequency of a collector drop with all of the droplets is given by [33]:

$$P_1 = \frac{N_2 \pi (r_1 + r_2)^2 v_{rel}}{V_{cell}} \quad (4.50)$$

where N_2 is the number of drops in the droplet parcel, $v_{rel} = |v_{i1} - v_{i2}|$ is the relative velocity between the collector and droplet parcels, r_1 and r_2 are the radii of the collector and droplet, respectively, and V_{cell} is the volume of the carrier-phase cell that includes the two parcels. The probability that the collector collides n times with drops is assumed to follow a Poisson distribution:

$$P(n) = \exp(-\bar{n}) \frac{\bar{n}^n}{n!} \quad (4.51)$$

with a mean value given by

$$\bar{n} = P_1 \Delta t = \frac{N_2 \pi (r_1 + r_2)^2 v_{rel} \Delta t}{V_{cell}} \quad (4.52)$$

where Δt is the computational time-step. In Eq. 4.52 the quantity $\pi (r_1 + r_2)^2 v_{rel} \Delta t$ is the collision volume which is simply the collision area $\pi (r_1 + r_2)^2$ multiplied by the distance traveled by a droplet in one time-step. Since there is a uniform probability that a droplet will be anywhere in the gas-phase cell, then the probability of the droplet being in the collision volume is the ratio of the collision volume to the gas-phase cell volume.

On the other hand, the probability of no collisions is given by

$$P_o = \exp(-\bar{n}) \quad (4.53)$$

In this case, a random number is chosen between zero and one to determine if collision occurs. If the value of the random number is less than P_o , no collision takes place, whereas if it is greater than or equal to P_o , then collision occurs.

If a collision occurs, the next step is to determine the outcome of the collision. The O'Rourke mode includes two collision outcomes, namely coalescence and grazing collision. In order to determine which outcome takes place, a critical impact parameter (b_{crit}) is calculated as follows:

$$b_{crit} = (r_1 + r_2) \min \left(1, \frac{2.4f}{We_c} \right) \quad (4.54)$$

where We_c is the collision Weber number introduced in Eq. 2.32b and f is given by

$$f = \left(\frac{r_1}{r_2} \right)^3 - 2.4 \left(\frac{r_1}{r_2} \right)^2 + 2.7 \left(\frac{r_1}{r_2} \right) \quad (4.55)$$

The actual collision impact parameter is given by $b = (r_1 + r_2)\sqrt{Y}$, where Y is a random number between zero and one. Then, the collision outcome is coalescence if $b < b_{crit}$, otherwise the outcome is grazing collision.

On the one hand, if the outcome of the event is grazing collision, the new drop velocities are computed according the conservation of momentum and kinetic energy. From the basis of assumed forms for the energy and angular momentum losses due to viscous dissipation, O'Rourke [33] derived the following expressions for the new collector and droplet velocities:

$$v_{i,1}^* = \frac{m_1 v_{i,1} + m_2 v_{i,2} + m_2 (v_{i,1} - v_{i,2})}{m_1 + m_2} \sqrt{1 - f_E} \quad (4.56a)$$

$$v_{i,2}^* = \frac{m_1 v_{i,1} + m_2 v_{i,2} + m_1 (v_{i,2} - v_{i,1})}{m_1 + m_2} \sqrt{1 - f_E} \quad (4.56b)$$

where the * superscript indicates the post-grazing collision velocity values and f_E is the fraction of energy dissipated in the collision, defined as:

$$f_E = 1 - \frac{(b - b_{crit})^2}{(r_1 + r_2 - b_{crit})^2} \quad (4.57)$$

In addition, grazing collisions only take place between the smaller number of drops between parcel 1 and parcel 2. For example, if parcel 1 has fewer drops than parcel 2, the updated velocities are given by

$$v_{i,1}^{n+1} = v_{i,1}^* \quad (4.58a)$$

$$v_{i,2}^{n+1} = \frac{N_1 v_{i,2}^* + (N_2 - N_1) v_{i,2}^n}{N_2} \quad (4.58b)$$

where the superscripts n and $n + 1$ refer to the previous and updated time-step values, respectively.

On the other hand, in the case of coalescence, the number of droplets that coalesce with a collector drop are determined through Eq. 4.51. The properties of the coalesced drops are found using the basic conservation laws (not shown here for brevity).

4.2.3.5 Drop Evaporation Modelling

Once the liquid spray is injected into the computational domain, a model is needed to convert the liquid into vapour. The standard approach considered in this thesis to describe the evaporation process is to consider a single-component model fuel and to assume phase equilibrium because of its simplicity and low consumption of computational resources [34]. In this way, the rate of change in the drop radius (\dot{R}) shown in Eqs. (2.10) and (2.20) due to vaporization can be expressed according to the Frossling correlation [31] as follows:

$$\dot{R} = \frac{dr}{dt} = -\frac{\rho_g D B Sh}{2\rho_{f_v} r} \quad (4.59)$$

where D is the mass diffusivity of fuel vapour in the gaseous phase of density ρ_g and B represents the mass transfer number, which can be related to the fuel mass fraction as:

$$B = \frac{Y_{f_v}^* - Y_{f_v}}{1 - Y_{f_v}^*} \quad (4.60)$$

where $Y_{f_v}^*$ denotes the fuel mass fraction at the drop surface, Y_{f_v} refers to the fuel mass fraction in the computational cell, the subscript f_v indicates the fuel vapour, and Sh is the Sherwood number [31], which in turn can be written as follows:

$$Sh = \left(2 + 0.6 Re_d^{1/2} Sc^{1/3}\right) \frac{\ln(1 + B)}{B} \quad (4.61)$$

where Re_d is the drop Reynolds number, Sc is the Schmidt number of the gas-phase, and $\ln(1 + B)/B$ is the Spalding function to consider the heat transfer modification in turbulent boundary layers.

As stated before, the partial pressure of fuel vapour can be assumed to be equal to the equilibrium vapour pressure, thus allowing to express the fuel mass fraction at the drop surface as:

$$Y_{f_v}^* = \frac{W_{f_v}}{W_{f_v} + W_g \left(\frac{p_g}{p_{f_v} T_d} - 1 \right)} \quad (4.62)$$

where W_{f_v} and W_g refer to the molecular weights of the vapour fuel and gas-phase, respectively, p_{f_v} and p_g are the vapour fuel pressure and air pressure, respectively, and T_d is the drop temperature.

On the other hand, the time rate of change in drop temperature (\dot{T}_d) introduced in Eqs. (2.19) and (2.22) can be directly obtained from the following energy balance:

$$\rho_l \frac{4}{3} \pi r^3 c_l \dot{T}_d - \rho_l 4\pi r^2 \dot{R} L_v = 4\pi r^2 \dot{Q}_d \quad (4.63)$$

where c_l represents the specific heat of the liquid-phase, L_v is the specific latent heat for vaporisation at a constant temperature T_d and \dot{Q}_d refers to the heat flux (i.e., the rate of heat conduction to the drop), which can be written as:

$$\dot{Q}_d = -\alpha_h (T_g - T_d) \quad (4.64)$$

where T_g refers to the gas temperature and α_h represents the heat transfer coefficient.

The heat transfer coefficient can be expressed as [35]:

$$\alpha_h = \frac{Nu}{2r} \lambda_{eff} \frac{\ln(1+B)}{B} \quad (4.65)$$

where λ_{eff} represents the effective thermal conductivity and Nu is the Nusselt number, given by the following expression [36, 37]:

$$Nu = 2 + 0.6Re^{1/2}Pr^{1/3} \quad (4.66)$$

where Re and Pr refers to the Reynolds and Prandtl numbers, respectively.

4.2.4 Numerical Methods

The numerical simulations of the swirling flow in an LDI combustor carried out in this investigation are conducted through CONVERGETM and OpenFOAM[®] CFD packages. Both codes are based in the finite volume method to numerically solve the integral form of the conservation equations.

Generally, the numerical methods in a CFD simulation consist of the following 3 steps:

1. The governing transport equations of fluid flow are integrated over all the control volumes of the domain.
2. The resulting integral equations are discretised into a system of algebraic equations.
3. An iterative numerical algorithm is applied to obtain a solution of the algebraic equations.

The governing transport equations presented in Sections 2.3.2 and 4.2.1 can be converted from its differential form into an integral form (step 1), as follows:

$$\frac{\partial \phi}{\partial t} + \frac{\partial(u\phi)}{\partial x} = 0 \Rightarrow \frac{d}{dt} \int_{V_c} \phi dV + \int_S u \cdot n\phi dS = 0 \quad (4.67)$$

where V_c is the cell volume, S is the surface area, and n is the surface normal. The resulting control volume integration denotes the conservation of a general flow variable ϕ for each discrete cell of the domain. Then, the integral form of the equation is solved by summing fluxes on the faces of the cells. However, in CONVERGETM and OpenFOAM[®], all values are colocated and stored at the center of the cell as shown in Figure 4.6. Thus, to solve the integral form of the equation, the velocity and ϕ must be interpolated to the cell surface (step 2).

There are several options in order to obtain the cell surface value (step 2). One option is to upwind the surface value for ϕ , which results in a first-order accurate spatial scheme:

$$\phi_{i+1/2} = \phi_i \quad (4.68a)$$

$$\phi_{i-1/2} = \phi_{i-1} \quad (4.68b)$$

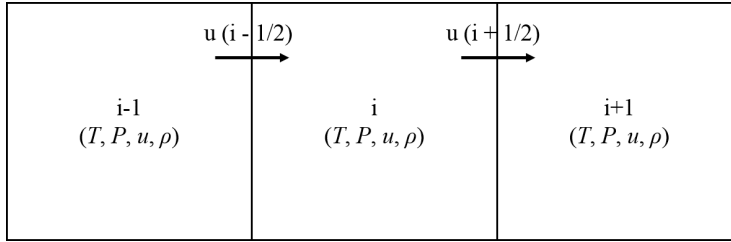


Figure 4.6: Sample three-cell of a one-dimensional spatial domain

Another option is to average the two adjacent cell values and place them on the surface, which results in a second-order accurate spatial scheme, the value of ϕ at the surface being given by:

$$\phi_{i+1/2} = \frac{1}{2}\phi_i + \frac{1}{2}\phi_{i+1} \quad (4.69a)$$

$$\phi_{i-1/2} = \frac{1}{2}\phi_i + \frac{1}{2}\phi_{i-1} \quad (4.69b)$$

Specifically, the second-order spatial accurate Monotonic Upstream-Centered Scheme for Conservation Laws (MUSCL) scheme [38] has been used in this study. The MUSCL scheme calculates the value of ϕ at a cell face using a blend of second order upwind and reconstructed central difference spatial discretisation schemes. Meanwhile, a flux limiter (e.g., CHARM [39], HQUICK [40], SUPERBEE [41]) is usually used together with the MUSCL scheme to preserve stability by restricting fluxes to meaningful values near discontinuities in the domain. Near these discontinuities, a flux limiter switches to a first-order spatial discretisation to avoid spurious oscillations in the solution. In the rest of the domain, however, the flux limiter function employs a higher-order spatial discretisation to improve solution accuracy.

Besides, for unsteady simulations, the governing transport equations need to be discretised in time. The expression for the time evolution of the scalar of a general flow variable ϕ is given by:

$$\frac{\partial \phi}{\partial t} = F(\phi) \quad (4.70)$$

where the function F includes any spatial discretisation. If the time derivative is discretised using backward differences, the corresponding first and

second-order accurate temporal discretisation schemes are given, respectively, by:

$$F(\phi) = \frac{\phi^{n+1} - \phi^n}{\Delta t} \quad (4.71a)$$

$$F(\phi) = \frac{3\phi^{n+1} - 4\phi^n + \phi^{n-1}}{2\Delta t} \quad (4.71b)$$

where n , $n + 1$, and $n - 1$ are the values at discrete times t , $t + \Delta t$, and $t - \Delta t$, respectively. For further details on the available discretisation schemes, the reader may also refer to the work by Versteeg and Malalasekera [1].

Finally, an iterative numerical algorithm is applied to obtain a solution of the algebraic equations (step 3). Figure 4.7 summarizes the order in which the transport equations are solved. At the start of each time-step, the values at the previous time-step ($t - 1$) are stored for all transported quantities. Next, explicit sources are calculated for each sub-model that is currently activated (e.g., spray sub-models presented in Section 4.2.3). The pressure-velocity linkage is then determined through the Pressure Implicit with Splitting of Operators (PISO) method [42]. Finally, the turbulence equations are resolved outside of the PISO loop for efficiency reasons.

The PISO algorithm, originally developed for unsteady compressible flow, starts with a predictor step where the momentum equation is solved. After the predictor, a pressure equation is derived and solved, which leads to a correction that is then applied to the momentum equation. This process of correcting the momentum equation and re-solving is repeated as many times as necessary to achieve the desired accuracy. After the momentum predictor and first corrector step have been completed, the other transport equations are solved in series. For further details on the PISO algorithm and other numerical algorithms, the reader may also refer to the work by Versteeg and Malalasekera [1].

4.3 Pre-processing

This section presents the pre-processing stage involving the complete case setup for both gaseous and liquid-fueled cases in both CONVERGE™ and OpenFOAM© codes. First, the definition of the computational domain and the appropriate boundary conditions as well as the fluid properties are shown

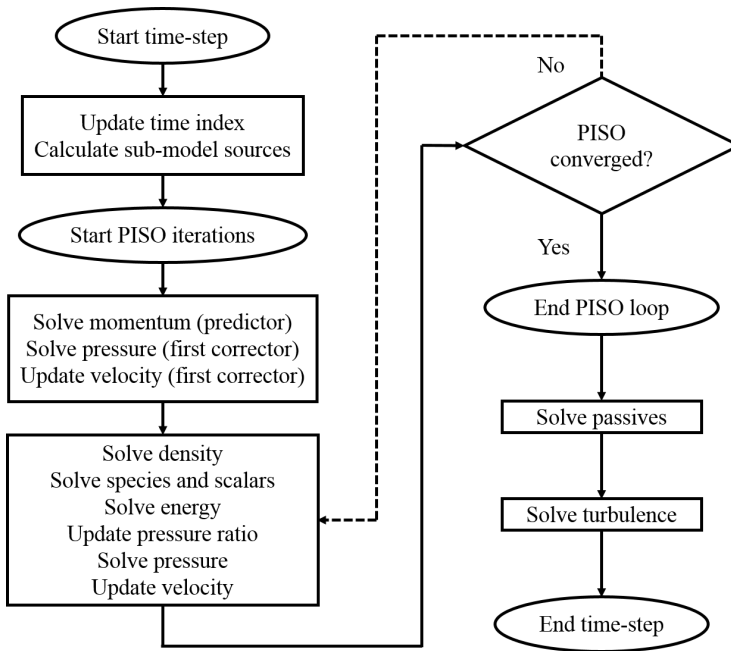


Figure 4.7: Numerical procedure to solve the discretised transport equations.

in Section 4.3.1. The computational grid and the two different meshing strategies considered are presented in Section 4.3.2. Finally, the numerical algorithms, discretisation schemes and solution strategy are reported in Section 4.3.3.

4.3.1 Computational Domain and Boundary Conditions

4.3.1.1 Gaseous-fueled case

The computational investigation concerning gaseous fuel injections has been carried out based on the experimental gaseous configuration of the CORIA burner [43–45], whose 3D model is depicted in Figure 4.8. This burner configuration contains four major components: a plenum to tranquilize the flow before entering the swirler, a radial-swirl injection system, a square cross-section combustion chamber ($100 \times 100 \times 260$ mm) and, finally, a convergent exhaust to prevent air recirculation. It is of primary interest to consider the flow across the plenum and swirler blades in order to eliminate any ambiguity in the inflow conditions as the flow dynamics and coherent structures within the combustion chamber are fundamentally characterized by the flow conditions at the exit of the swirler.

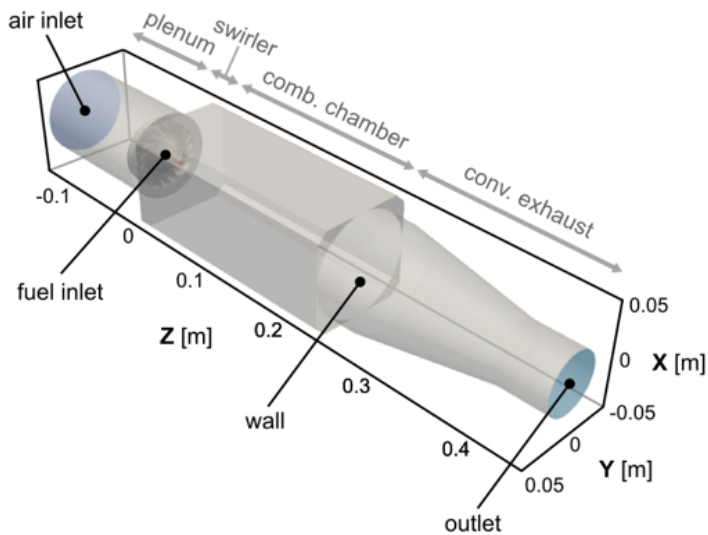


Figure 4.8: Overview of the CORIA single burner computational domain.

The combustor employs a radial swirler composed of 18 channels inclined at 45° with an external diameter of $D = 20$ mm. The swirler creates a swirling air flow in the combustion chamber, in which gaseous methane is injected through a tube ($d = 4$ mm) acting as a fuel injector located at the center of the swirler. The injector may be operated with premixed or non-premixed methane (CH_4) and air inflows. In the premixed mode (see the left side of Figure 4.9), both plenum and fuel injector are fed with a full mixture of methane and air. On the other hand, in the non-premixed mode (see right side of Figure 4.9), pure methane is injected through the nozzle while the air enters the combustion chamber across the plenum. The axial direction is referred to as the z -axis, corresponding to the main flow direction, while the x -axis and y -axis denote the transverse directions.

The operating and boundary conditions corresponding the experimental gaseous premixed [44] and non-premixed [46, 47] injection strategies are collected in Table 4.1. The results of the non-premixed study are not shown in this dissertation for the sake of brevity but can be found in the work by Payri et al. [48].

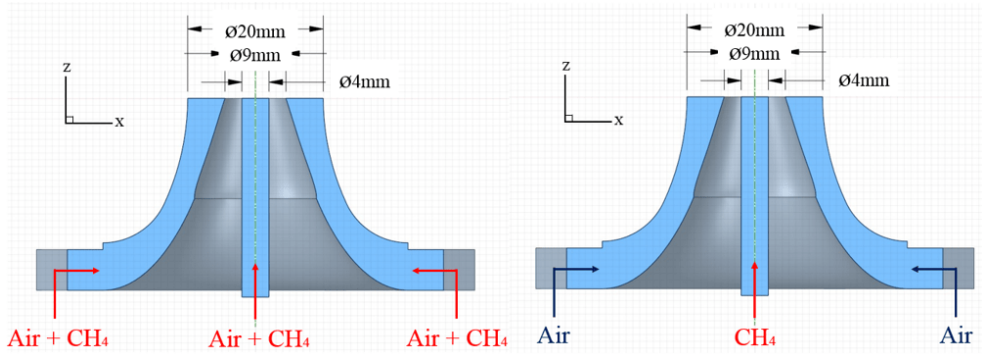


Figure 4.9: Sketch of the swirl-injection system showing both gaseous premixed (left) and non-premixed (right) injection strategies.

	Premixed Case [44]	Non-premixed Case [46]
T	298 K	298 K
p	1 atm	1 atm
Plenum injection	$\dot{m}_{air+CH_4} = 5.612$ g/s	$\dot{m}_{air} = 5.43$ g/s
Central injection	$\dot{m}_{air+CH_4} = 0.236$ g/s	$\dot{m}_{CH_4} = 0.234$ g/s
Equivalence Ratio	0.75	
U_{bulk}	37 m/s	27 m/s
\bar{Re}	35 000	33 000

Table 4.1: Operating and boundary conditions of the gaseous-fueled cases for both premixed and non-premixed injection strategies.

4.3.1.2 Liquid-fueled case

On the other hand, a liquid spray injection strategy has been simulated at atmospheric pressure for which experimental data are available [49, 50]. In this case, liquid n-heptane is injected through a simplex pressure-swirl atomizer (Danfoss, 1.46 kg/h, 80° hollow cone) located at the centre of the swirler. The operating condition corresponds to ultra-lean conditions and relevant parameters are gathered in Table 4.2. Meanwhile, the O'Rourke and Amsden heat transfer model [51] is employed to estimate the fluid-wall heat transfer.

As introduced in Section 4.2.3, a Lagrangian formulation is used to model the liquid fuel since the discrete-particle scales are much smaller than the smallest turbulent scales solved. The fuel spray is described by the injection of a series of discrete liquid parcels containing a certain number of drops. Parcels

Liquid-fueled Case [49, 50]	
p	1 atm
Plenum injection	$\dot{m}_{air} = 8.2 \text{ g/s}$
Central injection	$\dot{m}_{C_7H_{16}} = 0.33 \text{ g/s}$
Equivalence Ratio	0.61
T_{air}	416 K
$T_{C_7H_{16}}$	350 K
T_{wall}	387 K
U_{bulk}	70 m/s
\bar{Re}	50 000

Table 4.2: Operating and boundary conditions of the liquid-fueled case.

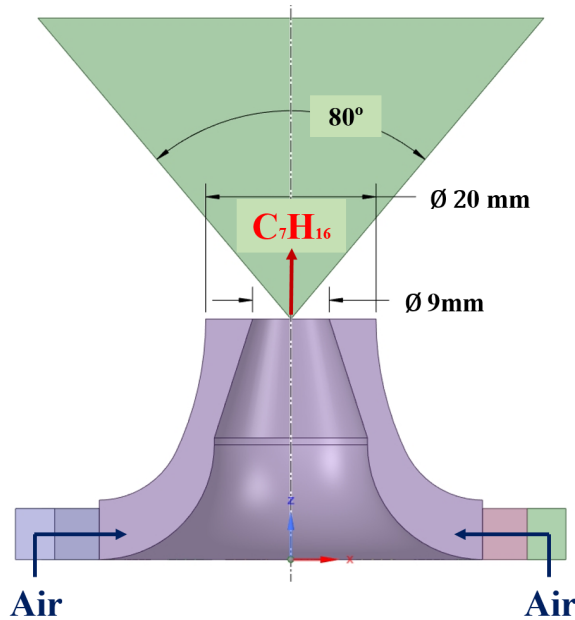


Figure 4.10: Sketch of the swirl-injection system showing the liquid spray injection strategy.

represent a group of drops (particles) of similar size, location and properties (e.g., velocity, temperature) into a single parcel before solving Lagrangian equations for averaged properties of the parcel.

Fuel is injected from the tip of the atomizer (see Figure 4.10) with the liquid mass flow rate and temperature imposed according to the experimental

operating conditions mentioned above. Moreover, experimental velocity and drop size results from PDA measurements [49] have been used to set the spray conditions in the model. From here, two different liquid injection modelling strategies are tested:

- **LISA case.** The liquid injection and primary atomisation is modelled using the LISA injection-atomisation model [18, 19] described in Section 4.2.3, whereas the TAB breakup model [20] is considered for secondary atomization. In this way, the hollow cone overall angle is set as 76° with a thickness of 8° (i.e., outer angle 80° and inner angle 72°), whereas the velocity on injected sheet parcels is initialised from the experimental injection pressure $p_{inj} = 11$ bar.
- **TAB case.** Fuel parcels are directly injected with a Rosin-Rammler distribution characterised by a Sauter Mean Diameter $D_{32} = 31$ μm and a width parameter $q = 2.3$ [49]. In this case, the hollow cone overall angle is also set in 76° with a thickness of 8° , but the velocity on injected sheet parcels is defined through the nozzle diameter in order to match experimental results in the near-injection region.

The number of total injected parcels has been set according to sensitivity analysis in the literature [52] in order to secure that all the possible droplet sizes are represented by at least one parcel. This can be done by dividing the total mass flow rate (0.33 g/s) by the mass of the biggest droplet reported experimentally (75 μm), leading to a number of 3 million parcels/s. Meanwhile, the O'Rourke Numerical Scheme [33] is employed to model coalescence and collision phenomena, whereas the Frossling correlation [53] is applied to model evaporation.

4.3.2 Computational Grid

The problem is addressed through two different CFD codes (OpenFOAM[®] and CONVERGE[™]) involving two different meshing strategies: an automatic mesh generation and adaptive refinement algorithms through CONVERGE[™] and a more traditional meshing technique in OpenFOAM[®].

4.3.2.1 CONVERGE[™] Mesh

CONVERGE[™] code uses an innovative modified cut-cell Cartesian method that eliminates the need for the computational grid to be morphed with the geometry of interest, while still precisely representing the exact boundary

shape [54]. This approach allows using simple orthogonal grids and automates the mesh generation process.

Therefore, an automatic domain decomposition technique is employed, allowing for efficient load balancing throughout the calculation. CONVERGE™ includes several tools illustrated in Figure 4.11 to control the grid size before and during a simulation:

- **Base Size** Side length of the hexahedral cells, from which the other grid control tools are defined.
- **Fixed Embedding (FE)** Refines the grid at user-specified locations (areas) and times where a finer resolution is critical to the accuracy of the solution (i.e., the flow behaviour within the small passages of the swirler), while allowing the rest of the grid to remain coarse to minimize simulation time. An embedding scale (a positive integer) must be specified for each fixed embedding area defined, including the refinement of the cells adjacent to walls.
- **Adaptive Mesh Refinement (AMR)** Automatically changes the grid based on fluctuating and moving conditions. Specifically, the AMR method adds embedding where the flow field is more under-resolved or where the sub-grid field is the largest without unnecessarily slowing the simulation with a globally refined grid. To do so, the AMR algorithm estimates the magnitude of the sub-grid field (ϕ'), computed as the difference between the actual field (ϕ) and the resolved field ($\bar{\phi}$), to determine where to add embedding. The scale of the sub-grid can be approximated by Eq. (4.72):

$$\phi' = -\frac{dx_k^2}{24} \frac{\partial^2 \bar{\phi}}{\partial x_k \partial x_k} \quad (4.72)$$

Then, a cell is embedded if the absolute value of the sub-grid given by Eq. (4.72) is above a user-specified value (called threshold value for the remainder of this dissertation). Conversely, a cell is released (i.e., the embedding is removed) if the absolute value of the sub-grid is below 1/5 of the user-specified value [14].

All these grid control techniques refine (or coarsen) the base mesh by cutting the cell dimensions in half (or doubling them) for each level of refinement (i.e., a 2 mm of base mesh size with three levels of fixed embedding would be

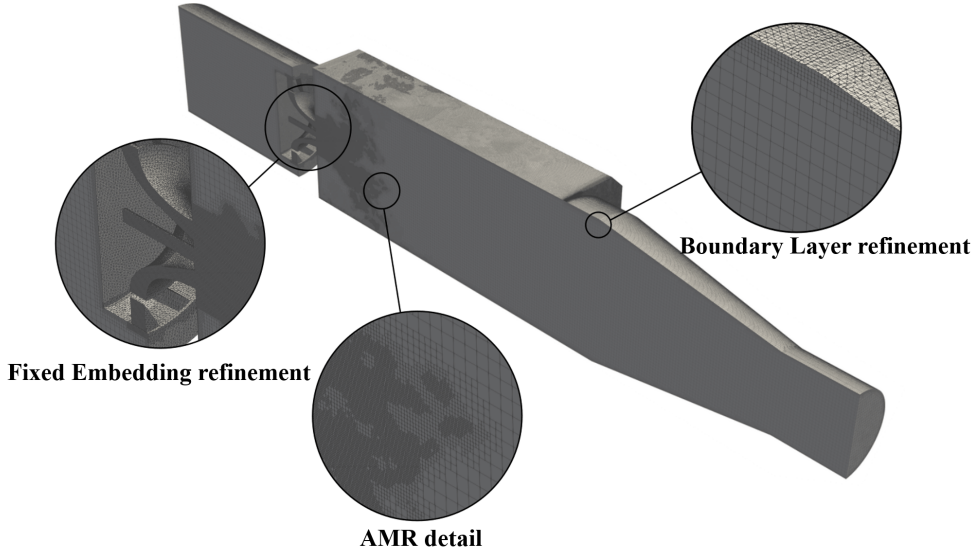


Figure 4.11: Computational mesh illustrating the strategy considered in CONVERGE™ consisting in 3 levels of fixed embedding, 3 levels of AMR, and 2 layers with 2 levels of wall refinement.

converted into 512 cells of 0.25 mm). In this way, the cell size is reduced by applying a grid-scale factor (r), according to:

$$L_{scaled} = \frac{L_{base}}{2^r} \quad (4.73)$$

For illustrating purposes, Figure 4.11 shows an example of a given mesh refinement through the selected grid-tools described previously. The influence of the grid control tools has been evaluated through a mesh sensitivity study for gaseous-fueled cases presented in Section 5.2.1.2.

Finally, the meshing strategy employed for the liquid-fueled case is selected from this well-defined methodology as a compromise between spatial resolution and computational cost in order to work out this multi-scale problem.

4.3.2.2 OpenFOAM© Mesh

The computational domain in OpenFOAM© simulations is spatially discretised by a traditional and static unstructured mesh composed of tetrahedral cells (see Fig. 4.12) generated with the ICEM CFD software [55]. A structured mesh would allow using higher-order discretisation schemes without leading to

numerical divergences, thus resulting in less numerical diffusion and commensurately higher accuracy. However, it would lead to some cells in regions of high geometric complexity having unavoidably large aspect ratios or substantial skewness, resulting in unacceptable discretisation errors. Please note that CONVERGE™, even using structure grids, does not present these problems thanks to the aforementioned automatic mesh cut-cell Cartesian method [54].

The meshing strategy consists of conical fixed embedding area regions placed near the injection system. In this way, different cell sizes are used in the concerned zones of interest: (1) the swirler and mixing region, (2) further downstream of the injection plane, (3) and the rest of the combustor far away of the critical flow.

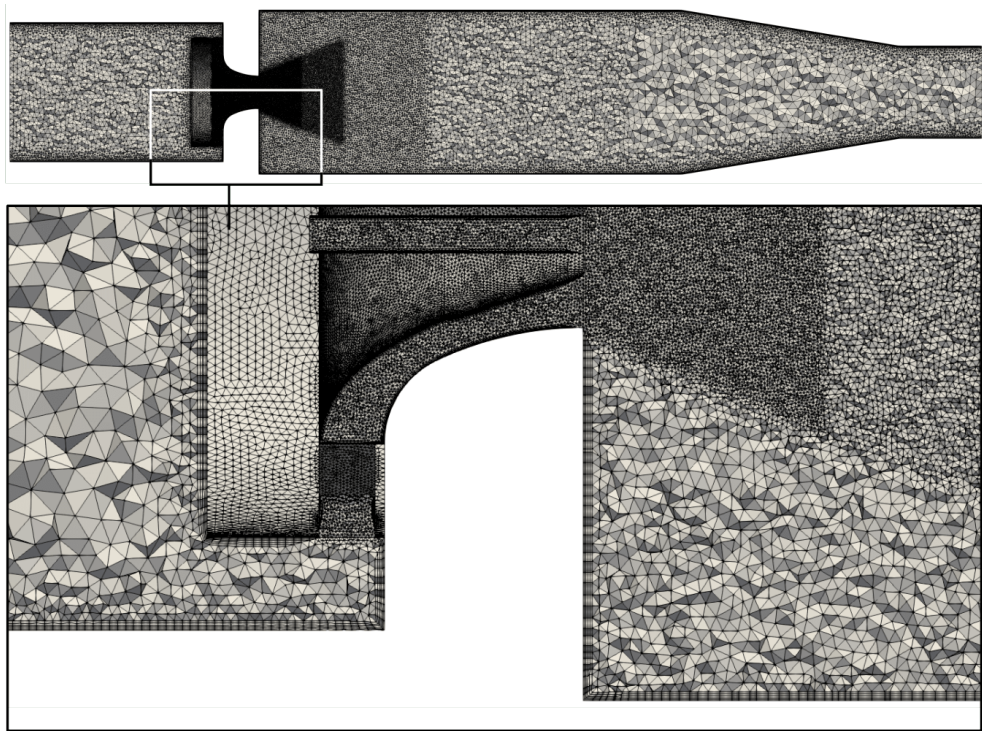


Figure 4.12: Computational mesh illustrating the strategy considered in OpenFOAM©.

Moreover, mesh refinement in near-wall regions ensures $30 < y^+ < 100$ at the swirler, convergent inlet walls and combustion chamber walls in order to allow wall models to work properly. Furthermore, additional mesh quality controls overruled mesh coarsening in regions having small curvature radii or

sharp corners. The impact of the meshing strategy and the turbulence modelling on the flow field is discussed in Section 5.2.1.1 where a mesh sensitivity study is performed for the premixed gaseous-fueled OpenFOAM© simulations.

4.3.3 Numerical Algorithms and Discretisation Schemes

This section presents a brief overview of the numerical algorithms, discretisation schemes and turbulence models considered both in the premixed gaseous-fueled and liquid-fueled simulations. The reader is referred to Table 4.3, where the relevant numerical parameters are compiled.

4.3.3.1 Numerical Setup in CONVERGE™

In the CONVERGE™ solver, all computed values are collocated at the center of the computational cell, where the conservation equations are solved using the finite volume method. A second-order-accurate spatial discretisation scheme is used for the governing conservation equations, while a second-order implicit formulation is set for time discretisation. The Rhie-Chow algorithm [56] is employed to prevent spurious oscillations (e.g., checker-boarding). Meanwhile, the transport equations are solved using the PISO algorithm described in Section 4.2.4. A variable time-stepping algorithm is used in the current investigation, where the time-step is automatically calculated each computational cycle, ensuring that the maximum CFL-number does not exceed 0.8 anywhere in the computational domain at any instant.

U-RANS (i.e., the Standard, Realizable and RNG $k-\epsilon$, and the LRR Reynolds Stress Model) and LES (i.e., the Smagorinsky, Dynamic Smagorinsky, and Dynamic Structure) modelling options for the treatment of turbulence (see Section 4.2.2) have been applied separately to characterize the unsteady non-reacting flow field in the gaseous-fueled cases presented in Section 5.2.1.2. However, in liquid-fueled simulations only the Dynamic Smagorinsky LES turbulence treatment has been considered. Additionally, a standard law-of-the-wall profile is used to determine the tangential components of the stress tensor at the wall in U-RANS simulations, whereas the Werner and Wengle wall model [57] is considered in LES. Even though the Werner and Wengle wall model is suitable for dealing with cells located at both the viscous ($y^+ \leq 5$) and buffer ($5 < y^+ < 30$) sub-layers, placing any cells at the buffer sub-layer region has been avoided through the AMR since the approximation of wall models at that region can result in errors around 10 – 20% that might compromise the accuracy of the overall results. The use of wall models in this kind of device dominated by the large-scale motions can be justified through

	CONVERGE	OpenFOAM
Discretisation Schemes	2^{nd} order (time and space)	
Time step control	Variable (1 – 4 μ s)	Fixed (1 μ s)
Turbulence model	<u>U-RANS</u> Standard, Realizable and RNG k- ϵ , and LRR-RSM <u>LES</u> Smagorinsky, Dynamic Smagorinsky and Dynamic Structure	<u>RANS</u> Standard k- ϵ <u>U-RANS</u> LRR-RSM <u>LES</u> Smagorinsky and Dy- namic Smagorinsky
Wall treatment	Law-of-the-wall ($y^+ \geq 30$)	
Numerical algorithm	PISO	
Time simulated	200 ms	

Table 4.3: Numerical setup of the simulations performed in CONVERGETM and OpenFOAM[®].

several LES reported in the literature considering the same experimental test rig [58]. In those simulations, a better agreement in terms of both pressure loss and velocity field has been found when considering wall-models instead of resolving the boundary layer.

Meanwhile, the variable time step sizes resulting from the aforementioned CFL restriction range among 2×10^{-6} and 4×10^{-6} s for U-RANS and 1×10^{-6} and 2.5×10^{-6} s for LES, the mean CFL number being around 0.001. For typical simulations, mesh scaling of twice the baseline mesh size was used to stabilize the flow field until 50 ms before automatically scaling down to the base mesh size and starting the fixed embedding and AMR tools. The simulations were run for additional 100 ms to stabilize the overall mass flow rate and velocity fields (i.e., the parameters considered to check the convergence in a statistical steady state) with the final mesh strategy. From here, temporal averages and higher-order moments started to be calculated in the gaseous-fueled simulations. In the liquid-fueled cases, in turn, liquid injection and the fixed embedding in the conical near-nozzle region started at this moment, running for another 50 ms to stabilise the flow and spray field with the final mesh strategy. Finally, statistics were computed during approximately

25 times the rotation flow scale (50 ms). This time scale is associated to some large coherent structures generated within the combustor, as presented in Section 2.2.1.

4.3.3.2 Numerical Setup in OpenFOAM©

The open-source *Foam Extend 3.2 pisoFoam* and *OpenFOAM v6 sprayFoam* solvers are employed in the gaseous and liquid-fueled simulations, respectively. These OpenFOAM© fork solvers are dedicated to handling the transient, compressible and turbulent flow, using the Pressure Implicit with Splitting of Operators (PISO) algorithm.

On the one hand, second-order accurate spatial discretisation schemes (i.e., Gauss linear - central differences) are employed to compute gradients and advective terms. Laplacian terms and normal surface gradients have been computed by linear second-order accurate schemes considering non-orthogonal explicit corrections to the cells with a high value of non-orthogonality in order to increase numerical stability. Meanwhile, an implicit second-order accurate backward scheme is employed for time-stepping. The van Driest damping function is considered for near-wall modelling in order to correct the over-dissipation of the model viscosity near walls. A constant time step of $1 \cdot 10^{-6}$ s ensured that the maximum CFL-number does not exceed 0.3 anywhere in the computational domain at any instant.

On the other hand, a coupled Diagonal Incomplete LU (DILU) Preconditioned Bi-Conjugate Gradient (PBiCCCG) solver has been employed to solve the momentum transport equation. For its part, a Geometric-Algebraic Multi-Grid (GAMG) solver with a Gauss-Seidel smoother was used to calculate the pressure field. Finally, the pressure-velocity coupling is imposed by the PISO method operating with 2 correctors (i.e., number of times the algorithm solves the pressure equation and momentum corrector in each step) and 3 non-Orthogonal correctors.

Gaseous-fueled simulations are carried out considering the following turbulence approaches for all considered meshes (see Section 5.2.1.1): the Standard $k-\varepsilon$ model (RANS), the Launder-Reece-Rodi Reynolds Stress model (U-RANS), and the Smagorinsky and Dynamic Smagorinsky models (LES). Meanwhile, in liquid-fueled simulations only Dynamic Smagorinsky LES turbulence treatment has been considered. To conduct the current study, a preliminary run was executed for each mesh using the RANS approach, both to set the fluid dynamics in place and to generate a map file of the variables in steady conditions. The code was then called to map the variables and

initialize the U-RANS and LES studies. The simulation was run during 150 ms until statistically steady flow was reached. From here, temporal averages and higher-order moments started to be calculated in gaseous-fueled cases and liquid injection started in liquid-fueled cases (with the same extra time for the stabilisation of the spray than in CONVERGE™). The statistics were computed during approximately 25 times the rotation flow scale, as stated for CONVERGE™ cases.

4.4 Post-processing

A considerable amount of development work has taken place in the post-processing field. On the one hand, the systematic algorithms developed to automatically post-process the raw data extracted from gaseous fuel and spray simulations are shown in Section 4.4.1. These computational routines allow a rapid comparison and validation against experimental data and an efficient assessment of the influence of both the mesh, the turbulence and the spray models on the flow solution. In this way, a rigorous procedure needs to be developed to quantify the CFD performance considering discrepancies between predicted and experimentally measured values, thus making it possible to assign an overall score for a quantitative comparison between simulations. To this end, a specific quality parameter has been adopted to quantify the accuracy of turbulent numerical statistics regarding the agreement with the experimental database available in the literature. On the other hand, Section 4.4.2 introduces the theoretical background of the modal decomposition techniques (i.e., Proper Orthogonal Decomposition and Dynamic Mode Decomposition) and the procedure implemented as a post-processing tool to extract the relevant coherent structures and the underlying dynamics of the combustor system.

4.4.1 Algorithms for Gaseous and Liquid Phase Characterisation

4.4.1.1 Definition of a Quality Parameter

A quality parameter needs to be defined to quantify the accuracy of turbulent numerical statistics regarding the agreement on key features with the experimental database available in the literature. The turbulent field of a given gaseous variable (e.g., pressure, velocity) obtained from U-RANS and LES simulations during runtime can be decomposed into the mean (time-

averaged), and root mean square (fluctuation) values, evaluated respectively by Eqs. (4.74) and (4.75):

$$\langle \psi(\mathbf{x}) \rangle = \frac{1}{T_m} \sum_{n=1}^{N_T} \psi(\mathbf{x}, t^n) \Delta t_m \quad (4.74)$$

$$\psi(\mathbf{x})_{RMS} = \sqrt{\langle \psi(\mathbf{x})^2 \rangle - \langle \psi(\mathbf{x}) \rangle^2} \quad (4.75)$$

where T_m is the recording duration (50 ms in most of the simulations, as stated in Section 4.3.3), N_T is the number of time steps, and Δt_m is the value of the time step. It is important to remark that the RMS value calculated by Eq. (4.75) does not account for the sub-grid scale contribution, which is expected to slightly modify the real value but with no substantial influence on the results presented in Section 5.2.

The accuracy of a given simulation is measured through the evaluation of the Normalised Mean Square Error (hereinafter referred to as *NMSE*), defined by Eq. (4.76) and widely used in literature [59, 60] to quantify CFD performance considering discrepancies between predicted and measured values:

$$NMSE = \frac{(\phi_N - \phi_E)^2}{|\phi_N \phi_E|} \quad (4.76)$$

where ϕ_N is the numerical mean (time-averaged) or RMS value of a given gaseous flow variable calculated through CFD in a given spatial location, whereas ϕ_E denotes the same flow variable value obtained experimentally in the same location. A perfect model would have $NMSE = 0$. Even though the quality acceptance criteria for this metric strongly depends on what the underlying data represent, reference studies [61] state $NMSE < 4$ as an acceptable quality criterion for a predictive model. However, these are not definite guidelines and it is essential to consider every performance indication when accepting the predictive capabilities of a model. In this study, the computed *NMSE* value has proven its suitability to compare the performance between different simulations.

The numerical mean (time-averaged) and RMS gaseous velocity components (i.e., axial, radial and tangential) have been computed at locations where experimental data are available [43–45], i.e., in the centerline and at several radial stations located at a given axial distance from the entrance of the combustion chamber, as shown in Figure 4.13.

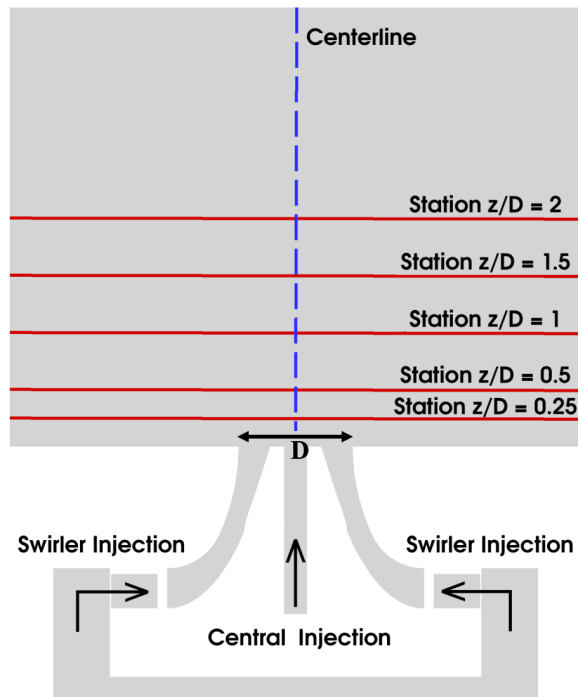


Figure 4.13: Overview of the measurement transverse cross-section where experimental data concerning the premixed gaseous case are available for comparison with CFD simulations: the centerline, and the radial stations located at five different axial positions. The location of the radial stations is normalised with the external diameter of the swirler exit.

The strategy followed to evaluate the prediction quality of a given CFD simulation is to obtain three differentiated *NMSE* values: one for the time-averaged axial velocity along the centerline (i.e., *NMSE-Centerline*), another one for the mean of the time-averaged components velocity in all the stations (i.e., *NMSE-Mean-Stations*) and a last one for the same variable but considering the RMS values (i.e., *NMSE-RMS-Stations*). To do so:

- **NMSE-Centerline** The time-averaged axial velocity value obtained numerically is compared with the experimental one at all the axial points along the centerline where experimental values are available, thus calculating a *NMSE* value at each location. Then, all the *NMSE* values obtained along the centerline are averaged, thus yielding a global *NMSE* for the time-averaged axial velocity along the centerline (i.e., *NMSE-Centerline*).

- **NMSE-Mean-Stations** The strategy to obtain a global *NMSE* for the time-averaged velocity in the stations is:
 1. For each point of a given station where experimental data for time-averaged velocity components are available, the comparison with CFD results provides a *NMSE* value.
 2. Next, the *NMSE* values of each velocity component at each of the five stations are averaged by stations, obtaining one *NMSE* value per velocity component and station.
 3. Then, the *NMSE* values of each station are averaged for a given velocity component, obtaining one value per velocity component.
 4. Finally, *NMSE* three values are averaged, resulting in a global *NMSE* for the time-averaged velocity in all the axial stations (i.e., *NMSE-Mean-Stations*).

- **NMSE-RMS-Stations** The same procedure is followed to obtain a global *NMSE* value for the root mean square of the velocity components in the stations (i.e., *NMSE-RMS-Stations*).

Please note that U-RANS $k-\varepsilon$ simulations are expected to obtain higher values of *NMSE-RMS-Stations* since the governing equations are ensemble-averaged before being solved and the isotropic turbulence hypothesis is assumed, meaning few fluctuations are expected.

4.4.1.2 Algorithm for liquid-phase post-processing

As stated in Section 4.2.3.1, the gaseous phase (considered as a continuum) is solved through the Navier-Stokes (NS) equations in an Eulerian framework (see Section 2.3.2), whereas the liquid phase (considered as discrete parcels) is computed in a Lagrangian framework (see Section 2.3.3) by tracking the spray parcels throughout the determined flow field. Therefore, a different strategy is required to suitably post-process the lagrangian disperse phase present in the liquid-fueled simulations before comparing the predicted liquid statistics with experimental data at the eulerian fixed locations where PDA measurements are available (see Figure 4.13).

The general procedure developed in Python to post-process the spray parcel's output in CONVERGE™ and OpenFOAM© (see Figure 4.14) imitates the experimental PDA detection strategy. The algorithm can be summarised as follows:

1. Each instantaneous spray parcel datum (e.g., position, velocity, radius, temperature and number of droplets) is saved during 20 ms every 0.025 ms (giving rise to a total of 800 saved time-steps) and converted to VTK format, which allows all the parcel data to be stored in a single file per time step.
2. A coordinate system conversion is made from cartesian to cylindrical coordinates (see Figure 4.15).
3. Spray parcels located within the planes of interest containing the radial stations shown in Figure 4.13 (where experimental data are available) are captured/retained, and their instantaneous values are stored for each time-step. Please note that working with planes at a given axial position (z/D) in cylindrical coordinates (z, r, ϕ) instead of radial stations in cartesian coordinates allows to significantly increase the sensitivity in the number of parcels captured, thus reducing the required time steps to achieve droplet statistical convergence.
4. Spray parcels detected in each plane are assigned to a given radial location (r/D) where experimental data are available. In other words, all parcels belonging to a single radial position are caught, which means that the detection zone is a set of concentric circles.
5. Mass-weighted average and root-mean-square velocity components (u_z, u_r, u_ϕ) are computed for the spray parcels gathered at each radial location in all planes of interest. The number of droplets contained in the parcel is considered for the computation.
6. The Mean and Sauter Mean Diameter (D_{10} and D_{32}) introduced in Section 2.4.2.1 are computed for the spray parcels gathered at each radial location in all planes of interest.
7. The Probability Density Function (PDF) introduced in Section 2.4.2.2 is computed at specific user-defined locations ($z/D, r/D$).
8. The temporal evolution of the liquid penetration length (see Section 2.4.2.3) is computed as the axial distance from the nozzle containing the 95% of the liquid mass.
9. The whole set of computed liquid-phase results are saved in .csv files that will be later load by a MATLAB routine in order to integrate them with the available experimental data and the gas-phase (and *NMSE*) outcomes.

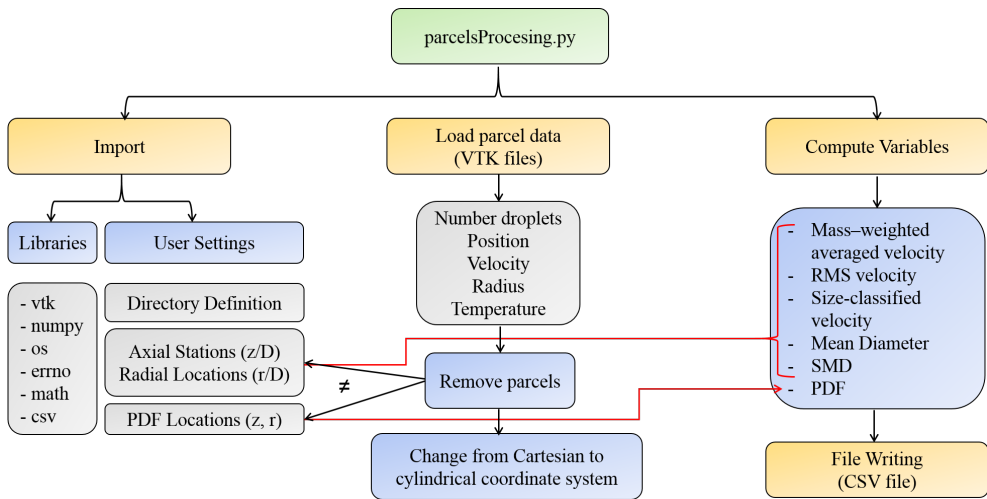


Figure 4.14: Diagram of the algorithm implemented in Python to post-process the liquid-phase statistics.

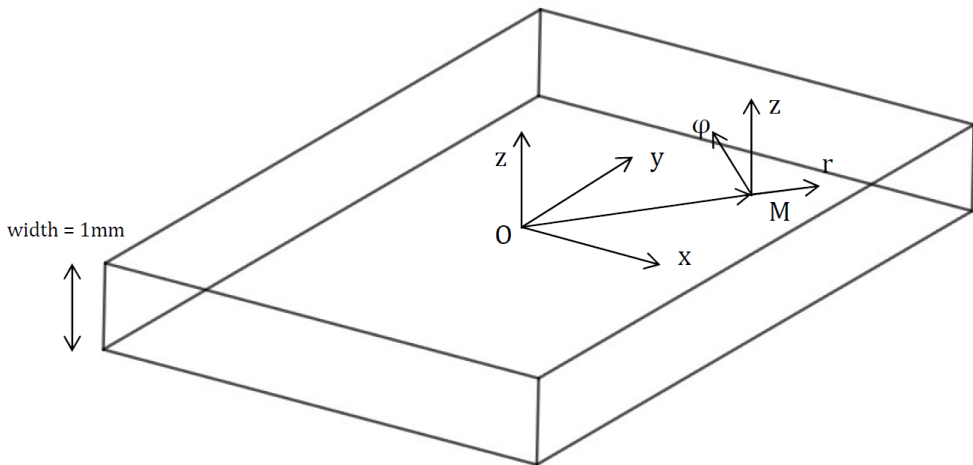


Figure 4.15: Parcel detection plane in cylindrical coordinates.

4.4.2 Modal Decomposition Techniques

Advanced combustion systems such as the swirl-stabilised LDI combustor studied in this thesis are designed to operate under lean conditions and thus have the potential to satisfy the regulatory requirements by keeping the pollutant emissions below stringent restrictions, as stated in Section 1.1. However,

local extinction may easily occur as the flame is operated closer to blow-off conditions. For this reason, it is necessary to demonstrate the ability to re-ignite the system from non-reactive conditions, which cannot be taken for granted at high altitude conditions. In addition, these systems are more susceptible to self-excited combustion and hydrodynamic instabilities, which in turn can negatively impact the engine performance and durability. Such phenomena are strongly unsteady and three-dimensional, giving rise to the formation of low-order coherent structures, which are complex to study experimentally and even numerically since they requires capturing a multi-scale phenomenon.

Traditional and basic data processing techniques utilised in instability spectral analysis are based in bandpass filtering of the signals around a frequency of interest at a given spatial location. In this way, Fast Fourier Transform (FFT) and Sound Pressure Level (SPL) analysis of the signal have been usually applied to determine the frequencies (or frequency ranges) of interest in a simple, straightforward manner [62, 63]. However, the filtered outcomes obtained in this way are too sensitive to factors such as the filter type, bandwidth, sample quality and spatial position. Furthermore, the need to manually select the frequencies of interest implies the risk of missing relevant frequencies (which are not known beforehand) and represents an increase of the workload of the design engineers. Finally, even though SPL does allow for detailed analysis of the frequency content of a given flow variable (in the form of time series), it is unable to provide an adequate description of the spatio-temporal nature of the underlying dynamics of the system (i.e., the time evolution of these spatial features is lost).

In this context, advanced statistical data processing techniques based on linear-algebra tools such as the Proper Orthogonal Decomposition (POD) [64, 65] and the Dynamic Mode Decomposition (DMD) [66, 67] have emerged in the recent past with the aim of shedding some light on the flow diagnostics to characterise their structure and extract complementary information detecting coherent spatial patterns. These two powerful tools complement each other and have been applied to extract the low-order coherent structures acting as precursors of the global self-sustained oscillations. Both POD and DMD techniques are equally applicable to experimental and numerical flow field data and are capable of working with the entire data set with minimal information loss. Furthermore, they do not require prior knowledge or pre-analysis of the data in order to obtain the dominant frequencies. The main advantages and disadvantages of POD and DMD techniques are collected in Table 4.4.

On the one hand, the POD technique (see Section 4.4.2.1) serves to identify the modes that represent the majority of the energy content through

	Strengths	Weaknesses
POD	<ol style="list-style-type: none"> 1. Provides an orthogonal set of basis vectors with the minimal dimension (useful to build a reduced-order model of the flow-field). 2. POD modes are simple to compute using either the (classical) spatial or snapshot methods. 3. Incoherent noise from the dataset can be suppressed by simply removing high-order modes from the expansion. 4. POD analysis can be used in a wide spectrum of studies. 	<ol style="list-style-type: none"> 1. Higher-order correlations are ignored. POD is based on second-order correlations. 2. The temporal coefficients of spatial POD modes generally contain a mix of frequencies. 3. POD modes are ranked considering the energy content instead of the dynamical importance. 4. Absence of absolute truncation criteria for keeping POD modes.
DMD	<ol style="list-style-type: none"> 1. Non a-priori assumptions or knowledge of the underlying dynamics are required (entirely data-driven analysis). Also in POD. 2. DMD can be applied to many types of data or even sequences of different data sources. Also in POD. 3. Gives a finite-dimensional approximation to the Koopman operator (an infinite-dimensional linear operator to describe non-linear dynamics). 4. DMD modes can isolate specific dynamic structures (associated to a particular frequency). 5. DMD has proven to be entirely customizable. 	<ol style="list-style-type: none"> 1. Typically requires regularly spatial and time resolved data. Also in POD. 2. There is no single correct way to rank eigenvalue importance (i.e., which modes are the most physically relevant). 3. If DMD is used for system identification, the resulting model will be linear. 4. DMD can be unreliable for non-linear systems (need to carefully choose a sufficiently rich set of measurements). 5. DMD outputs can be sensitive to noisy data.

Table 4.4: Strengths and weaknesses of POD and DMD techniques.

spatial correlations of a given flow field variable by diagonalizing the spatial correlation matrix computed from the snapshots [68]. However, even though the statistical analysis of flow fields using POD has been established as a valuable tool for the characterisation of coherent vortex structures, it is not well-considered for reacting flows since its decomposition technique does not account for density variations [69]. Furthermore, two significant shortcomings are associated with POD: (i) the flow energy may not be suitable to rank the coherent structures in all circumstances, and (ii) due to the selection of second-order statistics as a basis for the decomposition, relevant phase data is lost (see Table 4.4).

On the other hand, the DMD technique (see Section 4.4.2.2) has proved to overcome these POD drawbacks, allowing to detect in a more precise (less biased) way both the frequencies and the stability eigenmodes of the flow field through the extraction of spatial modal (low-dimensional coherent) structures and their corresponding growth/decay rates [70]. In many ways, DMD may be seen as a merging of the desirable features of both the POD and the discrete Fourier transform [71, 72], resulting in spatio-temporal coherent structures identified primarily from data.

4.4.2.1 Proper Orthogonal Decomposition (POD)

In the Proper Orthogonal Decomposition (POD) technique, a set of distributions or functions (ensemble) is decomposed into an optimal orthogonal set of eigenfunctions that represent the distributions of the ensemble (i.e., the flow field is decomposed into coupled spatial and temporal orthogonal modes). This decomposition technique, also called Principal Component Analysis (PCA), can be used to generate reduced-order models (ROMs) to study coherent large-scale structures of a flow field in general and a combustor in particular.

In this way, the set of distributions is represented as a weighted expansion of the eigenfunctions, which are considered optimal since they contain most of the information, thus allowing to capture the dominant features of a system while minimizing the basis functions. In fact, the spatial structures comprising most of the flow field energy are identified through the ordering of the contribution of each mode and the full flow field can be reconstructed through the superposition of all modes. Therefore, the examination of a few POD eigenfunctions permits to quickly recognize the most energetic structures thus determining where more detailed research is required.

The evolution of the flow field in CFD simulations is usually presented in

a sequence of N temporal snapshots (\mathbf{v}_i), gathered in a matrix \mathbf{V} :

$$\mathbf{V}_1^N = \{\mathbf{v}_1, \mathbf{v}_2, \dots, \mathbf{v}_N\} \quad (4.77)$$

These snapshots should be separated by a constant time step (Δt_{POD}) and usually contain a quantity M of scalar flow magnitudes such as velocity and vorticity components, density, pressure, or species, with each column containing the temporal data and each row comprising the spatial data.

In this way, POD can then be performed by solving the associated eigensystem of the diagonalised time-averaged correlation matrix $\mathbf{V}^T \mathbf{V}$. Nevertheless, since $\mathbf{V}^T \mathbf{V}$ resolution can be computationally expensive ($N \times N$ matrix) an alternative approach based on the Singular Value Decomposition (SVD) of \mathbf{V} [73] is generally preferred:

$$\mathbf{V} = \mathbf{U} \mathbf{\Sigma} \mathbf{W}^T \quad (4.78)$$

Here, the columns of \mathbf{U} ($M \times N$ matrix) represent the left-singular vectors known as POD spatial modes Ψ_i , which form an orthonormal basis of \mathbf{V} . The validity of this alternate approach is proved since the spatial modes are also the eigenvectors of $\mathbf{V}^T \mathbf{V}$. Next, $\mathbf{\Sigma}$ is a diagonal matrix of dimensions $M \times N$ whose non-zero elements correspond to the squared eigenvalues (σ_i) of $\mathbf{V}^T \mathbf{V}$ and thus represent the contribution of each spatial mode Ψ_i to the total energy of matrix \mathbf{V} (i.e., the relevance of each orthonormal mode in the total flow field [74]). Finally, \mathbf{W} corresponds to the right-singular vectors of \mathbf{V} , the temporal evolution $a_i(t)$ of each spatial mode Ψ_i being described by the rows of $\mathbf{\Sigma} \mathbf{W}^T$. It is important to note that the 1st POD mode represents the mean-field while the subsequent modes describe the flow dynamics (i.e., the fluctuations).

Therefore, the overall flow field can be understood as a linear superposition of spatial and temporal data, as shown in Eq. (4.79).

$$\mathbf{V}(\mathbf{x}, t) = \sum_{i=1}^N \Psi_i(\mathbf{x}) a_i(t) \quad (4.79)$$

The main interest of the POD technique is the possibility of dimensionality reduction, crucial in CFD simulations where output data are arranged in big matrices. In this way, the total flow field can be reconstructed by applying Eq. (4.79) taking into account a reduced number of modes L (being $L < N$) and ensuring that the reconstructed flow field $\tilde{\mathbf{V}}$ is the closest to the original by the minimisation of the Frobenius norm.

4.4.2.2 Dynamic Mode Decomposition (DMD)

The Dynamic Mode Decomposition (DMD) technique aims at grouping coherent spatial features into modes (eigenvectors) of a single temporal frequency, allowing the identification of coherent but weakly-energetic modes in highly transient regimes.

Recalling the matrix \mathbf{V}_1^N introduced in Section 4.4.2.1, containing N snapshots of the flow field, and assuming these to be linearly correlated through an unknown matrix \mathbf{A}_{DMD} :

$$\mathbf{v}_{i+1} = \mathbf{A}_{DMD}\mathbf{v}_i \quad (4.80)$$

Then, the evolution and dynamic characteristics of the flow field can be characterised by the eigenvalues (i.e., DMD eigenvalues) and eigenvectors (i.e., DMD modes) of this matrix. It should be clear that even if the flow field is non-linear, the matrix \mathbf{A}_{DMD} provides a linear approximation of the flow evolution. Eq. (4.77) and Eq. (4.80) can be combined in matrix form:

$$\mathbf{V}_2^N = \mathbf{A}_{DMD}\mathbf{V}_1^{N-1} \quad (4.81)$$

The eigendecomposition of \mathbf{A}_{DMD} is usually too computationally expensive to be performed directly. Thus, Singular Value Decomposition (SVD) can be used again as in Section 4.4.2.1 in order to obtain $\mathbf{V}_1^{N-1} = \mathbf{U}\mathbf{\Sigma}\mathbf{W}^T$, then reformulating Eq. (4.81) as:

$$\mathbf{V}_2^N = \mathbf{A}_{DMD}\mathbf{U}\mathbf{\Sigma}\mathbf{W}^T \quad (4.82)$$

Now, a new matrix $\tilde{\mathbf{S}}$ can be built through the manipulation of terms that are already known. The matrix $\tilde{\mathbf{S}}$ is constructed ensuring *matrix similarity* with \mathbf{A}_{DMD} , as:

$$\tilde{\mathbf{S}} \triangleq \mathbf{U}^T \mathbf{V}_2^N \mathbf{W} \mathbf{\Sigma}^{-1} = \mathbf{U}^T \mathbf{A}_{DMD} \mathbf{U} \quad (4.83)$$

Because of this similarity, the eigenvalues λ_i of $\tilde{\mathbf{S}}$ match those of \mathbf{A}_{DMD} , with the advantage that $\tilde{\mathbf{S}}$ is of reduced size and easier to solve. Then, the DMD modes (Φ_i) can be computed by mapping the eigenvectors y_i (eigenvector matrix \mathbf{Y}) of $\tilde{\mathbf{S}}$ into the non-reduced space through \mathbf{U} (note that \mathbf{U} is the POD basis of \mathbf{V}_1^{N-1}):

$$\Phi = \mathbf{U}\mathbf{Y} \quad (4.84)$$

Since the numerical routine implemented in the present thesis normalises the calculated eigenvectors, it is necessary to recover the modal amplitudes α_i . This can be easily done by solving the reconstructed flow field multiplied by the unknown amplitudes against any snapshot of the flow [75]:

$$\mathbf{V}_1 = \Phi \boldsymbol{\alpha} \Rightarrow \boldsymbol{\alpha} = \Phi^{-1} \mathbf{V}_1 = \mathbf{Y}^{-1} \mathbf{U}^* \mathbf{V}_1 \quad (4.85)$$

Please note that \mathbf{U} is unitary and thus its conjugate transpose \mathbf{U}^* is also its inverse. Now the system can be solved inverting \mathbf{Y} rather than the higher-order Φ . In this way, the full dynamics of the unsteady flow field, represented by the snapshot matrix at discrete time steps t_k , can be reconstructed by the linear superposition of the DMD modes:

$$\mathbf{V}(\mathbf{x}, t_k) = \Re \left\{ \sum_{i=1}^{N-1} \Phi_i(\mathbf{x}) \alpha_i \lambda_i^{k-1} \right\} = \Re \{ \Phi \mathbf{D}_{iag}(\boldsymbol{\alpha}) \mathbf{V}_{and}(\boldsymbol{\lambda}) \} \quad (4.86)$$

Where $\mathbf{D}_{iag}(\boldsymbol{\alpha})$ is the diagonal matrix of modal amplitudes, and $\mathbf{V}_{and}(\boldsymbol{\lambda})$ is the Vandermonde matrix of the eigenvalues. The real part of the complex eigenvalue denotes the growth/decay factor for the DMD mode, while the imaginary part of the complex eigenvalue provides its oscillation frequency. Furthermore, the single frequency (f_i) associated to each DMD mode can be recovered considering the time step (Δt_{DMD}) between snapshots:

$$f_i = \frac{\omega_i}{2\pi} = \frac{\Im \{ \ln(\lambda_i) \}}{2\pi \Delta t_{DMD}} \quad (4.87)$$

Finally, the calculated DMD modes need to be ranked in relevance. It can be difficult (or at least subjective) to determine which modes are the most physically relevant since (unlike in POD) there is no single correct way to rank eigenvalue importance. In this way, Kou and Zhang [76] have recently proposed a simple criterion that considers the evolution of each dynamic mode within the whole sampling space, and ranks them according to their contribution to all samples:

$$E_i = \sum_{j=1}^N \left| \alpha_i \lambda_i^{j-1} \right| \|\Phi_i\|_F^2 \Delta t_{DMD} \quad (4.88)$$

Since in this thesis the focus is put into an statistically steady-state of the combustor, short-lived evanescent modes are not expected nor of interest for

the objective of isolating the most energetic and relevant modes. Thus, the Kou and Zhang criterion will be used to rank the DMD modes.

4.4.2.3 Spectral Analysis Procedure

In order to apply the modal decomposition procedures, the instantaneous pressure field is exported to text files containing the cell centroid coordinates $[\mathbf{x} \ \mathbf{y} \ \mathbf{z}]$ and their corresponding static pressures \mathbf{p} . For this analysis, a total of 200 snapshots are gathered during a simulated physical time of 20 ms, which implies a spectral resolution of 50 Hz. Data are then exported every 0.1 ms, thus obtaining a sampling frequency of 5 kHz, which is enough to apply the Nyquist criterion [77] in order to isolate the relevant information. This allows optimizing both the processing computational cost and storage space.

However, since the adaptive mesh refinement algorithm is continuously modifying the number of cells, the spatial coordinates of each exported snapshot do not remain constant. Therefore, the raw data require some preliminary treatment as the decomposition techniques require constant spatial coordinates. In this previous step, a subset of 1 million random cells is selected from the first snapshot and taken as spatial reference, providing an adequate compromise between computational cost and spatial resolution.

The procedure to relate the coordinates of the cell centroids of subsequent snapshots (which will have changed due to the AMR, as stated) is to identify the nearest neighbour of each of the reference coordinates. To do so, a k - d tree data structure [78] is generated in order to organize the raw coordinates from each new snapshot. Then, a searcher algorithm [79] computes both the indices of the new snapshot cells that best match the reference coordinates and the Euclidean distance d_i between them. A validation is performed to discard cells whose computed distance d_i to their corresponding reference is greater than 1 mm, thus ensuring spatial consistency. Hence, only the pressure and velocity values of the suitable cells of a given snapshot are stored in the corresponding vector \mathbf{v}_i defined in Sections 4.4.2.1 and 4.4.2.2. Finally, once the snapshot matrix \mathbf{V} is assembled, rows with “NaN” values (from cells that failed the validation) are discarded, thus obtaining a suitable matrix of consistent and continuous pressure and velocity values at nearly constant spatial locations.

References

- [1] Versteeg, H. and Malalasekera, W. *Introduction to Computational Fluid Dynamics: The finite volume method*. 2nd Edition. Pearson Education Limited, 2007. DOI: 10.2514/1.22547.

- [2] Menon, S. and Patel, N. “Subgrid Modeling for Simulation of Spray Combustion in Large-Scale Combustors”. In: *AIAA Journal* 44.4 (2006), pp. 709–723. DOI: 10.2514/1.14875.
- [3] Patel, N. and Menon, S. “Simulation of spray-turbulence-flame interactions in a lean direct injection combustor”. In: *Combustion and Flame* 153 (2008), pp. 228–257. DOI: 10.1016/j.combustflame.2007.09.011.
- [4] Sirignano, W. *Fluid Dynamics and Transport of Droplets and Sprays*. 2nd Edition. New York, USA: Cambridge University Press, 2010.
- [5] Pope, S. *Turbulent Flows*. Cambridge University Press, 2000. DOI: 10.1017/CB09780511840531.
- [6] Gibson, M. and Launder, B. “Ground effects on pressure fluctuations in the atmospheric boundary layer”. In: *Journal of Fluid Mechanics* 86.3 (1978), pp. 491–511. DOI: 10.1017/S0022112078001251.
- [7] Sagaut, P. *Large eddy simulation for incompressible flows: an introduction*. Springer Science and Business Media, 2006.
- [8] Smagorinsky, J. “General Circulation Experiments with the primitive equations: I. The basic experiment”. In: *Monthly Weather Review* 91.3 (1963), pp. 99–164. DOI: 10.1175/1520-0493(1963)091<0099:GCEWTP>2.3.CO;2.
- [9] Germano, M., Piomelli, U., Moin, P., and Cabot, W. “A dynamic subgrid-scale eddy viscosity model”. In: *Physics of Fluids A: Fluid Dynamics* 3.7 (1991), pp. 1760–1765. DOI: 10.1063/1.857955.
- [10] Lilly, D. “A proposed modification of the Germano subgrid-scale closure method”. In: *Physics of Fluids A: Fluid Dynamics* 4.3 (1992), pp. 633–635. DOI: 10.1063/1.858280.
- [11] Pomraning, E. and Rutland, C. “Dynamic One-Equation Nonviscosity Large-Eddy Simulation Model”. In: *AIAA Journal* 40.4 (2002), pp. 689–701. DOI: 10.2514/2.1701.
- [12] Ashgriz, N. “Handbook of atomization and sprays: theory and applications”. In: Springer Science and Business Media, 2011. Chap. 9 - Atomization Models.
- [13] Faeth, G. “Mixing, transport and combustion in sprays”. In: *Progress in Energy and Combustion Science* 13.4 (1987), pp. 293–345. DOI: 10.1016/0360-1285(87)90002-5.

- [14] *CONVERGE 2.4 Manual*. Tech. rep. Convergent Science, Inc., Middleton, 2017.
- [15] *OpenFOAM 6.0 User Guide*. 2018. URL: <https://cfd.direct/openfoam/user-guide-v6/> (visited on 04/21/2020).
- [16] Ashgriz, N. “Handbook of atomization and sprays: theory and applications”. In: Springer Science and Business Media, 2011. Chap. 4 - Dynamics of Liquid Droplets.
- [17] Huh, K., Lee, E., and Koo, J. “Diesel spray atomization model considering nozzle exit turbulence conditions”. In: *Atomization and Sprays* 8 (1998), pp. 453–469. DOI: 10.1615/AtomizSpr.v8.i4.60.
- [18] Schmidt, D. et al. “Pressure-swirl atomization in the near field”. In: *SAE Technical Papers* 724 (1999). DOI: 10.4271/1999-01-0496.
- [19] Senecal, P. et al. “Modeling high-speed viscous liquid sheet atomization”. In: *International Journal of Multiphase Flow* 25 (1999), pp. 1073–1097. DOI: 10.1016/S0301-9322(99)00057-9.
- [20] O’Rourke, P. and Amsden, A. “The tab method for numerical calculation of spray droplet breakup”. In: *SAE Technical Papers* (1987). DOI: 10.4271/872089.
- [21] Reitz, R. and Bracco, F. “Mechanisms of Breakup of Round Liquid Jets”. In: *The Encyclopedia of Fluid Mechanics* 3 (1986), pp. 223–249.
- [22] Reitz, R. “Modeling atomization processes in high-pressure vaporizing sprays”. In: *Atomisation Spray Technology* 3 (1987), pp. 309–337.
- [23] Patterson, M. and Reitz, R. “Modeling the Effects of Fuel Spray Characteristics on Diesel Engine Combustion and Emission”. In: *International Congress and Exposition*. SAE International, 1998. DOI: <https://doi.org/10.4271/980131>.
- [24] Taylor, G. *The shape and acceleration of a drop in a high speed air stream*. Tech. rep. Cambridge University Press, 1963, pp. 457–464.
- [25] Han, Z., Parrish, S., Farrell, P., and Reitz, R. “Modeling atomization processes of pressure-swirl hollow-cone fuel sprays.” In: *Atomization and Sprays* 7.6 (1997), pp. 663–684.
- [26] Lefebvre, A. *Atomization and Sprays*. Hemisphere Publishing Corporation, 1989.
- [27] Lefebvre, A. and Ballal, D. *Gas turbine combustion: alternative fuels and emissions*. 3rd edition. Taylor and Francis, 2010.

- [28] Dombrowski, N. and Johns, W. “The aerodynamic instability and disintegration of viscous liquid sheets”. In: *Journal of Chemical Engineering Science* 18 (1963), pp. 203–214.
- [29] Dombrowski, N. and Hooper, P. “The effect of ambient density on drop formation in sprays”. In: *Chemical Engineering Science* 17.4 (1962), pp. 291–305. DOI: [https://doi.org/10.1016/0009-2509\(62\)85008-8](https://doi.org/10.1016/0009-2509(62)85008-8).
- [30] Lamb, H. *Hydrodynamics*. 6th edition. Dover Publications, 1945.
- [31] Amsden, A., O’Rourke, P., and Butler, T. “KIVA-II: A computer program for chemically reactive flows with sprays”. In: *Technical Report LA-11560-MS* (1989).
- [32] Crowe, C., Chung, J., and Troutt, T. “Particle mixing in free shear flows”. In: *Progress in Energy and Combustion Science* 14.3 (1988), pp. 171–194. DOI: [https://doi.org/10.1016/0360-1285\(88\)90008-1](https://doi.org/10.1016/0360-1285(88)90008-1).
- [33] O’Rourke, P. “Collective Drop Effects on Vaporizing Liquid Sprays”. PhD thesis. Princeton University, 1981.
- [34] Ayoub, N. and Reitz, R. “Multidimensional Computation of Multi-component Spray Vaporization and Combustion”. In: *International Congress Exposition*. SAE International, 1995. DOI: 10.4271/950285.
- [35] Law, C. “Recent advances in droplet vaporization and combustion”. In: *Progress in Energy and Combustion Science* 8.3 (1982), pp. 171–201. DOI: 10.1016/0360-1285(82)90011-9.
- [36] Ranz, W. and Marshall, W. “Evaporation from drops”. In: *Chemical Engineering Progress* 48 (1952), pp. 141–146.
- [37] Frolov, S., Posvianskii, V., and Basevich, V. “Evaporation and combustion of hydrocarbon fuel. Part I: Nonempirical model of single-component drop evaporation”. In: *Advanced Chemical Physics* 21 (2002), pp. 58–67.
- [38] Van Leer, B. “Towards the ultimate conservative difference scheme III. Upstream-centered finite-difference schemes for ideal compressible flow”. In: *Journal of Computational Physics* 23.3 (1977), pp. 263–275. DOI: [https://doi.org/10.1016/0021-9991\(77\)90094-8](https://doi.org/10.1016/0021-9991(77)90094-8).
- [39] Zhou, G. “Numerical Simulations of Physical Discontinuities in Single and Multi-Fluid Flows for Arbitrary Mach Numbers”. PhD thesis. Chalmers University of Technology, 1995.

- [40] Waterson, N. and Deconinck, H. “A unified approach to the design and application of bounded higher-order convection schemes”. In: *Numerical methods in laminar and turbulent flow* 9 (1995), pp. 203–214.
- [41] Roe, P. “Characteristic-Based Schemes for the Euler Equations”. In: *Annual Review of Fluid Mechanics* 18.1 (1986), pp. 337–365. DOI: 10.1146/annurev.fl.18.010186.002005.
- [42] Issa, R.I. “Solution of the implicitly discretised fluid flow equations by operator-splitting”. In: *Journal of Computational Physics* 62.1 (1986), pp. 40–65. DOI: [https://doi.org/10.1016/0021-9991\(86\)90099-9](https://doi.org/10.1016/0021-9991(86)90099-9).
- [43] Cordier, M. “Allumage et propagation de flamme dans les écoulements fortement swirlés : études expérimentales et numériques”. PhD thesis. Institut National des sciences appliquees (INSA), 2013.
- [44] Cordier, M., Vandael, A., Cabot, G., Renou, B., and Boukhalfa, A. “Laser-Induced Spark Ignition of Premixed Confined Swirled Flames”. In: *Combustion Science and Technology* 185.3 (2013), pp. 379–407. DOI: 10.1080/00102202.2012.725791.
- [45] Barré, D. “Simulation Numerique De L’Allumage Dans Les Chambres De Combustion Aeronautiques”. PhD thesis. Institut National Polytechnique de Toulouse (INP Toulouse), 2014.
- [46] Esclapez, L. “Numerical study of ignition and inter-sector flame propagation in gas turbine”. PhD thesis. Institut National Polytechnique de Toulouse (INP Toulouse), 2015. DOI: 10.1017/CB09781107415324.004.
- [47] Esclapez, L., Riber, E., and Cuenot, B. “Ignition probability of a partially premixed burner using les”. In: *Proceedings of the Combustion Institute* 35.3 (2015), pp. 3133–3141. DOI: 10.1016/j.proci.2014.07.040.
- [48] Payri, R., Novella, R., Carreres, M., and Belmar-Gil, M. “Study about the influence of an automatic meshing algorithm on numerical simulations of a Gaseous-Fueled Lean Direct Injection (LDI) Gas Turbine Combustor in Non-Reactive conditions”. In: *ILASS - Europe 2019, 29th Conference on Liquid Atomization and Spray Systems*. Paris, France, 2019.
- [49] Marrero-Santiago, J. “Experimental study of lean aeronautical ignition. Impact of critical parameters on the mechanisms acting along the different ignition phases.” PhD thesis. INSA de Rouen - Normandie, 2018.

- [50] Marrero-Santiago, J. et al. “Experimental study of airflow velocity, fuel droplet size-velocity and flame structure in a confined swirled jet-spray flame”. In: *ILASS - Europe 2016, 27th Conference on Liquid Atomization and Spray Systems*. September. Brighton, United Kingdom, 2016.
- [51] Amsden, A. “KIVA-3V: A block-structured KIVA program for engines with vertical or canted valves”. In: *Los Alamos National Laboratory Technical Report LA-13313-MS* (1997).
- [52] Alessandro, D., Stankovic, I., and Merci, B. “LES Study of a Turbulent Spray Jet: Mesh Sensitivity, Mesh-Parcels Interaction and Injection Methodology”. In: *Flow, Turbulence and Combustion* 103.2 (2019), pp. 537–564. DOI: 10.1007/s10494-019-00039-7.
- [53] Frossling, N. “The evaporation of falling drops (in German)”. In: *Gerlands Beitrage zur Geophysik* 52 (1938), pp. 170–216.
- [54] Senecal, P. et al. “A New Parallel Cut-Cell Cartesian CFD Code for Rapid Grid Generation Applied to In-Cylinder Diesel Engine Simulations”. In: 724 (2007), pp. 776–790. DOI: 10.4271/2007-01-0159.
- [55] *CFD ICEM Help Manual*. Tech. rep. ANSYS, Inc., 2018.
- [56] Rhie, C. and Chow, W. “Numerical study of the turbulent flow past an airfoil with trailing edge separation”. In: *AIAA Journal* 21.11 (1983), pp. 1525–1532. DOI: 10.2514/3.8284.
- [57] Wengle, H. and Werner, H. “Large-eddy Simulation of Turbulent Flow Over Sharp-edged Obstacles in a Plate Channel”. In: *Proceedings of the Eighth Symposium on Turbulent Shear Flows* 2 (1991). DOI: 10.1007/978-3-663-13986-7_26.
- [58] Barré, D., Kraushaar, M., Staffelbach, G., Moureau, V., and Gicquel, L. “Compressible and low Mach number LES of a swirl experimental burner”. In: *3rd INCA Colloquim* 341.1-2 (2013), pp. 277–287. DOI: 10.1016/j.crme.2012.11.010.
- [59] Hanna, S., Tehranian, S., Carissimo, B., Macdonald, R., and Lohner, R. “Comparisons of model simulations with observations of mean flow and turbulence within simple obstacle arrays”. In: *Atmospheric Environment* 36 (2002), pp. 5067–5079. DOI: 10.1016/S1352-2310(02)00566-6.
- [60] Gousseau, P., Blocken, B., and Heijst, G. van. “Quality assessment of Large-Eddy Simulation of wind flow around a high-rise building: Validation and solution verification”. In: *Computers and Fluids* 79 (2013), pp. 120–133. DOI: 10.1016/J.COMPFLUID.2013.03.006.

- [61] Hanna, S., Hansen, O., and Dharmavaram, S. “FLACS CFD air quality model performance evaluation with Kit Fox, MUST, Prairie Grass, and EMU observations”. In: *Atmospheric Environment* 38.28 (2004), pp. 4675–4687. DOI: 10.1016/j.atmosenv.2004.05.041.
- [62] Huang, C., Gejji, R., and Anderson, W. “Combustion Dynamics Behavior in a Single-Element Lean Direct Injection (LDI) Gas Turbine Combustor”. In: *50th AIAA/ASME/SAE/ASEE Joint Propulsion Conference*. Vol. 31. 0704. Cleveland, 2014.
- [63] Sharma, S., García-Tíscar, J., Allport, J., Jupp, M., and Nickson, A. “Impact of impeller casing treatment on the acoustics of a small high speed centrifugal compressor”. In: *Proceedings of the ASME Turbo Expo*. Vol. 2B. 2018, pp. 1–12. DOI: 10.1115/GT2018-76815.
- [64] Lumley, J. “The structure of inhomogeneous turbulent flows”. In: *Atmospheric Turbulence and Radio Wave Propagation (Eds. A.M. Yaglom and V.I. Tatarsky)* (1967), p. 166.
- [65] Lumley, J. *Stochastic Tools in Turbulence*. Academic Press, 1970.
- [66] Schmid, P. “Dynamic mode decomposition of numerical and experimental data”. In: *Journal of Fluid Mechanics* 656 (2010), pp. 5–28. DOI: 10.1017/S0022112010001217.
- [67] Schmid, P. “Applications of the dynamic mode decomposition”. In: *Journal of Fluid Mechanics* 25.1 (2010), pp. 249–259.
- [68] Berkooz, G., Holmes, P., and Lumley, J. “The Proper Orthogonal Decomposition in the Analysis of Turbulent Flows”. In: *Annual Review of Fluid Mechanics* 25.1 (1993), pp. 539–575.
- [69] Smith, T., Moehlis, J., and Holmes, P. “Low-Dimensional Modelling of Turbulence Using the Proper Orthogonal Decomposition: A Tutorial”. In: *Nonlinear Dynamics* 41 (2005), pp. 275–307. DOI: 10.1007/s11071-005-2823.
- [70] Taira, K. et al. “Modal Analysis of Fluid Flows: An Overview”. In: *AIAA Journal* 55.12 (2018). DOI: 10.2514/1.j056060.
- [71] Rowley, C., Mezi, I., Bagheri, S., Schlatter, P., and Henningson, D. “Spectral analysis of nonlinear flows”. In: *Journal of Fluid Mechanics* 641 (2009), pp. 115–127. DOI: 10.1017/S0022112009992059.
- [72] Chen, K., Tu, J., and Rowley, C. “Variants of dynamic mode decomposition: Boundary condition, Koopman, and fourier analyses”. In: *Journal of Nonlinear Science* 22.6 (2012), pp. 887–915. DOI: 10.1007/s00332-012-9130-9.

- [73] Abdi, H. and Williams, L. “Principal Component Analysis”. In: *Wiley Interdisciplinary Reviews: Computational Statistics* 2.4 (2010), pp. 433–459.
- [74] Nikiforov, V. “The energy of graphs and matrices”. In: *Journal of Mathematical Analysis and Applications* 326.2 (2007), pp. 1472–1475. DOI: 10.1016/j.jmaa.2006.03.072.
- [75] Futrzynski, R. and Efraimsson, G. *Dymode: A parallel dynamic mode decomposition software*. Tech. rep. KTH Royal Institute of Technology, 2015. DOI: 10.13140/RG.2.1.4087.9126.
- [76] Kou, J. and Zhang, W. “An improved criterion to select dominant modes from dynamic mode decomposition”. In: *European Journal of Mechanics, B/Fluids* 62 (2017), pp. 109–129. DOI: 10.1016/j.euromechflu.2016.11.015.
- [77] Nyquist, H. “Regeneration Theory”. In: *Bell System Technical Journal* 11.1 (1932), pp. 126–147. DOI: 10.1002/j.1538-7305.1932.tb02344.x.
- [78] Bentley, J. “Multidimensional Binary Search Trees Used for Associative Searching”. In: *Commun. ACM* 18.9 (1975), pp. 509–517. DOI: 10.1145/361002.361007.
- [79] Friedman, J., Bentley, J., and Finkel, R. “An Algorithm for Finding Best Matches in Logarithmic Expected Time”. In: *ACM Trans. Math. Softw.* 3.3 (1977), pp. 209–226. DOI: 10.1145/355744.355745.

Chapter 5

Computational Model Validation

“There exist families of logically consistent interpretations and theories that can match a given series of facts. Such insight should warn us that mere absence of nonsense may not be sufficient to make something true.”

—W. V. Quine

5.1 Introduction

The validation process consists of defining the scope to which a computational model is an accurate description of the real world from the standpoint of the expected utilisation of the model. The fundamental strategy of validation considered in this investigation involves the quantification of the deviation between the results predicted by the computational model and the available experimental data through the quality parameter introduced in Section 4.4.1.

On the one hand, this parameter of quality is considered in Section 5.2 to define a methodology to establish an optimal meshing strategy by solving the reference gaseous fuel case (which presents a reduced complexity when compared to the spray fuel case) while validating the gaseous-phase resolution through both CFD codes (OpenFOAM[©] and CONVERGE[™]) by assessing the influence of the mesh and turbulence model. The numerical results and the flow visualisation of the best gaseous-fueled case setup are also discussed in this section. On the other hand, the defined methodology is applied to

solve and validate the reference liquid-fueled case both in OpenFOAM© and CONVERGE™. In this way, the performance of the atomisation and breakup models, together with the turbulent spray dispersion is assessed and discussed in Section 5.3.

5.2 Gaseous-Fueled Reference Case

The results presented in this section contain the CONVERGE™ and OpenFOAM© premixed gaseous-fueled cases for all turbulence approaches considered and meshes proposed. The modelling methodology is defined by solving the reference gaseous fuel case through both CFD codes by assessing the influence of the mesh and the turbulence model (see Section 5.2.1) through the quality parameter defined in Section 4.4.1.1. An additional LES quality and reliability assesment based on measures of the turbulent resolution and viscosity is included in Section 5.2.2. Finally, the numerical results and the flow visualisation of the best gaseous-fueled case setup are discussed in Section 5.2.3.

5.2.1 Evaluation of the mesh and turbulence models influence

The impact of the meshing strategy and the turbulence modelling on the flow field and the $NMSE$ values calculated is shown in this section. In this way, the $NMSE$ is taken as an indicator to perform the mesh sensitivity study for the gaseous premixed OpenFOAM© and CONVERGE™ simulations. Please note that the absolute values of $NMSE$ are influenced by the magnitude of the variables involved, so they must be considered only to compare the relative performance among simulations.

5.2.1.1 Mesh sensitivity study for OpenFOAM simulations

Six different meshes have been proposed to evaluate the dependence on the numerical set-up and turbulence models in the gaseous-fueled case. The main characteristics of the meshes are listed in Table 5.1. The computational domain is discretised into fully unstructured meshes (as shown in Figure 4.12) using from 0.5 to 17 million tetrahedral cells, with length scales ranging from 2.0 to 0.4 mm in the swirler and the mixing region, from 3.0 to 1.1 mm in the downstream region of the combustion chamber, and from 6.0 to 1.5 mm in the rest of the combustor. Furthermore, additional mesh quality controls overruled mesh coarsening in regions having small curvature radii or sharp corners.

	0.5 M	0.8 M	1.2 M	3 M	6 M	17 M
Swirler and mixing region ($z = 20$ mm)	2.0 mm	1.5 mm	1.0 mm	0.8 mm	0.6 mm	0.4 mm
Downstream injection cone ($z = 40$ mm)	2.0 mm	1.5 mm	1.0 mm	0.8 mm	0.8 mm	0.6 mm
Near Zone ($z = 80$ mm)	3.0 mm	2.0 mm	1.5 mm	1.2 mm	1.2 mm	0.8 mm
Far zone ($z = 160$ mm)	4.0 mm	3.0 mm	3.0 mm	2.0 mm	2.0 mm	1.5 mm
Rest of burner (base size)	6.5 mm	5.0 mm	5.0 mm	4.0 mm	3.0 mm	2.0 mm

Table 5.1: Characteristics of the six meshes proposed to study the non-reactive premixed gaseous-fueled case in OpenFOAM®.

As introduced in Section 4.3.3, simulations are carried out considering the following turbulence approaches for all considered meshes: the Standard $k-\varepsilon$ model (U-RANS), the Launder-Reece-Rodi Reynolds Stress model (U-RANS), and the Smagorinsky and dynamic Smagorinsky models (LES), leading to a total of 24 simulations.

Figure 5.1 summarises the three $NMSE$ values reported for the full set of premixed gaseous-fueled OpenFOAM® simulations for both U-RANS and LES turbulence models. A significant difference between the U-RANS and LES behaviour when refining the mesh needs to be remarked. On the one hand, a RANS model continues to significantly influence the flow field resulting in no changes in the solution from a given spatial resolution since all the turbulent scales are modelled. This is appreciated in Figure 5.1, where numerical accuracy is notably improved from coarse grids (0.5 M - 1.2 M cells) to finer grids (3 M - 6 M cells), but no improvement is found when increasing to 17 M cells. On the other hand, the influence of a LES model on the flow field is still present even though the ratio between the solved and modelled (by the sub-grid model) energy increases as the mesh is refined. This results in a better agreement with experimental results when the total number of cells is increased.

Let us analyse Figure 5.1 in more detail together with Table 5.1, where mesh details were exposed, to identify the optimal mesh strategy depending on the turbulence model considered:

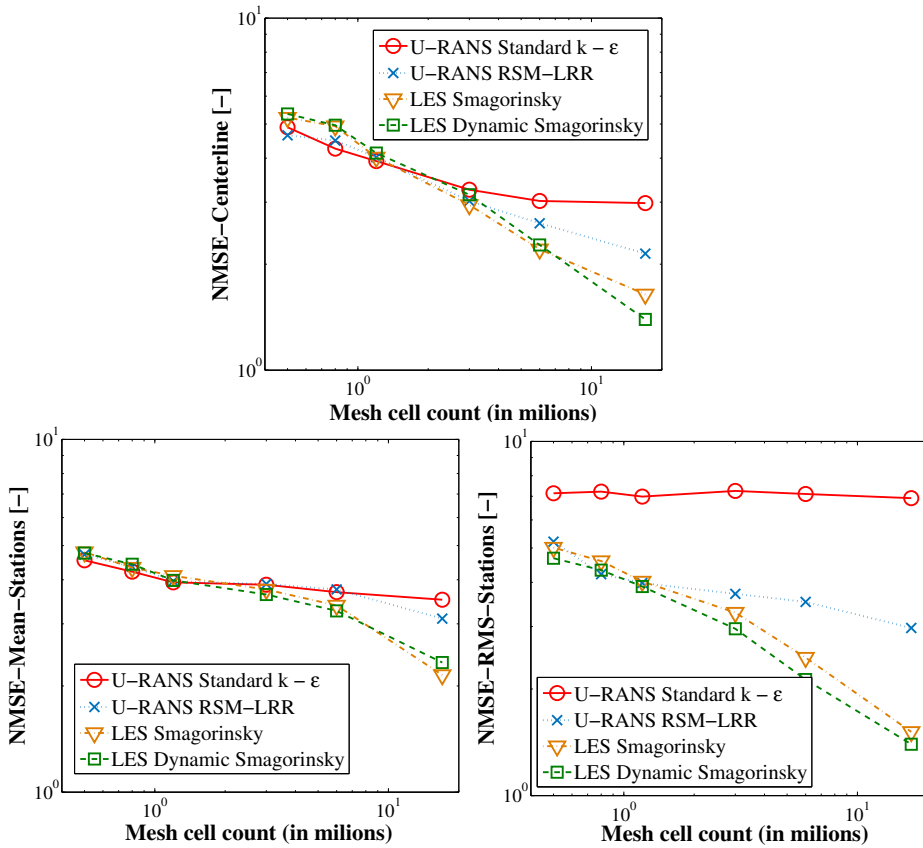


Figure 5.1: Mesh Sensitivity Study for RANS, U-RANS and LES Open-FOAM© simulations through NMSE-Centerline (top), NMSE-Mean-Stations (bottom left), and NMSE-RMS-Stations (bottom right) values reported.

- In the case of Standard $k-\epsilon$ U-RANS simulations, reducing the cell size in swirler and combustion chamber inlet from 2 mm (0.5 M cells) to 0.8 mm (3 M cells) improves the velocity field prediction significantly. Nevertheless, hardly no difference is seen when the cell size is reduced even more, up to 0.4 mm (17 M cells) and base size is reduced from 5 mm (3 M cells) to 3 mm (6 M cells). Note that the $k-\epsilon$ models are not capable, by definition (see Section 4.2.2), to capture the fluctuations and unsteadiness of the flow field (see the bottom right side of Figure 5.1).
- Meanwhile, for LRR Reynolds Stress Model U-RANS simulations, the solution behaviour in terms of NMSE-Centerline value is similar to the

one obtained with Standard $k-\epsilon$ up to 1.2 M cells. From here, a better agreement with experimental results is observed when the grid is refined in the swirler and injection zone from cell sizes of 1.2 mm (1.2 M cells) to 0.8 mm (3 M cells). Nonetheless, no significant accuracy is observed when refining in that region up to 0.4 mm (17 M cells). Therefore, the grid of 6 M cells positioned with the best ratio in terms of accuracy/-computational cost for the Reynolds Stress Model U-RANS simulations.

- Finally, a monotonous growth in accuracy as the number of cells in the mesh increases is noticed in LES cases. As known, mesh independence study is pointless when turbulence is solved through LES, but it is interesting to evaluate the *NMSE* values when the element size is decreased. The smaller the mesh elements size, the more the scales that LES can solve and the better the agreement with the experimental data. Furthermore, the *NMSE-RMS-Stations* value obtained indicates that the transient flow is captured more reliably, as expected. The best results are obtained with the dynamic Smagorinsky sub-grid model, since it can automatically adjust the Smagorinsky constant of the model as a function of the flow regime (see Section 4.2.2).

5.2.1.2 Mesh parametric study for CONVERGE simulations

As already stated, one of the objectives of the thesis is to understand how different mesh layouts and turbulence resolution can impact on the prediction of the flow field within the burner. The accuracy of the results in terms of the *NMSE-Centerline-Value* (the most representative curve in this kind of burners) is reported and discussed for several mesh strategies in CONVERGE™ through the evaluation of the available grid control tools described in Section 4.3.2.1. Given the high number of possible combinations between the potential meshing strategies and turbulence models, the simulations have been selected carefully to explore the tendency when modifying the parameters studied. In this way, two different objectives have been proposed:

1. To assess the influence of the grid control tools for a given turbulence model (U-RANS and LES).
2. To determine the influence of the turbulence model for a given mesh setup. The optimal mesh case setup extracted from the study of the point 1 is employed to explore whether the U-RANS and LES turbulence model influences the performance of the AMR and therefore the number of cells and/or the agreement with experimental results.

Assessment of the grid control tools

The sensitivity of the grid control tool is evaluated considering two different approaches:

- The Standard $k-\varepsilon$ U-RANS turbulence model is considered (due to fewer cell count and faster simulations are expected) to analyse the impact of the base size, fixed embedding and AMR tools on the flow solution (see Table 5.2).
- The dynamic Smagorinsky LES turbulence model is employed to evaluate the influence of the AMR algorithm in a LES framework both in terms of the computational cost (CPU hours for simulating 200 ms) and the agreement with experimental data.

Base Size	2, 3, 4, 5, and 6 mm (from $0.2D$ to $0.3D$)
Fixed Embedding	0 and 3 levels (swirler and combust. chamber inlet)
AMR	0, 3 and 4 levels (velocity gradients, threshold 0.1)

Table 5.2: Parameters considered to assess the influence of the CONVERGETM grid control tools for Standard $k-\varepsilon$ U-RANS simulations.

A set of 11 standard $k-\varepsilon$ U-RANS simulations performed through CONVERGETM to analyse the base size influence together with the fixed embedding and AMR is summarized in Figure 5.2, for which the *NMSE-Centerline* value is represented. The lines join simulations that keep all the parameters constant (i.e., a given zone of influence and levels of fixed embedding, and a given threshold and levels of AMR) except for the base size. It is important to remark that the number of cells reported in CONVERGETM is a result of time-averaging the instantaneous cell count during the same temporal window used to compute the turbulent statistics. As a consequence of the AMR action, the maximum and the minimum number of cells of a given simulation usually oscillates between $\pm 5 - 8\%$ about the mean value reported.

From the examination of the grid tools impact in Figure 5.2, it may be stated that:

- When no fixed embedding or AMR is considered, the tendency to reduce the base size from 4 mm (i.e., 0.07 M cells) to 2 mm (i.e., 0.52 M cells) is towards a better agreement with experimental data, as expected. Nevertheless, the absence of any specific refinement causes a

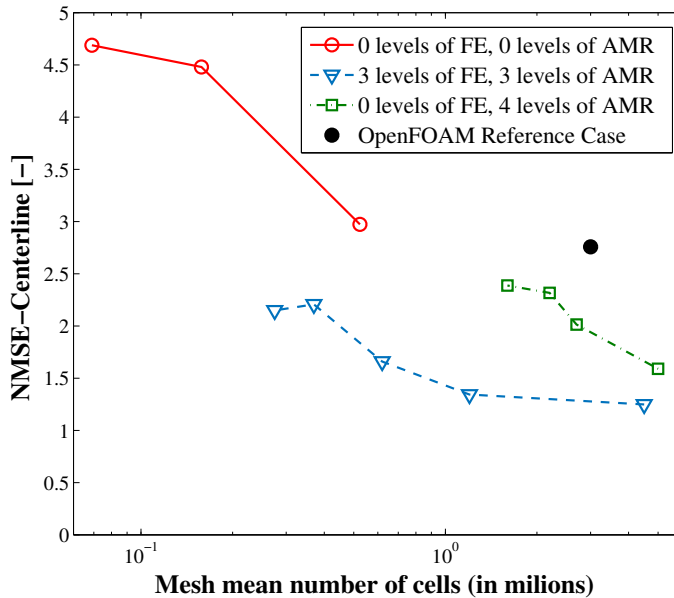


Figure 5.2: Influence of the grid control tools on the *NMSE-Centerline* value (Standard $k-\varepsilon$ U-RANS turbulence model). Each line represents the variation of the base size for a given strategy of AMR and fixed embedding refinement.

low resolution locally in the critical flow sections (i.e., the swirler and combustion chamber inlet), and unacceptable results are obtained with *NMSE-Centerline* values greater than 4.

- Regarding the application of three levels of fixed embedding and AMR, the baseline size was varied from 6 mm (i.e., 0.27 M cells) to 2 mm (i.e., 4.5 M cells). A clear improvement in the *NMSE* value compared with the previous non-locally refined strategy is observed. As expected, the Normalised Mean Square Error at the centerline presents better results as the base size is decreased up to 3 mm (i.e., the smallest cell size of 0.375 mm). Nevertheless, note that no apparent improvement is shown when reducing the base size to 2 mm, then discarding the need to reduce the cell size as much in zones far from the injection region for U-RANS simulations.
- Last, the influence of removing the fixed embedding and letting the AMR algorithm be the sole tool in charge of mesh refinement is evaluated. For this task, the base size has been changed from 6 mm to 3 mm. The

NMSE-Centerline value reported decreases monotonously as the base size is decreased, as expected. However, the improvement obtained is not compensated with the growth in the overall cell count, requiring three times more cells to compute with the same agreement than with the standard mesh setup. This can be attributed to the fact that the use of fixed embedding in regions where the presence of critical flow is expected (i.e., the swirler and the entrance of the combustor) acts as a trigger of the AMR in situations where otherwise it would not be activated due to a low flow resolution. From here, a significant conclusion can be drawn: a base size greater than 3 mm is not fine enough to correctly model the turbulence scales through U-RANS, even if the smallest cells located in the crucial flow regions are finer than those of the corresponding 3 mm case (i.e., 0.375 mm). This fact, together with the one extracted from the discussion above, results in an optimal mesh strategy for U-RANS cases consisting in a base size of 3 mm with 3 levels of both the AMR and the fixed embedding (in the swirler and entrance of the combustor region).

- Therefore, according to the discussion above, the Standard $k-\varepsilon$ U-RANS simulation performed considering this optimal grid strategy is taken as reference for the following discussion about the turbulence model influence.

On the other hand, the *NMSE-Centerline* obtained in the OpenFOAM© Standard $k-\varepsilon$ U-RANS simulation considering the fixed unstructured 1.8-million cell mesh (see Table 5.1) is also reported in Figure 5.2 for comparison purposes. When comparing the results of the CONVERGE™ optimal mesh case defined above with the OpenFOAM© reference case (see Table 5.3), it can be seen that the joint action of AMR and the fixed embedding allowed both an increase in accuracy and a reduction in computational resources.

Thus, the use of an automatic grid refinement tool in the vicinity of the zones with high velocity gradients allows:

- A smaller cell size at the entrance of the combustor (i.e., 0.375 mm for the optimal mesh defined in CONVERGE™, as opposed to the 0.6 mm of OpenFOAM© mesh), leading to a better performance of U-RANS models in modeling the smallest high-turbulent scales and therefore enhancing the agreement with experimental work. Please note that, for a licit comparison in terms of *NMSE*, achieving the same element sizes

CFD Code	Computational cost			Agreement experiments	
	Cells	CPU h	Memory	NMSE-Centerline	NMSE-Mean-Stations
CONVERGE TM (optimal case)	1.2 M	2300	23 GB	1.35	2.32
OpenFOAM [©] (reference case)	1.8 M	3700	12 GB	2.10	2.78

Table 5.3: Accuracy and computational requirements concerning the CONVERGETM optimal mesh case and OpenFOAM[©] reference case simulations (Standard $k-\varepsilon$ U-RANS turbulence model).

in the fixed OpenFOAM[©] mesh than those generated automatically by CONVERGETM would imply more than 10 million cells.

- Keeping the overall cell count relatively low (i.e., a mean of 1.2 M cells, versus the 1.8 M cells in OpenFOAM[©] mesh), which together with the structured cartesian mesh means an optimization of both the solution speed and the storage requirements. Nevertheless, additional computational resources are required for runtime load balancing and re-meshing in CONVERGETM in terms of RAM memory, so the performance of the two solvers (and meshing strategy) needs to be based both on RAM memory requirements and on the overall amount of CPU hours required to simulate the same amount of physical time (i.e., 200 ms, as reported in Section 4.3.3).

Thus, a proper application of the grid control tools available in CONVERGETM together with its automatic mesh generation algorithm has been demonstrated to be an attractive option to face this type of multi-scale problem.

On the other hand, the influence of the AMR algorithm has also been evaluated in a LES framework both in terms of the computational cost (CPU hours for simulating 200 ms) and the agreement with experimental data. In this respect, two different CONVERGETM cases involving dynamic Smagorinsky Large Eddy Simulation (see Table 5.4) have been considered to directly evaluate the implications of considering the use of AMR through the three computed *NMSE* values (i.e., *NMSE-Centerline*, *NMSE-Mean-Stations*, and *NMSE-RMS-Stations*). Both cases present the same base mesh size (i.e. 2 mm) and the same 3 levels of fixed embedding in the swirler region, but:

- Case with AMR: 3 levels of AMR have been used.
- Case without AMR: the lack of AMR is compensated with an additional fixed embedding refinement in the near-injection zone, considering conical zones of influence and the progressive use of 3, 2 and 1 levels of refinement as the flow moves away from the injector.

Please note that, in the case without AMR, both the size of the zone of influence and the levels of refinement of this extra fixed embedding have been carefully selected trying to obtain a similar mesh number of cells than those regarding the LES with AMR.

Case	Computational cost			Agreement experiments		
	Cells	CPU h	Memory	NMSE Center.	NMSE Mean-St.	NMSE RMS-St.
LES without AMR	16.7 M	27.7 k	255 GB	0.85	2.82	0.37
LES with AMR	17.1 M	30.6 k	290 GB	0.41	2.06	0.12

Table 5.4: Accuracy and computational requirements concerning the two dynamic Smagorinsky LES in CONVERGETM to evaluate the influence of the AMR algorithm.

A better agreement with experimental data is obtained in the LES case with AMR both in the mean and fluctuating terms of the three velocity components through the three computed NMSE values. This can be then directly attributed to the 3 automatic refinement levels of AMR in the near injection region (see Figure 4.11) as opposed to the eventual 1 and 2 levels of fixed embedding that are present in some local zones of this same region in the LES without AMR. It must be noted that the cost of this accuracy improvement is a moderate increase on the computational requirements both in CPU hours (10% higher) and in RAM memory (15% higher), as showed in Table 5.4. Therefore, the AMR algorithm has proved to be able to distribute the cells in a proper way for this lean direct injection multi-scale problem in a LES framework.

Turbulence Models Influence

The optimal mesh case setup extracted from the previous study employed to explore whether the U-RANS and LES turbulence model influences the

performance of the AMR and therefore the number of cells and/or the agreement with experimental results. To that end, U-RANS (i.e., Standard, Realizable and RNG $k-\varepsilon$, SST $k-\omega$ and LRR Reynolds Stress Model) and LES (i.e., Smagorinsky, Dynamic Smagorinsky, and Dynamic Structure) modelling options for the treatment of turbulence have been applied. Furthermore, for LES the base mesh size has been also reduced to 2 mm (i.e., smallest cells of 0.25 mm) and the wall refinement has been increased to two layers and levels. Regarding the turbulence approach considered, both U-RANS (for the optimal mesh case setup) and LES turbulence models influence are shown in Figures 5.3 and 5.4, respectively. In this case, the three values of $NMSE$ defined in Section 4.4.1.1 are depicted for a given turbulence model with a given mesh strategy (i.e., a given mean number of cells).

The first aspect worth mentioning is the difference in the mean overall cell count due to the specific behaviour of each model with the same 3 levels of AMR and 0.1 threshold value defined. The higher number of cells in RNG $k-\varepsilon$, $k-\omega$ SST and LRR RSM models was expected since RNG formulation involves a modified form of the ε -equation which attempts to account for the different scales of motion through changes to the production term [1]. In addition, RSM models require higher-level turbulence closures considering the anisotropy of the Reynolds stresses. On the other hand, the specific SST $k-\omega$ formulation in the inner parts of the boundary layer and the extra non-physical turbulence levels provided in regions with large normal strain also result in a moderate higher number of cells. Because of that, these formulations modify the resolved and sub-grid field computed by the AMR algorithm leading to distinct sensitivity responses to a given threshold.

In the case of the U-RANS turbulence models (see Figure 5.3), the Standard, RNG and Realizable $k-\varepsilon$, the SST $k-\omega$ and the Laufer-Reece-Rodi (LRR) Reynolds Stress Model (RSM) are tested. On the one hand, the Realizable and Standard $k-\varepsilon$ models show a similar response in terms of keeping a relatively low number of cells (i.e., 1.2 M cells). The Realizable variant was expected to present better results since it uses an improved formulation for the turbulent viscosity, thereby giving enhanced predictions for the spreading rate of jets, and superior ability to capture the mean flow of complex structures involving recirculation. Nevertheless, the Standard $k-\varepsilon$ offered a better precision in the $NMSE$ -Centerline value. Meanwhile, the application of the advanced SST $k-\omega$ model offered practically the same agreement with experiments that the Standard $k-\varepsilon$ but presenting a 50% higher number of cells. This identical performance reported in the accuracy levels (i.e., $NMSE$ -Centerline and $NMSE$ -Mean-Stations) was expected since phenomena such as

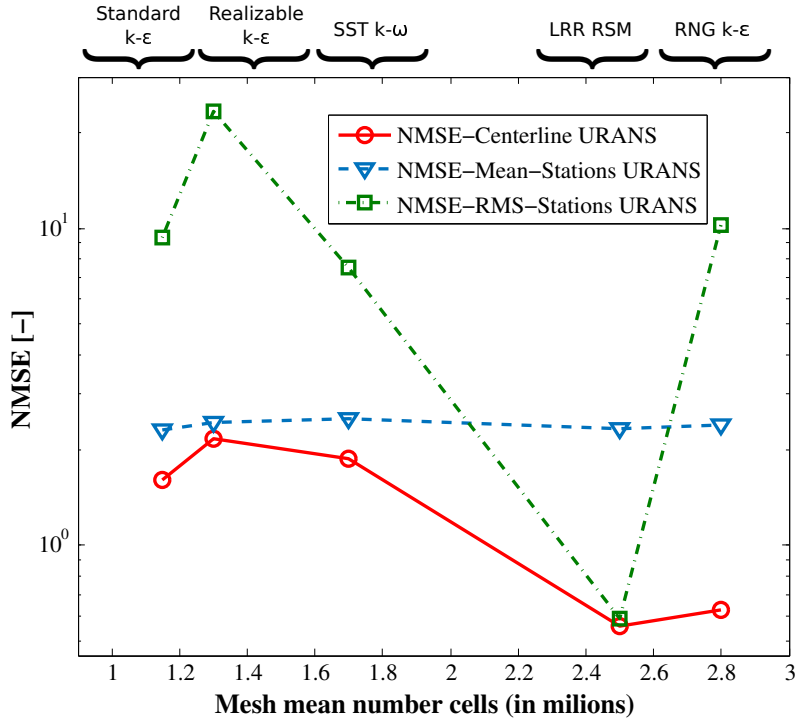


Figure 5.3: Influence of the U-RANS turbulence models on the *NMSE-Centerline*, *NMSE-Mean-Stations* and *NMSE-RMS-Stations* values.

adverse pressure gradients and separating flows (where better behaviour according to the claims in the literature is expected) do not play a crucial role in the problem here studied, thus not taking profit of the improved near-wall performance of the $k-\omega$ model. On the other hand, the RNG $k-\epsilon$ and LRR RSM results are similar concerning both the total number of cells (i.e., 2.8 M and 2.5 M cells, respectively) and the great ability to predict the centerline velocity field. The RNG $k-\epsilon$ and LRR RSM models lead to slightly lower values of *NMSE-Centerline* ($NMSE-Centerline < 1$) than those obtained with Standard $k-\epsilon$, but with more than twice the number of cells. Moreover, the *NMSE-Mean-Stations* reported for these models is slightly higher, so the preference in choosing the Standard $k-\epsilon$ (with acceptable *NMSE-Centerline* values) past the RNG is demonstrated.

Additionally, the *NMSE-RMS-Stations* value (i.e., a parameter defined as a measurement of the ability of a given simulation to predict the velocity fluctuations) reported for the LRR RSM in Figure 5.3 (*NMSE-RMS-Stations*

= 0.60) is much better than the one obtained by $k-\varepsilon$ models ($NMSE-RMS-Station > 10$), as expected. Note that, as previously discussed, the two-equation turbulence models ($k-\varepsilon$ and $k-\omega$) are not capable to capture the fluctuations of the flow field accurately. Therefore, if predicting the fluctuating components (instantaneous field) of a given transient simulation plays a major role in the reliability of the results (e.g., characterization of the turbulent dispersion of liquid spray), the LRR-RSM will be the most appropriate way to approach the turbulence when computational resources are limited and LES treatment is unaffordable.

On the other hand, in LES framework, the turbulence resolution length scale or filter width $\Delta_e(\mathbf{x})$ is specified subjectively in a flow-dependent manner. For that reason, characterizing the dependence of predictions on Δ_e (directly related to the grid resolution dx_k , and hence to the ability of AMR algorithm to refine regions) must be part of the overall LES methodology. The aim of the combination of meshing strategy and turbulence model here is to keep the fraction of the turbulent kinetic energy in the resolved motions below a specified tolerance everywhere in the domain. To do so, the LES sub-grid scale models have been tested through six different simulations (see Figure 5.4 and Table 5.5). In this way, both the performance, the computational requirements and the predictive capability accuracy of Smagorinsky, Dynamic Smagorinsky and Dynamic Structure SGS LES cases have been evaluated considering both the optimal mesh strategy (i.e., base size of 3 mm and smallest cells of 0.375 mm, hereinafter called coarse grid) and a more refined grid where the base mesh size has been reduced to 2 mm (i.e., smallest cells of 0.25 mm) and the wall refinement has been increased to two layers and levels. In general terms, an improvement in the $NMSE-Centerline$ reported by the three refined-grid LES is detected, enhancing the prediction of the velocity field performed by U-RANS models. Furthermore, the $NMSE-RMS-Station$ value obtained indicates that the unsteadiness of the flow is captured more reliably (i.e., $NMSE-RMS-Station < 0.2$).

On the one hand, the reduction in the base size carried out in the refined grid together with the higher sensitivity to a certain AMR threshold (for the same reason explained before) leads to a total cell count around 16 M. It is interesting to note how the ability to capture smaller turbulent structures in LES acts as a trigger of the AMR. Furthermore, a difference in the response regarding the mean number of cells generated is observed: those SGS models that use the turbulent viscosity to model the sub-grid stress tensor (i.e., Smagorinsky and Dynamic Smagorinsky) tend to produce a slightly higher number of cells than those using an additional equation to compute the sub-grid kinetic energy (i.e., Dynamic Structure) for the same mesh strategy.

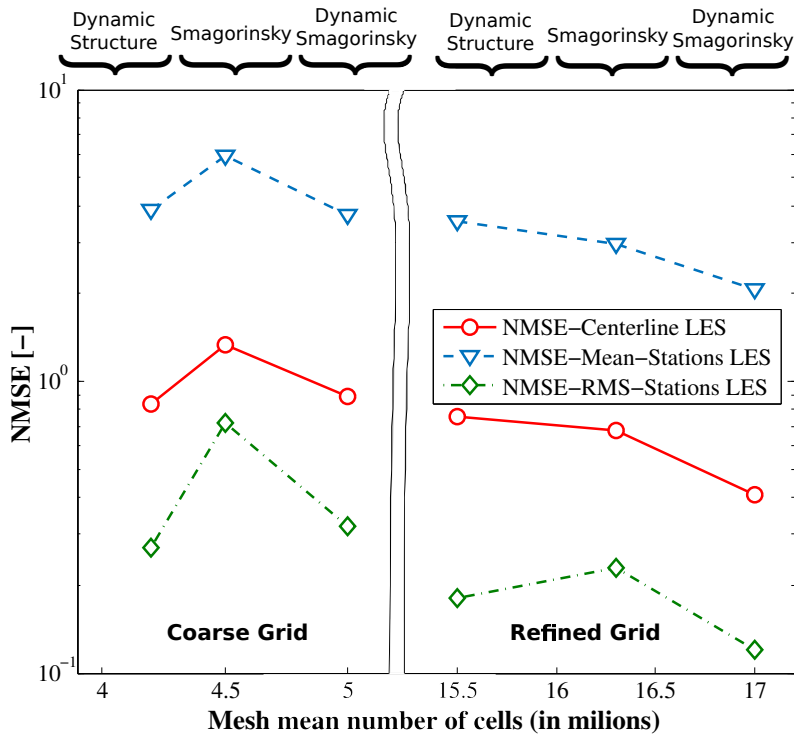


Figure 5.4: Influence of the SGS LES turbulence models on the NMSE-Centerline, NMSE-Mean-Stations and NMSE-RMS-Stations values.

Nevertheless, the evaluation of the convergence velocity shows that the Dynamic Structure one-equation model slightly increases both the CPU cost and memory requirements for the presented simulation, since it provides an independent SGS velocity scale and therefore accounts for non-equilibrium effects (see Table 5.5). It is interesting to note how this last consideration makes the one-equation Dynamic Structure model a more suitable option when dealing with coarser meshes, resulting in better values of $NMSE$ than those obtained with zero-equation models.

On the other hand, in dynamic approaches, the coefficients of the SGS model are determined as part of the computation, based on the energy content of the smallest resolved scales. These dynamic models are usually driven by concepts of scale similarity: if the turbulent motion possesses scale similarity, then a model that considers this similarity should be suitable at different scales (i.e., for different values of filter widths Δ_e). In fact, Jiménez and Moser [2] concluded that the physical basis for the good a posteriori performance of

SGS Model	Coarse Grid (Base Size = 3 mm)			Refined Grid (Base Size = 2 mm)		
	Cells	CPU h	Memory	Cells	CPU h	Memory
Dynamic Structure	4.2 M	23.4 k	200 GB	15.5 M	34.2 k	300 GB
Smagorinsky	4.5 M	18.0 k	160 GB	16.3 M	27.8 k	250 GB
Dynamic Smagorinsky	5.0 M	21.6 k	180 GB	17.1 M	30.6 k	290 GB

Table 5.5: Performance and computational requirements of the SGS LES models for the two meshing strategies considered.

the Dynamic Smagorinsky sub-grid models in LES appears to be only weakly related to their ability to correctly represent the sub-grid physics. The on-the-fly coefficient calculation of the dynamic models performed in this study (i.e., Dynamic Smagorinsky and Dynamic Structure) confirms the scale similarity of the flow within the burner since they report a more stable accuracy than the Smagorinsky model for different values of Δ_e when moving from coarse to refined grids (see Figure 5.4). Furthermore, it has been demonstrated that the fixed value of the Smagorinsky constant must be decreased in situations with high shear regions [3], leading to more unaccurate predictions of the Smagorinsky model, especially when these regions are under-resolved (which seems to occur in the coarse mesh cases of this study).

From previous analysis and values reported in Figure 5.4 and Table 5.5 it can be concluded that:

1. The Dynamic Smagorinsky SGS model provides the best prediction ability on the computed time-averaged statistics when employing a sufficiently refined grid (when dealing with turbulence resolution length scale of 0.25 mm).
2. The Dynamic structure model arises as the best option when dealing with a coarser mesh (turbulence resolution length scale of 0.375 mm).

The Dynamic Smagorinsky simulation considering the refined grid is taken for the LES quality assessment performed in Section 5.2.2 and the transient analysis carried out in Section 5.2.3 since it presents the best quality metrics for the three parameters computed.

5.2.2 LES Quality Assessment

The turbulence resolution in scale-resolved large eddy simulations (LES) depends both on the grid resolution and the modelling of the small scales. An important issue regarding LES is to know if the computational grid directly resolves a sufficient part of the turbulent flow energy. For such purpose, two criteria based on different approaches have been calculated for the Dynamic Smagorinsky LES (only the refined grid is considered for clarity) carried out in CONVERGE™ and presented in Section 5.2.1:

- The criterion proposed by Pope [4] based on the turbulence resolution is currently one of the most accepted methods to quantify the quality of a LES in predicting the velocity field. This index of quality (IQ_k) expresses the contribution of the resolved part of the turbulent kinetic energy, that is, the ratio between resolved and total (modelled + resolved) turbulent kinetic energy. In this work, the resolved part is deduced from the filtered turbulent fluctuations, computed as $k_{res} = \frac{1}{2} (\bar{u}_{x,RMS}^2 + \bar{u}_{y,RMS}^2 + \bar{u}_{z,RMS}^2)$, whereas the modelled part (sub-grid scale turbulent kinetic energy) is evaluated through Eq. (5.1) [5]:

$$k_{mod} = \frac{1}{(C_m \Delta_e)^2} \nu_{sgs}^2 \quad (5.1)$$

Where Δ_e is the filter width (i.e., the characteristic length of the grid cell: cube root of the cell volume), C_m is a model constant whose value has been taken as 0.091 [5] and ν_{sgs} is the sub-grid scale viscosity. In this context, a good quality LES is defined when at least 80% of the turbulent kinetic energy is resolved ($IQ_k > 0.8$). Figure 5.5 (left) shows the IQ_k criterion on the transversal x-cut exhibiting that the Pope requirement is globally satisfied inside the combustion chamber (particularly near the injection system where the turbulence is predominant) except near the walls, where shear stresses arise from modelled processes yielding unresolved boundary layers (please note that the flow in these regions is not deemed to be critical since the physical phenomena in these burners does not involve high adverse pressure gradients and separating flow in near-wall regions). The small sub-grid scale contribution to the computed RMS values stated in Section 5.2.1 is here confirmed. Please also note that a null value is also obtained when evaluating the IQ_k index within in areas where turbulence is not of critical interest such as the plenum and fuel line, since no fluctuations are expected.

- A complementary index of quality based on the viscosity (IQ_ν) has been proposed [6] to describe LES resolution. This criterion evaluates the contribution relative to the laminar (ν), the sub-grid (ν_{sgs}), and the numerical (ν_{num}) viscosities according to Eq. (5.2):

$$IQ_\nu = \frac{1}{1 + \alpha_\nu \left(\frac{\nu_{sgs} + \nu + \nu_{num}}{\nu} \right)^n} \quad (5.2)$$

The two constants have been calibrated at $\alpha_\nu = 0.05$ and $n = 0.53$ through DNS results [7]. Celik et al. [6] suggested that IQ_ν values of 0.75 to 0.85 can be considered adequate for High-Reynolds-number flow. Results based on the computed IQ_ν value are shown on the right side of Figure 5.5 and reinforce the conclusion extracted from the Pope requirement, presenting acceptable index criteria values that demonstrate the consistency and the quality of the simulation.

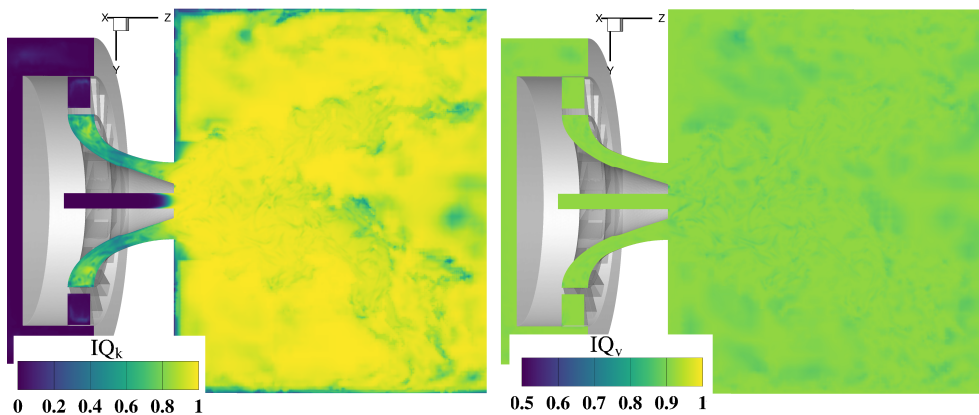


Figure 5.5: Assessment of the LES quality through two different criteria. Left: Index based on the turbulent resolution IQ_k . Right: Index based on the viscosity IQ_ν .

Therefore, LES quality and reliability of non-reactive flow has been assessed based on measures of the turbulent resolution and viscosity. Such criteria confirm the validity of the AMR threshold defined to calculate the sub-grid field from the LES filtering and allows certifying the compatibility when combining LES with AMR implementation. Since controlling processes occur in the resolved large scales in this burner and considering both criteria are satisfied for the kind of grid, the relatively low computational cost

methodology here presented supports the adopted numerical set-up for further liquid-fueled and reactive LES studies.

5.2.3 Numerical results: Validation and discussion

5.2.3.1 Flow Characterisation

An analysis of the time-evolving features and a close examination of the flow near the vicinity of the injection system is carried out in the present section in order to assess the presence of unsteady coherent structures within the combustor. From the discussion of Sections 5.2.1 and 5.2.2, results presented in this section are focused on the Dynamic Smagorinsky LES case carried out in CONVERGE™ since it has exhibited the highest agreement with experimental data through the 3 *NMSE* values computed.

As exposed in Section 2.2.1, when the S_w introduced in Eq. (2.3) exceeds a critical value in the swirler outlet region (typically 0.65 in such flows [8]), the phenomenon known as Vortex Breakdown Bubble (VBB) occurs, leading to the formation of a Central Toroidal Recirculation Zone. In the present premixed gaseous-fueled case, the swirl number evaluated in the injection plane of the combustion chamber is 0.76, implying that the formation of a VBB is expected. This phenomenon manifests itself as an abrupt change in the core of a slender vortex and usually develops downstream into a recirculation bubble or a spiral pattern.

Figure 5.6 shows the axial mean velocity field (normalised with the mean bulk velocity at the swirler exit region $\bar{U}^{ref} = 37$ m/s) and streamlines pattern in a central x -cut plane allowing to illustrate the characteristic flow structures that are typically observed in a gas turbine combustor [9]. These include (1) a Vortex Breakdown Bubble (VBB), which induces a Central Toroidal Recirculation Zone (CTRZ) with reverse flow and a stagnation point, (2) Corner Recirculation Zones (CRZ), and (3) strong shear layers originating from the swirled jet (SWJ) at the outer edge of the inlet annulus. All these unsteady, asymmetric and 3D flow features are influenced by the swirl strength and play an essential role in spray dispersion in the axial and radial directions.

LES simulations allow identifying the vortex structure and reveal the unsteady flow phenomena. The VBB can be described as the formation of a free stagnation point and a recirculation zone with a surrounding 3D spiral flow in the core. The axial location of the stagnation point (the first axial point with zero axial velocity) results from the equilibrium between the central jet and the reverse flow. Figure 5.7 shows the Vortex Breakdown Bubble identified through an iso-surface of zero mean streamwise velocity (the iso-surfaces close

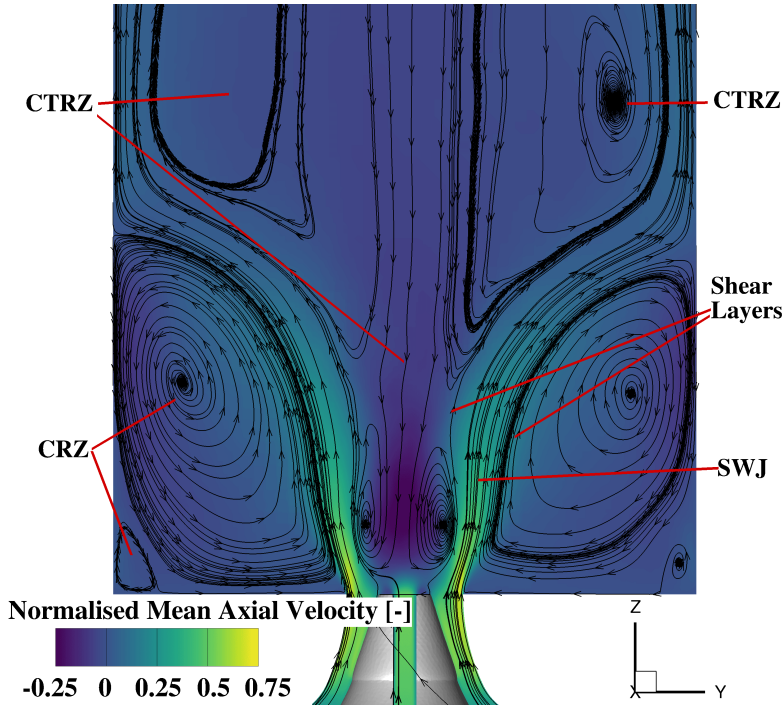


Figure 5.6: Mean (time-averaged) axial velocity field in a mid x -plane and streamlines patterns showing the characteristic flow pattern at 200 ms. Velocity values are normalised with the mean bulk velocity at the swirler exit ($\bar{U}^{ref} = 37 \text{ m/s}$).

to the walls upstream of the combustion chamber have been blanked for the sake of clarity), and the streamlines, coloured by the mean streamwise velocity, to demonstrate the spiral pattern of the flow. This swirling motion also creates an adverse pressure gradient in the axial direction that leads to the formation of the CTRZ. At high swirl numbers, a strong coupling is developed between axial and tangential velocity components and the axial adverse pressure gradient [9]. As the SWJ expands further downstream of the combustion chamber, the momentum conservation implies a decay of the tangential velocity. This causes a decay of the radial pressure gradient, and thus a widening of the CTRZ forming its characteristic *bottle-neck* shape. In confined environments like the present combustor geometry, the SWJ also induces reverse flow regions on its outer part, known as Corner Recirculation Zones (CRZ).

The left side of Figure 5.8 shows the contour of the instantaneous axial velocity field at 200 ms, whereas the right side of Figure 5.8 depicts the

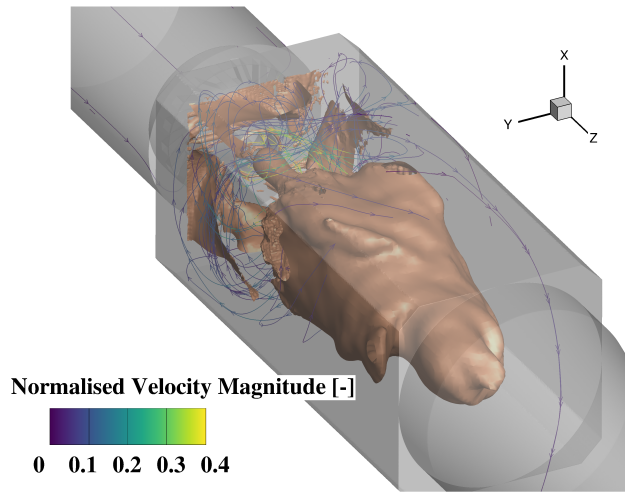


Figure 5.7: Vortex Breakdown Bubble identified using an iso-surface of zero mean streamwise velocity at 200 ms. Velocity values are normalised with the mean bulk velocity at the swirler exit ($\bar{U}^{ref} = 37$ m/s).

time-averaged axial velocity field. Even though the recirculation zones shown in Figure 5.8 (right) may appear to be confined to regions with well-defined boundaries (zero-axial velocity regions are highlighted in black) the instantaneous flow field is much more dynamic and complex. As can be seen, the time-averaged axial velocity field hides the highly general unsteadiness of the flow, turbulent mixing, and interactions that take place in this region. The boundary of the CTRZ is barely visible in the instantaneous field, which shows smaller and isolated recirculation zones with a high degree of unsteadiness. Furthermore, the contours show that the LES grid can resolve many small scale turbulent structures, as derived from Section 5.2.2. The generation of this CTRZ is crucial to provide enough residence time, and sufficiently high temperature and turbulent mixing to complete fuel combustion since it acts as an aerodynamic blockage and allows stabilizing the flame.

When the central vortex core starts precessing around the combustor axis of symmetry at a given frequency (f_{PVC}), it produces hydrodynamic instabilities. The frequency of precession is a function of the combustor design and the swirl intensity at the inlet. This instability caused by the vortex breakdown is called Precessing Vortex Core (PVC), and usually surrounds the CTRZ. The structure of the PVC captured by the LES simulation is displayed in Fig. 5.9 through an instantaneous iso-surface of the unsteady pressure field. The PVC's typical asymmetric shape tends to align with the central axis near the

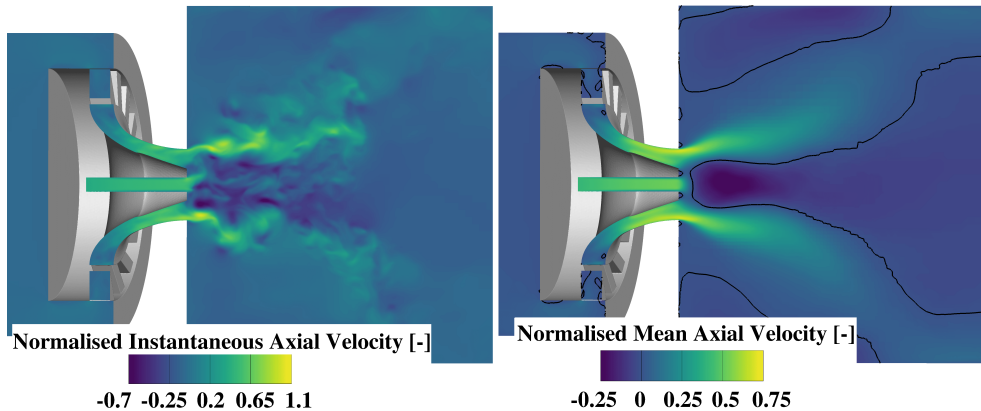


Figure 5.8: Contours of instantaneous (left) and time-averaged (right) axial velocity, and time-averaged tangential velocity at 200 ms. Velocity values are normalised with the mean bulk velocity at the swirler exit ($\bar{U}^{ref} = 37$ m/s).

inlet. Then, as it reaches the stagnation point (i.e. the first point on the z-axis where axial velocity is zero), the PVC transforms into a spiral further downstream the combustion chamber. Meanwhile, two rotating helicoidal branches coming out from the swirler into the chamber can be observed to be reoriented by the mean rotating flow. The swirl induces a centrifugal force, thus making vertical finger-like structures steer away from the axial axis. It is interesting to note how the Kelvin-Helmholtz instabilities cause these vortex spirals to evolve from the shear layer in both the axial and azimuthal directions. In fact, the presence of instantaneous negative axial and tangential velocities in the region near the centerline of the combustion chamber can be directly attributed to the existence of the PVC. In this way, the displacement of the vortex core compresses the flow field at one side against the chamber wall and causes a significant increase in the azimuthal velocity in the squeezed flow region due to the conservation of angular momentum [8]. Finally, further downstream of the injection position, turbulence breaks this large vortical structure into small scale ones, no coherent PVC being detected.

Meanwhile, a rotation time scale associated to the PVC can be defined through Eq. (2.4) introduced in Section 2.2.1 to identify some unsteady flow structures. For the premixed gaseous-fueled case here investigated, the rotation time scale evaluated at the combustion chamber inlet is around 2 ms. Figure 5.10 presents four different snapshots to show the development of the so-called branches of the PVC within one cycle of the precession obtained from the LES. As can be noticed, the number of branches can vary with the

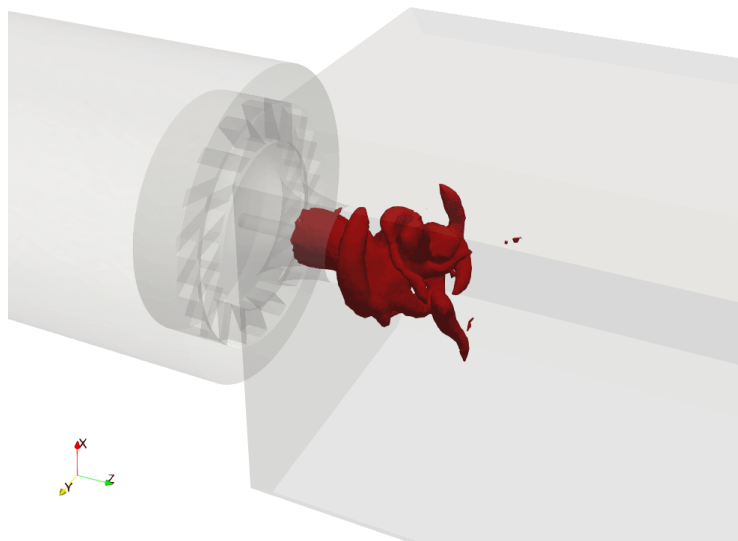


Figure 5.9: Instantaneous visualization of the Precessing Vortex Core identified through a pressure iso-surface of the instantaneous pressure $\bar{p} = 101.1$ kPa at 200 ms.

course of time since just one helicoidal finger-like structure is now visualized. The turnover (or one complete rotation) time of this vortex structure is estimated at $\tau_{PVC} = 2.0$ ms, close to the rotation time scale defined by Eq. (2.4), and corresponding to a precessing frequency of about $f_{PVC} = 500$ Hz. The structure at $t/\tau_{PVC} = 0$ (considering the arbitrary absolute time of 214 ms as the start of a given rotation -i.e., 0 ms-) is aligned to the central axis, but at $t/\tau_{PVC} = 0.25$, it is taken away from the core and turns in a spiral shape along the axial direction. The vortex spiral evolves from the shear layer due to Kelvin-Helmholtz instabilities in both the axial and azimuthal directions. Once the vortical structure has completed one cycle, it is again driven towards the central axis and spreads outward rapidly breaking up into small-scale structures. These helical filaments present counter-clockwise winding in space and clockwise rotation in time. Besides, velocity vectors around the PVC showed clockwise rotation all along the filament. Indeed, the outer edge was observed to have positive axial velocity, whereas the inner regions had reverse flow, as expected from Figure 5.6. This PVC motion affects the flow evolution in the combustion chamber and improves turbulence intensity and mixing levels. However, at given conditions a probable resonant coupling with low-frequency acoustic oscillations in the chamber can exist (these issues will be investigated more in-depth by spectral analysis in Chapter 6). Never-

theless, the behaviour and incidence of the PVC is more complex in reactive cases, not studied in the present work.

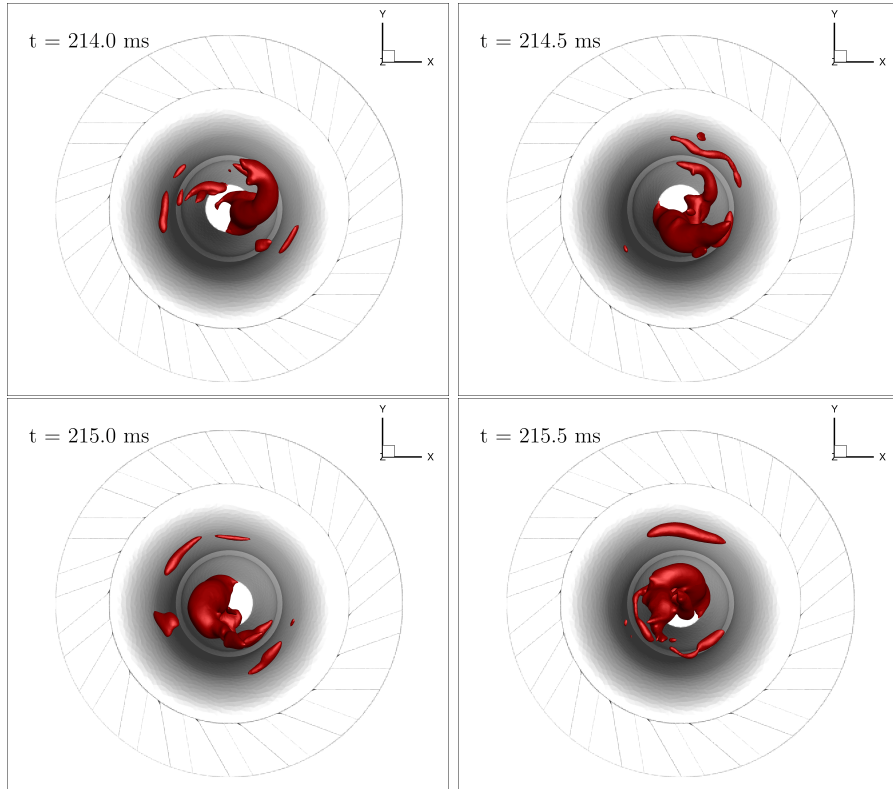


Figure 5.10: Time evolution of the PVC in one cycle of the precession motion. PVC is identified using an iso-surface of the instantaneous pressure $\bar{p} = 101.1 \text{ kPa}$.

The high intensity of turbulence in the CTRZ can be also demonstrated by the visualization of the Q-criterion captured by LES on the left side of Figure 5.11, which defines vortices as areas where the vorticity magnitude is greater than the magnitude of rate-of-strain. As the flow expands from the swirler exit and evolves downstream, strong shear layers are developed from the large velocity difference between the jet flow and the ambient fluid. Furthermore, the presence of swirl generates an azimuthal shear layer and centrifugal instabilities when the circulation decreases in the outward direction. In this regard, well-organized large vortical structures, arising from the shear layers downstream of the dump plane (illustrated on the left side of Figure 5.11), are convected downstream, and then become disordered and dissipated into

small-scale eddies due to the strong CTRZ. In fact, the CTRZ was found to intersect with the outer shear layer, setting a complex flow field near the injector exit.

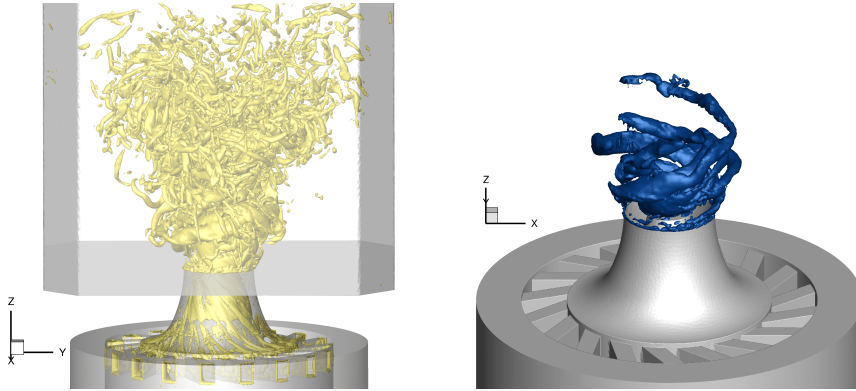


Figure 5.11: Left: Instantaneous iso- Q criterion ($Q = 10^7$) in the swirler and the combustor at 200 ms. Right: Instantaneous iso-surface of the tangential vorticity component (15000 s^{-1}) through the combustion chamber at 200 ms.

Meanwhile, Figure 5.11(right) shows a snapshot of an instantaneous positive tangential vorticity iso-surface. The flow field in the region $r/D > 0.75$ is blanked to provide a clearer picture of the spiral vortex structure. The evolution of these spiral vortex structures can be understood as a kind of vortex shedding with well-defined frequencies close to the rotation time scale of the PVC. Therefore, the combined axial and tangential shear layers become unstable due to the swirl motion and evolve to a modified form of the Kelvin-Helmholtz (KH) instability. In this kind of strong swirl flow, vorticity in the tangential shear layer, generated by the azimuthal velocity, grow and become comparable to the vorticity in the axial shear layer (not shown for clarity). Thus, this joint action of stretch/strain forces the swirling flow to continuously evolve in the axial and azimuthal directions. The aforementioned displacement of the vortex core congestions the flow at one side against the combustor wall, leading to a considerable increase in the tangential velocity in the squeezed flow region due to the conservation of angular momentum. The existence of the PVC also explains the occurrence of instantaneous tangential velocity near the centerline of the combustor.

To end with the transient analysis, Figure 5.12 shows a snapshot of the vorticity magnitude field in a central x -cut plane captured by LES. Vorticity is related to the flow circulation and presents a large magnitude, espe-

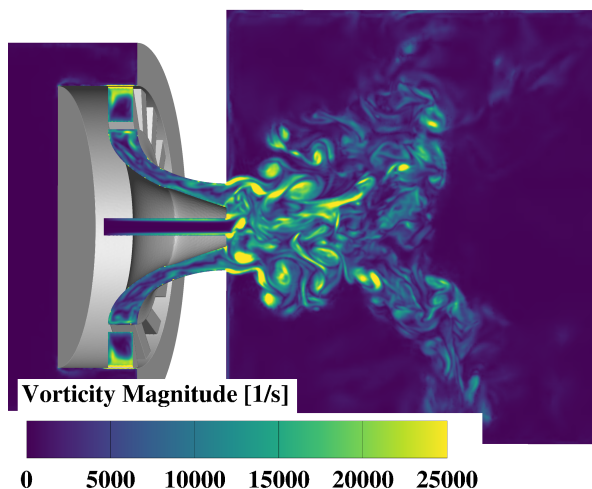


Figure 5.12: Snapshot of the vorticity magnitude field in a central x -cut plane at 200 ms.

cially in the outer shear layer. Well-organized large vortical structures, arising from the shear layers downstream of the dump plane ($z/D = 0$ plane), are observed to be convected downstream, and then become disordered and dissipated into small-scale eddies due to the strong CTRZ. Hence, the high turbulence-intensity region developed at the combustion chamber inlet as a precursor of liquid atomization and enhanced mixing is confirmed again.

5.2.3.2 Mean Features

The statistically averaged flow field (obtained by Eqs. (4.74) and (4.75)) allows comparing numerical and experimental time-averaged velocity profiles.

Figure 5.13 shows the time-averaged mean and RMS fields of the velocity components in the central x -normal plane of the Dynamic Smagorinsky LES with CONVERGETM. As can be seen, the highest axial velocity is located in the SWJ, at the point where it reaches the combustion chamber. The jet opening is first limited due to the presence of the PVC resulting in a narrow CTRZ while further downstream (where the large structure has disappeared) the SWJ is fully opened. The high velocity of the central jet injection is visible on the axial velocity component, characterized by an abrupt decrease near the stagnation point. In this zone, as the axial component quickly decreases, the conservation of the mass flow rate implies a rapid increase of the radial component. It is also interesting to note that the time-averaged position of

the CTRZ moves upstream towards the wall between the central jet and the SWJ. Besides, the high antisymmetric tangential velocity component confirms the strong swirl number of the injection system at the injection plane, reaching values as high as those obtained for the axial component, thus leading to the formation of the CTRZ. Meanwhile, the distributions of the RMS velocity components illustrate the flapping motion of the central jet and SWJ indicating that a high turbulence-intensity region is developed at the combustion chamber inlet. Besides, large velocity fluctuations are produced at this location because of the strong turbulent mixing in the shear layers between the incoming flow and the recirculation flows.

Figures 5.14 to 5.16 show the radial distributions ($x/D = 0$ corresponds to the centerline of the chamber) of the mean velocity components, and its root-mean-square, at five axial locations ($z/D = 0.25, 0.5, 1, 1.5$ and 2) within the CORIA burner. The results here presented correspond to the best numerical setups obtained from the methodology shown in Section 5.2.1: the 3 M LRR Reynolds Stress Model U-RANS and 17 M Dynamic Smagorinsky LES in CONVERGETM are plotted together with both the 17 M Dynamic Smagorinsky LES in OpenFOAM[®] and the experimental data available in literature [10–12]. For a licit analogy between LES cases in both codes, in the case of OpenFOAM[®] only the results for the 17 M mesh (i.e. smallest cell size of 0.4 mm $-0.02D-$) are reported, thus allowing a valid iso-number-of-cells comparison. Please recall that the number of cells reported in CONVERGETM (where the smallest cell size is reduced to 0.25 mm $-0.0125D-$ in LES) is a result of time-averaging the instantaneous cell count during the same temporal window used to compute the turbulent statistics.

In a first look, the global flow topology and the amplitude of the mean and RMS velocity profiles are well reproduced. The mean velocity profiles (left side of Figures 5.14 to 5.16) show that the computed velocity field is, qualitatively, in good agreement with experiments. Both the U-RANS and the LES seem to accurately capture the jet opening angle, denoted by the peaks of the mean velocity components around $x/D = 0.5$. Meanwhile, the turbulent velocity, given by the root mean square value (i.e., the RMS depicted on the right side of the Figures 5.14 to 5.16), is slightly over-predicted in all the simulations for axial and radial components. This could partly be attributed to the fact that the PIV resolution used for measurements is 1 mm [10], which is larger than the LES filter size in the near-injection zone, resulting in smaller measured RMS values due to averaging effect within the probe. Results show stronger turbulent velocities close to the chamber inlet, but an abrupt decay as the flow moves downstream. The different fluctuation profiles among three components

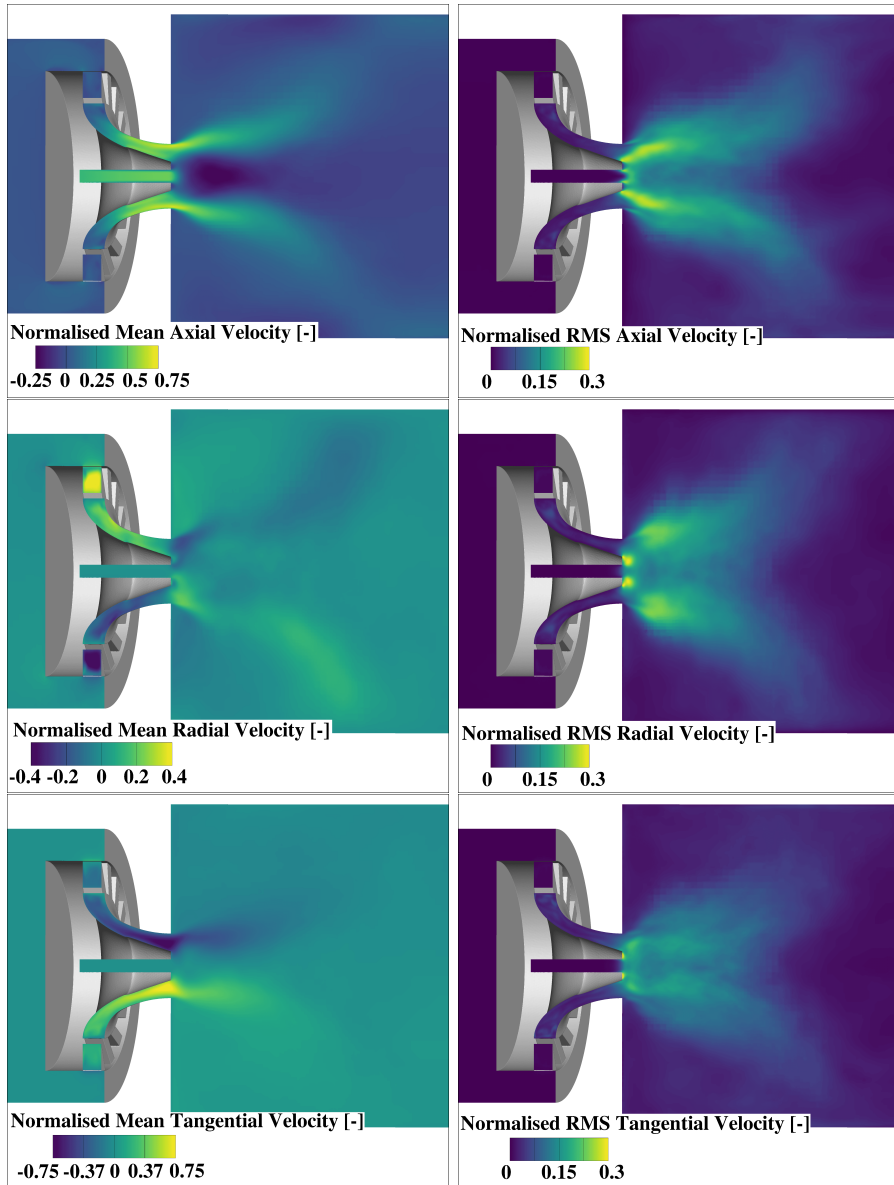


Figure 5.13: Mean (time-averaged) and RMS velocity components in a central x -cut plane through the combustion chamber of the Dynamic Smagorinsky LES with CONVERGETM. Velocity values are normalised with the mean bulk velocity at the swirler exit ($\bar{U}^{ref} = 37$ m/s).

up to $z/D = 1.5$ mm indicate the presence of an anisotropic Reynolds stress distribution produced by the strong swirling flow.

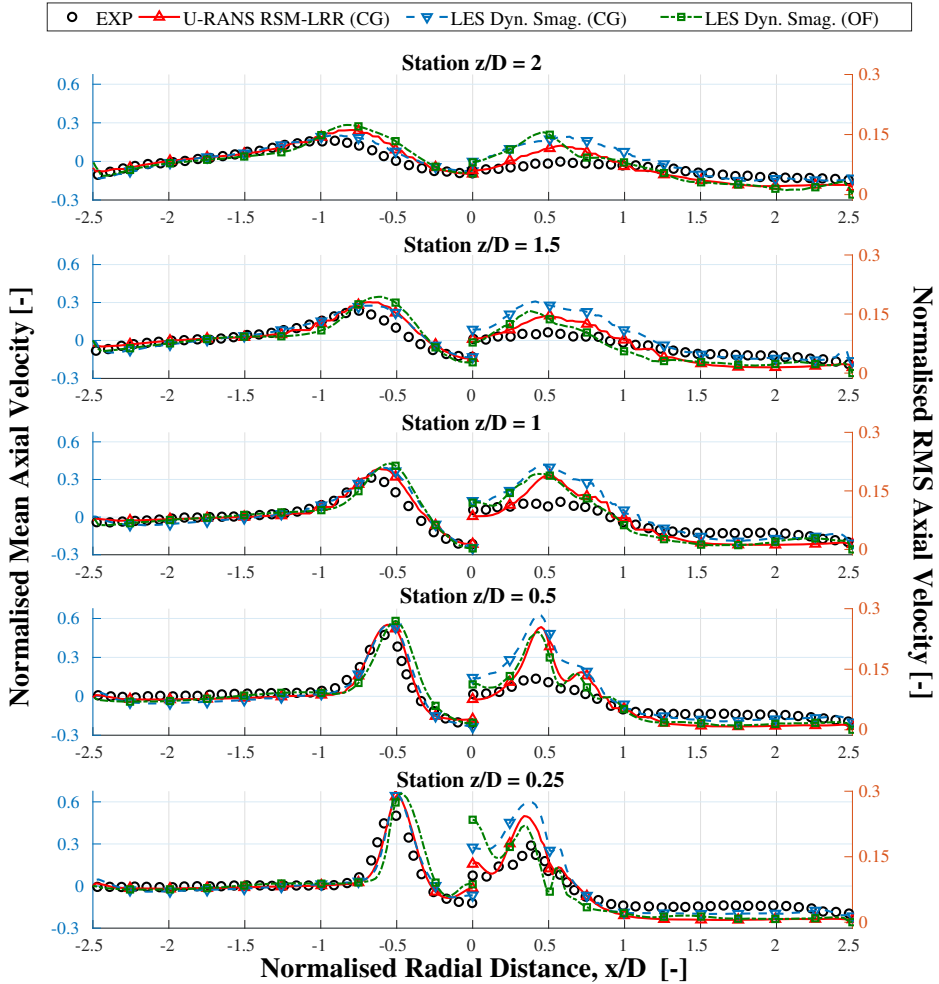


Figure 5.14: Mean and RMS Axial Velocity profiles obtained in U-RANS and LES simulations with CONVERGETM (CG) and OpenFOAM[®] (OF) at 5 axial locations. Velocity values are normalised with the mean bulk velocity at the swirler exit ($\bar{U}^{ref} = 37$ m/s).

The mean axial velocity peak observed at the location $z/D = 0.25$ in Figure 5.14 flattens out as the flow reaches stations far away from the combustion chamber inlet due to the expansion of the recirculation zone in the central region. Moreover, the computed axial velocity at the station $z/D = 0.25$

denotes a slightly stronger penetration of the central jet at $x/D = 0$ (more pronounced in OpenFOAM©), which appreciably modifies the velocity profile since a strong gradient is found near the stagnation point. Results also show the negative axial velocities in the central and corner regions, confirming the existence of recirculation zones.

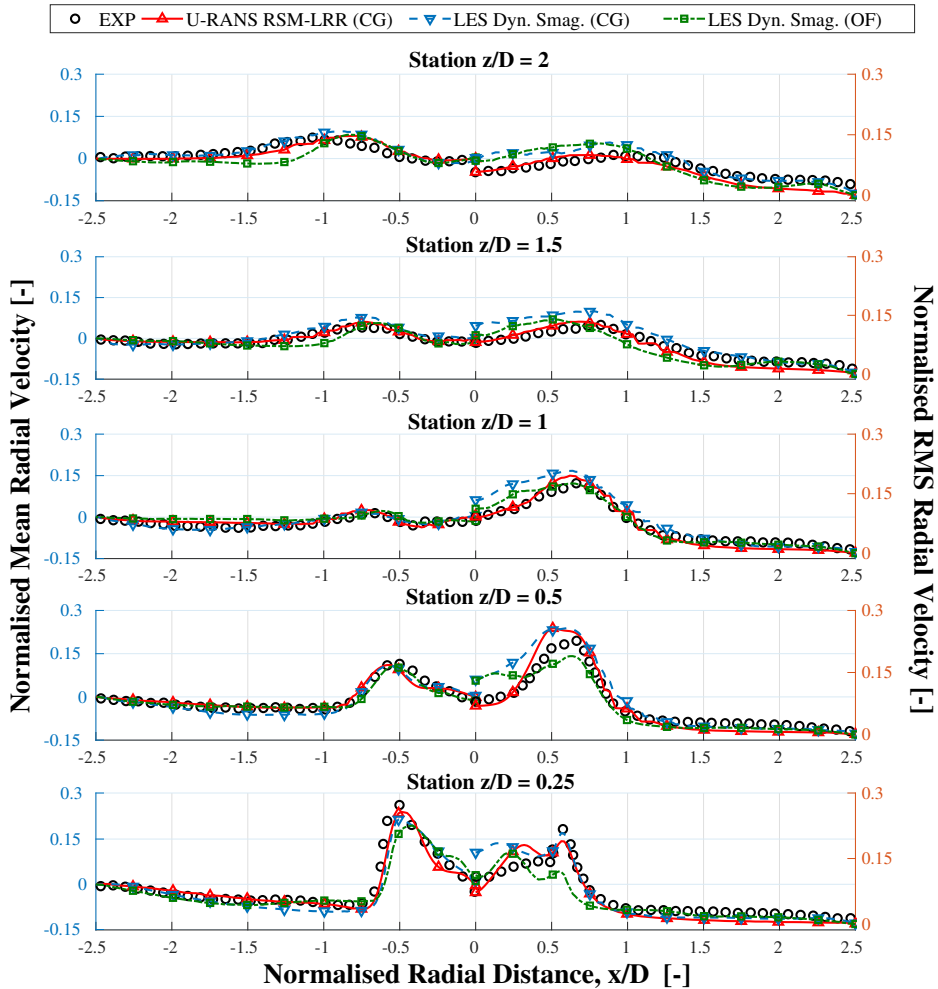


Figure 5.15: Mean and RMS Radial Velocity profiles obtained in U-RANS and LES simulations with *CONVERGE*TM (CG) and OpenFOAM© (OF) at 5 axial locations. Velocity values are normalised with the mean bulk velocity at the swirl exit ($\bar{U}^{ref} = 37$ m/s).

The computed results of Figure 5.15 exhibit the positive mean radial ve-

locities in the main flow passage generated as a consequence of the incoming flow from the swirler spreading outward from the central axis under the effect of the centrifugal force. The mean radial velocity presents a lower magnitude than the axial and tangential components, implying a quicker expansion downstream of the combustion chamber inlet.

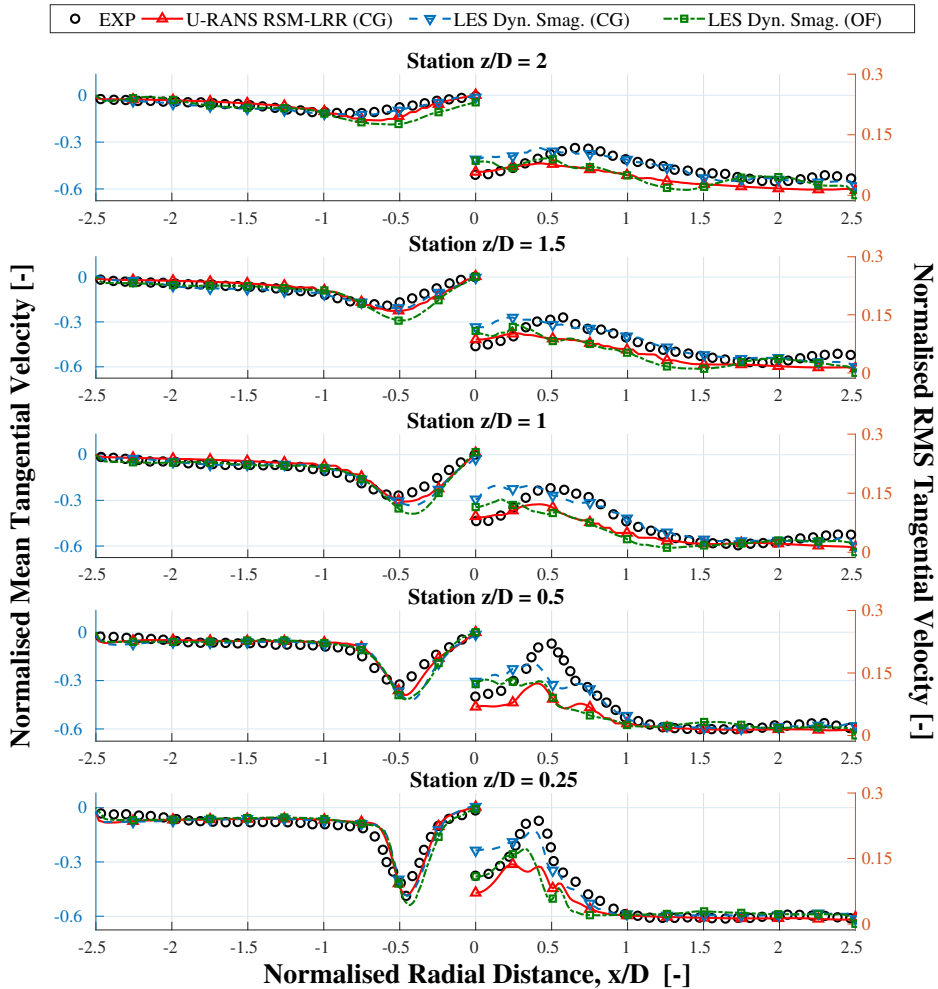


Figure 5.16: Mean and RMS Tangential Velocity profiles obtained in U-RANS and LES simulations with *CONVERGE*TM (CG) and *OpenFOAM*® (OF) at 5 axial locations. Velocity values are normalised with the mean bulk velocity at the swirler exit ($\bar{U}^{ref} = 37$ m/s).

Regarding the mean azimuthal velocity profiles shown in Figure 5.16, the

flow motion in the central region of the first axial stations is similar to a solid-body rotation and a free vortex structure, as observed in the PVC in Figure 5.9. Meanwhile, further downstream, the peak of mean tangential velocity moves outward and a solid vortex profile is established (recall the antisymmetric pattern shown in Figure 5.13). Besides, it is observed that the magnitude of the mean tangential velocities (which primarily represents the swirl of the flow) is much higher than the one corresponding to the mean radial velocities, even in stations further downstream from the combustion chamber inlet, as expected in these high swirling flows combustors.

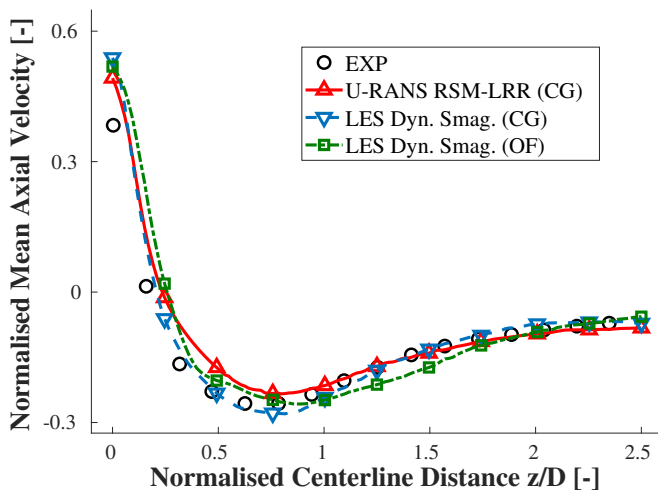


Figure 5.17: Mean Axial Velocity Profile along with the central axis of the burner. Velocity values are normalised with the mean bulk velocity at the swirler exit ($\bar{U}^{ref} = 37$ m/s).

Finally, the mean axial velocity profile along the central axis of the burner is shown in Figure 5.17 for the same three simulations exposed previously. Please note that the experimental values here presented are those used to compute the *NMSE-Centerline* reported in Section 4.4.1.1. The greater ability of the Dynamic Smagorinsky LES to capture the axial velocity along the centerline shown in Section 5.2.1 through the *NMSE-Centerline* can be appreciated. The increase in the turbulent scales solved from U-RANS to LES can significantly improve the central jet penetration prediction, but the position of the stagnation point (i.e., the axial location with zero axial velocity) is still not fully recovered, exhibiting an offset of about 1 mm with experiments.

Generally, the mean axial velocity is slightly over-predicted in the three cases up to $z/D = 0.5$ but fully recovered downstream.

5.3 Liquid-Fueled Reference Case

The emphasis of this section is to achieve a precise description of the swirling spray dispersion (e.g., droplet size and size-classified velocity) downstream of the injector for the liquid-fueled LES cases in CONVERGE™ and OpenFOAM© presented in Section 4.3.1, as well as the characterisation of the instantaneous, mean and fluctuating air and liquid velocities when compared to the available experimental data. The flow topology and spray visualisation is presented in Section 5.3.1 for the LISA and TAB cases in CONVERGE™, whereas the time-averaged features and validation against experiments are showed in Section 5.3.2 for the LISA and TAB cases in CONVERGE™ and the TAB case in OpenFOAM©.

5.3.1 Flow Characterisation

In the liquid-fuel case, the swirl number evaluated in the injection plane of the combustion chamber is 0.77 (the same value than in the gaseous-fueled case since the swirler has not experienced any geometrical change) implying that the formation of a VBB is expected. As introduced in Section 5.2.3, the VBB can be described as the formation of a recirculation zone established downstream of the area expansion close to the nozzle exit where negative velocities yield a stagnation region (enabling to hold the flame and shorten the flame length in reactive cases) with a surrounding 3D spiral flow in the core (see Figure 5.18). Meanwhile, Corner Recirculation Zones (CRZ) are again induced between the outer shear layer and the chamber walls by the confinement of the chamber and the abrupt flow development in the cross-section area when entering the combustion chamber. The higher the S_W , the higher the CTRZ region and, consequently, the smaller the CRZ volume. Due to the moderate swirl number, the CTRZ in the 2-D cut of the left side Figure 5.18 presents a small area in the centre of the combustor compared to the CRZ. Finally, in between both regions, the primary swirled air (SWJ) flows from the swirler outlet to the jet zone along with the chamber characterised by strong shear layers (presenting a high level of turbulence) interacting with the spray. All these unsteady, asymmetric and 3D flow features are influenced by the swirl strength and play an essential role in spray dispersion in axial and radial directions.

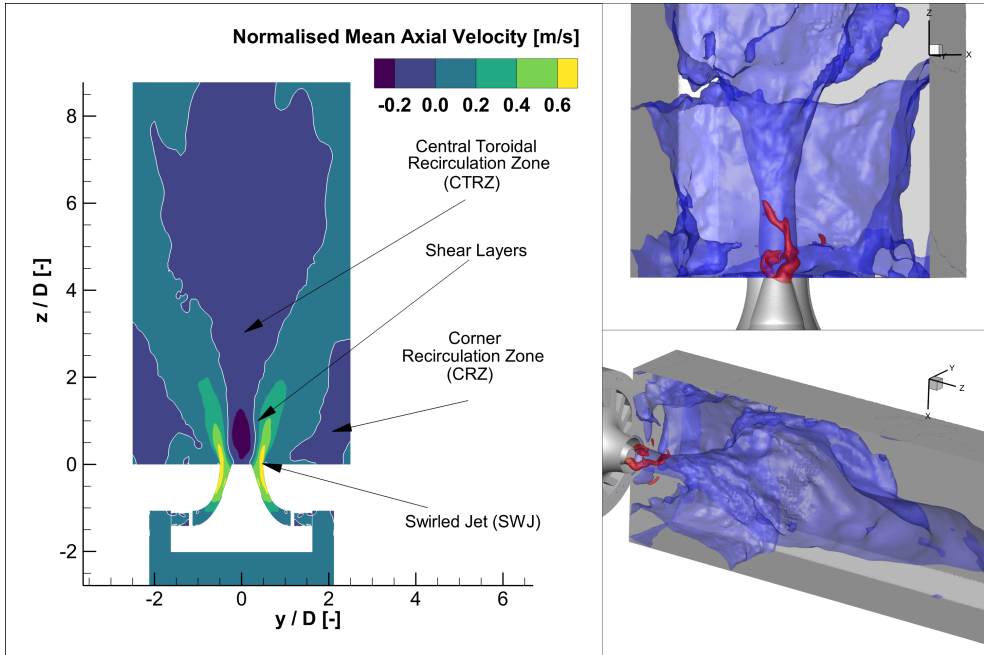


Figure 5.18: Left: Mean (time-averaged) axial velocity field in a central x -cut plane and streamlines patterns showing the characteristic flow pattern within the spray configuration of the CORIA LDI Combustor. Right: Instantaneous visualization of the PVC (red) and VBB (blue) structures at 200 ms. VBB past $r > 35$ mm is not shown to increase clarity. (TAB case in CONVERGETM).

The steady snapshot of the VBB identified in Figure 5.18 through an iso-surface of zero mean axial velocity appears as a single continuous and symmetric region presenting swirling mean flow into and around it. As it was already found in Figure 5.8, the instantaneous snapshot (not repeated here) is considerably different, presenting unsteady local asymmetry. The Precessing Vortex Core, originated from the swirler outlet region and essentially dominated by the inflow swirl dynamics is also visualised in Figure 5.18, using a pressure iso-surface at 100 kPa as a helical filament rotating around the VBB region. The coherence of the PVC is sustained for a certain area downstream of the injection plane until it finally dissipates into smaller and less coherent structures (this fact can be better appreciated in temporal evolution records). The rotation time scale associated to the PVC (defined through Eq. (2.4)) evaluated at the combustion chamber inlet for the liquid-fueled case investigated here is estimated at $\tau_{PVC} = 1$ ms (i.e., half of the one manifested in the

gaseous-fueled case), corresponding to a frequency of about 1 kHz (i.e., twice of the one exhibited in the gaseous-fueled case).

The spray dispersion is strongly governed by the interactions of the spray with the surrounding turbulent gas flow, specifically by the VBB pattern and the rotating motion of the PVC. The LES here presented allows capturing and visualising the instantaneous flow fields, thus accurately predicting the characteristic spiraling motion of the disperse phase in swirling flows accurately. Nevertheless, the spray dispersion (and therefore, the spray-air mixture) can be affected by the breakup modelling as reported in the studies conducted by Patel and Menon [13].

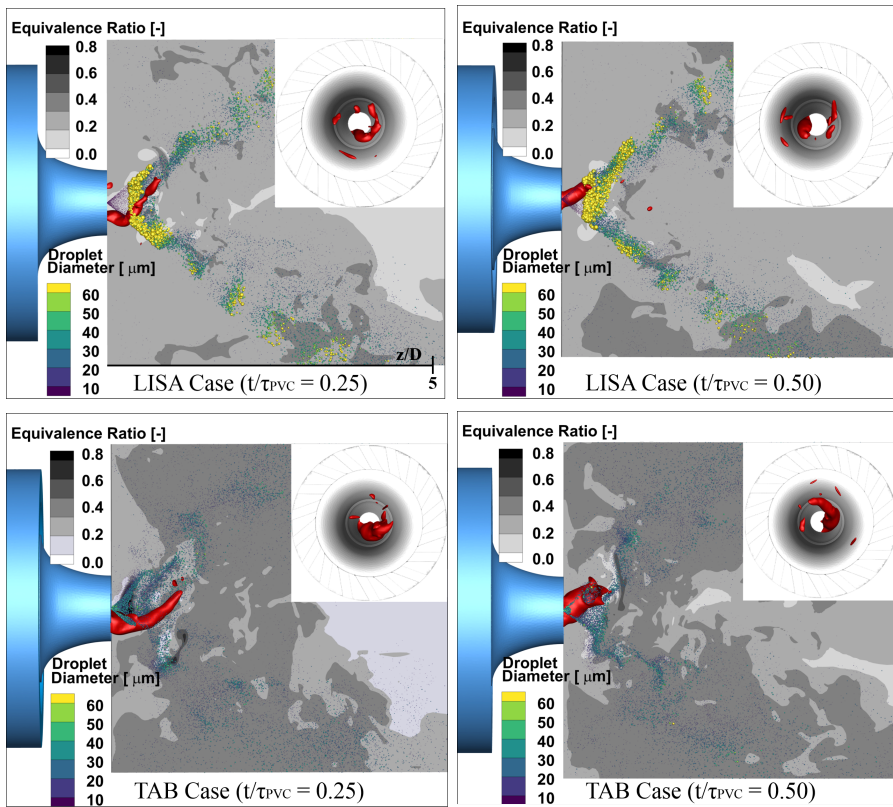


Figure 5.19: Representation of the instantaneous parcels at two instants for LISA and TAB simulations in CONVERGETM, the fuel reaction rate (dark-coloured) and the PVC (red).

In this way, Figure 5.19 shows the visualisation of the spray dispersion under the swirling effect as it evolves in time for the LISA (top) and TAB

(bottom) cases in CONVERGE™. It can be observed how fuel is injected in a hollow-cone shape to generate a quickly atomised spray and efficient fuel-air mixing downstream of the injector. Spray droplets are forced to a wide radial dispersion because of the increased swirling forces at the shear layer around the VBB. Besides, spray dispersion and mixing is further accentuated a few centimetres downstream the injection where randomly oriented structures are generated when the coherence of the PVC breaks down.

In general, the helical Kelvin-Helmholtz instabilities arise from (and synchronise with) the precessing motion of the carrier phase leading the spray both to resemble the spiral PVC pattern (due to the low-pressure inside the structure) and to get confined within the PVC and VBB forming dense pockets of parcels (except for parcels presenting large Stokes numbers). This implies the occurrence of high fluctuations in the local fuel concentration [14]. In this way, a high temporal and spatial dependence from the entrainment effect of the PVC on the spray can be established in the form of a spatial correlation between the parcel and PVC positions. Analysis reveals that big parcels in LISA Case ($d > 60 \mu\text{m}$) with high Stokes values travel downstream almost uninfluenced by the local unsteady flow structures due to their inertia (leading to equivalence ratio inhomogeneities), whereas a preferential accumulation of small parcels (low Stokes numbers) is detected around the PVC and captured by the CTRZ in the TAB Case. Such a preferred collection of parcels in low-vorticity regions has been also reported in past studies [13, 15]. This fact will be discussed in the following section.

5.3.2 Mean Features

The statistically averaged gaseous and liquid fields are now described and compared with measurements separately for the dynamic Smagorinsky LES in CONVERGE™ (LISA and TAB cases) and OpenFOAM© (TAB case). The analysis here presented is focused substantially on the predictions of the dispersed phase statistics (e.g., droplet velocity and size distributions). The liquid-phase results have been azimuthally-averaged, as explained in Section 4.4.1.2, to increase the statistically converged data.

5.3.2.1 Carrier Phase

The gaseous field resolution was validated in Section 5.2.3. Therefore, only a brief presentation of gaseous results is here included to confirm the low influence of the fuel spray droplets on the carrier-phase¹.

¹Only one case in CONVERGE™ is here presented since gaseous phase results in LISA and TAB cases are virtually identical.

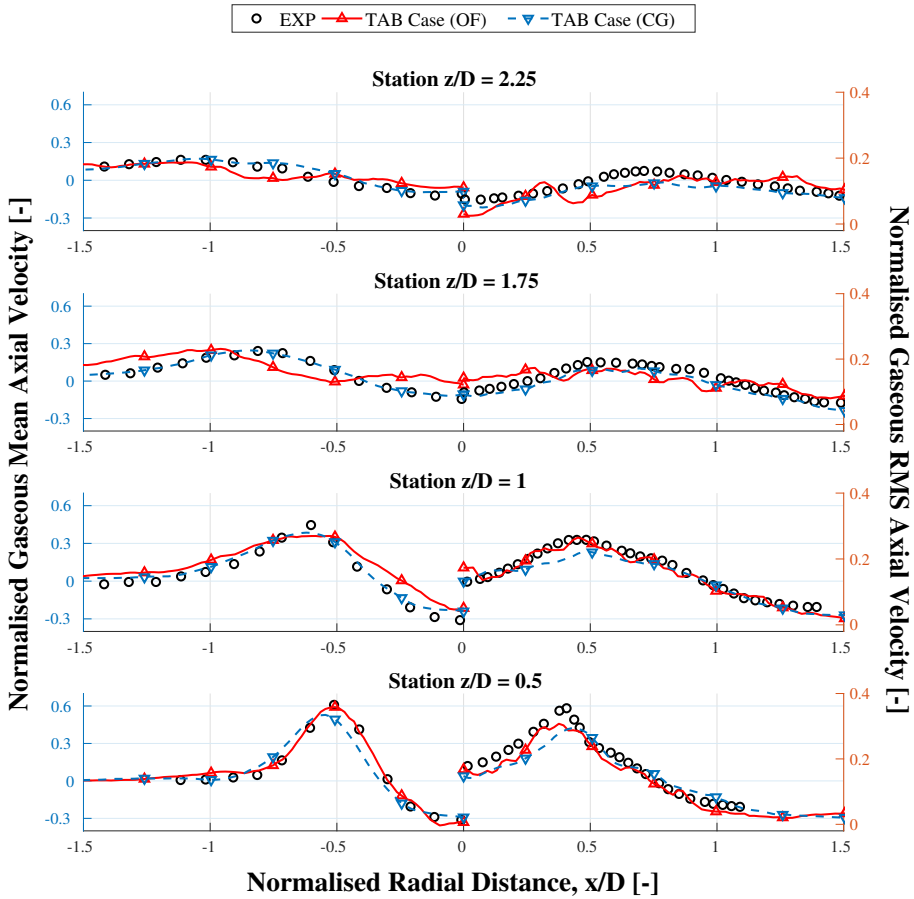


Figure 5.20: Gaseous Mean and RMS Axial Velocity profiles obtained in TAB cases with CONVERGE™ (CG) and OpenFOAM® (OF) at 4 axial locations. Velocity values are normalised with the mean bulk velocity at the swirler exit ($\bar{U}^{ref} = 70 \text{ m/s}$).

The axial and tangential components of the numerical time-averaged mean and root-mean-square velocity of the air are plotted in the radial profiles of Figures 5.20 and 5.21 at four streamwise locations within the CORIA LDI combustor where PDA air velocity measurements are available [16]. Both the mean and RMS velocity profiles obtained from the CFD results show that the computed velocity field is, qualitatively, in good agreement with experiments throughout the four stations. The LES data is able to capture the length and

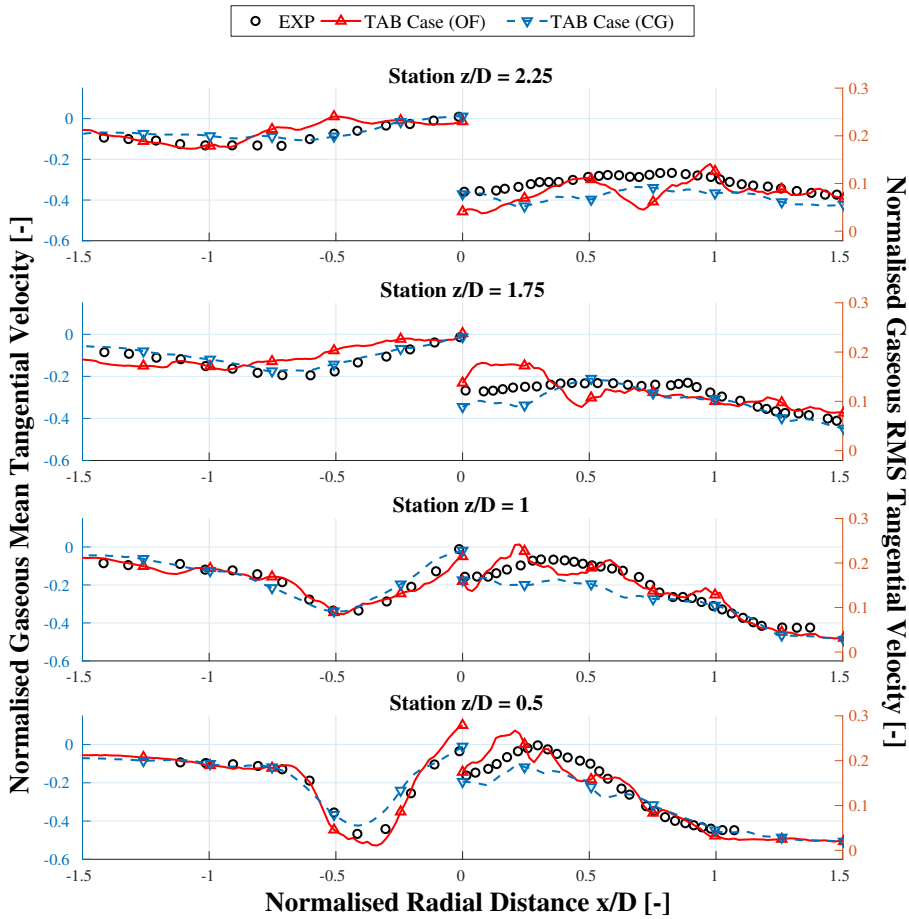


Figure 5.21: Gaseous Mean and RMS Tangential Velocity profiles obtained in TAB cases with CONVERGETM (CG) and OpenFOAM[®] (OF) at 4 axial locations. Velocity values are normalised with the mean bulk velocity at the swirler exit ($\bar{U}^{ref} = 70$ m/s).

strength of the CTRZ with the correct level of spreading angle, demonstrating the robustness of the numerical methodology and ratifying that the influence of the spray on the air mean velocity is negligible in the near-injection region and thus in the entire combustor.

On the one hand, the air mean axial velocity depicted on the left side of Figure 5.20 shows a co-flow peak of $0.6\bar{U}^{ref}$ (i.e., 40 m/s) at $z/D = 0.5$ and $x/D = 0.5$ which is rapidly diffused downstream up to $0.15\bar{U}^{ref}$ at

$z/D = 2.25$. This same trend occurs with the negative axial velocity peak of $-0.3\bar{U}^{ref}$ from $z/D = 0.5$ to $z/D = 1$, which then decreases downstream. Meanwhile, the maximum gaseous mean tangential velocity on the left-side of Figure 5.21 reaches a peak of $0.5\bar{U}^{ref}$, denoting a high swirling motion close to the axial component.

On the other hand, the right sides of Figures 5.20 and 5.21 show more substantial turbulent velocities close to the chamber inlet. Still, an abrupt decay is experienced as the flow moves both radially (towards zones outside the external shear layer of the air jet) and downstream. The different fluctuation profiles among three components (comparison of the radial component is not shown here for brevity) up to $z/D = 1$ indicate the presence of an anisotropic Reynolds stress distribution produced by the strong swirling flow. The fuel/air mixing is enhanced by these energetic velocity fluctuations, and the trajectories of all the droplets (already atomised when entering this region) are strongly influenced by the air motion (see the following section). Both mean and fluctuating air velocities are small in the CRZs so fuel vapour may have more prolonged residence times than in other regions.

5.3.2.2 Dispersed Phase

A more in-depth insight into the near field region, where the breakup model is expected to impact on the spray distribution field, is achieved through the computation of size and velocity droplet statistics.

With regard to the liquid velocity field, Figures 5.22 and 5.23 compare the drop axial and radial velocity components from the three CFD cases against the available experimental data [16]. Liquid mean (left) and RMS (right) velocity profiles (considering the whole drop sizes population) capture the general features and agree with PDA data overall, indicating converged parcel statistics. The main discrepancy is the apparent underprediction in the injected spray cone angle at the station $z/D = 0.75$ denoted by the mean axial velocity peak at $x/D = -0.5$, which seems to be fully recovered further downstream. This difference can be attributed to the slight imprecision in the predicted drop size distribution manifested in Figures 5.24 and 5.25 since both the angle and peak location differs depending on the droplet size, as will be later shown in the velocity-size correlations of Figure 5.26). Besides, the LISA case also overpredicts the peak of negative axial velocity of the parcels detected within the CTRZ due to the underprediction in the drop distribution (i.e., the small predicted drop sizes are influenced and accelerated by the reverse gas phase velocity). On the other hand, the TAB case in OpenFOAM® does not succeed in predicting the rapid reduction in the mean radial velocity

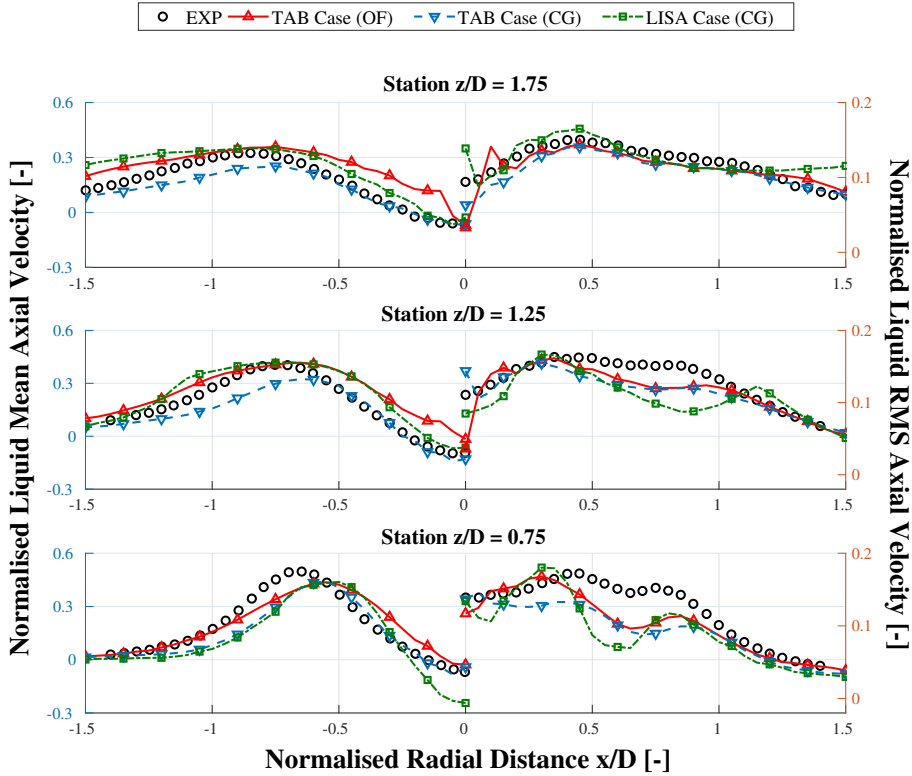


Figure 5.22: Liquid Mean and RMS Axial Velocity profiles obtained in TAB and LISA cases with CONVERGETM (CG) and TAB case with OpenFOAM[®] (OF) at 3 axial locations. Velocity values are normalised with the mean bulk velocity at the swirler exit ($\bar{U}^{ref} = 70$ m/s).

as the spray penetrates within the combustor. Meanwhile, the RMS quantities are fully resolved both in TAB and LISA cases at most axial stations and radial positions but underpredicted in others. In general terms, the TAB case in CONVERGETM offers the best overall predicting capabilities in resolving the liquid velocity field so it will be considered both in the remainder of the section and in the parametric study presented in Chapter 7.

An explicit description of droplet size at different axial stations is provided in Figure 5.24, where radial profiles of the time-averaged Sauter Mean Diameter (SMD or D_{32}) computed by the CFD cases are compared with experiments² [16]. It can be seen how the TAB Case in CONVERGETM accurately

²Note that the global experimental SMD value from which spray conditions of the com-

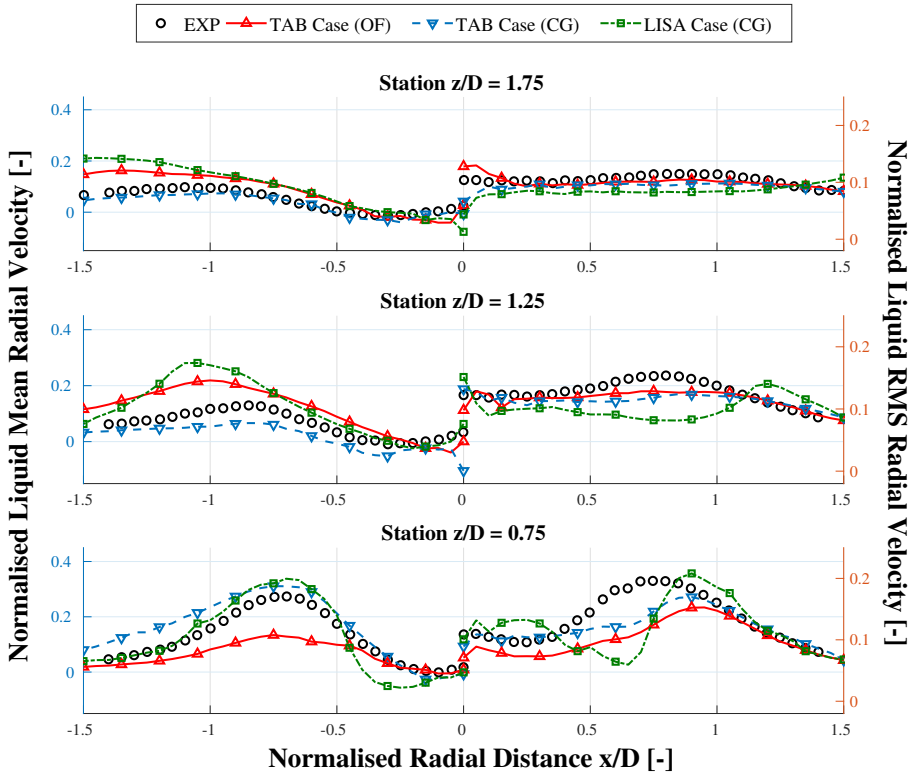


Figure 5.23: Liquid Mean and RMS Radial Velocity profiles obtained in TAB and LISA cases with *CONVERGE*TM (CG) and TAB case with *OpenFOAM*® (OF) at 3 axial locations. Velocity values are normalised with the mean bulk velocity at the swirler exit ($\bar{U}^{ref} = 70$ m/s).

predicts the overall trend and specific sizes along all stations. Experimental data show bounded profiles with SMD values ranging from 23 to 36 μm , where the smaller droplets (those presenting low Stokes numbers) are captured by the VBB and CRZ regions. SMD profiles become more uniform at further locations. Meanwhile, the presence of the SWJ pushes the emerging droplets further downstream before completing their break up processes and thus originating higher SMD values at the first axial stations.

A closer examination to the predicted spray size distribution downstream of the nozzle is depicted in Figure 5.25. In this way, two histograms are shown

putational atomisation models have been calibrated is equal to $D_{32} = 31$ μm .

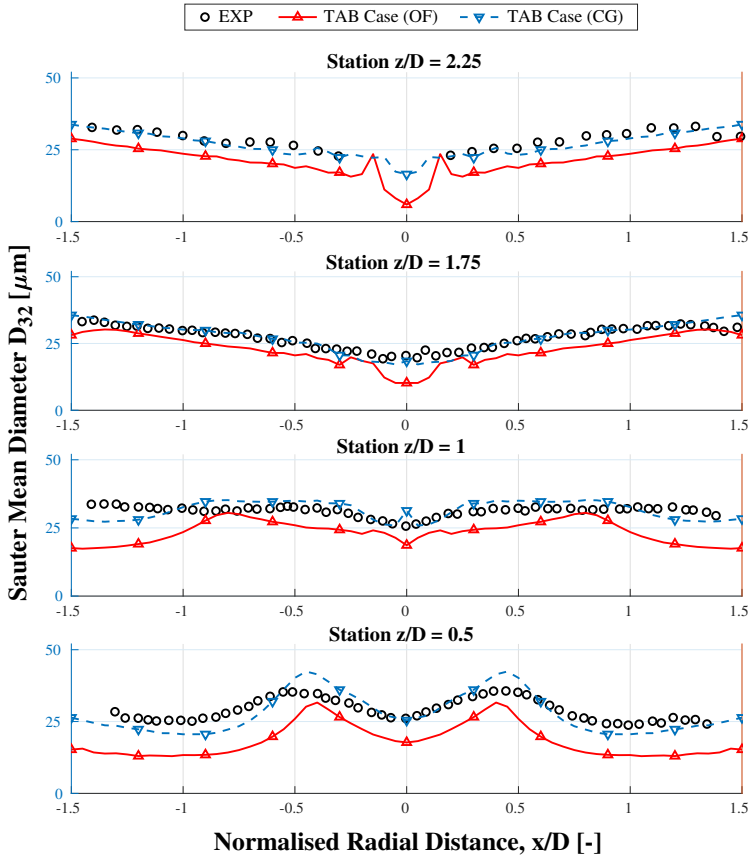


Figure 5.24: Sauter Mean Diameters (D_{32}) profiles obtained in TAB and LISA cases with CONVERGETM (CG) and TAB case with OpenFOAM[®] (OF) at 4 axial locations.

at representative locations where PDA data are available (i.e., in the CTRZ -left-, and in the outer edge of the spray cone angle -right-) in order to provide a more detailed characterisation in terms of the breakup model. For each location, the azimuthally averaged number of droplets contained in each parcel per bin size and the sum of droplets across all bins is considered to obtain the probability density function for each group size. Experimental measurements reveal a similar distribution in both locations presenting a locally heterogeneous population with diameters ranging from 5 to 50 μm . Nevertheless, the drop size distributions predicted numerically are narrower. The TAB case is

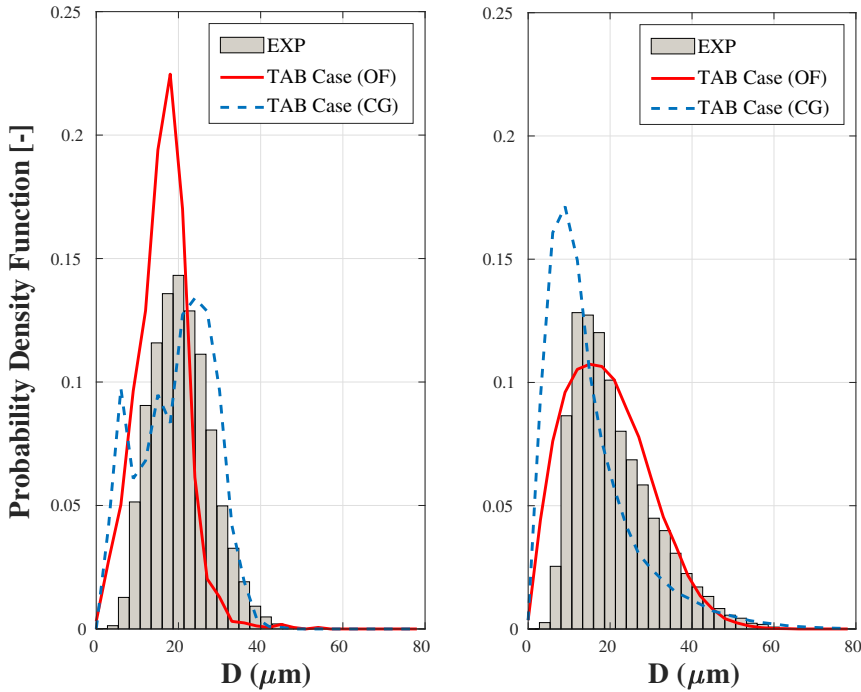


Figure 5.25: Particle size distribution obtained in TAB and LISA cases with CONVERGETM (CG) and TAB case with OpenFOAM[®] (OF) at 2 spatial locations. Left: CTRZ ($z/D = 0.5$, $r/D = 0$); Right: SWJ ($z/D = 1$, $r/D = 1$).

in overall good agreement with PDA size distributions, as occurred with the predicted SMD. In this way, the global trends are respected in TAB cases even not predicting the exact distribution values: no droplets larger than 40 μm are detected at the CTRZ, while drops up to 60 μm are captured in the SWJ region. Besides, the TAB model can predict that the SWJ contains more droplets ranging from 0 to 15 μm than the CTRZ.

Focusing on the velocity-size correlation, drop velocity components are computed for different groups/bins based on their diameter. Figure 5.26, 5.27 and 5.28 show the liquid mean (on the left side) and RMS (on the right side) velocity components for the size classes 0 – 10 μm , 20 – 30 μm and 40 – 50 μm corresponding to the TAB case in CONVERGETM (filled markers with lines) together with the available experimental data (hollow markers). In general, the time-averaged and fluctuating droplet velocity profiles show a reasonable

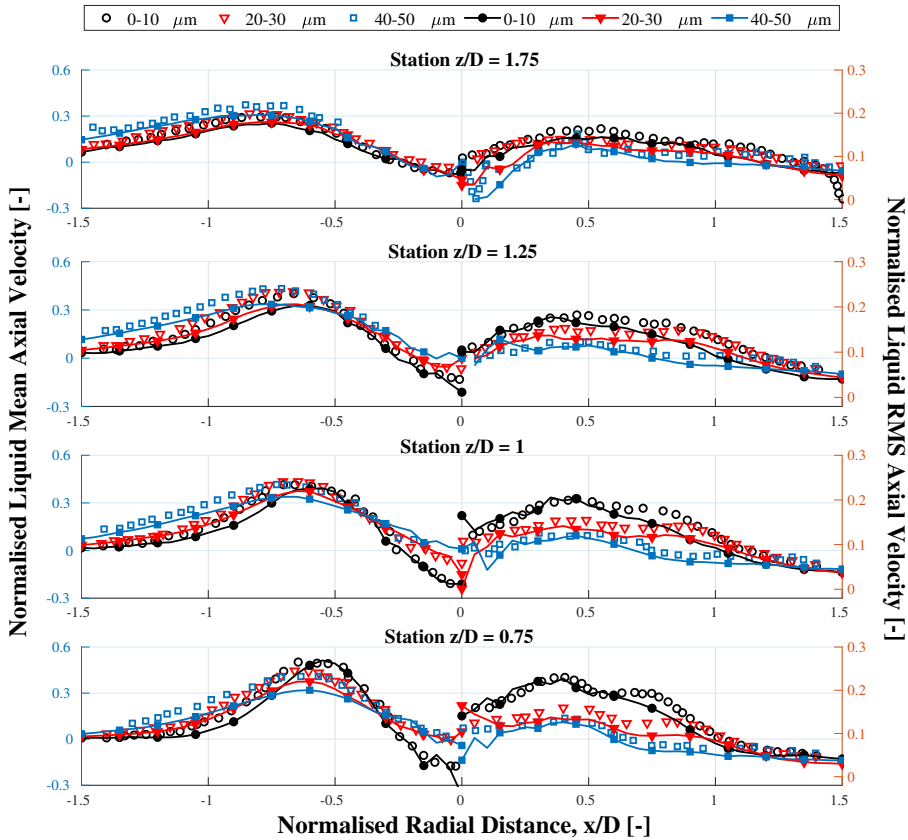


Figure 5.26: Liquid Mean and RMS Axial Velocity profiles classified by size groups obtained in TAB case with CONVERGETM (CG) at 4 axial locations (hollow markers: experimental data; lines with filled markers: LES). Velocity values are normalised with the mean bulk velocity at the swirler exit ($\bar{U}^{ref} = 70$ m/s).

agreement of drop statistics for the three considered bin sizes, thus confirming the success achieved by the Lagrangian tracking approach in conjunction with the TAB breakup model.

The time-averaged streamwise velocity (Figure 5.26) reveals how the smaller droplets are strongly accelerated by the co-flow in the first millimetres achieving higher axial velocity peaks (and thus a smaller injection cone angle) at $z/D = 0.75$, as anticipated earlier. However, both the 3-D expansion, the adverse pressure gradients and the drag effect experienced as the spray evolves further downstream decelerate its evolution lowering the velocity for all group

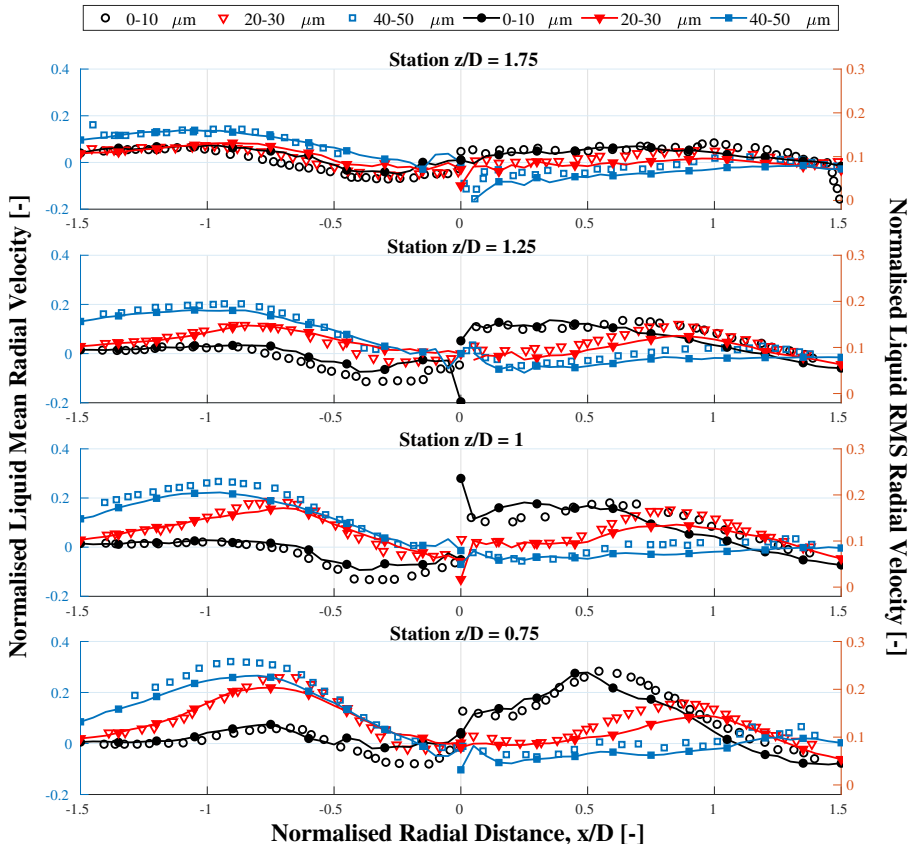


Figure 5.27: Liquid Mean and RMS Radial Velocity profiles classified by size groups obtained in TAB case with CONVERGETM (CG) at 4 axial locations (hollow markers: experimental data; lines with filled markers: LES). Velocity values are normalised with the mean bulk velocity at the swirler exit ($\bar{U}^{ref} = 70$ m/s).

sizes. This effect is much more accentuated in the small particles due to their lower inertia and higher interaction (faster momentum equilibrium) with the carrier phase, changing from almost $0.6 \bar{U}^{ref}$ at $z/D = 0.75$ to $0.3 \bar{U}^{ref}$ at $z/D = 1.75$.

The particle mean radial velocity profiles plotted in Figure 5.27 reflect how the radial motion of the spray increases with radial distance. The peak of maximum radial velocity decreases again with axial distance because of the 3D expansion. The negative radial velocity of the small droplets for $x/D < 0.75$ indicates how these low-Stokes particles are pushed towards the centerline

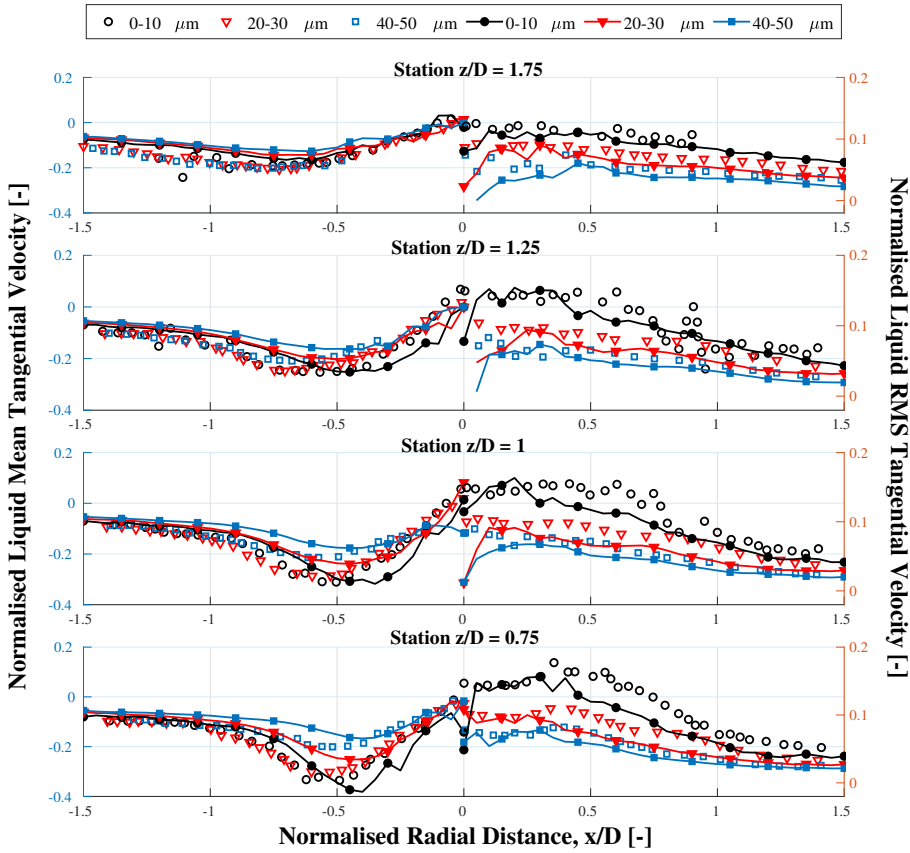


Figure 5.28: Liquid Mean and RMS Tangential Velocity profiles classified by size groups obtained in TAB case with CONVERGETM (CG) at 4 axial locations (hollow markers: experimental data; lines with filled markers: LES). Velocity values are normalised with the mean bulk velocity at the swirler exit ($\bar{U}^{ref} = 70$ m/s).

($x/D = 0$) and eventually captured by the CTRZ. On the other hand, larger spray droplets are ejected with high significant velocities ($0.3\bar{U}^{ref}$) following more ballistic trajectories.

Meanwhile, the drop mean tangential velocity profiles (Figure 5.28) show the opposite trend than the radial velocities. Here, the smaller drops present higher mean velocity values at low stations and are rapidly adapted to the airflow further downstream to approximately converge to the velocity of the other size groups, as occurred with the other velocity components.

Finally, the root mean square of the fuel droplet velocity, represented on the right side of Figures 5.26, 5.27 and 5.28, reveals higher fluctuations for smaller droplets, being the largest strain rates (about $0.25 \bar{U}^{ref}$) located at the SWJ core close to the nozzle ($z/D = 0.75$). It should also be noted that axial and radial RMS profiles exhibit about 30% more fluctuations than the azimuthal component, as observed in the carrier phase.

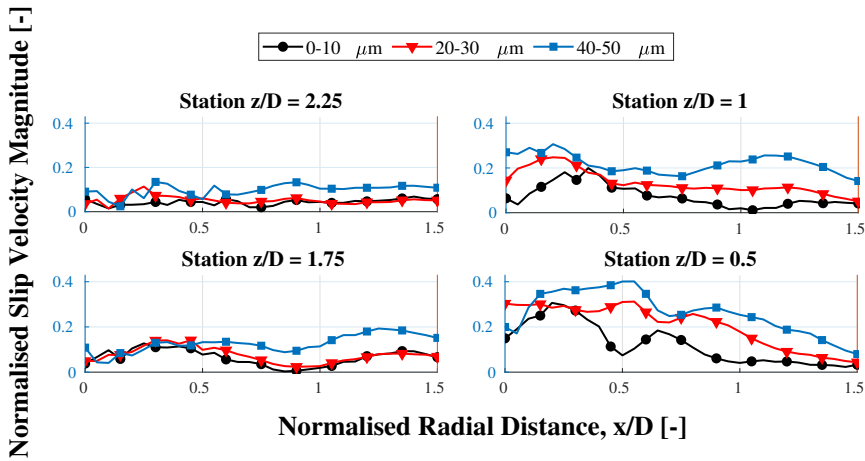


Figure 5.29: Liquid-gas mean slip velocity magnitude classified by size groups in TAB case with CONVERGETM (CG) at 4 axial locations. Velocity values are normalised with the mean bulk velocity at the swirler exit ($\bar{U}^{ref} = 70$ m/s).

To conclude with the liquid-phase analysis, the relative velocity magnitude between drops and air³ is displayed in Figure 5.29 for the same three bin groups dealt with before. These slip velocities experienced by fuel droplets are significant since they control the evaporation process (vapour production and local equivalence ratio) and thus the two-phase combustion in reactive cases. It can be directly observed how small drops (0 – 10 μm) present lower slip velocity values (i.e., match more strictly the airflow velocity) than large droplets, as expected. The maximum relative velocities are detected on the spray edges ($x/D = 0.5$) at lower axial distances ($z/D = 0.75$) for big droplets (40 – 50 μm), reaching values up to $0.4 \bar{U}^{ref}$. Significant slip velocities are found for the (40–50 μm) group, both close to the centerline and to the nozzle. Meanwhile, once the spray penetrates further downstream the combustion

³For each location, the air mean velocity has been subtracted to the liquid mean velocity.

chamber, the slip velocities for the three groups collapse toward values under $0.2\bar{U}^{ref}$. The higher slip velocities of the larger droplets (carrying most of the fuel mass) imply greater evaporation rates, thus contributing to the generation of significant fuel vapour mass. This vapour produced at the spray periphery faces a moderate airflow velocity region with high fluctuations (see Figures 5.20 and 5.21) and eventually falls into the CTRZ.

5.4 Conclusions

An academic gas turbine combustor with premixed gaseous and non-premixed liquid injections has been modelled through U-RANS and LES simulations by means of two distinctive codes, namely the opensource CFD package OpenFOAM[®] and the commercial CFD code CONVERGE[™], which provides advanced mesh handling features, including AMR algorithms. An optimal mesh strategy using adaptive mesh refinement has been defined, and its benefits against traditional fixed mesh approaches have been exploited. The applicability of grid control tools such as fixed embedding and AMR has been demonstrated to be an interesting option to face this type of multi-scale problem. A methodology has been presented to evaluate the influence on the accuracy of the grid control tools through a parametric mesh study. The main findings of the present chapter are summarised as follows:

- The Normalised Mean Square Error has been adopted and systematically applied as a validation metric to quantify the existing discrepancies between the CFD numerical results and the available experimental data, proving to be a promising indicator to the quality of different meshing strategies.
- The capability of CONVERGE[™] numerical code in resolving the complex swirling flow features and the recirculation flow regions with reasonable accuracy has been demonstrated. Agreement with experimental data was obtained both in U-RANS and LES in terms of predicted location and size of the CTRZ and CRZ as well as time-averaged and RMS values for air velocity components.
- The LES has revealed a flow pattern typical of highly swirled configurations similar to experimental observations. The macroscopical analysis of the main turbulent features given by the unsteady flow visualization has allowed identifying a coherent structure (i.e., the Precessing Vortex Core) at both the inner and outer shear layers resulting in a periodic

disturbance of the pressure and velocity fields. This hydrodynamic instability mode originates both single and double intermittent helical vortices wrapping the recirculation bubble. Furthermore, a rotation time scale associated to the PVC has been defined in order to identify its associated characteristic frequency.

- From a complete grid-tool parametric study carried out for gaseous premixed U-RANS cases, a well-defined mesh strategy has been established to work out this multi-scale problem. The automatic cartesian meshing algorithm together with the joint action of both fixed embedding and Adaptive Mesh Refinement have allowed capturing the critical regions of high-velocity gradients, enabling a larger base mesh size in areas where it was not required. This results in:
 - An optimisation of the use of the computational resources, since a fewer number of cells are needed to obtain similar *NMSE* values to those of traditional fixed meshes utilized in OpenFOAM®.
 - Better accuracy of the simulations carried out with the presented methodology in CONVERGE™ in terms of the *NMSE* for a given mean cell count due to an optimal mesh layout according to the flow characteristics.
- Meanwhile, in the LES framework considered in gaseous-fueled cases:
 - The AMR algorithm has proved to be able to distribute the cells in a proper way for this lean direct injection multi-scale problem. A better agreement with experimental data is obtained in the LES case with AMR both in the mean and fluctuating terms of the three velocity components through the three computed *NMSE* values. Nevertheless, it must be noted that the cost of this accuracy improvement is a moderate increase on the computational requirements both in CPU hours and in the RAM memory required when compared to LES cases without AMR.
 - LES quality and reliability of non-reactive flow has been assessed based on measures of the turbulent resolution and viscosity, reinforcing the selected turbulence resolution length scale. Such criteria confirm the validity of the AMR threshold defined to calculate the sub-grid field from the LES filtering and allows certifying the compatibility when combining LES with AMR implementation.

- The Dynamic Smagorinsky sub-grid scale model has provided the best prediction ability on both the computed time-averaged statistics and the dynamic behaviour of the turbulent flow scales when employing a sufficiently refined grid, while the non-viscous Dynamic Structure model arises as to the best option when dealing with a coarser mesh.
- Those SGS models that use the turbulent viscosity to model the sub-grid stress tensor (i.e., Smagorinsky and Dynamic Smagorinsky) have been manifested to act as a trigger of the AMR algorithm, thus producing a higher number of cells than those SGS models using an additional equation to compute the sub-grid kinetic energy (i.e., Dynamic Structure) for the same mesh strategy. The independent SGS velocity scale considered by the Dynamic Structure model modify the resolved field, and thus alleviates the sub-grid field computed by the AMR algorithm.
- Finally, the defined methodology has been satisfactorily applied to solve the reference spray fuel case both in CONVERGE™ and OpenFOAM®. In this way, the relevant phenomena associated to the liquid phase have been modelled, obtaining good agreement with experimental data. The capabilities of LISA and TAB breakup models in predicting droplet statistics (e.g., droplet velocity and size distributions) have been assessed. The TAB model together with the Lagrangian tracking formulation has been demonstrated to be able to solve the dispersed-phase field within the combustor accurately.

The outcome from the present research work is expected to be of interest to define a suitable meshing strategy for modellers in the field of multi-scale gas turbine combustors. It should be noted that, although the meshing strategy here defined has been applied for solving non-reactive cases, this methodology can be considered as a suitable ground to be extrapolated to more specific simulations involving reacting flows.

References

- [1] Yakhot, V., Orszag, S., Thangam, S., Gatski, T., and Speziale, C. “Development of turbulence models for shear flows by a double expansion technique”. In: *Physics of Fluids A* 4.7 (1992), pp. 1510–1520. DOI: 10.1063/1.858424.

- [2] Jiménez, J. and Moser, Robert D. “LES: Where are we and what can we expect”. In: *29th AIAA Fluid Dynamics Conference*. Vol. 38. 1998, pp. 1–11. DOI: 10.2514/6.1998-2891.
- [3] Blazek, J. *Computational Fluid Dynamics: Principles and Applications*. Ed. by Butterworth-Heinemann. 3rd Edition. 2015, p. 466.
- [4] Pope, S. “Ten questions concerning the large-eddy simulation of turbulent flows”. In: *New Journal of Physics* 6 (2004), p. 3. DOI: 10.1088/1367-2630/6/1/035.
- [5] Sagaut, P. *Large eddy simulation for incompressible flows: an introduction*. Springer Science and Business Media, 2006.
- [6] Celik, I., Cehreli, Z., and Yavuz, I. “Index of resolution quality for large eddy simulations”. In: *Journal of Fluids Engineering, Transactions of the ASME* 127.5 (2005), pp. 949–958. DOI: 10.1115/1.1990201.
- [7] Celik, I., Klein, M., and Janicka, J. “Assessment measures for engineering LES applications”. In: *Journal of Fluids Engineering, Transactions of the ASME* 131.3 (2009), pp. 0311021–03110210. DOI: 10.1115/1.3059703.
- [8] Huang, Y. and Yang, V. “Dynamics and stability of lean-premixed swirl-stabilized combustion”. In: *Progress in Energy and Combustion Science* 35.4 (2009), pp. 293–364. DOI: 10.1016/J.PECS.2009.01.002.
- [9] Syred, N. and Beér, J. “Combustion in swirling flows: A review”. In: *Combustion and Flame* 23.2 (1974), pp. 143–201. DOI: 10.1016/0010-2180(74)90057-1.
- [10] Cordier, M. “Allumage et propagation de flamme dans les écoulements fortement swirlés : études expérimentales et numériques”. PhD thesis. Institut National des sciences appliquees (INSA), 2013.
- [11] Cordier, M., Vandael, A., Cabot, G., Renou, B., and Boukhalfa, A. “Laser-Induced Spark Ignition of Premixed Confined Swirled Flames”. In: *Combustion Science and Technology* 185.3 (2013), pp. 379–407. DOI: 10.1080/00102202.2012.725791.
- [12] Barré, D. “Simulation Numerique De L’Allumage Dans Les Chambres De Combustion Aeronautiques”. PhD thesis. Institut National Polytechnique de Toulouse (INP Toulouse), 2014.
- [13] Patel, N. and Menon, S. “Simulation of spray-turbulence-flame interactions in a lean direct injection combustor”. In: *Combustion and Flame* 153 (2008), pp. 228–257. DOI: 10.1016/j.combustflame.2007.09.011.

-
- [14] Galley, D, Ducruix, S., Lacas, F., and Veynante, D. "Mixing and stabilization study of a partially premixed swirling flame using laser induced fluorescence". In: *Combustion and Flame* 158.1 (2011), pp. 155–171. DOI: <https://doi.org/10.1016/j.combustflame.2010.08.004>.
- [15] Yoon, C., Gejji, R., and Anderson, W. "Computational Investigation of Combustion Dynamics in a Lean Direct Injection Gas Turbine Combustor". In: *51st AIAA Aerospace Sciences Meeting including the New Horizons Forum and Aerospace Exposition* 20.0704 (2013). DOI: 10.2514/6.2013-166.
- [16] Marrero-Santiago, J. "Experimental study of lean aeronautical ignition. Impact of critical parameters on the mechanisms acting along the different ignition phases." PhD thesis. INSA de Rouen - Normandie, 2018.

Chapter 6

Spectral Analysis

“When you develop your opinions on the basis of weak evidence, you will have difficulty interpreting subsequent information that contradicts these opinions, even if this new information is obviously more accurate.”

—Nassim N. Taleb

6.1 Introduction

Once the preliminary analysis of the flow topology carried out for the gaseous-fueled (see Section 5.2) and liquid-fueled (see Section 5.3) cases has characterized the swirling flow dynamics and assessed the presence of time-evolving structures within the combustor, a more in-depth frequency-related analysis is required to a better characterisation on the dynamics of the governing helical coherent structures. In this way, the present section reports a detailed numerical study of the low-dimensional dynamics of the pressure and velocity field evolution both for the gaseous-fueled CORIA combustor (see Section 6.2) for which experimental frequency-related results are available in the literature [1, 2] and for the liquid-fueled case (see Section 6.3) for which no measurements have been published yet.

The primary motivation of this study is to develop systematic advanced mathematical procedures for the analysis of complex data sets used for comparison, validation and identification of physical mechanisms. The characterisation of non-reacting instabilities is of primary interest since one of the biggest

problems of the LDI technology is the eventual flame blow-outs and the consequent high-altitude relight from a non-reacting field. For this reason, several modal post-processing decomposition techniques such as Fast Fourier Transform (FFT), Proper Orthogonal Decomposition (POD) and Dynamic Mode Decomposition (DMD) introduced in Sections 4.4.2.1 and 4.4.2.2 are applied (according to the exposed in Section 4.4.2.3) to the gaseous-fueled and liquid-fueled (TAB Case) Dynamic Smagorinsky LES carried out in CONVERGE™. The predictive capability of these simulations was previously validated in Sections 5.2 and 5.3 where the unsteady behaviour of flow field features in the chamber and its complex interactions with the geometry was revealed.

6.2 Gaseous-fueled Case

A spectral analysis based on FFT (see Section 6.2.1), POD (see Section 6.2.2) and DMD (see Section 6.2.3) of the 3D flow field pattern is performed to capture the dominant coherent structures and confirm the occurrence of PVC in the swirler outlet region of the gaseous-fueled case.

6.2.1 Fast Fourier Transform (FFT) Analysis

The spatial distribution of the acoustic flow field for different frequencies of interest is first explored by performing the Fourier transform at a given spatial location in order to certify the energetic structures detected within the combustor and advanced in Section 5.2.3. In this research, the Fast Fourier Transform (FFT) algorithm is applied to estimate the Sound Pressure Level (SPL) following Welch's method [3]. This method involves sectioning the signal record (i.e., the fluctuating pressure and velocity fields), taking modified periodograms of these sections, and finally averaging these modified periodograms.

In FFT spectra, a signal can be described as a sum of harmonic waves of different frequency content and phase. Since the transformation assumes that the signal is of infinite length (or at least periodic), a compromise needs to be satisfied. In this way, the pressure and velocity signal should be steady (i.e., the first central moments should not vary with time) in order to guarantee a certain level of quality. In the present thesis, the mean (time-averaged) and RMS values of the velocity components were considered to judge the steadiness, concluding that 20 ms of the recorded signal are enough to achieve statistical convergence concerning the detected coherent structures.

The signal recorded at eight representative monitors (see bottom of Figure 6.1) located at the plenum, swirler, PVC, CTRZ, CRZ and the combustion

chamber further away from the PVC, is then subjected to a FFT on the pressure component (the spectra of the velocity components do not add any extra information) and represented in the top of Figure 6.1. Please note that the colouring of the streamlines is used just to distinguish the two originating planes and better appreciate how the flow mixes through the swirler and inside the chamber. The main peaks of the PVC probes occur at around 500 Hz and 1050 Hz and give good correlation with the experimental data (i.e., 507 Hz and 999 Hz, respectively) reported in the literature [1, 2]. Furthermore, fundamental harmonics of the PVC (i.e., multiples of the natural frequency of the PVC at around 1700 Hz, 2100 Hz, 2750 Hz, 3200 Hz, 3750 Hz and 4350 Hz) can be clearly identified in the spectra, dominated by the rotation time scale defined by Eq. (2.4). No definite frequency peak could be found in the rest of the probes, since minor fluctuations of swirl are recorded outside the recirculation and PVC zones (i.e., less frequency content), indicating that the most energetic coherent structures are PVC induced or derived.

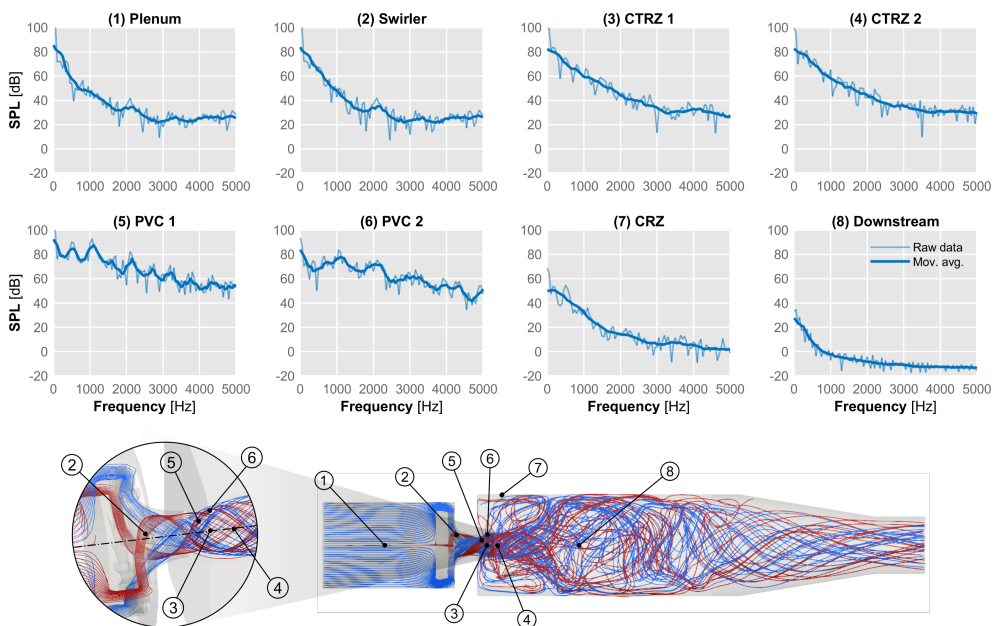


Figure 6.1: Sound Pressure Level (SPL) amplitude of the static pressure signal at eight representative locations and 3D streamlines pattern.

Additionally, coupled phenomena seem to impact the plenum and swirler producing 2100 Hz acoustic modes. The nature of these frequency peaks detected in the spectrum would need to be further investigated. Neverthe-

less, the unambiguous identification of hydrodynamic from acoustic modes¹ is rather intricate.

In Figure 6.2, the SPL of one million probes distributed at random locations through the whole domain is shown. The level of transparency indicates the overlapping of probes with a similar or coincident SPL. By applying transparency to the lines, it is possible to judge which spectra are more consistent and which spectra are more different from the rest.

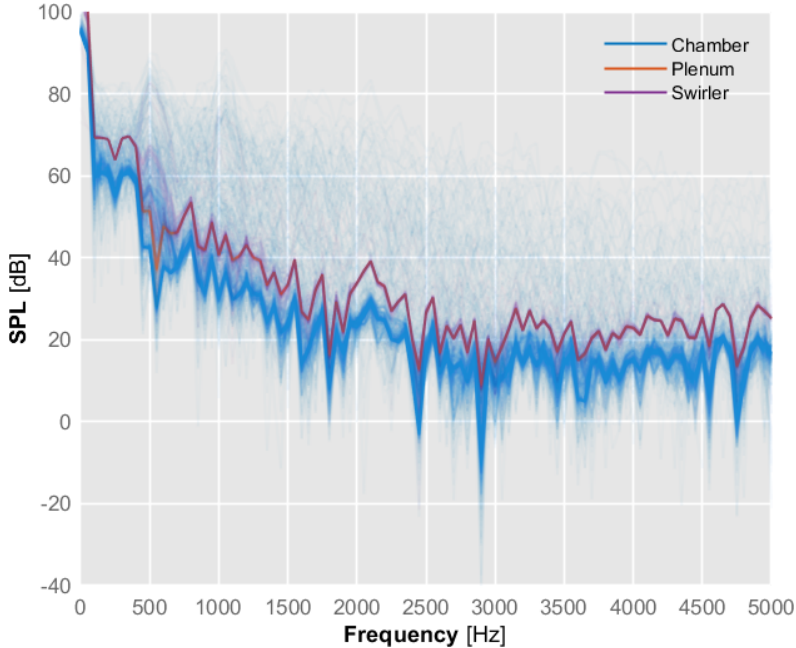


Figure 6.2: FFT amplitude of the static pressure signal recorded at 1 million random probes within the domain.

In this way, Figure 6.2 shows how the pressure spectra for the probes located in both the plenum, the swirler and the combustion chamber do resemble one another in the vast majority of the domain (except for those probes located at the PVC region with peaks in the PVC natural frequency and its corresponding harmonics), which is consistent with the elliptic nature of the

¹Note that, in the present thesis, the term *acoustic* is meant to refer directly to the total fluctuations of the pressure field and not to the acoustic field that results from splitting the pressure information into acoustic and hydrodynamic fluctuations. This is reasonable since an acoustic propagation to a possible far-field is not meaningful in this internal flow case with no combustion.

incompressible formulation of the Navier-Stokes equations. It can be seen that locations presenting spectral peaks at ~ 500 and ~ 1000 Hz are few, as denoted by their faded colour. In fact, the vast majority of the chamber features more uniformly decaying spectral signatures. These outcomes suggest that the information of the flow field fluctuations is transmitted everywhere in the computational domain almost immediately. Please note that the increased energy content in the spectra for the very low frequencies can be partly associated to the variations of the first central moments and are not conclusive given the spectral resolution of 50 Hz.

Furthermore, the spectral lines of each of the spatial points in Figure 6.2 are coloured according to their location in order to discern which are the more common spectra at each location (chamber, plenum or swirler). It can be observed that the plenum and swirler share almost the same typical spectrum, whereas the chamber features both a widely shared, non-tonal spectrum and a smaller subset of points with these ~ 500 and ~ 1000 Hz peaks. This figure exemplifies the difficulty of using just FFT to analyse the spatio-temporal behaviour of the pressure and to rank the importance of tonal noises. It also highlights how techniques such as POD and DMD can be useful in summarizing and synthesizing this information.

6.2.2 Proper Orthogonal Decomposition (POD) Analysis

Proper Orthogonal Decomposition is applied as described in Section 4.4.2.1 to obtain the orthonormal spatial modes Ψ_i (with their principal values σ_i) and their corresponding temporal evolution coefficients \mathbf{a}_i . The relevance of each mode is characterized by measuring their overall energy contribution (through the principal values) to the total energy of the snapshot matrix. As the mean pressure of the chamber is not subtracted, the first POD mode Ψ_1 is homogeneously distributed through the chamber, resulting in a singular value σ_1 that represents a high percentage of the matrix energy. Note that the mean pressure is around 100 kPa, so the acoustic fluctuations are small when compared to the mean component. Nevertheless, since the main interest of this study lies on extracting the unsteady structures within the combustor, the first mode related to the mean homogeneous pressure can be ignored. In this way, the remaining pulsating energy distribution among the subsequent modes is shown in the Pareto chart of Figure 6.3. It can be seen that POD modes Ψ_2 to Ψ_{17} gather approximately 40% of the remaining energy, with 20% being gathered just by modes Ψ_2 to Ψ_6 . Meanwhile, modes Ψ_2 to Ψ_{100} represent 80% of the remaining energy, with the rest of the modes ($\Psi_{101} - \Psi_{208}$) representing just 20% of the remaining energy.

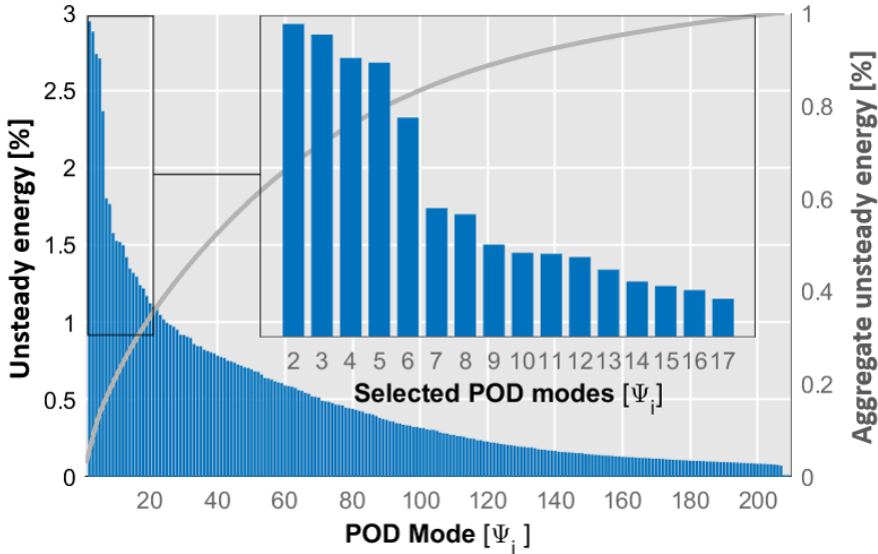


Figure 6.3: Pareto chart showing the singular values associated with POD modes Ψ_2 to Ψ_{208} and the aggregate contribution to the remaining energy after discarding the first mode related to the mean homogeneous pressure.

Besides the energy contribution of each mode, the analysis of its evolution in the frequency domain is carried out using the information contained within the time coefficients $\mathbf{a}_i = \sigma_i \mathbf{W}_i^T$. In this regard, Figure 6.4 shows the amplitude of the POD modes in the frequency domain based on normalised periodograms of right-singular vectors \mathbf{W}_i^T . The strength of the energy of each spatial mode is shown through the Power Spectral Density (PSD) function of the time coefficient associated with its corresponding mode. The high energy content exhibited by modes Ψ_2 to Ψ_6 in Figure 6.3 is here confirmed, and the spectral content of the higher-order modes (i.e., Ψ_7 to Ψ_{17}) appears nearly flat in comparison. It can also be seen how each of the most energetic POD modes (Ψ_2 to Ψ_6) only features a well-defined frequency of interest, making it possible to attribute a specific phenomenon of known frequency to each mode when combined with the analysis of the spatial distribution of the modal energy. Nevertheless, higher-order modes (Ψ_7 to Ψ_{17}) present some kind of spectral mixing with several dominant frequencies ascribed to them. Furthermore, it is interesting to note how the two dominant frequency peaks (i.e., 526 Hz and 1053 Hz) seem to have two different POD modes with the same spectrum associated. These peaks are in good agreement with the FFT results presented above (i.e., ~ 500 and ~ 1000 Hz) and the experimental mea-

surements (i.e., 507 Hz and 999 Hz, respectively) reported in the literature [1, 2].

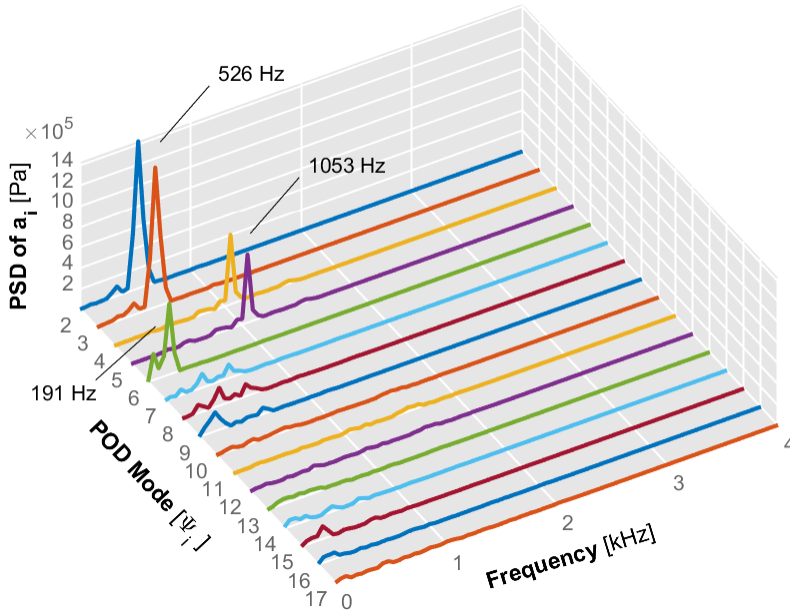


Figure 6.4: Power Spectral Density of the time coefficient associated with POD modes $\Psi_2 - \Psi_{17}$ in the frequency domain.

Finally, the spatial distribution of the POD modes can be visualized in Figure 6.5 by plotting the values of the left-singular vectors Ψ_i contained in the columns of \mathbf{U} associated with each of the reference coordinates that were selected when building the snapshot matrix \mathbf{V} . The POD modes $\Psi_2 - \Psi_{13}$ are then represented through an iso-surface of the 5% positive (red) and negative (blue) distribution of the real values of the mode $\Re\{\Psi_i\}$.

Inspecting the shapes of modes Ψ_2 and Ψ_3 in Figures 6.5 and 6.6, it is clearly seen how the higher amplitudes are oscillating in opposite sides at the periphery of the CTRZ. This single helical instability, born inside the swirler and reoriented by the mean rotating flow when entering the chamber, corresponds to the structure of the PVC defined in Section 2.2.1 and shown in Section 5.2.3. In fact, the computed frequency of 526 Hz associated to these POD modes completely matches the precession frequency of the PVC estimated by Eq. (2.4) and represented in the time evolution of the PVC (see Figure 5.10). Please note that red and blue iso-surfaces correspond to a single structure where instantaneous pressure assumes strong positive and strong

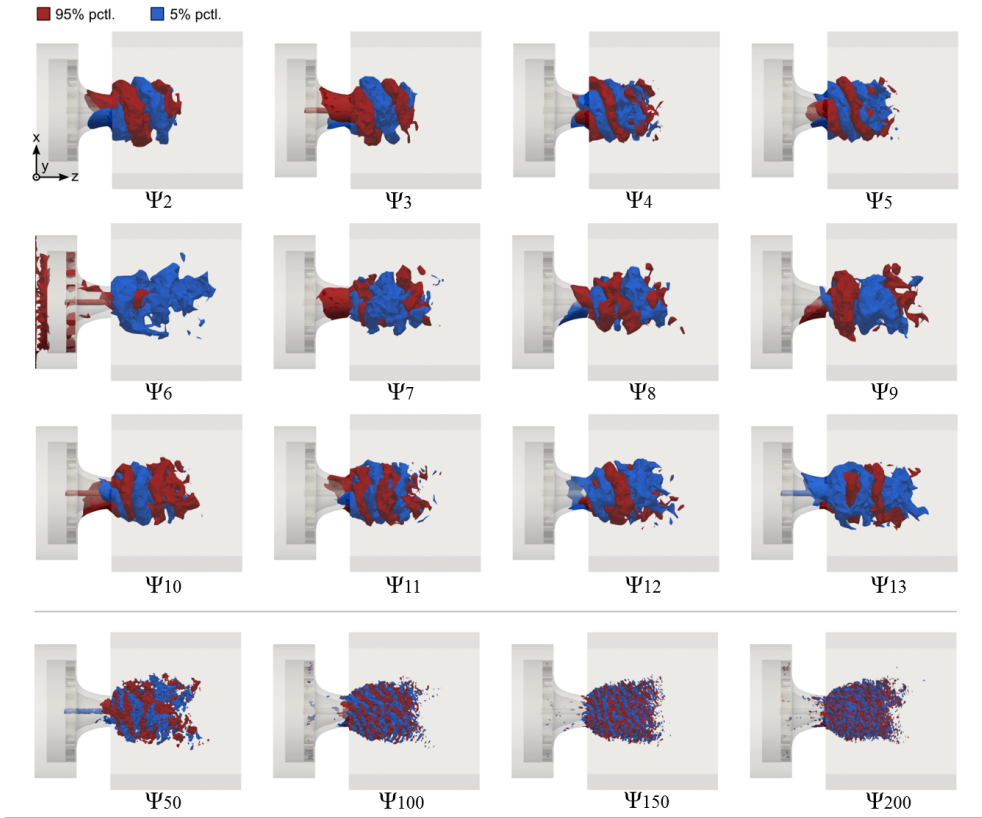


Figure 6.5: Spatial distribution of POD modes $\Psi_2 - \Psi_{13}$ and Ψ_{50} , Ψ_{100} , Ψ_{150} and Ψ_{200} within the combustor.

negative values separated by an angular distance of about π rad. Furthermore, these modes Ψ_2 and Ψ_3 resemble one another and are shifted in phase by $\pi/2$ rad (see Figure 6.6). As already observed by Oberleithner et al. [4] in a swirling jet facility composed by four tangential slots, this first pair of modes describes a travelling azimuthal wave with wavenumber $|m| = 1$ having a $\pi/2$ phase shift. For a comprehensive definition of the azimuthal wavenumber derived from linear stability analysis, the reader may refer to the work by Oberleithner et al. [4].

The next two modes (Ψ_4 and Ψ_5) in Figure 6.5 are interesting since their amplitudes are again predominantly gathered in the CTRZ, but featuring a PVC with double spiral pattern structures and twice its rotating frequency ($f = 1053$ Hz). These modes show a similar pattern to Ψ_2 and Ψ_3 but, in this

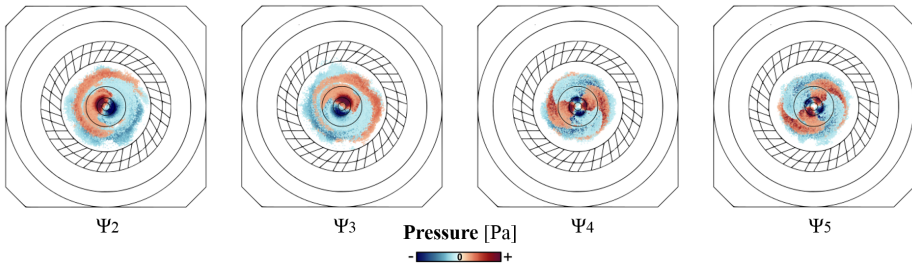


Figure 6.6: Frontal view of the spatial distribution of the first four POD modes $\Psi_2 - \Psi_5$. Both mode pairs describe rotating structures with the same frequency with azimuthal wavenumber $|m| = 1$ for modes Ψ_2 and Ψ_3 and with $|m| = 2$ for modes Ψ_4 and Ψ_5 .

case, characterised by the appearance of two vortices separated by an angular distance of about $\pi/2$ (see Figure 6.6). In such a case, the two modes seem rotated about $\pi/4$ with respect to each other, so that a travelling azimuthal wave with wavenumber $|m| = 2$ can be associated to them. The occurrence of this other coherent structure explains what was hinted in Figures 5.9 and 5.10, namely the intermittent emergence and disappearance of the branch-like structures of the PVC during the simulation. They describe coherent structures that are first growing and then decaying in the stream-wise direction. Since the angles of the two pair of modes ($\Psi_2 - \Psi_3$ and $\Psi_4 - \Psi_5$) are in a ratio of about 2 : 1 and being the azimuthal periods of the waves $|m| = 1$ and $|m| = 2$ in the same ratio, it can be established that the two pairs of modes rotate at the same frequency and that the double helix (POD modes Ψ_4 and Ψ_5) is a harmonic of the single helix (POD modes Ψ_2 and Ψ_3).

In contrast with previous modes, the maximum amplitudes of Ψ_6 are contained in a more uniform shape (see Figure 6.5). Moreover, the frequency content of this particular mode, peaking around 190 Hz (see Figure 6.4), is quite lower than the previous PVC modes. This spatial mode can be attributed to the generation of a well-defined CTRZ since its period of around 5 ms is really close to the minimum amount of simulated time that the instantaneous axial velocity component needs to be time-averaged in order to identify the CTRZ in the mean axial velocity field. Therefore, this axisymmetric fluctuation of the sixth-mode of the flow is related to the axial displacement of the vortex breakdown location and is not correlated with the identified harmonic structures.

Subsequent POD modes ($\Psi_7 - \Psi_{13}$) in Figure 6.5 present a pattern of low-frequency and low-energy coupled effects. Since the flow is not entirely

axisymmetric after passing through the 18 radial channels and emerging from the swirler, a high number of POD modes with similar but distorted shapes is expected as a consequence of the strong interaction among the unsteady PVC, the high turbulent CTRZ and the strong shear layers. Finally, higher-order POD modes (Ψ_{50} , Ψ_{100} , Ψ_{150} and Ψ_{200}) are represented to demonstrate the smaller size of these low-energetic structures and how, even so, they remain connected in a dominant spiral pattern, which might suggest potential acoustics coupling.

6.2.3 Dynamic Mode Decomposition (DMD) Analysis

As previously introduced in Section 4.4.2.2, Dynamic Mode Decomposition is a well-suited tool for an in-depth frequency analysis since it aims at grouping coherent spatial flow features into modes of a single temporal frequency, allowing the spatial morphology identification of coherent modes in highly transient regimes. Following the procedure outlined in the theoretical background, the relevance E_i of each mode is computed considering the totality of the snapshots and then normalized with $\max_i(E_i)$ to evaluate the relevance of the resulting DMD modes Φ_i .

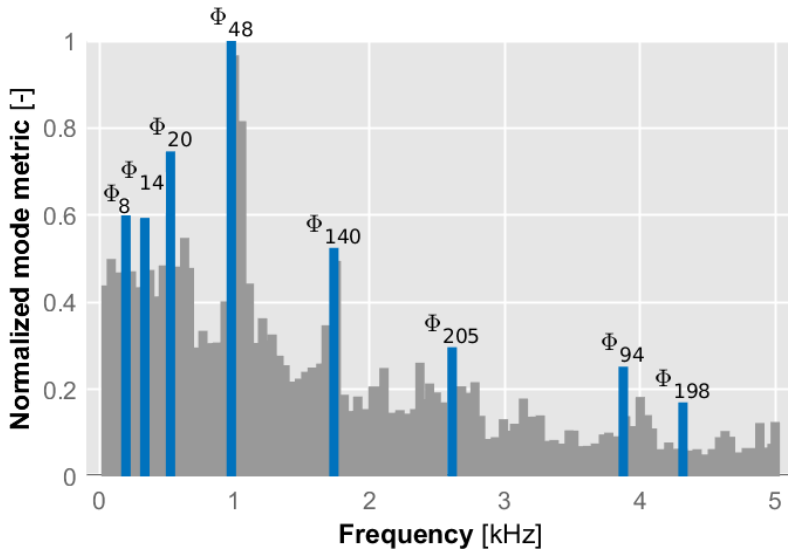


Figure 6.7: Normalised relevance $E_i/\max_i(E_i)$ of the spectrum of DMD modes, highlighting the eight most coherent modes at the frequencies of interest.

Figure 6.7 shows a chart where DMD modes have been ordered according to their associated frequency and ranked using a normalized Kou and Zhang criterion [5], highlighting the eight most coherent modes at the frequencies of interest. Furthermore, the spatial distribution of the high-energetic flow regions pulsating at these main mode frequencies is represented in Figure 6.8 by plotting the values of the left-singular vectors Φ_i contained in the columns of \mathbf{U} associated to each of the reference coordinates that were selected when building the snapshot matrix \mathbf{V}_2^N (see Section 4.4.2.2). The most relevant DMD modes according to the aforementioned criterion are then represented by iso-surfaces indicating the 2% positive (red) and negative (blue) distribution of the real values of each mode $\Re\{\Phi_i\}$.

The DMD spectrum of Figure 6.7 shows that three modes (i.e., Φ_8 , Φ_{20} and Φ_{48}) are peaking above those around them featuring oscillation frequencies of 197, 527 and 978 Hz, respectively. These frequencies are consistent with the dominant and sub-dominant frequency given by POD analysis. In fact, the spatial distributions and the modal relevance information of the dominant DMD modes (i.e., Φ_8 , Φ_{20} and Φ_{48}) represented in Figure 6.8 confirm and validate the correlations between frequency content and spatial morphology of the associated structures suggested by the POD energy ranking. Furthermore, the modes Φ_{14} and Φ_{20} seem to be located in a more compacted/confined region than the higher frequency ones, which seem to penetrate further downstream the combustion chamber and get more disordered.

As stated before, the benefit of DMD is that modes are organized in terms of a single frequency, unlike POD for which multiple frequencies are forced to be grouped together making the individual impact of a single frequency more difficult to discern. Hence, in addition to the main hydrodynamic PVC modes reported both in the POD analysis (see Section 6.2.2) and in the literature [1, 4, 6, 7], DMD here applied also allows detecting modal structures at higher frequencies, multiples of the natural frequency –527 Hz– of the PVC (e.g., 1735 Hz, 2610 Hz, 3877 Hz and 4318 Hz). Biswas and Qiao [8] have recently proposed that the higher-order modes could be related to a complex coupled mode of the whole combustor, whose longitudinal and transverse mixed modes arise at lower equivalence ratios like the ones studied in the present work. These higher modes show more spatial variation in the azimuthal direction (see the cross-sectional view in Figure 6.9), and a concomitant reduction in the scale of vortices when increasing frequency similar to the VBB harmonics modes reported in [9]. This seems to indicate a source flow phenomenon related to each individual channel of the swirler. Vortices appear to emanate from the swirler outlet region with decreasing vorticity towards the axial direction. In this way,

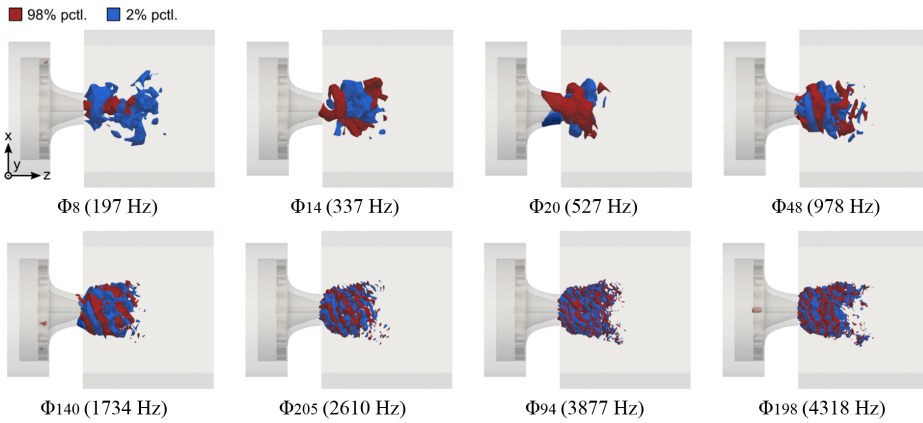


Figure 6.8: Spatial distribution of the eight more coherent DMD modes within the combustor. Each mode is represented by iso-surfaces indicating the 2% (red) and 98% (blue) percentiles of the spatial energy distribution of the real values of each mode $\Re\{\Phi_i\}$.

spiral structures with harmonically oscillating vorticity in the streamwise direction can be identified presenting a given number of branches equal to the corresponding multiple of the frequency of the first PVC mode (e.g., the mode Φ_{205} at 2610 Hz reveals 5 branches since $527 \text{ Hz} \times 5 \simeq 2610 \text{ Hz}$). This can be attributed to continued formation of shear layer vortices due to the higher shear strength of the structures emanating from each of the swirler channels and their interactions with the turbulence present in the recirculation zone.

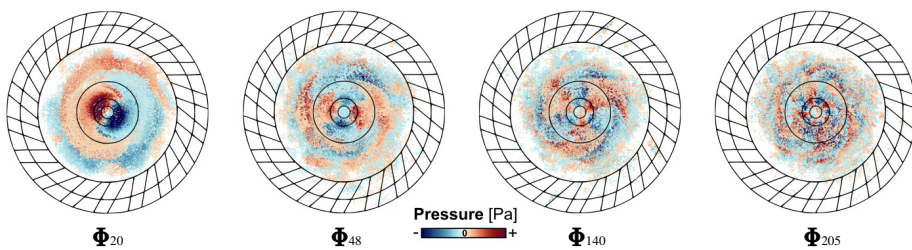


Figure 6.9: Frontal view of the spatial distribution of four DMD modes.

To close the discussion, the Strouhal numbers based on the main frequency peaks detected through FFT, POD and DMD are calculated. The Strouhal

number of a given perturbation can be evaluated through Eq. 6.1:

$$Sr = \frac{D_{ext}f}{U_{Swirler}} \quad (6.1)$$

with f being the frequency of the identified structure, D_{ext} the external diameter of the swirler exit and $U_{Swirler}$ the bulk velocity entering the combustion chamber from the swirler (i.e., the reference velocity \bar{U}^{ref}). The two peak Strouhal numbers are summarized in Table 6.1.

	PVC (1 st harmonic)				PVC (2 nd harmonic)			
	FFT	POD	DMD	EXP	FFT	POD	DMD	EXP
f [Hz]	500	526	527	507	1050	1053	978	999
Sr [-]	0.44	0.47	0.47	0.45	0.95	0.95	0.88	0.89

Table 6.1: Strouhal numbers for the main frequencies identified using FFT, POD and DMD techniques.

Regarding the Strouhal numbers found in the literature [10], a PVC is usually found for a Strouhal number higher than 0.8. Hence, the frequency of around 1000 Hz is identified as the dominant frequency of the PVC and the primary source of unsteadiness according to the FFT, POD and DMD analysis despite not having the highest amount of unsteady energy computed by POD, as shown in Figure 6.4. Therefore, the limitation of POD when attributing any physical significance to a particular frequency present in the flow-field is noted here again since some of that unsteady energy is distributed between the remaining modes instead of being grouped in a single frequency.

6.3 Liquid-fueled Case

A spectral analysis based on the POD (see Section 6.3.1) and DMD (see Section 6.3.2) techniques applied to the 3D pressure and fuel mass fraction fields is performed to the liquid-fueled TAB Dynamic Smagorinsky LES carried out in CONVERGETM to shed light and evaluate the specific influence of the dominant PVC on the spray dispersion occurred at the swirler exit region. In this section, a shorter analysis focused on the relation between gaseous structures and liquid fuel propagation is carried out since most of the particularities of the coherent structures have been already discussed in detail in Section 6.2.

6.3.1 Proper Orthogonal Decomposition (POD) Analysis

Proper Orthogonal Decomposition is applied to both the pressure and fuel mass fraction signals in order to identify some correlation between the generation of the main swirling structures and to determine its effect on the liquid fuel propagation. In this regard, Figures 6.10 and 6.11 show the amplitude of the POD modes obtained from the 3D pressure and mass fuel fraction data, respectively. Since the operating conditions of the liquid-fuel case originate a tangential velocity at swirler outlet region (see Figure 5.21) of twice the magnitude than the one manifested in the gaseous-fueled case (as shown in Figure 5.16), the rotation time scale associated to the single-helical co-rotating vortex structure (defined through Eq. (2.4)) evaluated at the combustion chamber inlet for this liquid-fueled case is estimated at $\tau_{PVC} = 1$ ms (i.e., half of the one manifested in the gaseous-fueled case), corresponding to a frequency of about 1 kHz (i.e., twice of the one exhibited in the gaseous-fueled case). Note that the frequency of this acoustic mode would also be slightly higher even if dealing with the same tangential velocity since the air temperature has been increased from 298 K to 416 K, denoting an increase of 14% in the speed of sound.

The characteristic swirling frequency of the single-branched PVC (i.e., 1088 Hz) presenting two different POD modes (modes $\Psi_2 - \Psi_3$) with the same associated spectrum is confirmed again in Figures 6.10 and 6.11. Such pair of modes are phase-shifted approximately $\pi/2$ rad both in time and space, as occurred in the gaseous-fueled case (see Section 6.2.2). Nevertheless, the intermittent emergence and disappearance of the second branch structure (i.e., modes at 2176 Hz: $\Psi_5 - \Psi_6$ in Figure 6.10 and $\Psi_4 - \Psi_5$ in Figure 6.11) associated to the hydrodynamic system is much weaker than the one exhibited by the gaseous-fueled case, and thus its associated energy content becomes practically unidentifiable when compared to the single helical instability. In experimental studies, the detection of the double helical mode has been reported to be very rare and highly sensitive even to small disturbances [11–13]. Besides, an intermediate frequency of around 1631 Hz is captured and attributed to these POD modes as a result of an eventual reduction on the rotation velocity of the second branch: both helices start separated by an angular distance of about π rad, but this gap is progressively reduced up to a given instant in which the main branch reaches and “swallows”/encompasses the secondary one. This complex coupled phenomenon has not been captured experimentally and therefore not explained yet, not even in the most recent studies reporting on a possible double helical motion [6, 14, 15]. Meanwhile, some low-frequency hydrodynamic instability modes (Ψ_6 in Figure 6.11) seem

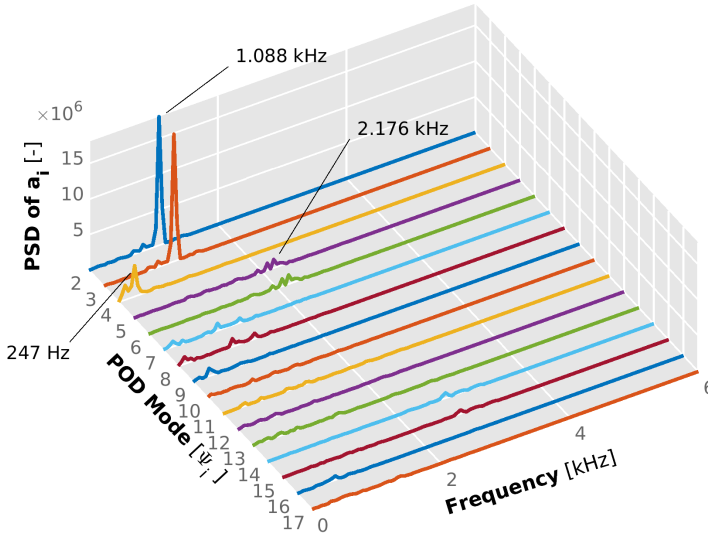


Figure 6.10: Power Spectral Density of the time coefficient associated with POD modes $\Psi_2 - \Psi_{17}$ obtained from the 3-D pressure signal in the frequency domain.

to be captured at 50 Hz, corresponding to leaking effects from the spectral resolution and the gradual slow diffusion of the fuel filling the combustion chamber, without any special physical significance.

On the other hand, it is interesting to note how the POD modes of the fuel mass fraction signal present the same dominant frequency peak than the ones extracted from the pressure signal for the spiral breakdown of the single helix PVC ($|m| = 1$). In fact, even the weaker modes ($\Psi_4 - \Psi_5$), related to the double helix PVC ($|m| = 2$), seem to exactly resemble each other for the two predicted pressure frequencies (1631 and 2176 Hz). The high correspondence between the extracted pressure and fuel POD modes is clearly confirmed in the spatial shape representation shown in Figure 6.12. Nonetheless, two subtle points should be highlighted here. On the one hand, the POD mode related to the formation of the CTRZ appears to present a higher energy content in the pressure signal spectrum (pressure mode Ψ_4) than the one exhibited for the CTRZ in the mass fuel fraction (fuel mode Ψ_6), thereby indicating a slight delay or impact of the turbulent CTRZ on the fuel droplets capture. On the other hand, the spatial distribution of mass fuel fraction modes $\Psi_4 - \Psi_5$ seems

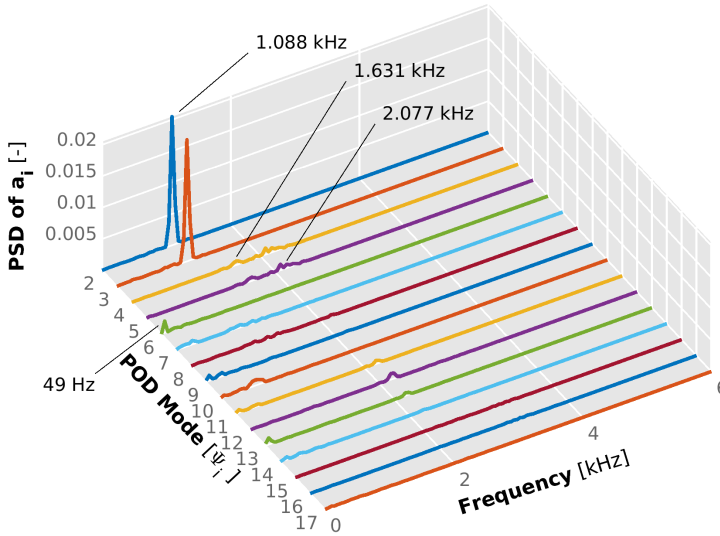


Figure 6.11: Power Spectral Density of the time coefficient associated with POD modes $\Psi_2 - \Psi_{17}$ obtained from the 3-D mass fuel fraction signal in the frequency domain.

to be more in between single and double helix than in a well-defined double helix, as seen for the pressure signal. This can be explained by the higher peak observed at the intermediate frequency of 1631 Hz by the fuel modes $\Psi_4 - \Psi_5$ in Figure 6.11 than the one reported by the pressure modes $\Psi_5 - \Psi_6$ in Figure 6.10. Last, it is important to note that modes Ψ_5 and Ψ_6 in Figure 6.11 seem to be considering some kind of fuel droplets reaching the walls and getting trapped by the corner recirculation zones. This high amount of fuel close to the walls is reasonable since it is a non-reacting case, but has been omitted in the analysis.

Nevertheless, even though the weaker gaseous structures are not observed to have an instantaneous impact on the fuel distribution, a high correlation between the Lagrangian spray dispersion and the Eulerian pressure field has been revealed, specifically with the main coherent structures generated in the near-field of interest. This is an important finding, since this observation will suggest (as anticipated from the visualisation of Figure 5.19) that it is possible to extract conclusions related to the spatio-temporal characterisation of the liquid-phase by only focusing on the analysis of the pressure data.

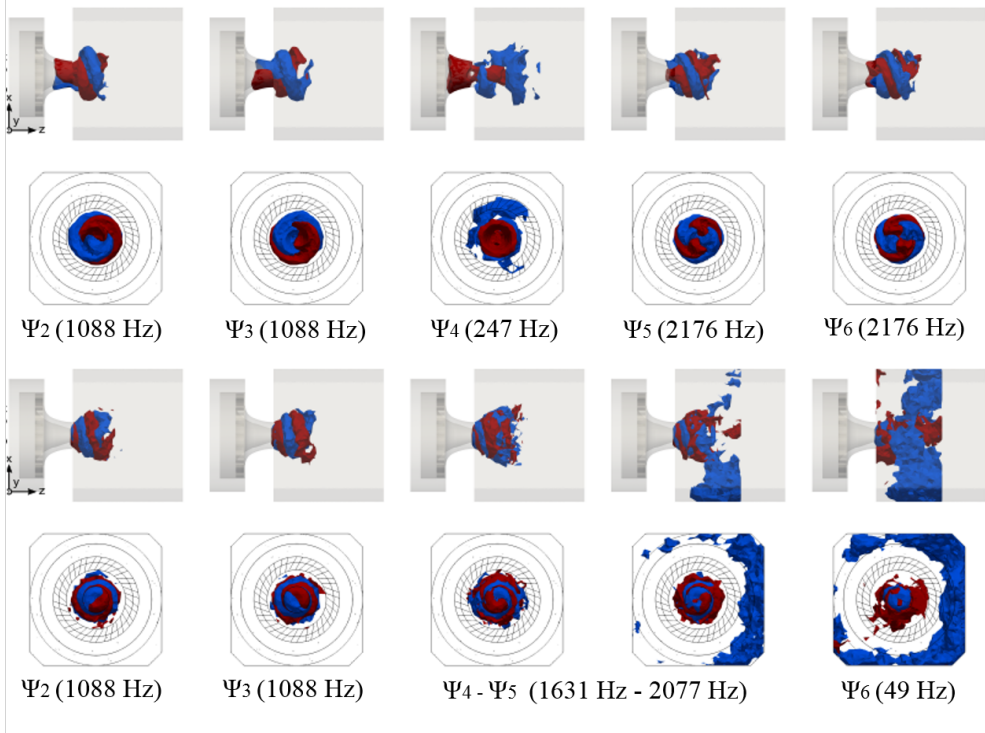


Figure 6.12: Spatial distribution of the first five pressure (top) and fuel (bottom) POD modes $\Psi_2 - \Psi_6$ within the combustor.

6.3.2 Dynamic Mode Decomposition (DMD) Analysis

Finally, the Dynamic Mode Decomposition technique is applied to the numerical spray data to further investigate the spray-turbulence interactions inside the combustion chamber. As previously done in Section 6.3.1, DMD is applied to both the pressure and fuel mass fraction signals to confirm and expand the POD analysis. In this regard, Figures 6.13 and 6.14 show the normalised relevance of the DMD modes according to their associated frequency obtained from the 3D pressure and mass fuel fraction data, respectively. Furthermore, the spatial distributions of the highlighted coherent and energetic modes at their identified oscillating frequencies are depicted in Figure 6.15.

The behaviour shown in Figure 6.15 evidences and confirms how the swirl-acoustic interactions led in the VBB and PVC oscillations play a crucial role in the way the fuel spray is internally forced by the PVC wavemaker travelling downstream the swirler and synchronized with its dominant frequency. In this

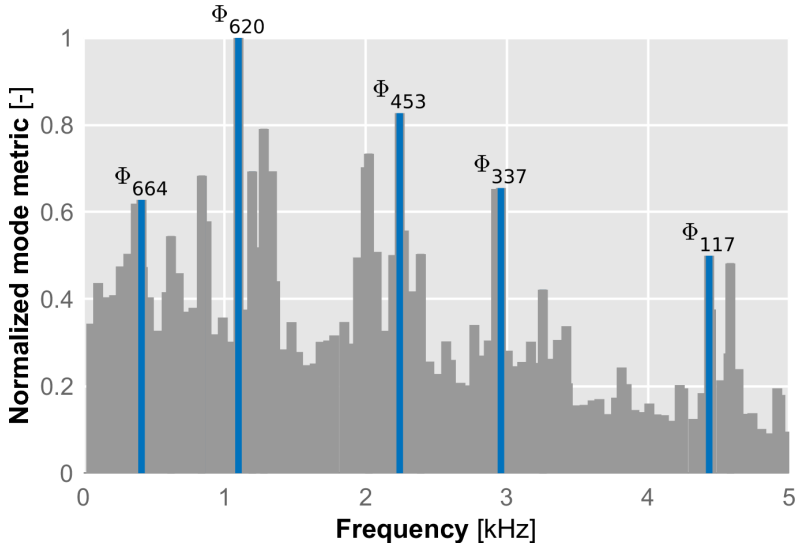


Figure 6.13: Normalised relevance $E_i/\max_i(E_i)$ of the spectrum of DMD modes obtained from the 3D pressure signal.

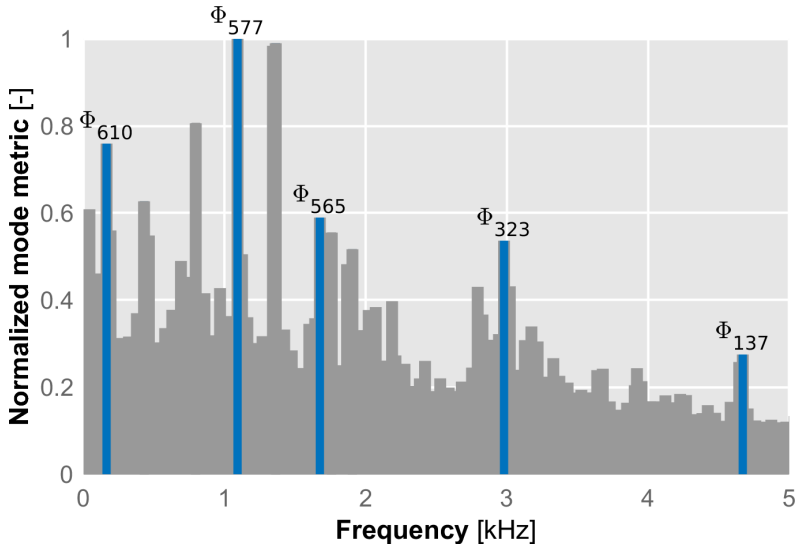


Figure 6.14: Normalised relevance $E_i/\max_i(E_i)$ of the spectrum of DMD modes obtained from the 3D mass fuel fraction signal.

way, the main single-branched PVC mode at 1105 Hz (i.e., Φ_{620} in the pressure signal) arises again as the most coherent flow structure, emerging from

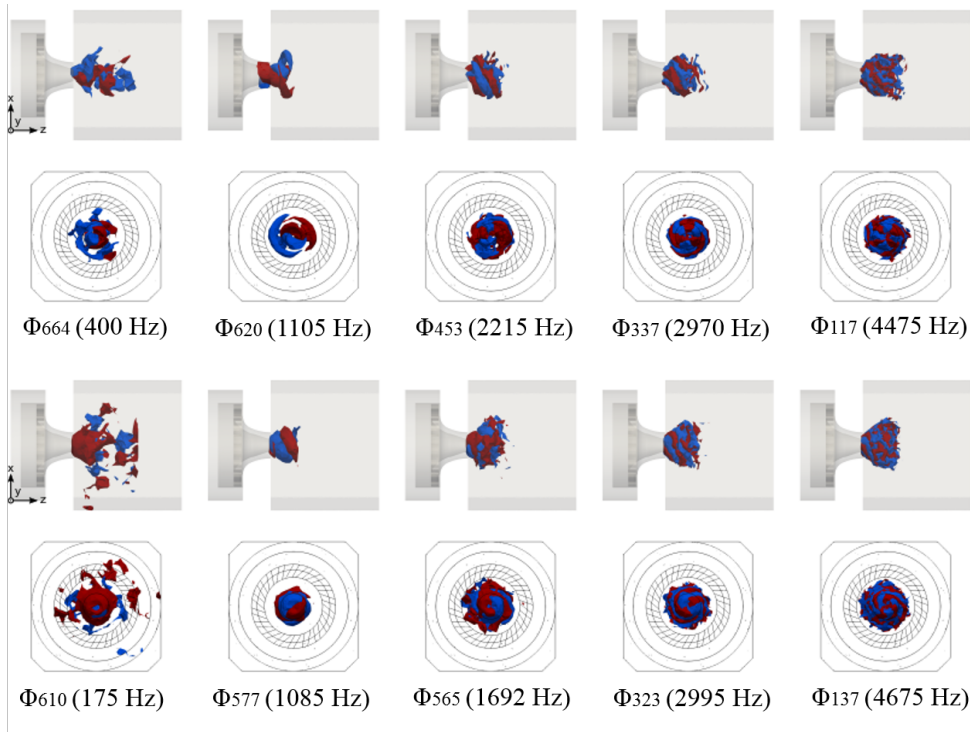


Figure 6.15: Spatial distribution of the more coherent pressure (top) and fuel (bottom) DMD modes within the combustor. Each mode is represented by iso-surfaces indicating the 2% (red) and 98% (blue) percentiles of the spatial energy distribution of the real values of each mode.

the swirler and getting twisted as soon as it enters the combustion chamber. Meanwhile, the strong analogous mode computed from the fuel fraction signal (Φ_{577}) seems to be a direct result/consequence from the aforementioned finding, since it presents the same shape but not as wrapped as the pressure mode, starting at the combustion chamber itself.

In addition, it is important to highlight that the intermediate frequency detected in the pressure POD analysis between 1000 Hz and 2000 Hz due to the intermittency between single and double helical PVC branches is not manifested here. The reason is the fact that DMD forces the grouping of coherent spatial flow features into modes of a single temporal frequency. In this way, the two different frequencies that were attributed to a single POD mode are here split, isolating and attributing the effects to a well-defined double-helical PVC rotating at 2215 Hz (pressure mode Φ_{453}). Nevertheless, according to

the mass fuel fraction spectrum of Figure 6.14, the spray distribution can be affected by this intermittency between single and double helical branches of the PVC, thus leading to the detection of intermediate frequencies between the two associated values even in DMD results (fuel mode Φ_{565} at 1682 Hz in Figure 6.14) but without presenting a clear predominant spatial distribution (see Figure 6.15). This intermediate DMD frequency in the fuel signal is consistent with the higher peak at the intermediate frequency (1631 Hz) reported on the fuel fraction POD analysis of Figure 6.11 when compared with the pressure POD spectrum of Figure 6.10.

On the other hand, one fact that draws attention is how the higher intermittency of the second branch (i.e., the higher amount of simulated time at which the second branch is present) can also lead to more distorted harmonics. Since these harmonics are a result of both the frequency of the main single-branched mode (multiples of 1105 Hz) and the double-branched mode (multiples of 2215 Hz), some mixture and blur in both the resulting frequencies associated to the harmonics and their spatial distribution can be found (mainly in the fuel mass fraction modes) due to this intermittency. In this regard, it can be observed how the pressure mode at 2970 Hz (Φ_{337}), corresponding to the third harmonic of the main pressure mode (Φ_{620}), clearly shows three well-defined branches. Meanwhile, the fuel mode at practically the same 2995 Hz (Φ_{323}) only presents two branches, being more related with the pressure mode at 2215 Hz (Φ_{453}). Nevertheless, the fourth harmonic at 4675 Hz is able to retrieve the expected four branches both in the pressure (Φ_{117}) and fuel (Φ_{137}) DMD modes. Besides, it is interesting to note how the branches seem to be more twisted in the latter, unlike the trend observed in the main mode. This is an important finding, since this observation was not possible using POD.

Finally, in addition to the PVC-like modes, a low-frequency dominant mode on the order of 175 Hz (i.e., Φ_{610}) is revealed in the DMD spectrum of the mass fuel fraction (see Figure 6.14). The interpretation of its modal structure in Figure 6.15 allows the explanation of the trends and suggests that it could be related to the transient shift of the spray edge not being affected by the dominant PVC nor by the shear layers. In fact, DMD studies of experimental liquid injection measurements recently carried out by Leask et al. [16] attributed this low-frequency mode to slow and periodic changes in the spray edge, either in the form of the spray angle increasing and decreasing, or in the form of the spray edge preferentially moving left or right. On the other hand, the low-frequency DMD mode from the pressure signal (i.e., Φ_{664} at 197 Hz) is delimited in a more uniform shape and can be attributed to the generation of a well-defined CTRZ. Please note that it presents a higher

			PVC				CTRZ
			1 st harm.	2 nd harm.	3 rd harm.	4 rd harm.	
LQ	POD	Pres.	1088 Hz	2176 Hz	-	-	247 Hz
		Fuel	1088 Hz	2077 Hz	-	-	49 Hz
	DMD	Pres.	1105 Hz	2215 Hz	2970 Hz	4475 Hz	400 Hz
		Fuel	1085 Hz	1692 Hz	2995 Hz	4675 Hz	175 Hz
GC	POD		526 Hz	1053 Hz	-	-	191 Hz
	DMD		527 Hz	978 Hz	1734 Hz	2610 Hz	197 Hz

Table 6.2: Main frequencies of the coherent flow structures of the liquid-fueled and gaseous-fueled cases identified using POD and DMD techniques. LC: Liquid-fueled Case, GC: Gaseous-fueled Case.

frequency than the corresponding CTRZ mode presented in the gaseous-fueled case for the same reason that has been explained at the beginning of Section 6.3.1. In order to synthesise the results from the techniques and facilitate the comparison among them, the associated frequencies of the main coherent flow structures identified both in the liquid-fueled and the gaseous-fueled cases through POD and DMD techniques are compiled in Table 6.2.

6.4 Conclusions

An in-depth frequency-related analysis of the non-reactive Large Eddy Simulations of both the gaseous-fueled and liquid-fueled CORIA LDI combustor have been carried out for a complete characterisation on the dynamics of the governing helical coherent structures. In this way, three approaches have been considered in order to identify the self-sustained instabilities occurring in the combustor: filtering techniques (i.e., Fast Fourier Transform - Sound Pressure Level) and modal decomposition procedures (i.e., Proper Orthogonal Decomposition and Dynamic Mode Decomposition). The implementation of these routines has allowed retrieving information about the flow dynamics and provide a systematic approach to identify the main mechanisms that sustain instabilities in the combustor. By considering the pressure information of the entire computational domain at once, including complex geometries such

as the radial swirler, the overall amplitude for each frequency has been adequately identified according to the overall unsteady energy available in the flow.

On the one hand, the pressure and velocity fluctuations have been used to compute the spectral signatures through the Sound Pressure Level (SPL) amplitude at multiple locations, allowing the detection of fundamental harmonics of the PVC in the spectra dominated by the rotation time scale. Meanwhile, the pressure spectra for the probes located both at the plenum, the swirler and the combustion chamber resemble one another in the vast majority of the geometry. This can imply coupled effects and quasi-instantaneous transmission of the pressure waves throughout the entire domain both in positive and negative axial directions.

On the other hand, the numerical identification of the main acoustic modes in the chamber through Proper Orthogonal Decomposition (POD) and Dynamic Mode Decomposition (DMD) has allowed overcoming the FFT shortcomings and understanding the propagation of the hydrodynamic instability disturbances. In this way, both the POD and DMD analyses have extracted similar flow dynamics results associated to a global self-excited oscillatory mode, namely the Precessing Vortex Core (PVC), having a single dominant frequency. This hydrodynamic instability mode results in double-helical vortices and leads to a counter-rotating co-winding helical structure located between the inner and the outer shear layer, enveloping the recirculation bubble. Furthermore, both decomposition techniques allowed detecting two distinct eigenfunctions corresponding to azimuthal wavenumbers $|m| = 1$ and $|m| = 2$, which have been found to yield a helical or double-helical breakdown mode, respectively, that dominate the dynamics of the whole flow. Thus, the flow oscillations are coherent with the dominant frequency of the global mode and, taking into account the phase shift between the decomposition results, the precession of the vortex core can be attributed to the same frequency.

In addition, the implemented DMD method has also allowed identifying some complex pulsating, intermittent and cyclical spatial patterns related to the harmonic helical branches of the PVC, not detected in previous investigations. In this way, spiral structures with harmonically oscillating vorticity in the streamwise direction have been identified presenting a given number of branches equal to the corresponding multiple of the frequency of the first PVC mode. This can be attributed to the continued formation of shear layer vortices due to the higher shear strength of the structures emanating from each of the swirler channels, opening the door to specific design modifications. Since DMD generates a global frequency spectrum in which each mode

corresponds to a specific discrete frequency, its application has been demonstrated to be more efficient than POD when dealing with temporally coherent problems. Nevertheless, the price to pay is to require a more diffuse metric than in POD, raising DMD as a less appropriate option to perform Reduced-Order-Models (ROMs) in some circumstances. Nevertheless, in the view of the results, DMD technique has proved to be a more systematic, efficient and robust tool that can give more accurate and consistent interpretations of the periodic physics underlying hydrodynamic instabilities in the Lean Direct Injection burner studied in the present investigation.

Finally, it can be concluded that both the FFT, POD and DMD techniques have successfully extracted the flow dynamics associated to the dominant global instability mode, corresponding to a double-helical precessing vortex structure. Nevertheless, the traditional bandpass-filtering technique has demonstrated to be mostly dependent on the results of a-priori PSL analysis (not known beforehand), which can be tricky. Furthermore, global acoustic responses can be easily confirmed by examining several locations along the burner, but there are high-frequency responses that can be more challenging to pinpoint. In this way, the implementation and application of POD and DMD techniques has removed most of the manual decisions linked to these traditional techniques thus allowing a complete automation of the post-processing: the mode frequencies, their respective spatial distributions and the ranking of their contribution to the total field are obtained automatically and always using the same exact criterion, with no need of user intervention or observation.

References

- [1] Cordier, M. “Allumage et propagation de flamme dans les écoulements fortement swirlés : études expérimentales et numériques”. PhD thesis. Institut National des sciences appliquees (INSA), 2013.
- [2] Barré, D. “Simulation Numerique De L’Allumage Dans Les Chambres De Combustion Aeronautiques”. PhD thesis. Institut National Polytechnique de Toulouse (INP Toulouse), 2014.
- [3] Welch, P. “The Use of Fast Fourier Transform for the Estimation of Power Spectra: A Method Based on Time Averaging Over Short, Modified Periodograms”. In: *IEEE Transactions on Audio and Electroacoustics* 15.2 (1967), pp. 70–73. DOI: 10.1109/TAU.1967.1161901.

- [4] Oberleithner, K. et al. “Three-dimensional coherent structures in a swirling jet undergoing vortex breakdown: Stability analysis and empirical mode construction”. In: *Journal of Fluid Mechanics* 679 (2011), pp. 383–414. DOI: 10.1017/jfm.2011.141.
- [5] Kou, J. and Zhang, W. “An improved criterion to select dominant modes from dynamic mode decomposition”. In: *European Journal of Mechanics, B/Fluids* 62 (2017), pp. 109–129. DOI: 10.1016/j.euromechflu.2016.11.015.
- [6] Cozzi, F., Sharma, R., and Solero, G. “Analysis of coherent structures in the near-field region of an isothermal free swirling jet after vortex breakdown”. In: *Experimental Thermal and Fluid Science* 109 (2019), p. 109860. DOI: 10.1016/j.expthermflusci.2019.109860.
- [7] Karlis, E., Liu, Y., Hardalupas, Y., and Taylor, A. “H₂ enrichment of CH₄ blends in lean premixed gas turbine combustion: An experimental study on effects on flame shape and thermoacoustic oscillation dynamics”. In: *Fuel* 254 (2019), p. 115524. DOI: 10.1016/j.fuel.2019.05.107.
- [8] Biswas, S. and Qiao, L. “Combustion instabilities of ultra-lean premixed H₂-Air mixtures by prechamber turbulent jet ignition”. In: *Journal of Propulsion and Power* 34.5 (2018), pp. 1166–1177. DOI: 10.2514/1.B36927.
- [9] Huang, C., Gejji, R., and Anderson, W. “Combustion Dynamics Behavior in a Single-Element Lean Direct Injection (LDI) Gas Turbine Combustor”. In: *50th AIAA/ASME/SAE/ASEE Joint Propulsion Conference*. Vol. 31. 0704. Cleveland, 2014.
- [10] Syred, N. “A review of oscillation mechanisms and the role of the precessing vortex core (PVC) in swirl combustion systems”. In: *Progress in Energy and Combustion Science* 32.2 (2006), pp. 93–161. DOI: 10.1016/J.PECS.2005.10.002.
- [11] Sarpkaya, T. “On stationary and travelling vortex breakdowns”. In: *Journal of Fluid Mechanics* 45.3 (1971), pp. 545–559. DOI: 10.1017/S0022112071000181.
- [12] Escudier, M. and Zehnder, N. “Vortex-flow regimes”. In: *Journal of Fluid Mechanics* 115 (1982), pp. 105–121. DOI: 10.1017/S0022112082000676.
- [13] Billant, P., Chomaz, J., and Huerre, P. “Experimental study of vortex breakdown in swirling jets”. In: *Journal of Fluid Mechanics* 376 (1998), pp. 183–219. DOI: 10.1017/S0022112098002870.

-
- [14] O'Connor, J. and Lieuwen, T. "Recirculation zone dynamics of a transversely excited swirl flow and flame". In: *Physics of Fluids* 24.7 (2012). DOI: 10.1063/1.4731300.
- [15] Vanierschot, M., Percin, M., and Van Oudheusden, B. "Double helix vortex breakdown in a turbulent swirling annular jet flow". In: *Physical Review Fluids* 3.3 (2018). DOI: 10.1103/PhysRevFluids.3.034703.
- [16] Leask, S., Li, A., McDonell, V., and Samuelsen, S. "Preliminary Development of a Measurement Reference Using a Research Simplex Atomizer". In: *Journal of Fluids Engineering, Transactions of the ASME* 141.12 (2019), pp. 1–11. DOI: 10.1115/1.4044072.

Chapter 7

Analysis of the influence of the combustor geometrical features on the non-reacting flow

*“One needs to exit doubt in order to produce science;
but few people heed the importance of not exiting from it prematurely”*

—Simon Foucher

7.1 Introduction

The present thesis aims at studying the non-reacting flow field in a Lean Direct Injection gas turbine combustor by means of Eulerian-Lagrangian Large Eddy Simulations. Once the computational tools and methodology have been presented (Chapter 4) together with computed reference gaseous and liquid-fueled cases that ensured the validation of the computational model (as shown in Chapter 5) and the proper implementation of advanced spectral post-processing tools (Chapter 6), it is time to benefit from the potential of the developed methodology through its application in preliminary design stages. Results of this study can help identifying possible areas for optimisation to LDI designs that may improve individual swirler performance and to expand

this early technology for future aircraft engines. This task is treated in the present chapter.

Fundamental research to elucidate the effect of geometric parameters on the combustor performance is of paramount importance since aspects such as the air swirler vane angle, the number of swirler vanes or the axial location of the injector fuel tip are expected to strongly affect first the flow field and atomisation/mixing phenomena, then the flame structure/response, and finally the engine efficiency and emissions. In order to carry out the analysis, a Design of Experiments (DoE) is proposed in Section 7.2 to determine the key geometrical features of the burner that could have more influence onto the flow field. Such a statistical study should also allow identifying geometric solutions that promote eventual re-ignitions in altitude from a non-reacting field after non-desired but conceivable flame blowouts.

The geometrical impact is first evaluated on the gaseous and liquid field outcomes in Section 7.3. This includes the obtaining of qualitative visualisations and quantitative characterisations of the main self-excited turbulent flow structures, which play a crucial role into the degree of atomisation (i.e., fuel droplet size distribution and size-classified velocity), spray dispersion and fuel-air mixing process. Besides, the governing precessing vortex core is quantitatively characterised through advanced modal decomposition techniques in Section 7.4. In this way, the spectral analysis can reveal how a geometrical modification can redistribute the energy between detected modes, changing its frequency, intensity and shape, and thus making some of them more important than before.

7.2 Design of Experiments (DoE)

Complex systems such as LDI burners abound in interdependencies difficult to detect and in non-linear responses. In such conditions, simple casual associations can be confusing since it is challenging both to establish the causality and to explain specific evidence by looking at individual parts. In this context, Design of Experiments (DoE) techniques may be beneficial to assess the response of the system to the modification of geometrical factors.

In order to understand the interdependences and trade-offs of various combustor parameters and to optimise the performance of the liquid spray injection (and therefore the efficiency of the subsequent combustion process), high-fidelity CFD simulations are a crucial tool. In this way, the methodology developed and validated in this thesis allows easy changes in design parame-

ters and ensures consistent and comparable accuracy in the outcomes between design iterations.

From the literature review (see Chapter 3), it is known that the performance of an LDI combustor can be impacted by a significant number of design parameters. For this study, four geometrical parameters with three different levels are considered (see Table 7.8). However, a full factorial design would lead to 81 (3^4) simulations, so a reduced set from all potential combinations needs to be selected. To this end, a robust design of calculations based on the Taguchi theory [1] is applied to systematically design a suitable set of simulations in which all the level settings appear an equal number of times.

Factor	Acronym	Level 1	Level 2	Level 3
Swirler vane angle [°]	A	30	45	60
Combustion chamber width [mm]	W	80	100	120
Number of swirler vanes [-]	S	6	12	18
Axial position nozzle tip [mm]	N	0	5	10

Table 7.1: Geometrical parameters and levels considered to conduct the parametric study (values of the baseline geometry in bold)

The Taguchi method employs a particular set of orthogonal arrays to minimise the number of experiments/simulations required to provide the full information of all the factors that affect a specific performance parameter. This method lies in deciding correctly the level combinations of the design variables for each experiment. Following this procedure, a Taguchi's orthogonal array L9 is taken to reduce the study to 9 computations, which are compiled in Table 7.2.

Therefore, the individual contribution of the number of swirler vanes, the swirler vane angle (swirl number), the combustion chamber width and the axial position of the nozzle tip into both the flow field pattern, the spray size distribution and the occurrence of instabilities in the combustion chamber is evaluated throughout nine simulations. Please note that the axial location of the nozzle tip (N) is shifted upstream of the corresponding to the reference case, so the level 3 means that the nozzle tip position is situated at $z = -10$ mm, as shown in Figure 7.1¹. It is also worth mentioning that the action of moving the injection system upstream the swirler exit region also leads to a

¹The triangles of the computational domain in Figure 7.1 do not correspond and are not related to the mesh, but to the specific surface preparation in CONVERGE™ on which the automatic meshing grid tools works.

Case	Nomenclature	A	W	S	N	Cells
1	S6-A30-N0-W4	30°	80 mm	6	0 mm	10.85 M
2	S12-A30-N5-W5	30°	100 mm	12	5 mm	13.72 M
3	S18-A30-N10-W6	30°	120 mm	18	10 mm	15.86 M
4	S12-A45-N10-W4	45°	80 mm	12	10 mm	12.63 M
5	S18-A45-N0-W5	45°	100 mm	18	0 mm	13.10 M
6	S6-A45-N5-W6	45°	120 mm	6	5 mm	16.14 M
7	S18-A60-N5-W4	60°	80 mm	18	5 mm	11.77 M
8	S6-A60-N10-W5	60°	100 mm	6	10 mm	15.93 M
9	S12-A60-N0-W6	60°	120 mm	12	0 mm	14.28 M

Table 7.2: Taguchi's orthogonal array L9 proposed to study the influence of the geometrical parameters on the non-reacting field (reference case in bold). *A*: swirler vane angle, *W*: combustion chamber width (values in the nomenclature are normalised with the external diameter of the swirler exit, $D = 20$ mm), *S*: number of swirler vanes, *N*: axial position of the nozzle tip.

change in the convergent section found immediately downstream of the swirler blades entrance.

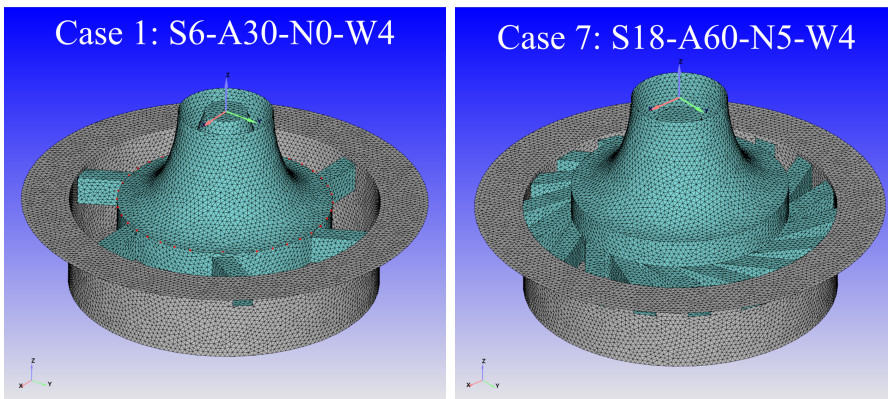


Figure 7.1: Zoom to the swirler system to illustrate the modifications in key features such as the number of swirler vanes, the swirler angle vane and the axial position of the nozzle tip.

It is important to mention that this analysis is performed on the nominal operating conditions and the meshing strategy used for the liquid-fueled reference case (case 5 in Table 7.2). On the other hand, the study of double

interactions between parameters on aggregated impacts and the effect of other factors, such as the equivalence ratio, mass flow rate, and temperature and pressure in the chamber are left for future works.

7.3 Statistical Analysis of Variance (ANOVA)

The analysis of variance or ANOVA analysis consists of a powerful statistical technique for studying the effect of one or more factors among group means [2]. The basic idea is the decomposition of the total variability observed in some data into the parts associated with each factor considered and a residual part that may include other factors not taken into account. A statistical analysis of variance (ANOVA) of the results obtained from the 9 simulations is performed to identify the individual contribution of the geometrical parameters on the designated response variables. These response variables are first defined in Section 7.3.1 and later analysed in Section 7.3.2. Then, a brief discussion about the non-linearity results is presented Section 7.3.3 in order to better define and expand the scope of the analysis of Section 7.3.2. Finally, an optimal geometrical design is proposed and evaluated in Section 7.3.4 as an example of the potential of the established methodology.

7.3.1 Definition of the response variables

A successful aerodynamic design demands knowledge of flow recirculation, jet penetration and air-fuel mixing, as well as a proper characterisation of the pressure losses of the flow across the air swirler [3]. In this way, the parameters contemplated as response variables in the ANOVA have been carefully selected and are mostly related to the size and intensity of the typical flow structures generated within an LDI combustor. Some of these variables are defined from the contours of mean axial velocity depicted in Figure 7.2 and further specified in Table 7.3 with their corresponding preferred units. From the literature review (Chapter 3), it is apprehended that the changes found between the axial and tangential velocity fields, the shape, size and intensity of the recirculation zones and the turbulence distribution end up impacting first on the atomisation, evaporation and mixing processes, and then into the subsequent flame structure, temperature distribution and emission characteristics.

The size and intensity of the large scale coherent flow structures such as the Central Toroidal Recirculation Zone (CTRZ) induced by the Vortex Breakdown Bubble (VBB), the Corner Recirculation Zones (CRZ), and the Swirled Jet (SWJ) are normalised to facilitate comparison between cases. Regarding

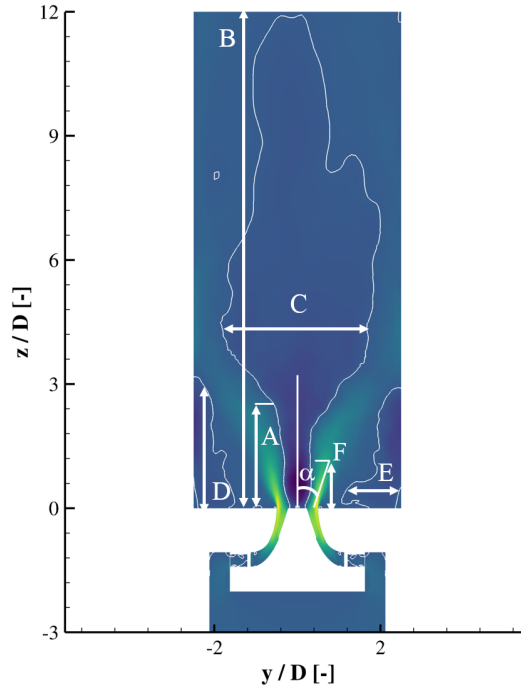


Figure 7.2: Definition of the response variables considered to characterise the self-excited structures identified through an iso-surface of zero mean stream-wise velocity

the spray characterisation, both the global drop sizes (D_{10} and D_{32}) and the spray penetration are considered in the analysis. The latter is defined as the furthest axial distance from the nozzle tip that contains the 95% of the liquid fuel mass. Finally, some critical parameters in LDI combustors such as the pressure loss² and the swirl number at the swirler exit plane are also computed as:

$$S_W = \frac{1}{R} \frac{\int_0^R \int_0^{2\pi} UV r^2 dr d\theta}{\int_0^R \int_0^{2\pi} U^2 r dr d\theta} \quad (7.1)$$

$$\Delta P_{loss} = \frac{P_{chamber} - P_{plenum}}{P_{plenum}} \cdot 100 \quad (7.2)$$

²Before reaching the combustion chamber, the air travels through the swirler, which can impose significant pressure losses together with an associated temperature change.

Label	Acronym	Meaning	Units
A	$L_{VBB,bot}$	Length of the VBB bottle-neck	[-]
B	$L_{VBB,top}$	Maximum length of the VBB	[-]
C	W_{VBB}	Maximum width of the VBB	[-]
	U_{CTRZ}^{min}	Minimum axial velocity at the CTRZ	[-]
D	L_{CRZ}	Length of the CRZ	[-]
E	W_{CRZ}	Width of the CRZ	[-]
	S_{CRZ}	Equivalent size of the CRZ	[-]
	U_{CRZ}^{min}	Minimum axial reverse velocity at the CRZ	[-]
F	$L_{SWJ}^{0.2ref}$	SWJ length with velocity 20% of reference case	[-]
α	α_{SWJ}	Half SWJ cone angle	[°]
	U_{SWJ}^{max}	Maximum axial velocity at the SWJ	[-]
	V_{SWJ}^{max}	Maximum tangential velocity at the SWJ	[-]
	S_W	Swirl number at the swirler exit plane	[-]
	ΔP_{loss}	Pressure loss of the flow along the swirler	[%]
	D_{10}	Global mean arithmetic diameter of the spray	[μm]
	D_{32}	Global sauter mean diameter of the spray	[μm]
	S_{spray}	Spray penetration (axial distance from nozzle tip)	[-]

Table 7.3: Definition of the response variables considered for the analysis of variance. The distances and velocities are normalised with the external diameter of the swirler exit and with the mean bulk velocity of the reference case at the swirler exit ($D = 20$ mm and $\bar{U}^{ref} = 70$ m/s).

where U and V here represent the axial and tangential velocity components.

7.3.2 Statistical Analysis (linear)

A first qualitative representation of the flow pattern is presented through the mean axial and tangential velocity contours of the 9 cases in Figures 7.3 and 7.4, respectively. Meanwhile, the values of the response variables considered for the 9 simulations are compiled in Tables 7.4 and 7.5. Please note that the effects of W_{CRZ} are collected in S_{CRZ} (i.e., $S_{CRZ} = \sqrt{L_{CRZ} \cdot W_{CRZ}}$). As it

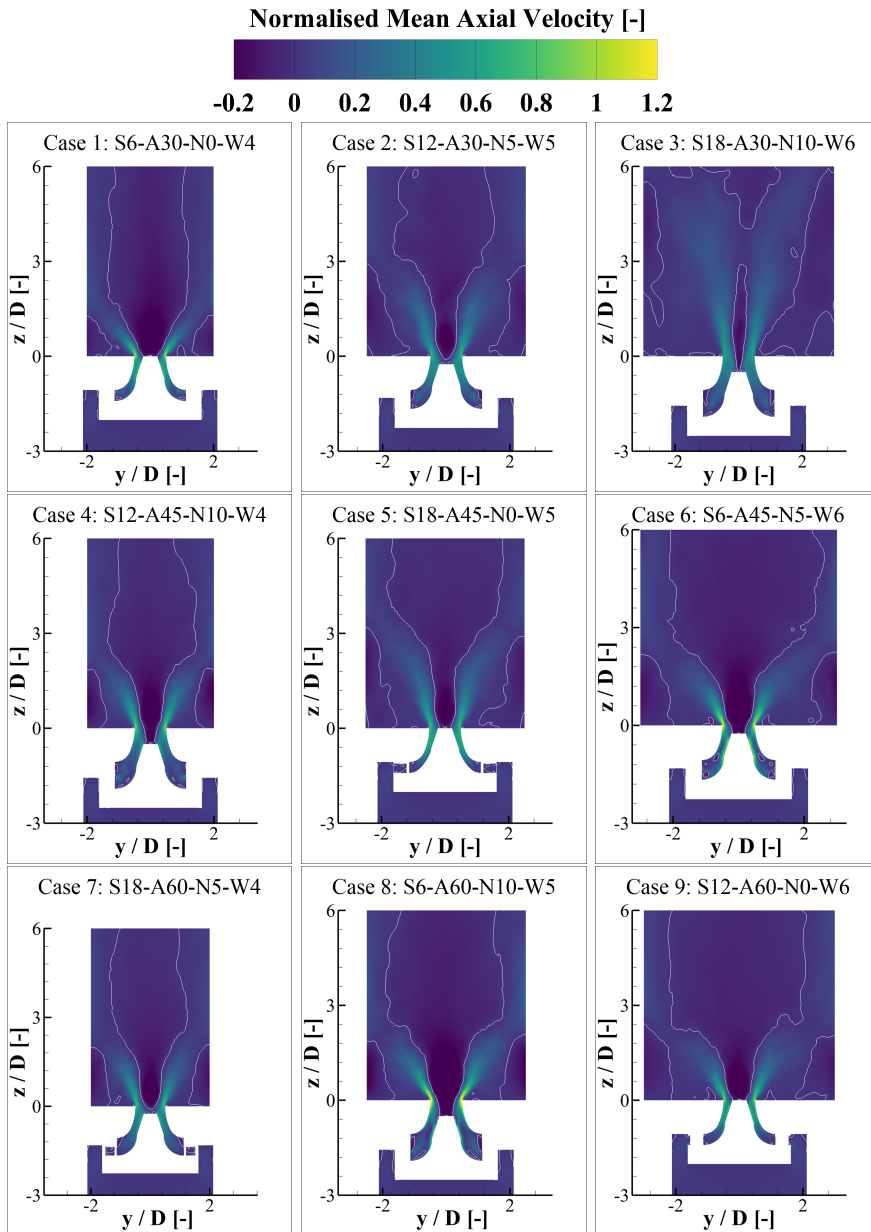


Figure 7.3: Contours of time-averaged axial velocity at 200 ms for the simulations of the L9 array. Velocity values are normalised with the mean bulk velocity at the swirler exit of the reference case ($\bar{U}^{ref} = 70$ m/s).

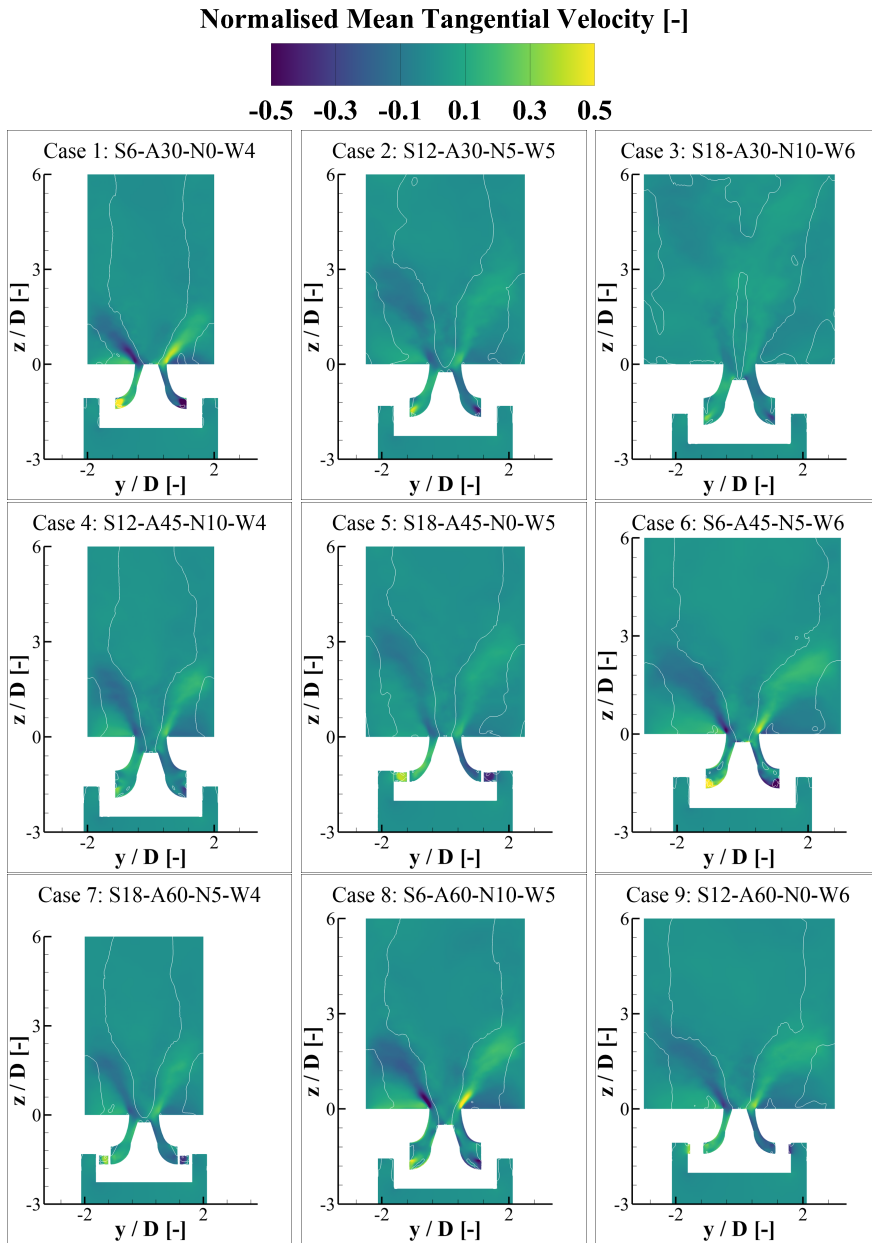


Figure 7.4: Contours of time-averaged tangential velocity at 200 ms for the simulations of the L9 array. Velocity values are normalised with the mean bulk velocity at the swirler exit of the reference case ($\bar{U}^{ref} = 70 \text{ m/s}$).

Case	$L_{VBB,bot}$	$L_{VBB,top}$	W_{VBB}	U_{CTRZ}^{min}	L_{CRZ}	S_{CRZ}	U_{CRZ}^{min}	S_W
1	1.5	17.0	2.5	- 0.35	1.3	0.93	- 0.08	1.07
2	2.1	9.1	3.3	- 0.30	2.9	1.86	- 0.07	0.78
3	0.0	2.8	0.5	- 0.18	5.9	2.97	- 0.04	0.63
4	1.9	14.8	2.7	- 0.36	1.9	1.07	- 0.13	0.83
5	2.0	11.9	3.5	- 0.30	2.9	1.94	- 0.01	0.76
6	2.2	15.8	4.4	- 0.45	2.2	1.41	- 0.04	1.14
7	2.4	12.3	2.5	- 0.35	2.0	1.22	- 0.03	0.85
8	2.2	16.9	3.4	- 0.48	1.9	1.23	- 0.17	1.11
9	2.2	15.4	4.1	- 0.36	2.4	1.38	- 0.07	1.01

Table 7.4: Values of the response variables considered for the analysis of variance for the simulations of the L9 array (1/2).

Case	$L_{SWJ}^{0.2ref}$	α_{SWJ}	U_{SWJ}^{max}	V_{SWJ}^{max}	ΔP_{loss}	D_{10}	D_{32}	S_{spray}
1	0.80	40.4	1.08	0.47	8.24	19.6	32.4	3.42
2	1.60	24.2	0.72	0.20	2.76	19.2	30.7	4.75
3	2.25	11.8	0.60	0.08	1.29	22.4	35.4	6.25
4	1.25	25.3	0.93	0.26	4.03	17.7	28.4	3.88
5	1.50	19.4	0.78	0.16	1.97	18.1	41.0	5.53
6	1.00	34.2	1.33	0.50	12.50	14.4	23.3	4.32
7	1.40	24.2	0.80	0.22	3.37	17.3	28.0	3.54
8	0.75	52.6	1.48	0.64	14.70	13.8	23.0	3.86
9	0.90	31.9	1.02	0.37	5.27	19.2	30.5	4.61

Table 7.5: Values of the response variables considered for the analysis of variance for the simulations of the L9 array (2/2).

can be observed, the shape, size and intensity of the main structures shift to some extent, thereby altering the fuel atomisation and mixing performance, and affecting the residence time within the combustion region. On the other hand, it is important to highlight that the CTRZ is not originated in Case 3, mainly because the swirl number (see Table 7.4) is below the threshold of the vortex breakdown onset (typically 0.65 in such flows [4]).

However, since three geometric parameters are modified among each pair of simulations, it would be tricky to directly attribute changes into the resulting response variables from any single parameter variation without resorting to statistical analysis. With the aim of quantifying this specific influence, Table

7.6 shows the computed ANOVA results for the maximum axial velocity of the swirled jet (U_{SWJ}^{max}) as an example of the data provided by the software Statgraphics Centurion v.18 [5]. The results shown in the table are briefly discussed below:

- The total sum of squares represents the total variability of the response variable and is calculated as the sum for all points (9) of the square of the difference of each value of U_{SWJ}^{max} (denoted as U in the following equations) minus the mean value of the 9 values:

$$SS_T = \sum_1^9 (U_i - \bar{U}_T)^2 \quad (7.3)$$

- The total degrees of freedom is the number of experiments minus one (i.e., $9 - 1 = 8$).
- The sum of squares of each geometrical factor represents the variability of the response variable due to the variation of each factor. It is obtained as the sum of three terms (since each factor is varied 3 different levels), each one equal to the difference between the mean U_{SWJ}^{max} found for that level and the mean value of the 9 cases and multiplied by the number of cases on which the average of each level has been obtained (3). So, for example, the sum of squares of the factor related to the swirler vane angle (A) is computed as:

$$SS_A = \sum_1^3 (\bar{U}_{A_{level,i}} - \bar{U}_T)^2 \quad (7.4)$$

- The degrees of freedom of each factor to be included in the model is restricted to 1 since the study is limited to analyse the principal effects without considering double interactions.
- The residual sum of squares represents the variability of U_{SWJ}^{max} that is not due to the variation of the 4 considered factors. This may be due to other factors not considered in the analysis.
- The residual degrees of freedom are calculated as the total degrees of freedom minus the sum of the different factors (i.e., $8 - 4 = 4$).

	SS	DF	Mean Square	F-Ratio	P-Value
A	0.1305	1	0.1305	12.29	0.0248
W	0.0029	1	0.0029	0.28	0.6261
S	0.4931	1	0.4931	46.44	0.0024
N	0.0028	1	0.0028	0.26	0.6362
Residual	0.0425	4	0.0106		
Total	0.6718	8			

Table 7.6: Results of the analysis of variance for the the maximum axial velocity of the swirled jet U_{SWJ}^{max} . SS: Sum of Squares, DF: Degrees of Freedom.

The ratios between each sum of squares and their degrees of freedom are denominated mean squares. Meanwhile, the mean square for the residual is an estimation of the variance existing in the experiments carried out. On the other hand, the ratios between the different mean squares and the residual mean square (F-Ratio) are distributed following a Fisher's F-distribution as long as meeting the null hypothesis that the effects on the result variable are null. On the contrary, if an effect is not null, the corresponding F-Ratio is on average greater than a Fisher's F. The null hypothesis is rejected (indicating the significance of the factor) if the F-Ratio is greater than the critical value $F(\alpha)$ obtained in tables for a predetermined α risk of the first species³.

Finally, the last column of the ANOVA analysis in Table 7.6 is the P-Value and represents the probability that a Fisher's F-distribution exceeds the value of the F-Ratio, so that:

- If the probability is equal to or greater than 0.05, the null hypothesis is met, indicating that the effect of the factor considered is not significant with a confidence level of 95%.
- If the probability is less than 0.05, the null hypothesis is rejected, indicating that the effect of the factor in question is significant with a confidence level of 95%.

Therefore, from Table 7.6 it can be inferred that the factors A (angle of the swirler vanes) and S (number of swirler vanes) have a significant statistical influence on the result variable, U_{SWJ}^{max} , with a 95% confidence (P-Value <0.05).

³ $F(\alpha)$ is the value such that the probability of being exceeded by a Fisher's F is equal to α .

Besides, the results indicate a negligible effect of the width of the combustion chamber (W) and the axial position of the injector tip (N) on the maximum swirled jet velocity.

This procedure has been performed for each of the response variables previously defined. In this way, the effect of each geometrical factor on the most representative response variables is compiled into the P-value shown in Table 7.7 and Figure 7.5. The cells in Table 7.7 are coloured depending on the degree in which the factor affects the response variable: green indicates a statistically significant influence with a confidence level of 95%, yellow denotes a considerable influence (confidence level of 90% – 95%) and white means statistically non-significant influence. Furthermore, a Pareto chart of standardised effects has been considered (not shown for the sake of brevity) to determine which factors increase or decrease the response variables. As a result, the P-values of the factors that have a negative influence are coloured in red.

At the first look at Table 7.7 and Figure 7.5, it becomes clear that the number of swirler vanes (S) and the angle of these vanes (A) have much more influence on most of the response variables than the other two geometrical factors. As it may be observed, the former is, by far, the parameter which principally influences to a greater extent the computed response variables when compared to the effect the other design parameters. Besides, as it was already observed in Figure 7.3 and here confirmed again in Table 7.7 and Figure 7.5, the VBB or CTRZ width is not significantly influenced by any geometric factor.

A closer observation of Table 7.7 and Figure 7.5 allows detecting specific pairs of response variables presenting opposed behaviour or tendency. This occurs, for example, between the size/intensity of the CTRZ ($L_{VBB,bot}$, $L_{VBB,top}$ and U_{CTRZ}^{min}) and the size/intensity of the CRZ (L_{CRZ} , S_{CRZ} and U_{CRZ}^{min}), since a larger and stronger CTRZ always leads to smaller and weaker CRZs.

It is important to highlight that, although the tendency of the response variables related to the maximum and minimum axial velocities could seem opposite to the trend expected at a first glance, it is only due to the particular way they have been defined. Since the negative sign is conserved in the minimum reverse axial velocities (as shown in Table 7.4), a negative influence means “more negative” values (i.e., stronger reverse flow). This has to be kept in mind to maintain the consistency in the following reasonings.

Another pair of response variables closely linked is the angle of the swirled jet at the swirler exit region (α_{SWJ}) and the axial distance from the swirler exit at which the SWJ velocity decreases to a 20% of the reference bulk velocity ($L_{SWJ}^{0.2ref}$). As would be expected from momentum conservation, the greater

	A	W	S	N
$L_{VBB,bot}$	0.097	0.398	0.369	0.341
$L_{VBB,top}$	0.013	0.052	0.003	0.055
W_{VBB}	0.172	0.614	0.168	0.196
S_{CRZ}	0.026	0.010	0.010	0.128
L_{CRZ}	0.022	0.007	0.006	0.038
U_{CRZ}^{min}	0.452	0.389	0.082	0.126
ΔP_{loss}	0.107	0.561	0.058	0.444
D_{32}	0.117	0.975	0.041	0.115
S_{spray}	0.073	0.012	0.020	0.687
$L_{SWJ}^{0.2ref}$	0.001	0.018	0.0001	0.004
α_{SWJ}	0.067	0.407	0.005	0.881
S_W	0.014	0.818	0.0008	0.082
U_{CTRZ}^{min}	0.013	0.450	0.006	0.973
U_{SWJ}^{max}	0.025	0.626	0.002	0.636
V_{SWJ}^{max}	0.021	0.994	0.001	0.901

Table 7.7: P -values for the defined response variables. Dark green cell: P -value ≤ 0.01 ; light green cell: $0.01 < P$ -value ≤ 0.05 ; yellow cell: $0.05 < P$ -value ≤ 0.10 . Values in red indicates that the geometrical factors have a negative influence on the response variable.

the jet angle, the lower the axial distance at which the SWJ penetrates. Please note that the same relation can be attributed to the liquid spray penetration length (S_{spray}). Besides, not surprisingly from inspection of Figure 7.3, the higher α_{SWJ} , the bigger and stronger the size and intensity of the CTRZ, with the same implications to the characteristics of the CRZ mentioned above.

Finally, a last recurrent trend between coupled variables can be highlighted: the higher the maximum axial velocity of the swirled jet at the swirler exit region (U_{SWJ}^{max}) the more significant the pressure losses undergone by the flow across the swirler (ΔP_{loss}), as expected. This strong correlation requires a trade-off in the combustor design, aiming to achieve adequate mixing and stable flow pattern with minimal pressure loss.

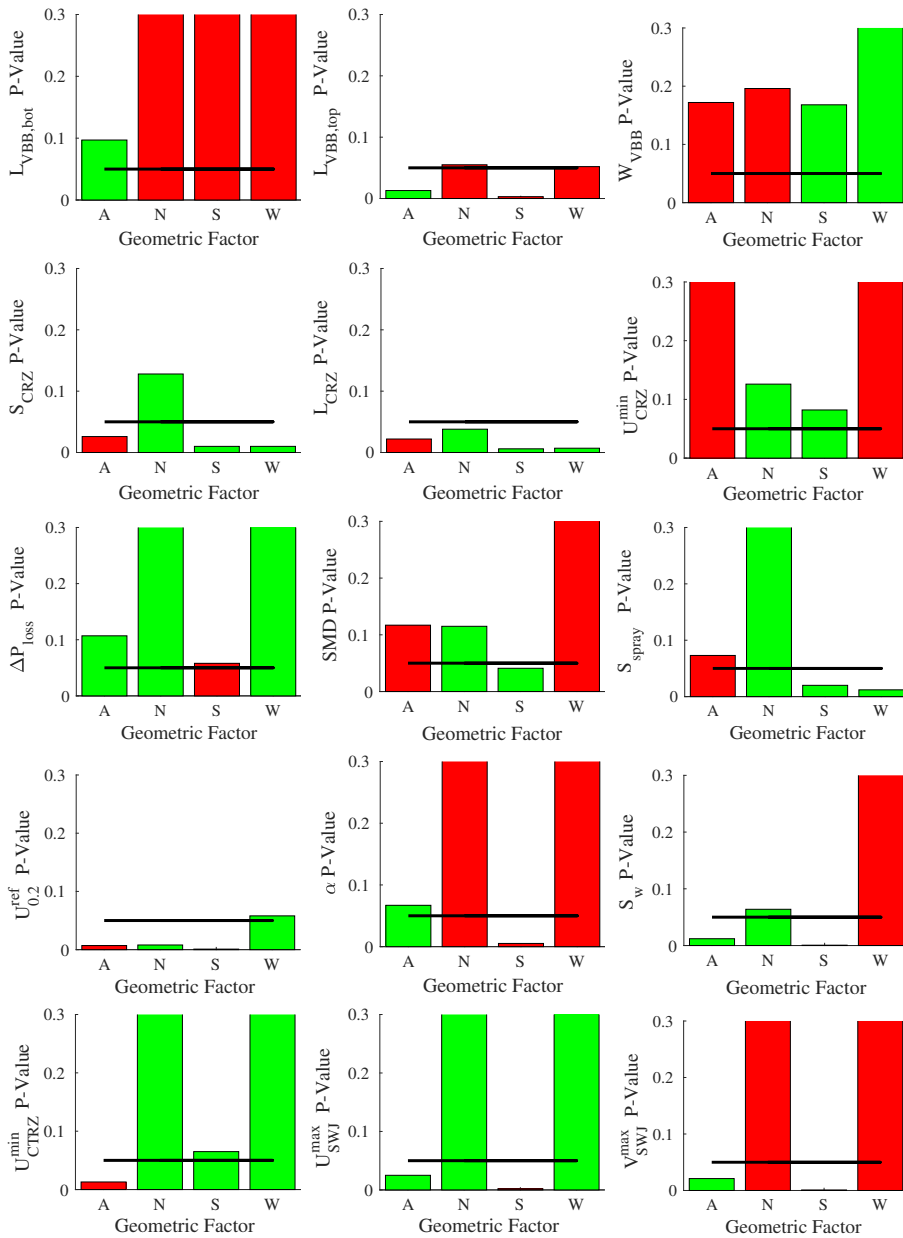


Figure 7.5: P-values for the defined response variables. Green and red bars represent positive and negative influence on the response variable, respectively. Open bars denote $P\text{-value} \geq 0.3$ and thick line means $P\text{-value} = 0.05$.

Before further analysing the Table 7.7 and Figure 7.5, it could be interesting to introduce some additional images and considerations on which to build the main discussion about the specific influence of the geometrical factors on the response variables. Since the liquid fuel is directly injected in the combustion chamber as a poly-disperse hollow-cone spray, the mixture fraction can undergo inhomogeneities due to fuel stratification that could lead to later undesired unsteady responses of the swirled flame structure. In fact, from the literature review (Chapter 3), it is well-known that self-excited combustion fluctuations generated within LDI burners are associated to spray motion variations. In order to illustrate the variation in spray parcels behaviour and mixing performance with the changes in geometry, a comparison concerning spray dispersion and the equivalence ratio field is shown in Figure 7.6. This qualitative description reveals a transition in liquid distribution among cases in line with the transition in flow states reported in Figure 7.3 and 7.4. As it can be seen in Figure 7.6, the spray pattern is sensitive to the swirl intensity and, thereby, the number of droplets detected in the centre of the hollow cone rises with increasing air swirler angle and decreasing number of swirler vanes (discussed in more detail below). On the other hand, in the opposite extreme case (i.e., Case 3, with 18 vanes at 30°), the recirculating flow patterns are not even generated, and the liquid spray cone trajectory travels practically undisturbed, thereby preventing proper atomisation and dispersion with incoming swirled air.

Let us now evaluate the influence of each geometrical parameter on the response variables from Table 7.7 and Figure 7.5, starting with the number of vanes of the air swirler (S). It is important to notice that, as the mass flow rate is preserved among experiments, the change in the number of swirler vanes directly leads to a change in the flow velocity obtained across the swirler due to the change of the total effective area. In this way, the lower the number of vanes, the higher the axial (U_{SWJ}^{max}) and tangential (V_{SWJ}^{max}) velocity at the swirler exit region. These two response variables are strongly correlated, as will be better appreciated in Section 7.3.3. Since the increase in the tangential component is produced to a greater extent (in percentage terms) than the increase in the axial one, the swirl number (S_W) is considerably increased (recall from Eq. 7.1 that S_W essentially depends on the ratio $U \cdot V/U^2$). The reduction of the number of swirl vanes also leads to a substantial increase of the swirled jet angle (α_{SWJ}), proportionally magnifying the intensity of the central recirculating zone (U_{CTRZ}^{min}), ultimately due to the increase of S_W mentioned above. As a result, the superposition of all these effects induce a lower spray penetration length S_{spray} (see its transient evolution in Figure 7.7 from which the mean values presented in Table 7.5 have been computed)

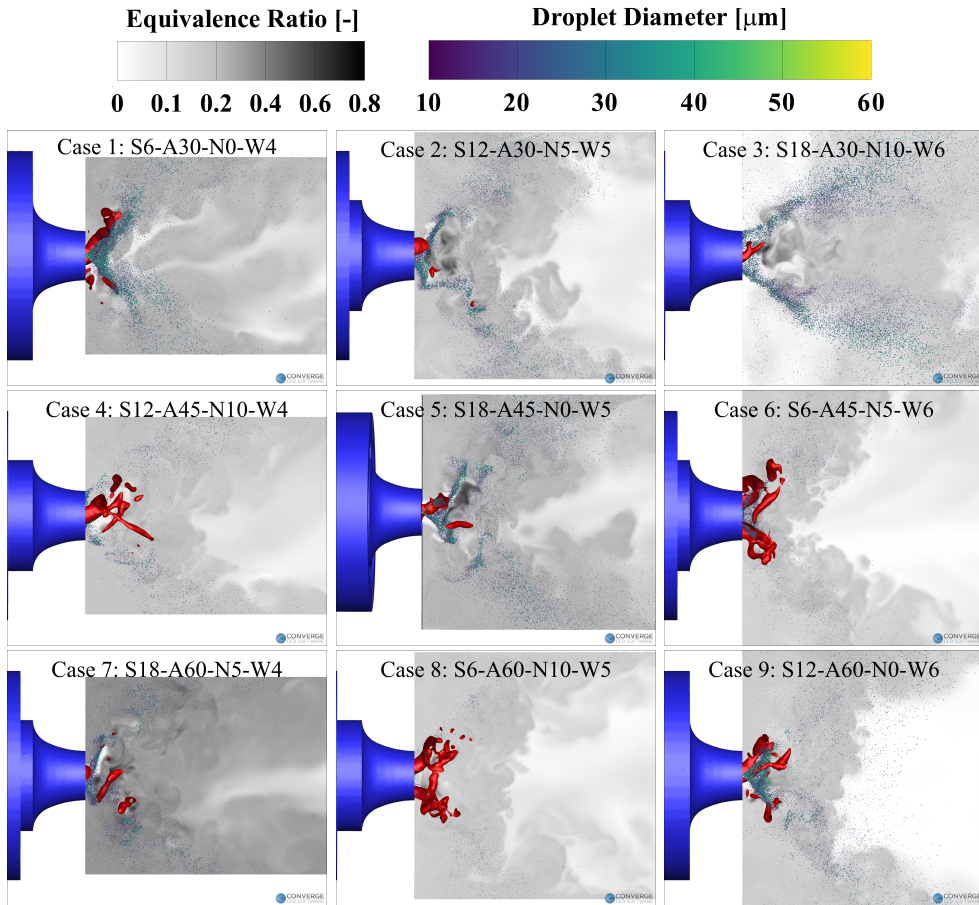


Figure 7.6: Representation of the spray pattern (instantaneous parcels), fuel reaction rate (dark-coloured) and PVC (red) at 200m for the simulations of the L9 array.

and more energetic interactions of the spray with these more turbulent flow structures, which promotes the secondary breakup and assists in reaching lower drop sizes (D_{32}). This conclusion is crucial since the injection model employed is based on a given initial distribution based on a Sauter Mean Diameter (as exposed in Section 4.3.1.2). Therefore, the disparity in the final drop sizes reached can be attributed to how the geometry is influencing in the atomisation phenomenon predicted by the TAB breakup model.

As shown in Figure 7.6, a stronger CTRZ and a faster and more uniform fuel-air mixing are confirmed in the cases presenting a low number of swirl

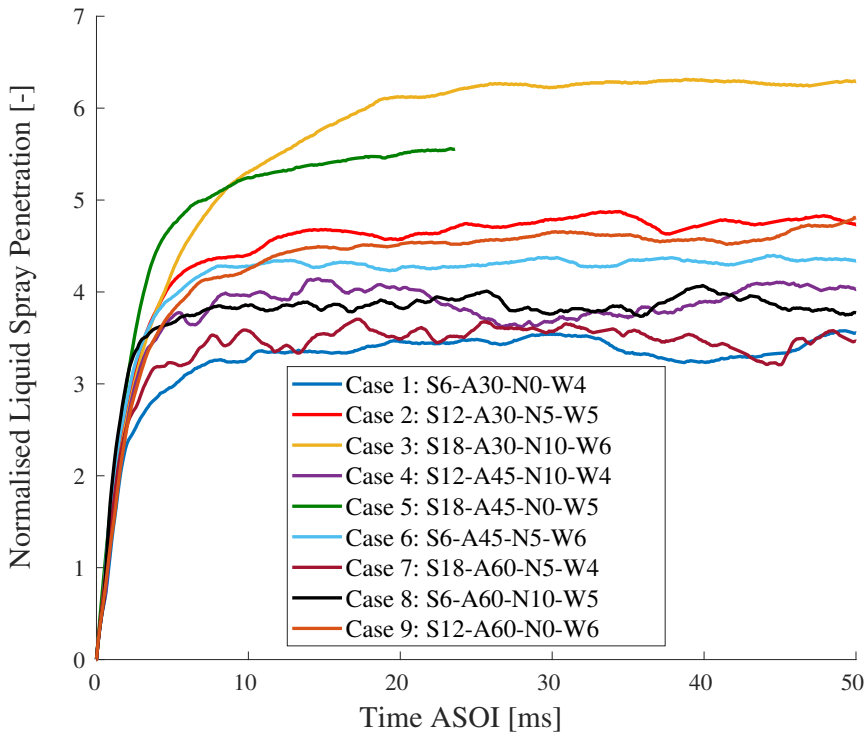


Figure 7.7: Liquid spray penetration profiles for the simulations of the L9 array. The penetration is normalised with the external diameter of the swirler exit ($D = 20$ mm). ASOI: After Start Of Injection.

vanes (Cases 6 and 8). Meanwhile, the contrary is appreciated in Cases 3, 5 and 7, as they present higher local fuel concentrations that would lead to subsequent slower-burning rates and unstable aerodynamic flames. This better spray-air interaction when decreasing the number of swirler vanes is also denoted by the reduction of $L_{SWJ}^{0.2ref}$, indicating a greater air diffusion, thereby enhancing fuel distribution.

Nevertheless, the decrease in the number of swirl vanes generally results in a significant increase in pressure losses (ΔP_{loss}). As shown in Table 7.5, the pressure drop across the air swirler can reach a 12%, as expected because of the higher velocities and smaller effective area. On the other hand, the reduction of the number of swirl blades allows increasing both the length ($L_{VBB,top}$) and width (W_{VBB}) of the VBB and, even though not statistically significant with a 95% of confidence (i.e., P-value ≥ 0.05 in Table 7.7 and

Figure 7.5), the length and width of the bottle-neck ($L_{VBB,bot}$), as it can be seen in Cases 1, 6 and 8 of Figure 7.3. Nonetheless, such a resulting large and powerful CTRZ (which has been demonstrated to affect the average residence time of fuel and burned products within the combustion zone) may not be useful or beneficial since it could retain excessively burned products and prevent or difficult their the exhaust. Furthermore, taking into account that an increase of the size and intensity of the CTRZ implies a reduction of the CRZ size S_{CRZ} and intensity (U_{CRZ}^{min}) and that an increase in the swirled jet angle means a broader radial spray dispersion, it may be possible that with a too low number of swirler vanes some unburned fuel drops are excluded from entering the primary reaction zone and even not being captured by the (small) CRZ to redirect them towards the combustion. Therefore, further research on reacting cases is required to a more consistent evaluation of the role the CRZs on the specific response variables defined for reacting cases. Only under that circumstance, it will be possible to elucidate if a trade-off between the CTRZ and CRZ is preferred instead of just maximising the CTRZ.

On the other hand, equivalent effects on the response variables to those reported above when decreasing the number of swirler vanes (S) are observed (to a lesser extent) when increasing the air swirler angle (A). In this way, the statistical ANOVA confirms that the greater the air swirler angle, the higher the maximum axial and tangential velocity at the swirler exit (the latter again to a greater extent, thereby increasing the swirl number), the wider the SWJ angle (although a higher influence on it could be expected) and the larger and stronger the CTRZ (to the detriment of the CRZ). As mentioned earlier, the characteristics of the CTRZ are deemed to have an important influence on spray penetration length while the higher swirl number results in better atomisation.

Consequently, as observed when increasing the number of swirler blades, lower air swirler angle results in larger droplets travelling further downstream along with the combustion chamber, thus leading to higher fluctuations of the local equivalence ratio (see Figure 7.6) that could promote combustion instabilities in reactive cases. Similarly, the higher the air swirler angles, the higher the pressure losses of the flow across the swirler, although not being as statistically significant (P-value = 0.107 according to Table 7.7 and Figure 7.5) as those observed when reducing the number of swirler vanes.

As far as the width of the combustion chamber size (W) is concerned, a low significant influence is generally observed on most of the response variables. On the one hand, larger corner recirculation zones are generated as the combustor size is increased. This increase leads to a slight reduction in the

size/intensity of the CTRZ. Besides, the distance at which the SWJ velocity reaches 20% of the reference is significantly increased, indicating lower and slower diffusion and turbulent mixing at the near-injection zone. Meanwhile, the SWJ angle seems to be slightly reduced when increasing the combustor size, thus involving a moderately greater axial momentum of airflow. The contribution of all these undesired effects ends up causing high spray penetration lengths, being the combustor size, in fact, the most influential geometrical factor on this response variable. On the other hand, despite not being significant from a statistical point of view on the resulting spray size, the combustion chamber width is influencing the fuel distribution, as can be qualitatively appreciated in Figure 7.6. In this way, the lower the combustion chamber width (smaller combustor), the more concentrated the fuel is in the available volume, as expected. Nevertheless, it is difficult to extract conclusions concerning fuel field patterns since this study concerns only non-reacting flow. Therefore, it precludes the characterisation of critical reacting factors such as the lower flammability limit or the flame extent, which are deemed to be crucial requirements to determine the optimal chamber dimensions.

Finally, regarding the axial location of the spray injector tip (N), it is worth recalling that the action of moving the injection system upstream the swirler exit region also leads to a change in the convergent section found immediately downstream of the swirler blades entrance. The more the injection system is shifted upstream, the greater the undiscovered effective section (see Figure 7.3), and therefore the slower the flow velocity achieved across the swirler in a similar way to the aforementioned effect when increasing the effective area with the number of swirler vanes. In addition, the displacement of the injector also modifies the swirler outlet discharge section to the combustion chamber (at $z/D = 0$), going from a ring 20 mm and 9 mm of external and internal diameter, respectively, to merely a circular section of $D = 20$ mm (see Figure 7.3). Consequently, it is necessary to separate these possible coupled effects in order to identify the original cause behind the influence on the response variables.

As it can be seen in Table 7.7 and Figure 7.5, moving the injection system upstream of the swirler exit region produces an increment in the size of the CRZ and therefore a reduction in the VBB and the CTRZ. Since it presents the same tendency as the one observed when increasing the number of swirler blades, the increment in the passage section immediately downstream of the swirler blades entrance can be attributed as the cause.

Otherwise, even though the nozzle displacement does not seem to have an evident influence on the maximum axial and tangential SWJ velocities,

a particular impact is observed on the computed swirl number. This slight decrease in the swirl number when moving the spray injection tip upstream is due, therefore, to the change in the swirler discharge section discussed above. Please note that the swirl number presented in Table 7.5 is calculated by integrating along the radial distance of this discharge section at $z/D = 0$ (see equation 7.1). The reader is referred to Figure 7.8 for further comprehension about the evolution of the swirl number computed at several axial locations from the air swirler inlet ($z/D = -2$) up to the discharge into the combustion chamber entrance ($z/D = 0$). This illustrates the deviation in the behaviour experienced by the flow across the swirler with respect to the reference case.

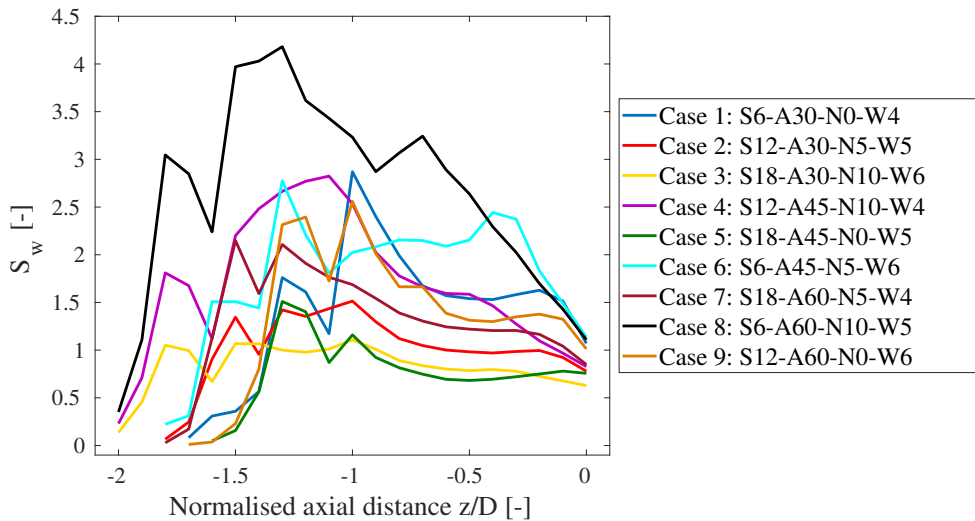


Figure 7.8: Evolution of the Swirl Number along the swirler. The axial length is normalised with the external diameter of the swirler exit ($D = 20$ mm).

Finally, it can be observed how shifting the location of the nozzle tip upstream can have a beneficial effect on the resulting spray atomization, despite not being significant from the statistical point of view. As stated early, the swirl number slightly decreases when shifting the injection position upstream, so the cause for the higher degree of atomisation (smaller D_{32}) can be found in the larger distances (higher residence time) that the liquid sheet will have to interact with the flow structures. Since the flow structures are not quite influenced by the nozzle tip location, it could seem that moving it upstream as much as possible is beneficial. Nevertheless, a trade-off could appear at real-engine operating conditions since displacing it too much upstream would

imply abandoning the direct injection strategy itself, tending to partially pre-mixed combustion, which could suppose the apparition of flashback with the consequent damage to the swirler structure.

7.3.3 Discussion about non-linearity on the response variables

A brief discussion about the non-linearity results is here presented in order to better define the scope of the ANOVA analysis exposed in Section 7.3.2. The ANOVA analysis has been valuable to identify and quantify the specific global influence of the geometrical factors on the response variables, but at the risk of precluding/masking specific trends of the outcomes with the geometry levels.

Therefore, some examples of the dispersion results of several response variables are presented in Figure 7.9 in an attempt to overcome the aforementioned limitations related to the linear assumptions and to shed some light for a better interpretation of the non-linear behaviour. The reader is referred to Appendix A for the complete set of dispersion results concerning both the whole response variables and design factors. These dispersion graphs allow important observations in how a key response variable changes when the values of each factor are modified.

On the one hand, the dispersion results reinforce some of the reasonings of the ANOVA analysis. For example, as it may be appreciated on the first row of images in Figure 7.9, the variability (increase) of the maximum tangential velocity component at the swirler outlet region (V_{SWJ}^{max}) when reducing the number of swirler vanes (S) is confirmed to be produced to a greater extent (in percentage terms) than the increase in the axial one (U_{SWJ}^{max}), thus resulting in the aforementioned considerable increment of the swirl number (S_W). Besides, the strong correlation highlighted from the P-values in Section 7.3.2 between both U_{SWJ}^{max} , V_{SWJ}^{max} , and U_{CTRZ}^{min} (please recall the sign convection for reverse axial velocities) can be here better appreciated.

On the other hand, the dispersion scatterplot can also be helpful to clarify and expand the conclusions obtained from the statistical analysis. As discussed in Section 7.3.2, the reduction of the number of swirler blades (S) allowed increasing the length ($L_{VBB,top}$) of the VBB, but the P-value results attributed a not statistically significance (with a 95% of confidence, i.e., P-value ≥ 0.05 in Table 7.7 and Figure 7.5) to the width of the VBB (W_{VBB}) and the length of the bottle-neck ($L_{VBB,bot}$). Nonetheless, as it can be seen in the second row of images in Figure 7.9, even though the low influence of the number of swirler vanes on W_{VBB} is reinforced, the low influence regarding the $L_{VBB,bot}$ (also applicable to intensity of the corner recirculation zones

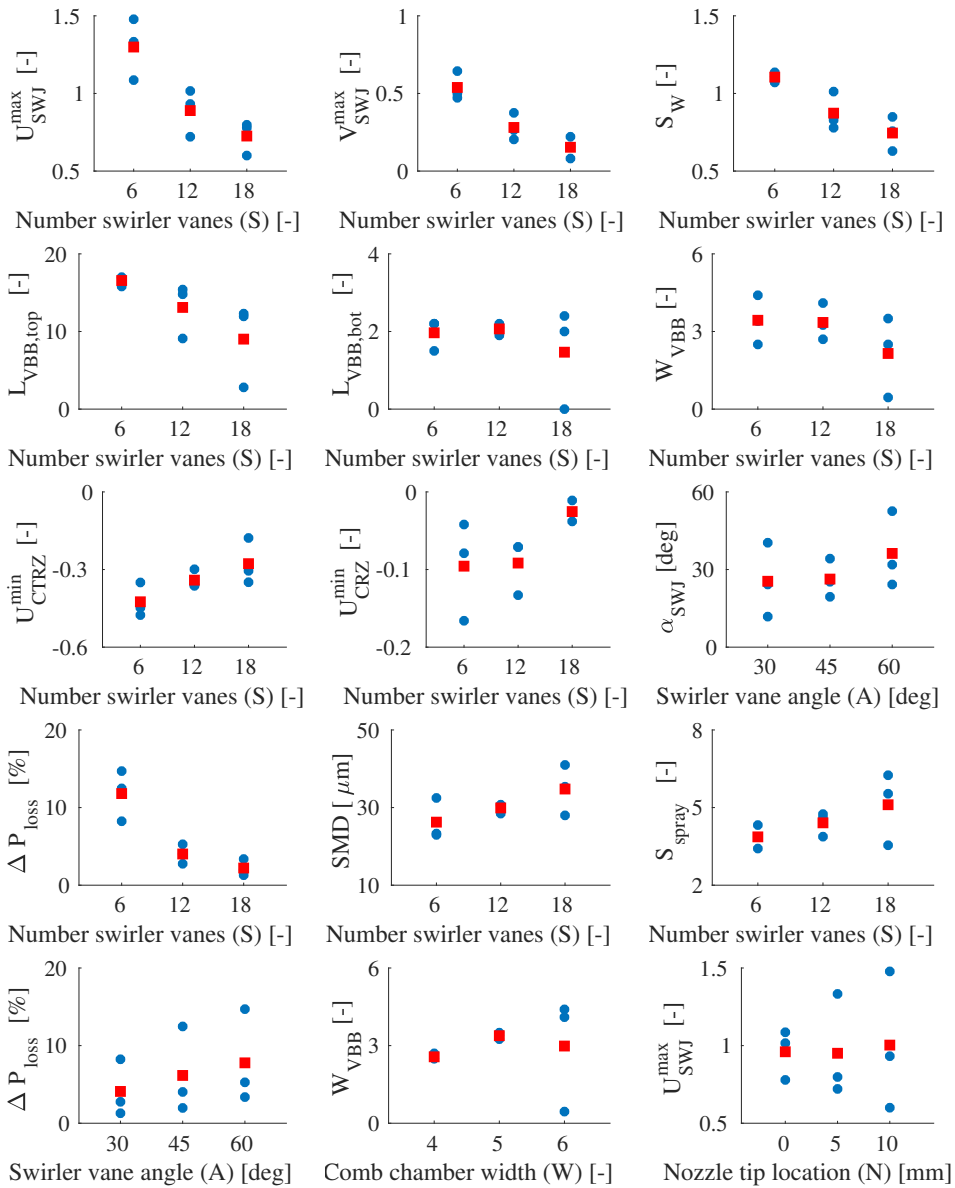


Figure 7.9: Dispersion values of some example response variables as a function of a given design parameter. Blue circles: the values of the response variable for each of the 9 simulations. Red squares: average of the 3 values for each level of the considered geometric factor.

U_{CRZ}^{min}) is more inconclusive since the high spread induced by the exceptional value of Case 3 appears to be masking the trend and leading to misleading P-values⁴.

A similar conclusion can be extracted from the dispersion pattern of the W_{VBB} with respect the width of the combustion chamber (W). A distorted result was displayed in the ANOVA results (P-Value of 0.64) because of the low value presented in Case 3. Nevertheless, Figure 7.9 manifests an apparent growing trend with the combustor width but moderated by the value of Case 3. This makes it evident that detailed observation of these complementary results (see Appendix A) is prudent and necessary to reveal key design parameters not detected as statistically significant at a first glance but that so far from reality are being decisive on the response variables.

Similarly, the influence highlighted and discussed in the ANOVA analysis about pressure losses with the number and angle of the swirler vanes is here confirmed: the higher the air swirler angles (A), the higher the pressure losses of the flow across the swirler (ΔP_{loss}), although not being denominated as statistically significant by the ANOVA (i.e., P-Value = 0.107) as those observed when reducing the number of swirler vanes (S). Besides, the higher the number of vanes the lower the non-linearity and the less critical the variation between levels, to the point where little reductions in pressure losses are reported for the cases concerning 18 swirler blades with respect its homologous of 12 vanes. This fact, together with the significantly worst degree of atomisation and spray penetration reported when increasing the number of vanes (see the SMD vs S and S_{spray} vs S plots in Figure 7.9), gives an initial conception of a possible way toward a potential trade-off optimisation between pressure losses and atomisation performance.

Furthermore, the dispersion results can be useful to reinforce the conclusions about the possible coupled effects originated when shifting the axial location of the spray injector tip (N) in order to identify and associate the original cause⁵ behind the influence on the response variables. In this way, the observation of (for example) the patterns concerning the maximum axial velocity at the swirler outlet (U_{SWJ}^{max}) can be compared between the number of swirler (S) and axial position of the nozzle (N) to dilucidate and better attribute the specific causality (e.g., the 3 points corresponding to those cases with 6 swirler vanes are explicitly revealed).

⁴Recall that the VBB/CTRZ is not generated in Case 3.

⁵Please recall that the action of moving the injection system upstream the of swirler exit region also leads to a change in the convergent section found immediately upstream of the swirler exit.

7.3.4 Multiple Response Optimisation

Finally, a Figure of Merit (FoM) [6] or a Cost Function (CF) [7] could have been derived from the analysis here presented in an effort to quantitatively characterise the performance of the LDI combustor towards an optimal design trade-off. Nevertheless, these quantities would have needed to consider additional contributions related to specific response variables defined for reacting cases such as combustion efficiencies and/or even NO_x emissions levels, which would have definitely affected the weighting factors in case of being defined from this study concerning non-reacting flow. Therefore, since the FoM/CF would be highly sensitivity to these calibration factors, their definition through regression algorithms is left for future works.

On the other hand, a faster Multiple Response Optimisation (MRO) analysis [8] can be performed to obtain a trade-off design to maximise/minimise the desired response variables. This is done by constructing a desirability function, based on the values of the response variables, which is then maximized. Nonetheless, this analysis would present the same aforementioned limitations: the selection of the response variables from an incomplete knowledge of a reacting field and the high sensitivity of the calculated optimal solution to the user-defined weights or desirability factors applied to each response variable (e.g., would it be beneficial from the point of view of the flame stability to have the stronger CTRZ as possible or would it be more beneficial to have a compromise between CTRZ and CRZ sizes and intensities taking in mind their opposed trends?). In order to illustrate the applicability of a MRO, two different possibilities are proposed:

- Optimal Case 1: To maximise the degree of atomisation (i.e., minimise the SMD) while minimising the pressure losses (assuming equal weights and impacts).
- Optimal Case 2: To maximise both the degree of atomisation and the size/intensity of the CTRZ, while minimising the pressure losses (assuming pressure losses weights to be double of the other responses).

The optimal design resulting from these two MRO analysis is presented in Table 7.8. Nevertheless, the superposition of the mentioned limitations together with the linear assumptions on how the effect of each factor on each response is estimated [8] can reduce the consistency of the conclusions that can be drawn.

Factor	Ref. Case	Opt. Case 1	Opt. Case 2
Swirler vane angle [°]	60	60	60
Combustion chamber width [mm]	100	83	80
Number of swirler vanes [-]	18	18	13
Axial position nozzle tip [mm]	0	9.7	2.9

Table 7.8: Geometrical parameters values of the optimal cases resulted from two Multiple Response Optimisation (MRO) analysis

7.4 Spectral Analysis

A spectral analysis is finally conducted to the L9 array in order to complete the previous discussion through a quantitative characterisation of the governing large-scale coherent structure within the LDI burner: the Precessing Vortex Core (PVC). An in-depth definition of the PVC is crucial since, as exposed in Section 2.2.1, its self-excited generation can provoke thermoacoustic oscillations and modulate the fuel distribution, thus altering the combustion process (e.g., the location of the flame front). Besides, the characterisation of the PVC in non-reacting cases is justified since it has been demonstrated to reappear after being suppressed at low equivalence ratios due to the coupling of swirled flames with acoustic modes [9].

As derived from Chapter 6, the Dynamic Mode Decomposition (DMD) would be a suitable technique to analyse more in detail the broad spectrum of main modes and harmonics present in the combustion chamber. Nevertheless, the DMD outcomes are highly sensitive to the specific criterion considered to sort the energy content of the modes. Moreover, several different modes can be detected close around of the frequency of interest. This fact can hinder the application of a uniform criterion to consistently detect the modes in a parametric study. On the other hand, since POD aims at grouping and automatically ranking the most energetic modes in a straightforward procedure, a more consistent criterion can be selected to compare the results between cases (see Section 4.4.2). Therefore, the POD technique is chosen in this particular case to gain further understanding on how the geometrical modifications can activate determined PVC modes, thus affecting its frequency, intensity and shape.

In this way, following the procedure shown in Sections 6.2.2 and 6.3.1, the energy contribution and spatial distribution of each POD mode have been obtained from the instantaneous 3D pressure field⁶ for the simulations of the

⁶Please recall the high correlation revealed in Section 6.2.2 between the Lagrangian spray

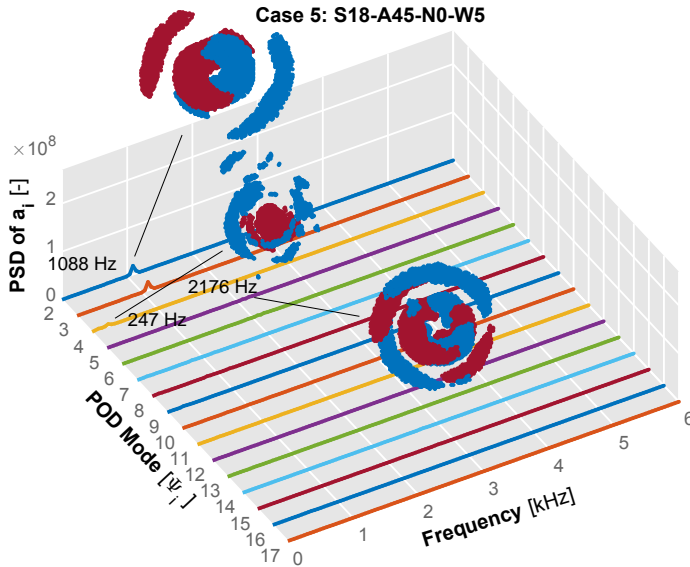


Figure 7.10: Power Spectral Density and spatial distribution of the time coefficient associated with POD modes $\Psi_2 - \Psi_{17}$ obtained from the 3D pressure signal for the reference case.

L9 array (see Figures 7.10 and 7.11). Besides, both the frequency and intensity/amplitude of the detected modes have been compiled in Table 7.9 for a quantitative comparison between cases. Please recall from Section 4.4.2.1 that the values σ_i represent the contribution of each orthonormal spatial mode Ψ_i to the total energy of matrix [10]. For this reason, they have been selected as a response variable to quantify the relevance of each POD mode on the total flow field.

As it can be observed in Figure 7.11 and Table 7.9, the changes in key design parameters produce substantial impacts on the energy spectrum due to the way that the hydrodynamic modes interact and couple with the acoustic ones. Generally, the dominant PVC mode corresponding to the single-helical PVC structure (1st harmonic) is in the 1.1 - 2.2 kHz range, whereas a 2.1 - 3.6 kHz range is detected in those cases where the double helix PVC (2nd harmonic) is manifested. It is important to note how the energy content in Cases 6 and 8 (and 3 to a slightly lesser extent) is much more intense than dispersion and the Eulerian pressure field, specifically with the main coherent structures generated in the near-field of interest, allowing to extract conclusions related to the spatio-temporal characterisation of the liquid-phase only focusing on the analysis of the pressure data.

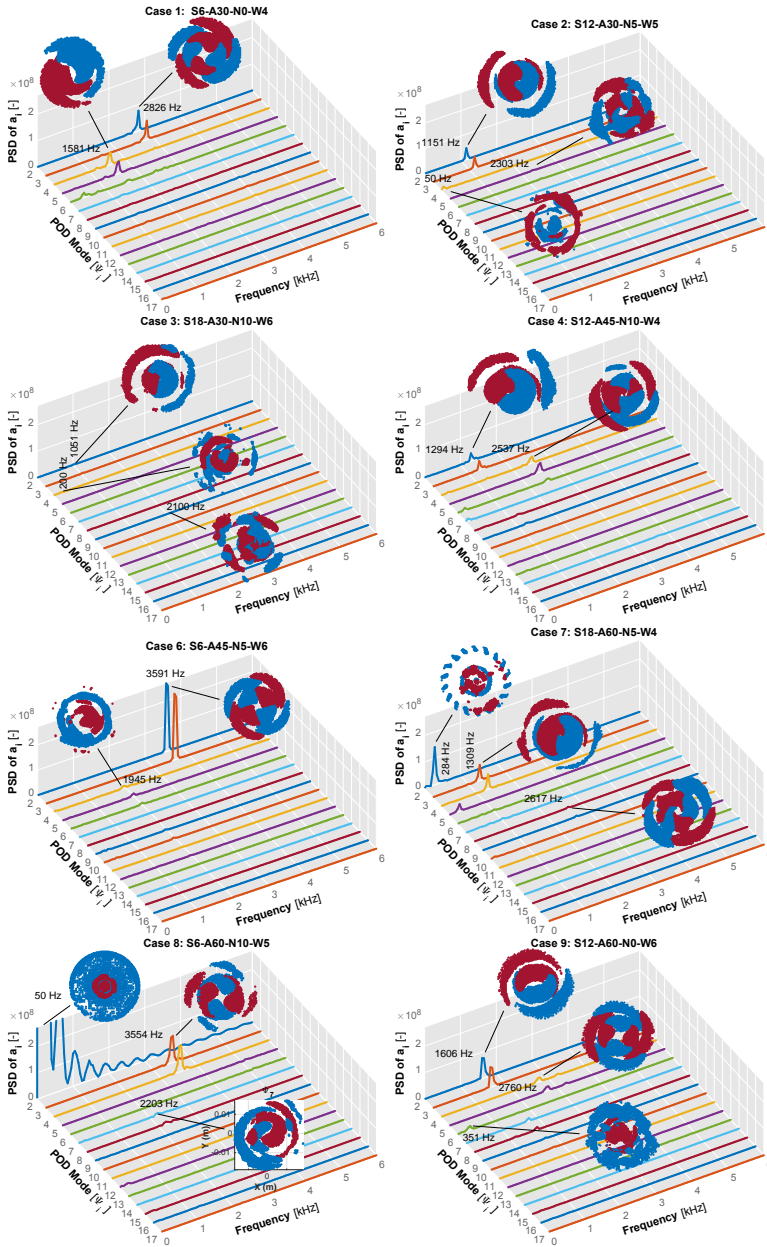


Figure 7.11: Power Spectral Density and spatial distribution of the time coefficient associated with POD modes $\Psi_2 - \Psi_{17}$ obtained from the 3D pressure signal for the simulations of the L9 array.

PVC modes						
Case	1 st harm.			2 nd harm.		
	Modes	Frequency	σ_i [-]	Modes	Frequency	Sigma [-]
1	Ψ_4 - Ψ_5	1581 Hz	$2.28 \cdot 10^6$	Ψ_2 - Ψ_3	2826 Hz	$2.55 \cdot 10^6$
2	Ψ_2 - Ψ_3	1151 Hz	$1.71 \cdot 10^6$	Ψ_5 - Ψ_6	2303 Hz	$0.58 \cdot 10^6$
3	Ψ_2 - Ψ_3	1051 Hz	$0.56 \cdot 10^6$	Ψ_9 - Ψ_{10}	2100 Hz	$0.28 \cdot 10^6$
4	Ψ_2 - Ψ_3	1294 Hz	$2.05 \cdot 10^6$	Ψ_4 - Ψ_5	2537 Hz	$1.85 \cdot 10^6$
5	Ψ_2 - Ψ_3	1088 Hz	$1.10 \cdot 10^6$	Ψ_5 - Ψ_6	2176 Hz	$0.65 \cdot 10^6$
6	Ψ_5 - Ψ_6	1945 Hz	$1.40 \cdot 10^6$	Ψ_2 - Ψ_3	3591 Hz	$4.80 \cdot 10^6$
7	Ψ_3 - Ψ_4	1309 Hz	$2.05 \cdot 10^6$	Ψ_8 - Ψ_9	2617 Hz	$0.81 \cdot 10^6$
8	Ψ_7 - Ψ_8	2203 Hz	$1.41 \cdot 10^6$	Ψ_3 - Ψ_4	3554 Hz	$2.93 \cdot 10^6$
9	Ψ_2 - Ψ_3	1606 Hz	$2.77 \cdot 10^6$	Ψ_4 - Ψ_5	2760 Hz	$1.73 \cdot 10^6$

Table 7.9: Frequency and intensity associated to the POD modes obtained from the 3-D pressure signal for the simulations of the L9 array. Values in bold denote the most energetic POD mode.

in all other cases. This result can be explained by the higher pressure losses experienced by those cases (recall Table 7.5), which could finally lead to higher pressure oscillations and thus, higher instability amplitudes. Therefore, this pressure loss along the swirler, together with the one exerted by the high velocity at the swirler outlet seem to be critical to the PVC dynamics⁷.

Furthermore, the high σ_i values exhibited by the cases with a lower number of swirler vanes (Cases 1, 6 and 8) are associated to the double-helical PVC structure (please recall from Section 7.3.2 the strong influence of the number of swirler vanes on those response variables, which is also reinforced below on the particular spectral response variables). In fact, these powerful double-helix modes are also observed to present higher values of frequency than those manifested by the cases with a higher number of swirler vanes (i.e., Cases 3, 5 and 7, with both lower frequencies and an insignificant double-helical PVC).

On the other hand, a particular behaviour is observed in Cases 1 and 4, which present a similar energy content referred to both pairs of modes (see

⁷This strong correlation is consistent since the PVC structure is identified as a low-pressure flow region.

Table 7.9), thus indicating the PVC is undergoing a higher and faster alternancy between 1 and 2 branches (see discussion at the end of this section). This could be detrimental since it could provoke stronger thermoacoustic oscillations than the ones produced by a more stable (although powerful) single or doubled-branched PVC.

Analogously to what was done in Section 7.3.2, the effect of each geometrical factor on both the frequency and intensity of the two main PVC modes are compiled into the P-value in Table 7.10, whereas their dispersion values are shown in Figure 7.12. Several conclusions can be extracted from here:

- The number of swirler vanes (S) stands as the most influencing factor on both the frequency and intensity of the PVC. In this way, the higher the number of blades, the smaller the rotating velocity and the associated energy of the PVC, as induced from Table 7.9. Besides, the strong influence of S on the presence of an energetic double-helix PVC is here confirmed, being the exclusive geometrical parameter with remarkable statistical influence on its intensity ($\sigma_{PVC,2}$).
- A joint look at Figures 7.9 and 7.12 allows to reveal a strong correlation among the responses of $\sigma_{PVC,2}$ and ΔP_{loss} to the change of S . This observation reinforces the previous reasoning about the possible dependence of the two-branch PVC intensity and the pressure losses.
- The frequency of both the single and double-helical PVC is strongly affected by the angle of the swirler vanes (A), as expected from the rotation time scale associated to the PVC defined in Eq. (2.4). This is justified due to the patent and self-evident interdependence between the swirler vane angle and the tangential velocity component at the swirler outlet region, as demonstrated in Table 7.7 and Figure 7.5.
- No significant influence of the location of the nozzle tip (N) and the combustion chamber width (W) on the PVC frequency and intensity is noticed. In some literature studies concerning reacting cases [11], it is hypothesised that a shift of the injector tip position may lead to non-linear distortions on the flame behaviour, thus affecting the acoustic oscillations and consequently the instability amplitudes and dominant pressure modes. Nevertheless, the axial placement of the spray injector is not essential for the characteristics of the detected modes in the non-reacting flow and the LDI geometry here investigated.

- The intensity of the single-helical PVC is not statistically affected by any geometrical factor (their dispersion graphs can be found in Figure A.6 of the Appendix A). Nevertheless, it seems to be closely related and follow the same trends that the size of the vortex breakdown bubble ($L_{VBB,bot}$ and $L_{VBB,top}$) and the maximum tangential velocity component (V_{SWJ}^{max}). Besides, the intensity of the single-branch presents the opposite trend that the spray penetration (S_{spray}) and the swirled-air diffusion length ($L_{SWJ}^{0.2ref}$), as expected. Therefore, even the aforementioned detrimental effects, a strong single-branched PVC could be beneficial (at least in a non-reacting case) by inducing a shorter fuel penetration length and enhancing the fuel-air mixing.

	A	W	S	N
$f_{PVC,1}$	0.014	0.2611	0.002	0.441
$\sigma_{PVC,1}$	0.334	0.341	0.418	0.236
$f_{PVC,2}$	0.046	0.472	0.007	0.511
$\sigma_{PVC,2}$	0.429	0.532	0.022	0.956

Table 7.10: *P*-values for the response variables of the spectral analysis. Dark green cell: P -value ≤ 0.01 ; light green cell: $0.01 < P$ -value ≤ 0.05 ; yellow cell: $0.05 < P$ -value ≤ 0.10 . Values in red indicates that the geometrical factors have a negative influence on the response variable.

Finally, an important consideration about the validity of the spectral results presented in this section is required. In the reference case, the temporal evolution of the pressure field showed an alternance (every few milliseconds) between a single and double-branched PVC, as mentioned in previous Chapters 5 and 6. Besides, since the presence of both modes is mutually exclusive or disjoint (i.e., they cannot both occur at the same time), the energy that the POD technique is assigning to each instability mode is directly proportional to the specific amount of time the concerned mode (single or double-branched PVC) is active in the recorded temporal window. Therefore, since all the cases studied in the L9 array present (to a greater or lesser extent) some energy content of both single and double-helix PVC, one might question if the considered temporal window of 20 ms (see Section 4.4.2.3) is enough to quantitatively represent the energy content consistently. In fact, it might be possible that the limited 20 ms temporal window would be hindering the

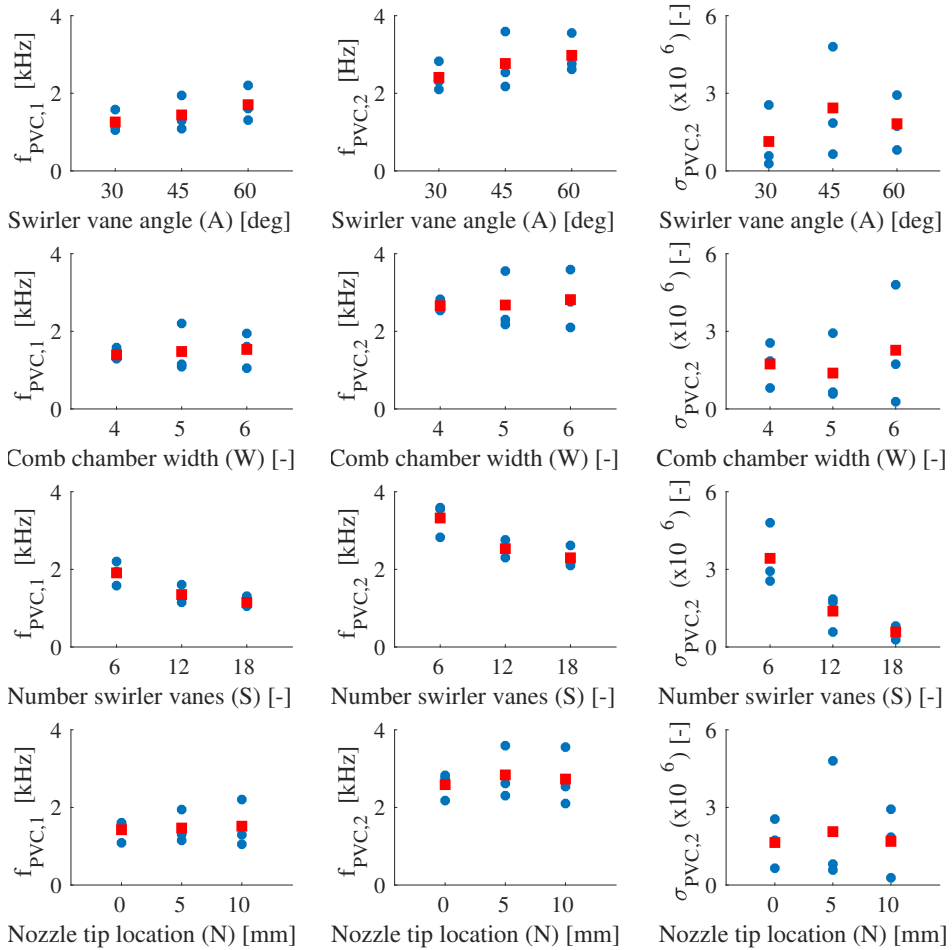


Figure 7.12: Dispersion values of the spectral response variables for each design parameter. Blue circles: the values of the response variable for each of the 9 simulations. Red squares: average of the 3 values for each level of the considered geometric factor.

physical mechanism, and the POD would be attributing a misleading energy content three times greater than the single-branched mode. Nevertheless, it should also be noted that the more important a given mode is, the more the time it is active, and thus the more the probabilities to be captured during the considered 20 ms temporal window. Anyway, a close observation into a wider recorded temporal window should be considered in future works in order to completely characterise the way of activation and energy of these self-excited modes.

7.5 Conclusions

Once the computational model has been validated, fundamental research has been undertaken to elucidate the effects of key geometrical parameters on the flow field and atomisation characteristics within an LDI burner. A Design of Experiments (DoE) has been proposed to quantify the influence of critical design factors on the defined response variables. In this way, the individual contribution of some functional parameters (namely the number of swirler vanes, the swirler vane angle, the combustion chamber width and the axial position of the nozzle tip) into both the flow field pattern, the spray size distribution and the occurrence of instabilities in the combustion chamber are evaluated throughout a Taguchi's orthogonal array L9. This has allowed minimising the number of simulations required to provide the full information of all the factors that affect a specific performance parameter.

From such a statistical study, it has become clear that most of the response variable outcomes mainly depend on the factors linked to the swirler (i.e., the number and angle of the swirler vanes). In this regard, stronger recirculation zones leading to an improved atomisation and mixing performance have been found both when decreasing the number of swirler blades and increasing the vane angle. Nevertheless, it has been also noticed how the higher the global degree of atomisation achieved, the more significant the pressure losses undergone by the flow across the swirler (this influence is more important at a low number of swirler vanes). Therefore, this strong correlation requires a trade-off in the combustor design, aiming to achieve adequate mixing and stable flow pattern with minimal pressure loss.

As far as the width of the combustion chamber size is concerned, a low significant influence is generally observed on most response variables. The lower the combustion chamber width, the more concentrated the fuel is in the available volume and the smaller the corner recirculation zones. Nevertheless, it is difficult to extract conclusions concerning fuel field patterns since this study concerns only non-reacting flow. Therefore, it precludes the characterisation of critical reacting factors such as the lower flammability limit or the flame extent, which are deemed to be crucial requirements to determine the optimal chamber dimensions.

On the other hand, it can be demonstrated how shifting the location of the nozzle tip upstream can have a beneficial effect on the resulting spray atomization, despite not being significant from the statistical point of view. This can be justified in the larger distances (higher residence time) that the liquid sheet will have to interact with the flow structures. Since the flow

structures are not quite influenced by the nozzle tip location, it could seem beneficial to move it upstream as much as possible. Nevertheless, a trade-off could appear at real-engine operating conditions since displacing it too much upstream would imply abandoning the direct injection strategy itself, tending to partially premixed combustion, which could suppose the apparition of flashback with the consequent damage to the swirler structure.

The ANOVA analysis has been valuable to identify and quantify the specific global influence of the geometrical factors on the response variables, but at the risk of precluding/masking specific trends of the outcomes with the geometry levels. For this reason, a brief discussion about the non-linearity on the dispersion results has allowed a better definition of both the scope and limitations (related to linear assumptions) of the statistical analysis.

Finally, the governing precessing vortex core has been quantitatively characterised through the POD technique. In this way, the spectral analysis has revealed how a geometrical modification can redistribute the energy between detected modes, changing its frequency, intensity and shape, and thus activating particular modes that can become more important than in the reference case. The number of swirler vanes has been observed again to be the most influencing factor on both the frequency and intensity of the PVC. In this regard, the higher the number of swirler blades, the smaller the rotating velocity and the associated energy of the PVC. Besides, the number of swirler blades has been revealed to be crucial into both the activation the energetic content of the double-helix PVC.

In conclusion, such a statistical study supposes a good starting point for subsequent studies of injection, atomisation and combustion on LDI burners. The methodology here presented can be exploited as a potential tool in the design phase, allowing to optimise the performance of the LDI combustor towards an optimal design trade-off at a faster and lower cost than the one that an experimental campaign would imply. Nevertheless, the selection of the definite response variables to optimise and the high sensitivity of the calculated optimal solution to the user-defined weights applied to each response variable precludes any concluding optimisation from a non-reacting case. These quantities should consider additional coupled contributions related to specific response variables defined for reacting cases such as combustion efficiencies and/or even NO_x emissions levels.

References

- [1] Ross, P. “Taguchi techniques for quality engineering”. In: *Mc, Graw Hill* (1998).
- [2] Montgomery, D. *Design and analysis of experiments*. John Wiley & Sons, 2017.
- [3] Lefebvre, A. and Ballal, D. *Gas turbine combustion: alternative fuels and emissions*. 3rd edition. Taylor and Francis, 2010.
- [4] Huang, Y. and Yang, V. “Dynamics and stability of lean-premixed swirl-stabilized combustion”. In: *Progress in Energy and Combustion Science* 35.4 (2009), pp. 293–364. DOI: 10.1016/J.PECS.2009.01.002.
- [5] *Statgraphics Centurion 18*. 2020. URL: <https://www.statgraphics.com/centurion-xviii> (visited on 09/21/2020).
- [6] Lorber, A. “Error propagation and figures of merit for quantification by solving matrix equations”. In: *Analytical Chemistry* 58.6 (1986), pp. 1167–1172. DOI: 10.1021/ac00297a042.
- [7] Haupt, R. and Haupt, S. *Practical Genetic Algorithms*. 2nd edition. John Wiley & Sons, 2004.
- [8] Vera-Candiotti, L., De-Zan, M., Cámara, M., and Goicoechea, H. “Experimental design and multiple response optimization. Using the desirability function in analytical methods development”. In: *Talanta* 124 (2014), pp. 123–138. DOI: <https://doi.org/10.1016/j.talanta.2014.01.034>.
- [9] Syred, N. and Beér, J. “Combustion in swirling flows: A review”. In: *Combustion and Flame* 23.2 (1974), pp. 143–201. DOI: 10.1016/0010-2180(74)90057-1.
- [10] Nikiforov, V. “The energy of graphs and matrices”. In: *Journal of Mathematical Analysis and Applications* 326.2 (2007), pp. 1472–1475. DOI: 10.1016/j.jmaa.2006.03.072.
- [11] Gejji, R., Huang, C., Fugger, C., Yoon, C., and Anderson, W. “Parametric investigation of combustion instabilities in a single-element lean direct injection combustor”. In: *International Journal of Spray and Combustion Dynamics* 11 (2018), p. 1756827718785851. DOI: 10.1177/1756827718785851.

Chapter 8

Conclusions and Future Works

*“Science progresses best when observations
force us to alter our preconceptions”*

—Vera Rubin

The main conclusions of the dissertation are synthesised in this chapter, highlighting how they can lead to further analysis and future works. For more specific conclusions, the reader is referred to the final section of Chapters 5, 6 and 7.

8.1 Conclusions

The non-reacting flow field and the liquid spray injection in a Lean Direct Injection gas turbine combustor have been investigated along this thesis by means of Eulerian-Lagrangian Large Eddy Simulations. This thesis constitutes the development and establishment of a methodological basis in the *Departamento de Máquinas y Motores Térmicos* (DMMT) to investigate the LDI technology. As the first experience of the DMMT in the field, the proposed approach has been numerical, giving the tools and guidelines for further numerical and experimental research in the following years.

In LDI combustors, a highly swirling air is admitted into the combustor where the liquid fuel is directly injected at a lean equivalence ratio close to

the lean blow-out limit. The turbulent swirling flow promotes both the atomisation of the injected liquid sheet and the mixing of the atomised sprays and generates a high-turbulent recirculation region downstream of the injection system. As a result from the literature review, it became clear that an accurate characterisation of the degree of atomisation of the liquid spray fuel, the turbulent dispersion and evaporation of liquid drops and the fuel-air mixing quality was deemed to be essential since those phenomena strongly influenced the subsequent combustion performance and pollutant emissions. The laboratory-scale swirled-stabilised CORIA Spray Burner was taken as the experimental geometry of reference to carry out the numerical investigation.

In the first place, reference cases concerning premixed gaseous and non-premixed liquid injections were modelled through U-RANS and LES simulations by means of two distinctive codes. An optimal mesh strategy using Adaptive Mesh Refinement (AMR) algorithms was defined, and its benefits against traditional fixed mesh approaches were exploited. The applicability of grid control tools such as fixed embedding and AMR demonstrated to be an interesting option to face this type of multi-scale problem. Besides, a methodology was presented to evaluate the influence on the accuracy of the grid control tools through a parametric mesh study. To that end, the Normalised Mean Square Error was adopted and systematically applied as a validation metric to quantify the existing discrepancies between the CFD numerical results and the available experimental data, proving to be a promising indicator to the quality of different meshing strategies. The following conclusions could be extracted from such a study:

- The capability of the CFD numerical codes in resolving the complex swirling flow features and the recirculation flow regions with reasonable accuracy was demonstrated. Agreement with experimental data was obtained both in U-RANS and LES in terms of predicted location and size of the recirculation zones as well as the mean and fluctuating air velocity components.
- The LES revealed a flow pattern typical of highly swirled configurations similar to experimental observations. The macroscopical analysis of the main turbulent features given by the unsteady flow visualization allowed identifying the Precessing Vortex Core (PVC) at both the inner and outer shear layers resulting in a periodic disturbance of the pressure and velocity fields. This hydrodynamic instability mode originated both single and double intermittent helical vortices wrapping the recirculation bubble. Furthermore, a rotation time scale associated to the PVC was defined in order to identify its associated characteristic frequency.

- A complete grid-tool parametric study carried out for gaseous premixed U-RANS cases allowed to establish a well-defined mesh strategy to work out the multi-scale problem. Besides, an automatic cartesian meshing algorithm together with the joint action of both fixed embedding and AMR allowed capturing the critical regions of high-velocity gradients, enabling a larger base mesh size in areas where it was not required. This resulted in:
 - An optimisation of the use of the computational resources, since a fewer number of cells were needed to obtain similar *NMSE* values to those of traditional fixed meshes.
 - Better accuracy in terms of the *NMSE* for a given mean cell count due to an optimal mesh layout according to the flow characteristics.
- Meanwhile, in the LES framework considered in gaseous-fueled cases:
 - The AMR algorithm proved to be able to distribute the cells in a proper way for this lean direct injection multi-scale problem. A better agreement with experimental data was obtained in the LES case with AMR both in the mean and fluctuating terms of the three velocity components through the three computed *NMSE* values. Nevertheless, it must be noted that the cost of this accuracy improvement was a moderate increase on the computational requirements both in CPU hours and in the RAM memory required when compared to LES cases without AMR.
 - LES quality and reliability of non-reacting flow was assessed based on measures of the turbulent resolution and viscosity, reinforcing the selected turbulence resolution length scale. Such criteria confirmed the validity of the AMR threshold defined to calculate the sub-grid field from the LES filtering and allowed certifying the compatibility when combining LES with AMR implementation.
 - Those SGS models that used the turbulent viscosity to model the sub-grid stress tensor (i.e., Smagorinsky and Dynamic Smagorinsky) were manifested to act as a trigger of the AMR algorithm, thus producing a higher number of cells than those SGS models using an additional equation to compute the sub-grid kinetic energy (i.e., Dynamic Structure) for the same mesh strategy. The independent SGS velocity scale considered by the Dynamic Structure model modified the resolved field, and thus alleviated the sub-grid field computed by the AMR algorithm.

- The Dynamic Smagorinsky sub-grid scale model provided the best prediction ability on both the computed time-averaged statistics and the dynamic behaviour of the turbulent flow scales when employing a sufficiently refined grid, while the non-viscous Dynamic Structure model arose as to the best option when dealing with a coarser mesh.
- Finally, the defined methodology was satisfactorily applied to solve the reference spray fuel case concerning liquid injections with both CFD codes. In this way, the relevant phenomena associated to the liquid phase were satisfactorily modelled after a significant amount of work selecting and calibrating the existing models, and finally obtaining good agreement with experimental data. The capabilities of LISA and TAB breakup models in predicting droplet statistics (e.g., droplet velocity and size distributions) were assessed. The TAB model together with the Lagrangian tracking formulation has been demonstrated to be able to solve the dispersed-phase field within the combustor accurately.

The outcome of this methodology is expected to be of interest to define a suitable meshing strategy for modellers in the field of multi-scale gas turbine combustors. It should be noted that, although the meshing strategy defined was applied for solving non-reactive cases, the methodology could be considered as a suitable ground to be extrapolated to more specific simulations involving reacting flows.

Once the methodology was presented and the computed reference cases ensured the validation of the computational model, an in-depth frequency-related analysis of both the gaseous-fueled and liquid-fueled CORIA LDI combustor was carried out for a complete characterisation on the dynamics of the governing helical coherent structures. In this way, three approaches were considered in order to identify the self-sustained instabilities occurring in the combustor: filtering techniques (i.e., Fast Fourier Transform - Sound Pressure Level) and data-driven modal decomposition procedures (i.e., Proper Orthogonal Decomposition and Dynamic Mode Decomposition). The implementation of these routines allowed retrieving information about the flow dynamics and provided a systematic approach to identify the main mechanisms that sustained instabilities in the combustor. By considering the pressure information of the entire computational domain at once, including complex geometries such as the radial swirler, the overall amplitude for each frequency was adequately identified according to the overall unsteady energy available in the flow.

On the one hand, the pressure and velocity fluctuations were used to compute the spectral signatures through the Sound Pressure Level (SPL) amplitude at multiple locations, allowing the detection of fundamental harmonics of the PVC in the spectra dominated by the rotation time scale. Meanwhile, the pressure spectra for the probes located both at the plenum, the swirler and the combustion chamber resembled one another in the vast majority of the geometry. This could imply coupled effects and quasi-instantaneous transmission of the pressure waves throughout the entire domain both in positive and negative axial directions.

On the other hand, the numerical identification of the main acoustic modes in the chamber through Proper Orthogonal Decomposition (POD) and Dynamic Mode Decomposition (DMD) allowed overcoming the FFT shortcomings and understanding the propagation of the hydrodynamic instability disturbances. In this way, both the POD and DMD analyses extracted similar flow dynamics results associated to a global self-excited oscillatory mode, namely the Precessing Vortex Core (PVC), having a single dominant frequency. This hydrodynamic instability mode resulted in double-helical vortices and led to a counter-rotating co-winding helical structure located between the inner and the outer shear layer, enveloping the recirculation bubble. Furthermore, both decomposition techniques allowed detecting two distinct PVC behaviours in time, which were found to yield a helical or double-helical breakdown mode, respectively, that dominated the dynamics of the whole flow. Thus, the flow oscillations were coherent with the dominant frequency of the global mode and, taking into account the phase shift between the decomposition results, the precession of the vortex core could be attributed to the same frequency.

In addition, the implemented DMD method also allowed identifying some complex pulsating, intermittent and cyclical spatial patterns related to the harmonic helical branches of the PVC. In this way, spiral structures with harmonically oscillating vorticity in the streamwise direction were identified presenting a given number of branches equal to the corresponding multiple of the frequency of the first PVC mode. This could be attributed to the continued formation of shear layer vortices due to the higher shear strength of the structures emanating from each of the swirler channels, opening the door to specific design modifications. Since DMD generated a global frequency spectrum in which each mode corresponds to a specific discrete frequency, its application was demonstrated to be more efficient than POD when dealing with temporally coherent problems. Nevertheless, the price to pay was to require a more diffuse metric than in POD, raising DMD as a less appropriate option to perform Reduced-Order-Models (ROMs) in some circumstances. Nevertheless,

in the view of the results, DMD technique proved to be a more systematic, efficient and robust tool that could give more accurate and consistent interpretations of the periodic physics underlying hydrodynamic instabilities in the Lean Direct Injection burner studied in the present investigation.

From the spectral analysis of the reference cases, it could be concluded that both the FFT, POD and DMD techniques successfully extracted the flow dynamics associated to the dominant global instability mode, corresponding to a double-helical precessing vortex structure. Nevertheless, the traditional bandpass-filtering technique demonstrated to be mostly dependent on the results of a-priori SPL analysis (not known beforehand), which could be tricky. Furthermore, global acoustic responses could be easily confirmed by examining several locations along the burner, but there were high-frequency responses that could be more challenging to pinpoint. In this way, the implementation and application of POD and DMD techniques removed most of the manual decisions linked to those traditional techniques thus allowing a complete automation of the post-processing: the mode frequencies, their respective spatial distributions and the ranking of their contribution to the total field were obtained automatically and always used the same exact criterion, with no need of user intervention or observation.

Finally, once the computational model was validated and the modal decomposition techniques were assessed, fundamental research was undertaken to elucidate the effects of key geometrical parameters on the flow field and atomisation characteristics within the LDI burner. A Design of Experiments (DoE) was proposed to quantify the influence of critical design factors on the defined response variables. In this way, the individual contribution of some functional parameters (namely the number of swirler vanes, the swirler vane angle, the combustion chamber width and the axial position of the nozzle tip) into both the flow field pattern, the spray size distribution and the occurrence of instabilities in the combustion chamber were evaluated throughout a Taguchi's orthogonal array L9. This allowed minimising the number of simulations required to provide the full information of all the factors that affect a specific performance parameter.

From such a statistical (ANOVA) study, it became clear that most of the response variable outcomes mainly depended on the factors linked to the swirler (i.e., the number and angle of the swirler vanes). In this regard, stronger recirculation zones leading to an improved atomisation and mixing performance were found both when decreasing the number of swirler blades and increasing the vane angle. Nevertheless, it was also noticed how the higher the global degree of atomisation achieved, the more significant the

pressure losses undergone by the flow across the swirler (this influence is more important at a low number of swirler vanes). Therefore, this strong correlation requires a trade-off in the combustor design, aiming to achieve adequate mixing and stable flow pattern with minimal pressure loss.

As far as the width of the combustion chamber size is concerned, a low significant influence was generally observed on most response variables. The lower the combustion chamber width, the more concentrated the fuel was in the available volume and the smaller the corner recirculation zones. Nevertheless, it is difficult to extract conclusions concerning fuel field patterns since this study concerns only non-reacting flow. Therefore, it precludes the characterisation of critical reacting factors such as the lower flammability limit or the flame extent, which are deemed to be crucial requirements to determine the optimal chamber dimensions.

On the other hand, it could be demonstrated how shifting the location of the nozzle tip upstream could have a beneficial effect on the resulting spray atomization, despite not being significant from the statistical point of view. This could be justified in the larger distances (higher residence time) that the liquid sheet will have to interact with the flow structures. Since the flow structures were not quite influenced by the nozzle tip location, it could seem beneficial to move it upstream as much as possible. Nevertheless, a trade-off could appear at real-engine operating conditions since displacing it too much upstream would imply abandoning the direct injection strategy itself, tending to partially premixed combustion, which could suppose the apparition of flashback with the consequent damage to the swirler structure.

The ANOVA analysis was valuable to identify and quantify the specific global influence of the geometrical factors on the response variables, but at the risk of precluding/masking specific trends of the outcomes with the geometry levels. For this reason, a brief discussion about the non-linearity on the dispersion results allowed a better definition of both the scope and limitations (related to linear assumptions) of the statistical analysis.

Finally, the governing Precessing Vortex Core was quantitatively characterised through the POD technique. In this way, the spectral analysis revealed how a geometrical modification could redistribute the energy between detected modes, changing its frequency, intensity and shape, and thus activating particular modes that could become more important than in the reference case. The number of swirler vanes was observed again to be the most influencing factor on both the frequency and intensity of the PVC. In this regard, the higher the number of swirler blades, the smaller the rotating velocity and the associated energy of the PVC. Besides, the number of swirler blades was re-

vealed to be crucial into both the activation and the energetic content of the double-helix PVC.

In conclusion, such a statistical study supposes a good starting point for subsequent studies of injection, atomisation and combustion on LDI burners. The methodology here presented can be exploited as a potential tool in the design phase, allowing to optimise the performance of the LDI combustor towards an optimal design trade-off at a faster and lower cost than the one that an experimental campaign would imply.

8.2 Future works

Along the present thesis, the non-reacting flow field and the liquid spray injection inside a Lean Direct Injection gas turbine combustor have been exhaustively analysed by means of Eulerian-Lagrangian Large Eddy Simulations. However, since this investigation has constituted the development and establishment of a methodological basis at the research centre, many questions remain uncovered and should be further reviewed in order to reach a more reliable understanding of LDI technology.

To this end, the following tasks, would help to shedding more light on the topic:

- Numerical characterisation of the laboratory-scale atmospheric continuous-flow LDI test rig developed at the department, whose first measurements have been recently published. Since the design and setup of the test facility were very premature at the beginning of this thesis, it was decided to take the CORIA Spray Burner as the experimental geometry of reference to carry out the numerical investigation.
- Extension of the study to a multi-point (multi-injector) LDI geometry. Even though most laboratory-scale combustors only consider a single injector strategy, multiple injectors are present in many combustion chambers of current engine configurations. Therefore, a thorough study should be addressed in an MP-LDI version of the baseline case in order to understand the complex physics such as ignition sequence, PVC interactions and flame propagation between injectors/burners, and combustion dynamics.
- LES of the internal flow inside the atomiser used in the experimental campaigns. This task is essential since, while experimental measurements only allow collecting data downstream of the injector, the CFD

results would make it possible to define a more realistic boundary condition than the one currently considered in the simulations of the complete combustion chamber in the thesis. This would allow improving the accuracy obtained in the computed liquid phase size-velocity correlations. Furthermore, subsequent internal/external flow simulations could be proposed to solve at once the internal fuel features and the external atomisation, evaporation and combustion phenomena.

- Statistical study to evaluate the influence of modifying factors related to the operating conditions, such as the equivalence ratio, mass flow rate, and temperature and pressure in the chamber. However, as reviewed in the thesis, comprehensive research on the influence of high-pressure conditions in LDI devices is an area with limited progress. This absence of experimental results in representative operating conditions of the flight regimes of an aircraft would make the correct calibration challenging. Therefore, it would be necessary to first resolve the aforementioned internal flow case at those operating conditions due to the great uncertainty in the definition of the characteristics of the spray (e.g., velocity and angle at the injection plane) when varying temperature and pressure. The study could also be extended in order to take into account double interactions between parameters. Moreover, the maximum and minimum levels of some parameters can be further restricted by taking into account the geometric constraints induced by real combustor engines.
- Application of the Dynamic Mode Decomposition (DMD) technique to a broader temporal window in the statistical study carried out in Chapter 7. The spectral analysis based on the Proper Orthogonal Decomposition (POD) tool carried out has allowed quantitatively characterising the most energetic modes of the governing Precessing Vortex Core when modifying key geometrical factors. However, DMD would allow (if a consistent criterion involving all the cases would be defined) both to identify higher PVC harmonics and to try to elucidate under which conditions the alternancy between single and double-helix is generated.
- Extension of the study towards reacting cases. The results of this thesis have entirely characterised the non-reacting flow, which is known to be a crucial step in LDI combustor research since the success or failure of ignition (and re-ignition at high-altitude) is known to directly depend on local conditions just before ignition, especially on the mixture quality

and the turbulence level at the near-injection region. In this way, numerical tools are now ready to study both the ignition phenomena and the reacting field. Since the LDI technology can promote coupling effects among acoustics, hydrodynamics and combustion, a complete characterisation of the reacting field is crucial to understand the amplification mechanisms of these combustion instabilities.

- Application of POD and DMD techniques to reacting cases. The combustion chamber can be seriously damaged if the self-excited acoustic waves coincide with the natural frequency of the system (resonance). In this way, this spectral analysis could help to:
 - Elucidate and characterise the coupling and complex interaction between combustion (heat release) and acoustic modes, which is also deemed to induce flame extinction.
 - Give an idea of the exact mechanisms by which the reported suppression of the PVC occurs under particular reacting conditions.
 - Identify the leading cause of acoustic noise from combustion and try to reduce or redistribute those modes to higher frequencies that are not audible to humans.
- Definition of a Figure of Merit (FoM) from a reacting case to quantitatively characterise the performance of the LDI combustor towards an optimal design trade-off. A Multiple Response Optimisation (MRO) analysis has been performed in this study to try to obtain a trade-off design to maximise/minimise the desired response variables. Nevertheless, the selection of the definite response variables to optimise and the high sensitivity of the calculated optimal solution to the user-defined weights applied to each response variable precludes any concluding optimisation from a non-reacting case. These quantities should consider additional coupled contributions related to specific response variables defined for reacting cases such as combustion efficiencies and/or even NO_x emissions levels.
- Exploitation of the methodology to perform industrial simulations for design studies of realistic Gas Turbine burners. Nevertheless, it is important to highlight that the main obstacles when performing LES in such real engines are the extra modelling challenges induced by the restricted set of available measurements for validation purposes.

Appendices

Appendix A

Full set of results for the L9 orthogonal array parametric study on the geometrical features

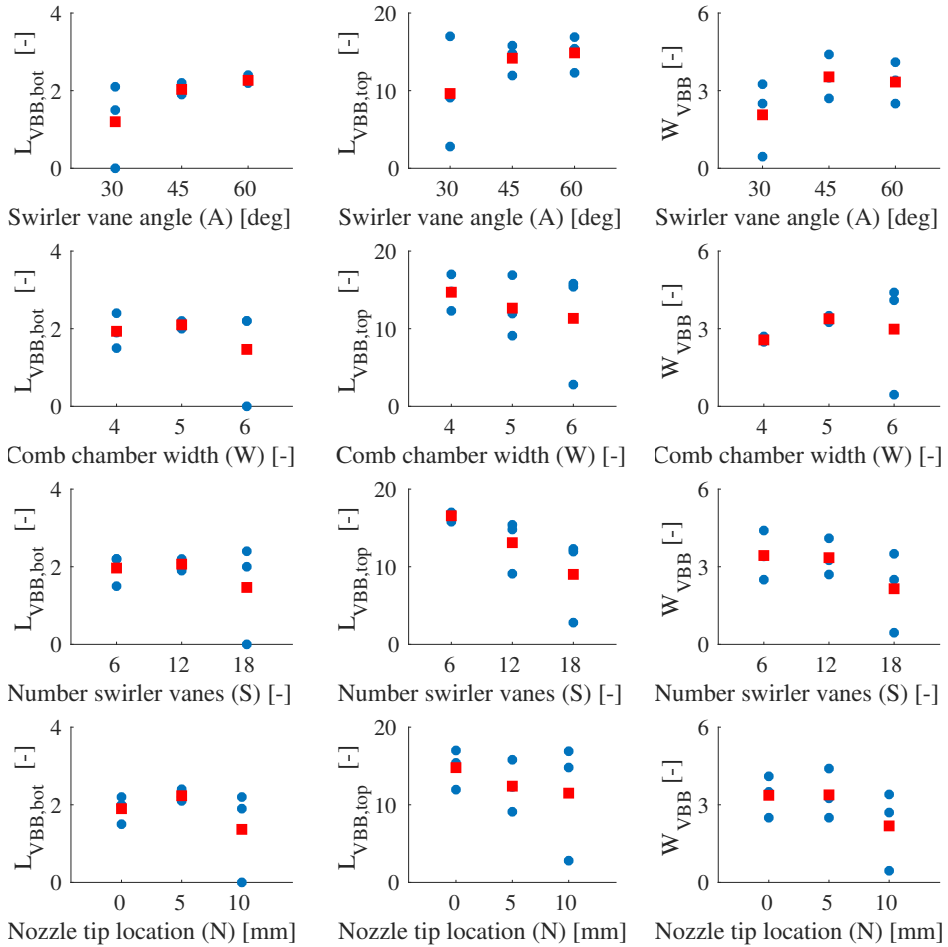


Figure A.1: Dispersion values of the response variables for each design parameter (1 of 7). Blue circles: the values of the response variable for each of the 9 simulations. Red squares: average of the 3 values for each level of the considered geometric factor.

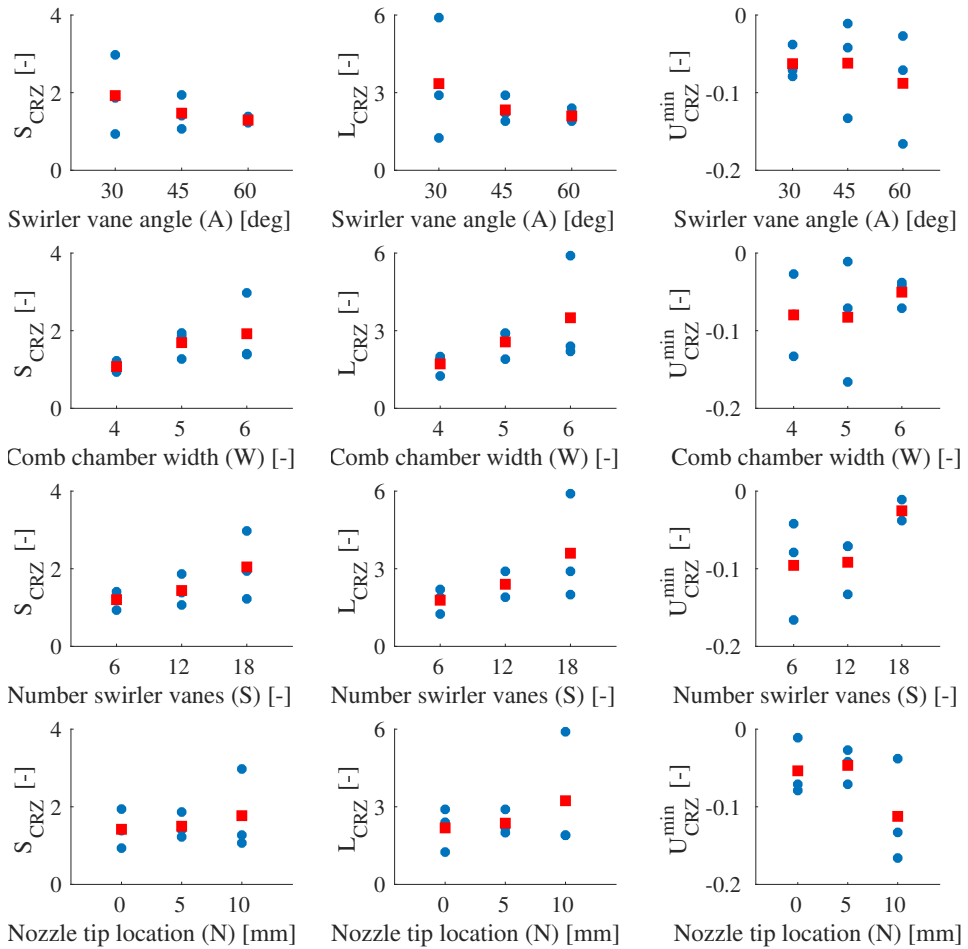


Figure A.2: Dispersion values of the response variables for each design parameter (2 of 7). Blue circles: the values of the response variable for each of the 9 simulations. Red squares: average of the 3 values for each level of the considered geometric factor.

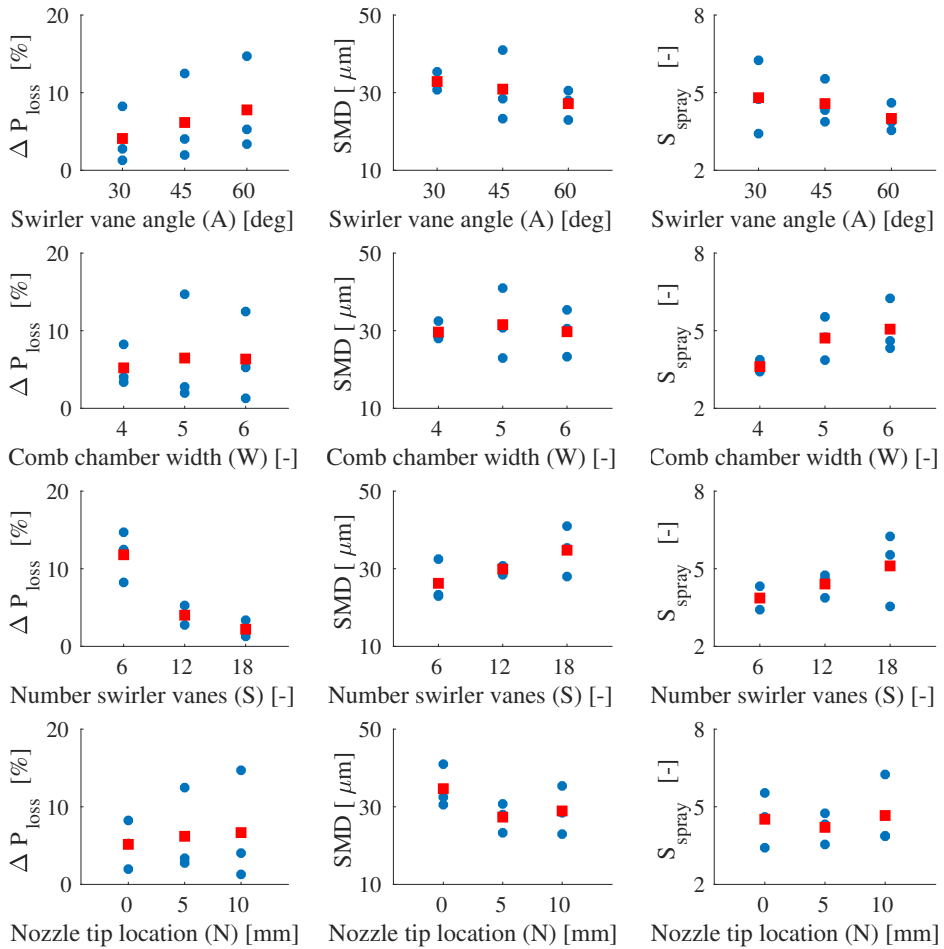


Figure A.3: Dispersion values of the response variables for each design parameter (3 of 7). Blue circles: the values of the response variable for each of the 9 simulations. Red squares: average of the 3 values for each level of the considered geometric factor.

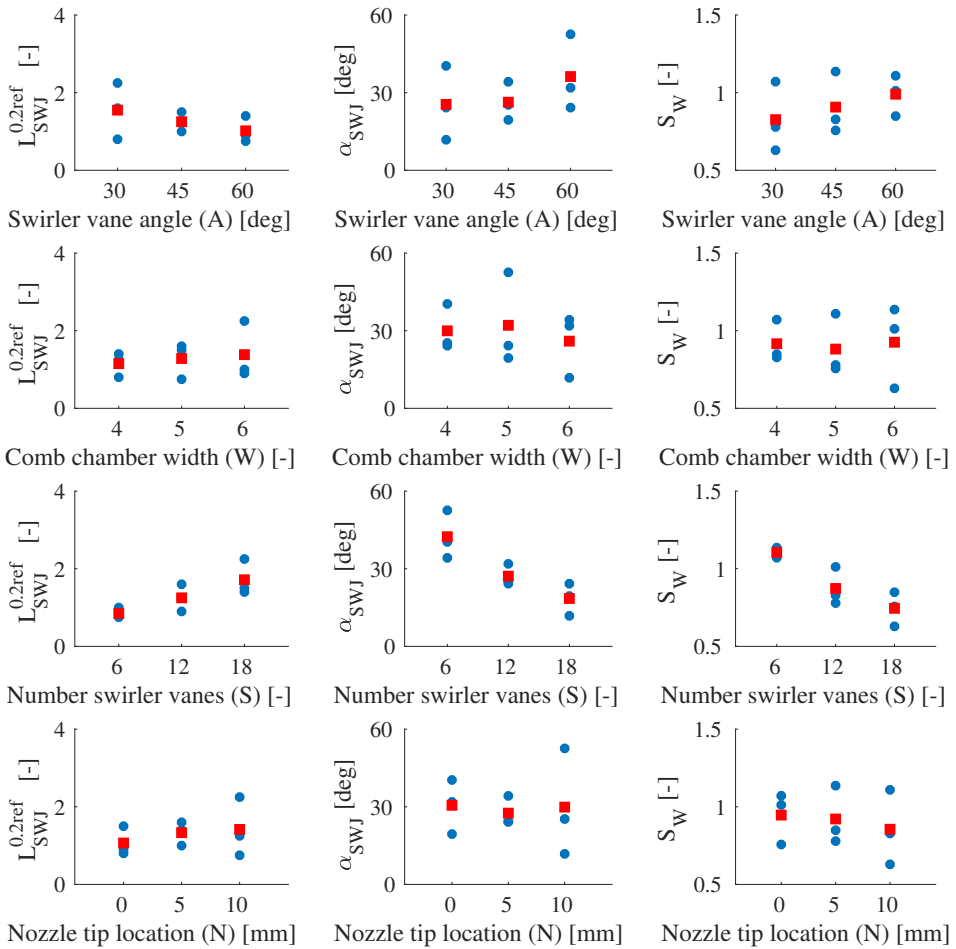


Figure A.4: Dispersion values of the response variables for each design parameter (4 of 7). Blue circles: the values of the response variable for each of the 9 simulations. Red squares: average of the 3 values for each level of the considered geometric factor.

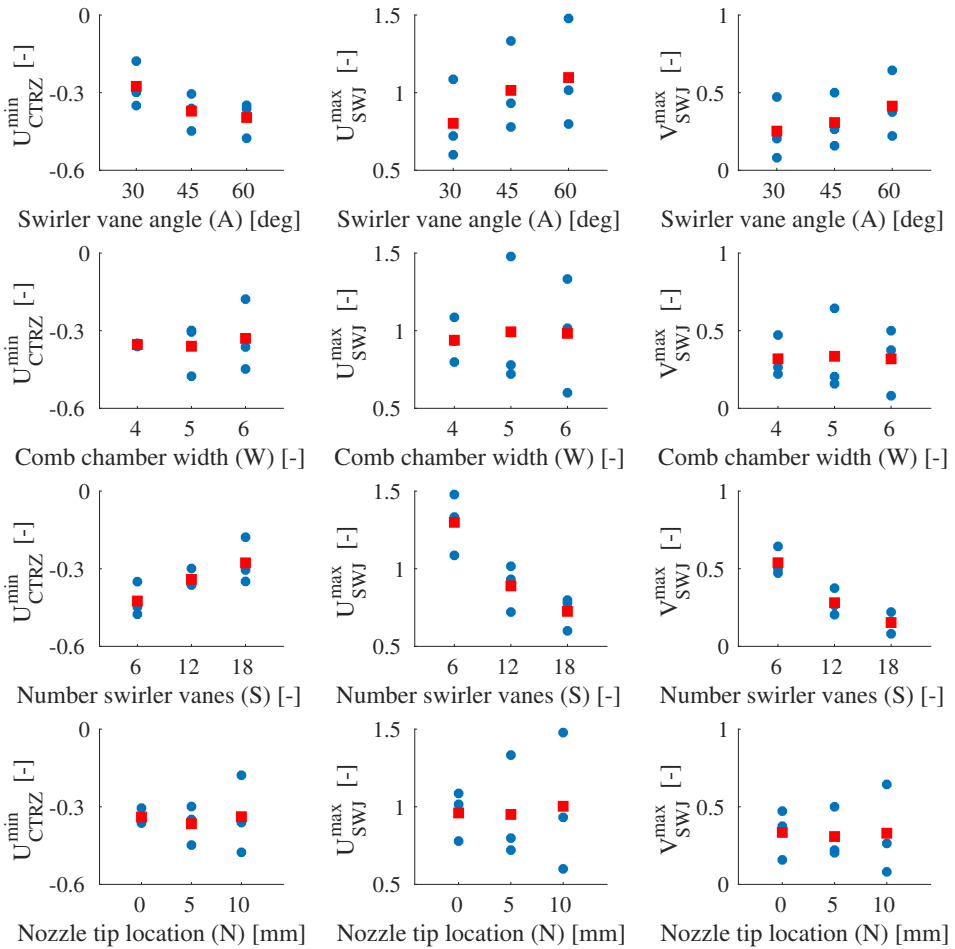


Figure A.5: Dispersion values of the response variables for each design parameter (5 of 7). Blue circles: the values of the response variable for each of the 9 simulations. Red squares: average of the 3 values for each level of the considered geometric factor.

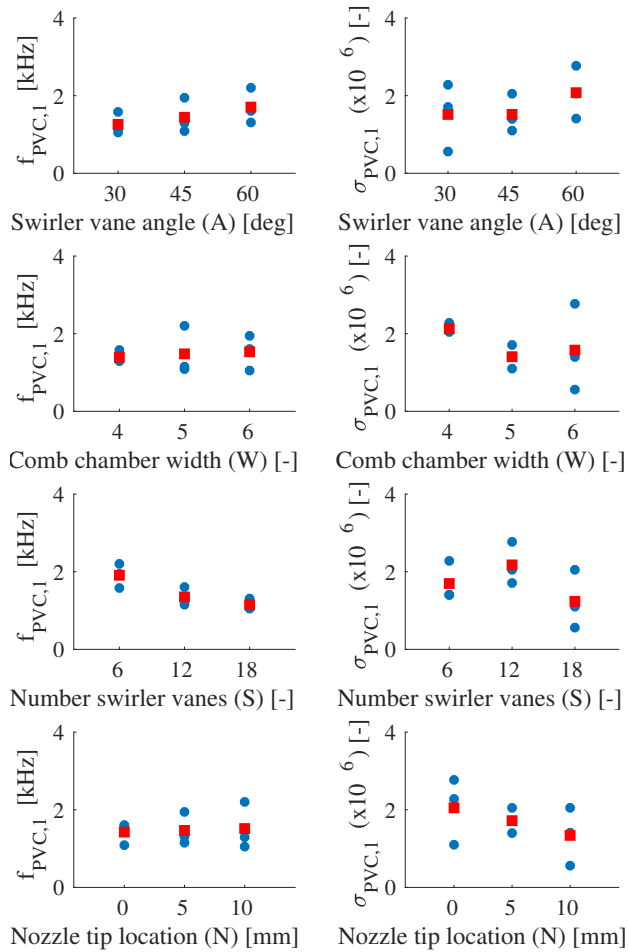


Figure A.6: Dispersion values of the spectral response variables for each design parameter (6 of 7). Blue circles: the values of the response variable for each of the 9 simulations. Red squares: average of the 3 values for each level of the considered geometric factor.

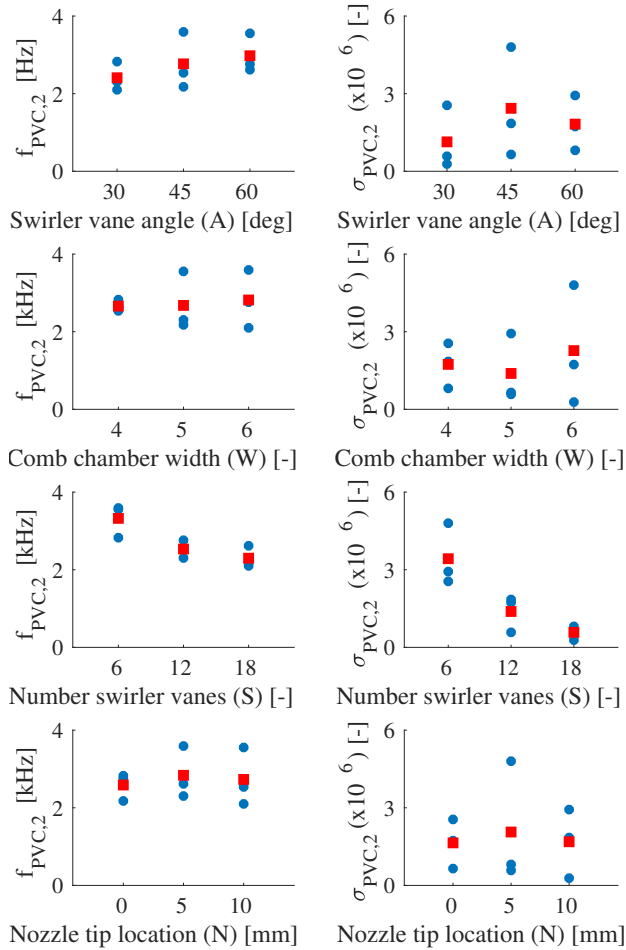


Figure A.7: Dispersion values of the spectral response variables for each design parameter (7 of 7). Blue circles: the values of the response variable for each of the 9 simulations. Red squares: average of the 3 values for each level of the considered geometric factor.

Global Bibliography

- Al-Abdeli, Y. and Masri, A. “Turbulent Swirling Natural Gas Flames: Stability Characteristics, Unsteady Behavior and Vortex Breakdown”. In: *Combustion Science and Technology* 179.1-2 (2007), pp. 207–225. DOI: 10.1080/00102200600809092 (cited on pages 65, 70, 72, 79).
- Al-Abdeli, Y., Masri, A., Marquez, G., and Starner, S. “Time-varying behaviour of turbulent swirling nonpremixed flames”. In: *Combustion and Flame* 146.1 (2006), pp. 200–214. DOI: <https://doi.org/10.1016/j.combustflame.2006.03.009> (cited on page 65).
- Al-Abdeli, Yasir M. and Masri, Assaad R. “Review of laboratory swirl burners and experiments for model validation”. In: *Experimental Thermal and Fluid Science* 69 (2015), pp. 178–196. DOI: 10.1016/j.expthermflusci.2015.07.023 (cited on page 63).
- Abdi, H. and Williams, L. “Principal Component Analysis”. In: *Wiley Interdisciplinary Reviews: Computational Statistics* 2.4 (2010), pp. 433–459 (cited on page 156).
- Abraham, J. and Magi, V. “A Model for Multicomponent Droplet Vaporization in Sprays”. In: *SAE Transactions* 107 (1998), pp. 603–613. DOI: 10.2307/44736555 (cited on page 45).
- Abramzon, B. and Sirignano, W. “Approximate theory of a single droplet vaporization in a convective field: effects of variable properties, Stefan flow and transient liquid heat”. In: *Proceedings of the American Society of Mechanical Engineers*. Honolulu, Hawaii, United States of America, 1987 (cited on page 44).

- Abramzon, B. and Sirignano, W. “Droplet vaporization model for spray combustion calculations”. In: 32.9 (1988), pp. 1605–1618. DOI: 10.2514/6.1988-636 (cited on page 45).
- Ajmani, K., Mongia, H., and Lee, P. “CFD evaluation of a 3rd generation LDI combustor”. In: *53rd AIAA/SAE/ASEE Joint Propulsion Conference, 2017*. 2017. DOI: 10.2514/6.2017-5017 (cited on pages 76, 82).
- Alekseenko, S., Dulin, V., Kozorezov, Y., and Markovich, D. “Effect of High-Amplitude Forcing on Turbulent Combustion Intensity and Vortex Core Precession in a Strongly Swirling Lifted Propane/Air Flame”. In: *Combustion Science and Technology* 184.10-11 (2012), pp. 1862–1890. DOI: 10.1080/00102202.2012.695239 (cited on page 84).
- Alekseenko, S. et al. “Coherent structures in the near-field of swirling turbulent jets: A tomographic PIV study”. In: *International Journal of Heat and Fluid Flow* 70 (2018), pp. 363–379. DOI: <https://doi.org/10.1016/j.ijheatfluidflow.2017.12.009> (cited on page 84).
- Alessandro, D., Stankovic, I., and Merci, B. “LES Study of a Turbulent Spray Jet: Mesh Sensitivity, Mesh-Parcels Interaction and Injection Methodology”. In: *Flow, Turbulence and Combustion* 103.2 (2019), pp. 537–564. DOI: 10.1007/s10494-019-00039-7 (cited on page 140).
- Alkabie, H. and Andrews, G. “Reduced NO_x Emissions Using Low Radial Swirler Vane Angles”. In: *Proceedings of the ASME: International Gas Turbine and Aeroengine Congress and Exposition*. Orlando, Florida (USA), 1991. DOI: 10.1115/91-GT-363 (cited on pages 5, 60).
- Alkabie, H., Andrews, G., and Ahmad, N. “Lean Low NO_x Primary Zones Using Radial Swirlers”. In: *Turbo Expo: Power for Land, Sea and Air*. 1988. DOI: 10.1115/88-GT-245 (cited on page 4).
- Amsden, A. “KIVA-3V: A block-structured KIVA program for engines with vertical or canted valves”. In: *Los Alamos National Laboratory Technical Report LA-13313-MS* (1997) (cited on pages 48, 138).
- Amsden, A., O’Rourke, P., and Butler, T. “KIVA-II: A computer program for chemically reactive flows with sprays”. In: *Technical Report LA-11560-MS* (1989) (cited on pages 127, 131).
- Anderson, D. “Effect of Equivalence Ratio and Dwell Time on Exhaust Emissions From an Experimental Premixing Prevaporizing Burner”. In: *NASA Technical Report NASA-TMX-71592* (1975) (cited on page 61).
- Anderson, D. “Ultra-Lean Combustion at High Inlet Temperatures”. In: *Proceedings of the ASME Turbo Expo*. Vol. 2. 1989. DOI: 10.1115/81-GT-44 (cited on page 61).

- Andrews, G., N., Escott, A., Al-Shaikhly, and H., Al-Kabie. "Counter-rotating radial swirlers for low NO_x emissions with passage fuel injection". In: *International Symposium on Air Breathing Engines (ISABE)*. 1995 (cited on page 62).
- Aouina, Y., Maas, U., Gutheil, E., Riedel, U., and Warnatz, J. "Mathematical modeling of droplet heating, vaporization, and ignition including detailed chemistry". In: *Combustion Science and Technology* 173 (2001), pp. 1–29. DOI: 10.1080/00102200108935842 (cited on page 45).
- Apte, S., Mahesh, K., Gorokhovski, M., and Moin, P. "Stochastic modeling of atomizing spray in a complex swirl injector using large eddy simulation". In: *Proceedings of the Combustion Institute* 32.2 (2009), pp. 2257–2266. DOI: 10.1016/j.proci.2008.06.156 (cited on page 72).
- Apte, S.V., Gorokhovski, M., and Moin, P. "LES of atomizing spray with stochastic modeling of secondary breakup". In: *International Journal of Multiphase Flow* 29.9 (2003), pp. 1503–1522. DOI: 10.1016/S0301-9322(03)00111-3 (cited on page 71).
- Archer, S. and Gupta, A. "Effect of Swirl and Combustion on Flow Dynamics in Lean Direct Injection Gas Turbine Combustion". In: *41st Aerospace Sciences Meeting and Exhibit, AIAA 2003-1343*. 2003, pp. 1–9. DOI: 10.1115/DETC2003/CIE-48253 (cited on pages 63, 69).
- Arienti, M., Li, X., Soteriou, M., Eckett, C., and Jensen, R. "Coupled Level-Set/Volume-of-Fluid Method for the Simulation of Liquid Atomization in Propulsion Device Injectors". In: *AIAA/ASME/SAE/ASEE Joint Propulsion Conference* July (2010), pp. 1–10 (cited on page 72).
- Ashgriz, N. "Handbook of atomization and sprays: theory and applications". In: Springer Science and Business Media, 2011. Chap. 24 - Spray Nozzles (cited on pages 24, 26).
- Ashgriz, N. "Handbook of atomization and sprays: theory and applications". In: Springer Science and Business Media, 2011. Chap. 4 - Dynamics of Liquid Droplets (cited on page 117).
- Ashgriz, N. "Handbook of atomization and sprays: theory and applications". In: Springer Science and Business Media, 2011. Chap. 6 - Droplet Deformation and Breakup (cited on page 38).
- Ashgriz, N. "Handbook of atomization and sprays: theory and applications". In: Springer Science and Business Media, 2011. Chap. 9 - Atomization Models (cited on pages 116, 121).

- Ashgriz, N. and Givi, P. “Binary collision dynamics of fuel droplets”. In: *International Journal of Heat and Fluid Flow* 8.3 (1987), pp. 205–210. DOI: 10.1016/0142-727X(87)90029-4 (cited on page 41).
- Ashgriz, N. and Poo, J. “Coalescence and separation in binary collisions of liquid drops”. In: *Journal of Fluid Mechanics* 221 (1990), pp. 183–204. DOI: 10.1017/S0022112090003536 (cited on pages 42–44).
- El-Asrag, H. and Menon, S. “Large eddy simulation of bluff-body stabilized swirling non-premixed flames”. In: *Proceedings of the Combustion Institute* 31 II (2007), pp. 1747–1754. DOI: 10.1016/j.proci.2006.07.251 (cited on page 71).
- El-Asrag, Hossam A. and Braun, Markus. “Effect of turbulence non-isotropy modeling on spray dynamics for an evaporating Acetone spray jet”. In: *International Journal of Multiphase Flow* 68 (2015), pp. 100–120. DOI: 10.1016/j.ijmultiphaseflow.2014.10.009 (cited on pages 73, 81).
- Ayoub, N. and Reitz, R. “Multidimensional Computation of Multicomponent Spray Vaporization and Combustion”. In: *International Congress Exposition*. SAE International, 1995. DOI: 10.4271/950285 (cited on pages 45, 131).
- Bahr, D. “Technology for the design of high temperature rise combustors”. In: *Journal of Propulsion and Power* 3 (1987), pp. 179–186. DOI: 10.2514/3.22971 (cited on pages 2, 3).
- Barré, D. “Simulation Numerique De L’Allumage Dans Les Chambres De Combustion Aeronautiques”. PhD thesis. Institut National Polytechnique de Toulouse (INP Toulouse), 2014 (cited on pages 7, 136, 148, 192, 219, 221, 225).
- Barré, D., Kraushaar, M., Staffelbach, G., Moureau, V., and Gicquel, L. “Compressible and low Mach number LES of a swirl experimental burner”. In: *3rd INCA Colloquim* 341.1-2 (2013), pp. 277–287. DOI: 10.1016/j.crme.2012.11.010 (cited on pages 68, 78, 145).
- Barré, D. et al. “Flame propagation in aeronautical swirled multi-burners: Experimental and numerical investigation”. In: *Combustion and Flame* 161.9 (2014), pp. 2387–2405. DOI: 10.1016/j.combustflame.2014.02.006 (cited on pages 6, 68, 78, 81).
- Beér, J. and Chigier, N. *Combustion aerodynamics*. London, Applied Science Publishers, 1972 (cited on page 19).
- Bentley, J. “Multidimensional Binary Search Trees Used for Associative Searching”. In: *Commun. ACM* 18.9 (1975), pp. 509–517. DOI: 10.1145/361002.361007 (cited on page 159).

- Berkooz, G., Holmes, P., and Lumley, J. “The Proper Orthogonal Decomposition in the Analysis of Turbulent Flows”. In: *Annual Review of Fluid Mechanics* 25.1 (1993), pp. 539–575 (cited on page 155).
- Billant, P., Chomaz, J., and Huerre, P. “Experimental study of vortex breakdown in swirling jets”. In: *Journal of Fluid Mechanics* 376 (1998), pp. 183–219. DOI: 10.1017/S0022112098002870 (cited on page 232).
- Biswas, S. and Qiao, L. “Combustion instabilities of ultra-lean premixed H₂-Air mixtures by prechamber turbulent jet ignition”. In: *Journal of Propulsion and Power* 34.5 (2018), pp. 1166–1177. DOI: 10.2514/1.B36927 (cited on page 229).
- Bizon, K., Continillo, G., Lombardi, S., Sementa, P., and Vaglieco, B. “Independent component analysis of cycle resolved combustion images from a spark ignition optical engine”. In: *Combustion and Flame* 163 (2016), pp. 258–269. DOI: 10.1016/j.combustflame.2015.10.002 (cited on page 83).
- Bizon, K., Continillo, G., Mancaruso, E., Merola, S., and Vaglieco, B. “POD-based analysis of combustion images in optically accessible engines”. In: *Combustion and Flame* 157.4 (2010), pp. 632–640. DOI: 10.1016/j.combustflame.2009.12.013 (cited on page 83).
- Blazek, J. *Computational Fluid Dynamics: Principles and Applications*. Ed. by Butterworth-Heinemann. 3rd Edition. 2015, p. 466 (cited on page 181).
- Boileau, M., Staffelbach, G., Cuenot, B., Poinso, T., and Bérat, C. “LES of an ignition sequence in a gas turbine engine”. In: *Combustion and Flame* 154.1-2 (2008), pp. 2–22. DOI: 10.1016/j.combustflame.2008.02.006 (cited on pages 74, 75, 79).
- Boileau, M. et al. “Investigation of Two-Fluid Methods for Large Eddy Simulation of Spray Combustion in Gas Turbines”. In: *Flow, Turbulence and Combustion* 80.3 (2007), pp. 291–321. DOI: 10.1007/s10494-007-9123-1 (cited on page 72).
- Bracho, G. “Experimental and theoretical study of the direct diesel injection process at low temperatures”. PhD thesis. Universitat Politècnica de València, 2011 (cited on page 9).
- Broatch, A., García-Tíscar, J., Roig, F., and Sharma, S. “Dynamic mode decomposition of the acoustic field in radial compressors”. In: *Aerospace Science and Technology* 90 (2019), pp. 388–400. DOI: 10.1016/j.ast.2019.05.015 (cited on pages 83, 84).

- Broatch, A., Novella, R., Gomez-Soriano, J., Pal, P., and Som, S. “Numerical Methodology for Optimization of Compression-Ignited Engines Considering Combustion Noise Control”. In: *SAE International Journal of Engines* 11.6 (2018), pp. 625–642. DOI: 10.4271/2018-01-0193 (cited on page 10).
- Broatch, A., Olmeda, P., Margot, X., and Gomez-Soriano, J. “Numerical simulations for evaluating the impact of advanced insulation coatings on H2 additivated gasoline lean combustion in a turbocharged spark-ignited engine”. In: *Applied Thermal Engineering* 148.November 2018 (2019), pp. 674–683. DOI: 10.1016/j.applthermaleng.2018.11.106 (cited on page 10).
- Cai, J, Tacina, R., and Jeng, S. “The Structure of a Swirl-Stabilized Reacting Spray Issued From an Axial Swirler”. In: *43rd AIAA Aerospace Sciences Meeting and Exhibit*. January. 2005 (cited on pages 5, 63, 66, 69, 75, 79, 80).
- Caraeni, D., Bergström, C., and Fuchs, L. “Modeling of liquid fuel injection, evaporation and mixing in a gas turbine burner using large eddy simulations”. In: *Flow, Turbulence and Combustion* 65.2 (c), pp. 223–244. DOI: 10.1023/A:1011428926494 (cited on page 71).
- Carreres, M. “Thermal Effects Influence on the Diesel Injector Performance through a Combined 1D Modelling and Experimental Approach”. PhD thesis. Universitat Politècnica de València, 2016 (cited on page 9).
- Caux-Brisebois, V., Steinberg, A., Arndt, C., and Meier, W. “Thermo-acoustic velocity coupling in a swirl stabilized gas turbine model combustor”. In: *Combustion and Flame* 161.12 (2014), pp. 3166–3180. DOI: 10.1016/j.combustflame.2014.05.020 (cited on page 83).
- Cavaliere, D., Kariuki, J., and Mastorakos, E. “A Comparison of the Blow-Off Behaviour of Swirl-Stabilized Premixed, Non-Premixed and Spray Flames”. In: *Flow, Turbulence and Combustion* 91.2 (2013), pp. 347–372. DOI: 10.1007/s10494-013-9470-z (cited on page 68).
- Celik, I., Cehreli, Z., and Yavuz, I. “Index of resolution quality for large eddy simulations”. In: *Journal of Fluids Engineering, Transactions of the ASME* 127.5 (2005), pp. 949–958. DOI: 10.1115/1.1990201 (cited on page 183).
- Celik, I., Klein, M., and Janicka, J. “Assessment measures for engineering LES applications”. In: *Journal of Fluids Engineering, Transactions of the ASME* 131.3 (2009), pp. 0311021–03110210. DOI: 10.1115/1.3059703 (cited on page 183).
- CFD ICEM Help Manual*. Tech. rep. ANSYS, Inc., 2018 (cited on page 142).

- Chen, H., Hung, D., Xu, M., Zhuang, H., and Yang, J. “Proper orthogonal decomposition analysis of fuel spray structure variation in a spark-ignition direct-injection optical engine”. In: *Experiments in Fluids* 55.4 (2014), p. 1703. DOI: 10.1007/s00348-014-1703-y (cited on page 83).
- Chen, H., Reuss, D., and Sick, V. “Analysis of misfires in a direct injection engine using proper orthogonal decomposition”. In: *Experiments in Fluids* 51.4 (2011), pp. 1139–1151. DOI: 10.1007/s00348-011-1133-z (cited on page 83).
- Chen, K., Tu, J., and Rowley, C. “Variants of dynamic mode decomposition: Boundary condition, Koopman, and fourier analyses”. In: *Journal of Non-linear Science* 22.6 (2012), pp. 887–915. DOI: 10.1007/s00332-012-9130-9 (cited on pages 84, 155).
- Chen, R. and Driscoll, J. “The role of the recirculation vortex in improving fuel-air mixing within swirling flames”. In: *Symposium (International) on Combustion* 22.1 (1989), pp. 531–540. DOI: [https://doi.org/10.1016/S0082-0784\(89\)80060-8](https://doi.org/10.1016/S0082-0784(89)80060-8) (cited on page 62).
- Chigier, N. and Beer, J. “Velocity and Static-Pressure Distributions in Swirling Air Jets Issuing From Annular and Divergent Nozzles”. In: *Journal of Basic Engineering* 86.4 (1964), pp. 788–796. DOI: 10.1115/1.3655954 (cited on page 20).
- Chou, W. and Faeth, G. “Temporal properties of secondary drop breakup in the bag breakup regime”. In: *International Journal of Multiphase Flow* 24.6 (1998), pp. 889–912. DOI: 10.1016/S0301-9322(98)00015-9 (cited on page 38).
- Chrigui, M., Masri, A., Sadiki, A., and Janicka, J. “Large eddy simulation of a polydisperse ethanol spray flame”. In: *Flow, Turbulence and Combustion* 90.4 (2013), pp. 813–832. DOI: 10.1007/s10494-013-9449-9 (cited on page 73).
- Chryssakis, C. and Assanis, D. “A unified fuel spray breakup model for internal combustion engine applications”. In: *Atomization and Sprays* 18 (2008), pp. 375–426. DOI: 10.1615/AtomizSpr.v18.i5.10 (cited on page 38).
- Collin-Bastiani, F. et al. “A joint experimental and numerical study of ignition in a spray burner”. In: *Proceedings of the Combustion Institute* 37.4 (2019), pp. 5047–5055. DOI: 10.1016/j.proci.2018.05.132 (cited on pages 78, 82).
- Compact Helical Arranged combustors with lean LIFTed flames*. 2020. URL: <https://cordis.europa.eu/project/id/831881> (visited on 02/11/2020) (cited on page 6).

- CONVERGE 2.4 Manual*. Tech. rep. Convergent Science, Inc., Middleton, 2017 (cited on pages 116, 124, 128, 141).
- Cooper, J. et al. “Fuel nozzle assembly for reduced exhaust emissions”. Google Patent 6389815. 2002 (cited on page 4).
- Cordier, M. “Allumage et propagation de flamme dans les écoulements fortement swirlés : études expérimentales et numériques”. PhD thesis. Institut National des sciences appliquées (INSA), 2013 (cited on pages 7, 68, 136, 148, 192, 219, 221, 225, 229).
- Cordier, M., Vandel, A., Cabot, G., Renou, B., and Boukhalfa, A. “Laser-Induced Spark Ignition of Premixed Confined Swirled Flames”. In: *Combustion Science and Technology* 185.3 (2013), pp. 379–407. DOI: 10.1080/00102202.2012.725791 (cited on pages 7, 68, 70, 78, 81, 136–138, 148, 192).
- Correia-Rodrigues, H., Tummers, M., van-Veen, E., and Roekaerts, D. “Effects of coflow temperature and composition on ethanol spray flames in hot-diluted coflow”. In: *International Journal of Heat and Fluid Flow* 51 (2015), pp. 309–323. DOI: <https://doi.org/10.1016/j.ijheatfluidflow.2014.10.006> (cited on pages 68, 70).
- Correia-Rodrigues, H., Tummers, M., van-Veen, E., and Roekaerts, D. “Spray flame structure in conventional and hot-diluted combustion regime”. In: *Combustion and Flame* 162.3 (2015), pp. 759–773. DOI: <https://doi.org/10.1016/j.combustflame.2014.07.033> (cited on pages 68, 70).
- Cozzi, F., Sharma, R., and Solero, G. “Analysis of coherent structures in the near-field region of an isothermal free swirling jet after vortex breakdown”. In: *Experimental Thermal and Fluid Science* 109 (2019), p. 109860. DOI: 10.1016/j.expthermflusci.2019.109860 (cited on pages 84, 229, 232).
- Crapper, G. and Dombrowski, N. “A note on the effect of forced disturbances on the stability of thin liquid sheets and on the resulting drop size”. In: *International Journal of Multiphase Flow* 10.6 (1984), pp. 731–736 (cited on page 35).
- Crialesi, M. “Analysis of primary atomization in sprays using Direct Numerical Simulation”. PhD thesis. Universitat Politècnica de València, 2019 (cited on page 9).
- Crowe, C. “Modeling turbulence in multiphase flow”. In: *Engineering Turbulence Modelling and Experiments* (1993), pp. 899–913. DOI: <https://doi.org/10.1016/B978-0-444-89802-9.50088-5> (cited on page 40).

- Crowe, C., Chung, J., and Troutt, T. "Particle mixing in free shear flows". In: *Progress in Energy and Combustion Science* 14.3 (1988), pp. 171–194. DOI: [https://doi.org/10.1016/0360-1285\(88\)90008-1](https://doi.org/10.1016/0360-1285(88)90008-1) (cited on pages 40, 41, 128).
- Crowe, C., Sommerfeld, M., Schwarzkopf, J., and Tsuji, Y. *Multiphase Flows with Droplets and Particles*. 2nd Edition. New York, USA: Taylor and Francis (cited on page 45).
- Custer, J. and Rizk, N. "Influence of design concept and liquid properties on fuel injector performance". In: *Journal of Propulsion and Power* 4.4 (1988), pp. 378–384. DOI: 10.2514/3.23077 (cited on page 49).
- Danby, S. and Echehki, T. "Proper orthogonal decomposition analysis of autoignition simulation data of nonhomogeneous hydrogen-air mixtures". In: *Combustion and Flame* 144.1-2 (2006), pp. 126–138. DOI: 10.1016/j.combustflame.2005.06.014 (cited on page 83).
- Daroukh, M., Moreau, S., Gourdain, N., Boussuge, J., and Sensiau, C. "Tonal Noise Prediction of a Modern Turbofan Engine With Large Upstream and Downstream Distortion". In: *Journal of Turbomachinery* 141.2 (2019). DOI: 10.1115/1.4042163 (cited on page 84).
- Davoudzadeh, F., Liu, N., and Moder, J. "Investigation of swirling air flows generated by axial swirlers in a flame tube". In: *Proceedings of the ASME Turbo Expo* 1 (2006), pp. 891–902. DOI: 10.1115/GT2006-91300 (cited on pages 75, 76, 79).
- De la Morena, J. "Estudio de la influencia de las características del flujo interno en toberas sobre el proceso de inyección Diesel en campo próximo". PhD thesis. Universitat Politècnica de València, 2011 (cited on page 9).
- Desantes, J., Salvador, F., Lopez, J., and De la Morena, J. "Study of mass and momentum transfer in diesel sprays based on X-ray mass distribution measurements and on a theoretical derivation". In: *Experiments in Fluids* 50.2 (2011), pp. 233–246. DOI: 10.1007/s00348-010-0919-8 (cited on page 62).
- Desjardins, O., Moureau, V., and Pitsch, H. "An accurate conservative level set/ghost fluid method for simulating turbulent atomization". In: *Journal of Computational Physics* (2008). DOI: 10.1016/j.jcp.2008.05.027 (cited on page 72).
- Development of the Lean Azimuthal Flame as an Innovative aviation gas turbine low-NOX combustion concept*. 2020. URL: <https://cordis.europa.eu/project/id/831804> (visited on 02/11/2020) (cited on page 6).

- Dewanji, D. and Rao, A. “Spray combustion modeling in lean direct injection combustors, part I: Single-element LDI”. In: *Combustion Science and Technology* 187.4 (2015), pp. 537–557. DOI: 10.1080/00102202.2014.965810 (cited on pages 75, 76).
- Dewanji, D. and Rao, A. “Spray combustion modeling in lean direct injection combustors, part II: Multi-point LDI”. In: *Combustion Science and Technology* 187.4 (2015), pp. 558–576. DOI: 10.1080/00102202.2014.958476 (cited on pages 75, 76, 82).
- Dombrowski, N. and Fraser, R. “A photographic investigation into the disintegration of liquid sheets”. In: *Journal of Mathematical and Physical Sciences* 247 (1954), pp. 101–130. DOI: 10.1098/rsta.1954.0014 (cited on page 35).
- Dombrowski, N. and Hooper, P. “The effect of ambient density on drop formation in sprays”. In: *Chemical Engineering Science* 17.4 (1962), pp. 291–305. DOI: [https://doi.org/10.1016/0009-2509\(62\)85008-8](https://doi.org/10.1016/0009-2509(62)85008-8) (cited on page 122).
- Dombrowski, N. and Johns, W. “The aerodynamic instability and disintegration of viscous liquid sheets”. In: *Journal of Chemical Engineering Science* 18 (1963), pp. 203–214 (cited on pages 35, 121, 123).
- Drennan, S. and Kumar, G. “Demonstration of an Automatic Meshing Approach for Simulation of a Liquid Fueled Gas Turbine with Detailed Chemistry”. In: *AIAA Propulsion and Energy Forum 2014* 3 of 9 (2014), pp. 2590–2597. DOI: 10.1081/E-EEE2-120046011 (cited on page 10).
- Drennan, S., Kumar, G., Steinthorsson, E., and Mansour, A. “Unsteady Simulations of a low NO_x LDI combustor for environmentally responsible aviation engines”. In: *Turbine Technical Conference and Exposition GT2015* (2015) (cited on page 10).
- Dressler, L., Sacomano Filho, F., Sadiki, A., and Janicka, J. “Influence of Thickening Factor Treatment on Predictions of Spray Flame Properties Using the ATF Model and Tabulated Chemistry”. In: *Flow, Turbulence and Combustion* (2020). DOI: 10.1007/s10494-020-00149-7 (cited on page 73).
- Dumouchel, C. “On the experimental investigation on primary atomization of liquid streams”. In: *Experiments in Fluids* 45 (2008), pp. 371–422 (cited on page 35).

- Duwig, C., Ducruix, S., and Veynante, D. “Studying the Stabilization Dynamics of Swirling Partially Premixed Flames by Proper Orthogonal Decomposition”. In: *Journal of Engineering for Gas Turbines and Power* 134.10 (2012), p. 101501. DOI: 10.1115/1.4007013 (cited on page 84).
- Elghobashi, S. and Truesdell, G. “On the two way interaction between homogeneous turbulence and dispersed solid particles. I: Turbulence modification”. In: *Physics of Fluids A: Fluid Dynamics* 5.7 (1993), pp. 1790–1801. DOI: 10.1063/1.858854 (cited on page 27).
- Esclapez, L. “Numerical study of ignition and inter-sector flame propagation in gas turbine”. PhD thesis. Institut National Polytechnique de Toulouse (INP Toulouse), 2015. DOI: 10.1017/CB09781107415324.004 (cited on pages 137, 138).
- Esclapez, L., Riber, E., and Cuenot, B. “Ignition probability of a partially premixed burner using LES”. In: *Proceedings of the Combustion Institute* 35.3 (2015), pp. 3133–3141. DOI: 10.1016/j.proci.2014.07.040 (cited on pages 78, 81, 137).
- Escudier, M. “Vortex breakdown: Observations and explanations”. In: *Progress in Aerospace Sciences* 25.2 (1988), pp. 189–229. DOI: 10.1016/0376-0421(88)90007-3 (cited on page 19).
- Escudier, M. and Zehnder, N. “Vortex-flow regimes”. In: *Journal of Fluid Mechanics* 115 (1982), pp. 105–121. DOI: 10.1017/S0022112082000676 (cited on pages 19, 232).
- Faeth, G. “Evaporation and combustion of sprays”. In: *Progress in Energy and Combustion Science* 9.1 (1983), pp. 1–76. DOI: [https://doi.org/10.1016/0360-1285\(83\)90005-9](https://doi.org/10.1016/0360-1285(83)90005-9) (cited on page 40).
- Faeth, G. “Mixing, transport and combustion in sprays”. In: *Progress in Energy and Combustion Science* 13.4 (1987), pp. 293–345. DOI: 10.1016/0360-1285(87)90002-5 (cited on page 116).
- Faeth, G., Hsiang, L., and Wu, P. “Structure and breakup properties of sprays”. In: *International Journal Of Multiphase Flow* 21 (1995), pp. 99–127 (cited on page 37).
- Fogleman, M., Lumley, J., Rempfer, D., and Haworth, D. In: *Journal of Turbulence* 5 (2004). DOI: 10.1088/1468-5248/5/1/023 (cited on page 83).
- Fraser, R. “Liquid fuel atomization”. In: *Sixth Symposium (International) on Combustion*. New York, United States of America, 1957, pp. 687–701 (cited on page 35).

- Fraser, R., Dombrowski, N., and Routley, J. “The atomization of a liquid sheet by an impinging air stream”. In: *Journal of Chemical Engineering Science* 18 (1963), pp. 339–353 (cited on page 35).
- Fraser, R. and Eisenklam, P. “Research into the performance of atomizers for liquids”. In: *Journal of the Imperial College Chemical Engineering Society* 7 (1953), pp. 52–68 (cited on pages 34, 35).
- Fraser, R., Eisenklam, P., Dombrowski, N., and Hasson, D. “Drop formation from rapidly moving sheets”. In: *Journal of American Institute of Chemical Engineers* 8.5 (1962), pp. 672–680 (cited on page 35).
- Friedman, J., Bentley, J., and Finkel, R. “An Algorithm for Finding Best Matches in Logarithmic Expected Time”. In: *ACM Trans. Math. Softw.* 3.3 (1977), pp. 209–226. DOI: 10.1145/355744.355745 (cited on page 159).
- Frolov, S., Posvianskii, V., and Basevich, V. “Evaporation and combustion of hydrocarbon fuel. Part I: Nonempirical model of single-component drop evaporation”. In: *Advanced Chemical Physics* 21 (2002), pp. 58–67 (cited on page 132).
- Frossling, N. “The evaporation of falling drops (in German)”. In: *Gerlands Beitrage zur Geophysik* 52 (1938), pp. 170–216 (cited on page 140).
- Fu, Y., Jeng, S., and Tacina, R. “Characteristics of the swirling flow in a multipoint LDI combustor”. In: *45th AIAA Aerospace Sciences Meeting, AIAA 2007-846*. 2007. DOI: 10.2514/6.2007-846 (cited on pages 66, 70, 75, 79, 82).
- Futrzynski, R. and Efraimsson, G. *Dymode: A parallel dynamic mode decomposition software*. Tech. rep. KTH Royal Institute of Technology, 2015. DOI: 10.13140/RG.2.1.4087.9126 (cited on page 158).
- Galley, D, Ducruix, S., Lacas, F., and Veynante, D. “Mixing and stabilization study of a partially premixed swirling flame using laser induced fluorescence”. In: *Combustion and Flame* 158.1 (2011), pp. 155–171. DOI: <https://doi.org/10.1016/j.combustflame.2010.08.004> (cited on page 201).
- García-Rosa, N. “Phénomènes d’allumage d’un foyer de turbomachine en conditions de haute altitude”. PhD thesis. Institut Supérieur de l’Aéronautique et de l’Espace - ONERA, 2008 (cited on pages 65, 70, 80, 81).
- García-Rosa, N., Linassier, G., Lecourt, R., Villedieu, P., and Lavergne, G. “Experimental and Numerical Study of High-Altitude Ignition of a Turbojet Combustor”. In: *Heat Transfer Engineering* 32 (2011), pp. 949–956. DOI: 10.1080/01457632.2011.556377 (cited on pages 66, 70).

- Gejji, R., Huang, C., Fugger, C., Yoon, C., and Anderson, W. “Parametric investigation of combustion instabilities in a single-element lean direct injection combustor”. In: *International Journal of Spray and Combustion Dynamics* 11 (2018), p. 1756827718785851. DOI: 10.1177/1756827718785851 (cited on pages 64, 274).
- Germano, M., Piomelli, U., Moin, P., and Cabot, W. “A dynamic subgrid-scale eddy viscosity model”. In: *Physics of Fluids A: Fluid Dynamics* 3.7 (1991), pp. 1760–1765. DOI: 10.1063/1.857955 (cited on page 115).
- Gibson, M. and Launder, B. “Ground effects on pressure fluctuations in the atmospheric boundary layer”. In: *Journal of Fluid Mechanics* 86.3 (1978), pp. 491–511. DOI: 10.1017/S0022112078001251 (cited on page 114).
- Gimeno, J. “Desarrollo y aplicación de la medida de flujo de cantidad de movimiento de un chorro Diesel”. PhD thesis. Universitat Politècnica de València, 2008. DOI: 10.4995/Thesis/10251/8306 (cited on page 9).
- Giridharan, M., Mongia, H., and Jeng, S. “Swirl Cup Modeling Part VIII : Spray Combustion in CFM-56 Single Cup Flame Tube”. In: *AIAA Paper* January (2003), pp. 1–11 (cited on page 20).
- Gounder, J., Kourmatzis, A., and Masri, A. “Turbulent piloted dilute spray flames: Flow fields and droplet dynamics”. In: *Combustion and Flame* 159.11 (2012), pp. 3372–3397. DOI: <https://doi.org/10.1016/j.combustflame.2012.07.014> (cited on pages 65, 70, 73, 81).
- Gousseau, P., Blocken, B., and Heijst, G. van. “Quality assessment of Large-Eddy Simulation of wind flow around a high-rise building: Validation and solution verification”. In: *Computers and Fluids* 79 (2013), pp. 120–133. DOI: 10.1016/J.COMPFLUID.2013.03.006 (cited on page 148).
- Grimm, F., Dierke, J., Ewert, R., Noll, B., and Aigner, M. “Modelling of combustion acoustics sources and their dynamics in the PRECCINSTA burner test case”. In: *International Journal of Spray and Combustion Dynamics* 9.4 (2017), pp. 330–348. DOI: 10.1177/1756827717717390 (cited on page 84).
- Grimm, F. et al. “Combustion Noise Dependency on Thermal Load and Global Equivalence Ratio in a Swirl-Stabilized Combustor”. In: *AIAA SciTech Forum*. 2019, pp. 1–24. DOI: 10.2514/6.2019-1582 (cited on page 84).
- Güner, H., Thomas, D., Dimitriadis, G., and Terrapon, V. “Unsteady aerodynamic modeling methodology based on dynamic mode interpolation for transonic flutter calculations”. In: *Journal of Fluids and Structures* 84 (2019), pp. 218–232. DOI: 10.1016/j.jfluidstructs.2018.11.002 (cited on page 83).

- Gupta, A., Lilley, D., and Syred, N. *Swirl flows*. Abacus Press, 1984 (cited on pages 19, 23).
- H., Simmons and C., Harding. “Some effects on using water as a test fluid in fuel nozzle spray analysis”. In: ASME Paper 80-GT-90, 1980 (cited on page 47).
- Hadef, R. and Lenze, B. “Measurements of droplets characteristics in a swirl-stabilized spray flame”. In: *Experimental Thermal and Fluid Science* 30.2 (2005), pp. 117–130. DOI: 10.1016/J.EXPHERMFLUSCI.2005.05.002 (cited on page 62).
- Hadef, R. and Lenze, B. “Effects of co- and counter-swirl on the droplet characteristics in a spray flame”. In: *Chemical Engineering and Processing: Process Intensification* 47.12 (2008), pp. 2209–2217. DOI: 10.1016/J.CEP.2007.11.017 (cited on page 62).
- Han, J. and Tryggvason, G. “Secondary breakup of axisymmetric liquid drops. II. Impulsive acceleration”. In: *Physics of Fluids* 13.6 (2001), pp. 1554–1565. DOI: 10.1063/1.1370389 (cited on page 38).
- Han, Z., Parrish, S., Farrell, P., and Reitz, R. “Modeling atomization processes of pressure-swirl hollow-cone fuel sprays.” In: *Atomization and Sprays* 7.6 (1997), pp. 663–684 (cited on page 119).
- Hanna, S., Hansen, O., and Dharmavaram, S. “FLACS CFD air quality model performance evaluation with Kit Fox, MUST, Prairie Grass, and EMU observations”. In: *Atmospheric Environment* 38.28 (2004), pp. 4675–4687. DOI: 10.1016/j.atmosenv.2004.05.041 (cited on page 148).
- Hanna, S., Tehranian, S., Carissimo, B., Macdonald, R., and Lohner, R. “Comparisons of model simulations with observations of mean flow and turbulence within simple obstacle arrays”. In: *Atmospheric Environment* 36 (2002), pp. 5067–5079. DOI: 10.1016/S1352-2310(02)00566-6 (cited on page 148).
- Haupt, R. and Haupt, S. *Practical Genetic Algorithms*. 2nd edition. John Wiley & Sons, 2004 (cited on page 269).
- Hayashi, S., Yamada, H., Shimodaira, K., and Machida, T. “NO_x emissions from non-premixed, direct fuel injection methane burners at high-temperature and elevated pressure conditions”. In: *Symposium (International) on Combustion* 27.2 (1998), pp. 1833–1839. DOI: 10.1016/S0082-0784(98)80025-8 (cited on page 60).

- Heath, C., Hicks, Y., Anderson, R., and Locke, R. “Optical Characterization of a Multipoint Lean Direct Injector for Gas Turbine Combustors: Velocity and Fuel Drop Size Measurements.” In: *Proceedings of the ASME Turbo Expo*. Vol. 2. 2010, pp. 791–802. DOI: 10.1115/GT2010-22960 (cited on pages 66, 67, 70).
- Hicks, Y., Heath, C., Anderson, R., and Tacina, K. “Investigations of a Combustor Using a 9-Point Swirl-Venturi Fuel Injector: Recent Experimental Results”. In: *20th International Symposium on Air Breathing Engines (IS-ABE)*. Göteborg (Suecia), 2011 (cited on pages 5, 67, 70).
- Hsiang, L. and Faeth, G. “Near-limit drop deformation and secondary breakup”. In: *International Journal of Multiphase Flow* 18.5 (1992), pp. 635–652. DOI: 10.1016/0301-9322(92)90036-G (cited on page 38).
- Hu, Y., Kai, R., Kurose, R., Gutheil, E., and Olguin, H. “Large eddy simulation of a partially pre-vaporized ethanol reacting spray using the multiphase DTF/flamelet model”. In: *International Journal of Multiphase Flow* 125 (2020), p. 103216. DOI: 10.1016/j.ijmultiphaseflow.2020.103216 (cited on page 73).
- Hu, Y. and Kurose, R. “Nonpremixed and premixed flamelets LES of partially premixed spray flames using a two-phase transport equation of progress variable”. In: *Combustion and Flame* 188 (2018), pp. 227–242. DOI: <https://doi.org/10.1016/j.combustflame.2017.10.004> (cited on page 73).
- Huang, C., Gejji, R., and Anderson, W. “Combustion Dynamics Behavior in a Single-Element Lean Direct Injection (LDI) Gas Turbine Combustor”. In: *50th AIAA/ASME/SAE/ASEE Joint Propulsion Conference*. Vol. 31. 0704. Cleveland, 2014 (cited on pages 153, 229).
- Huang, Y., Wang, S., and Yang, V. “Systematic Analysis of Lean-Premixed Swirl-Stabilized Combustion”. In: *Aiaa Journal* 44 (2006), pp. 724–740. DOI: 10.2514/1.15382 (cited on page 84).
- Huang, Y. and Yang, V. “Dynamics and stability of lean-premixed swirl-stabilized combustion”. In: *Progress in Energy and Combustion Science* 35.4 (2009), pp. 293–364. DOI: 10.1016/J.PECS.2009.01.002 (cited on pages 21, 24, 84, 184, 187, 254).
- Huh, K., Lee, E., and Koo, J. “Diesel spray atomization model considering nozzle exit turbulence conditions”. In: *Atomization and Sprays* 8 (1998), pp. 453–469. DOI: 10.1615/AtomizSpr.v8.i4.60 (cited on page 118).

- Hussain, U., Andrews, G., Cheung, W., and Shahabadi, A. "Low NO_x Primary Zones Using Jet Mixing Shear Layer Combustion". In: *Proceedings of the ASME Turbo Expo*. Vol. 3. 1988. DOI: 10.1115/88-GT-308 (cited on page 61).
- Hwang, S., Liu, Z., and Reitz, R. "Breakup mechanisms and drag coefficients of high speed vaporizing liquid drops". In: *Atomization and Sprays* 6.3 (1996). DOI: 10.1615/AtomizSpr.v6.i3.60 (cited on page 39).
- Ianiro, A., Lynch, K., Violato, D., Cardone, G., and Scarano, F. "Three-dimensional organization and dynamics of vortices in multichannel swirling jets". In: *Journal of Fluid Mechanics* 843 (2018), pp. 180–210. DOI: 10.1017/jfm.2018.140 (cited on page 84).
- Ibrahim, E., Yang, H., and Przekwas, A. "Modeling of spray droplets deformation and breakup". In: *Journal of Propulsion and Power* 9.4 (1993), pp. 651–654. DOI: 10.2514/3.23672 (cited on page 38).
- Innovative Technologies of Electrochemical Suppression and Electromagnetic Decomposition for NO_x Reduction in Aeroengines*. 2020. URL: <https://cordis.europa.eu/project/id/831848> (visited on 02/11/2020) (cited on page 6).
- Issa, R.I. "Solution of the implicitly discretised fluid flow equations by operator-splitting". In: *Journal of Computational Physics* 62.1 (1986), pp. 40–65. DOI: [https://doi.org/10.1016/0021-9991\(86\)90099-9](https://doi.org/10.1016/0021-9991(86)90099-9) (cited on page 135).
- Jaegle, F. et al. "Eulerian and Lagrangian spray simulations of an aeronautical multipoint injector". In: *Proceedings of the Combustion Institute* 33 (2011), pp. 2099–2107. DOI: 10.1016/j.proci.2010.07.027 (cited on page 73).
- James, S., Zhu, J., and Anand, M. "Large eddy simulations of turbulent flames using the filtered density function model". In: *Proceedings of the Combustion Institute* 31.2 (2007), pp. 1737–1745. DOI: 10.1016/j.proci.2006.07.160 (cited on page 75).
- Janus, B., Dreizler, A., and Janicka, J. "Experiments on swirl stabilized non-premixed natural gas flames in a model gasturbine combustor". In: *Proceedings of the Combustion Institute* 31 II (2007), pp. 3091–3098. DOI: 10.1016/j.proci.2006.07.014 (cited on pages 5, 64, 69).
- Janus, B., Dreizler, A., and Janicka, J. "Experimental Study on Stabilization of Lifted Swirl Flames in a Model GT Combustor". In: *Flow, Turbulence and Combustion* 75.1 (2005), pp. 293–315. DOI: 10.1007/s10494-005-8583-4 (cited on pages 64, 69).

- Jenny, P., Roekaerts, D., and Beishuizen, N. “Modeling of turbulent dilute spray combustion”. In: *Progress in Energy and Combustion Science* 38.6 (2012), pp. 846–887. DOI: 10.1016/j.pecs.2012.07.001 (cited on page 18).
- Jia, X., Yang, J., Zhang, J., and Ni, M. “An experimental investigation on the collision outcomes of binary liquid metal droplets”. In: *International Journal of Multiphase Flow* 116 (1992), pp. 80–90. DOI: 10.1016/j.ijmultiphaseflow.2019.04.008 (cited on page 42).
- Jiménez, J. and Moser, Robert D. “LES: Where are we and what can we expect”. In: *29th AIAA Fluid Dynamics Conference*. Vol. 38. 1998, pp. 1–11. DOI: 10.2514/6.1998-2891 (cited on page 180).
- Jones, W. P., Lettieri, C., Marquis, A. J., and Navarro-Martinez, S. “Large Eddy Simulation of the two-phase flow in an experimental swirl-stabilized burner”. In: *International Journal of Heat and Fluid Flow* 38 (2012), pp. 145–158. DOI: 10.1016/j.ijheatfluidflow.2012.09.001 (cited on pages 73, 74, 81).
- Jones, W., Marquis, A., and Vogiatzaki, K. “Large-eddy simulation of spray combustion in a gas turbine combustor”. In: *Combustion and Flame* 161.1 (2014), pp. 222–239. DOI: 10.1016/j.combustflame.2013.07.016 (cited on pages 77, 81).
- Joseph, D., Belanger, J., and Beavers, G. “Breakup of a liquid drop suddenly exposed to a high-speed airstream”. In: *International Journal of Multiphase Flow* 25 (1999), pp. 1263–1303. DOI: 10.1016/j.ijmultiphaseflow.2003.11.004 (cited on page 38).
- Joyce, J. “The Atomisation of Liquid Fuels”. In: *The Journal of the Royal Aeronautical Society* 58.518 (1954). DOI: 10.1017/S0368393100097832 (cited on page 50).
- Al-Kabie, H. and Andrews, G. “Ultra low NO_x emissions for gas and liquid fuels using radial swirlers”. In: *Proceedings of the ASME Turbo Expo*. Vol. 3. 1989. DOI: 10.1115/89-GT-322 (cited on pages 60, 61).
- Al-Kabie, H. and Andrews, G. “Radial swirlers with peripheral fuel injection for ultra-low NO_x emissions”. In: *Proceedings of the ASME Turbo Expo*. Vol. 3. 1990. DOI: 10.1115/90-GT-102 (cited on page 60).
- Karlis, E., Liu, Y., Hardalupas, Y., and Taylor, A. “H₂ enrichment of CH₄ blends in lean premixed gas turbine combustion: An experimental study on effects on flame shape and thermoacoustic oscillation dynamics”. In: *Fuel* 254 (2019), p. 115524. DOI: 10.1016/j.fuel.2019.05.107 (cited on pages 84, 229).

- Karlis, E. et al. "Thermoacoustic phenomena in an industrial gas turbine combustor at two different mean pressures". In: *AIAA SciTech Forum*. January. San Diego, California, 2019, pp. 1–17. DOI: 10.2514/6.2019-0675 (cited on page 84).
- Kennedy, J. "High weber number SMD correlations for pressure atomizers". In: *Journal of Engineering for Gas Turbines and Power* 108.1 (1986), pp. 191–195. DOI: 10.1115/1.3239870 (cited on page 47).
- Kim, J., Jung, W., Hong, J., and Sung, H. "The Effects of Turbulent Burning Velocity Models in a Swirl-Stabilized Lean Premixed Combustor". In: *International Journal of Turbo and Jet Engines* 35.4 (2018), pp. 365–372. DOI: 10.1515/tjj-2016-0053 (cited on page 84).
- Kim, S., Menon, S., and Darin, J. "Large-Eddy Simulation of a High-Pressure, Single-Element Lean Direct-Injected Gas-Turbine Combustor". In: *52nd Aerospace Sciences Meeting*. 2014. DOI: 10.2514/6.2014-0131 (cited on pages 71, 84).
- Kirkpatrick, M. "A large eddy simulation code for industrial and environmental flows". PhD thesis. The University of Sydney, 2002 (cited on page 72).
- Kirtas, M., Patel, N., Sankaran, S., and Menon, S. "Large-Eddy Simulation of a Swirl-Stabilized, Lean Direct Injection Spray Combustor". In: *Proceedings of the ASME Turbo Expo*. 2006, pp. 903–914. DOI: 10.1115/GT2006-91310 (cited on page 75).
- Knudsen, E. and Pitsch, H. "Large Eddy Simulation of a Spray Combustor Using a Multi-regime Flamelet Approach". In: *Annual Research Briefs, Center for Turbulence Research (Stanford University)* (2010), pp. 337–350 (cited on page 75).
- Kou, J. and Zhang, W. "An improved criterion to select dominant modes from dynamic mode decomposition". In: *European Journal of Mechanics, B/Fluids* 62 (2017), pp. 109–129. DOI: 10.1016/j.euromechflu.2016.11.015 (cited on pages 158, 229).
- Krzeczkowski, S. "Measurement of liquid droplet disintegration mechanisms". In: *International Journal of Multiphase Flow* 6.3 (1980), pp. 227–239. DOI: 10.1016/0301-9322(80)90013-0 (cited on page 37).
- Kumar, G. and Drennan, S. "A CFD Investigation of Multiple Burner Ignition and Flame Propagation with Detailed Chemistry and Automatic Meshing". In: *AIAA Propulsion and Energy 2016 Conference* 4 of 9 (2016), pp. 20–54. DOI: 10.1081/E-EEE2-120046011 (cited on page 10).

- Lamarque, N. “Schémas numériques et conditions limites pour la simulation aux grandes échelles de la combustion diphasique dans les foyers d’hélicoptère”. PhD thesis. Institut National Polytechnique de Toulouse - CERFACS, 2007 (cited on page 73).
- Lamb, H. *Hydrodynamics*. 6th edition. Dover Publications, 1945 (cited on page 125).
- Law, C. “Recent advances in droplet vaporization and combustion”. In: *Progress in Energy and Combustion Science* 8.3 (1982), pp. 171–201. DOI: 10.1016/0360-1285(82)90011-9 (cited on page 132).
- Leask, S., Li, A., McDonell, V., and Samuelsen, S. “Preliminary Development of a Measurement Reference Using a Research Simplex Atomizer”. In: *Journal of Fluids Engineering, Transactions of the ASME* 141.12 (2019), pp. 1–11. DOI: 10.1115/1.4044072 (cited on page 238).
- Lecourt, R., Bismes, G., and Heid, G. “Experimental Investigation of Ignition of an Air-Kerosene Spray in Altitude Conditions”. In: *International Symposium on Air Breathing Engines (ISABE)*. 2009 (cited on page 66).
- Lecourt, R., Linassier, G., and Lavergne, G. “Detailed Characterisation of a Swirled Air/Kerosene Spray in Reactive and Non-Reactive Conditions Downstream From an Actual Turbojet Injection System”. In: *Proceedings of the ASME Turbo Expo*. Vol. 2. 2011, pp. 185–194. DOI: 10.1115/GT2011-45173 (cited on page 65).
- Lecourt, R., Rossoni, Laurent, Goyer, Stephen, and Linassier, Guillaume. “Gas Phase Velocity Measurements in a Swirled Air/Kerosene Burning Spray downstream from an Actual Turbojet Injection System”. In: *50th AIAA/ASME/SAE/ASEE Joint Propulsion Conference*. 2014. DOI: 10.2514/6.2014-3659 (cited on page 65).
- Lefebvre, A. “The prediction of sauter mean diameter for simplex pressure-swirl atomisers”. In: *Atomisation Spray Technology* 3.1 (1987), pp. 37–51 (cited on page 47).
- Lefebvre, A. *Atomization and Sprays*. Hemisphere Publishing Corporation, 1989 (cited on pages 24, 26, 119).
- Lefebvre, A. “Properties of Sprays”. In: *Particle and Particle Systems Characterization* 6.1-4 (1989), pp. 176–186. DOI: 10.1002/ppsc.19890060129 (cited on pages 33, 47, 50, 51).
- Lefebvre, A. and Ballal, D. *Gas turbine combustion: alternative fuels and emissions*. 3rd edition. Taylor and Francis, 2010 (cited on pages 1, 3, 5, 24, 120, 249).

- Lefebvre, A. and Suyari, M. “Film thickness measurements in a simplex swirl atomizer”. In: *Journal of Propulsion and Power* 2.6 (1986), pp. 528–533. DOI: 10.2514/3.22937 (cited on page 47).
- Lefebvre, A.H. “Factors controlling gas turbine combustion performance at high pressures”. In: *Cranfield International Symposium Series* 10 (1968), pp. 211–226 (cited on page 49).
- Legier, J., Poinso, T., and Veynante, D. “Dynamically Thickened Flame LES model for Premixed and Non-premixed Turbulent Combustion”. In: *Proceedings of the Summer Program, Center for Turbulence Research (Stanford University)* (2000), pp. 157–168 (cited on page 75).
- Legrand, M., Nogueira, J., Lecuona, A., Nauri, S., and Rodríguez, P. “Atmospheric low swirl burner flow characterization with stereo PIV”. In: *Experiments in Fluids* 48 (2009), pp. 901–913. DOI: 10.1007/s00348-009-0775-6 (cited on page 84).
- Lengani, D. et al. “Identification and quantification of losses in a LPT cascade by POD applied to LES data”. In: *International Journal of Heat and Fluid Flow* 70 (2018), pp. 28–40. DOI: <https://doi.org/10.1016/j.ijheatfluidflow.2018.01.011> (cited on page 83).
- Lew, H., Carl, D., Vermes, G., and DeZubay, E. “Low NO_x heavy fuel combustor concept program. Phase 1: Combustion technology generation”. In: *NASA Technical Report NASA-CR-165482* (1981) (cited on page 61).
- Li, Guoqiang and Gutmark, Effie. “Effects of Swirler Configurations on Flow Structures and Combustion Characteristics”. In: vol. 1. 2004. DOI: 10.1115/GT2004-53674 (cited on pages 63, 69).
- Li, X. and Soteriou, M. “High-fidelity simulation of fuel atomization in a realistic swirling flow injector”. In: *Atomization and Sprays* 23 (2013), pp. 1049–1078. DOI: 10.1615/AtomizSpr.2013007395 (cited on page 33).
- Lilley, D. “Swirl Flows in Combustion: A Review”. In: *AIAA Journal* 15.8 (1977), pp. 1063–1078. DOI: 10.2514/3.60756 (cited on page 23).
- Lilly, D. “A proposed modification of the Germano subgrid-scale closure method”. In: *Physics of Fluids A: Fluid Dynamics* 4.3 (1992), pp. 633–635. DOI: 10.1063/1.858280 (cited on page 115).
- Lin, S. *Breakup of Liquid Sheets and Jets*. Cambridge University Press, 2003. DOI: 10.1017/CB09780511547096 (cited on page 35).

- Linassier, G., Lecourt, R., Villedieu, P., Lavergne, G., and Verdier, H. “Numerical and Experimental study of aircraft engine ignition”. In: *ILASS - Europe 2010, 23rd Annual Conference on Liquid Atomization and Spray Systems*. 2010, pp. 1–10 (cited on pages 65, 70).
- Linassier, G. et al. “Application of numerical simulations to predict aircraft combustor ignition”. In: *Comptes Rendus Mécanique* 341.1-2 (2013), pp. 201–210. DOI: 10.1016/J.CRME.2012.11.009 (cited on page 5).
- Linne, M., Paciaroni, M., Berrocal, E., and Sedarsky, D. “Ballistic imaging of liquid break-up processes in dense sprays”. In: *Proceedings of Combustion Institute* 32.2 (2009), pp. 2147–2161. DOI: 10.1016/j.proci.2008.07.040 (cited on page 62).
- Lippert, A. and Reitz, R. “Modeling of Multicomponent Fuels Using Continuous Distributions with Application to Droplet Evaporation and Sprays”. In: *International Fuels and Lubricants Meeting and Exposition*. SAE International, 1997. DOI: <https://doi.org/10.4271/972882> (cited on page 45).
- Liu, A., Mather, D., and Reitz, R. “Modeling the Effects of Drop Drag and Breakup on Fuel Sprays”. In: *International Congress Exposition*. SAE International, 1993. DOI: <https://doi.org/10.4271/930072> (cited on pages 39, 41).
- Liu, N., Shih, T., and Wey, C. “Numerical Simulations of Two-Phase Reacting Flow in a Single-Element Lean Direct Injection (LDI) Combustor Using NCC”. In: *NASA Technical Report NASA/TM-217031* (2011) (cited on pages 75, 76, 80).
- Liu, N., Shih, T., and Wey, T. “Comprehensive combustion modeling and simulation: Recent progress at NASA Glenn Research Center”. In: *International Symposium on Air Breathing Engines (ISABE)*. 2007 (cited on page 75).
- Liu, Y. et al. “Review of modern low emissions combustion technologies for aero gas turbine engines”. In: *Progress in Aerospace Sciences* 94 (2017), pp. 12–45. DOI: 10.1016/j.paerosci.2017.08.001 (cited on pages 2, 60).
- Liu, Z. and Reitz, R. “An analysis of the distortion and breakup mechanisms of high speed liquid drops”. In: *International Journal of Multiphase Flow* 23.4 (1997), pp. 631–650. DOI: 10.1016/S0301-9322(96)00086-9 (cited on pages 37, 38).

- Lorber, A. “Error propagation and figures of merit for quantification by solving matrix equations”. In: *Analytical Chemistry* 58.6 (1986), pp. 1167–1172. DOI: 10.1021/ac00297a042 (cited on page 269).
- Lucca-Negro, O. and O’Doherty, T. “Vortex breakdown: A review”. In: *Progress in Energy and Combustion Science* 27 (2001), pp. 431–481. DOI: 10.1016/S0360-1285(00)00022-8 (cited on page 19).
- Lumley, J. “The structure of inhomogeneous turbulent flows”. In: *Atmospheric Turbulence and Radio Wave Propagation (Eds. A.M. Yaglom and V.I. Tatarsky)* (1967), p. 166 (cited on pages 83, 153).
- Lumley, J. *Stochastic Tools in Turbulence*. Academic Press, 1970 (cited on page 153).
- Luo, J. “Design optimization of the last stage of a 4.5-stage compressor using a POD-based hybrid model”. In: *Aerospace Science and Technology* 76 (2018), pp. 303–314. DOI: <https://doi.org/10.1016/j.ast.2018.01.043> (cited on page 83).
- Luo, K., Pitsch, H., Pai, M. G., and Desjardins, O. “Direct numerical simulations and analysis of three-dimensional n-heptane spray flames in a model swirl combustor”. In: *Proceedings of the Combustion Institute* 33.2 (2011), pp. 2143–2152. DOI: 10.1016/j.proci.2010.06.077 (cited on pages 76, 80).
- Mahesh, K. et al. “Large-eddy simulation of reacting turbulent flows in complex geometries”. In: *Journal of Applied Mechanics* 73.3 (2006), p. 374. DOI: 10.1115/1.2179098 (cited on page 76).
- Malalasekera, W., Ranga-Dinesh, K., Ibrahim, S., and Masri, A. “LES of recirculation and vortex breakdown in swirling flames”. In: *Combustion Science and Technology* 180.5 (2008), pp. 809–832. DOI: 10.1080/00102200801894018 (cited on pages 72, 73, 79).
- Marchione, T., Ahmed, S., and Mastorakos, E. “Ignition of turbulent swirling n-heptane spray flames using single and multiple sparks”. In: *Combustion and Flame* 156.1 (2009), pp. 166–180. DOI: 10.1016/J.COMBUSTFLAME.2008.10.003 (cited on page 6).
- Marrero-Santiago, J. “Experimental study of lean aeronautical ignition. Impact of critical parameters on the mechanisms acting along the different ignition phases.” PhD thesis. INSA de Rouen - Normandie, 2018 (cited on pages 138–140, 202, 204, 205).

- Marrero-Santiago, J. et al. “Experimental study of airflow velocity, fuel droplet size-velocity and flame structure in a confined swirled jet-spray flame”. In: *ILASS - Europe 2016, 27th Conference on Liquid Atomization and Spray Systems*. September. Brighton, United Kingdom, 2016 (cited on pages 68, 70, 78, 82, 138, 139).
- Martí-Aldaraví, P. “Development of a computational model for a simultaneous simulation of internal flow and spray break-up of the Diesel injection process”. PhD thesis. Universitat Politècnica de València, 2014. DOI: 10.4995/Thesis/10251/43719 (cited on page 9).
- Masri, A. and Gounder, J. “Turbulent Spray Flames of Acetone and Ethanol Approaching Extinction”. In: *Combustion Science and Technology* 182.4-6 (2010), pp. 702–715. DOI: 10.1080/00102200903467754 (cited on page 65).
- Masri, A., Kalt, P., Al-Abdeli, Y., and Barlow, R. “Turbulence-chemistry interactions in non-premixed swirling flames”. In: *Combustion Theory and Modelling* 11.5 (2007), pp. 653–673. DOI: 10.1080/13647830701213482 (cited on page 65).
- Masri, A., Kalt, P., and Barlow, R. “The compositional structure of swirl-stabilised turbulent nonpremixed flames”. In: *Combustion and Flame* 137.1 (2004), pp. 1–37. DOI: <https://doi.org/10.1016/j.combustflame.2003.12.004> (cited on page 65).
- McVey, J. et al. “Evaluation of low NOX combustor concepts for aeroderivative gas turbine engines”. In: *ASME 1992 International Gas Turbine and Aeroengine Congress and Exposition*. Vol. 3. 1992. DOI: 10.1115/92-GT-133 (cited on page 60).
- Meadows, J. and Agrawal, A. “Time-resolved PIV of lean premixed combustion without and with porous inert media for acoustic control”. In: *Combustion and Flame* 162.4 (2015), pp. 1063–1077. DOI: 10.1016/j.combustflame.2014.09.028 (cited on page 83).
- Mehring, C. and Sirignano, W. “Review of theory of distortion and disintegration of liquid streams”. In: *Progress in Energy and Combustion Science* 26 (2000), pp. 609–655 (cited on page 35).
- Meier, Ulrich, Heinze, Johannes, Freitag, Stefan, and Hassa, Christoph. “Spray and flame structure of a generic injector at aeroengine conditions”. In: *Journal of Engineering for Gas Turbines and Power* 134.3 (2012), pp. 1–9. DOI: 10.1115/1.4004262 (cited on pages 65, 69, 77, 81).

- Meier, W., Keck, O., Noll, B., Kunz, O., and Stricker, W. "Investigations in the TECFLAM swirling diffusion flame: Laser Raman measurements and CFD calculations". In: *Applied Physics B: Lasers and Optics* 71.5 (2000), pp. 725–731. DOI: 10.1007/s003400000436 (cited on pages 63, 69).
- Meier, W., Weigand, P., Duan, X., and Giezendanner-Thoben, R. "Detailed characterization of the dynamics of thermoacoustic pulsations in a lean premixed swirl flame". In: *Combustion and Flame* 150.1-2 (2007), pp. 2–26. DOI: 10.1016/j.combustflame.2007.04.002 (cited on pages 65, 69).
- Ménard, T., Tanguy, S., and Berlemont, A. "Coupling level set/VOF/ghost fluid methods: Validation and application to 3D simulation of the primary break-up of a liquid jet". In: *International Journal of Multiphase Flow* 33.5 (2007), pp. 510–524. DOI: 10.1016/j.ijmultiphaseflow.2006.11.001 (cited on page 72).
- Menon, S. and Patel, N. "Subgrid Modeling for Simulation of Spray Combustion in Large-Scale Combustors". In: *AIAA Journal* 44.4 (2006), pp. 709–723. DOI: 10.2514/1.14875 (cited on pages 71, 107).
- Mira, D. et al. "Numerical Characterization of a Premixed Hydrogen Flame Under Conditions Close to Flashback". In: *Flow, Turbulence and Combustion* 104.2-3 (2020), pp. 479–507. DOI: 10.1007/s10494-019-00106-z (cited on page 84).
- Moin, P. and Apte, S. "Large-eddy simulation of realistic gas turbine combustors". In: *AIAA Journal* 44.4 (2006), pp. 698–708 (cited on pages 71, 76).
- Mongia, H. "TAPS: A Fourth Generation Propulsion Combustor Technology for Low Emissions". In: *AIAA International Air and Space Symposium and Exposition* July (2003), pp. 1–11. DOI: 10.2514/6.2003-2657 (cited on pages 3, 4).
- Montgomery, D. *Design and analysis of experiments*. John Wiley & Sons, 2017 (cited on page 249).
- Mosier, S. and R., Pierce. "Advanced Combustion Systems for Stationary Gas Turbine Engines: Volume 1 Review and Preliminary Evaluation". In: *U.S. Environmental Protection Agency Technical Report EPA-600/7-80-017a* (1980) (cited on page 2).
- Moureau, V., Domingo, P., and Vervisch, L. "Design of a massively parallel CFD code for complex geometries". In: *Comptes Rendus Mécanique* 339.2 (2011), pp. 141–148. DOI: 10.1016/j.crme.2010.12.001 (cited on page 78).

- Moureau, V., Domingo, P., and Vervisch, L. “From Large-Eddy Simulation to Direct Numerical Simulation of a lean premixed swirl flame: Filtered laminar flame-PDF modeling”. In: *Combustion and Flame* 158.7 (2011), pp. 1340–1357. DOI: 10.1016/j.combustflame.2010.12.004 (cited on pages 76, 77, 80).
- Mugele, R. and Evans, H. “Droplet Size Distribution in Sprays”. In: *Industrial and Engineering Chemistry* 43.6 (1951), pp. 1317–1324. DOI: 10.1021/ie50498a023 (cited on page 46).
- Mulla, I., Godard, G., Cabot, G., Grisch, F., and Renou, B. “Quantitative imaging of nitric oxide concentration in a turbulent n-heptane spray flame”. In: *Combustion and Flame* 203 (2019), pp. 217–229. DOI: 10.1016/j.combustflame.2019.02.005 (cited on page 68).
- Neophytou, A., Mastorakos, E., and Cant, R. S. “DNS of spark ignition and edge flame propagation in turbulent droplet-laden mixing layers”. In: *Combustion and Flame* 157.6 (2010), pp. 1071–1086. DOI: 10.1016/j.combustflame.2010.01.019 (cited on page 71).
- Nguyen, L. and Bittker, D. “Investigation of low NO_x staged combustor concept in high-speed civil transport engines”. In: *NASA Technical Report NASA-TM-101977* (1989) (cited on page 61).
- Nikiforov, V. “The energy of graphs and matrices”. In: *Journal of Mathematical Analysis and Applications* 326.2 (2007), pp. 1472–1475. DOI: 10.1016/j.jmaa.2006.03.072 (cited on pages 156, 271).
- Novick, A. and Troth, D. “Low NO_x heavy fuel combustor concept”. In: *NASA Technical Report NASA-CR-165367* (1981) (cited on page 61).
- Nukiyama, S. and Tanasawa, Y. “Experiments on the atomization of liquids in an airstream”. In: *Trans. Soc. Mech. Eng. Jpn* 5 (1939), pp. 68–75 (cited on page 48).
- Nyquist, H. “Regeneration Theory”. In: *Bell System Technical Journal* 11.1 (1932), pp. 126–147. DOI: 10.1002/j.1538-7305.1932.tb02344.x (cited on page 159).
- Oberleithner, K., Paschereit, C., Seele, R., and Wygnanski, I. “Formation of Turbulent Vortex Breakdown: Intermittency, Criticality, and Global Instability”. In: *AIAA Journal* 50 (2012), pp. 1437–1452. DOI: 10.2514/1.J050642 (cited on page 84).
- Oberleithner, K. et al. “Three-dimensional coherent structures in a swirling jet undergoing vortex breakdown: Stability analysis and empirical mode construction”. In: *Journal of Fluid Mechanics* 679 (2011), pp. 383–414. DOI: 10.1017/jfm.2011.141 (cited on pages 84, 226, 229).

- O'Connor, J. and Lieuwen, T. "Recirculation zone dynamics of a transversely excited swirl flow and flame". In: *Physics of Fluids* 24.7 (2012). DOI: 10.1063/1.4731300 (cited on page 232).
- OpenFOAM 6.0 User Guide*. 2018. URL: <https://cfd.direct/openfoam/user-guide-v6/> (visited on 04/21/2020) (cited on pages 116, 124).
- O'Rourke, P. "Collective Drop Effects on Vaporizing Liquid Sprays". PhD thesis. Princeton University, 1981 (cited on pages 28, 39, 44, 128–130, 140).
- O'Rourke, P. and Amsden, A. "The tab method for numerical calculation of spray droplet breakup". In: *SAE Technical Papers* (1987). DOI: 10.4271/872089 (cited on pages 38, 118, 124, 126, 140).
- O'Rourke, P. and Bracco, F. "Modelling of drop interactions in thick sprays and a comparison with experiments". In: *Stratified Charge Automotive Engine, IMechE*. 1980 (cited on pages 39, 41).
- Ortman, J. and Lefebvre, A. "Fuel distributions from pressure-swirl atomizers". In: *Journal of Propulsion and Power* 1 (1985), pp. 11–15. DOI: 10.2514/3.22752 (cited on page 51).
- Papadogiannis, D. et al. "Assessment of the Indirect Combustion Noise Generated in a Transonic High-Pressure Turbine Stage". In: *Journal of Engineering for Gas Turbines and Power* 138.4 (2015). DOI: 10.1115/1.4031404 (cited on page 84).
- Patel, N. and Menon, S. "Simulation of spray-turbulence-flame interactions in a lean direct injection combustor". In: *Combustion and Flame* 153 (2008), pp. 228–257. DOI: 10.1016/j.combustflame.2007.09.011 (cited on pages 6, 20, 74, 75, 79, 84, 107, 200, 201).
- Patterson, M. and Reitz, R. "Modeling the Effects of Fuel Spray Characteristics on Diesel Engine Combustion and Emission". In: *International Congress and Exposition*. SAE International, 1998. DOI: <https://doi.org/10.4271/980131> (cited on page 118).
- Payri, R., Novella, R., Carreres, M., and Belmar-Gil, M. "Study about the influence of an automatic meshing algorithm on numerical simulations of a Gaseous-Fueled Lean Direct Injection (LDI) Gas Turbine Combustor in Non-Reactive conditions". In: *ILASS - Europe 2019, 29th Conference on Liquid Atomization and Spray Systems*. Paris, France, 2019 (cited on pages 10, 137).

- Payri, R., Novella, R., Carreres, M., and Belmar-Gil, M. “Modeling gaseous non-reactive flow in a lean direct injection gas turbine combustor through an advanced mesh control strategy”. In: *Proceedings of the Institution of Mechanical Engineers, Part G: Journal of Aerospace Engineering* 234.11 (2020), pp. 1788–1810. DOI: 10.1177/0954410020919619 (cited on page 10).
- Payri, R., Salvador, F., Gimeno, J., and Cardona, S. “Experimental study of the influence of the boundary conditions on the atomization process in an unconfined atmospheric burner”. In: *ILASS - Europe 2019, 29th Conference on Liquid Atomization and Spray Systems*. Paris, France, 2019 (cited on page 10).
- Pera, C. and Reveillon, J. “Direct numerical simulation of spray flame/acoustic interactions”. In: *Proceedings of the Combustion Institute* 31 II (2007), pp. 2283–2290. DOI: 10.1016/j.proci.2006.07.153 (cited on page 71).
- Percin, M., Vanierschot, M., and Oudheusden, B. van. “Analysis of the pressure fields in a swirling annular jet flow”. In: *Experiments in Fluids* 58.12 (2017), p. 166. DOI: 10.1007/s00348-017-2446-3 (cited on page 84).
- Pomraning, E. and Rutland, C. “Dynamic One-Equation Nonviscosity Large-Eddy Simulation Model”. In: *AIAA Journal* 40.4 (2002), pp. 689–701. DOI: 10.2514/2.1701 (cited on page 115).
- Pope, S. *Turbulent Flows*. Cambridge University Press, 2000. DOI: 10.1017/CB09780511840531 (cited on pages 111, 113).
- Pope, S. “Ten questions concerning the large-eddy simulation of turbulent flows”. In: *New Journal of Physics* 6 (2004), p. 3. DOI: 10.1088/1367-2630/6/1/035 (cited on page 182).
- Puggelli, S. “Towards a unified approach for Large Eddy Simulation of turbulent spray flames”. PhD thesis. Universita degli studi Firenze, 2018 (cited on page 3).
- Qian, J. and Law, C. “Regimes of coalescence and separation in droplet collision”. In: *Journal of Fluid Mechanics* 331 (1997), pp. 59–80. DOI: 10.1017/S0022112096003722 (cited on page 44).
- Radcliffe, A. “Fuel Injection, High Speed Aerodynamics and Jet Propulsion”. In: *Technical Report XIX* 11 (1960), p. 84 (cited on page 47).
- Rajpal, D., Gillebaart, E., and De Breuker, R. “Preliminary aeroelastic design of composite wings subjected to critical gust loads”. In: *Aerospace Science and Technology* 85 (2019), pp. 96–112. DOI: <https://doi.org/10.1016/j.ast.2018.11.051> (cited on page 83).

- Ramaekers, W., Tap, F., and Boersma, B. "Subgrid Model Influence in Large Eddy Simulations of Non-reacting Flow in a Gas Turbine Combustor". In: *Flow, Turbulence and Combustion* 100.2 (2018), pp. 457–479. DOI: 10.1007/s10494-017-9853-7 (cited on pages 78, 82).
- Raman, V. and Pitsch, H. "Large-eddy simulation of a bluff-body-stabilized non-premixed flame using a recursive filter-refinement procedure". In: *Combustion and Flame* 142.4 (2005), pp. 329–347. DOI: 10.1016/j.combustflame.2005.03.014 (cited on page 71).
- Rangel, R. and Sirignano, W. "The linear and non-linear shear instability of a fluid sheet". In: *Physics of Fluids* 3 (1999), pp. 2392–2400 (cited on page 35).
- Ranz, W. and Marshall, W. "Evaporation from drops". In: *Chemical Engineering Progress* 48 (1952), pp. 141–146 (cited on page 132).
- Reddemann, M., Mathieu, F., and Kneer, R. "Transmitted light microscopy for visualizing the turbulent primary breakup of a microscale liquid jet". In: *Experiments in Fluids* 54.11 (2013), p. 1607. DOI: 10.1007/s00348-013-1607-2 (cited on page 62).
- Reichel, T., Goeckeler, K., and Paschereit, O. "Investigation of Lean Premixed Swirl-Stabilized Hydrogen Burner With Axial Air Injection Using OH-PLIF Imaging". In: *Journal of Engineering for Gas Turbines and Power* 137.11 (2015). DOI: 10.1115/1.4031181 (cited on page 84).
- Reitz, R. "Modeling atomization processes in high-pressure vaporizing sprays". In: *Atomisation Spray Technology* 3 (1987), pp. 309–337 (cited on page 118).
- Reitz, R. and Bracco, F. "Mechanisms of Breakup of Round Liquid Jets". In: *The Encyclopedia of Fluid Mechanics* 3 (1986), pp. 223–249 (cited on pages 118, 122).
- Renaud, A., Tachibana, S., Arase, S., and Yokomori, T. "Experimental Study of Thermo-Acoustic Instability Triggering in a Staged Liquid Fuel Combustor Using High-Speed OH-PLIF". In: *Journal of Engineering for Gas Turbines and Power* 140.8 (2018), p. 081505. DOI: 10.1115/1.4038915 (cited on page 84).
- Renksizbulut, M., Bussmann, M., and Li, X. "A Droplet Vaporization Model for Spray Calculations". In: *Particle and Particle Systems Characterization* 9.1 (1992), pp. 59–65. DOI: 10.1002/ppsc.19920090110 (cited on page 45).

- Renksizbulut, M., Nafziger, R., and Li, X. “A mass transfer correlation for droplet evaporation in high-temperature flows”. In: *Chemical Engineering Science* 46 (1991), pp. 2351–2358 (cited on page 45).
- Report of the High Level Group on Aviation Research*. Tech. rep. European Commission. 2011. DOI: 10.2777/50266 (cited on page 1).
- Reveillon, J. and Demoulin, F. X. “Evaporating droplets in turbulent reacting flows”. In: *Proceedings of the Combustion Institute* 31 II (2007), pp. 2319–2326. DOI: 10.1016/j.proci.2006.07.114 (cited on page 71).
- Rhie, C. and Chow, W. “Numerical study of the turbulent flow past an airfoil with trailing edge separation”. In: *AIAA Journal* 21.11 (1983), pp. 1525–1532. DOI: 10.2514/3.8284 (cited on page 144).
- Riber, E., Moureau, V., García-Rosa, M., Poinso, T., and Simonin, O. “Evaluation of numerical strategies for large eddy simulation of particulate two-phase recirculating flows”. In: *Journal of Computational Physics* 228.2 (2009), pp. 539–564. DOI: 10.1016/j.jcp.2008.10.001 (cited on page 71).
- Richecoeur, F., Hakim, L., Renaud, A., and Zimmer, L. “DMD algorithms for experimental data processing in combustion”. In: *Center for Turbulence Research (Stanford University)*. 2012, pp. 459–468 (cited on page 84).
- Rittler, A., Proch, F., and Kempf, A. “LES of the Sydney piloted spray flame series with the PFGM/ATF approach and different sub-filter models”. In: *Combustion and Flame* 162 (2015), pp. 1575–1598. DOI: 10.1016/J.COMBUSTFLAME.2014.11.025 (cited on page 73).
- Rizk, N. and Lefebvre, A. “Prediction of velocity coefficient and spray cone angle for simplex swirl atomizers”. In: *Proc. 3rd Int. Conf. Liquid Atomization and Spray Systems, 111C/2/1-16*. 1985. DOI: 10.2514/6.1992-463 (cited on page 50).
- Rizk, N. and Mongia, H. “Performance of hybrid airblast atomizers under low power conditions”. In: *30th Aerospace Sciences Meeting and Exhibit*. 1992. DOI: 10.2514/6.1992-463 (cited on page 49).
- Roe, P. “Characteristic-Based Schemes for the Euler Equations”. In: *Annual Review of Fluid Mechanics* 18.1 (1986), pp. 337–365. DOI: 10.1146/annurev.fl.18.010186.002005 (cited on page 134).
- Rosfjord, T. “Evaluation of synthetic fuel character effects on rich-lean stationary gas turbine combustion systems. Vol. 1: Subscale test program”. In: *Electric Power Research Institute Technical Report AP-2822* (1981) (cited on page 61).

- Rosin, P. and Rammler, E. “The laws governing the fineness of powdered coal”. In: *Journal of the Institute of Fuel* 7 (1933), pp. 29–36 (cited on page 48).
- Ross, P. “Taguchi techniques for quality engineering”. In: *Mc, Graw Hill* (1998) (cited on page 247).
- Rowley, C., Mezi, I., Bagheri, S., Schlatter, P., and Henningson, D. “Spectral analysis of nonlinear flows”. In: *Journal of Fluid Mechanics* 641 (2009), pp. 115–127. DOI: 10.1017/S0022112009992059 (cited on pages 84, 155).
- Ruan, C. et al. “Principles of non-intrusive diagnostic techniques and their applications for fundamental studies of combustion instabilities in gas turbine combustors: A brief review”. In: *Aerospace Science and Technology* 84 (2019), pp. 585–603. DOI: 10.1016/j.ast.2018.10.002 (cited on page 62).
- Ruith, M., Chen, P., Meiburg, E., and Maxworthy, T. “Three-dimensional vortex breakdown in swirling jets and wakes: Direct numerical simulation”. In: *Journal of Fluid Mechanics* 486.486 (2003), pp. 331–378. DOI: 10.1017/S0022112003004749 (cited on page 84).
- Russell, P., Beal, G., and Hinton, B. “Low NOx heavy fuel combustor concept program”. In: *NASA Technical Report NASA-CR-165512* (1981) (cited on pages 4, 60).
- Sadanandan, R., Stöhr, M., and Meier, W. “Simultaneous OH-PLIF and PIV measurements in a gas turbine model combustor”. In: *Applied Physics B: Lasers and Optics* 90.3-4 (2008), pp. 609–618. DOI: 10.1007/s00340-007-2928-8 (cited on page 65).
- Sagaut, P. *Large eddy simulation for incompressible flows: an introduction*. Springer Science and Business Media, 2006 (cited on pages 114, 182).
- Sakowitz, A. and Mihăescu M. and Fuchs, L. “Flow decomposition methods applied to the flow in an IC engine manifold”. In: *Applied Thermal Engineering* 65 (2014), pp. 57–65 (cited on pages 83, 84).
- Salvador, F.J. “Estudio teórico experimental de la influencia de la geometría de toberas de inyección Diésel sobre las características del flujo interno y del chorro”. PhD thesis. Universitat Politècnica de València, 2003 (cited on page 9).
- Sampath, Ramgopal and Chakravarthy, Satyanarayanan R. “Investigation of intermittent oscillations in a premixed dump combustor using time-resolved particle image velocimetry”. In: *Combustion and Flame* 172 (2016), pp. 309–325. DOI: 10.1016/j.combustflame.2016.06.018 (cited on page 84).

- Sanjosé, M. et al. “LES of two-phase reacting flows”. In: *Proceedings of the Summer Program (Center for Turbulence Research)* (2008), pp. 251–263 (cited on page 73).
- Sanjosé, M. et al. “Fuel injection model for Euler-Euler and Euler-Lagrange large-eddy simulations of an evaporating spray inside an aeronautical combustor”. In: *International Journal of Multiphase Flow* 37.5 (2011), pp. 514–529. DOI: 10.1016/j.ijmultiphaseflow.2011.01.008 (cited on pages 73, 80).
- Sankaran, V. and Menon, S. “LES of spray combustion in swirling flows”. In: *Journal of Turbulence* 3 (2002). DOI: 10.1088/1468-5248/3/1/011 (cited on pages 72, 79).
- Sarpkaya, T. “On stationary and travelling vortex breakdowns”. In: *Journal of Fluid Mechanics* 45.3 (1971), pp. 545–559. DOI: 10.1017/S0022112071000181 (cited on pages 19, 232).
- Sazhin, S. “Advanced models of fuel droplet heating and evaporation”. In: *Progress in Energy and Combustion Science* 32 (2006), pp. 162–214. DOI: 10.1016/j.pecs.2005.11.001 (cited on page 45).
- Schmid, P. “Applications of the dynamic mode decomposition”. In: *Journal of Fluid Mechanics* 25.1 (2010), pp. 249–259 (cited on pages 84, 153).
- Schmid, P. “Dynamic mode decomposition of numerical and experimental data”. In: *Journal of Fluid Mechanics* 656 (2010), pp. 5–28. DOI: 10.1017/S0022112010001217 (cited on pages 84, 153).
- Schmidt, D. et al. “Pressure-swirl atomization in the near field”. In: *SAE Technical Papers* 724 (1999). DOI: 10.4271/1999-01-0496 (cited on pages 118–120, 140).
- Schultz, D. and Wolfbrandt, G. “Flame tube parametric studies for control of fuel bound nitrogen using rich-lean two stage combustion”. In: *NASA Technical Report NASA-TM-81472* (1980) (cited on page 61).
- Semerjian, H., Ball, I., and A., Vranos. “Pollutant Emissions from Partially Mixed Turbulent Flames”. In: *17th International Symposium on Combustion*, pp. 679–6879 (cited on page 61).
- Semlitsch, B. and Mihaescu, M. “Flow phenomena leading to surge in a centrifugal compressor”. In: *Energy* 103 (2016), pp. 572–587. DOI: 10.1016/j.energy.2016.03.032 (cited on page 84).

- Senecal, P. et al. "Modeling high-speed viscous liquid sheet atomization". In: *International Journal of Multiphase Flow* 25 (1999), pp. 1073–1097. DOI: 10.1016/S0301-9322(99)00057-9 (cited on pages 35, 118, 119, 121, 123, 140).
- Senecal, P. et al. "A New Parallel Cut-Cell Cartesian CFD Code for Rapid Grid Generation Applied to In-Cylinder Diesel Engine Simulations". In: 724 (2007), pp. 776–790. DOI: 10.4271/2007-01-0159 (cited on pages 141, 143).
- Senoner, J. "Simulation aux Grandes Échelles de l'écoulement diphasique dans un bruleur aéronautique par une approche Euler-Lagrange". PhD thesis. Institut National Polytechnique de Toulouse - CERFACS, 2010 (cited on page 67).
- Senoner, J. et al. "Eulerian and Lagrangian Large-Eddy Simulations of an evaporating two-phase flow". In: *Comptes Rendus Mécanique* 337.6-7 (2009), pp. 458–468. DOI: 10.1016/J.CRME.2009.06.002 (cited on page 73).
- Shaffar, S. and Samuelsen, G. "A Liquid Fueled, Lean Burn, Gas Turbine Combustor Injector". In: *Combustion Science and Technology* 139.1 (1998), pp. 41–57. DOI: 10.1080/00102209808952080 (cited on pages 5, 62).
- Sharma, S., García-Tíscar, J., Allport, J., Jupp, M., and Nickson, A. "Impact of impeller casing treatment on the acoustics of a small high speed centrifugal compressor". In: *Proceedings of the ASME Turbo Expo*. Vol. 2B. 2018, pp. 1–12. DOI: 10.1115/GT2018-76815 (cited on page 153).
- Sheen, H., Chen, W., Jeng, S., and Huang, T. "Correlation of swirl number for a radial-type swirl generator". In: *Experimental Thermal and Fluid Science* 12.4 (1996), pp. 444–451. DOI: [https://doi.org/10.1016/0894-1777\(95\)00135-2](https://doi.org/10.1016/0894-1777(95)00135-2) (cited on page 20).
- Sirignano, W. *Fluid Dynamics and Transport of Droplets and Sprays*. 2nd Edition. New York, USA: Cambridge University Press, 2010 (cited on pages 45, 107).
- Smagorinsky, J. "General Circulation Experiments with the primitive equations: I. The basic experiment". In: *Monthly Weather Review* 91.3 (1963), pp. 99–164. DOI: 10.1175/1520-0493(1963)091<0099:GCEWTP>2.3.CO;2 (cited on page 114).
- Smith, T., Moehlis, J., and Holmes, P. "Low-Dimensional Modelling of Turbulence Using the Proper Orthogonal Decomposition: A Tutorial". In: *Nonlinear Dynamics* 41 (2005), pp. 275–307. DOI: 10.1007/s11071-005-2823 (cited on page 155).

- Soltani, M., Ghorbanian, K., Ashjaee, M., and Morad, M. “Spray characteristics of a liquid-liquid coaxial swirl atomizer at different mass flow rates”. In: *Aerospace Science and Technology* 9.7 (2005), pp. 592–604. DOI: 10.1016/J.AST.2005.04.004 (cited on page 62).
- Sommerfeld, M. and Qiu, H. “Detailed measurements in a swirling particulate two-phase flow by a phase-Doppler anemometer”. In: *International Journal of Heat and Fluid Flow* 12.1 (1991), pp. 20–28. DOI: 10.1016/0142-727X(91)90004-F (cited on pages 76, 80).
- Sovani S. Sojka, P. and Lefebvre, A. “Effervescent Atomization”. In: *Progress in Energy and Combustion Science* 27 (2001), pp. 483–521 (cited on page 25).
- Sreedhara, S. and Huh, K. “Assessment of closure schemes in second-order conditional moment closure against DNS with extinction and ignition”. In: *Combustion and Flame* 143.4 (2005). DOI: 10.1016/j.combustflame.2005.08.015 (cited on page 75).
- Staffelbach, G., Gicquel, L., Boudier, G., and Poinso, T. “Large Eddy Simulation of self excited azimuthal modes in annular combustors”. In: *Proceedings of the Combustion Institute* 32 II.2 (2009), pp. 2909–2916. DOI: 10.1016/j.proci.2008.05.033 (cited on pages 74, 80).
- Statgraphics Centurion* 18. 2020. URL: <https://www.statgraphics.com/centurion-xviii> (visited on 09/21/2020) (cited on page 255).
- Stein, O. and Kempf, A. “LES of the Sydney swirl flame series: A study of vortex breakdown in isothermal and reacting flows”. In: *Proceedings of the Combustion Institute* 31 II (2007), pp. 1755–1763. DOI: 10.1016/j.proci.2006.07.255 (cited on page 72).
- Steinberg, A., Boxx, I., Stöhr, M., Carter, C., and Meier, W. “Flow-flame interactions causing acoustically coupled heat release fluctuations in a thermo-acoustically unstable gas turbine model combustor”. In: *Combustion and Flame* 157.12 (2010), pp. 2250–2266. DOI: 10.1016/j.combustflame.2010.07.011 (cited on page 83).
- Stickles, R. and Barrett, J. *TAPS II Technology Final Report*. Tech. rep. 2013 (cited on page 4).
- Stöhr, M., Arndt, C M, and Meier, W. “Effects of Damköhler number on vortex-flame interaction in a gas turbine model combustor”. In: *Proceedings of the Combustion Institute* 34.2 (2013), pp. 3107–3115. DOI: <https://doi.org/10.1016/j.proci.2012.06.086> (cited on pages 65, 84).

- Stöhr, M., Sadanandan, R., and Meier, W. "Phase-resolved characterization of vortex-flame interaction in a turbulent swirl flame". In: *Experiments in Fluids* 51.4 (2011), pp. 1153–1167. DOI: 10.1007/s00348-011-1134-y (cited on page 84).
- Syred, N. "A review of oscillation mechanisms and the role of the precessing vortex core (PVC) in swirl combustion systems". In: *Progress in Energy and Combustion Science* 32.2 (2006), pp. 93–161. DOI: 10.1016/J.PECS.2005.10.002 (cited on page 231).
- Syred, N. and Beér, J. "Combustion in swirling flows: A review". In: *Combustion and Flame* 23.2 (1974), pp. 143–201. DOI: 10.1016/0010-2180(74)90057-1 (cited on pages 19, 23, 184, 185, 270).
- Syred, N. and Dahman, K. "Effect of high levels of confinement upon the aerodynamics of swirl burners". In: *Journal of Energy* 2.1 (1978), pp. 8–15. DOI: 10.2514/3.47950 (cited on page 23).
- Tacina, K., Chang, C., He, Z., Dam, B., and Mongia, H. "A Second Generation Swirl-Venturi Lean Direct Injection Combustion Concept". In: *NASA Technical Report NASA-E-662715* (2014) (cited on pages 67, 70).
- Tacina, K., Podboy, D., Dam, B., and Lee, F. "A Third-Generation Swirl-Venturi Lean Direct Injection Combustor With a Prefilming Pilot Injector". In: 2019. DOI: 10.1115/GT2019-90484 (cited on pages 68, 76, 82).
- Tacina, Kathleen M. et al. "A comparison of three second-generation swirl-venturi lean direct injection combustor concepts". In: *52nd AIAA/SAE/ASEE Joint Propulsion Conference, 2016*. 2016. DOI: 10.2514/6.2016-4891 (cited on pages 67, 70).
- Tacina, R. "Low NO_x potential of gas turbine engines". In: *28th Aerospace Sciences Meeting*. 1990, pp. 1–19. DOI: 10.2514/6.1990-550 (cited on page 61).
- Tacina, R., Lee, P., and Wey, C. "A Lean-Direct-Injection Combustor Using a 9 Point Swirl-Venturi Fuel Injector". In: *International Symposium on Air Breathing Engines (ISABE)*. 2005 (cited on pages 66, 67).
- Tacina, R., Mao, C., and Wey, C. "Experimental Investigation of a Multiplex Fuel Injector Module for Low Emission Combustors". In: *41st Aerospace Sciences Meeting and Exhibit*. 2003, pp. 1–16 (cited on page 63).
- Tacina, R., Mao, C., and Wey, C. "Experimental investigation of a multiplex fuel injector module with discrete jet swirlers for low emission combustors". In: *NASA Technical Report NASA-TM-212918* (2004) (cited on pages 63, 64).

- Tacina, R., Wey, C., Laing, P., and Mansour, A. “A low NO_x lean-direct injection, multipoint integrated module combustor concept for advanced aircraft gas turbines”. In: *NASA Technical Report NASA-TM-211347* (2002) (cited on pages 63, 69).
- Tacina, R. et al. “An assessment of combustion dynamics in a low-NO_x second-generation swirl-venturi lean direct injection combustion concept”. In: *International Symposium on Air Breathing Engines (ISABE)*. 2015 (cited on pages 67, 70).
- Taira, K. et al. “Modal Analysis of Fluid Flows: An Overview”. In: *AIAA Journal* 55.12 (2018). DOI: 10.2514/1.j056060 (cited on page 155).
- Tanner, F. “Liquid jet atomization and droplet breakup modeling of non-evaporating diesel fuel sprays”. In: *SAE Technical Papers* 412 (1997). DOI: 10.4271/970050 (cited on page 38).
- Taylor, G. *The shape and acceleration of a drop in a high speed air stream*. Tech. rep. Cambridge University Press, 1963, pp. 457–464 (cited on page 118).
- Terhaar, S., Bobusch, B., and Paschereit, C. “Effects of outlet boundary conditions on the reacting flow field in a swirl-stabilized burner at dry and humid conditions”. In: *Journal of Engineering for Gas Turbines and Power* 134.11 (2012), pp. 1–9. DOI: 10.1115/1.4007165 (cited on page 20).
- Torregrosa, A., Broatch, A., García-Tíscar, J., and Gomez-Soriano, J. “Modal decomposition of the unsteady flow field in compression-ignited combustion chambers”. In: *Combustion and Flame* 188 (2018), pp. 469–482. DOI: 10.1016/j.combustflame.2017.10.007 (cited on pages 10, 83, 84).
- Tratnig, A. and Brenn, G. “Drop size spectra in sprays from pressure-swirl atomizers”. In: *International Journal of Multiphase Flow* 36.5 (2010), pp. 349–363. DOI: 10.1016/J.IJMULTIPHASEFLOW.2010.01.008 (cited on page 62).
- Tyliszczak, A., Cavaliere, D., and M. “LES/CMC of Blow-off in a Liquid Fueled Swirl Burner”. In: *Flow, Turbulence and Combustion* 92.1 (2014), pp. 237–267. DOI: 10.1007/s10494-013-9477-5 (cited on page 6).
- Valera-Medina, A., Syred, N., and Griffiths, A. “Visualisation of isothermal large coherent structures in a swirl burner”. In: *Combustion and Flame* 156 (2009), pp. 1723–1734. DOI: 10.1016/J.COMBUSTFLAME.2009.06.014 (cited on page 23).

- Van Leer, B. “Towards the ultimate conservative difference scheme III. Upstream-centered finite-difference schemes for ideal compressible flow”. In: *Journal of Computational Physics* 23.3 (1977), pp. 263–275. DOI: [https://doi.org/10.1016/0021-9991\(77\)90094-8](https://doi.org/10.1016/0021-9991(77)90094-8) (cited on page 134).
- Vanierschot, M. and Ogus, G. “Experimental investigation of the precessing vortex core in annular swirling jet flows in the transitional regime”. In: *Experimental Thermal And Fluid Science* 106 (2019), pp. 148–158 (cited on page 84).
- Vanierschot, M., Percin, M., and Van Oudheusden, B. “Double helix vortex breakdown in a turbulent swirling annular jet flow”. In: *Physical Review Fluids* 3.3 (2018). DOI: 10.1103/PhysRevFluids.3.034703 (cited on pages 84, 232).
- Vera-Candioti, L., De-Zan, M., Cámara, M., and Goicoechea, H. “Experimental design and multiple response optimization. Using the desirability function in analytical methods development”. In: *Talanta* 124 (2014), pp. 123–138. DOI: <https://doi.org/10.1016/j.talanta.2014.01.034> (cited on page 269).
- Verdier, A. et al. “Experimental study of local flame structures and fuel droplet properties of a spray jet flame”. In: *Proceedings of the Combustion Institute* 36.2 (2017), pp. 2595–2602. DOI: 10.1016/j.proci.2016.07.016 (cited on page 68).
- Verdier, A. et al. “Local extinction mechanisms analysis of spray jet flame using high speed diagnostics”. In: *Combustion and Flame* 193 (2018), pp. 440–452. DOI: 10.1016/J.COMBUSTFLAME.2018.03.032 (cited on page 68).
- Versteeg, H. and Malalasekera, W. *Introduction to Computational Fluid Dynamics: The finite volume method*. 2nd Edition. Pearson Education Limited, 2007. DOI: 10.2514/1.22547 (cited on pages 6, 106, 111, 113, 135).
- Vié, A., Jay, S., Cuenot, B., and Massot, M. “Accounting for polydispersion in the eulerian large eddy simulation of the two-phase flow in an aeronautical-type burner”. In: *Flow, Turbulence and Combustion* 90.3 (2013), pp. 545–581. DOI: 10.1007/s10494-012-9440-x (cited on page 73).
- Viera, A. “Effect of multiple injection strategies on the diesel spray formation and combustion using optical diagnostics”. PhD thesis. Universitat Politècnica de València, 2019 (cited on page 9).

- Vinha, N., Meseguer-Garrido, F., De Vicente, J., and Valero, E. “A dynamic mode decomposition of the saturation process in the open cavity flow”. In: *Aerospace Science and Technology* 52 (2016), pp. 198–206. DOI: 10.1016/j.ast.2016.02.036 (cited on page 84).
- Wang, P., Fröhlich, J., Maas, U., He, Z., and Wang, C. “A detailed comparison of two sub-grid scale combustion models via large eddy simulation of the PRECCINSTA gas turbine model combustor”. In: *Combustion and Flame* 164 (2016), pp. 329–345. DOI: 10.1016/j.combustflame.2015.11.031 (cited on pages 77, 82).
- Wang, P., Platova, N., Fröhlich, J., and Maas, U. “Large Eddy Simulation of the PRECCINSTA burner”. In: *International Journal of Heat and Mass Transfer* 70 (2014), pp. 486–495. DOI: 10.1016/j.ijheatmasstransfer.2013.11.025 (cited on page 77).
- Wang, X. and Lefebvre, A. “Mean drop sizes from pressure-swirl nozzles”. In: *Journal of Propulsion and Power* 3.1 (1987), pp. 11–18. DOI: 10.2514/3.22946 (cited on page 47).
- Waterson, N. and Deconinck, H. “A unified approach to the design and application of bounded higher-order convection schemes”. In: *Numerical methods in laminar and turbulent flow* 9 (1995), pp. 203–214 (cited on page 134).
- Weigand, P., Meier, W., Duan, X., Stricker, W., and Aigner, M. “Investigations of swirl flames in a gas turbine model combustor: I. Flow field, structures, temperature, and species distributions”. In: *Combustion and Flame* 144.1-2 (2006), pp. 205–224. DOI: 10.1016/j.combustflame.2005.07.010 (cited on pages 5, 65, 66, 69, 76, 77, 80, 82).
- Welch, P. “The Use of Fast Fourier Transform for the Estimation of Power Spectra: A Method Based on Time Averaging Over Short, Modified Periodograms”. In: *IEEE Transactions on Audio and Electroacoustics* 15.2 (1967), pp. 70–73. DOI: 10.1109/TAU.1967.1161901 (cited on page 220).
- Wengle, H. and Werner, H. “Large-eddy Simulation of Turbulent Flow Over Sharp-edged Obstacles in a Plate Channel”. In: *Proceedings of the Eighth Symposium on Turbulent Shear Flows* 2 (1991). DOI: 10.1007/978-3-663-13986-7_26 (cited on page 144).
- Wierzba, A. “Deformation and breakup of liquid drops in a gas stream at nearly critical Weber numbers”. In: *Experiments in Fluids* 9.1-2 (1990), pp. 59–64. DOI: 10.1007/BF00575336 (cited on page 37).
- Williams, F. *Combustion Theory*. 2nd edition. Taylor and Francis, 1985 (cited on pages 27, 31).

- Wu, P. and Faeth, G. “Aerodynamic effects primary breakup of turbulent liquids”. In: *Atomization and Sprays* 3 (1993), pp. 265–289 (cited on page 37).
- Xu, L. et al. “Experimental and modeling study of liquid fuel injection and combustion in diesel engines with a common rail injection system”. In: *Applied Energy* 230 (2018), pp. 287–304. DOI: 10.1016/j.apenergy.2018.08.104 (cited on page 10).
- Yakhot, V., Orszag, S., Thangam, S., Gatski, T., and Speziale, C. “Development of turbulence models for shear flows by a double expansion technique”. In: *Physics of Fluids A* 4.7 (1992), pp. 1510–1520. DOI: 10.1063/1.858424 (cited on page 177).
- Yi, T. and Santavicca, D. “Combustion Instability in a Turbulent Liquid-Fueled Swirl-Stabilized LDI Combustor”. In: *Experiments, to be presented at the 45th AIAA/ASME/SAE/ASEE Joint Propulsion Conference & Exhibition*. Denver, Colorado (USA), 2009 (cited on page 64).
- Yoon, C., Gejji, R., and Anderson, W. “Computational Investigation of Combustion Dynamics in a Lean Direct Injection Gas Turbine Combustor”. In: *51st AIAA Aerospace Sciences Meeting including the New Horizons Forum and Aerospace Exposition* 20.0704 (2013). DOI: 10.2514/6.2013-166 (cited on page 201).
- Yuan, R., Kariuki, J., Dowlut, A., Balachandran, R., and Mastorakos, E. “Reaction zone visualisation in swirling spray n-heptane flames”. In: *Proceedings of the Combustion Institute* 35.2 (2015), pp. 1649–1656. DOI: <https://doi.org/10.1016/j.proci.2014.06.012> (cited on pages 68, 70).
- Yuan, R., Kariuki, J., and Mastorakos, E. “Measurements in swirling spray flames at blow-off”. In: *International Journal of Spray and Combustion Dynamics* 10.3 (2018), pp. 185–210. DOI: 10.1177/1756827718763559 (cited on pages 68, 70).
- Yuan, Z. and Michaelides, E. “Turbulence modulation in particulate flows: A theoretical approach”. In: *International Journal of Multiphase Flow* 18.5 (1992), pp. 779–785. DOI: [https://doi.org/10.1016/0301-9322\(92\)90045-I](https://doi.org/10.1016/0301-9322(92)90045-I) (cited on page 40).
- Zhou, G. “Numerical Simulations of Physical Discontinuities in Single and Multi-Fluid Flows for Arbitrary Mach Numbers”. PhD thesis. Chalmers University of Technology, 1995 (cited on page 134).
- Zhu, G., Reitz, R., Xin, J., and Takabayashi, T. “Modelling characteristics of gasoline wall films in the intake port of port fuel injection engines”. In: *International Journal of Engine Research* 2.4 (2001), pp. 231–248. DOI: 10.1243/1468087011545451 (cited on page 45).